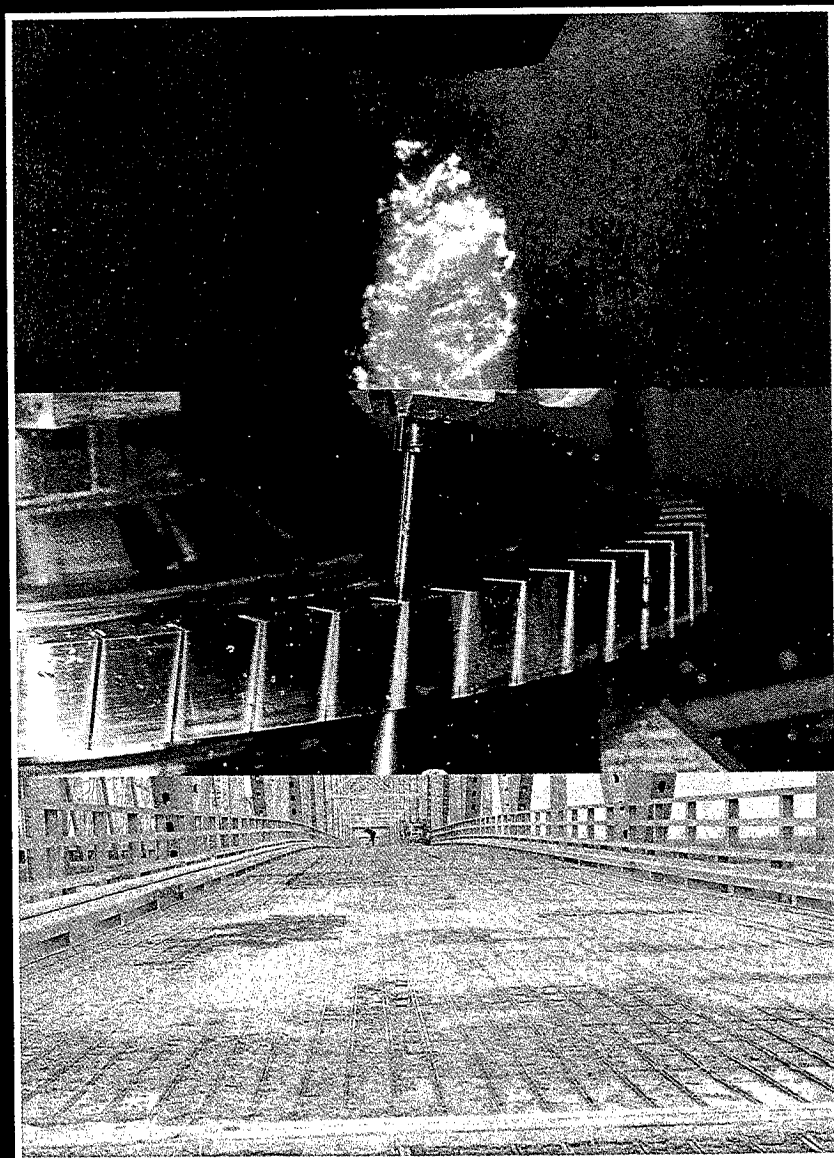


Proceedings of the 7th American Water Jet Conference

Volume I



Edited by Mohamed Hashish

August 28-31, 1993
Seattle, Washington

Proceedings of the 7th American Water Jet Conference

Volume I

**August 28-31, 1993
Seattle, Washington**

Edited by

Mohamed Hashish

Published by the

Water Jet Technology Association

Cover:

The three photographs shown on the cover reflect the three main sessions presented at the conference: technology developments, manufacturing, and contractors' applications. The top picture shows the development of cavitation bubbles in a submerged waterjet (*photograph courtesy of National Research Council of Canada*). The middle picture shows an abrasive-waterjet machining slots in an aircraft component (*photograph courtesy of General Electric Aircraft Engines*). The bottom picture shows a bridge deck scarified using a waterjet (*photograph courtesy of Flow International Corporation*). In the background is the Space Needle, which is a landmark in Seattle.

Proceedings of the 7th American Water Jet Conference

Published by the

Water Jet Technology Association
818 Olive Street, Suite 918
St. Louis, MO 63101-1598 USA

Copyright © 1993 by the Water Jet Technology Association

All rights reserved. No part of this book may be reproduced or transmitted in any form or by any means, electronic or mechanical, including photocopying, recording, or by any information storage and retrieval system, without the written permission of the Publisher.

ISBN: 1-880342-02-2 (Volume I)
1-880342-04-9 (2 Volume Set)

Printed in the United States of America
August 1993

Copies obtainable from:

Water Jet Technology Association
818 Olive Street, Suite 918
St. Louis, MO 63101-1598 USA
Telephone: (314)241-1445
Fax: (314)241-1449

Price: \$150 (payable in advance)

FOREWORD

The mission of the Water Jet Technology Association is to advance the state of the art of water jet technology. Water jet technology has made significant contributions to industry productivity, and the pace of improvement is accelerating. One method of advancing the art is to provide a forum where innovative people engaged in water jet technology can meet and discuss new insights and applications. The publication of a record of these discussions encourages others to use their ingenuity to gain more insight into water jet technology and to explore new applications of the technology. The present volume is the seventh in a series of published proceedings dating back to 1981. We proudly offer the Proceedings of the 7th American Water Jet Conference as evidence that water jet technology is a vibrant technology with a bright future. We expect that many readers will be inspired to investigate water jet technology. We trust that they will find more applications for this exciting technology and thereby increase the effectiveness and productivity of society.

GEORGE A. SAVANICK, Ph.D.
President
Water Jet Technology Association

Since 1972, when the 1st International Symposium on Jet Cutting Technology was held in the U.K., the water jet technology has rapidly spread worldwide and with it the appetite for more knowledge, as evidenced by the fact that there are more conferences in the field than ever before and the founding of a new *International Journal on Water Jet Technology*. I am confident that this Conference, like the ones before, will make it possible to share the knowledge gained around the world, as indicated by the large number of papers from many countries presented and included in this publication.

The success of the Conference is due to sharing of the work by many individuals in the Organizing Committee, the Conference Administrators and the International Advisors. However, this "Foreword" will be incomplete without special gratitude to Dr. Mohamed Hashish, the Conference Chairman, and his associates Dr. Andrew Conn, Prof. Thomas Kim, Prof. Thomas Labus and Prof. Mamidala Ramulu, the Conference Co-Chairmen.

I am indeed fortunate, privileged and honored to write this "Foreword." I am sure you will go home, like I always do, better informed and better equipped to pursue and enhance the areas of your interest in water jet technology. I sincerely thank you for enriching the Conference by your presence and I wish you all the best in your future endeavors.

MOHAN M. VIJAY, Ph.D.
Chairman of the Board
Water Jet Technology Association

ORGANIZING COMMITTEE

Dr. Mohamed Hashish (Chairman)

QUEST Integrated, Inc.
Kent, WA

Dr. Andrew Conn

Conn Consulting
Baltimore, MD

Prof. Thomas Kim

University of Rhode Island
Kingston, RI

Prof. Thomas Labus

University of Wisconsin
Fontana, WI

Prof. Mamidala Ramulu

University of Washington
Seattle, WA

Mr. Bill Hall Jr.

Waterjet Consulting
Minnetonka, MN

Mr. George Rankin

Aqua-Dyne, Inc.
Houston, TX

Dr. George Savanick

U.S. Bureau of Mines
Minneapolis, MN

Mr. Forrest Shook

NLB Corporation
Wixom, MI

Dr. David Summers

University of Missouri-Rolla
Rolla, MO

Dr. Mohan Vijay

National Research Council of Canada
Ottawa, Ontario

Dr. Fun-Den Wang

Colorado School of Mines
Golden, CO

Mr. John Wolgamott

StoneAge, Inc.
Durango, CO

INTERNATIONAL ADVISORS

Australia:	<i>Mr. J. Link</i> Melbourne, Victoria	Hungary:	<i>Dr. S. Toth</i> Debrecen, Hungary
Austria:	<i>Dr. H. Peters</i> Xuzhou, Jiangsu	India:	<i>Mr. M.F. Engineer</i> Dadar, Bombay, India
Belgium:	<i>Dr. D.S. Kriene</i> Willebrook, Belgium	Italy:	<i>Dr. R. Ciccu</i> Cagliari, Italy
Chili:	<i>Dr. M.A. Bejar</i> Santiago, Chili	Japan:	<i>Dr. H. Kiyohashi</i> Sendai, Japan
China:	<i>Dr. D. Cheng</i> Jiangsu, China	Malaysia:	<i>Dr. B. Ujang</i> Seianger D.E. Malaysia
Czechoslovakia:	<i>Dr. J. Vasek</i> Ostrava-Poruba, Czechoslovakia	New Zealand:	<i>Mr. M.J. Simpson</i> Christchurch, New Zealand
Egypt:	<i>Dr. M. Farid</i> Alexandria, Egypt	Poland:	<i>Dr. A. Klich</i> Pawilon, Poland
England:	<i>Dr. D.H. Saunders</i> Bedford, England	Sinapore:	<i>Dr. J. Cheung</i> Jiangsu, China
Finland:	<i>Dr. S. Patjas</i>	Sweden:	<i>Mr. G. Grinnal</i>
France:	<i>Dr. D. Fourmaintraux</i> Paris La Defense, France	Taiwan:	<i>Mr. B. Wang</i> Hsin Chu, Taiwan, R.O.C.
Germany:	<i>Dr. H. Louis</i> Hannover, Germany	Ukraine:	<i>Dr. G.A. Atanov</i> Donetsk, UKSSR

PREFACE

The proceedings for the 7th American Water Jet Conference is being presented in two volumes due to the record number of papers received - 71. These papers were presented in three main sessions at the conference: a general technology session that was held concurrently with two workshop sessions on manufacturing and contractors' applications.

The papers in this proceedings reflect the great advances that have been made in waterjet technology over the past 20 years. In the 1970s, major advances were related to waterjet tool and process developments primarily for mining, construction, rock cutting, cleaning, and a few manufacturing applications. A conference proceedings in the 1970s typically contained an average of 35 papers. In the 1980s, most advances that occurred were related to the introduction of the abrasive-waterjet technology. The number of papers presented at jet cutting conferences jumped noticeably to about 50 papers per conference, and the word "machining" started to replace the word "cutting" in many papers, due to the fact that the main applications for abrasive-waterjets were found in manufacturing where more accurate material removal was required. The increased number of papers may also have been due to the increased number of applications for both waterjets and AWJs.

In the 1990s, especially with this conference, we have observed another major jump, but we are not able to attribute it to a single factor. It is my opinion that the technological advances in the 1990s will not be singular and will be realized with the development of abrasive suspension jets, low-cost high-pressure direct drive pumps, and 3-D machining systems for the average size machine shop. Both nuclear and demilitarization applications will grow significantly in the 1990s, requiring further developments in nonabrasive jetting techniques. The need for these developments and for the continuing evolution of existing technologies to enable reliable and widespread use is more important to the growth of jet cutting technology than is the seeking of alternative approaches.

The success of this conference belongs to every participant. I would like to thank the authors for their technical contributions and for making these proceedings possible. A special thanks goes to those authors who are not proficient in English but yet elected to write and share their findings with us. The great professional and tireless efforts by David Birenbaum & Associates in organizing this conference have been most critical to its success. I would especially like to express my gratitude to Mark Birenbaum, Ken Carroll, LeAnn Hampton, Rhonda Stevens, and Jan Tubbs. I would also like to acknowledge the help and guidance of the conference co-chairmen: Dr. Andy Conn, Dr. M. Ramulu, Professor Thomas Kim, and Professor Thomas Labus. The assistance of Dr. Pawan Singh, Dr. Ed Ting, and Dr. Mohan Vijay was most useful in developing the subject index. Thanks are also due Kristie Hammond and Christa Ramey at QUEST for their assistance on this project. Finally, I must express my continuing gratitude to my wife, Nadia, for her ongoing patience and understanding.

MOHAMED HASHISH, Ph.D
Editor & Conference Chairman

TABLE OF CONTENTS

Page Number

FOREWORD	iii
COMMITTEES	iv
PREFACE	v

Volume I

Paper #

JET-MATERIAL INTERACTION

1 "Surface Structure and Kerf Geometry in Abrasive Water Jet Cutting: Formation and Optimization," by N.S. Guo, H. Louis, and G. Meier, University of Hannover, Germany	1
2 "Experimental Study of the Striation Formation and Spectral Analysis of the Abrasive Waterjet Generated Surfaces," by J. Chao and E. Geskin, New Jersey Institute of Technology, Newark, New Jersey	27
3 "Mechanisms of Material Removal in Abrasive Waterjet Machining of Common Aerospace Materials," by D. Arola and M. Ramulu, University of Washington, Seattle, Washington	43
4 "An Optical Technique to Visualize the Abrasive Waterjet Generated Stress Fields," by H. Yeh, F.X. Wang, and M. Ramulu, University of Washington, Seattle, Washington	65
5 "Target Responses to the Impact of High-Velocity, Non-Abrasive Water Jets," by S-W. Kang, T. Reitter, and G. Carlson, Lawrence Livermore National Laboratory, Livermore, California, and J. Crutchmer, D. Garrett, P. Kramer, and B. Do, Mason & Hanger, Pantex Plant, Amarillo, Texas	71
6 "Transient Boiling Heat Transfer to a High Speed Water Jet Impinging Onto a Heated Material and the Thermal Shock Fracture," by H. Kiyohashi, M. Ogasawara, and M. Kyo, Tohoku University, Japan	87
7 "Performances of HP Fluid Jet to Cut Food Products," by C. Merle, AQUARESE Industries, France, and M. Bouix, M. Sionneau, and J. Vasseur, Ecole Nationale Supérieure des Industries Agro-Alimentaire (ENSIA), France	103

MODELING AND ANALYTICAL STUDIES

8 "A Model for Milling With Abrasive Water Jets," by A. Laurinat, H. Louis, and G. Meier-Wiechert, University of Hannover, Germany	119
9 "A Transient Model for Material Removal in the Abrasive Waterjet Machining Process," by S.P. Raju, and M. Ramulu, University of Washington, Seattle, Washington	141
10 "On a Simplified Model for Hydro Abrasive Jet Machining Prediction, Control and Optimization," by E. Capello, Politecnico di Milano, Italy, and R. Groppetti, Università degli Studi di Perugia, Italy	157
11 "Parameter Prediction and Cost Analysis in Abrasive Waterjet Cutting Operations," by J. Zeng and T.J. Kim, University of Rhode Island, Kingston, Rhode Island	175

MODELING AND ANALYTICAL STUDIES, continued

- 12 "Cost Optimization of Abrasive Waterjet Cutting Systems," by *P.J. Singh and J. Munoz, Ingersoll-Rand Waterjet Cutting Systems, Farmington Hills, Michigan* 191
- 13 "Prediction Models for AWJ Machining Operations," by *M. Hashish, QUEST Integrated, Inc., Kent, Washington* 205
- 14 "Detection of Abrasive Waterjet Nozzle Wear Using Acoustic Signature Analysis," by *R. Kovacevic, L. Wang, and Y.M. Zhang, University of Kentucky, Lexington, Kentucky* 217

FLUID AND JET MECHANICS

- 15 "Enhancing the Performance of Cavitating Water Jets," by *M.M. Vijay, S.G. Hu, and M.K.Y. Lai, National Research Council of Canada, Ottawa, Ontario* 233
- 16 "The Influence of Ambient Pressure and Nozzle Shape on Submerged Water Jet Velocity and Spreading," by *K.M. Kalumuck, G.L. Chahine, and G.S. Frederick, DYNAFLOW, Inc., Fulton, Maryland* 251
- 17 "Examination of the Range of Jet Action in an Aqueous Medium," by *A. Kalukiewicz, University of Mining and Metallurgy, Poland* 263
- 18 "A Numerical Investigation of Turbulent Behaviors of Water Flow Inside Nozzle," by *M.E.H. Khan and E.S. Geskin, New Jersey Institute of Technology, Newark, New Jersey* 273
- 19 "Mathematical Modeling of the Accelerating Process of Particles in DIA-Jet," by *C. Guo, D. Cheng, and L. Liu, China University of Mining and Technology, China* 287
- 20 "Study on a Direct Injection Abrasive Jet (DIAJet) System," by *Y. Ming-qing, Z. Hai, and C. Zi-Pu, Jiaozuo Mining Institute, China and C. Da-zhong, Mining University of China, China* 295

HIGH PRESSURE TECHNOLOGY

- 21 "Fatigue Strength of Steel in High Pressure Water," by *W.A. Lees, Rogan and Shanley, Inc., Houston, Texas, and F. Zacharias and P.S.J. Crofton, Imperial College, England* 307
- 22 "Pressure Fluctuation and Operating Efficiency of Intensifier Pumps," by *E.J. Chalmers, Jet Edge, Inc., Minneapolis, Minnesota* 327
- 23 "Simulation and Control of Discharge Pressure Fluctuation of Ultra High Pressure Waterjet Pump," by *F. Hu and J. Robertson, HYDRO-PAC, Inc., Fairview, Pennsylvania* 337
- 24 "Advances in Direct-Drive Pump Technology Brings the Competitive Edge Back to Ultrahigh-Pressure Waterjets," by *T.D. Alkire, Flow International Corporation, Kent, Washington* 351

WATER AND ABRASIVES

- 25 "Abrasives: Their Characteristics and Effect on Waterjet Cutting," by J.L. Ohman,
Barton Mines Corporation, North Creek, New York 363
- 26 "Influence of Properties of Garnet on Cutting Process," by J. Vasek, P. Martinec,
*J. Foldyna, and L. Hlavac, Institute of Geonics Academy of Sciences of the
Czech Republic, The Czech Republic* 375
- 27 "Water Treatment Methodologies Used to Meet Standards for Discharge or Reuse in
Water Jet Applications," by M.D. Hanrahan, *Advanced Water Systems, Inc., Woodinville, Washington* . . . 389
- 28 "Water Soluble Abrasives," by M.J. Woodward, *Aqua-Dyne, Inc., Houston, Texas* 397

ROCK CUTTING AND FRAGMENTATION

- 29 "Preweakening of Hard Rocks with Water Jets," by M.M. Vijay, *National Research Council of
Canada, Ottawa, Ontario and J. Remisz, Applied Fluid Mechanics Inc., Canada* 405
- 30 "The Influence of Rock Properties on Waterjet Performance," by M. Agus, A. Bortolussi,
R. Ciccu, W.M. Kim, and P.P. Manca, University of Cagliari, Italy 427
- 31 "Abrasive Water Jet Cutting of Portuguese Marbles," by R.M. Miranda and P. Lousa, *Instituto
de Soldadura e Qualidade, Portugal, A.J. Mouraz Miranda, Instituto Superior Tecnico,
Portugal, and T.J. Kim, University of Rhode Island, Kingston, Rhode Island* 443
- 32 "Development and Applications of a Hydraulic Pulse Generator,"
by J.J. Kollé, *QUEST Integrated, Inc., Kent, Washington* 459

Volume II**MINING**

- 33 "Application of Water Jet Energy in the Borehole Mining," by A. Klich, *University of
Mining and Metallurgy, Poland, W. Jura, Mining Consultant, Poland, and M. Mazurkiewicz,
University of Missouri-Rolla, Rolla, Missouri* 473
- 34 "Borehole Mining of Gold from Frozen Placers," by A.L. Miller and G.A. Savanick,
U.S. Bureau of Mines, Minneapolis, Minnesota 485
- 35 "Certain Chosen Problems of Hydromechanical Mining with Disk Tools," by A. Klich
and K. Kotwica, *University of Mining and Metallurgy, Poland, and M. Mazurkiewicz,
University of Missouri-Rolla, Rolla, Missouri* 501
- 36 "Studies on Catastrophe Mechanism of Self-Controlled Hydro-Pick Cutting Rock,"
by X. Duan, D.Z. Cheng, and L. Yu, *China University of Mining and Technology, China* 515

DRILLING AND CONSTRUCTION

- 37 "Jet Assisted Mechanical Drilling of Oil and Gas Wells," by *S.D. Veenhuizen, T.J. Butler, and D.P. Kelley, FlowDril Corporation, Kent, Washington* 523
- 38 "Pulsed Jet Nozzle for Oilwell Jetting Drilling," by *L. Zhen-Fang and T. Chuan-lin, Chongqing University, China* 537
- 39 "Performance Enhancement of DIADrill Operations," by *D.E. Wright and D.A. Summers, University of Missouri-Rolla, Rolla, Missouri* 549
- 40 "Recent Developments in Water Jet Usage in Ground and Traffic Area Rebuilding," by *A.W. Momber, WOMA Apparatebau GmbH, Germany* 561
- 41 "Hydrodemolition: Why 'Yes' and Why 'No'," by *J. Remisz, Applied Fluid Mechanics, Inc., Canada, and W. Remisz, Remisz & Associates Engineering, Ltd., Canada* 573

COATING AND RUST REMOVAL

- 42 "Thermal Spray Removal with Ultrahigh-Velocity Waterjets," by *J.D. Watson, Flow International Corporation, Kent, Washington* 583
- 43 "Waterjet Nozzle Design for Complex Surfaces," by *D.J. Harbaugh and H. Fincher, Pratt and Whitney, Huntsville, Alabama* 599
- 44 "Advances in Cleaning and Coating Removal Using Ultra-High Pressure Water Jet Technology," by *S.T. Johnson, Jet Edge, Inc., Minneapolis, Minnesota* 607
- 45 "The Large Aircraft Robotic Paint Stripping (LARPS) System," by *S.A. Hofacker, Pratt & Whitney, Huntsville, Alabama* 613
- 46 "The Premajet Derusting and the Abrasive Recovery System," by *B. Liu, B. Jia, and D. Zhang, Huainan Mining Institute, China, and C. Wang, N. Li, H. Yao, Huainan Coal Mining Bureau, China* 629
- 47 "Experimental Study on Rust-Removing With Abrasive Waterjet," by *H. Jun, Mining Institute of Xian, China* 643
- 48 "Equipment and Test Research of High Pressure Water Jet for Rust Removal," by *X. Shengxiong, H. Wangping, Z. Sheng, S. Da-jun, General Machinery Research Institute, China* 653

SAFETY AND ENVIRONMENTAL ISSUES

- 49 "On the Job - An Overview of Occupational Safety and Health Act Regulations, Standards, and Requirements in the Workplace," by *M. Rankin, Attorney At Law, Houston, Texas* 663
- 50 "Water as a Tool: Alternative Methods of Reducing the Environmental and Human Health Risks in Paint Stripping," by *F.E. Scharwat, WOMA Corporation, Everett, Washington* 685

SAFETY AND ENVIRONMENTAL ISSUES, continued

- 51 "Environmental Protection in High Pressure Waterblasting," by *M.T. Gracey*,
Hydro Environmental Services Limited Partnership, Missouri City, Texas 689
- 52 "Environmental and Safety Attributes of Waterjet Cutting," by *C. Burnham*
and R. Sepe, Flow International Corporation, Kent, Washington 697

NUCLEAR AND HAZARDOUS APPLICATIONS

- 53 "Personnel and Environmental Risk Reduction Through High Pressure Jet
Cleaning of NORM," by *A. McArthur, Central Environmental, Inc., Houston, Texas* 701
- 54 "Nuclear Reactor Repair by High Pressure Hydroabrasive Jet," by *B. Mainbourg*,
FRAMATOME RTI, France, and P. Pontvianne, AQUARESE Industries, France 729
- 55 "Developing a Scarifier to Retrieve Radioactive Waste From Hanford Single-Shell
Tanks," by *J.A. Bamberger, Pacific Northwest Laboratory, Richland, Washington*,
and D.E. Steele, QUEST Integrated, Inc., Kent, Washington 737
- 56 "Air Jet Cutting Technology for Repairing Clay Cover at Radioactive Waste
Storage Sites," by *H. Yoshida and T. Isobe, Kajima Technical Research Institute, Japan*,
R. Kobayashi, Tohoku University, Japan, T. Yahiro, Tokai University, Japan, M. Takei,
Waseda University, Japan, and K. Horii, Shirayuri Women's College, Japan 747
- 57 "Safe Water Abrasive Cutting of Ammunition," by *H.H. Alba, Dr. Ing. Haber*,
Dipl.-Ing. Wilhelm, and J. Thode, Genflo Engineering GmbH, Germany 759

NEW MACHINING PROCESSES

- 58 "Abrasive Waterjet Milling: An Experimental Investigation," by *K.M.C. Öjmertz*,
Chalmers University of Technology, Sweden 777
- 59 "Diamond Polishing with Abrasive Suspension Jets," by *M. Hashish and D. Bothell*,
QUEST Integrated, Inc., Kent, Washington 793
- 60 "Machining of Titanium Using Water Jet Assistance Through the Insert," by *F.C.*
Schoenig, Jr., A.K. Khan, and A. Atherton, Cleveland State University, Ohio,
and R.R. Lindeke, University of Minnesota, Duluth, Minnesota 801
- 61 "The Removal of Excessive Resin From Semiconductor Leadframes With
Spot-Shot Waterjets," by *R. Yasui, A. Yanari, and F.M. Carletti, RIX Corporation, Japan* 813

AUTOMATED MACHINING SYSTEMS

- 62 "A New Abrasive-Waterjet Nozzle for Automated and Intelligent Machining,"
by M. Hashish, D.O. Monserud, P.D. Bondurant, J.C. Hake, S.J. Craigen, G.B. White and
W.J. Coleman, *QUEST Integrated, Inc., Kent, Washington* 829
- 63 "Successful Implementation of Two & Three Dimensional Hydro Machining,
Abrasive & Non-Abrasive, Within Automotive and Aerospace Industries,"
by J.R. Schibley, *ASI Robotic Systems, Clawson, Michigan* 843
- 64 "High Pressure Integration of Waterjet Special Systems," by G. Ayers and
B. Amundsen, *Flow International Corporation, Kent, Washington* 853
- 65 "On the Adaptive Control Constraint (ACC) of Hydro-Abrasive Jet Machining,"
by R. Groppetti, *Universita degli Studi di Perugia, Italy, and M. Bocchi and
R. Romano, Politecnico di Milano, Italy* 863

ADVANCED MACHINING AND FUTURE NEEDS

- 66 "Waterjet Machining in Relationship to Design Engineering for Manufacturability,"
by R.F. Woolman, *Hydro-Abrasive Machining, Inc., Los Angeles, California* 877
- 67 "Application of Advanced Abrasive Waterjet Machining at GE Aircraft
Engines," by J.M. Whalen, *GE Aircraft Engines, Cincinnati, Ohio* 883
- 68 "Expanding the Market for Abrasive Jet Cutting Systems,"
by D.S. Miller, *BHR Group Limited, U.K.* 899

MISCELLANEOUS PAPERS

The following papers contain valuable contributions to jet cutting technology. The editor sincerely thanks the authors for their efforts in preparing the papers in English, which is not their mother tongue. Accordingly, they have been scanned and slightly edited to improve their readability.

- 69 "Studying The Movement Parameters of Space Type Rotary Waterjet Head," by Z. Leyao,
Z. Qizhuang, and J. Yang, *Beijing Yanshan Petrochemical Corporation, China* 907
- 70 "The Cleaning Technology of High Pressure Water Jet For the Fouling of Heat
Exchanger," by Z. Leyao, Z. Qizhuang, and J. Yang, *Beijing Yanshan
Petrochemical Corporation, China, and L. Fanhua, Beijing Duoke Company, China* 915
- 71 "High Efficient Cutting - Experimental Study on Deep Slotting with Parallel
Swinging Oscillating Waterjet (PSOWJ)," by M. Jingming, *Shanghai Institute of
Coal Mining & Science, China* 929

LATE SUBMISSIONS

72 "The Application of Sensors for Process Monitoring in High Pressure
Water Jet Technology," by *Dipl. Ing. M. Knaupp, FORACON Maschinen-und
Anlagenbau GmbH Bretten, Germany* 935

73 "Innovative Designs For X-Y Cutting Systems," by *C.E. Johnston,
Chukar Industries, Ephrata, Washington* 951

AUTHOR'S INDEX A1

SUBJECT INDEX S1

SURFACE STRUCTURE AND KERF GEOMETRY
IN ABRASIVE WATER JET CUTTING:
FORMATION AND OPTIMIZATION

N.S. Guo, H. Louis, G. Meier
Institute of Material Science*
University of Hannover, Hannover, Germany

ABSTRACT

In this paper the physics of the formation process and the characteristics of a surface produced by cutting with abrasive water jets are discussed.

Using Fourier transformation the geometric structure of the cut surface is analysed and characterised at first. While the surface profile in the region of finish cutting is random and is dominated by the surface roughness, the grooves are the main component of the surface profile in the region of rough cutting.

Afterwards, the cutting process which leads to the formation of the geometric structure of a cut surface, is investigated three-dimensionally by interrupting the cutting procedure and by attacking a second sample by the jet when leaving the work piece. It was observed that the jet oscillates unsteady perpendicular to the direction of traverse in the region of rough cutting during the cutting process.

Based on the results described above the formation process of the surface produced by cutting with abrasive water jets is discussed. It was found, that there is a strong correlation between the surface structure and the physics of the cutting process.

* Head of Institute: Prof. Dr.-Ing. H. Haferkamp

1. INTRODUCTION

Machining quality in case of cutting procedure in general can be characterised by the change in material properties, the topography of the generated surface and the geometry of the kerf.

Due to the special advantages of abrasive water jet cutting especially metallurgical and thermal effects are not relevant (Blickwedel et al., 1989 and Hashish, 1989).

The geometry of the kerf includes the rounding at the inlet (Guo et al., 1992), the formation of the burr of ductile materials (Groppetti et al., 1992) and the formation of the chipping of brittle materials at the bottom (Guo et al., 1992) as well as the width and the straightness of the kerf (Matsui et al., 1990 and Guo et al., 1992). Although the geometry of the kerf is a characteristic criterion for abrasive water jet cutting, it may occur under certain conditions and can be reduced or optimised by means of suitable cutting conditions.

The surface topography of a cut by abrasive water jets, characterised in Figure 1, originates from the physics of the cutting process. Many authors have attempted to analyse and to describe the surface structure.

Blickwedel et al. (1990), Kovacevic (1991) and Singh et al. (1991) reported experimental results. Chao et al. (1992) discussed the correlation between the vibration of the nozzle and the waviness of the surface profiles. Using visualisation data from Hashish (1984) Tan (1986) formulated a model describing the surface structure. In a recent paper, Hashish (1992) presented a physical model to describe the phenomenon of waviness (striation), which is also based on the cutting process developed by visualisation (Hashish, 1988). The model shows a qualitative agreement with experimental data of surface waviness.

As described above the formation process of the surface structure is not completely understood up to now, even though some investigations on the cutting quality have been conducted.

The cutting quality is influenced by internal and external effects. The vibration of the work piece or the nozzle and the fluctuation of cutting parameters can be described as external influences. The physics of the process is the internal effect. This paper focuses essentially on the physics of the process.

Figure 2 shows the main factors affecting the cutting results. The cutting results, that means the cutting efficiency and the cutting quality, are caused by the interaction between

the abrasive particles, the target material and the abrasive water jet, which depends on the parameters such as pressure, nozzle diameter, abrasive flow rate and geometry of the focus as well as the hydrodynamics of the three phases jet while cutting. These three determinant factors influence each other temporarily and locally.

In this paper, the cutting process that leads to the formation of the surface structure, will be analysed three-dimensionally. The characteristics and the formation process of the cut surface produced by abrasive water jets will be discussed. The surface structure will be correlated with the cutting process. The influence of important parameters on the topography of the surface and aspects of the optimisation in abrasive water jet cutting will also be addressed to produce a surface with high quality.

2. ANALYSIS OF SURFACE STRUCTURE

The structure of each technical surface documents their formation progress (von Weingraber et al. 1989). To investigate this process and to identify the important parameters influencing the surface structure, the surface produced by abrasive water jet was analysed at first. The surface profiles were measured by an optical non-contacting laser surface measuring system (Model RM600, manufactured by Rodenstock Company) and analysed with aid of Fourier transformation.

2.1 Characteristics of the Cut Surface

Figure 3 shows the surface profiles of an aluminum sample measured at several typical depth. To eliminate surface structure caused by the jet deflection in the lower part of the cut, the sample was cut through completely. To ensure this, the thickness of the sample was 80% of the kerfing depth obtained with the same cutting parameters as given in Figure 3. The thickness of the material was 29.5 mm.

Figure 3a gives the surface profile 5 mm below the top of the work piece. This surface profile is typical for the zone of finish cutting (see Fig. 1). While the surface profile at the depth of 15 mm (Fig. 3b) represents the transition region from finish cutting to rough cutting, the surface profile at the depth of 20 mm (Fig. 3c) is located in the region of rough cutting. The last picture (Fig. 3d) shows the surface profile at the lower part of the cut (27 mm).

The amplitudes of surface profiles increase with the depth of measuring position. In the finish cutting region at the top, the surface profile is more random. In lower parts of the cut, however, the profiles are characterised by periodical appearance of peaks and valleys.

Fourier spectral analysis has been used to investigate the causes of this surface structure. The power spectra belonging to the surface profiles described in Figure 3 are presented in Figure 4. The horizontal scale shows the frequency of waves in 1/mm, which gives the number of waves per length unit. Inverse frequency delivers the wave length. The vertical scale is the power spectral density, which expresses the relative amplitude of waves at the frequency f . In the presentation of power spectra the Fourier-coefficients (from 1 to 10, that is equivalent to the frequencies up to 0.179 [1/mm]) representing the component of the surface profile with the large wave length, were omitted. A more detailed investigation shows that these long waves are caused by external effects like nozzle vibration etc. (Guo, 1993), so that the characteristics of surface caused by the cutting process can be described separately. Beside this the coefficients at higher frequencies than 5 [1/mm] are only relevant to the surface roughness produced by the acting of single particles.

From these power spectra the characteristics of surface produced by abrasive water jets along the depth of the work piece are clearly presented. In the upper part of cut (Fig. 4a) the spectrum distributes in a broad range of frequency and does not show a significant difference compared to the components with different wave length. This means, that the surface profile is almost random and does not possess a characteristic wave length.

With increasing depth of measuring position the spectral distribution is concentrated in a narrow range of frequency (Figure 4c and d, range of frequencies about from 0.179 to 0.804 [1/mm]), which demonstrates a dominant harmonic component in the surface profiles. This dominant component will be more and more marked when measuring in increasing depth. It is also obvious, that the highest peaks of power spectra are found approximately at same frequency for different depth of cut in the region of rough cutting. Figure 4b shows the spectrum for the surface profile in the transition zone, in which the characteristics of surface change from random surface profiles to surface profiles with dominant components.

The surface characteristics presented above are created by the cutting process itself. In the upper part a comparatively continuous cutting wear mode dominates the material removal process (Hashish 1988). The material removal results essentially from the sum of each micro-removal by abrasive particle. Therefore the surface profile is random and charac-

terised by the surface roughness. The roughness value of the surface depends on the interaction between the abrasive particle and the target material.

In the transition zone steps begin to form (Hashish, 1988 and Blickwedel, 1990). After this the cutting process is dominated by the development and motion of steps, which will be discussed later in detail. With regard to this fact the surface structure is dominated by waviness.

Using Fourier synthesis the dominant wave components of the surface profile can be reconstructed by inverse transformation of Fourier-coefficients from significant ranges in Figure 4. For example, Figure 5 shows the comparison between the measured profile of surface (Fig. 5a), the reconstructed profile of surface (Fig. 5b, synthesis using all coefficients) and the dominant wave component (Fig. 5c, synthesis using the coefficients from 10 to 45, that corresponds with frequencies from 0.179 to 0.804 [1/mm]) at the depth of 20 mm, which is equivalent to the measuring positions in Figure 3c. It demonstrates clearly, that the profile produced by inverse transformation of Fourier-coefficients is the same as the measured one. The curvature of the retransformed wave component shows a similar behaviour as the measured surface profile. This means, that the surface profile is dominated by the wave component.

2.2 Correlation between Cutting Parameters and dominant Wave Component

The frequency and the amplitude of the dominant wave component as well as the surface profile depend strongly on the cutting parameters and the thickness of the work piece. A variation of the diameter of the jet, which is related to the diameter of the focus, influences substantially the characteristics of the dominant wave component.

Figure 6 shows the measured profiles of surfaces cut by three different focus diameters (0.6, 0.9 and 1.25 mm) at corresponding measuring position. The related power spectra from Fourier transformation are illustrated in Figure 7.

It shows, that the frequency of the dominant wave components decreases with increasing focus diameter. Indeed there is a strong correlation between focus diameter and the frequency (wave length) of the significant wave component (see the schematic drawing at the bottom of Fig. 7). With increasing focus diameters the significant signal of power spectra is displaced to lower frequencies (larger wave length). That means, that the wave length on the cut surface is affected by the focus diameter. This effect is illustrated in Figure 8 by examples of cutting of an aluminum alloy. At focus diameters of 0.6 and 1.25 mm the picture shows clearly the different sizes of the grooves.

2.3 Influence of Parameters on Topography of Surface

With regard to the analyses mentioned above the cut surface is in general composed of two regions according to the structure of the surface in case of the rough cutting. The surface in the upper part is dominated by the roughness, which is depending on the interaction between single particle and material. The grooves dominate in the lower part of the cut surface. They are caused by the behaviour of the jet itself. The cutting parameters must have an influence on the topography of the surface.

To describe the surface topography in both regions the arithmetic mean deviation of the profile R_a was chosen. This parameter has the advantage, that the typical appearance in both regions can be described by the same parameter as long as the transfer function of the roughness measurement equipment is fit correctly to the expected roughness data. For the tests a cut-off of 8 mm was used. This means, that stochastic as well as periodical parts of the surface profile up to a wave length of 8 mm will be transferred by more than 75%. In this way the R_a -value in the upper part of the cut surface is dominated by the microstructure (roughness) and in the lower part by the macrostructure (waviness), and the measured data are comparable.

For instance, the surfaces of an aluminum alloy cut with two different focus diameters were measured. The results are given in Figure 9. In this case the depth of kerfs are nearly equal. In the upper part of the cut the R_a -value increases just slightly with increasing depth of cut. The difference between the R_a -values for the focus diameters of 0.6 mm and 0.9 mm demonstrates once more the effects of the particle size. The abrasives used at the focus diameter of 0.6 mm were smaller than at 0.9 mm. If a specific cutting depth is exceeded, the general behaviour of the curves shows a rapid increase of R_a -values with increasing depth of cut. A focus with a larger diameter leads to increasing values. The reason will be discussed in the following chapter.

In case of finish cutting the surface quality is characterised by the surface roughness, which is influenced by the particle size (Fig. 9). The influence of the particle size of the abrasive (Garnet) on different materials is shown in Figure 10. It gives the arithmetic mean deviation of the profile R_a , which is measured at the depth of 2 mm with a cut-off of 0.8 mm, versus the average particle size for aluminum alloy (3.4364), titan alloy (TiAl6V4) and ceramic (Al_2O_3). The roughness increases with increasing size of the particles. However the values are influenced by the sample material. The value R_a is a characteristic data for the combination of target material and abrasive particle (material, shape and size).

3. VISUALISATION OF CUTTING PROCESS

Using high-speed camera Hashish (1988) and Blickwedel (1990) observed the interaction between the abrasive water jet and the work piece in transparent material while cutting. It was observed that a steady-state interface exists at the top of the kerf. This zone is termed as cutting wear zone, in which the material removal occurs by particle impacts at shallow angles. In the lower part, however, a step is formed in the material and so a more discontinuous deformation wear process is dominant.

The cutting process leads to the two characteristic surface regions. While the upper part is free from jet-induced structures, in the lower part the deformation wear mode leads to the striation marks as characteristic structure (Hashish, 1988 and 1992).

The observation was only conducted in plane constituted by the direction of traverse and the direction of jet. However, the interaction between the abrasive water jet and the target material is three-dimensional. To understand the cutting process completely, in particular the formation of the surface topography, a three-dimensional observation of the interaction between the jet and the material had to be carried out.

3.1 Inclination of Jet

By interrupting the cutting procedure a leading edge was obtained. This appearance demonstrates the interaction between the jet and the material at a certain moment and gives information about the formation and movement of the step during the cutting process. This step is illustrated in Figure 11 at perspex, which shows the formation and the moving of the step in the direction of the traverse and perpendicular to it. The formed step is deviated from the original axial direction of the jet during the cutting process (right picture). This phenomenon was also observed at different materials such as aluminum alloy, titan alloy, steel and ceramic materials.

3.2 Oscillation of Jet

To quantify the motion of the steps tests were carried out to attack a second sample by the jet after leaving the work piece. This experiment is given schematically in Figure 12 on the right. The material to be cut was perspex of different thicknesses. Beneath the perspex a steel sample was positioned, loaded by the jet emerging after cutting through the perspex.

The traces of removed material at the steel sample represent the distribution of the intensity of the jet emerging from the kerf of perspex sample at different thicknesses.

Figure 12 on the left shows the traces of material removal at the steel sample. In this case the thickness of the perspex sample amounted to 75 percent of the depth of kerf. The traces of material removal caused by the emerging jet can be seen as a series of dents of removal at the steel sample. It demonstrates that the process is periodical, discontinuous and three-dimensional. It is evident, that the dents are either found at the midline in turns nor form a continuous line. They oscillate unsteadily. This corresponds with the illustration in Figure 11.

The trajectory of the moving of the step is dependent on the local loading condition, which is caused by the jet and by the geometry of the target material at the loading position. While the step begins to incline to one side from the midline in the first cycle, the next step will be propelled by the jet to the other side. This recurrent oscillation of the step movement occurs in the course of the cutting process and is due to the erosion effects. The amplitude and the frequency of this oscillation are essential dependent on process parameters as seen before.

By cutting perspex of different thicknesses it can be observed, that this oscillation of the traces will be observed only when the thickness of perspex sample is larger than the zone of finish cutting. In this case the amplitude of the oscillation of the traces increases with the material thickness to be cut. This phenomenon is caused by the inclination of jet during the progress of cut and proves that the inclination and the unsteady oscillation of the steps start with the beginning of the formation of the steps.

4. FORMATION OF SURFACE TOPOGRAPHY

4.1 Correlation between the Surface Structure and the Cutting Process

From the analysis of the surface structure in the lower region of the cut surfaces described above a wave component was detected, which dominates the surface profile. The visualisation of the cutting process illustrates, that the abrupt oscillation of the jets around the midline occurs periodically during cutting. To examine the influence of the cutting process on the surface structure, the cut gaps at different depth are given in Figure 13. The surface profiles present the measured data and their dominant wave components are made by the inverse transformation of Fourier-coefficients in the significant range illustrated in Figure

4 (synthesis using the coefficients from 10 to 45, that corresponds with the frequencies from 0.179 to 0.804 [1/mm]). Underneath an example of the appearance of the cut looked from the bottom is represented.

It demonstrates clearly, that the wave component dominates the profile of the surface. The oscillation of steps can be recognised easily from the structure of the cut gaps. Because the cut gaps show clearly an oscillation, which is in accordance with the physics of the cutting process observed above, the wave component is caused by the unsteady oscillation of the jet during the cutting process. The steps are moved by the jet with a lateral inclination, therefore the amplitude of the oscillation as well as the amplitude of the dominant wave component will increase with increasing depth of cut. However, the length of the dominant waves remains nearly constant (see Fig. 4). As Figure 7 demonstrates, the wave length depends on the diameter of the jet.

Comparing the whole surface profile and the waves (groove), another component of surface profile can be found. Its wave length is smaller than the wave length of the groove and larger than the "wave length" of the surface roughness.

To examine the formation of this component, the surface profile at the depth of 20 mm, where all of the components can be observed clearly, was reconstructed by Fourier inverse transformation. The result is given in Figure 14 (on the left). The formation process of the surface structure is illustrated schematically on the right.

As described before the grooves (Fig. 14c) are reconstructed by synthesis using the Fourier coefficients in the significant range of power spectrum (from 10 to 45, that corresponds with frequencies from 0.179 to 0.804 [1/mm]). The surface roughness (Fig. 14a) will be reconstructed by synthesis using the coefficients higher than 300 (frequencies higher than 5.357 [1/mm]). That means that the "wave length" of the roughness is smaller than 0.187 mm, which is in accordance with the half of the average diameter of the abrasive particles. The formation process of these both components was discussed as before.

The coefficients of power spectrum from 46 to 299 were transformed inversely and the obtained component of the surface profile is illustrated in Figure 14b. It shows a convex form, which is caused by the overlapping of penetrations of the adjacent jets. This part of the surface profile with relative small wave length will be called as the striation.

The Combination of the three components gives the whole surface profile (Fig. 14d). The roughness dominates in the upper part of the surface and the wave component (groove) dominates in the lower part.

4.2 Formation Process of the Surface Structure

The effects described above occurs during the cutting process not separately but concerted. Figure 15 shows a general view of the surface formation process.

The surface topography is formed by the cutting process, which is caused by interaction between abrasive particles, abrasive water jet and the material. They influence each other during the cutting process.

The interaction between the single abrasive particle and the material, which is based on the abrasion and erosion by solid impact, leads to a material removal. This micro-chipping process leads to the microstructure of cut surface (surface roughness), which dominates the surface profile in the region of finish cutting but can be detected in deeper regions too.

The macroscopic geometry of the cut surface results from the accumulation of removals of material by impacts of single particles. During the cutting process the geometrical condition of the interaction between abrasive particles and material is changed temporally and locally. This influences the abrasive water jet flow and so the motion of the particles leading to the formation of three-dimensional steps.

With the beginning of the formation of steps at a specific depth of cut the formation process of the cut surface is dominated by the shape of steps and by the hydrodynamics of the jet. On one hand, the formation process of steps and their overlapping in the direction of traverse leads to a striation component of the surface profile. On the other hand, the inclination and unsteady oscillation of the jet lead to a three-dimensional development and movement of steps during the cutting process. This motion of steps causes the formation of grooves, which are essential characteristics of surface profiles in the region of rough cutting.

In addition external influences (vibration of nozzle or work piece) affect the structure of the cut surface depending on the kinds of the external influencing factors (Guo, 1993).

The geometry of the cut surface consists in general of surface roughness, striations, grooves and additional external effects. The proportion of each components varies along the depth of the cut as described above. Their superposition leads to the surface profile.

5. CONCLUSIONS

From investigations described above the topography of the surface, which includes the surface roughness, striation and groove, varies along the depth of the cut. In case of just cutting through the surface can be in general characterised by the region of finish cutting and the region of rough cutting according to the structure of the surface. While in the region of finish cutting the surface is quite smooth and random, there is an increase roughness due to striations and grooves in the lower part of the cut.

The physics of cutting process is dominated in the region of finish cutting by a continuous micro-chipping process. In the region of rough cutting, however, the formation and the motion of steps dominate. The cutting process takes place discontinuously and three-dimensional in case of rough cutting. The jet inclines and oscillates unsteadily perpendicular to the direction of traverse during the cutting process.

There is a distinct correlation between the surface structure and the physics of cutting process. While the surface roughness is caused by the interaction between single particles and material and the striation with short wave length is formed by the overlapping of penetrations of the adjacent jets, the inclination and the unsteady oscillation of the jet lead to the formation of grooves with large wave length. While the surface is dominated by the surface roughness in the upper part, grooves are the main component of the profile in the lower part of cut.

The particle size influences essential the surface roughness. The frequency (wave length) of the grooves as well as the frequency of the striations are largely depending on the diameter of the jet. Beside these, other cutting parameters may affect the surface profile. Their quantitative relations will be the subject of further investigations.

6. REFERENCES

- Blickwedel, H., Haferkamp, H., Laurinat, A., and Louis, H., "Kalter Schnitt - Abrasivstrahlschneiden metallischer Werkstoffe im Vergleich zu anderen Trennverfahren," *Maschinenmarkt*, pp. 80-83, No. 49, 1989.
- Blickwedel, H., Guo, N.S., Haferkamp, H., and Louis, H., "Prediction of Abrasive Jet Cutting Performance and Quality," *Proceedings of the 9th International Symposium on Jet Cutting Technology*, pp. 163-179, BHRA, Fluid Engineering Centre, Cranfield, UK., 1990.

- Blickwedel, H., "Erzeugung und Wirkung von Hochdruck-Abrasive-Strahlen," Dissertation, Universität Hannover, 1990, in: Fortschritt-Berichte VDI, Reihe 2: Fertigungstechnik, Nr. 206, VDI Verlag, 1990.
- Chao, J., Geskin, E.S., and Chung, Y., "Investigations of the Dynamics of the Surface Topography Formation during Abrasive Waterjet Machining," Proceedings of the 11th International Symposium on Jet Cutting Technology, pp. 593-603, Kluwer Academic Publishers, Dordrecht, NL., 1992.
- Groppetti, R., and Monno, M., "A Contribution to the Study of Burr Formation in Hydro Abrasive Jet Machining," Proceedings of the 11th International Symposium on Jet Cutting Technology, pp. 621-633, Kluwer Academic Publishers, Dordrecht, NL., 1992.
- Guo, N.S., Haferkamp, H., Laurinat, A., and Louis, H., "Einsatzmöglichkeiten des Wasserabrasivstrahlschneidens zum Trennen von schwerschneidbaren Werkstoffen und Verbundsystemen," Abschlußbericht DVS 8236 / AiF 6.110, Interner Technischer Report, Institut für Werkstoffkunde, Universität hannover, 1992.
- Guo, N.S., "Bildungsvorgang der Schnittflächenstruktur beim Wasserabrasivstrahlschneiden," Interner Technischer Report, Institut für Werkstoffkunde, Universität Hannover, 1993.
- Hashish, M., "On the Modeling of Abrasive-Waterjet Cutting," Proceedings of the 7th International Symposium on Jet Cutting Technology, pp. 249-265, BHRA, Fluid Engineering Centre, Cranfield, UK., 1984.
- Hashish, M., "Visualization of the Abrasive-Waterjet Cutting Process," Experimental Mechanics, pp. 159-169, June, 1988.
- Hashish, M., "Characteristics of Surfaces Machined with Abrasive-Waterjets," In: Machining Characteristics of Advanced Materials (eds. M. Ramulu and M. Hashish), pp. 23-32, Presented at Winter Annual Meeting of ASME, San Francisco, 1989.
- Hashish, M., "On the Modelling of Surface Waviness Produced by Abrasive-Waterjets," Proceedings of the 11th International Symposium on Jet Cutting Technology, pp. 17-34, Kluwer Academic Publishers, Dordrecht, NL., 1992.
- Kovacevic, R., "Surface Texture in Abrasive Waterjet Cutting," Journal of Manufacturing

Systems, Vol. 10, No. 1, pp. 32-40, 1991.

Matsui, S., Matsumura, H., Ikemoto, Y., Tsujita, K., and Shimizu, H., "High Precision Cutting Method for Metallic Materials by Abrasive Waterjet," Proceedings of the 10th International Symposium on Jet Cutting Technology, pp. 263-278, BHRA, Fluid Engineering Centre, Cranfield, UK., 1990.

Singh, P.J., Chen, W.L., and Munoz, J., "Comprehensive Evaluation of Abrasive Waterjet Cut Surface Quality," Proceedings of the 6th American Water Jet Conference, pp. 139-161, Water Jet Technology Association, ST. Louis, Missouri, 1991.

Tan, D.K.M., "A Model for the Surface Finish in Abrasive-Waterjet Cutting," Proceedings of the 8th International Symposium on Jet Cutting Technology, pp. 309-313, BHRA, Fluid Engineering Centre, Cranfield, UK., 1986.

von Weingraber, H., and Abou-Aly, M., "Handbuch Technische Oberflächen," Friedr. Vieweg & Sohn, Braunschweig/Wiesbaden, Germany, 1989.

7. NOMENCLATURE

a	Thickness of workpiece	mm
d_D	Nozzle diameter	mm
d_F	Focus diameter	mm
f	Frequency	1/mm
h_{rb}	Region of rough cutting	mm
h_{rf}	Region of finish cutting	mm
k	Depth of kerf	mm
l_F	Focus length	mm
l_t	Measuring length	mm
l_e	Cut-off length	mm
\dot{m}_p	Abrasive flow rate	g/s
n	Trailback	mm
p	Pressure	bar
R_a	Arithmetic mean deviation of the profile	μm
s	Stand-off distance	mm
v	Traverse rate	mm/min
z	Measuring position	mm

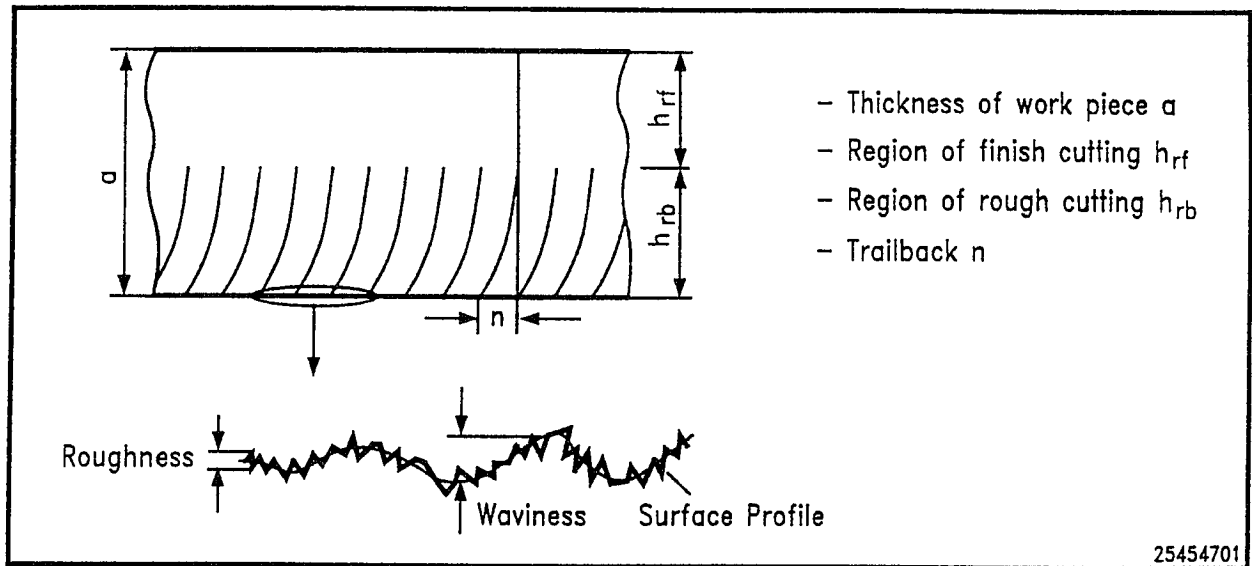


Fig. 1: General Characteristics of Cut Surface

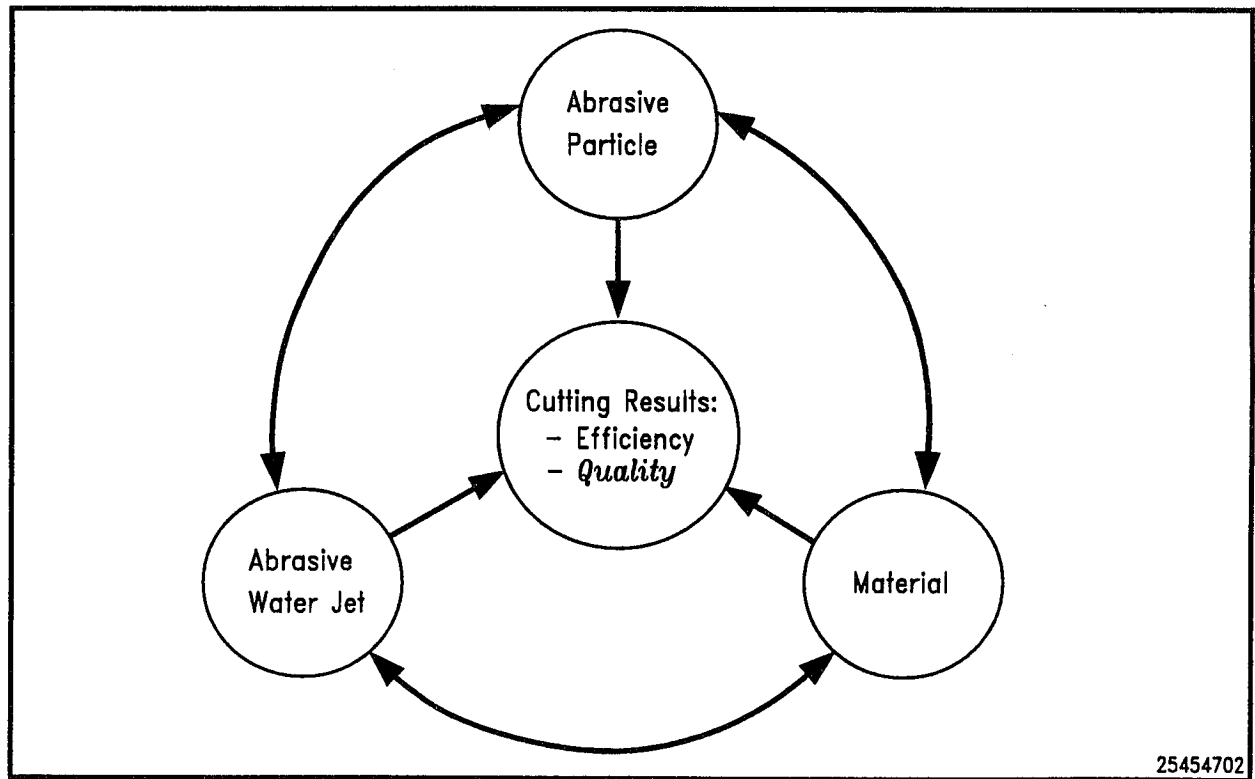


Fig. 2: Schematic of Interaction in Abrasive Water Jet Cutting

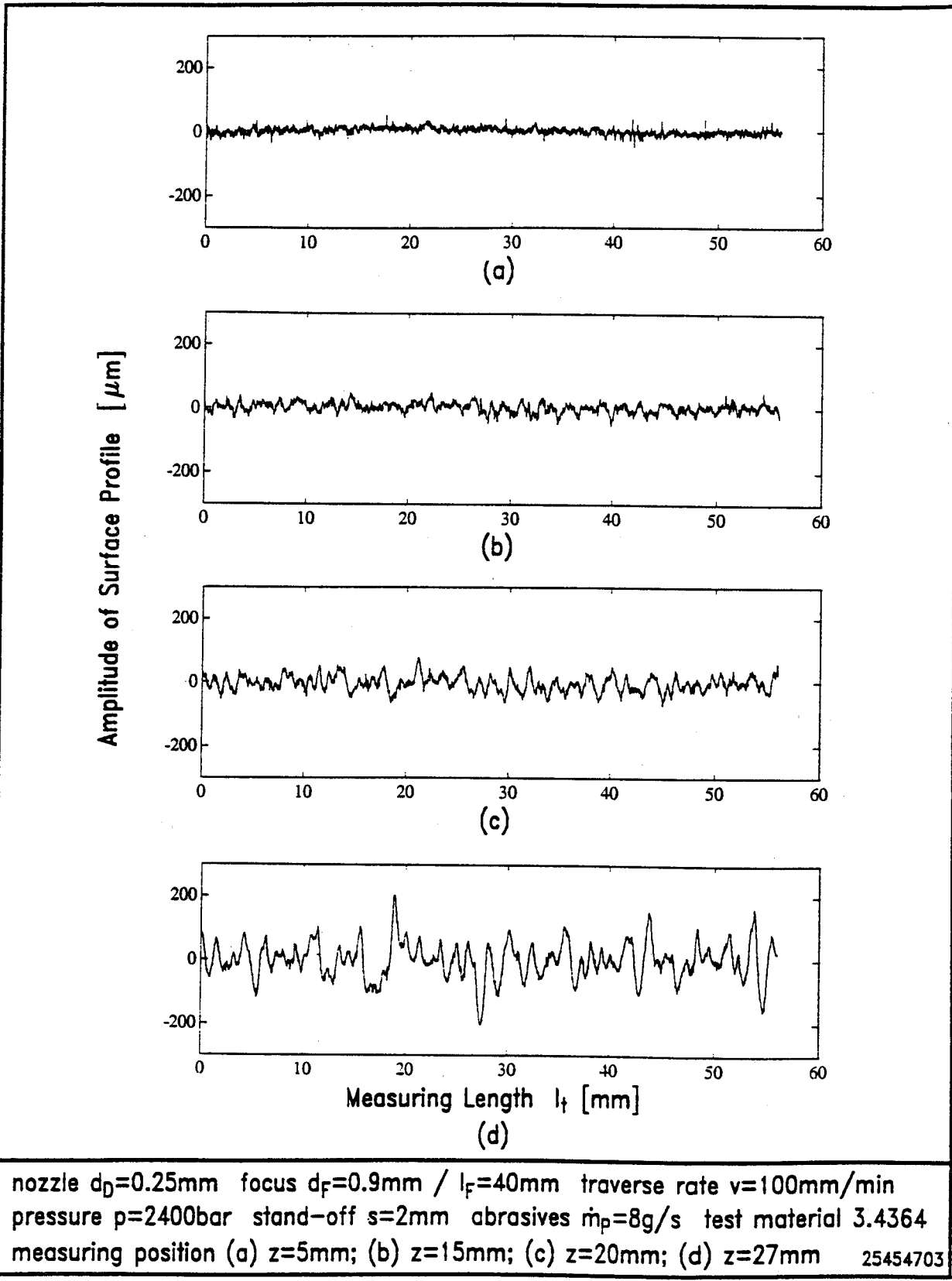


Fig. 3: Surface Profiles at Various Depth of Cut

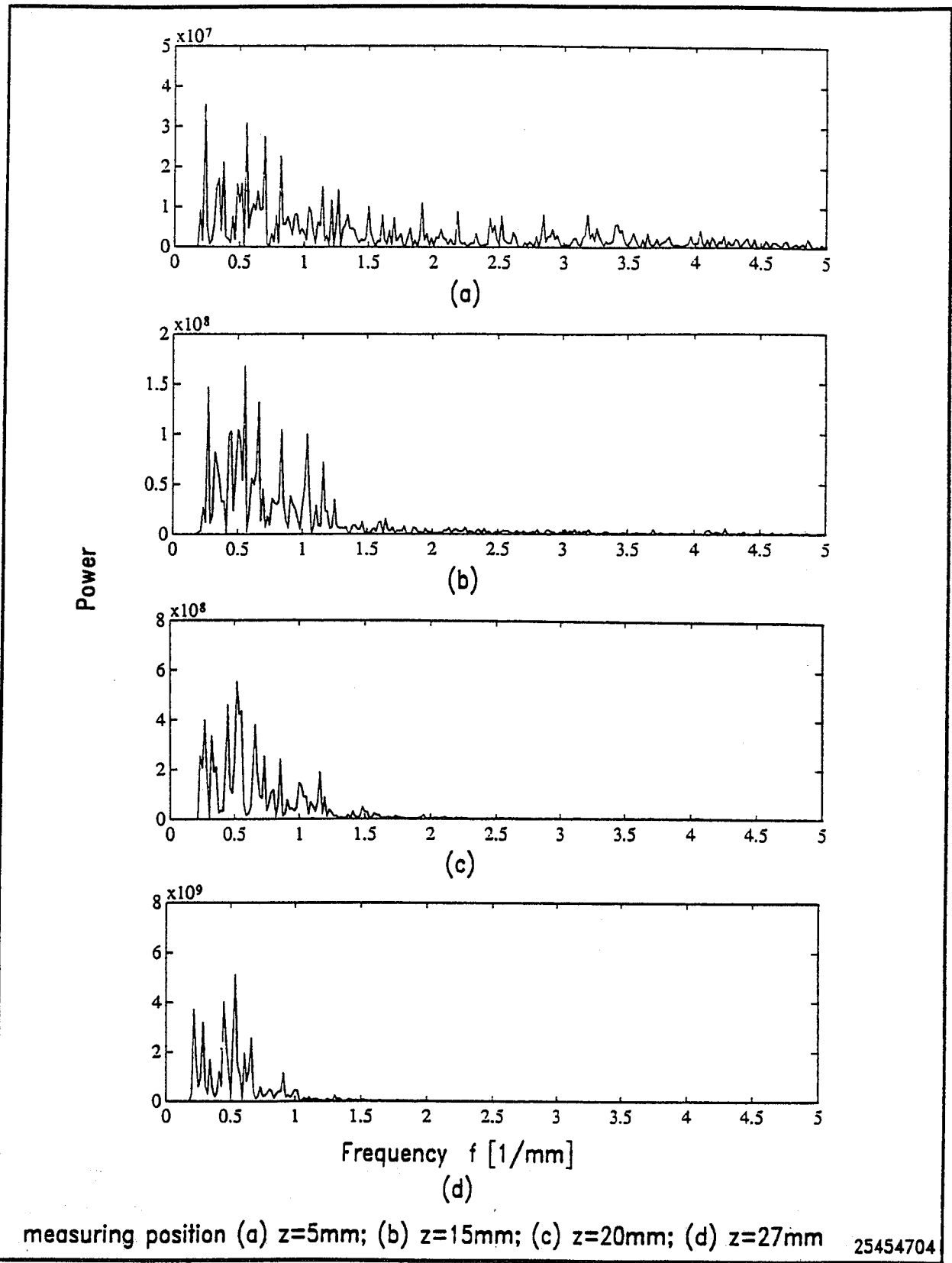


Fig. 4: Power-Spectrum of Surface Profiles at Various Depth of Cut

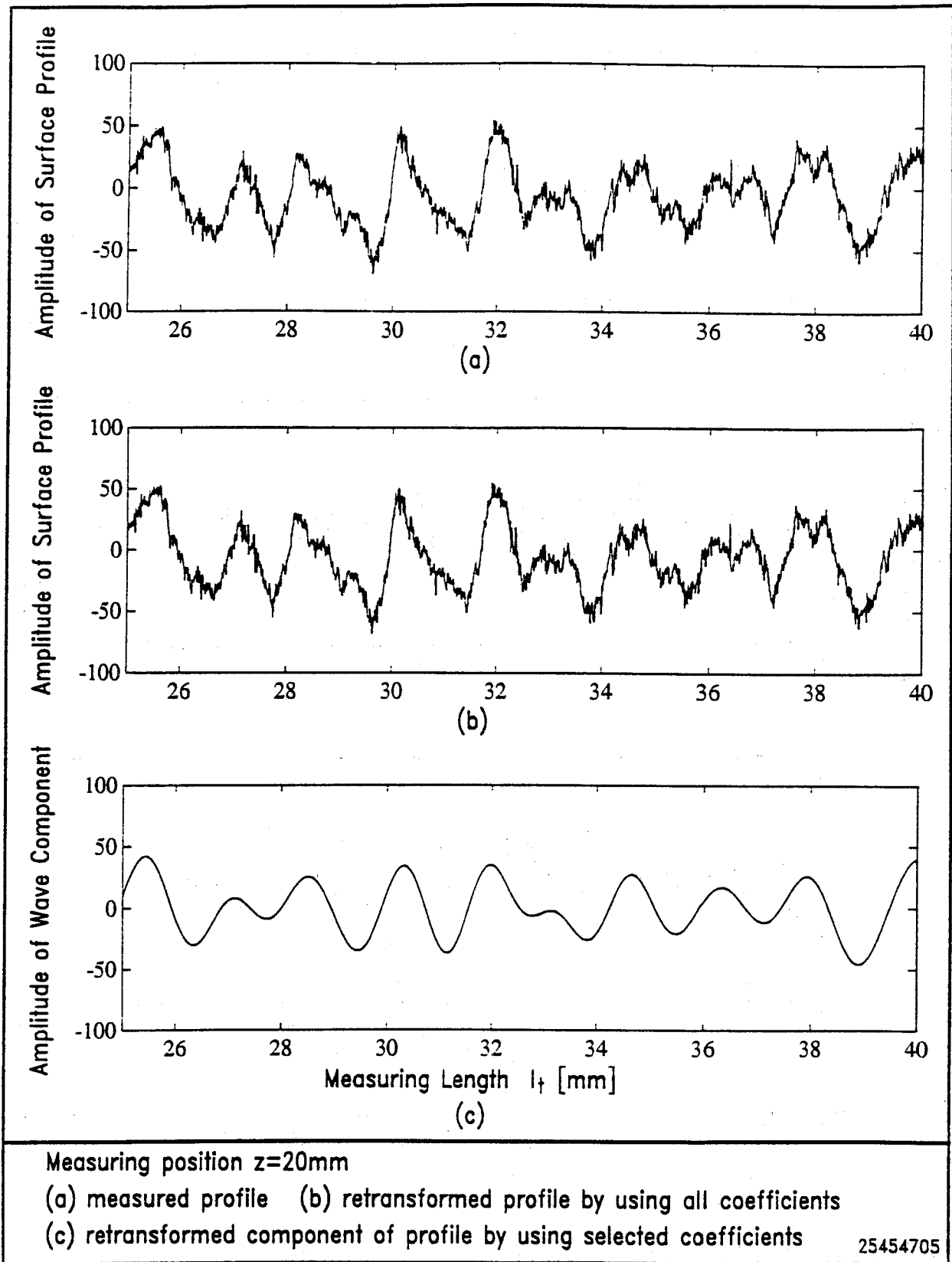


Fig. 5: Comparison between Surface Profile and Wave Component

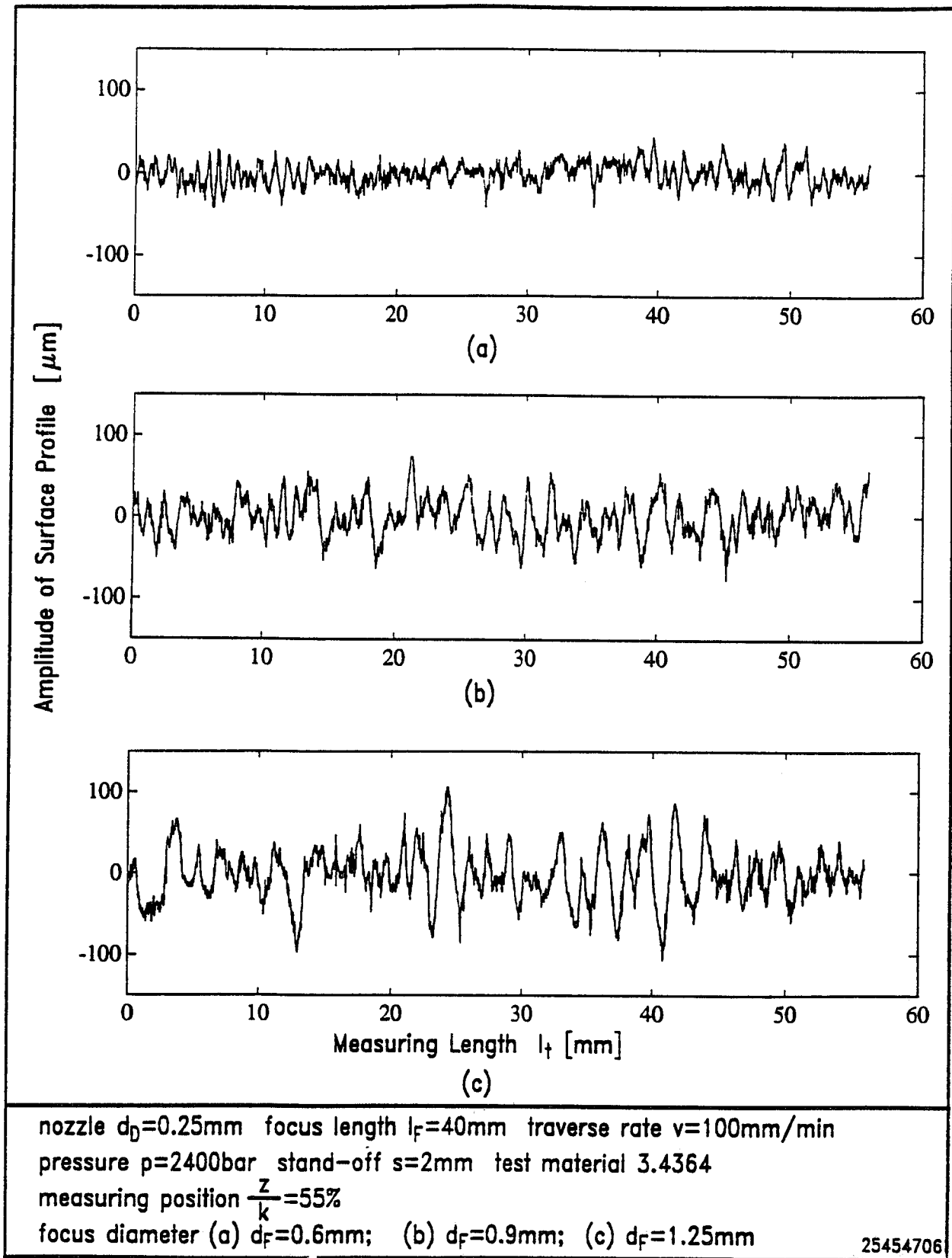


Fig. 6: Surface Profiles for Different Focus Diameters

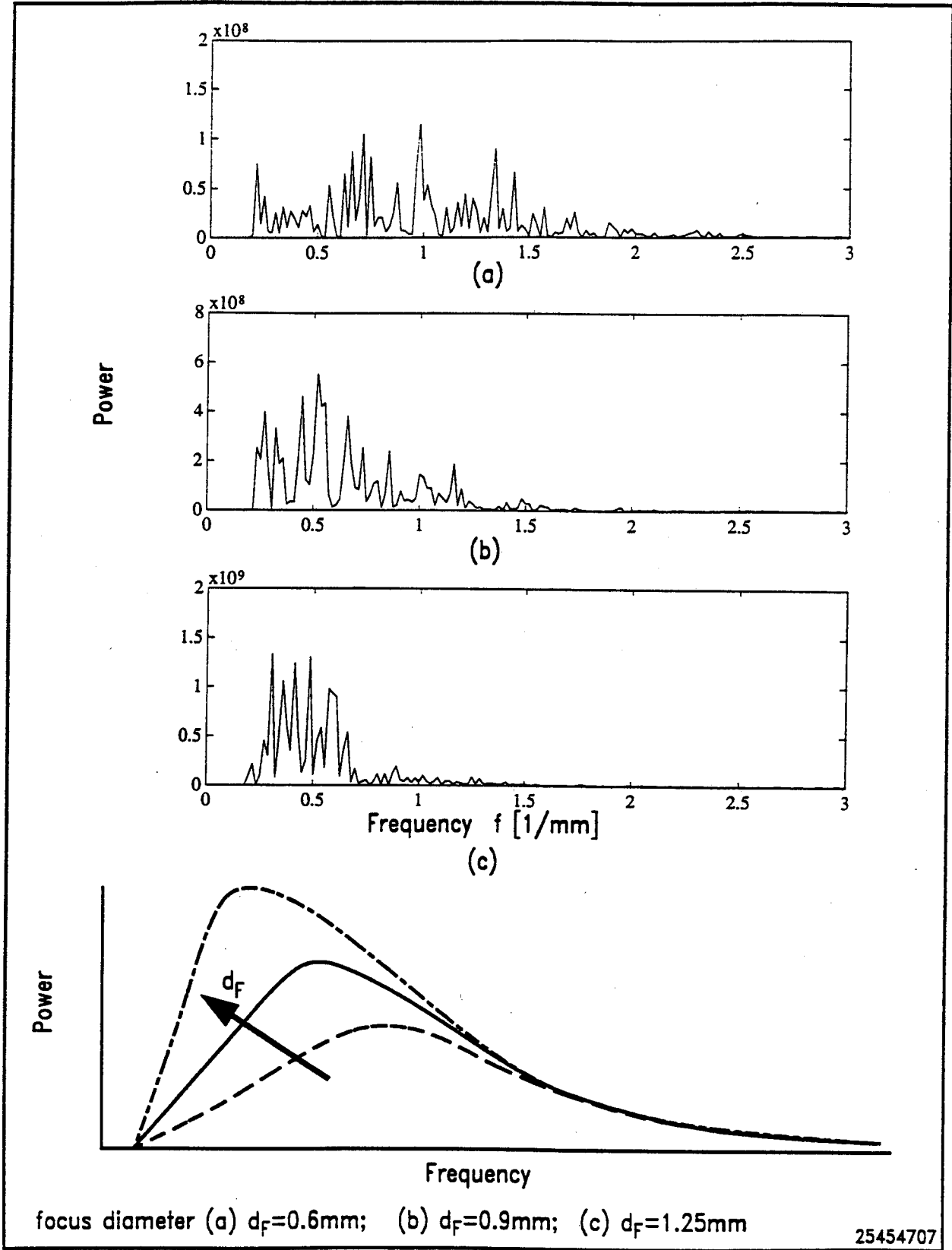


Fig. 7: Power-Spectrum of Surface Profiles for Different Focus Diameters

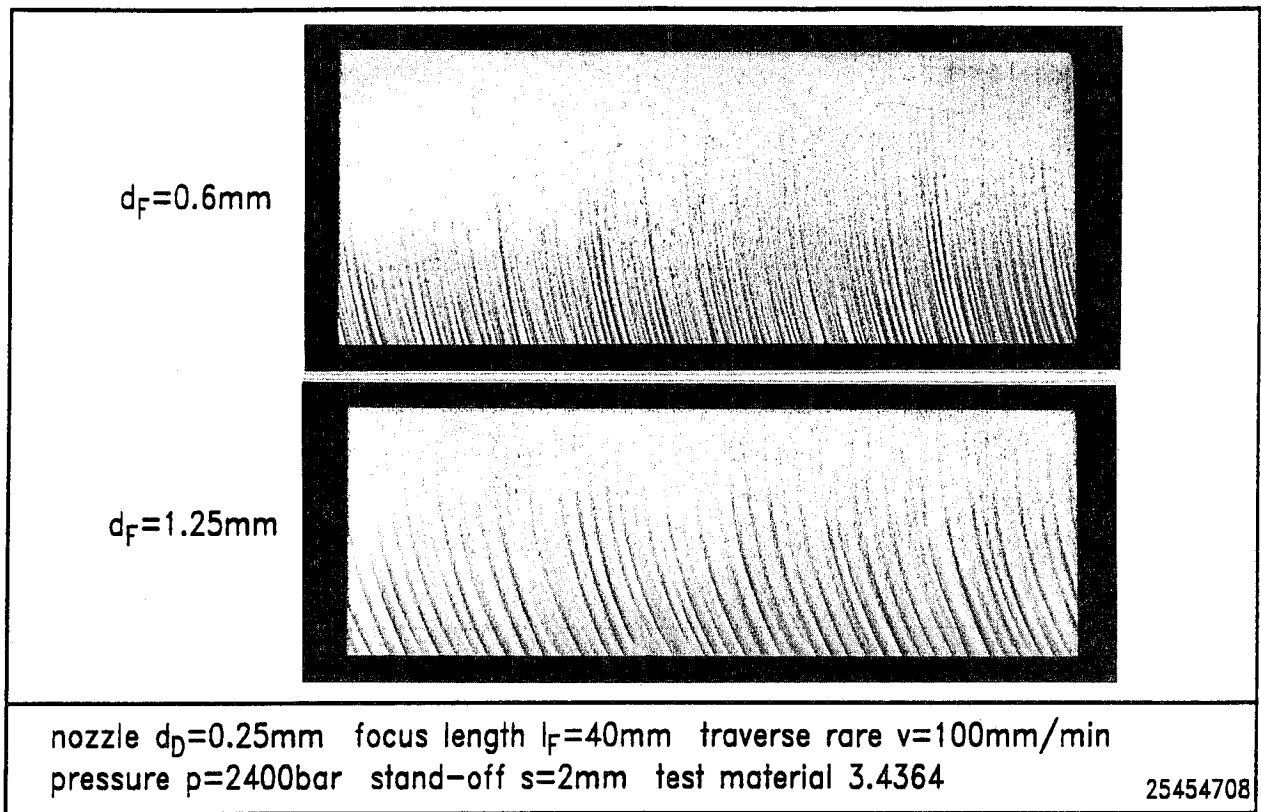


Fig. 8: Effect of Focus Diameter on Surface Structure

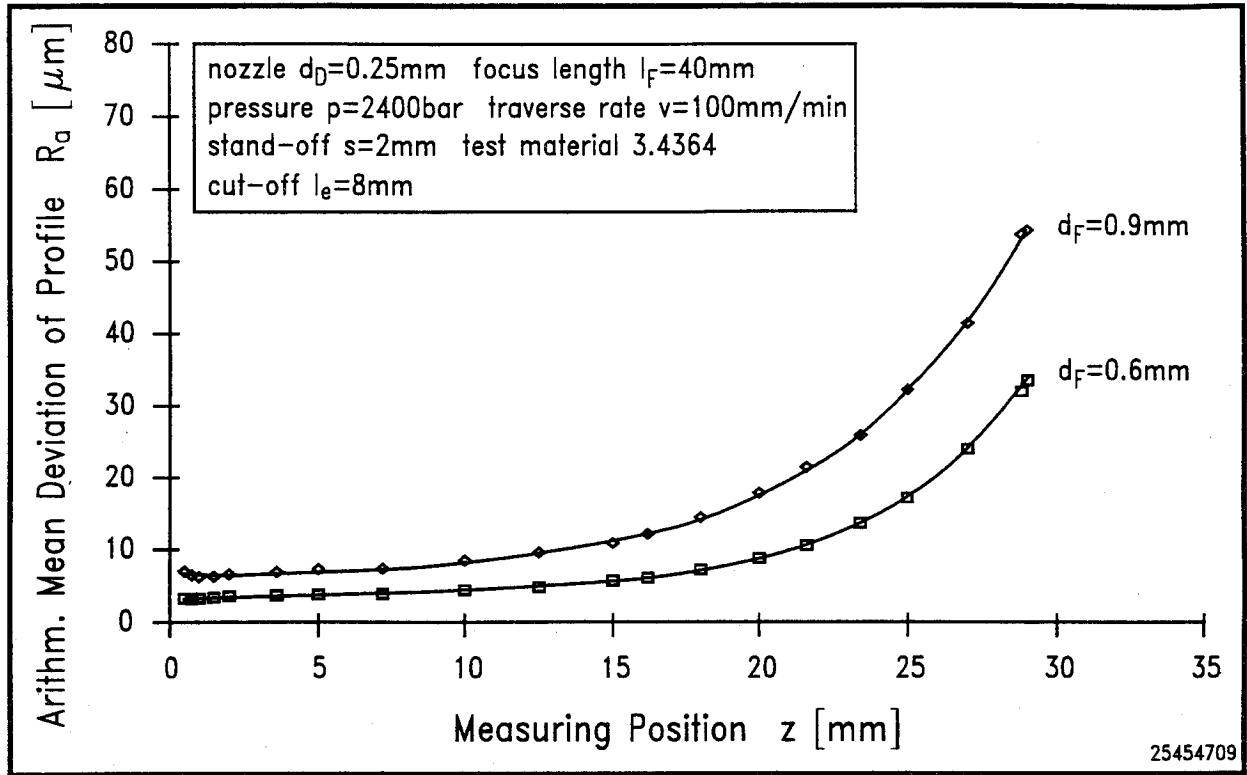


Fig. 9: Effect of Focus Diameter on Surface Topography

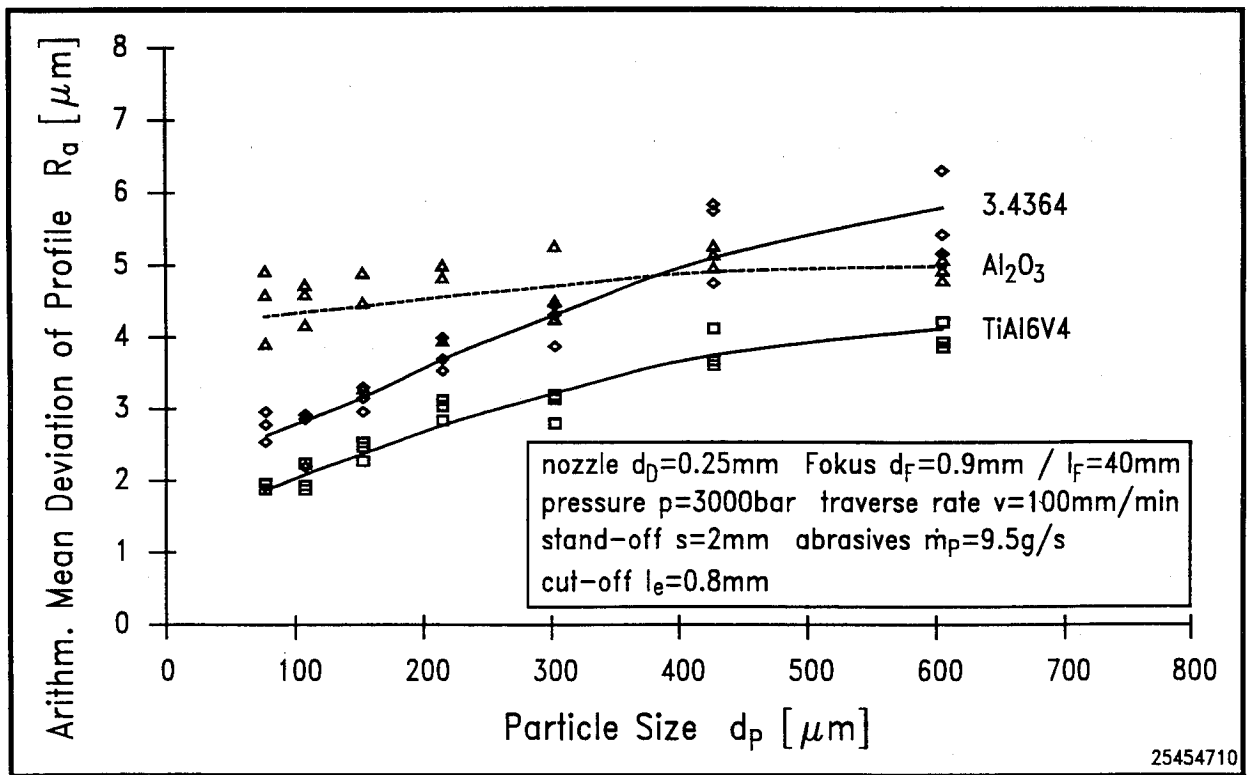


Fig. 10: Effect of Particle Size on Surface Roughness

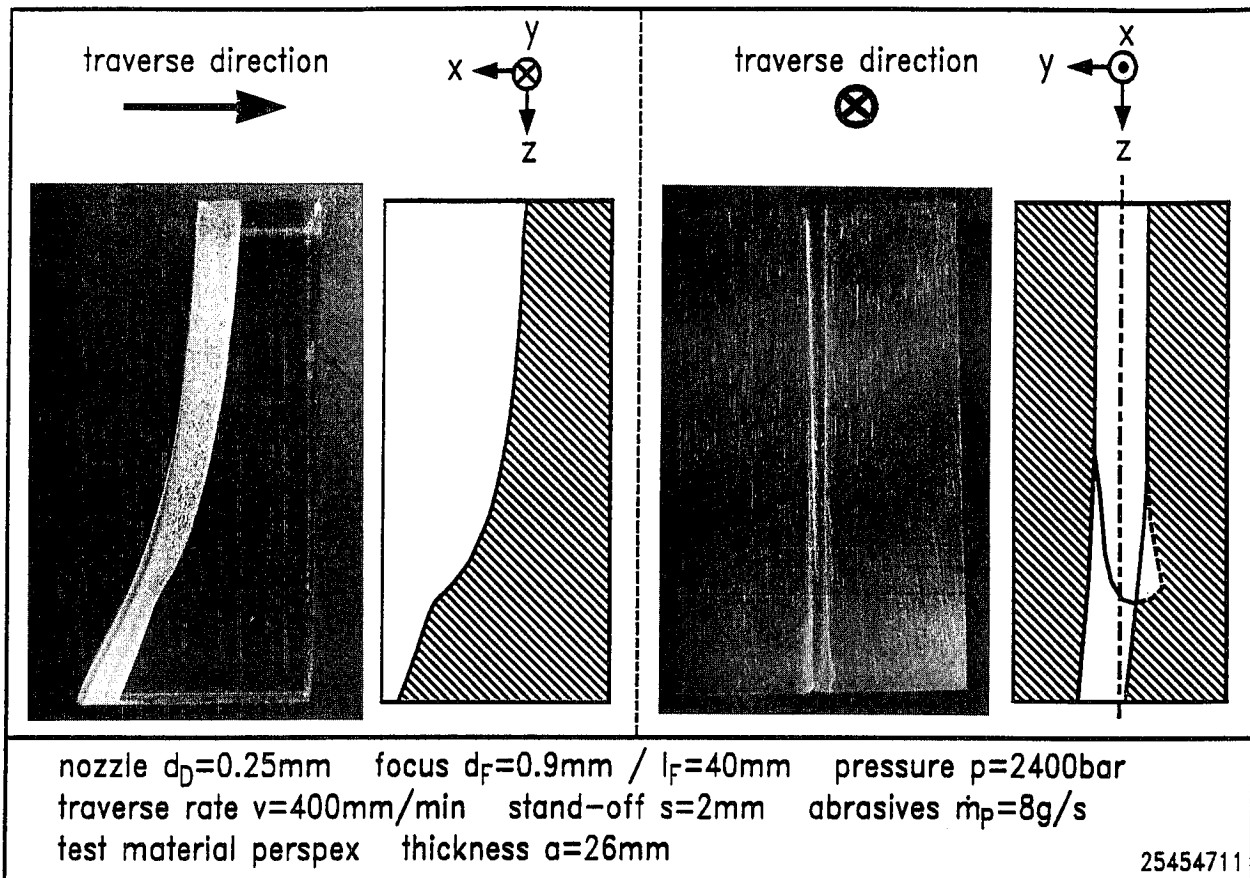


Fig. 11: Inclination of Step during Cutting Process

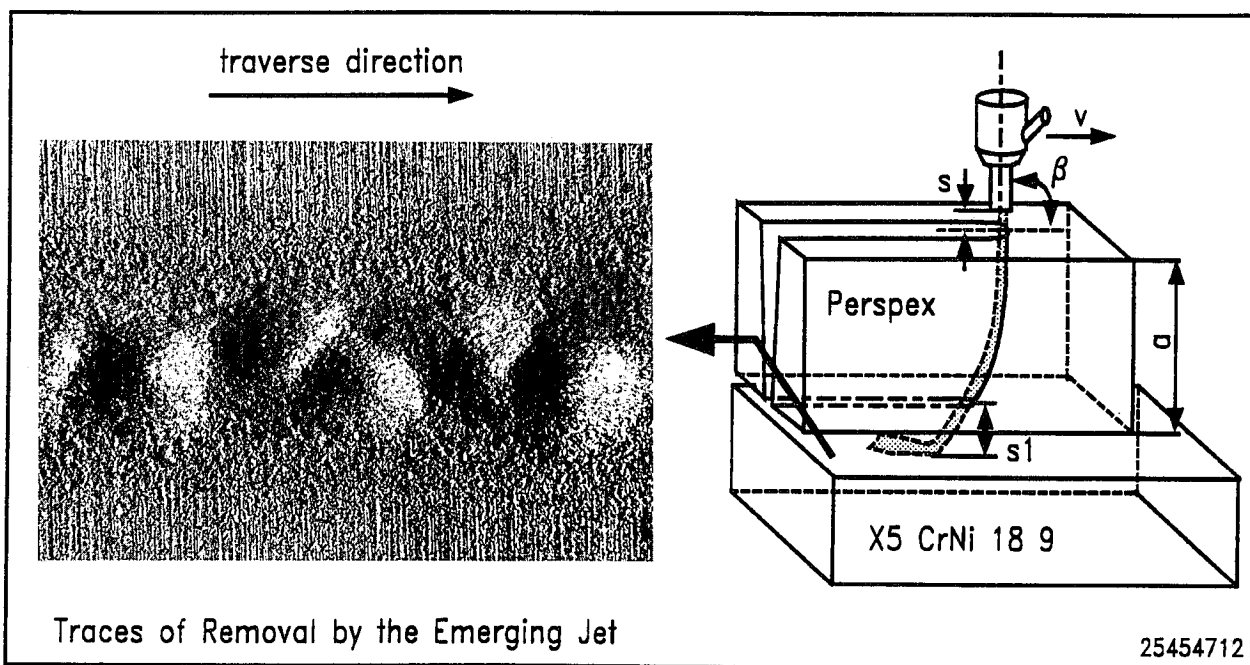


Fig. 12: Traces of Removal by the Emerging Jet

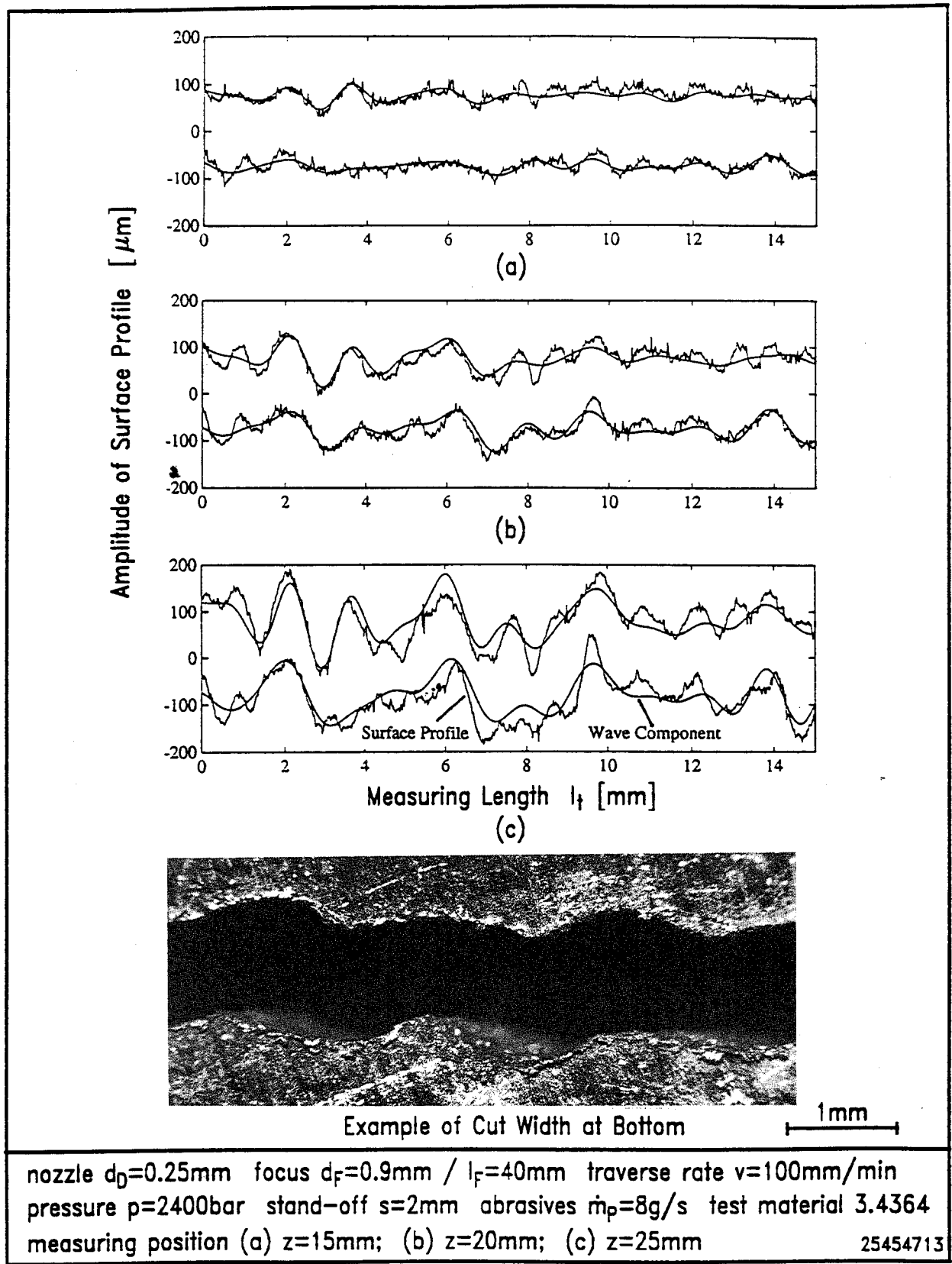


Fig. 13: Width of the Cut at Various Depth in the Region of Rough Cutting

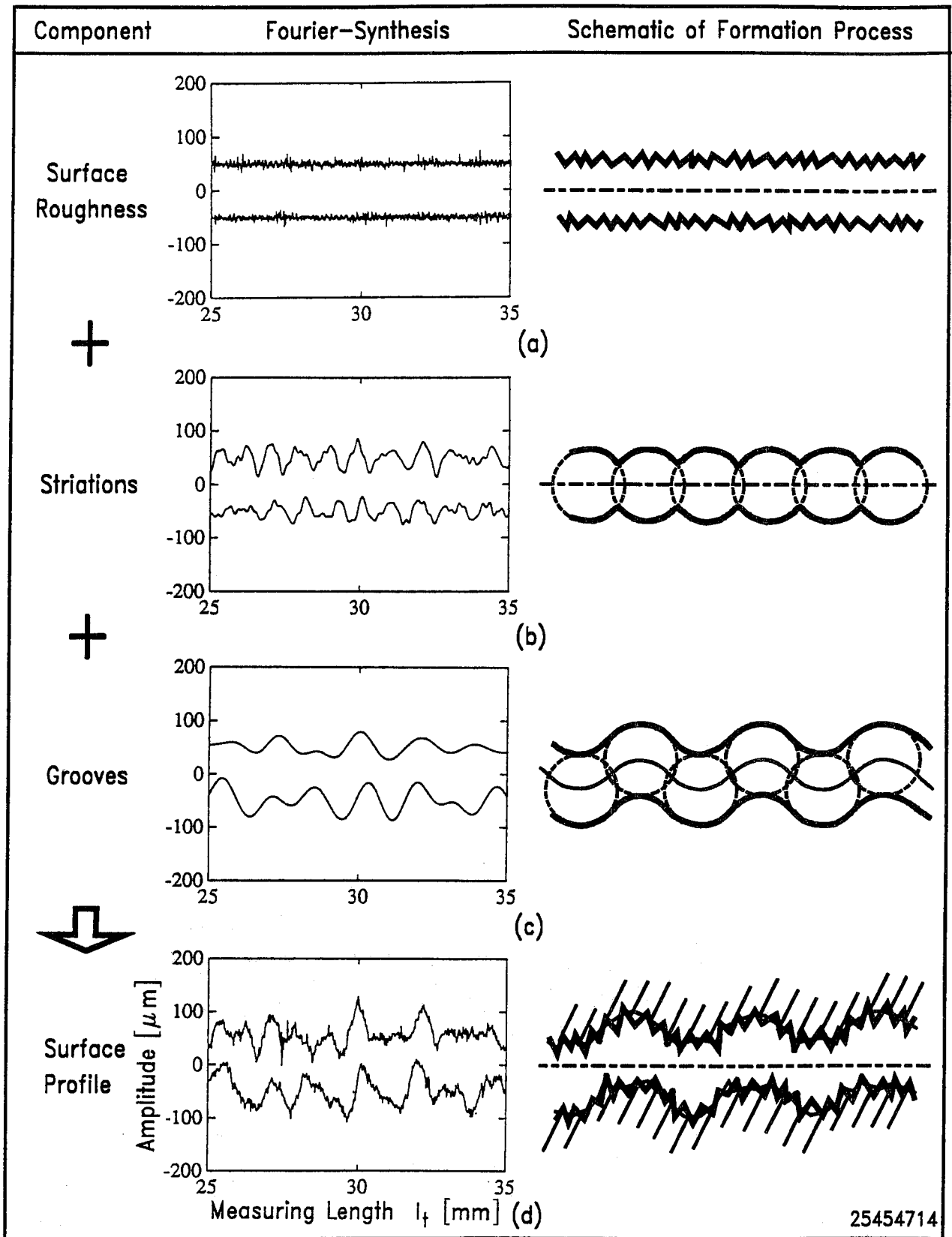


Fig. 14: Constitution of Surface profile

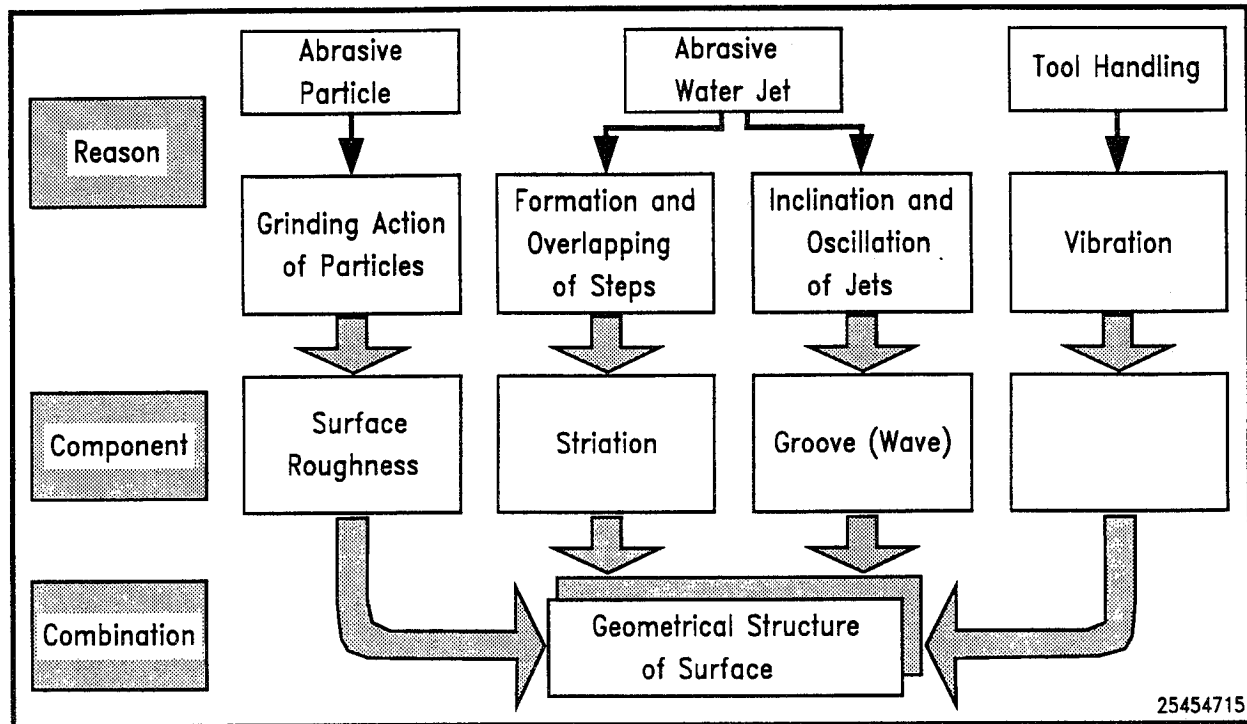


Fig. 15: Formation Process of Cut Surface

EXPERIMENTAL STUDY OF THE STRIATION FORMATION AND SPECTRAL ANALYSIS OF THE ABRASIVE WATERJET GENERATED SURFACES

J. Chao and E. Geskin
Department of Mechanical and Industrial Engineering
New Jersey Institute of Technology, Newark, NJ 07102

ABSTRACT

This study describes the investigation of the formation of surface topography during abrasive waterjet cutting. We observed that the direction of cutting dramatically changes the striation pattern in the waterjet cutting system been study. The power spectral of surface topography shows a dominant frequency when cutting was done in the Y direction and multi-peaks when cutting was done in the X direction and the amplitude are much different. The amplitude of the dominant peaks were found generated at different cutting speeds to be second order polynomial function of the distance from the top of cut.

A series of experiment were carried out. It was found that the machine vibration is the main cause of striation formation in the abrasive waterjet cutting system. The motor-drive system and rack/pinion transmission were identified as the sources of vibration which cause severe striation marks on the kerf edge.

1. INTRODUCTION

Abrasive waterjet (AWJ) machining is a relatively new manufacturing technique. Due to acceptable cutting speed, absence of a heat-affected zone and thermal distortion, and the ability to cut all materials of interest, AWJ is widely used in a number of industrial applications. AWJ has the potential of becoming one of the principal material removal technologies, however, several shortcomings substantially inhibit the use of this technology.

One of the principal deficiencies of AWJ is excessive waviness (striation) of generated sidewall surfaces. Usually, the sidewall surface generated by AWJ consists of a smooth upper and a wavy bottom zone (Blickwedel et al., 1990, and Hunt et al., 1988). The upper smooth zone has a random, moderately isotropic texture, with a height distribution that is nearly Gaussian. The surface quality in this zone is comparable to the quality generated using milling and turning techniques (Matsui et al., 1990). The depth of the upper zone depends on the specific energy delivered by the jet per unit of workpiece area. Reductions of the cutting speed or increase of the jet velocity results in deepening of the smooth zone. A desirable surface finish can be obtained if the thickness of the workpiece is less than the depth of the smooth zone, otherwise additional finishing operations are required (Souda, 1990, and Zhou et al., 1992). Obviously, striation phenomenon substantially reduces practical application of AWJ technology and minimization of this problem would constitute a substantial improvement in material shaping.

Striation formation is a phenomenon typical to all existing high energy beam technologies. The general pattern observed on surfaces generated during laser, plasma, and flame cutting is similar to that generated by AWJ. Despite the importance of elimination or minimization of this phenomenon, the knowledge of the mechanism of striation formation is inadequate.

The current explanation of AWJ generated striation is based on the experiment of Hashish (1984 and 1988), involving visualization of AWJ cutting of transparent materials. In this experiment, the author attempted to demonstrate the existence of two modes of jet-workpiece interaction, as well as the periodic character of this interaction. Thus, striation appears at the portion of a workpiece below the level of the transition between the two modes. Using this observation, Hashish suggested that the cause of striation is the change of the mode of material destruction. He also presented a detailed theory based on the above hypothesis. This theory was accepted by the most of the waterjet research community, and used for an explanation of the factors pertinent to striation formation.

From Hashish's experiments, it follows that striation is an intrinsic feature of AWJ machining and thus its elimination appears to be impossible. This conclusion is shared by the community of waterjet researchers. Little additional study is being reported and the technology appears to be encumbered by this important practical limitation.

More recently, Hashish (1991) hypothesized that striation can be caused by changing operational conditions during cutting. These conditions include water pressure, abrasive flow rate, and traverse rate. During the early phase of our experiments we observed other conditions that influence the formation of striations. For example, the direction of cutting dramatically changes the striation pattern. It was also found that the entire kerf geometry has a periodic character. These observations together with the general formation of striation with all beam machining techniques enabled us to suggest that motion control and robot vibration might contribute, at least partially, to the striation formation.

This hypothesis formed the basis in this study. In the experiments to be described, we studied the dynamic motion of the cutting head, as well as cutting of different materials attempted to

correlate this information with the observed striation. The study of the robot dynamics showed that the vibration in the nozzle guidance system is the main cause of the normally observed striation formation. This information makes imperative the development of means for vibration reduction, which would lead to suppression of striations, or at least greatly extend the depth of the smooth zone.

2. EXPERIMENTAL SETUP AND METHODS

The waterjet machine made by Ingersoll-Rand company was used in this study. This system is based on (Figure 1) a 5-axis gantry robot. The cutting head is mounted on the gantry. The translation along the X-axis is controlled by a rack and pinion system. For translations along the Y- and Z-axes are controlled by two motorized ball-screws. Two rotary axes, perpendicular to each other, one in the horizontal (i.e. the pitch motion) and the other one in the vertical direction respectively (i.e. the roll motion), permit angular displacements within 200 and 360 degrees. The 5-axis motion of the cutting head is controlled by an Allen Bradley 8200 series CNC controller.

The surface topographies of all the samples are measured by the Matrix Videometrix Econoscope. It comprises a general purpose computer (HP-9000 series), a 3-axis positioning control system, and a digital image processor and part monitor section. The data representing the surface profiles include the X, Y, and Z coordinates of the measured points. They are stored in the computer and then downloaded to a 80386 based personal computer via the RS-232 port for further analysis.

A non-contact laser displacement meter (LDM) LC-2010 made by Keyence Corp. was used to measure the nozzle displacement. The LDM was held by a vise and placed on the top of the catcher. The laser beam was pointed to a flat surface on the cutting head. The analog output data of the LC-2000 controller was displayed on a Nicolet digital oscilloscope and then downloaded to a PC via the RS-232 port for further processing.

2.1 Compliance Measurement

Compliance is the ratio between the displacement and input force. In robotics, it represents the flexibility of the robot in the force-applied direction. The compliance is an inherent characteristic of a robot (ElMaraghy et al., 1988). In the waterjet cutting system, the cutting head is mounted on the frame of the gantry robot. The robot structure is subjected to the force induced by the jet. If the robot structure is not sufficiently rigid, it is possible that the structure resonance is excited when the jet is on. The compliance was measured at four locations as shown in Figure 2 by using a force transducer to push the robot as the source of displacement. The displacement at the corresponding position was measured by LDM. The force versus displacement plot is depicted in Figures 3a-3d. It can be noted that the displacement at the location "a" is higher than that at other three sites. This phenomenon most probably is due to the soft wrist element in the rotational joint A.

2.2 Modal Testing

The compliance represents the static characteristic of the structure. Thus its values were used to evaluate the flexibility of structure in the direction in which semi-static forces were applied. The dynamic characteristics of the structure can be determined experimentally or theoretically. For a simple system such as a single mass-spring-damper system, mathematical description of the

dynamic behavior is readily available. For a complex system such as the 5-axes robot, theoretical construction of a mathematical model is difficult. An experimental technique is used to identify the vibration characteristic of this system. The experimental determination of vibration behavior is termed modal testing. The natural frequency of robot upper arm in X and Y directions are shown in Figures 4a and 4b. These frequencies are 20 and 26 Hz, respectively. The modal testing result of end-effector is shown in Figure 4c. Frequencies of 1 Hz and 3.5 Hz were observed.

3. RESULTS AND DISCUSSIONS

3.1 Spectral Analysis of Surface Profiles

Two titanium samples of 20 mm thick that were generated at identical process parameters but at the different directions of nozzle motion. The observed patterns of the striation marks are quite different. The surface profiles were measured from 2 mm (at the top of cut) to 16 mm (almost at the bottom of the cut) from the top of sample. The power spectral density functions of the surface profiles are depicted in Figures 5a and 5b, respectively. The cut-off frequency 4.33 Hz was selected since all the amplitude above the cut-off frequency are much smaller than the amplitude of lower frequencies.

Figure 5a shows the surface spectra of the sample that was cut in X-direction. At the depths 14 mm and 16 mm multi-peaks distributed in frequency range from 0 to 2 Hz are observed while at the frequency above 2 Hz and the surface spectra of depths 2 mm to 12 mm, no clear peak can be identified. The sample that was cut in the Y-direction shows only a single peak at the frequency of 1 Hz for all depths, as shown in Figure 5b. It can be readily noticed that the amplitude of power spectral density functions of sample cut in Y-direction is much larger than that of sample cut in the X-direction.

3.2 Effects of the Cutting Parameters

Due to the different striation patterns generated when cutting was done in the different directions, experiments of cut steel sample with different speeds at the same location, and with the same cutting speed but at different locations were carried out to determine the effects of structural dynamics on surface topography. Figure 6a shows plot of surface amplitude versus cutting speeds, for samples cut at same location of the 5-axes waterjet machine. It can be noticed that amplitude at different depths can fit a second degree polynomial function and the trend is same for different cutting speeds but amplitude increases with higher cutting speed. This is due to the jet penetration rate decreases as the depth of penetrate increases and the penetration rate is decreasing linearly with the depth of penetrate. Figure 6b illustrates that the surface dominant frequency is subject to small changes when cut with different speeds. Table 1 shows the dominant frequencies of samples cut with same cutting speed, but at different locations. It can be noticed that except for the first cut which shows a higher dominant surface frequency, these frequencies are almost same when cutting is done at same location, but the frequency changes significantly with the change of cutting location.

3.3 Dynamic Characteristics of the Robotic Traverse System

Because the dominant striation frequency is independent of the cutting speed and the compliance shows joint A (rotation about Y-axis) has the highest compliance, as shown in the Figure 3, we can suggest that the periodicity of the striation marks is due to jet exciting the pitch resonance of

end-effector. The different dominant frequencies generated at different locations are probably caused by different dynamic characteristics of the gantry robot at various locations. To prove this hypothesis, the natural frequencies of the waterjet cutting system in X and Y directions were determined by the modal testing, as shown in Figure 4. From Figure 4c it is apparent that 1 Hz frequency of vibration matches the surface dominant frequency and is the main cause of the striation marks when cutting is done in the Y-direction.

3.4 Vibrations Measured Under Machine Dwell Conditions

The vibration signal measured at the nozzle tip under machine dwell conditions was also investigated. The signal appears while the drive was on, but after turning off the drive of traverse system, the signal disappeared immediately. It was then suggested that there is a small but measurable vibration which appears once the drive is turned on without the robot movement and without the jet flow. It was noticed also from the read-out of the LDM controller that the vibration in the X-direction has a larger amplitude (about 20 μm .) than in Y-direction and it is periodic, as shown in Figures 7a and 7b. It was found also that the 1 Hz frequency of the vibration signal is the dominant frequency of the vibration measured at the nozzle tip in X-direction which matched the 1 Hz frequency measured from modal testing as well as the surface dominant frequency. Thus we can assume that the 1 Hz frequency measured in modal testing experiment is not a natural frequency of the end-effector but was some other cause and the 3.5 Hz frequency is the lowest mode of the end-effector.

Further experiments involved measuring the vibrations at three other locations with the machine in a dwell status (*b*, *c*, *d* in Figure 2). The plots of the displacement and the corresponding spectrum are depicted in Figures 7b, 7c, 7d, 7f, 7g and 7h. The vibration that was measured at location "*b*" (Figure 7b) shows the same dominant frequency and about the same amplitude as the vibration measured at the location "*a*" (Figure 7a). The vibrations measured at the locations "*c*" and "*d*" (Figure 7c and 7d) show much smaller amplitudes than the vibrations in locations "*a*" and "*b*" and do not have single dominant frequencies as do the vibrations in locations "*a*" and "*b*". Thus the dominant frequencies measured at locations "*a*" and "*b*" matched the dominant striation frequency when the cutting was done in the Y-direction of the waterjet machine. The power spectra of the vibration measured at locations "*c*" and "*d*" had multi-peaks. The characteristic agrees with that of the surface spectra generated when the cutting was done in the X-direction of the waterjet machine. These results clearly indicate that the cutting head vibration of force type is the main cause of striations in the waterjet machining studied.

3.5 Source of the Vibration

To identify the source of the forced vibration, we examined the driving mechanism of the waterjet machining system. As shown in Figure 8, the motors that enabled manipulating the end-effector in X- and Y-directions were mounted on the support frame of the gantry robot, with their axes along Y-direction. The translation of the cutting head in Y direction is activated by the motor Y through a ball-screw. The cutting head translation in the X direction is activated by the motor X through a pinion-rack mechanism. The vibratory motion of the cutting head was not due to the pitch motor (which rotates the cutting head about a horizontal axis as shown in Figure 9) because the vibrations measured at location "*a*" and at location "*b*" were almost the same in magnitude. The vibration displacement at location "*a*" should have been much larger than that at location "*b*" if the pitch motor had been a main source of vibration. The roll motor (which rotates the cutting head

about a vertical axis marked by B in Figure 8) was not a cause of the cutting head vibration for the same reason. Motor Z was not the main cause because if this was the case, then the vibration spectra measured at locations "a", "b", "c" and "d" should all have had a high degree of similarity due to the Z direction of this motor's axis. It can be concluded that motor X and motor Y are the main sources of mechanical structure vibration in the waterjet machining system used in our study. The excitations from these two motors could be due to the motor vibration in the direction perpendicular to the motor axis and/or due to the motor rotation wandering an amount corresponding to one bit of encoder measurement or digital quantization in the servo control. This knowledge of sources of the cutting head vibration is necessary in order to develop means for vibration reduction which in turn would lead to suppression of striations and improvement of surface quality.

3.6 Vibrations due to the Rack/Pinion Transmission

The striation marks were found to have same distance apart when cut in X-direction at different operating conditions and different workpiece materials. Figure 10 shows the samples cut at different speeds. All surfaces depicted in Figure 10 exhibit striation marks with separation equal to 8 mm. Examination of the waterjet machine showed that the pinion and rack have a circular pitch of 8 mm (Figure 11) which is equal to the distance between the striation marks. We can conclude now that the smoothness of the traverse system is an important factor of striation mark formation during the abrasive waterjet machining.

3.7 Amplitude Characteristics of AWJ Generated Surfaces

The results in Figure 6 shows the amplitude of striation increases abruptly as the jet penetrate deeper. An important question to address is why the striations occur only well below surface. To understand this, consider that sometimes the vibration amplitude is so small that striations would not be expected to be visible. This small amplitude case corresponds to the smooth zone striation. However, deep enough in the material the spent water flows back along the already cut channel. When there is vibration, there is a sideways velocity component added to the forward motion of the moving jet. Thus the spent water has a sideways component which cuts into the sidewall. The expected result that the striation is in-phase with the amplitude of the vibration at the top and in-phase with the velocity at the bottom of the side wall and deeper. As described in the preceding section, the amplitude of striation marks is a second degree polynomial function of penetration depth. This phenomenon is same as the striation marks can be characterized as a parabola in cutting depth coordinate (Zeng et al., 1991).

4. CONCLUSIONS

The spectral analysis of the topography of the surface generated by AWJ determines the frequency characteristics of these surfaces. The AWJ generated surface does not contain distinctive regions. The differences between various regions are qualitative. The surface spectra show strong correlation with the structure dynamics of the traverse system. The jet-induced waviness has not been observed in our study. The amplitude of the striation marks is a second-degree polynomial function of the distance from the top of cut and is also a function of speed.

The dynamic test of the traverse system enables us to determine the real dynamic characteristics of the system which are helpful for the understanding of the striation formation in

abrasive waterjet machining. The obtained results show that the vibration plays an important role in the striation formation. The driving motors and the gear/pinion transmission system were identified as the vibration sources in the waterjet machining system. The straightness of the kerf edge is affected by the accuracy of the waterjet machining system. This knowledge of the sources of the cutting head vibration is useful for development of means for vibration reduction, which would lead to suppression of striations and improvement of surface quality.

REFERENCES

- Blickwedel, H., N. S. Guo, H. Haferkamp, and H. Louis. "Prediction of Abrasive Jet Cutting Efficiency and Quality." *Proceedings of the 10th. Int. Symp. on Jet Cutting Technology*, Amsterdam, 1990.
- Hunt, C. D., T. J. Kim, and M. Reuber. "Surface Finish Optimization for Abrasive Waterjet Cutting." *Proceedings of the 9th. Int. Symp. on Jet Cutting Technology*, Sendai, Japan, 1988.
- Matsui, S., H. Matsumura, Y. Ikemoto, K. Tsujita, and H. Shimizu. "High Precision Cutting Method for Metallic Materials by Abrasive Waterjet." *Proceedings of the 10th. Int. Symp. on Jet Cutting Technology*, Amsterdam, Paper No. G3, 1990.
- Souda, V. *Implementation of an Integrated High Energy Beam Workcell*. Master Thesis, New Jersey Institute of Technology, Newark, NJ, 1990.
- Zhou, G., M. Leu, E. Geskin, Y. Chung, and J. Chao. "Investigation of Topography of Waterjet Generated Surfaces." *Proceedings of ASME Winter Annual Meeting*, LA, 1992.
- Hashish, M. "A Model Study of Metal Cutting With Abrasive Waterjets." *ASME Journal of Engineering Materials and Technology*, Vol. 106, pp. 88-100, 1984.
- Hashish, M. "Visualization of the Abrasive-Waterjet Cutting Process." *Experimental Mechanics*, pp. 159-169, 1988.
- Hashish, M. "Characteristics of Surfaces Machined With Abrasive-Waterjets." *ASME Journal of Engineering Materials and Technology*, Vol. 113, pp. 354-362, 1991.
- ElMaraghy, H. A., and B. Johnson. "An Investigation Into the Compliance of SCARA Robots. Part II: Experimental and Numerical Validation." *ASME Journal of Dynamic Systems, Measurement, and Control*, Vol. 110, pp. 23-30, 1988.
- Zeng, J., R. Heines, and T. Kim. "Characterization of Energy Dissipation Phenomenon in Abrasive Waterjet Cutting." *Proceedings of the 6th. American Water Jet Conference*, pp. 163-177, Houston, 1991.

Table 1 Dominant frequencies of surface spectra cut in different locations of the waterjet cutting system. Case I cut at the location (x, y, z, A, B) = (135,387,-180.71,-0.5,-180). Case II cut at the location (x, y, z, A, B) = (858,387,-179,-0.5,-180).

No.	Dominant Frequency (Hz)	
	I	II
1	1.0173	0.7452
2	0.9157	0.6112
3	0.9137	0.6173
4	0.8995	
5	0.9299	
6	0.9035	
Average	0.9124 (Hz)	0.6143 (Hz)

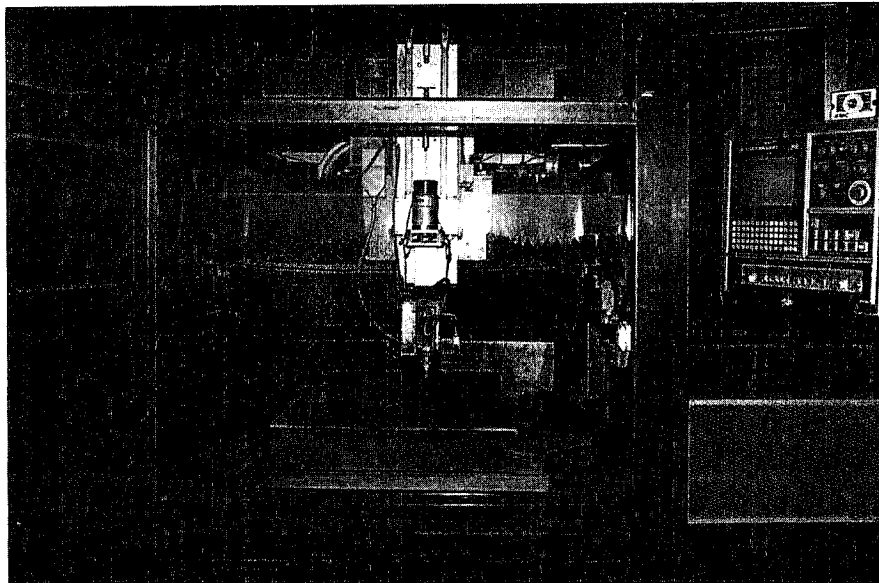


Figure 1 5-axis waterjet cutting system

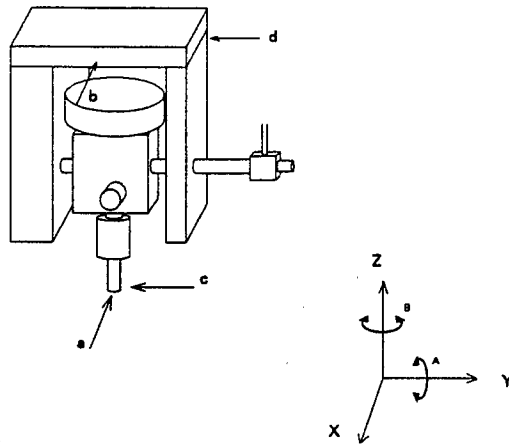


Figure 2 Schematic of the end-effector showing four locations where measurements were made.

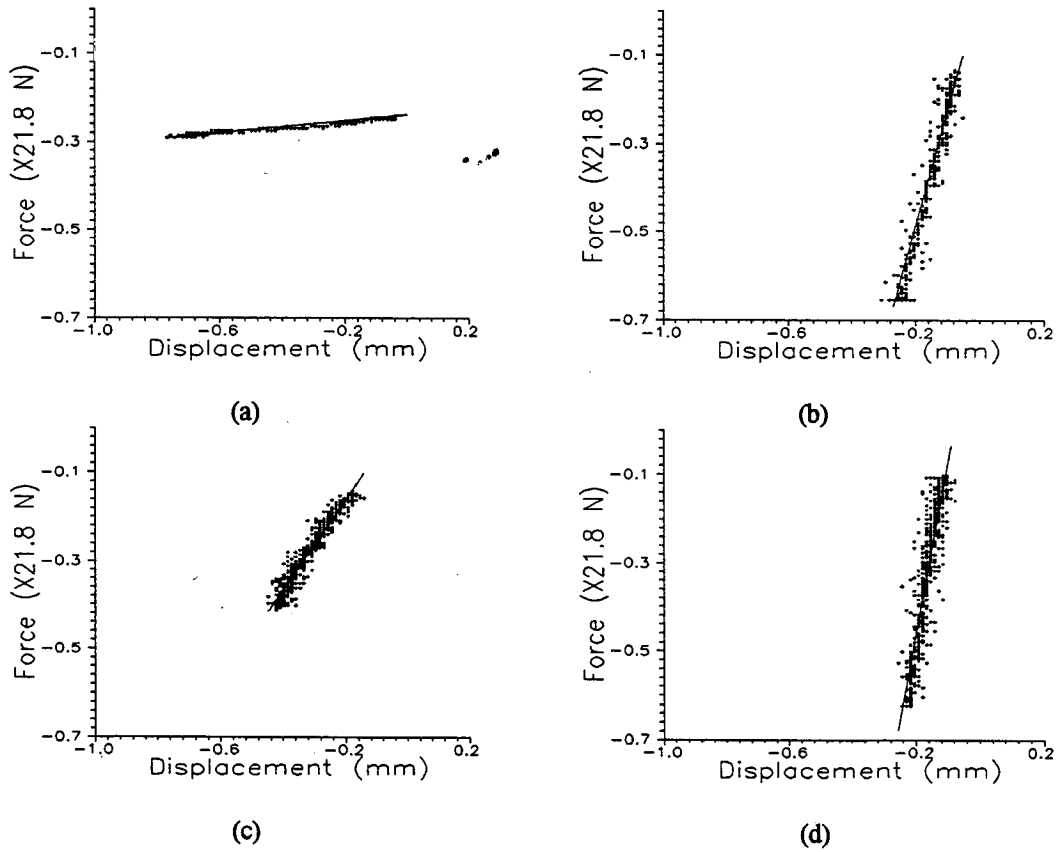
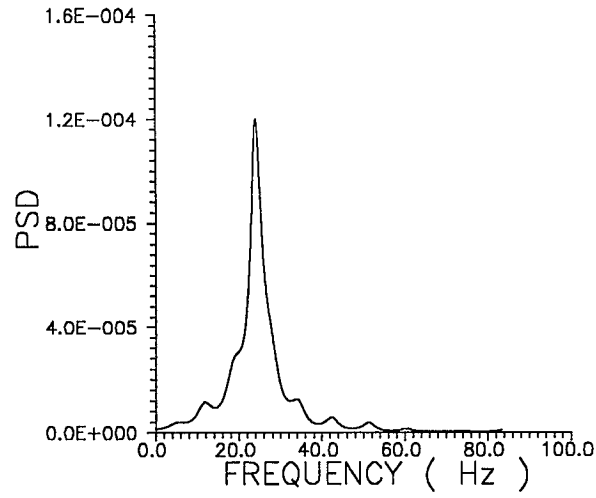
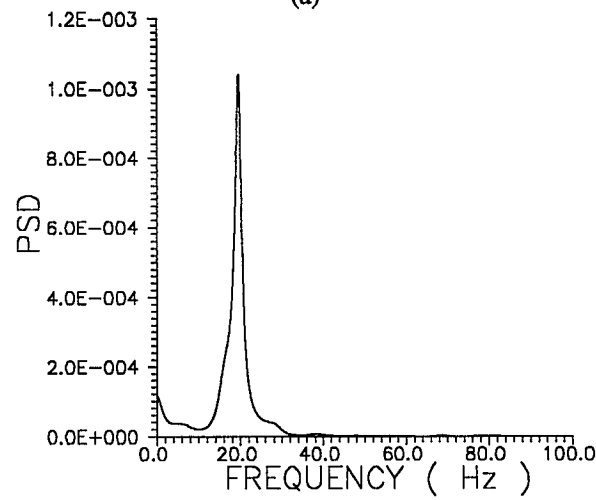


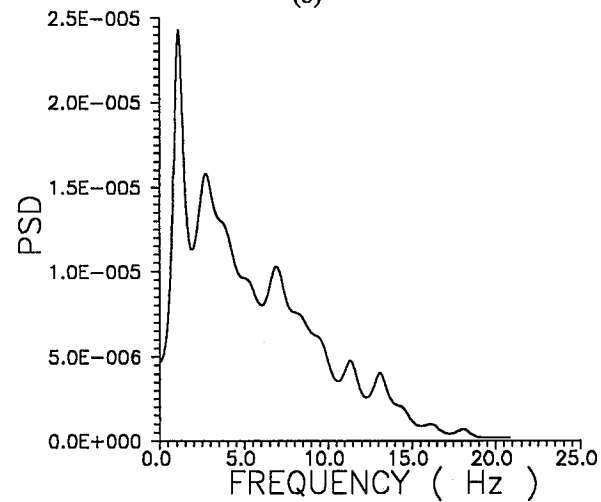
Figure 3 The force versus displacement measured from positions a,b,c and d of figure 4 for the 5-axis gantry robot.



(a)

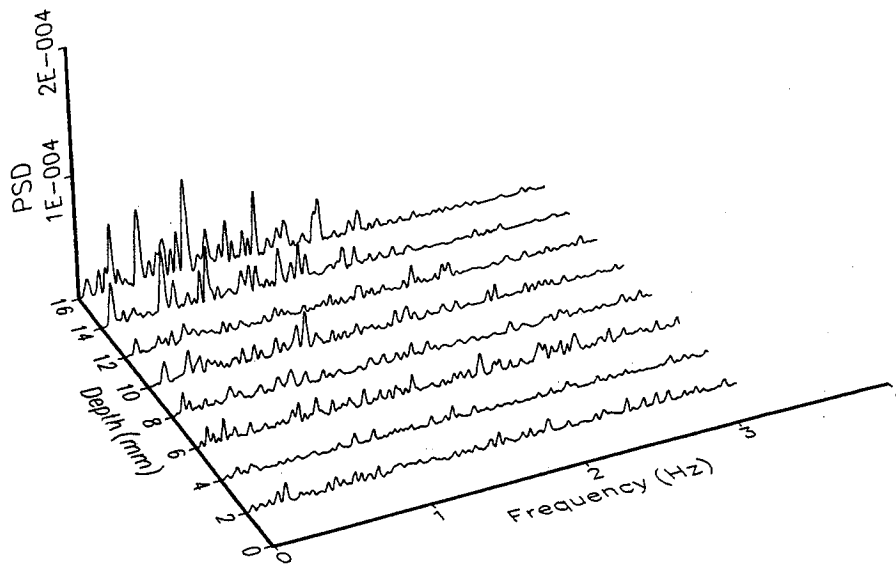


(b)

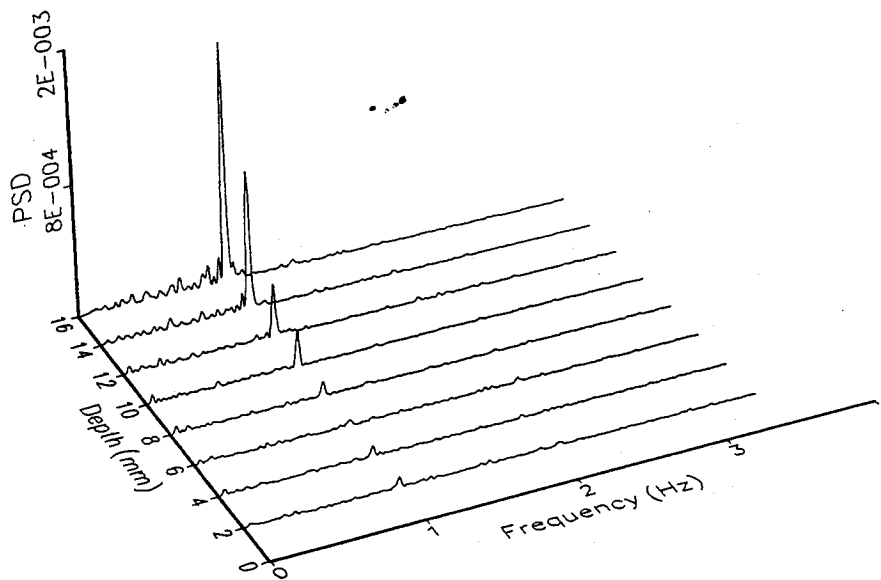


(c)

Figure 4 Power spectra of structure vibration measured at robot arm in (a) Y-direction (b) X-direction, and (c) Y-direction of the end-effector.

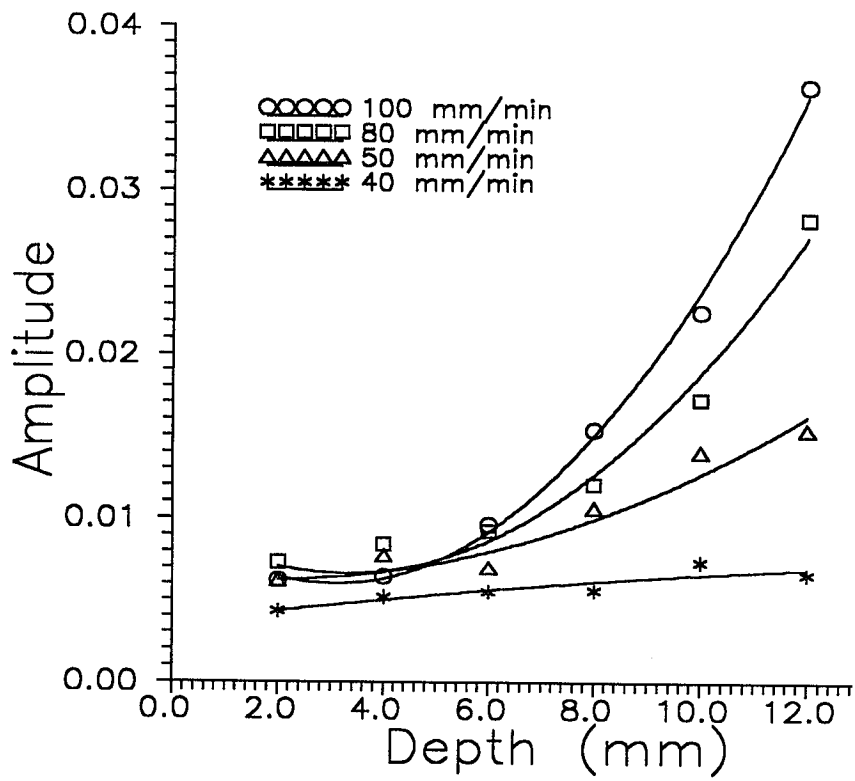


(a)

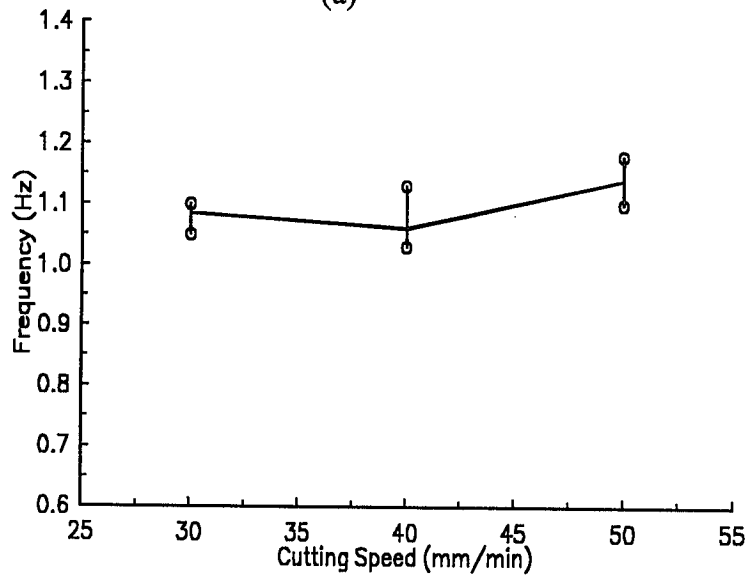


(b)

Figure 5 Power spectral densities measured from different depths. Cutting was done in (a) X-direction and (b) Y-direction.

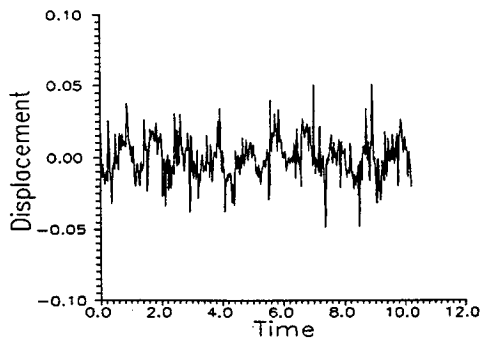


(a)

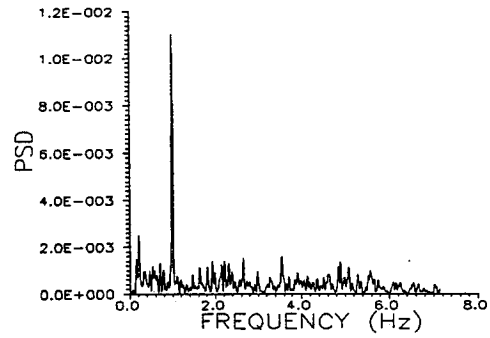


(b)

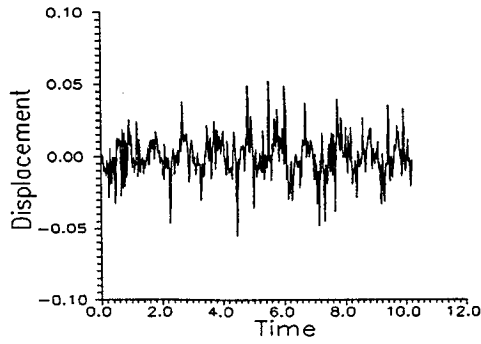
Figure 6 (a) Plot of amplitude of dominant striation versus depth of cut at different cutting speeds. (b) Dominant striation frequency of surface spectra generated at different cutting speeds at the same location.



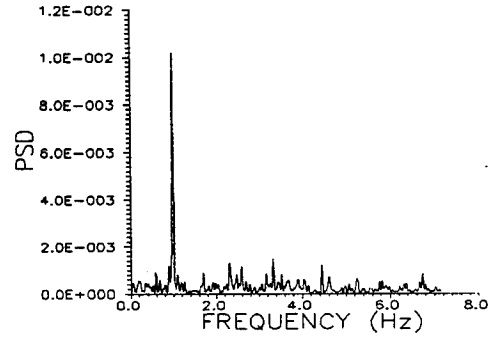
(a)



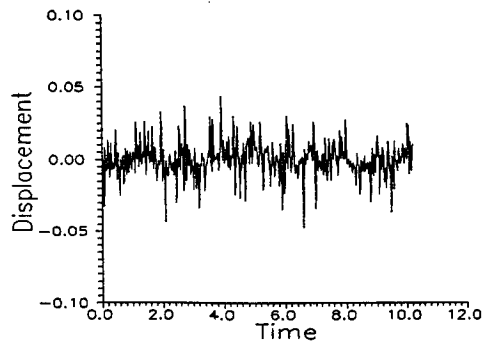
(e)



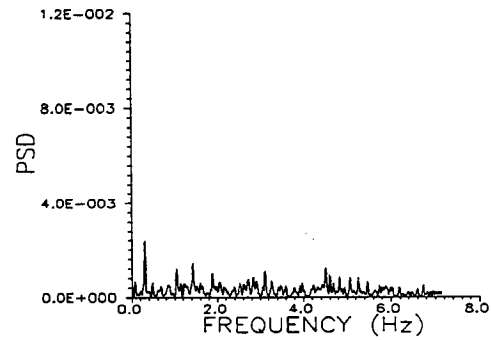
(b)



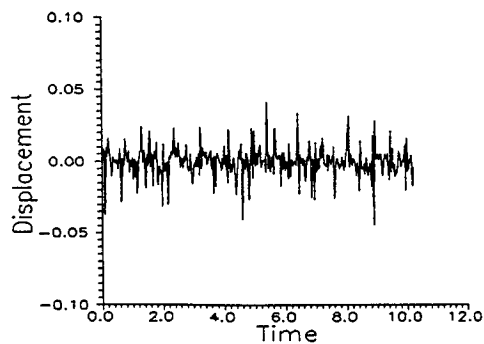
(f)



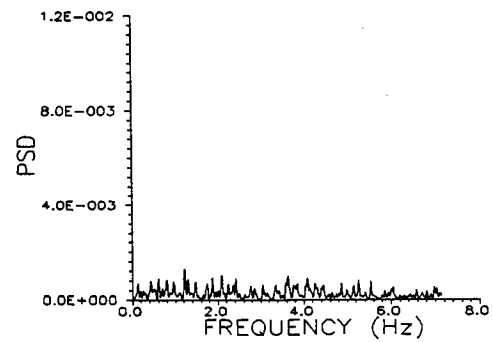
(c)



(g)



(d)



(h)

Figure 7 (a), (b), (c) and (d) are the displacement measured at the positions a,b,c and d shown in the figure 2 . (e) (f) (g) and (h) are the power spectral density of the (a) (b) (c) and (d).

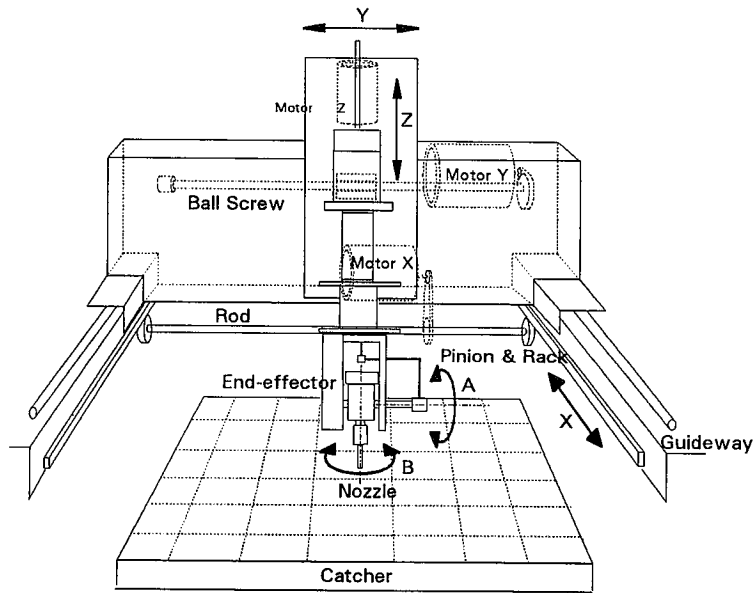


Figure 8 Schematic of the 5-axes robotic machining system.

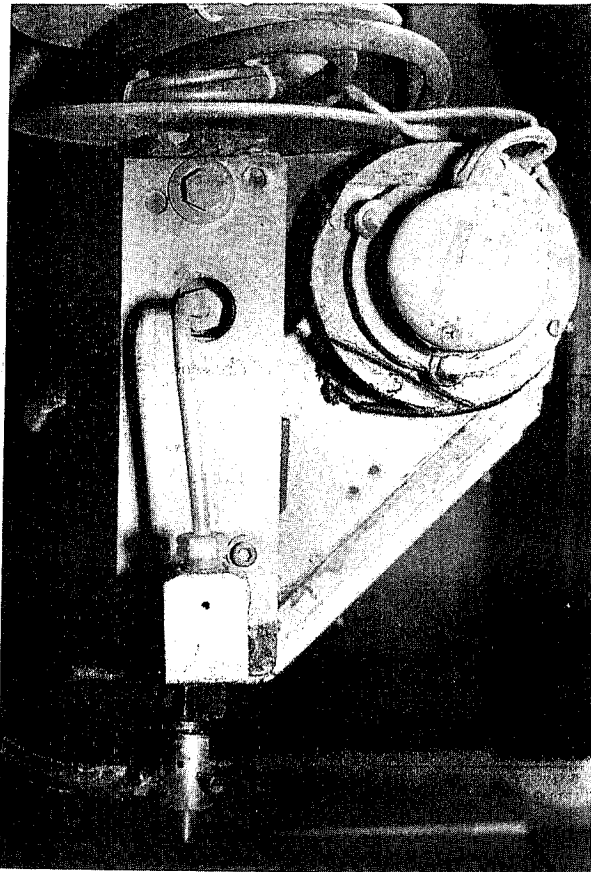


Figure 9 Photograph of pitch motor.

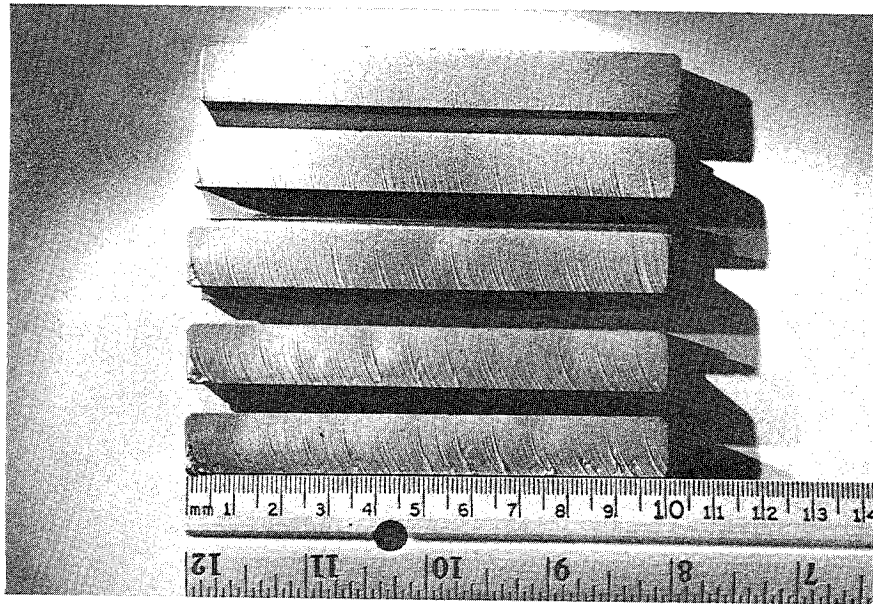


Figure 10 The surfaces were generated at different speeds show the striation marks with same distance apart (8 mm).

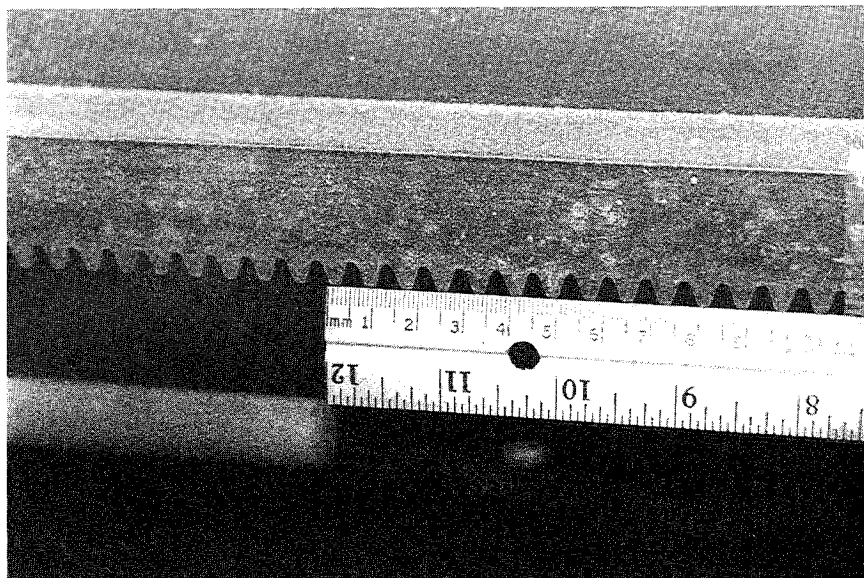


Figure 11 Photograph of the rack with circular pitch equal to 8 mm.

MECHANISMS OF MATERIAL REMOVAL IN ABRASIVE WATERJET MACHINING OF COMMON AEROSPACE MATERIALS

Arola, D. and Ramulu, M.
Department of Mechanical Engineering, FU-10
University of Washington
Seattle, Washington, 98195
USA

ABSTRACT

Two common aerospace structural materials were machined with an abrasive waterjet to distinguish the mechanisms of material removal indicative of the erosion process. Gr/Ep laminate with [0/90/45/-45]_{ns} lay-up and 7075-T6 aluminum were machined with various parametric combinations to inspect change of removal mechanisms as a function of cutting depth and material properties. A machined surface inspection of both the quasi-brittle Gr/Ep and ductile aluminum suggest that material removal occurs predominantly by abrasive micro machining. Abrasive shearing induced brittle fracture mechanisms are predominate in composite machining with limited post-processed constituent disruption and high interstitial integrity. Mechanisms of material removal when machining aluminum are a product of ductile shear induced by scooping and plowing actions of the abrasive particles. Although material removal is deformation induced at jet impingement, ductile shearing mechanisms dominate material removal below this region and throughout the cutting depth. Despite kerf geometry changes with cutting depth, micro-mechanisms of material removal in AWJ machining of both brittle and ductile materials remain constant with cutting depth and are governed by material properties.

INTRODUCTION

The abrasive waterjet (AWJ) is currently utilized for a variety of manufacturing applications. Omni-directional cutting potential as well as minimal thermal and mechanical loading are just a few of the advantages realized when cutting with a water driven abrasive slurry. Most recently the AWJ has been suggested for use in post-mold shaping of composite materials[1-3], particularly Graphite/Epoxy composites[4-6]. Based on drawbacks of conventional shaping techniques with respect to composite trimming and drilling[1,7,8], the aerospace industry has adopted the AWJ for net-shaping component parts molded from FRP's. However, despite current and a continuing development of interest in this machining process, only a limited understanding of material removal mechanisms in AWJ cutting exists. Furthermore, the influence of material properties on the mechanisms of material removal and change in mechanisms with cutting depth have not been reported.

Mechanisms of material removal present in AWJ machining have often been described using theoretical studies of solid particle impact induced erosion. Hashish[9] concluded from a visualization of the cutting process in Plexiglas that material removal may occur by cutting wear and deformation wear, two distinct modes of material removal. Both "cutting wear" and "deformation wear" are definitions derived from theoretical studies of solid particle impact induced erosion by Finnie[10] and Bitter[11,12] respectively. Material removal within these two domains is differentiated by the particle attack angle and ensuing deformation of the material. Erosion at small angles of particle impact is defined as cutting wear. Cutting wear material removal occurs when the shear strength of the material is

exceeded due to abrasive particle shear loading. The "cutting wear zone" is typically identified on an AWJ machined surface by the uppermost portion of the eroded kerf which exhibits a high quality surface texture with limited visible macroscopic variation. Deformation wear erosion is induced by repeated particle bombardment at large impact angles (greater than 20°) and was defined by Bitter[11]. In this mode of abrasive removal the parent material is plastically deformed, work hardened with continual bombardment, and eventually removed due to plastic embrittlement. The "deformation wear zone" in AWJ cutting exists below the cutting wear zone and is typically identified by waviness patterns caused by severe jet deflection. Waviness patterns have been noted in AWJ machining of a variety of materials with uniquely different mechanical properties, both ductile and brittle.

Surface features observed in AWJ cutting of various materials have been defined using the analogy of material removal provided by Hashish[3,9]. Consequently, distinction between the cutting wear and deformation wear mechanisms of material removal in AWJ studies are differentiated by waviness patterns on the kerf. In a number of studies[13-16] it was noted that the geometry of waviness patterns including size and shape appear to be influenced by parametric cutting conditions including pressure, abrasive size and flow rate, and traverse speed. Parametric influence on waviness geometry implies that the choice of cutting parameters may inadvertently influence the mechanisms of material removal. Alternately, this phenomena may imply that waviness patterns are a function of the energy of the impinging jet, not the mechanisms of material removal. Waviness patterns are observed when cutting both ductile and brittle materials which suggests that these patterns are a function of jet energy, not a product of material removal mechanisms. Subsequently, it appears that the mechanisms of material removal remain constant with cutting depth and within both cutting zones. For example, Ramulu et al.[5] observed when machining Graphite/Epoxy laminates that the mechanisms of material removal remain constant with cutting depth. An understanding of the mechanisms of material removal inherent to a machining process is important due to their effect on structural performance. External forces applied to create a new surface through mechanical work can result in a near sub-surface stress field[17]. Interestingly, Burnham et al.[18] found that the cutting force during AWJ machining of alumina, steel, and Gr/Ep increased with jet penetration depth. An increase in cutting force may influence the size and distribution of the residual stress field near the surface in a material susceptible to work hardening. For materials where plastic deformation or brittle fracture occurs, surface properties of the workpiece material may change during material removal.

In this study a common quasi-brittle and ductile aerospace material were machined with an AWJ. Graphite/Epoxy composite laminate and 7075-T6 aluminum were machined with numerous parametric combinations to promote varying degrees of cutting wear and deformation wear zones on the machined surfaces. For each material a visual analysis was conducted to distinguish and differentiate mechanisms of material removal as a function of cutting depth and material properties. Scanning Electron Microscope analysis was conducted at various penetration depths to examine the mechanisms of material removal on a microscopic level. Material removal is discussed with regards to material properties and as a function of the depth of cut in AWJ machining.

EXPERIMENTAL

All experiments were performed with a PowerJet model waterjet, which is driven by a Model 20-35 waterjet pump. Traverse bi-axial feed is produced by the addition of a modified Hardinge milling machine table. Two Dayton Model 42140 DC motors and Model 6x165 motor controllers were fixed to the Hardinge table to provide adjustable, reliable, table feed rates. The milling table is adapted with an aluminum cutting table to support the workpiece and provide a source for clamping the workpiece. Primary components of the nozzle

assembly for this study consist of a 0.3mm diameter sapphire jewel which transforms the high pressure water into a collimated jet, and a 1.0mm diameter carbide waterjet nozzle insert. All machining was conducted with garnet abrasives.

A 16mm thick Graphite/Epoxy laminate composed of 3501-6 resin and IM-6 fibers with stacking sequence $[(0/90/45/-45)_n]_s$ was used for all composite cutting experiments in this study. The average diameter of the graphite fibers is $6\mu\text{m}$ and the volume fraction of the material is near 0.65. A 16mm thick 7075-T6 aluminum stock was also chosen for this study based on its use within the aerospace industry and relatively ductile mechanical properties. Elastic constants for both Gr/Ep and 7075-T6 Aluminum are listed in Table 1.

Graphite/Epoxy specimens were machined from laminate stock parallel to one of the primary fiber directions resulting in fiber directions of 0° , 90° , 45° and -45° realized through the depth of cut. A schematic diagram of specimen geometry and the associated cutting terminology is shown in Figure 1. All specimens were machined a traverse distance of at least 25mm to insure constant cutting conditions were achieved. Design of experiments (DOE) of Taguchi was used in obtaining a total of 27 Gr/Ep specimens involving various parametric combinations of pressure, standoff distance, traverse speed, and grit size. Surface roughness and kerf taper models for AWJ machining of Gr/Ep composites were formulated and previously reported with use of these experiments[5]. A visual analysis indicated varying degrees of waviness on the kerf surface between specimens machined with different parametric combinations. Two specimens which exhibited different degrees of waviness were chosen to conduct further analysis regarding mechanisms of material removal in this study. Two aluminum specimens were machined with the AWJ using parametric levels of the two Gr/Ep specimens chosen for further analysis. Parametric levels used in obtaining the two specimens of each material are listed in Table 2. Scanning Electron Microscope (SEM) analysis was conducted to inspect micro-features of the machined specimens with a Jeoul JSM-T330A Scanning Electron Microscope. SEM micrographs were obtained at various depths along the jet penetration depth to document micro features of abrasive removal.

RESULTS

Graphite/Epoxy

The machined surface of the Graphite/Epoxy laminate specimens are shown in Figure 2. Variation in the macro-features between the two specimens indicates an influence of cutting parameters on removal characteristics. From both a visual and profilometric examination it was noted that the machined surface can be characterized by three macro regions of surface topography. An initially rough region was observed near the jet entrance distinguished by the rounded kerf edge and relatively rough surface texture. This region of the kerf will be referred to as the initial damage zone. The entrance region was followed by a region of notably smooth surface texture with limited damage phenomenon, typically referred to as the cutting wear zone. The third region of surface topography exists from the end of the cutting wear zone to the jet exit edge and is characterized by a rough surface texture and waviness patterns that outline the path of jet deflection. This zone is commonly referred to as the deformation wear zone. These regions of material removal in the machining of Gr/Ep laminates have been discussed previously in terms of surface profilometry by Ramulu et al[5]. Size of these three regions on the face of the machined specimens is dependent on the level of the machine parameters. Note the relatively low degree of waviness on the

surface of Specimen 1 in Figure 2(a) and contrasting well defined waviness patterns of Specimen 2 in 2(b). Specimen 2 exhibits a larger initial damage region due to the higher standoff distance and a well defined, large deformation wear zone attributed to the use of #150 Garnet.

Scanning Electron Microscope analysis was performed to observe micro phenomena of the machined surfaces throughout the cutting depth. Figure 3, 4, and 5 shows micrographs taken within the initial damage, cutting wear, and deformation wear domains of Specimen 1; depth at which the micrographs were obtained are noted as well. For comparison, the removal features of the machined surface are very similar to those reported in a recent study on AWJ machined unidirectional Graphite/Epoxy[4]. As can be seen from Figures 3-5(a), the surface of the 90° plies suggests that abrasive induced brittle removal, including shearing and abrasive micro-machining, are the dominate modes of material removal. The fractured surface of the fibers and surrounding matrix appear to be machined, contrary to regions of macro-fracture induced by cantilever bending which are the effects of sustained loading forces. The cut surface is random in nature due to the host of abrasive attack angles at the face of the penetrating jet. Features of the post-machined fibers and interstitial matrix indicate that independent fracture of the constituents occurs during material removal. Nearly all matrix adjacent to the fibers remains intact in its supportive position after machining. Degrees of fiber pullout and fiber/matrix delamination are limited, possibly a function of the high interfacial bond strength between the constituents coupled with localized cutting forces of the AWJ.

Features of the 0° plies of Specimen 1 at three observation depths are shown in Figures 3-5(b). Again, similar to the 90 degree plies, inspection of the machined surface suggests that abrasive shearing and brittle fracture account for the dominant portions of material removal. Although the surface of some exposed fibers are fractured, the matrix remains intact on the machined surface. Shallow abrasive wear tracks can be distinguished perpendicular to the fiber axis and are caused by stray abrasive particles at the exterior of the penetrating jet. This phenomena is most predominant near the jet entrance region (3b) with combinations of high supply pressure and large abrasives (small Garnet #). Note the increase in wear track angle with cutting depth which is due to the increase in jet deflection with penetration depth. Severity and depth of wear track penetration decreases with observation depth due to the reduction in abrasive kinetic and potential energies.

The surface of +45° and -45° fiber oriented plies along the penetration depth of Specimen 1 are shown in Figures 3-5(c) and (d) respectively. The +45° fibers are those at a positive (clockwise) angle of 45° with reference to the traverse direction and -45° fibers are at angles of 135° with reference to the traverse direction. A +45° fiber ply on one side of the kerf will be oriented at -45° on the corresponding opposite side of the kerf. Similar to the machined surface of the 90° and 0° plies, nearly all the supporting matrix remains intact on the machined surface. The fractured surface of the fibers in the +45° orientation are most often parallel to the machined surface which can be seen in Figures 3-5(c). However, fibers in the -45° orientation are often fractured perpendicular to the fiber axis. Variation in the fracture planes of fibers in these two orientations is attributed to the deflection force of the penetrating jet. Deflection forces compress the fiber within their matrix pocket in the +45° direction, facilitating shearing of the fully supported fibers. However, fibers in the -45° direction are pushed away from their interstitial position within the matrix due to deflection forces. Brittle fracture often occurs perpendicular to the fiber axis due to shear and axial stress distribution due to a combination of cantilever bending and shearing. Features characteristic to AWJ machining of -45° plies are shown in Figure 3-5d. Despite these features, macro damage features including fiber pullout and evidence of either interlaminar or intralaminar delamination are unapparent.

Figures 6-8(a-d) contain micrographs of the machined surface within the three material removal regions of Gr/Ep Specimen 2. As can be seen from these micrographs, distinctions in machined surface characteristics between Specimens 1 and 2 are difficult to make on the micro level. Material removal of the four ply orientations occurred by brittle fracture induced by shear loading of the abrasive particles. The only notable difference in removal features between the two Gr/Ep specimens is that the abrasive wear tracks on the 0° plies of Specimen 2 are not as well defined as those on Specimen 1. This difference is solely due to the smaller abrasive particles used in machining Specimen 2.

Aluminum

Two aluminum specimens were machined with the AWJ using the same parametric combinations as those used in obtaining the two Gr/Ep specimens. Figure 9 provides a macro view of the machined surface of Specimen 1 and Specimen 2. Similar to the machined surface of the Gr/Ep specimens, three zones exhibiting unique surface features can be identified on the kerf wall which vary in magnitude between the two specimens. Specimen 2 exhibits a relatively large and distinct initial damage and deformation wear zone in relation to Specimen 1 which can be distinguished by kerf rounding and the large degree of waviness. Difference in size of these zones is due to the higher standoff distance (2.5mm) and smaller abrasives used in obtaining Specimen 2.

Scanning Electron Micrographs were obtained along the cutting depth of the two aluminum specimens to study the micro-mechanisms of material removal. Micrographs of Specimen 1 obtained at depths of 0.05, 0.2, 2, 4, 8, 12, and 16mm are shown in Figure 10(a-g) respectively. By comparing features in these figures it is easy to distinguish the contrast of the machined surface in Figure 10(a) from the remaining micrographs. Within the initial damage zone considerable deformation has occurred due to the nearly normal repeated impact of abrasives on the exterior of the jet with the ductile aluminum. Repeated normal bombardment of the surface within the domain of the initial damage zone has caused material deformation and displacement but limited material removal. Features of cutting seen in Figures 10(b-g) are quite different from 10(a). Definite wear patterns are easily identified which outline the path of the abrasive particles along the penetration depth. Material removal has occurred by ductile shearing of the aluminum by abrasive scooping and scratching action of the garnet. The only contrasting feature within Figures 10(b-g) is the increasing deflection and more random attack angle of the abrasives with cutting depth. Deflection angle increases with cutting depth as a result of the reduction in the jet capacity for material removal.

Figures 11(a-g) contain micrographs of Specimen 2 along the machined surface at depths of observation previously indicated for Specimen 1. General characteristics of the machined surface exhibited by Specimen 2 are very similar to those noted on Specimen 1. The initial damage zone is larger than that of the first specimen due to the increase in standoff distance used when machining this sample. An increase in standoff distance allows the jet to expand prior to impingement. Initial damage attributed to the normal impact of abrasives on the impingement surface are visible to an approximate depth of 300µm as evident in both Figures 11(a) and (b). Although the size of the initial damage zone of Specimen 2 is considerably larger, the magnitude of material deformation appears to be lower. This is primarily due to the lower energy and potential for deformation of the #150 Garnet in comparison to the larger abrasive used in machining Specimen 1. Below the initial damage zone shear cutting mechanisms are predominant and remain constant with penetration to the point of jet exit. Features of the machined surface which are attributed to abrasive shearing induced by scooping and scratching of the particles are nearly identical to those observed on the surface of the first aluminum specimen in Figures 10(b-g). Size of the indentations on the surface of Specimen 2 are shallow due to the size and lower energy of the smaller

abrasive particles. With an increase in cutting depth the deflection angle and randomness in abrasive particle attack angle increases similar to the trend observed on Specimen 1.

DISCUSSION

Three macro regions were noted on the machined surface of the Gr/Ep and aluminum specimens. The first region begins from the jet entrance and extends to a depth which is dependent on the level of the AWJ cutting parameters. Quality and depth to which this region extends were found to be dependent on the grit size and standoff distance for both materials. Characteristics of this mode include initial damage on the top of the specimen and rounding of the entrance kerf. On the two Gr/Ep specimens, abrasive wear tracks were formed on the face of the kerf in the 0° plies due to fracture of the brittle fibers. The extent of the initial damage region is more severe on Specimen 2 (Gr/Ep) due to the brittle fracture characteristics of this material. In contrast, the initial damage region on both the aluminum specimens is characterized by extensive plastic deformation due to the normal component of the impacting abrasives. Aluminum specimens were able to absorb energy from normal impact of the abrasives through plastic deformation.

The second characteristic macro region on the surface of the machined specimens exists between the initial "damage" zone and the beginning of the waviness patterns at greater cutting depths. This region is typically referred to as the cutting wear zone[9,15]. Limited surface variations within this domain result from a combination of optimum coherency of the abrasive slurry with low exterior abrasive particle energy and minimal jet deflection. The abrasive slurry in this region has a bell-shaped energy density with high interior energy and low exterior intensity. Low energy levels of the outer region of the jet are a result of the imposition of drag from the kerf/jet interaction. Material removal in AWJ machining of the Gr/Ep specimens within this region occurs by brittle shearing mechanisms as shown in Figures 3-5(b-c) and 6-8(b). Ductile shearing mechanisms were responsible for material removal in AWJ machining of the aluminum specimens within this cutting zone. Figures 10(b-e) and 11(c, d) provide views of ductile removal on the kerf of the two aluminum specimens. Comparison in surface features presented by the aforementioned figures illustrates the similarity in abrasive particle path along the kerf surface of both materials. Abrasives within the slurry in this region are only slightly influenced by deflection forces of the reaction between slurry and kerf material. The path of the dominant portion of abrasives are primarily parallel with little randomness attributed to impact related or water current induced deflection. This property of the jet within the cutting wear domain is responsible for the uniformity in surface texture with minimal variation.

The third region of surface texture with distinct macro features is located below the cutting wear zone and extends to the jet exit edge on the kerf surface. This zone is evident by the formation of waviness patterns due to deflection of the penetrating jet as seen in Figures 2, and 9. Although deflection patterns were noted on all 4 specimens in this study, waviness was most predominant on the surface of the Gr/Ep and aluminum Specimen 2. Specimen 2 was machined with #150 Garnet. The mechanisms of material removal within this zone can be observed in Figures 5, and 8 for the Gr/Ep specimens and in Figures 10(f-g), and Figures 11(e-g) for the aluminum specimens. In both materials it was found that the mechanisms of material removal remained constant with AWJ parameters by comparing Specimens 1 and 2. Similarly, mechanisms of removal remained constant with cutting depth in both materials despite the increase in jet deflection and formation of waviness patterns. Brittle shear mechanisms were responsible for cutting of the quasi-brittle Gr/Ep specimens due to properties of the brittle fibers. However, ductile shear mechanisms including scooping and abrasive scratching were responsible for material removal of both aluminum specimens. These observations are in agreement with those in a previous study

by Ramulu et al[5] in Gr/Ep machining and those of Bitter[11,12]. Bitter observed in abrasive erosion of both brittle and ductile materials that the degree of either cutting wear or deformation wear material removal is dependent on the parent material properties. Despite the abrasive impact angle, material removal is governed by the material properties.

Observations of this study may appear to conflict with results from a study by Burnham et al.[18] in which he observed that cutting force in AWJ machining increases with cutting depth for both brittle and ductile materials. These trends are easily described. An increase in cutting force with penetration depth is primarily a result of longer loading duration during material removal with greater cutting depths. Elements from fracture mechanics can be used when machining brittle materials to suggest that crack initiation and growth is much lower at greater cutting depths due to lower particle velocities. A reduction in impact energy reduces crack initiation and severely reduces ensuing growth. Thus on a micro level, the duration of loading is greater due to the absence of fracture induced unloading creating higher cutting forces. For ductile materials a similar argument is used without the use of fracture mechanics. The duration of loading at greater cutting depths increases when machining ductile materials due to the decrease in material removal with jet energy and particle velocity. A decrease in material removal results in an increase in absorbed energy and inherent cutting force.

Definitions used to describe macro regions on the surface of an AWJ machined material have developed an inaccurate understanding of material removal indicative of this process. Despite the use of the terms cutting wear and deformation wear by Bitter they do not address the mechanisms of material removal within these regions in AWJ machining. When machining brittle materials, material removal occurs by shearing induced brittle fracture. Contrary to machining brittle materials, ductile shearing mechanisms are responsible for material removal in ductile materials except within the initial damage zone. Within this region deformation wear material removal occurs due to the nearly normal impact of abrasives with the target material and its ability to absorb impact energy under deformation. From an outline of the abrasive particle path with penetration depth provided by Figures 3-8 in Gr/Ep and by Figures 10 and 11 for aluminum we see that abrasives follow a piece-wise continuous path along the deflected jet. Contrary to previous assumptions, deformation wear does not at greater cutting depths. If deformation wear occurred with increased cutting depth a discontinuity in abrasive path would be noted which outlines normal abrasive impact with rebounding and glancing deflections.

From the observations and simple descriptions provided by this study a more thorough understanding of material removal in AWJ machining is developed. However, with this understanding we realize that waviness patterns on the surface of the kerf must be a function of jet energy only. Formation and geometry of these patterns are inadvertently a function of material properties which influence jet energy. Ductile materials are able to absorb jet energy through both elastic and plastic deformation. For this reason, jet deflection induced waviness is more severe in ductile materials. This was noted by comparing surface features of the aluminum and Gr/Ep surfaces of both Specimens 1 and 2. The cyclic nature and regularity of these patterns must be attributed to hydrodynamic factors of the jet combined with aspects of abrasive slurry and parent material interaction. Additional work in this area is needed and will enhance our understanding of these phenomena in AWJ machining.

CONCLUSIONS

A Graphite/Epoxy composite laminate and 7075-T6 aluminum were machined with an AWJ to distinguish and study the influence of cutting depth and material properties on the mechanisms of material removal. From a thorough micro-analysis of the machined surfaces the following conclusions can be made.

Material removal when machining Graphite/Epoxy occurs by brittle shearing mechanisms which fracture and micro-machine the constituents of the composite material.

AWJ machining of aluminum is a product of ductile shearing mechanisms including abrasive scooping and scratching of the parent material. These mechanisms are fully described by cutting wear.

Mechanisms of material removal present in when machining both Gr/Ep and aluminum do not change with cutting parameters. AWJ cutting parameters influence the macro features of the machined surface only.

Within the initial damage zone material removal may occur by deformation wear due to the normal impact of abrasives with the parent material. The degree of deformation wear is governed by the ductility of the material; a low ductility results in low degrees of deformation wear and high ductility will be subject to higher degrees of deformation.

Mechanisms of material removal below the initial damage zone in AWJ machining of both ductile and brittle materials do not change with cutting depth despite the macro features observed.

REFERENCES

- 1] König W., Wulf, Ch., Grab, P., and Willerscheid, H., "Machining of Fibre Reinforced Plastics", Annals of the CIRP, Vol. 34, No. 2, 1985, pp. 537-548.
- 2] Hamatani, G. and Ramulu, M., "Machinability of High Temperature Composites by Abrasive Waterjet", Journal of Engineering Materials and Technology, September 22, 1989.
- 3] Hashish, Mohamed, "Machining of Advanced Composites with Abrasive-Waterjets", Manufacturing Review, Vol. 2, No. 2, June 1989, pp. 142-150.
- 4] Ramulu, M., and Arola, D., "Waterjet and Abrasive Waterjet Cutting of Unidirectional Graphite/Epoxy Composite", Composites, Vol. 24, No. 2, 1992.
- 5] Ramulu, M., and Arola D., "The Influence of Abrasive Waterjet Cutting Conditions on the Surface Quality of Graphite/Epoxy Laminates", Accepted for publication in IJMTM, 1992.
- 6] Arola D. "Surface and Subsurface Topography of an Abrasive Waterjet Machined Graphite/Epoxy", Masters Thesis, University of Washington, 1991.
- 7] Colligan K., and Ramulu M., "The Effect of Edge Trimming on Composite Surface Plies", Manufacturing Review, Vol. 5, No. 4, 1992, pp. 274-283.
- 8] Wern, C. W., Ramulu, M., Colligan, K., "A Study of the Surface Texture of Composite Drilled Holes", Journal of Material Processing and Technology, Vol. 37, No. 1-4, 1993, pp. 373-389.
- 9] Hashish, M., "On the Modeling of Abrasive Waterjet Cutting", 7th Int Symp. of Jet Cutting Technology, Ottawa Canada, June 26-28, 1984, pp. 249-265.

- 10] Finnie, I., "The Mechanism of Erosion of Ductile Metals", Proc. 3rd National Congress of Applied Mechanics, ASME, 1958, pp. 527-532.
- 11] Bitter, J. G. A., "A Study of Erosion Phenomenon-Part I", Wear, 6, 1963, pp. 5-21.
- 12] Bitter, J. G. A., "A Study of Erosion Phenomenon-Part II", Wear, 6, 1963, pp. 169-190.
- 13] Tan, D. K., "A Model for the Surface Finish in Abrasive Waterjet Cutting", 8th Int. Symp. on Jet Cutting Technology, Durham, England, September 9-11, 1986, pp. 309-313.
- 14] Blickwedel, H., Guo, N. S., Haferkamp, H., and Louis, H., "Prediction of Abrasive Jet Cutting Performance and Quality", Proc. of 10th International Conference on Jet Cutting Technology, 1991, pp. 163-179.
- 15] Hashish, M., "Characteristics of Surfaces Machined with Abrasive-Waterjets", ASME Conference Proceedings, San Francisco, California, Dec 10-15, pp.23-32.
- 16] Kovacevic, R., Liaw, H. H., Barrows, J. F., "Surface Finish and its Relationship to Cutting Parameters", SME Technical Paper, MR88-589, Proceeding on the Third International Grinding Conference, Fontana, Winsconsin, October 4-6, 1988.
- 17] Kruszynski, B. W., Van Luttervelt, K. A., "The Influence of Manufacturing Processes on Surface Properties", Advanced Manufacturing Engineering, Vol. 1, July 1989.
- 18] Burnham, C. D., and Kim, T. J., "Statistical Characterization of Surface Finish Produced by a High Pressure Abrasive Waterjet", 5th American Waterjet Conference, Toronto, Canada, August 29-31, 1989, pp. 165-175.

Table 1 Mechanical Properties

Properties	Graphite/Epoxy		7075-T6 Aluminum	
	0 degrees	90degrees	Yield	Ultimate
Tensile Strength (MPa)	1378	41.34	4	579
Tensile Modulus (GPa)	117.1-137.8	7.6-11.0	7.2	N/A
Compressive Strength (MPa)	1309	N/A	69	N/A
Compressive Modulus (GPa)	106.8-124.0	N/A	7.2	N/A

Table 2 Gr/Ep and Aluminum Machining Conditions

Machine Parameters	Specimen 1	Specimen 2
Pressure (MPa)	241	241
Standoff Distance (mm)	1	2.5
Traverse Speed (mm/s)	3.9	3.9
Grit Size (Garnet #)	80	150

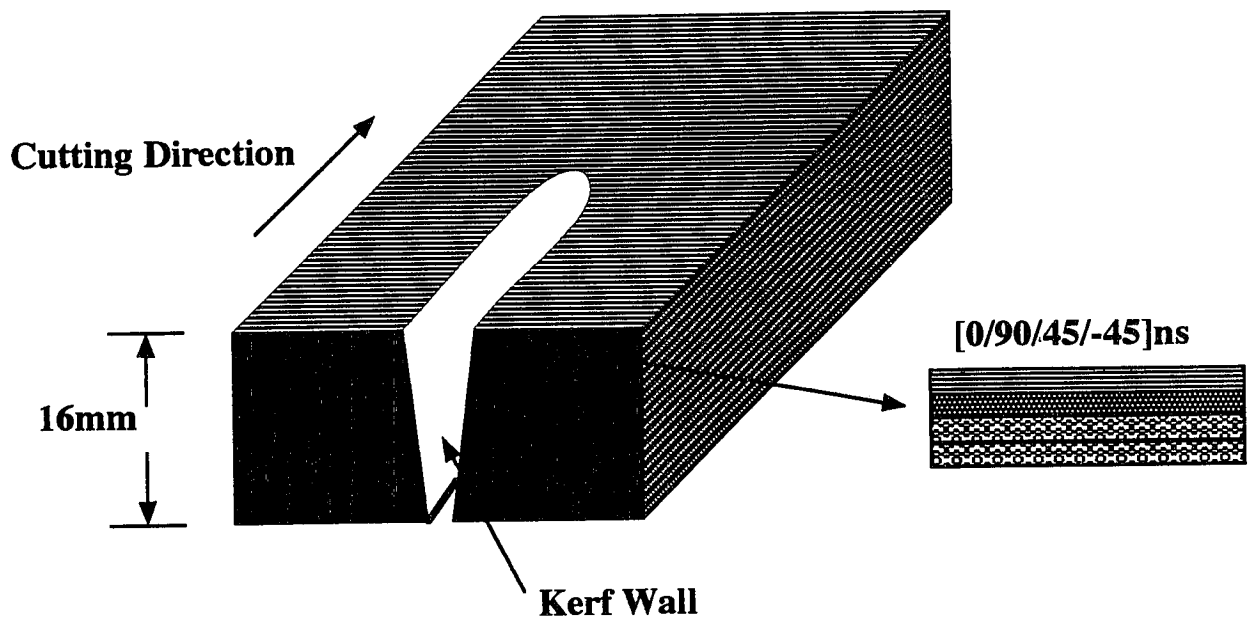
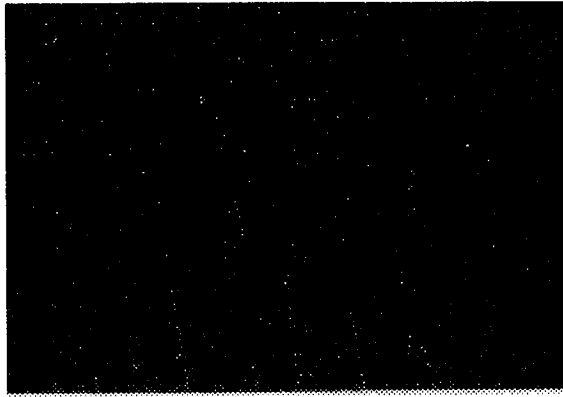
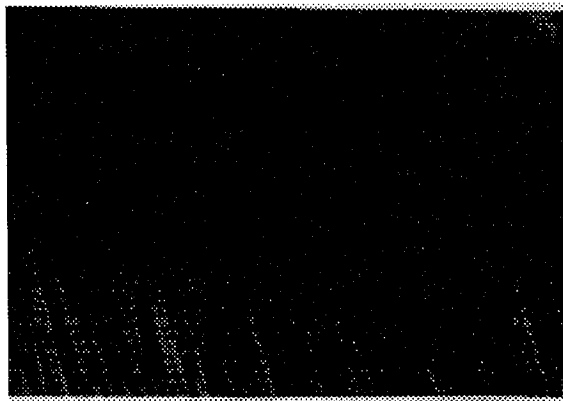


Figure 1 Schematic Diagram of AWJ Machined Gr/Ep Laminate

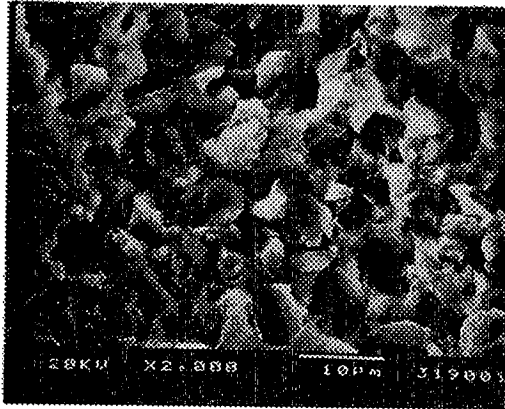


a) Specimen 1

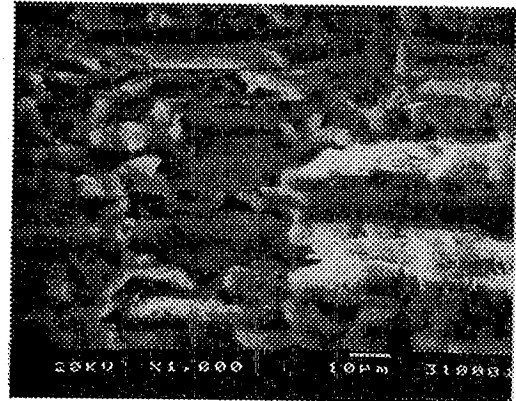


b) Specimen 2

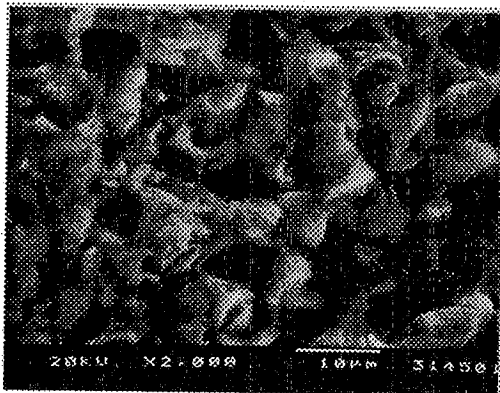
Figure 2 AWJ Machined Graphite/Epoxy Laminate Specimens



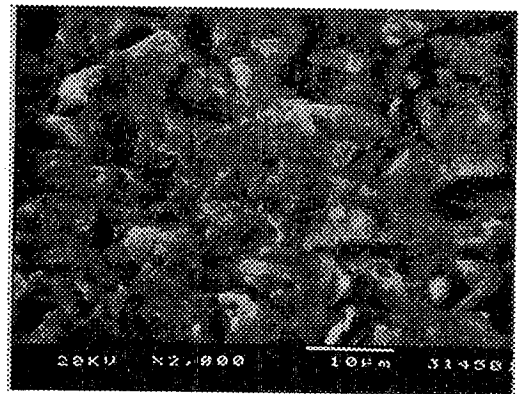
a) 90° ply at 100µm depth



b) 0° ply at 300µm depth

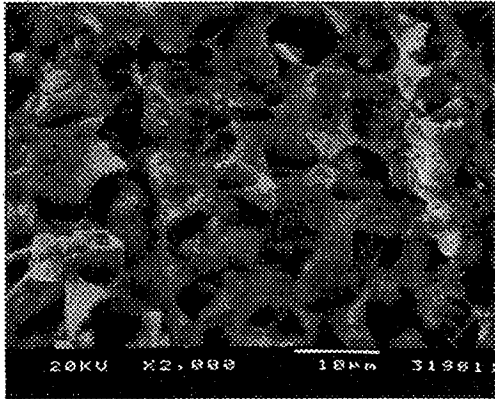


c) 45° ply at 500µm depth

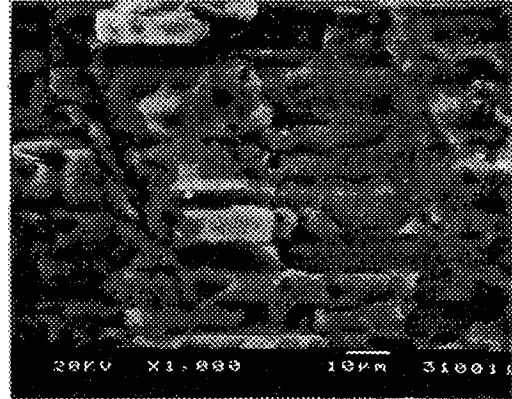


d) -45° ply at 700µm depth

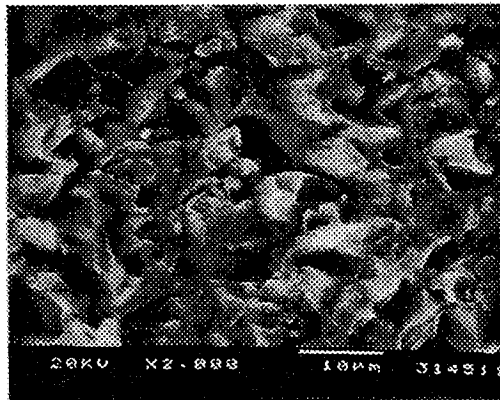
Figure 3 Initial Damage Zone of AWJ Machined Gr/Ep Laminate Specimen 1



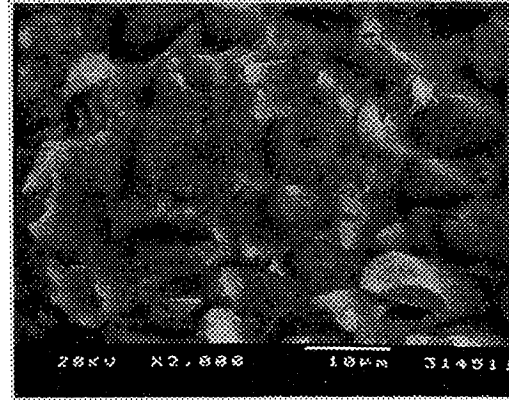
a) 90° ply



b) 0° ply

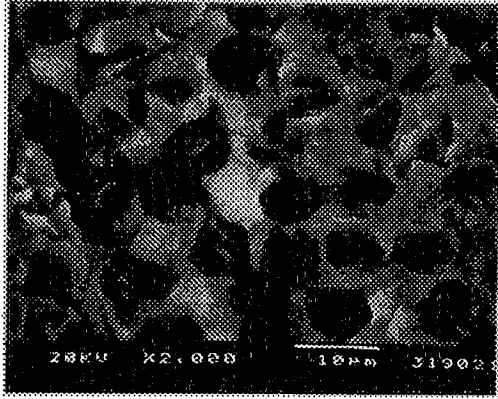


c) 45° ply

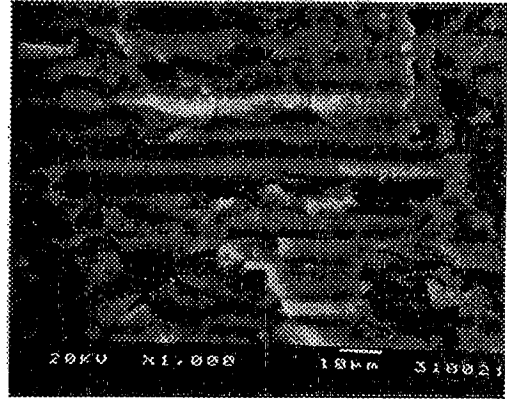


d) -45° ply

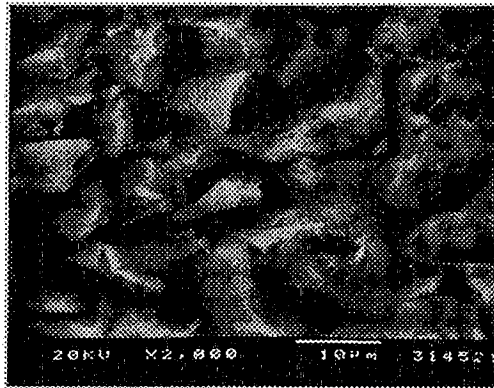
Figure 4 AWJ Machined Gr/Ep Laminate Specimen 1 at 5.0mm depth



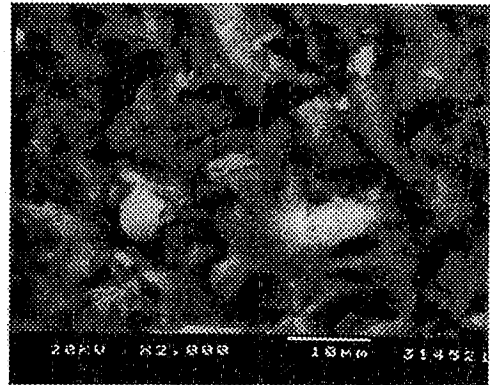
a) 90° ply



b) 0° ply

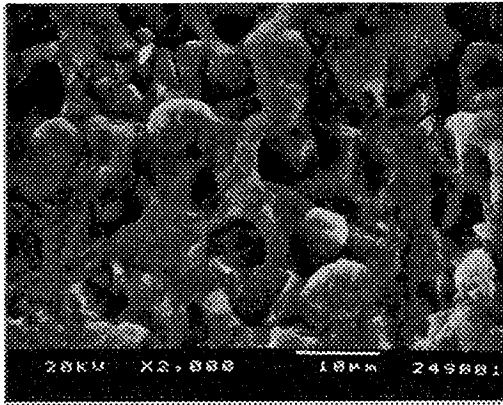


c) 45° ply

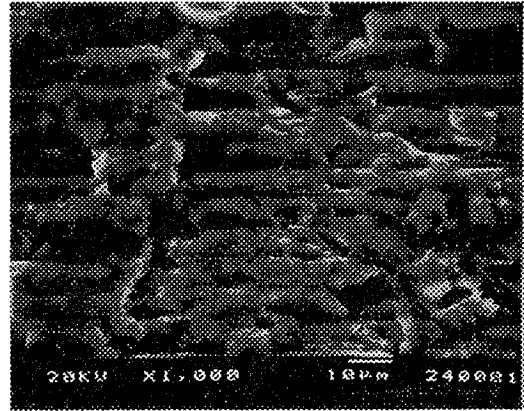


d) -45° ply

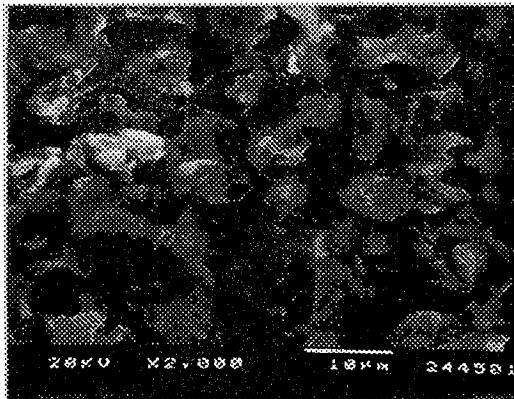
Figure 5 AWJ Machined Gr/Ep Laminate Specimen 1 at 12.0mm depth



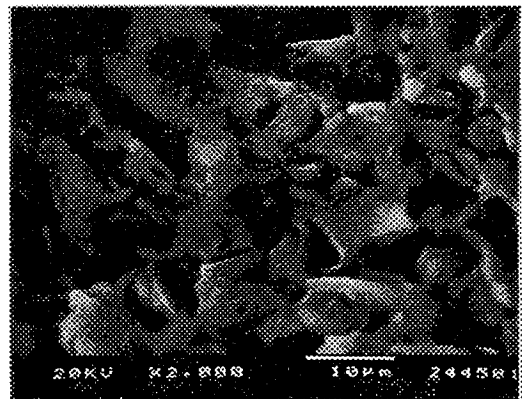
a) 90° ply at 100µm depth



b) 0° ply at 300µm depth

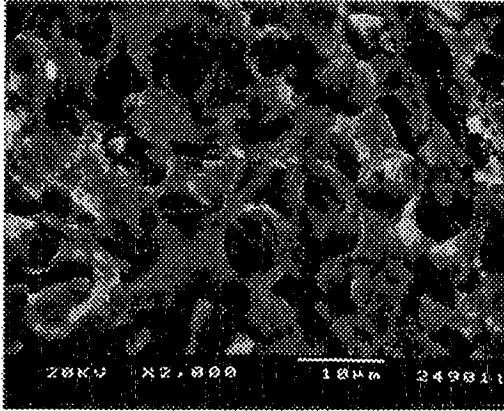


c) 45° ply at 500µm depth

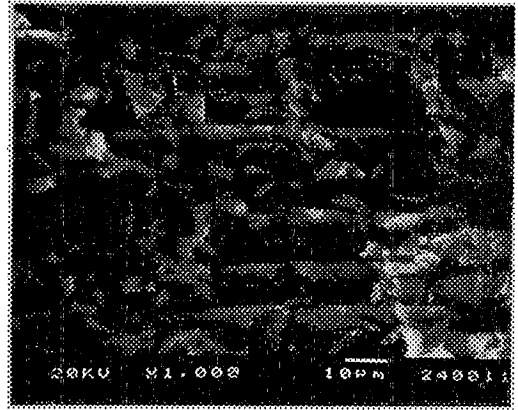


d) -45° ply at 700µm depth

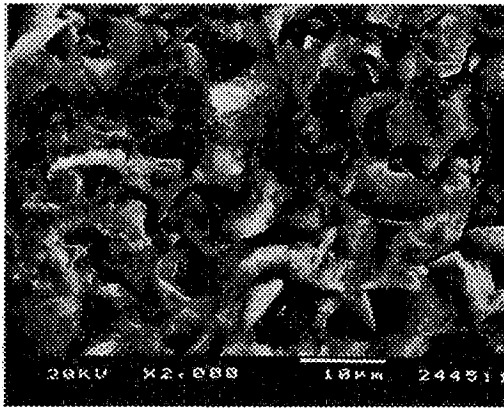
Figure 6 Initial Damage Zone of AWJ Machined Gr/Ep Laminate Specimen 2



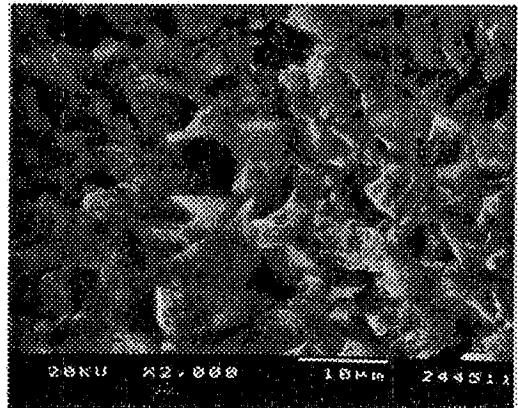
a) 90° ply



b) 0° ply

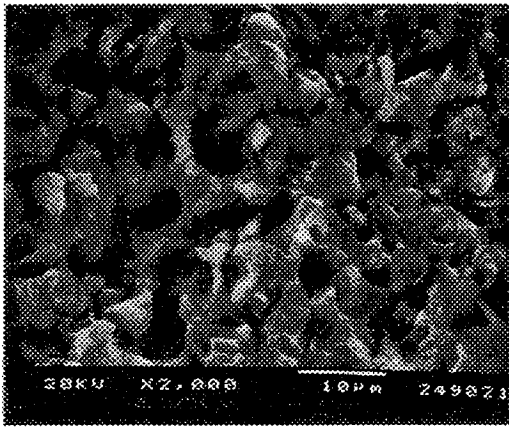


c) 45° ply

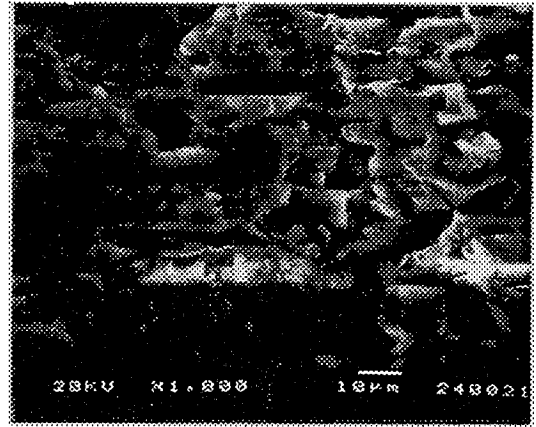


d) -45° ply

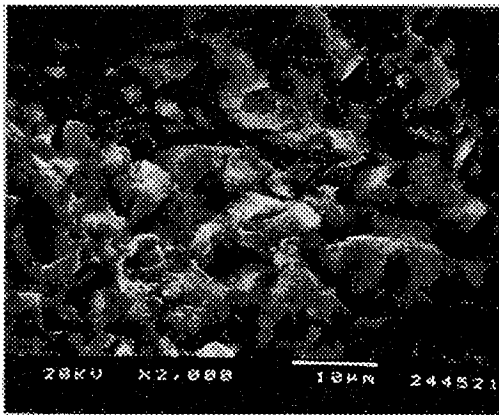
Figure 7 AWJ Machined Gr/Ep Laminate Specimen 2 at 5.0mm depth



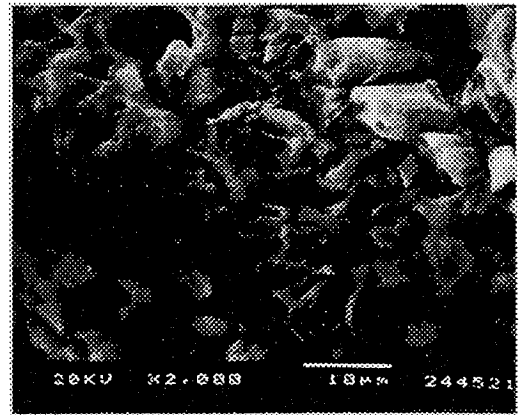
a) 90° ply



b) 0° ply

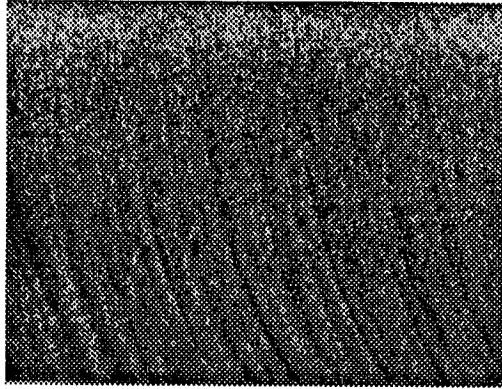


c) 45° ply

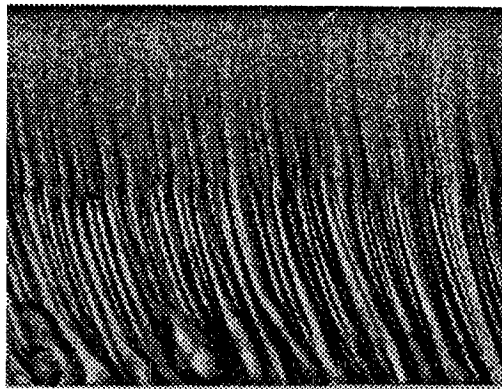


d) -45° ply

Figure 8 AWJ Machined Gr/Ep Laminate Specimen 2 at 12.0mm depth



a) Specimen 1

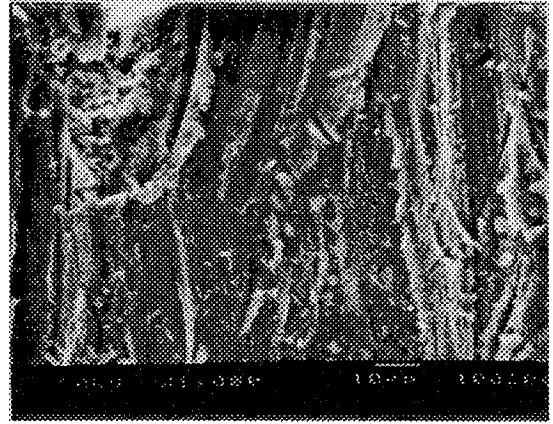


b) Specimen 2

Figure 9 AWJ Machined 7075-T6 Aluminum Specimens



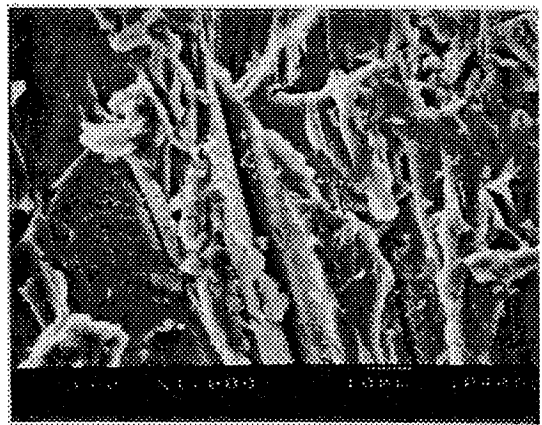
a) 50 μ m



b) 200 μ m



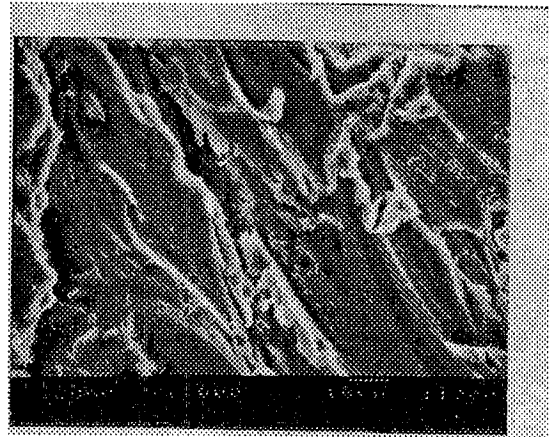
c) 2mm



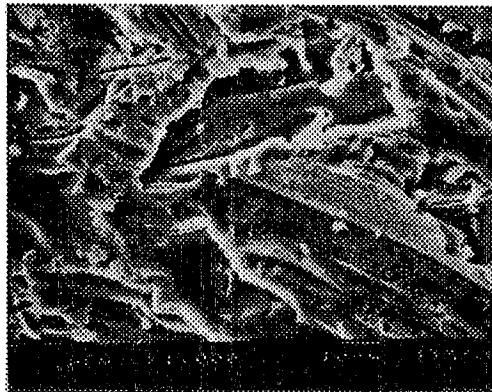
d) 4mm



e) 8mm

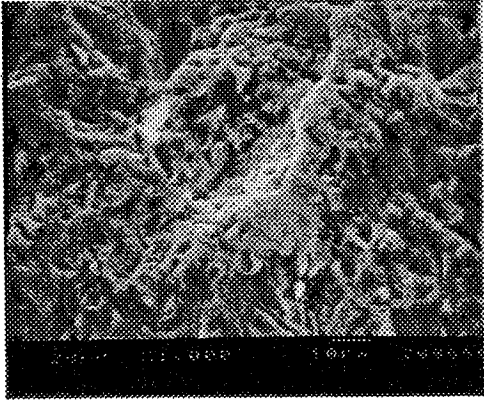


f) 12mm



g) 16mm

Figure 10 AWJ Machined 7075-T6 Aluminum Specimen 1 Micrographs.
Depth of observation noted



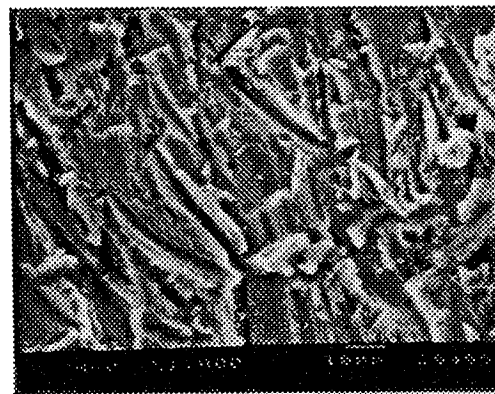
a) 50 μ m



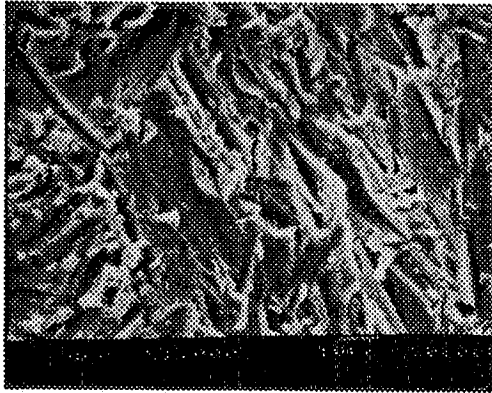
b) 200 μ m



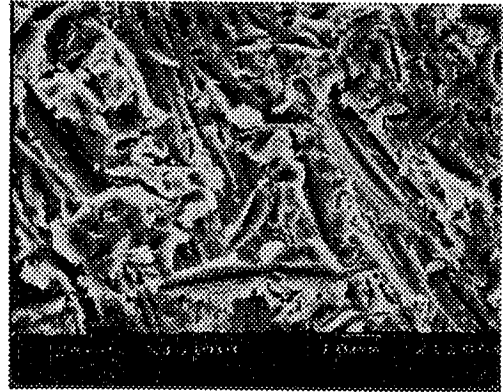
c) 2mm



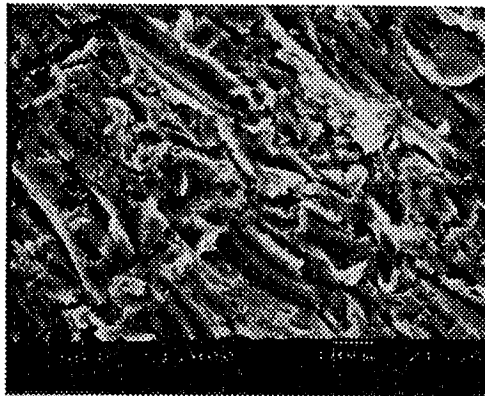
d) 4mm



e) 8mm



f) 12mm



g) 16mm

Figure 11 AWJ Machined 7075-T6 Aluminum Specimen 2 Micrographs.
Depth of observation noted

AN OPTICAL TECHNIQUE TO VISUALIZE THE ABRASIVE WATERJET GENERATED STRESS FIELDS

H. Yeh, F. X. Wang, and M. Ramulu
Department of Mechanical Engineering, FU-10
University of Washington
Seattle, WA, 98195 U.S.A.

ABSTRACT

An optical technique was developed to determine the principle stresses associated with the jet penetration process by simultaneously recording the on-line isochromatics and isopachics. A two dimensional dynamic photoelastic method is used to obtain isochromatics at the jet impingement zone in a specimen which is made of a polycarbonate epoxied on a Plexiglas. A new approach by using reflective interference optical method is conducted to record simultaneously the summation of the principle stresses in the vicinity of the impacting zone. By synchronized operation of these two methods, a real time stress state of the abrasive waterjet penetration process can be found. Some preliminary results are shown here to demonstrate the possibility of this new approach.

1. INTRODUCTION

Abrasive waterjet (AWJ) machining process has been introduced to industry for almost ten years[1]. Improving the ability of the AWJ cutting process, especially in its application to hard-to-cut material is growing [2-6]. However the mechanics of abrasive waterjet cutting is complex and our knowledge of the machining process is limited. Understanding the stress field associated with the jet cutting allow one to optimize the equipment and process, such that cutting energy and material system can be used in more economic ways. To meet such a requirement, investigations applying two dimensional dynamic photoelastic technique on the waterjet piercing process have been conducted. Daniel et al. [6] were the first to utilize dynamic photoelasticity in characterizing material failure due to waterjet impact. In addition, they found that the fragmentation and material removal phenomena is related to stress waves induced fracture, and the material properties. Wong [7], and Ramulu et al [8] successfully applied dynamic photoelasticity by using an Imacon high speed camera system to record the maximum shear stress state at the initial stage of the abrasive waterjet penetration process in polycarbonate material. Recently Ramulu et. al. [9] reported additional experimental results comparing the stress field of waterjet and the abrasive waterjet impingement process. So the mechanism within each stage of time during the penetration is defined. The stress field associated with the process in terms of the difference of the principle stresses, $\sigma_1 - \sigma_2$ were evaluated.

However, knowledge of the maximum shear stress within the abrasive waterjet impact region is not sufficient to fully understand the mechanism of material removal. To enhance our realization of material removal at the vicinity of jet impingement, knowledge of individual stress components and its distribution is essential . Thus, an effort was made to optically record the summation of the principle stresses simultaneously during jet penetration. The combination of $\sigma_1 - \sigma_2$ and $\sigma_1 + \sigma_2$, can be used to evaluate the stress distributions of σ_1 and σ_2 separately. Although there are many methods available to obtain $\sigma_1 + \sigma_2$, but they either have difficulties to apply on dynamic situation like abrasive waterjet impingement process or do not fulfill our real time requirement. In this paper, we report a new approach called *carrier wave method* used in conjunction with photoelasticity to record the isopachics (summation of principal stresses) and the isochromatics (difference of the principle stresses) by synchronizing the two optical systems in real time.

2. CARRIER WAVE METHOD

The concept of the carrier wave method is to combines the laser holography and the traditional photoelasticity which makes it possible to get the summation of the principle stresses $\sigma_1 + \sigma_2$. As we know, the strain in the thickness direction can be written as

$$\varepsilon_z = \frac{-\nu}{1-\nu}(\varepsilon_x + \varepsilon_y) = -\frac{\nu}{E}(\sigma_x + \sigma_y) \quad (1)$$

or

$$\varepsilon_z = \frac{\Delta t}{t} \quad (2)$$

where t is the thickness of the material.

To measure the variation of the specimen thickness Δt , we utilized the reflective properties of material and wave length of the light source. A collimated light is used to illuminate on a transparent specimen strained under applied load. As the light enters the specimen, the reflected

light from the rear surface will interfere with the reflected light from the front surface. Gratings thus formed due to such interference is named as carrier waves. The thickness of the specimen can be related to wave length and reflective index of the work as:

$$t = K \frac{\lambda}{4n} \quad K=0, 1, 2, \dots \quad (3)$$

where λ is the wavelength of the light source, e.g. for He-Ne laser, $\lambda \cong 632.8$ nm, K is integer, n is the reflective index of the specimen. An illustration describes this concept is shown in Figure 1. The grating will be in dark field when K is odd, and light field for K is even. The difference in the thickness can be obtained by subtracting these gratings before and after the deformation of the specimen.

When carrier wave gratings are used, a density of around 5~20 lines/mm is recommended to achieve sufficient resolution. By double exposure of a frame of the film when taking pictures for zero-load and loaded specimen we will obtain a new set of fringes formed by the intersected nodal points of those two original carrier waves. This set of new fringes represents the summation of principle stresses, $\sigma_1 + \sigma_2$. The light intensity on that frame of film is

$$I_{\text{total}} = 2C \left(1 - \cos \frac{\theta}{2} \cos \frac{\theta + 2\alpha}{2}\right) \quad (4)$$

where C is a constant,
 $\alpha = 2kN_0t_0$,

$$\theta = kt_0 \left(A + B - \frac{2N_0 \nu}{E}\right) (\sigma_1 + \sigma_2).$$

θ and α are the phase differences before and after loading, and k represents the wave number which is equal to $2\pi/\lambda$. And N_0 , t_0 is the material reflective index and the thickness respectively before loading. A , B are the reflective constant in the principle directions. θ varies slower than α , which produced the "beat" phenomenon on the film in which low spatial frequency fringes overlap on carrier waves. Such circumstance implies that the low frequency fringes were carried by the original high frequency gratings. However, if we let $\theta = N_p \pi$, $N_p = 1, 3, 5, \dots$, these are dark field fringes. With some additional mathematical simplification, we will have the stress-optic relation as

$$\sigma_1 + \sigma_2 = \frac{N_p f_p}{2t_0}, \text{ in other words these fringes are isopachic fringes. Where } f_p \text{ is a material constant}$$

and has to be determined experimentally by using diametral compression test. By combining this relation with the isochromatic stress-optic law will yield σ_1 and σ_2 independently.

3. EXPERIMENTAL WORK

In current tests, we use a Powerjet model 20-35 high pressure abrasive waterjet system to conduct the jet impact process on the specimen. The polycarbonate specimen of 6.35 mm thick is epoxied to a piece acrylic of the same thickness. A layer of aluminum of about 80 nm thick is coated on the acrylic surface to enhance light reflection without significantly reducing light passage through the specimen. An illustration of the specimen geometry is shown in Figure 2. A 20 mW He-Ne polarized laser of wavelength 632.8 nm has been used as the light source with a spatial filter and an aspherical lens were used to generate collimate light. Two Nikon F-3HP cameras without lenses were used to record photoelasticity and the carrier wave method images synchronically. Two 50 mm focal length Plano-convex lenses were used in front of each camera to form the image directly on the film.

An electronic system which was used to trigger the high speed camera system [8]. An illustration depicting the entire experimental setup is shown in Figure 3. A series of experiments were performed using a water supply pressure of 103.4 MPa, garnet abrasive of size #80, and the abrasive flow rate of 3 g/s. Isochromatic and isopachic fringe patterns were recorded continuously and simultaneously during the jet exposure time of one second.

Figure 4 show the typical dynamic photoelastic fringe patterns associated with the abrasive waterjet penetration process. Note that the difference in principal stress field clearly decreased with the jet exposure time and the depth of jet penetration. The results are consistent with our previously reported results. The corresponding dynamic isopachic fringe patterns are shown in Figure 5. Each fringe line shown in the fringe record represents the constant value of the sum of the principal stresses.

4. SUMMARY

The possibility of utilizing the carrier wave method in combination with photoelasticity to record the stress distribution of the abrasive waterjet impingement process has been demonstrated. By using this approach a full field data can be recorded in real time and with a data reduction algorithm in progress, the distributions of σ_1 and σ_2 are yield separately. This could enhance our understanding on the mechanics of material removal during abrasive waterjet machining process.

5. REFERENCES

1. Hashish, M., " Visualization of the Abrasive Waterjet Cutting Process" *Experimental Mechanics*, Vol. 28, No. 2, 1988, pp. 159-169.
2. Hamatani, G., and Ramulu, M., " Machinability of High Temperature Composites by Abrasive Waterjet" *ASME PED-35* , 1988, pp. 49-62.
3. Ramulu, M., and Arola. D., " Waterjet and Abrasive Waterjet Cutting of Unidirectional Graphite/Epoxy Composite" *Composites* , Vol. 24, No. 4., 1993.
4. Kim, T. J., Sylvia, J.G., and Posner, L., " Piercing and Cutting of Ceramics by Abrasive Waterjet", *ASME PED-Vol. 17*, ASME, 1985, pp.19-25.
5. Hashish, M., " Machining of Advanced Composites with Abrasive Waterjets" *Manufacturing Review* , Vol. 2, No. 2, 1989, pp.142-150.
6. Daniel, I. M., Rowland, R. E., Labus, T. J., "Photoelasticity Study of Waterjet Impact," *Proceedings of the Second International Symposium on Jet Cutting Technology*, Paper A1, BHRA, Cambridge, UK, 1974.
7. Ramulu, M., Wong, K.-P., "Preliminary Investigations of Abrasive Water Jet Piercing Process by Dynamic Photoelasticity," *International Journal of Water Jet Technology*, Vol. 1, No. 2, Sep. 1991.
8. Wong, K.-P., "Photoelastic Investigation of Abrasive Waterjet Machining," *Master Thesis*, Department of Mechanical Engineering, University of Washington, 1990.
9. Ramulu, M., Yeh, H., Wong, K.-P., Raju, S. P., "Photoelastic Investigation of Jet Piercing Process," *Proceedings of the sixth American Water Jet Conference*, pp.1-15, Water Jet Technology Association, Houston, Texas, 1991.

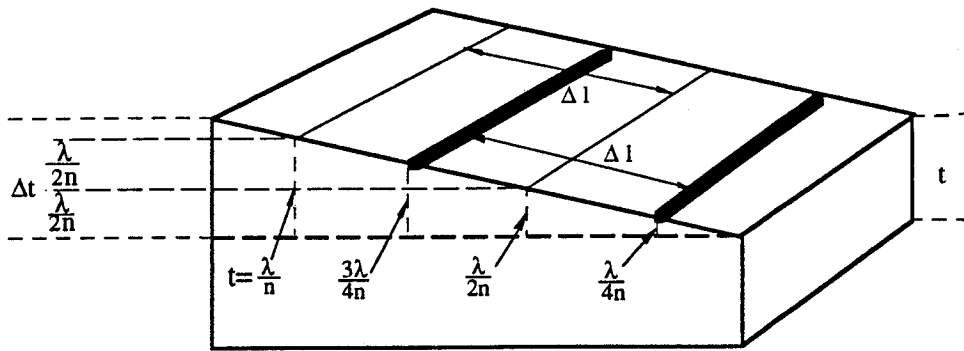


Figure 1. The Formation of Fringes on a Transparent Specimen

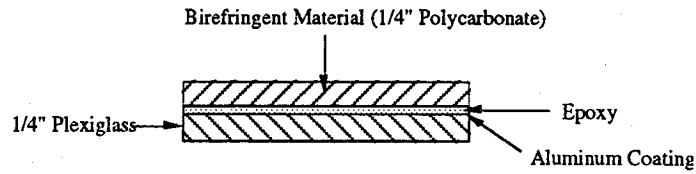


Figure 2. Specimen

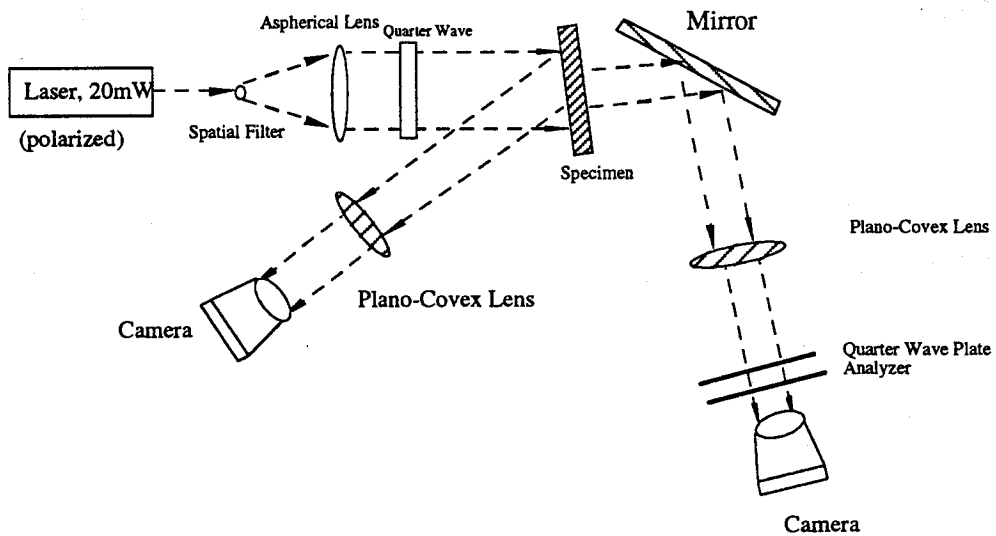


Figure 3. Experimental Setup

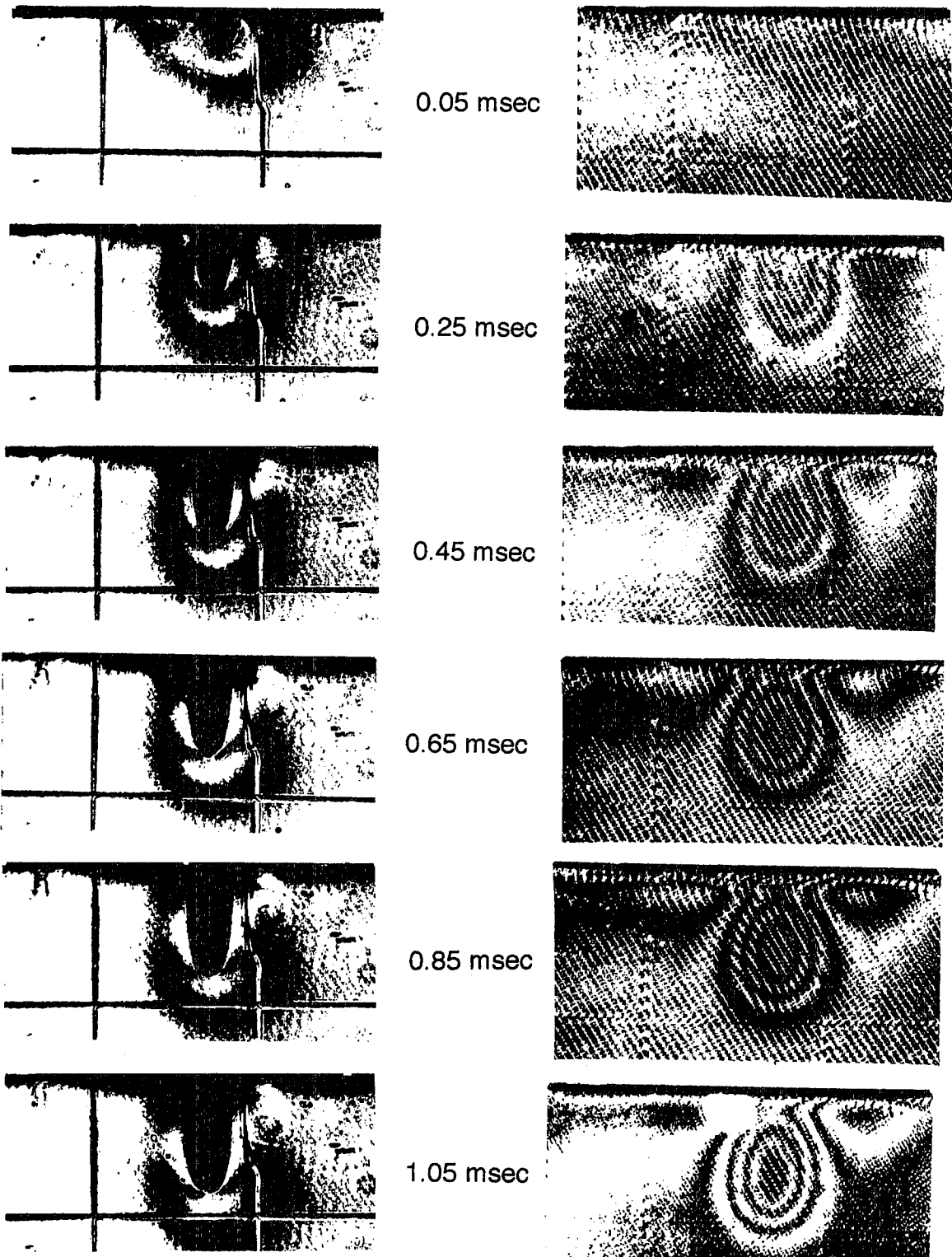


Figure 4. Dynamic Isochromatic Fringes

Figure 5. Dynamic Isopachic Fringes

TARGET RESPONSES TO THE IMPACT OF HIGH-VELOCITY, NON-ABRASIVE WATER JETS

S-W. Kang, T. Reitter, G. Carlson
Lawrence Livermore National Laboratory, Livermore, CA 94550

J. Crutchmer, D. Garrett, P. Kramer, B. Do
Mason & Hanger, Pantex Plant, Amarillo, TX 79177

ABSTRACT

Theoretical and experimental investigations have been performed on the effects of a non-abrasive water jet impinging on a solid surface. The theoretical analysis treats the time-dependent, two-dimensional case of an axisymmetric jet impacting on a rigid or non-rigid surface at various velocities, up to 1500 m/s. The numerical results obtained include time-dependent pressure distributions and jet geometry near the surface. The maximum calculated pressures agree well with the "water-hammer" values when modified for high-velocity jets. Impact and machining experiments were conducted with various materials with water jet reservoir pressures up to 276 MPa (40,000 psi). Test results show that maximum mass removal rate takes place when the standoff distance is several hundred nozzle diameters from the nozzle, suggesting that at this long distance the jet has disintegrated into a series of ligaments and drops impinging on the surface. Analytical and experimental efforts are continuing on determining the dominant mechanisms for the target response to high-velocity jets.

Work performed under the auspices of the U.S. Department of Energy by Lawrence Livermore National Laboratory under Contract W-7405-Eng-48, and at Pantex Plant.

1. INTRODUCTION

We are interested in ultimately determining dominant mechanisms governing the material cutting processes with non-abrasive water jets. In this paper we describe the preliminary approaches taken on this complex phenomenon, and will concentrate our discussion on the problem of efficient mass removal processes.

A survey of literature on water jet cutting technology reveals many approaches and insights, ranging from the use of simple water jets to abrasive and cavitating jets in an effort to accomplish effective removal of the target material.

The subject of material removal by high velocity water is not new, judging from the number of publications available in the open literature on this topic. Many aspects of the phenomena have been investigated, from steady-jet cutting to multiple-droplet erosions in both ductile and brittle materials. Sample publications are: Bowden and Brunton (1961), Field (1966), Leach and Walker (1966), Franz (1974), Neusen and Schramm (1978), Hashish and duPlessis (1978a, 1978b, 1979), Louis and Schikorr (1982), Pidsley (1983), Whiting et al. (1990), Springer (1976) and Tikhomirov et al. (1992).

We are particularly interested in identifying the physics governing the most efficient mass removal process when a material is subjected to water jet impacts. Many mechanisms have been proposed and analyzed in the literature: see, for example, Bowden and Brunton (1961).

One major issue seems to be whether the most efficient mass removal is due to a steady, intact jet impinging on a material or due to multiple drop impacts. See Franz (1974) and Conn (1974). This question appears to be still relevant.

On the other hand, there seems to be a consensus on the existence of an "optimum" standoff distance at which the mass removal rate is greatest. Reference is made to the works of Louis and Schikorr (1982), Hashish et al. (1978b) and Franz (1974), among others.

Because we are primarily concerned with identifying the most efficient mass removal rate, our first task in tackling the complex jet cutting phenomena was to conduct some preliminary experiments and initiate theoretical analyses. On the experimental front measurements were made of the removal rate of aluminum vs. the standoff distance under various nozzle designs and pressure conditions. On the analytical front, the related problem of determining the pressure characteristics when a jet impinges on a material has been addressed, both when the material surface is rigid and when the material is deformable. The rigid case was first investigated to obtain the maximum attainable pressure levels for a given jet impact velocity.

In subsequent sections we describe the experiments and the theoretical analyses performed and the preliminary results obtained from both of these efforts.

2. EXPERIMENTAL AND THEORETICAL ANALYSES

2.1. Jet Cutting Experiments

2.1.1. Experimental Setup.

Two nozzles were used to produce high-velocity water jet cutting on 6061-T0 and 6061-T6 aluminum bars 25 mm x 25 mm x 150 mm (1" x 1" x 6") with a feed rate of 2 mm per second (5 in. per minute). Figure 1 shows the detailed cross-sectional view of one of the nozzles, (nozzle A). The internal configuration of the other nozzle (nozzle B) is not shown here because of the proprietary nature of its design. Both nozzles are designed and produced by A.M. Gatti Corp.

For the tests the following typical operating parameters were used:

Nozzle reservoir pressure = 69 MPa (10,000 psi) to 276 MPa (40,000 psi);

Nozzle diameter = 0.25 mm (0.01 in.) and 0.36 mm (0.014 in.);

Nozzle length to diameter ratio = 2;

Ambient gas = air at 1 atm.;

Other parameters not mentioned above will be given as they occur in the text.

2.1.2. Preliminary Test Results.

Although we have obtained many test data under a variety of conditions, only some relevant and representative results will be presented here. Specifically, we discuss three aspects of the results: (a) The jet velocities and structures; (b) The mass removal rate vs. standoff distance; and (c) Optimum standoff distance vs. pressure.

The Jet Velocities and Structures. The velocity of water jets produced by the nozzles A and B was measured by the method of volume conservation. Table 1 lists the exit velocities of the jet at various reservoir pressures for the nozzle diameter of 0.35 mm (0.014 in.). The table shows that the velocities from nozzle A are somewhat larger than those from nozzle B. This is attributed to differences in the two nozzle designs.

In addition, the jet shapes emanating from each nozzle also differ widely from each other. This can be most clearly seen from the photographs taken of the jet core by using an infra-red film with the exposure time of 0.5 microseconds (Figure 2). The jet structure from nozzle A is shown in Figure 2A, wherein the jet begins to spread soon after exiting from the nozzle. By contrast, the jet stream from nozzle B (shown in Figure 2B) is remarkably coherent and remains so for a long distance from the nozzle.

Test results show that nozzle B is more efficient than nozzle A in removing mass from the target material, and therefore our subsequent discussion will deal with the results obtained using nozzle B.

Mass Removal Rate vs. Standoff Distance. Figure 3 shows the removal rate of 6061-T0 aluminum as a function of the standoff distance for nozzle B when the reservoir pressure is 138 MPa (20,000 psi). From Table 1 the jet stagnation pressure is 53 MPa (7650 psi), which is less than the material yield strength of 124 MPa (18,000 psi). Thus the effects of the jet-stagnation pressure alone are unlikely to cause any mass removal from the aluminum surface.

In Figure 3 we observe no mass removal in the first 15 mm (0.6 in.) from the nozzle exit. However, mass removal is observed beyond this distance. The maximum removal rate occurs at a distance of 145 mm (5.7 in.), about 405 nozzle diameters from the nozzle.

Similar results have been obtained for higher reservoir pressures. For instance, the case of 276 MPa (40,000 psi) is shown in Figure 4. The stagnation pressure for this case has been measured to be 109 MPa (15,900 psi), which is still lower than the target yield strength of 124 MPa (18,000 psi).

Again, no mass removal is observed in the first 12 mm (0.5 in.). Beyond this distance the jet begins to cut the material, and its cutting (removal) rate is larger than that for the lower pressure. The maximum removal rate occurs at about 175 mm (6.9 in.) from the nozzle exit, i.e., at about 495 nozzle diameters.

We reiterate that while no mass removal takes place at certain standoff distances, at other distances the jet can cut the material, even though the jet stagnation pressure at these locations is lower than the failure stress of the material. Therefore, some physical factors other than the stagnation pressure- effect appear to be at work in eroding the target material. This will be discussed later in Section 2.1.3.

Optimum Standoff Distance vs. Pressure. Inspection of the mass removal rate vs. standoff distance in Figures 3 and 4 yields the conclusion that there exists an optimum standoff distance at which the removal rate is maximum. This finding is not new, but is consistent with the previous analyses, notably Franz (1974), Conn (1974) and Louis and Schikorr (1982), among others. The present results on the measured optimum distance as a function of the reservoir pressure are shown in Figure 5. A monotonic increase in the standoff distance is observed for the pressure range of 69 MPa (10,000 psi) and 276 MPa (40,000 psi). Since the nozzle diameter is 0.35 mm (0.014 in.), these optimum lengths are sizable in terms of the nozzle diameter. For instance, at the lowest tested pressure of 76 MPa (11,000 psi) the optimum distance is about 280 nozzle diameters, and at 276 MPa (40,000 psi) it is about 500 nozzle diameters. Granting that the jet from nozzle B is very coherent, such lengths are nevertheless remarkably long distances from the nozzle exit.

2.1.3. Discussion of Test Results.

The results presented in the previous section, albeit highly preliminary, suggest that:

- (a) the material can be cut only at certain standoff distances;
- (b) there exists an optimum distance at which the rate is maximum;
- (c) this optimum distance is located very far from the nozzle exit.

Because our primary interest lies in the dominant processes involved in the maximum removal rate, we confine our subsequent discussions to the removal behavior at the optimum standoff distance only. That is, our discussion will center on the jet-material interaction in what Louis and Schikorr (1982) call "Regime III" .

The question arises as to whether at these optimum standoff distances the jet stream impinges on the surface as an intact jet, or as a disintegrated jet. This question is relevant, because different kinds of impact characteristics will be imposed on the target material depending upon the jet stream shapes.

Therefore the jet-flow phenomena constitute an important aspect of the mass removal processes using water jets. And indeed survey of literature supports this, considering the large number of publications on the subject, notably Tikhomirov et al. (1992), Grant and Middleman (1966), Kusui (1968), Dunn (1974), Yanaida and Ohashi (1978), Phinnney (1975), Mansour and Chigier (1990), Hiroyasu et al. (1982), and Shimizu et al. (1988).

Our particular interest is in estimating the intact jet length under given flow conditions. For the nozzle geometry used in the present tests and for the reservoir pressures ranging from 69 MPa (10,000 psi) to 276 MPa (40,000 psi), the estimate of the intact jet length is less than 200 nozzle diameters, based on Hiroyasu et al. (1982), Tikhomirov et al. (1992). These estimates are consistent with the present results; for example, for the case of 138 MPa (20,000 psi) reservoir pressure the intact length for nozzle A was estimated to be 63 mm (about 180 nozzle diameters), while that for nozzle B was 71 mm (2.8 in.), or equivalently, about 200 nozzle diameters.

By comparison, the optimum standoff distances for the most efficient mass removal far exceed the jet-intact lengths (about 200 nozzle diameters), as can be seen from Figure 5. In fact, the optimum standoff distances are sometimes as large as 500 nozzle diameters.

Therefore, we interpret the present test results as follows:

- (a) The maximum mass removal takes place at a distance far beyond the intact length of the jet;
- (b) The jet structure arriving at the material is no longer intact, and consist mainly of ligaments and drops;
- (c) These ligaments and drops then impinge on the target material in a series of "water hammer" blows, whose instantaneous pressures exceed the material yield strength, thus eroding the target material.

2.2. Theoretical Analyses of the Target Responses to Jet Impacts.

In view of the above preliminary test results on the jet impacts on the target surface, we have initiated analytical efforts to calculate the target response to a jet impact and the flow field as a function of time. We first analyze the case of a cylindrical jet impacting on a rigid surface. This will yield the maximum possible pressure that can be imposed on a target material. Following this, we address the case of a jet impacting on a deformable material and analyze the target responses as a function of time.

For analysis of both these cases a "hydrodynamics" numerical code called CALE2D was utilized. This code, developed at LLNL by Tipton (1992), computes both the fluid and solid characteristics for two-dimensional (i.e., axisymmetric or planar), inviscid and compressible flow situations. Although the code can use both the Lagrangian and Eulerian meshes in an arbitrary manner, we have performed the numerical calculations in the pure Eulerian mode. Details of the analysis can be found in Reitter and Kang (1993).

2.2.1. Jet Impact on a Rigid Surface.

Here we consider a circular water jet impinging on a rigid, non-deformable surface. This problem is important in that the peak pressure obtained at the rigid surface sets an upper bound to the pressure that any material can experience during the entire jet impact processes.

The jet diameter for this case is taken to be 0.127 mm (5 mil). The velocity of the jet varied from 200 m/s to 1,500 m/s.

Numerical results obtained for the above cases all display qualitatively similar behaviors. Therefore, the results for the jet velocity of 1,000 m/s will be discussed in greater detail here as a representative case.

Figure 6 shows the pressure history at the centerline stagnation point, labeled Location X. The first peak pressure is seen to be about 3800 MPa (550 ksi) and represents the highest pressure that the surface will experience. This magnitude is much greater than the nominal jet stagnation pressure of 500 MPa (72.5 ksi). As discussed by Brunton (1966) and others, the centerline jet behavior at the moment of impact simulates the one-dimensional "water-hammer" responses.

We now give an expression for the pressure across a one-dimensional water-hammer compression wave. The pressure has been experimentally measured by Cook, et al. (1962), and the test data have been correlated by Heymann (1968):

$$p_1 - p_0 = \rho_0 C_0 V_j \left(1 + 2 \frac{V_j}{C_0} \right) \quad (1)$$

where the term p denotes pressure, ρ the liquid density, C the sound speed, and V_j the flow velocity. The subscripts 0 and 1 signify conditions in the undisturbed liquid region and the compressed liquid region, respectively. Huang et al. (1973) have also derived a correlation expression, but Eq.(1) is deemed to be a sufficiently accurate correlation.

The correlation given above is general, in that it applies to low velocities as well as high velocities, up to about 2,000 m/s. We note that at low velocities, Eq.(1) reduces to the more-familiar expression, $p = \rho_0 C_0 V_j$.

When the present numerical result for the first peak pressure at the stagnation point is compared with Eq.(1), the agreement is excellent. Such an agreement with the one-dimensional expression suggests that the pressure at Location X is one-dimensional at the moment of impact, at least for a brief period of time. However, owing to the two-dimensionality of the flow, this peak value is short-lived, since the jet now begins to expand in a radial direction. The time lapse when the "one-dimensional" water-hammer pressure magnitude begins to decrease depends upon the radius of the jet, and in the present case of 1,000 m/s velocity and 0.127 mm jet diameter, this time has been calculated to be approximately 0.05 microseconds.

Other Velocity Cases. We now discuss the theoretical calculations made for velocities other than 1,000 m/s. The velocities considered are: 200 m/s, 440 m/s, 720 m/s and 1,500 m/s, the latter being the water sound speed under standard conditions. The peak-pressure histories at Location X are shown in Figure 7. All of these pressure histories show a peak at first impact and then gradually subsiding to their respective nominal stagnation pressures. As in the case for 1,000 m/s jet velocity, these peak values closely agree with the magnitudes estimated from the one-dimensional water-hammer values.

This problem has also been addressed by others, for example, Pritchett and Riney (1974). We shall see that the present results, employing different numerical schemes, agree well with their results, as well as the measured impact pressures by Brunton (1966), confirming the validity of the present approach.

We briefly summarize this section by stating that: (a) the peak pressure at the centerline stagnation point upon first impact is momentarily one-dimensional; and (b) therefore we can estimate this maximum pressure by the simple water-hammer expression given in Eq. (1). This is a useful result, inasmuch as such a step obviates the need to engage in complicated calculation procedures for two-dimensional, time-dependent flows just to obtain the maximum impact pressure levels.

We emphasize, however, that two-dimensional flow analysis must be used to obtain any other, more general, flow and material response characteristics.

2.2.2. Jet Impact on a Deformable Material.

Having performed the calculations of the two-dimensional flow field and the pressure histories of a jet impinging on a rigid surface at various velocities, we now turn our attention to the case of a jet impacting on a deformable material. For this purpose, 6061-T6 aluminum was used as the benchmark target material, as it is also being used as one of the materials for our mass-removal experiments.

Analysis of this case requires as input conditions not only the equation of state for water but also the dynamic response characteristics of the solid material. The appropriate material properties for aluminum have been incorporated into the numerical code. The material failure criterion for the T6-aluminum was taken to be 290 MPa (42,000 psi) yield stress. When the local material stress exceeds this magnitude, that material is given zero strength, so that it is "removed" from the material when it is subsequently subjected to a momentum away from the surface.

Numerical calculations were performed for the case of 1,000 m/s jet velocity. Some preliminary results have been obtained, and we present two of these preliminary results, viz., the pressure history at the centerline impact point, and the material deformation shape at some moments after the jet impact.

Figure 8 shows the pressure history at the centerline impact point. The peak pressure is about 2,900 MPa (420 ksi). This magnitude is greater than the jet stagnation value and, as expected, is lower than the water-hammer value on a rigid surface.

The deformation characteristics of the material following jet impact is shown in Figure 9 at 0.7 microseconds after impact. The deformation of the material is observed, its extent being more pronounced along the centerline. The water jet also shows deflections near the surface as a result of the ever-deforming target. This is unlike the rigid-surface case, where the jet has spread along the target surface and showed no detachment from the surface.

We emphasize that the results presented above are highly preliminary, and clearly more work is needed to make general statements on the response characteristics of a deformable target material following jet impact. Efforts are currently continuing on this problem.

3. CONCLUDING REMARKS

In this paper we have presented some preliminary results obtained from the analytical and experimental efforts conducted at the Lawrence Livermore National Laboratory and at Mason & Hanger, Pantex Plant.

A particular question addressed was to determine the optimum standoff distances for the maximum removal rate of the target material when subjected to jet impacts. As with previous analyses the existence of the optimum standoff distance was verified. The results from the present tests show these optimum standoff distances to be much greater than the jet intact lengths, suggesting multiple ligament impacts on the target surface. Two-dimensional, time-dependent analyses of the flow field and the target response were conducted; the calculational results demonstrate that the peak pressure at the first moment of impact on a rigid surface closely matches the value from the one-dimensional "water-hammer" expression. The case of the jet impact on aluminum has also been analyzed, and preliminary results display deformation of the material under sustained impact of the jet stream.

We plan to continue both the experimental and analytical efforts to ultimately determine the dominant factors involved in the most efficient mass removal rate. In the near term, analysis of the deformable material response to jet impact will continue, in conjunction with the experimental program to verify the theoretical predictions.

ACKNOWLEDGMENTS

We wish to acknowledge the contributions made by many individuals at the Lawrence Livermore National Laboratory, and by R. Bruse and T. Flower at Pantex Plant. Special thanks are due A.L. Austin of LLNL for the wide-ranging and stimulating discussions on the jet cutting technology.

REFERENCES

- Bowden, F.P., and Brunton, J.H., "The Deformation of Solids by Liquid Impact at Supersonic Speeds," *Proceedings of the Royal Society, Series A*, Vol. 263, pp.433-450, 1961.
- Brunton, J.H., "The Physics of Impact and Deformation: I. High Speed Liquid Impact," *Philosophical Transactions of the Royal Society of London, Series A*, Vol. 260, pp. 79-85, July 1966.
- Cole, R.H., *Underwater Explosions*, Princeton University Press, Princeton, NJ., 1948.
- Conn, A.F., Discussion of the paper by Franz (1974), *Proceedings of the 2nd International Symposium on Jet Cutting Technology*, pp. X16-19, BHRA, United Kingdom, 1974.
- Cook, M.A., Keyes, R.T., and Ursenbach, W.O., "Measurements of Detonation Pressure," *Journal of Applied Physics*, Vol. 33, pp. 3413-3421, December 1962.
- Daily, J.W., and Harleman, D.R., *Fluid Dynamics*, Addison-Wesley, Reading, MA, 1966.
- Dunn, J.C., "Stability of a High Velocity Water Jet in a Cutting Environment," Ph.D. Thesis, The Rutgers Univ., New Brunswick, NJ., 1974.
- Field, J.F., "Stress Waves, Deformation and Fracture Caused by Liquid Impact," *Philosophical Transactions of the Royal Society of London, Series A*, Vol. 260, pp. 86-93, July 1966.
- Franz, N.C., "The Influence of Standoff Distance on Cutting with High Velocity Fluid Jets," *Proceedings of the 2nd International Symposium on Jet Cutting Technology*, Paper B3, pp. 37-46, BHRA, United Kingdom, 1974.
- Grant, R.P., and Middleman, S., "Newtonian Jet Stability," *A.I.Ch.E. Journal*, Vol. 12, No. 4, pp. 669-678, July 1966.
- Hashish, M., and dePlessis, M.P., "Theoretical and Experimental Investigation of Continuous Jet Penetration of Solids," *Journal of Engineering for Industry*, Trans. ASME, Vol. 100, pp. 88-94, February 1978.
- Hashish, M., and dePlessis, M.P., "The Application of a Generalized Jet Cutting Equation," *Proceedings of the 4th International Symposium on Jet Cutting Technology*, Paper F1, pp. 1-16, BHRA, United Kingdom, 1978.
- Hashish, M., and dePlessis, M.P., "Prediction Equations Relating High Velocity Jet Cutting Performance to Stand Off Distance and Multipasses," *Journal of Engineering for Industry*, Trans. ASME, Vol. 101, pp. 311-318, August 1979.
- Heymann, F.J., "On the Shock Wave Velocity and Impact Pressure in High-Speed Liquid-Solid Impact," *Journal of Basic Engineering*, Trans, ASME, Vol. 90, pp. 400-402, September 1968.
- Hiroyasu, H., Shimizu, M., and Arai, M., "The Breakup of High Speed Jet in a High Pressure Gaseous Atmosphere," *Proceedings of the 2nd International Conf. Liquid Atomization and Spray Systems*, Madison, WI pp. 69-74, 1982.
- Huang, Y.C., Hammit, F.G., and Yang, W.J., "Mathematical Modeling of Normal Impact between a Finite Cylindrical Liquid Jet and Non-Slip, Flat Rigid Surface," *Proceedings of the 1st International Symposium on Jet Cutting Technology*, Paper A4, pp. 57-68, BHRA, United Kingdom, 1972.
- Huang, Y.C., Hammit, F.G., and Mitchell, T.M., "Note on Shock-Wave Velocity in High-Speed Liquid-Solid Impact," *Journal of Applied Physics*, Vol. 44, pp. 1868-1869, April 1973.
- Kusui, T., "Liquid Jet Flow into Still Gas," *Bulletin of the Japan Society of Mechanical Engineers*, Vol. 11, No. 48, pp. 1084-1090, 1968.

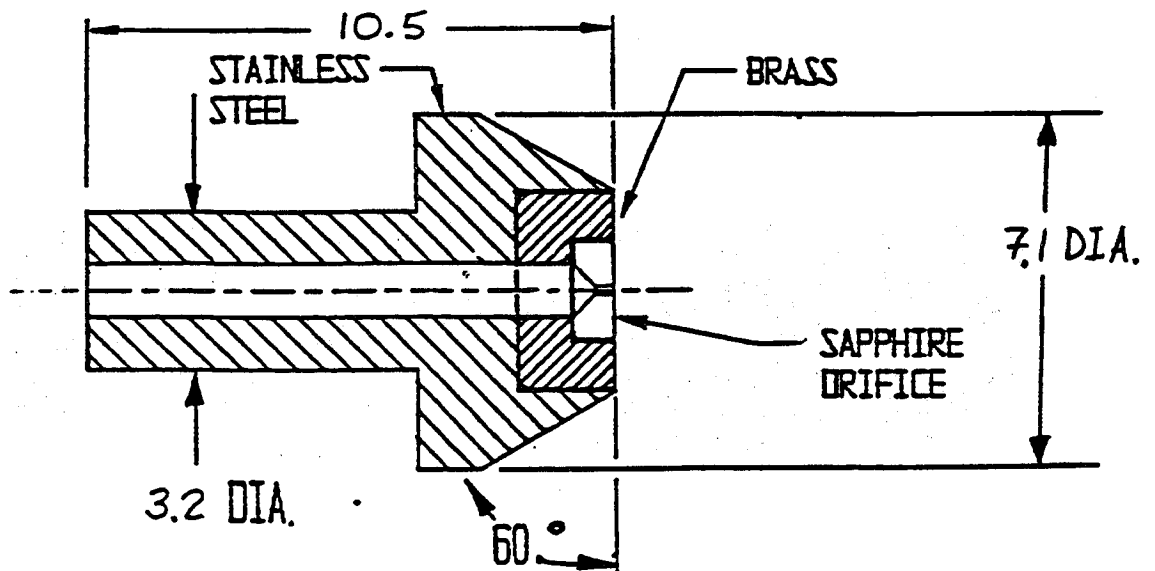
- Leach, S.J., and Walker, G.L., "Some Aspects of Rock Cutting by High Speed Water Jets," *Philosophical Transactions of the Royal Society of London, Series A*, Vol. 260, pp. 295-308, July 1966.
- Louis, H., and Schikorr, W., "Fundamental Aspects in Cleaning with High-Speed Water Jets," *Proceedings of the 6th International Symposium on Jet Cutting Technology*, Paper E3, pp. 217-228, BHRA, United Kingdom, 1982.
- Mansour, A., and Chigier, N., "Disintegration of Liquid Sheets," *Physics of Fluids*, Vol. 2, pp. 706-719, 1990.
- Neusen, K.F., and Schramm, S.W., "Jet Induced Target Material Temperature Increases during Jet Cutting," *Proceedings of the 4th International Symposium on Jet Cutting Technology*, Paper E4, pp. 45-52, BHRA, United Kingdom, 1978.
- Phinney, R.E., "Breakup of a Turbulent Liquid Jet in a Low-Pressure Atmosphere," *A.I.Ch.E. Journal*, Vol. 21, No. 5, pp. 996-999, September 1975.
- Pidsley, P., "A Numerical Investigation of Water Drop Impact," *Proceedings of the 6th International Conference on Erosion by Liquid and Solid Impact*, Paper 18, pp. 1-6, Cavendish Laboratory, Cambridge, England, 1983.
- Pritchett, J.W., and Riney, T.D., "Analysis of Dynamic Stresses Imposed on Rocks by Water Jet Impact," *Proceedings of the 2nd International Symposium on Jet Cutting Technology*, Paper B2, pp. 12-36, BHRA, United Kingdom, 1974.
- Reitter, T., and Kang, S-W., "Analysis of Maximum Pressure Attainable by WaterJet Impact," Lawrence Livermore National Laboratory Tech. Report, (in preparation) 1993.
- Shimizu, M., Arai, M., and Hiroyasu, H., "Disintegrating Process of a High Speed Liquid Jet," *Bulletin of the Japan Society of Mechanical Engineers*, Trans. B, Vol. 54, No. 504, pp. 2236-2244, August 1988.
- Springer, G.S., *Erosion by Liquid Impact*, John Wiley & Sons, New York, 1976.
- Tikhomirov, R.A., Babanin, V.F., Petukhov, E.N., Starikov, I.D., and Kovalev, V.A., *High-Pressure Jet Cutting*, American Society of Mechanical Engineers, New York, 1992.
- Tipton, B., "CALE User's Manual," Lawrence Livermore National Laboratory Tech. Report, 1992.
- Whiting, C.E., Graham, E.E., and Ghorashi, B., "Evaluation of Parameters in a Fluid Cutting Equation," *Journal of Engineering for Industry*, Trans, ASME, Vol. 112, pp. 240-244, August 1990.
- Yanaida, K., and Ohashi, A., "Flow Characteristics of Water Jets in Air," *Proceedings of the 4th International Symposium on Jet Cutting Technology*, Paper A3, pp. 39-54, BHRA, United Kingdom, 1978.

NOMENCLATURE

C	:	Sound speed
p	:	Pressure
V	:	Flow velocity
ρ	:	Density

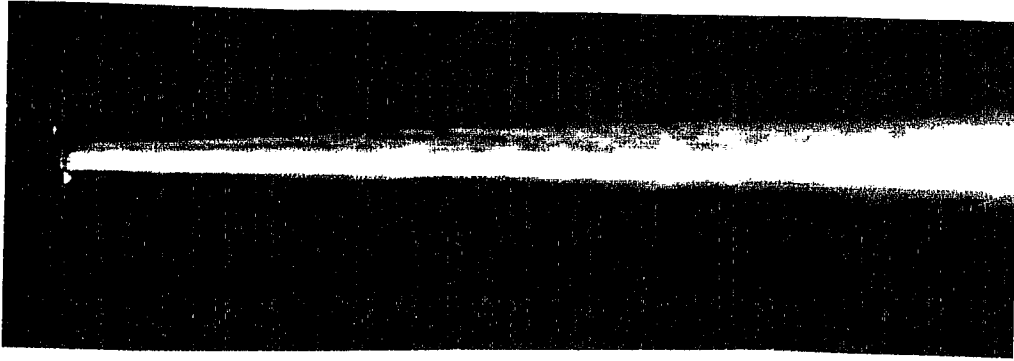
Subscripts

- o : Undisturbed region in the fluid
- 1 : Compressed region in the fluid

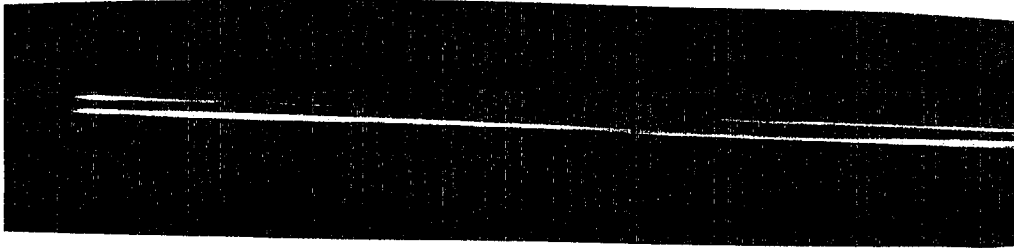


TYPE 2720
(Dimensions are in mm)

Figure 1. Structure of Nozzle A.



(A) From Nozzle A



(B) From Nozzle B

Figure 2. Jet Structures from Nozzles.
(Nozzle diameter: 0.35mm (0.014 in.);
Reservoir pressure: 138 MPa (20,000 psi))

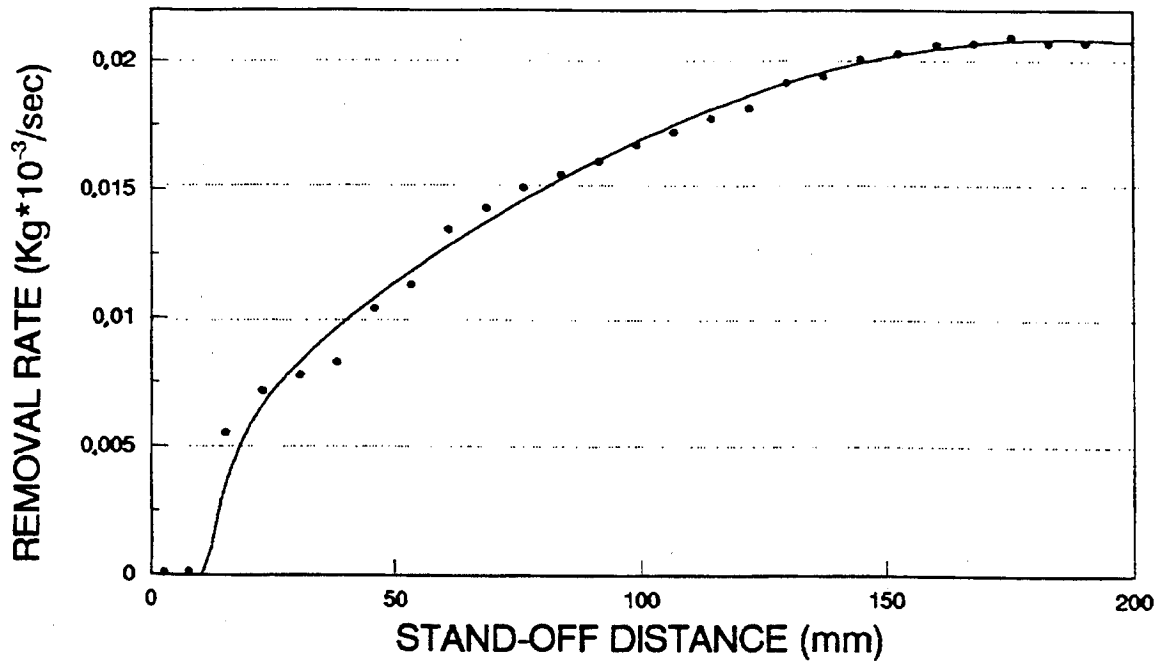


Figure 3. 6061-T0 Al removal rate as a function of stand-off distance for 0.356-mm nozzle B at 138 MPa

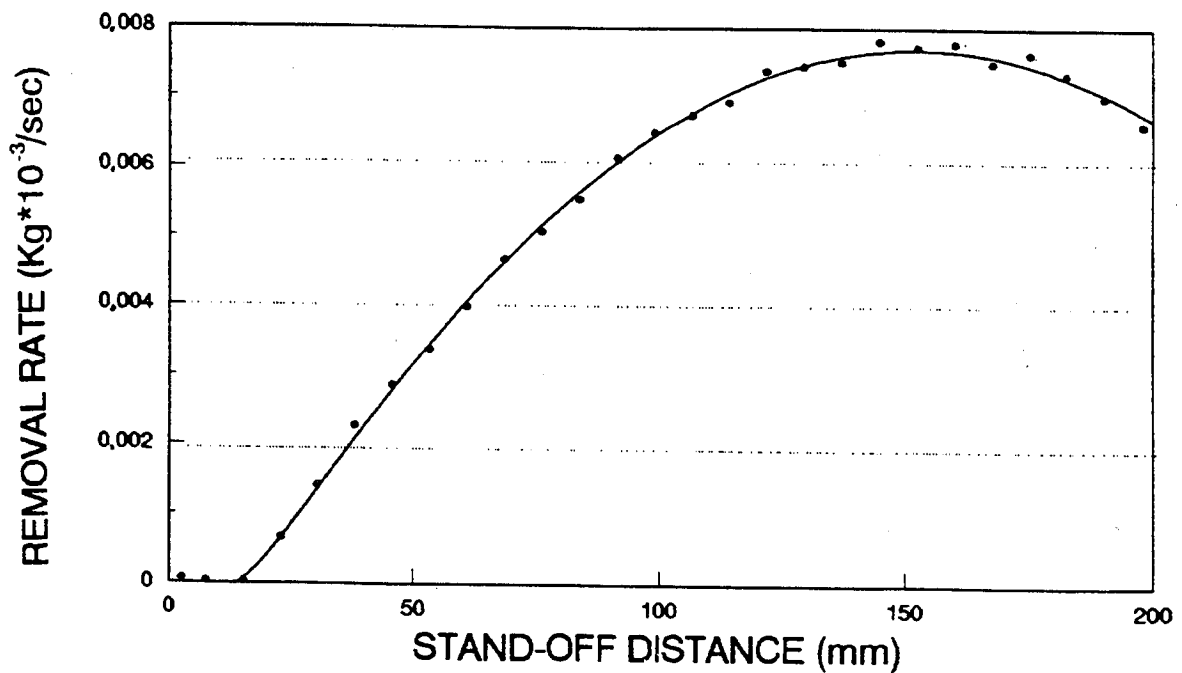


Figure 4. 6061-T0 Al removal rate as a function of stand-off distance for 0.356-mm nozzle B at 276 MPa

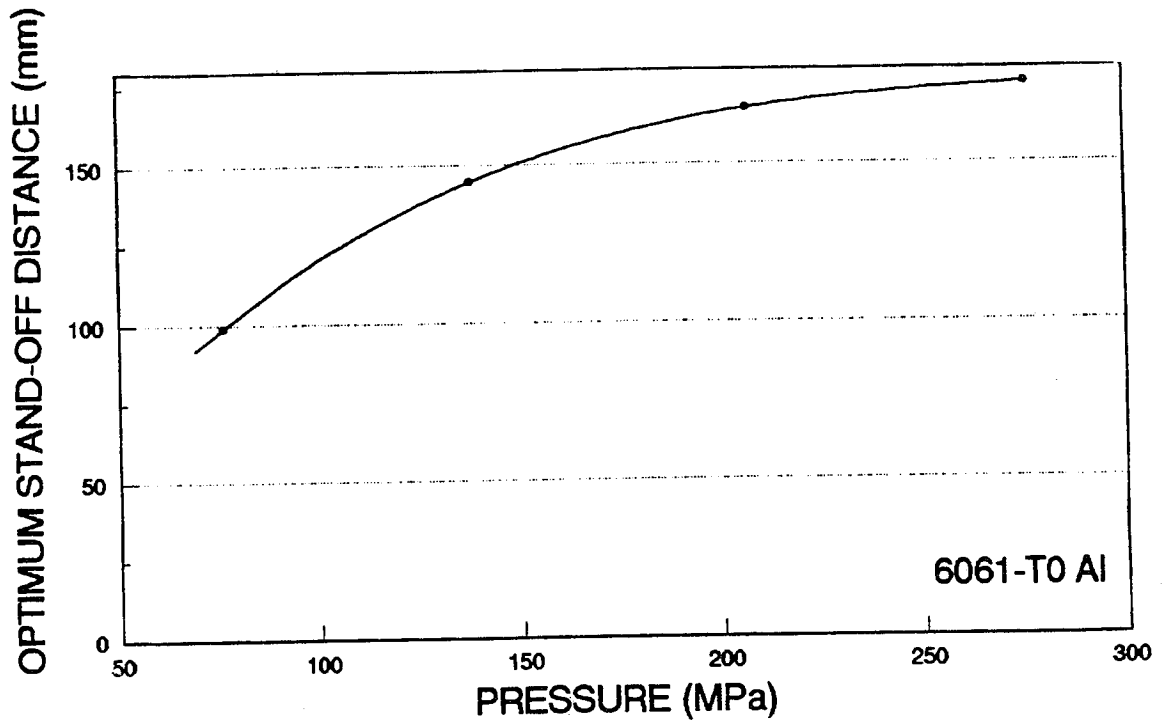


Figure 5. The optimum stand-off distance as a function of pressure for 0.356-mm nozzle B.

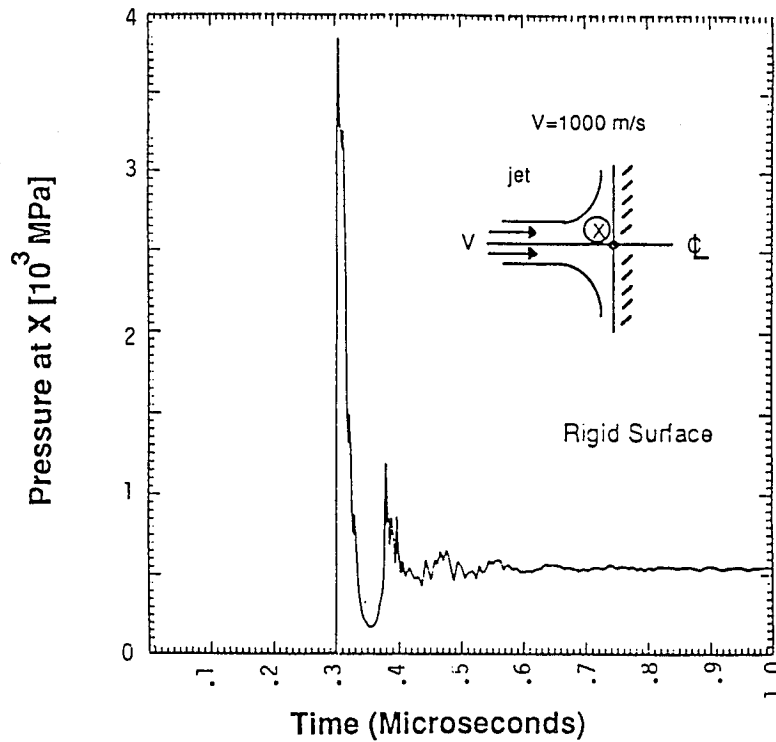


Figure 6. Calculated Pressure History at the Stagnation Point Following Jet Impact on a Rigid Surface (Jet Velocity = 1,000 m/s)

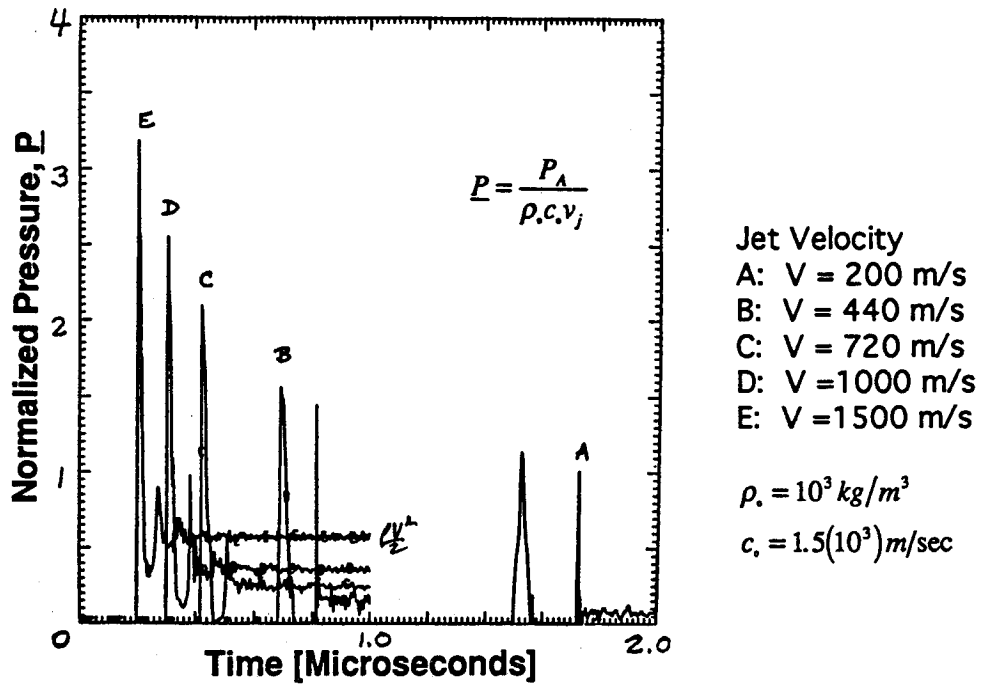


Figure 7. Calculated Pressure History at the Stagnation Point Following Jet Impact on a Rigid Surface for Various Jet Velocities

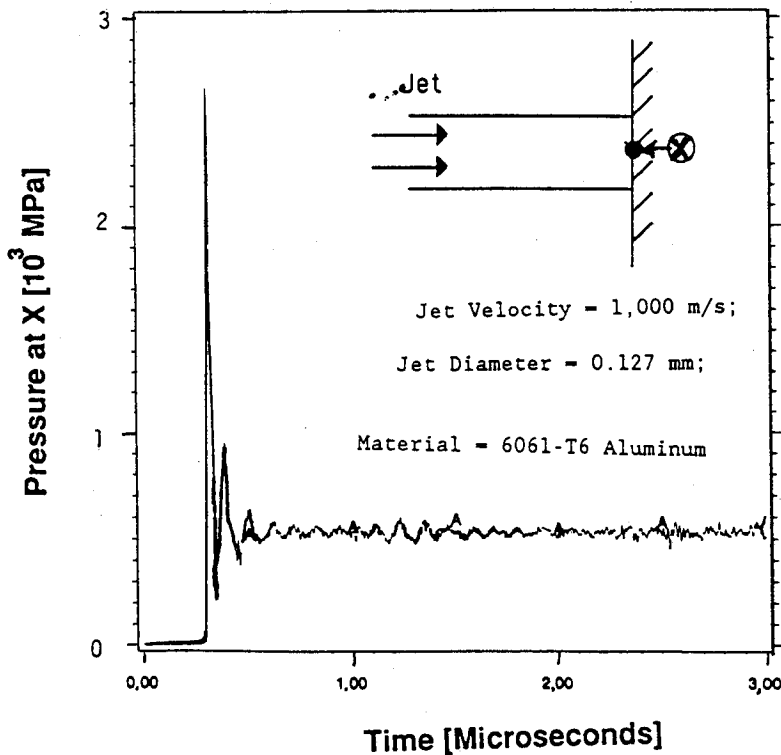


Figure 8. Calculated Pressure History at Location X Following Jet Impact on a Deformable Material.

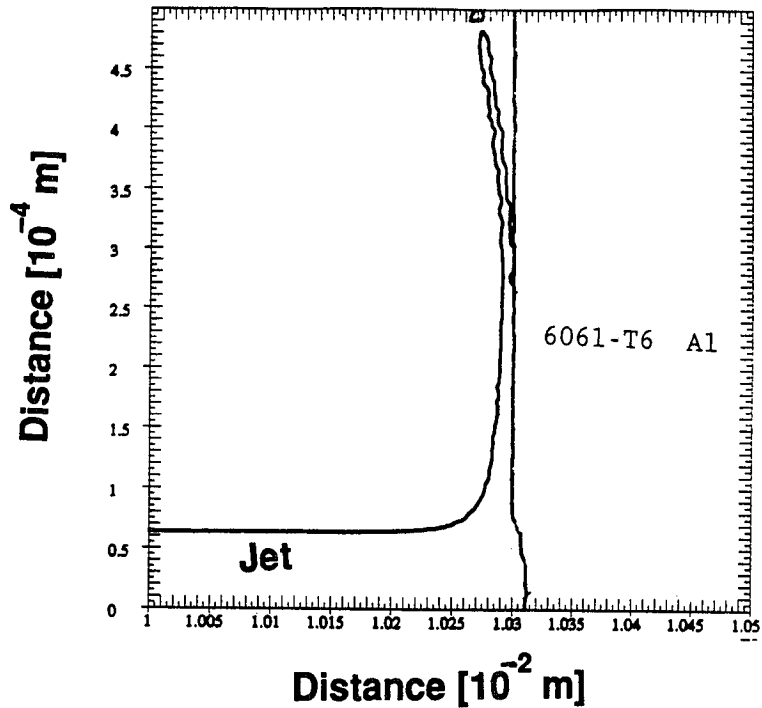


Figure 9. Calculated Material Deformation at 0.7 Microseconds after Jet Impact. Jet Velocity = 1,000 m/s; Jet Diameter = 0.127 mm

Table 1. Exit Jet Velocity from the Nozzles at Various Pressures

(A). Nozzle A.

Pressure [MPa] (ksi)	69 (10)	138 (20)	207 (30)	276 (40)
Velocity (m/s)	229	342	434	516
Velocity Coefficient	0.616	0.650	0.674	0.694
Stagnation Pressure [MPa] (psi)	26 (3795)	58 (8450)	94 (13628)	133 (19265)

(B). Nozzle B.

Pressure [MPa] (ksi)	69 (10)	138 (20)	207 (30)	276 (40)
Velocity (m/s)	223	324	396	469
Velocity Coefficient	0.599	0.618	0.615	0.630
Stagnation Pressure [MPa] (psi)	26 (3588)	53 (7638)	78 (11346)	109 (15876)

**TRANSIENT BOILING HEAT TRANSFER TO A HIGH SPEED WATER JET IMPINGING
ONTO A HEATED MATERIAL AND THE THERMAL SHOCK FRACTURE**

H. Kiyohashi, M. Ogasawara and M. Kyo
Tohoku University
Sendai 980, Japan

ABSTRACT

Thermal shock phenomena in hot insulating materials, which appear in the materials as thermal stresses or thermal shock fractures by impingement of the high speed water jets, have been observed in various engineering field. The objective of this study is to clarify the characteristics of the transient boiling heat transfer to a high speed water jet impinging onto a circular heated rod. In this study, temperature changes in the rod of stainless steel with time were measured at each three points for vertical and radial directions under eighteen conditions. Heat flux and heat transfer coefficient on a surface of the rod were evaluated for initial temperatures from 200 to 800°C and water jet velocities at nozzle exit from 36 to 110m/s. The thermal shock fractures appearing in an insulating material have also been discussed from these results.

1. INTRODUCTION

Thermal shock phenomena in hot insulating materials, which appear in the materials by impingement of the high speed water jets, are observed in various engineering fields, for example, on the water jet hot cleaning of clinker grown on the inner surface of the kiln for making industrial cement (Sugai, 1972), and on the jet cooling and cleaning of hot steel plate at continuous casting and rolling in the steel industry (Kikuchi et al., 1982). Furthermore, its application is considered as forthcoming technologies; (1) Water jet drilling and cutting of hot dry rocks and magma, which are considered as promising methods with reference to establishment of technology for extracting heat from them (Kiyohashi et al., 1978, Kiyohashi et al., 1980, Kiyohashi et al., 1981, Armsted and Tester, 1987 and Kiyohashi, 1987), (2) Technology for reduction of thermal shock fractures which may arise from heavy rain impingement in insulating materials to protect the surface of aerospace planes from aerodynamic heating when they return to the earth (Aihara, 1990) and (3) Establishment of an evaluating method of thermal-shock-resistance characteristics of engineering fine ceramics at high temperatures, using impingement of high speed water jets. Qualitative and quantitative characteristics of the transient boiling heat transfer between the impinging water jet and the hot surface are very important to elucidate their mechanisms.

For stable, unsubmerged, uniform velocity laminar jets in the absence of phase change, jet impingement cooling of uniformly heated surfaces were investigated analytically and experimentally by Liu et al. (1991). They obtained predictive formulae for the local Nusselt numbers from the stagnation point to radii of up to 40 diameters. Recently, they (Lienhard V, et al., 1992) also investigated splattering and heat transfer due to impingement of an unsubmerged, fully turbulent liquid jet experimentally and analytically.

Kunioka, et al. (1979) experimentally studied relations between the boiling heat transfer coefficient on a heated surface and the velocity of water jets impinging onto the surface in experimental ranges of initial surface temperatures from 200 to 800°C and jet velocities at nozzle exit from 2 to 8m/s. Then they obtained experimental formulae for their relations. Monde (1987) also studied experimentally critical heat flux during forced convection boiling on an open heated disk supplied with saturated liquids through a small round jet which impinged on the center of the disk employing refrigerant R12 at comparatively high pressures from 0.6 to 2.8MPa. Generalized correlations, predicting the CHF within an experimental range of liquid-to-vapor density ratio 5.3-41.25 and the reciprocal of Weber number 2×10^{-3} - 2×10^{-7} , were given for three different characteristic regimes: V-regime where the CHF increases with an increase in the jet velocity, I-regime where the CHF is nearly constant with jet velocity, and an HP-regime where the CHF appears only at high pressure and again rises with an increase in the jet velocity. In a recent study of a novel, flexible, long slender cryoprobe for cryosurgery of malignancy and cancers using a micro-impinging jet of liquid nitrogen (LN₂) (Aihara et al., 1993), the boiling heat transfer characteristics of the micro-imping-

ing jet were clarified in detail using different types of probe tips. The effects of the mass flow rate of LN_2 , standoff distance, shape of the probe tip, and surface roughness on boiling heat transfer were examined experimentally. The critical heat flux on the heat transfer area by Aihara et al. (1993) was 20-25% higher than the value evaluated with Monde's experimental formula (Monde, 1987), which was derived from the data on impinging jet boiling of water, R12, and R113 in free space, and was little influenced by the roughness of heat transfer surface.

Few studies on the impinging of a liquid jet on a hot porous surface have been made. However, the impact of a liquid droplet on the hot porous surface has been studied extensively because of its significance in a wide variety of applications (Fatehi and Kaviani, 1990, Chandra and Avedisian, 1992). Chandra and Avedisian (1992) experimentally studied the dynamic aspects of droplet impingement on a porous ceramic surface by single-shot flash photography. The primary parameter was the surface temperature in the range from 22 to 200°C. The liquid was n-heptane. The measured value of spreading rate of droplet on a porous surface at 22°C was lower than that on a stainless steel surface. No transition to film boiling was observed with the porous surface at a surface temperature of 200°C, unlike that seen with a stainless steel surface. The evolution of wetted area and spreading rate, both of a droplet on a porous surface and on a stainless steel surface, were found to be independent of surface temperature during the early period of impact. The maximum value of the diameter of droplet which spreads on the surface was lower on the ceramic surface than that on the stainless steel surface at the same temperature.

Recently, the present authors (Kiyohashi et al. 1992), reported a experimental study on the characteristics of the transient boiling heat transfer system composed of conduction in a circular stainless steel rod and forced convection between a flat surface of the rod and impinging water jets. Temperature changes with time at central three points below the surface of the rod were measured under the conditions of initial rod temperatures: $T_{s0}=200$ to 800°C, dimensionless standoff distances: $L/D_0=80$ to 300, and jet velocities: $U_0=7$ to 20m/s. The results obtained in the study were summarized as follows; (1) Transient heat transfer phenomena between the hot surface and the impinging water jet could be classified according to their characteristics varied with the degree of superheat on the heat transfer surface, $\Delta T_{SAT}=T_s-T_{SAT}$ (T_s : surface temperature, T_{SAT} : saturated temperature), into the following two types, i.e., the forced convection and radiation heat transfer for $\Delta T_{SAT}>300^\circ\text{C}$, and the forced convection and subcooled boiling heat transfer phenomena for $\Delta T_{SAT}\approx 20\sim 100^\circ\text{C}$. (2) Heat transfer coefficient, α , increased rapidly with impinging time, τ , during shorter time than $\tau=3\text{s}$, independently of U_0 and L/D_0 . However, for longer time and for $T_s<100^\circ\text{C}$, U_0 and L/D_0 affected α . (3) U_0 and L/D_0 almost never affected relations between α and ΔT_{SAT} . (4) The α rapidly decreased with larger values of ΔT_{SAT} and was affected by T_{s0} .

The objective of this study is to make clear the characteristics of the transient boiling heat transfer with respect to much higher speed water jets im-

pinging onto a flat end surface of heated circular rod. Temperature changes with time in the rod are measured at each three points for vertical and radial directions under eighteen conditions. Heat flux is evaluated from the sub-surface temperatures, and the thermophysical properties of the rod. From their results and the jet temperature in the nozzle exit, the heat transfer coefficients on the rod surface are calculated. The thermal shock fractures appearing in an insulating material are also discussed from these results.

2. EXPERIMENTAL APPARATUS

An experimental apparatus used is shown schematically in Fig. 1. The apparatus mainly consists of three parts; (1) the water jet generating system (A to S), (2) the heat transfer rod and its heating system (U to Y), and (3) the measuring system. The test liquid (pure water) introduced in the water bomb (H) is pressurized by the high pressure N_2 gas (maximum pressure :15MPa) in the N_2 gas bomb (E). The pressurized water is jetted from the nozzle (s) via the high pressure hose and the solenoid operated valve (Q). Pressure and temperature of the water jet at exit of the nozzle (S) is measured by the pressure transducer (O) and thermocouple (T_L) immersed in the nozzle assembly (R), respectively. The heat transfer rod (Y) is heated by the electric furnace (U) of which capacity is 5kW. Temperature of the rod (Y) is controlled by the thermocouple (T_{c2}) attached on the rod surface and a temperature controller, and also monitored by the thermocouple (T_{c1}).

The measuring system consists of a temperature measuring system and a remote operating system shown in Fig. 2. Temperature changes at the eight positions shown with solid points (T_1 to T_8) in the heat transfer rod (S), water jet temperature at the nozzle exit, T_s (T_L in Fig. 1), and temperature of the electric furnace, T_{10} (T_{c1} in Fig. 1), are measured by the high speed digital multimeter (TR6861, Takeda-riken Co.) (D) via the terminal box (F) and the high speed scanner (10 channels) (E). Data of the temperatures are processed by the personal computer (PC8801, NEC) (A), showed on the display (B) and/or recorded in the floppy disk unit (C). The remote operating system for jetting of water consists of the fiber (I), photoelectric detector (H), the remote relay box (G), the solenoid operated valve (J), the pressure transducer (K), the amplifier (L) and the pen type pressure recorder (M). Both the digital multimeter (D) for measuring the temperatures, and the remote relay box (G) for opening and closing the solenoid operated valve (G) can also be operated by the personal computer (A). The two sensing parts of the fibers were so fixed at about 20mm over the electric furnace (O) as to cross at right angles the axis of light from the fiber and the axis of the water jet. The electric furnace (O) are controlled by the thermocouple, T_{11} (T_{c2} in Fig. 1) and the temperature controller (N).

Figure 3 shows the heat transfer rod and the temperature measuring points in the rod in detail. Diameter and height of the rod were 75mm and 156mm, respectively. Temperature measuring points, T_1 , T_2 and T_3 , were set along the

central axis of the rod. Also, the points, T_4 and T_5 , and T_6 , T_7 and T_8 set on a concyclic imaginary surface with radius of 4mm, and one with radius of 8mm, respectively, shown in Fig. 3. C-A sheathed thermocouples of 1.6mm in diameter were used to measure the temperature of these measuring points. In this experiment, two nozzles in different diameter, $D_o=4\text{mm}$ and 6mm, were used. Figure 4 shows the schematic drawing of them. The lengths of the straight part of the nozzle exit, L_N , were 12mm and 18mm for the nozzle of $D_o=4.0\text{mm}$ and 6.0mm, respectively. The L_N was decided from the law of similarity of flow in the different nozzles. To obtain water jets having low level of turbulence, L_N/D_o of them was designed by three.

3. MEASURING METHOD OF TRANSIENT HEAT FLUX AND HEAT TRANSFER COEFFICIENTS

3.1 Inverse Heat Conduction Problem

If the heat flux or temperature histories at the surface of a solid are given as functions of time, then the temperature distribution can be obtained from the values. This approach is called a direct problem. In many dynamic heat transfer situations, the surface heat flux and temperature histories of a solid are determined by measuring transient temperatures at one or more interior locations; this is an inverse problem. In particular, the special case of estimating a surface condition from interior measurements has come to be known as the inverse heat conduction problem (IHCP). It is much more difficult to solve the IHCP analytically than the direct problem. However, the technique has been often used to measure the temperature history on the heated surface of a solid, although it is very easy to accurately measure the temperature history at an interior location or at an insulated surface of the body. One of the earliest papers on the IHCP was published by Stolz (1960). Papers over 300 have been written to date on the IHCP or closely related problems (Beck, et al, 1985). Burggraf (1964) obtained an exact solution of temperatures and heat flux at a boundary and internal locations by specifying the boundary conditions (in case of temperatures and heat flux, given simultaneously at a single location in a solid). Shoji (1978) solved analytically the inverse problem of one dimensional unsteady heat conduction in case of given temperatures at two locations in the solid using Laplace transform. He also examined calculating procedure, accuracy of the resultant answers and limitations of this analysis for a specified application. In the present study the authors try to use his technique to obtain the heat flux from the heated rod and the heat transfer coefficients between the surface of the heated rod and the high speed impinging water jets.

3.2 Principle of Measuring Method

The flow condition indicated in Fig. 5 is supposed. A water jet of velocity, U_o , and temperature, T_L , at the nozzle exit flows radially over a flat surface after impinging on the surface. If the surface conditions are such that $T_s > T_L$, convection heat transfer will occur on the surface. The local heat

flux, q_r , may be expressed as

$$q_r = \alpha_r (T_{s,r} - T_L) \quad (1)$$

where α_r is the local heat transfer coefficient. Because the flow conditions vary along the surface from stagnation point ($r=0$) to outer point ($r=r$), both q_r and α_r vary radially. The heat flux, q_r , may be in general a function of both position, r , and time, τ . It is assumed that lateral conduction can be neglected compared to the heat flow in direction normal to the surface. Thus the net surface heat flux as a function of time is estimated from temperatures obtained from two interior temperature sensors at positions, x_1 and x_2 , as shown in Fig. 5. The measurements are made at discrete times, t_1, t_2, \dots or in general at any time, τ_i , whose temperature is denoted T_i . To estimate the surface heat flux history it is necessary to have a mathematical model of the heat conduction process. In the case shown in Fig. 5, the semi-infinite body is assumed to be a single material, homogeneous and isotropic. Then the energy equation can be written as for the body,

$$(\partial T / \partial \tau) = a (\partial^2 T / \partial x^2) \quad (2)$$

where, $a (= \lambda / \rho c)$ is the thermal diffusivity of the material. The thermal conductivity, λ , density, ρ , and specific heat, c , are postulated to be known functions of temperature. If any one of these thermal properties varies with temperature, the IHCP becomes nonlinear. The initial temperature distribution, $T_0(x)$, is also taken as known. The locations, x_1 and x_2 , of the sensor are assumed to be measured and to have negligible error. Resultant calculating formulae of the temperature, $T_{s,r,i}$, and heat flux, $q_{r,i}$, on the surface are obtained as the solutions of Eq. (2) by using Laplace transformation (Shoji, 1978) as follows for the case of $r=0$:

$$T_{s,r,i} = T_{1,i} - (h_1/h_2) (\lambda_b/\lambda_a) (T_{2,i} - T_{1,i}) + [h_1(h_1+h_2)/4] (1/a_1) (\lambda_1/\lambda_a) (T_{1,i+1} - T_{1,i-1}) / \Delta t \quad (3)$$

$$q_{r,i} = -\lambda_s \{ (h_1/h_2) [1/(h_1+h_2)] (T_{2,i} - T_{1,i}) - [(1/h_1) + 1/(h_1+h_2)] (T_{1,i} - T_{s,i}) \} \quad (4)$$

where, $T_{1,i}$ and $T_{2,i}$ are measured values of the temperature at the locations, x_1 and x_2 at time $\tau = i \cdot \Delta \tau$, and h_1 and h_2 distances from the heat transfer surface to the location x_1 , and from the location x_1 to x_2 , respectively, shown in Fig. 5. The $\Delta \tau$ is a time interval. From the analytical results on the error estimation the time interval $\Delta \tau$ was determined to be 150ms. Thermo-physical properties of the material, SUS304, are given as functions of temperature according to literature data (Touloukian and Ho, 1970) as follows;

$$\begin{aligned} \lambda_1 &= 15.4 + 0.0125 T_1 && [W/(m \cdot K)] \\ \lambda_a &\doteq \lambda_1 \\ \lambda_b &= 15.4 + 0.0125 (T_1 + T_2) / 2 && [W/(m \cdot K)] \\ \lambda_s &= 15.4 + 0.0125 T_s && [W/(m \cdot K)] \end{aligned}$$

$$a_i = (15.4 + 0.0125T_i) / 7820(4.41 + 1.92 \times 10^{-3} \times T_i) \text{ [m}^2/\text{s]}$$

Local heat transfer coefficients, α_i , are calculated from Eqs. (1), (3), (4) and the equation,

$$\alpha_{r,i} = q_{r,i} / (T_{s,r,i} - T_L) \text{ [W/(m}^2 \cdot \text{K)]}. \quad (5)$$

In this experiment, C-A sheathed thermocouples of 1.6mm in diameter (diameters of naked Chromel and Alumel wires are both 0.1mm) were used as the sensors. The 63.2% response time, τ_R , of their thermocouples was 150ms. Temperature corrections for the response delay of these thermocouples at arbitrary time $\tau = n \cdot \tau_R$ were made by the use of a following equation derived by the authors;

$$T_n = [1/(1-c)] T_n' - \left\{ \sum_{m=1}^{n-2} c^{n-m-1} \times T_{m+1} + [1/(1-c)] c^{n-1} T_1 \right\} \quad (6)$$

where, $c=0.368$, and T_n and T_n' are true and measured temperatures, respectively.

4. EXPERIMENTAL METHOD AND CONDITIONS

The heat transfer surface was polished with emery papers #400, #700 and #1500 in this order before each test run. Experimental methods of one test run of this experiment are shown in Fig. 6 as flowchart. The experiments were conducted under the nominal condition: initial rod temperatures, $T_{s,0}=200, 400$ and 800°C ; a fixed dimensionless standoff distance, $L/D_0=50$; and water jet velocities at nozzle exit, $U_0=36, 68$ and 110m/s . Diameters of the nozzle made of SUS304, D_0 , are 4.0 and 6.0mm; and the temperature of the water jet, T_L , at the nozzle exit was kept at air temperature in a test chamber. Diameter and length of the rod are 75 and 156mm, respectively. Material of the rod is stainless steel, SUS304. The rod is automatically heated up to the tested temperature in the electric furnace with an insulating cap. Surface temperatures of the rod may be predicted by inversed heat conduction technique from temperatures measured with the thermocouples immersed in the rod. The actually tested values of $T_{s,0}$, U_0 and T_L are shown in Table 1.

5. EXPERIMENTAL RESULTS AND DISCUSSIONS

5.1 Characteristics of the Water Jets

The general structure of a free water jet in air consists of several regions; the initial region with a constant jet axial dynamic pressure, the main region with a constant jet axial velocity, and the final region (Kiyohashi, 1980). Relations between the jet diameter, D_j , at the standoff distance, L , and the dimensionless standoff distance, L/D_0 , for different jet velocities at nozzle exit, U_0 , were obtained by photographic measurements of the configuration of the water jet taken under the reflective light illumination. Figure 7 shows

the configurations of the water jets of $U_o=31.3$, 62.7 and 109 m/s in the case of $D_o=6.0$ mm. These reveal that divergence of D_L increases with increasing U_o and L/D_o . Values of D_L obtained with $L/D_o=50$ are as follows: In the case of $D_o=4.0$ mm, $D_L\approx 6.0$ mm for $U_o=31.3$ m/s, $D_L\approx 10.0$ mm for $U_o=62.7$ m/s and $D_L\approx 13.0$ mm for $U_o=109$ m/s. In the case of $D_o=6.0$ mm, $D_L\approx 8.0$ mm for $U_o=31.3$ m/s, $D_L\approx 12.0$ mm for $U_o=62.7$ m/s and $D_L\approx 18.0$ mm for $U_o=109$ m/s. The authors have estimated that the water jets used in this experiment maintain the initial region or the transition region of them at the impinging surface of $L/D_o=50$.

5.2. Cooling Curves of the Heat Transfer Rod.

Figure 8 shows the histories of the temperatures at the two interior locations, T_1 and T_2 , and at the central point, $T_{s,r=0}$ on the surface of the heat transfer rod in the case of $D_o=6.0$ mm and $U_o=62.8$ m/s. Figures 8 (a), (b) and (c) also present the histories of which initial temperatures of the heat transfer rod, T_{s_0} , are at about 200 , 400 and 800°C , respectively. Symbols of ellipse and triangle show experimental values at the locations of T_1 and T_2 , respectively, and those of square show the estimated values at the point, $T_{s,r=0}$, obtained from Eq. (3) and the experimental values. From the figures, it is found that the curves of the temperature histories at the point, T_1 , in the cases of $T_{s_0}=200$ and 400°C are characteristic of their shape. Both the T_1 values in the above cases drop steeply at a certain temperature from about 110 to 120°C .

Figure 9 shows also the temperature histories at the interior location, T_1 , of the heat transfer rod as a parameter of the water jet velocity at nozzle exit, U_o , in the case of $D_o=6.0$ mm. Again, Figures (a), (b) and (c) in Fig. 9 indicate the histories of which the initial temperatures of the heated rod are at $T_{s_0}=200$, 400 and 800°C , respectively. Symbols of ellipse, triangle and square denote the data of $U_o\approx 33.0$, 62.0 and 108 m/s, respectively. Flow models of water jets impinging onto a heated surface, reported previously by the authors (Kiyohashi et al., 1992), may also be supported by these temperature histories of T_1 and $T_{s,r=0}$ in spite of much higher jet velocities than 20 m/s.

5.3 Transient Heat Transfer Coefficients

Figure 10 shows variations of heat transfer coefficient, α , with time, τ , in the case of $D_o=6.0$ mm. Figures 8 (a) and (b) illustrate the relations between α and τ at the stagnation point ($r=0$ mm), for the initial heated rod temperature, $T_{s_0}\approx 400$ and 800°C , respectively, as a parameter of the water jet velocity, $U_o\approx 33$, 62 and 108 m/s and Figure 10 (C) for $T_{s_0}\approx 800^\circ\text{C}$ and $U_o\approx 109$ m/s as a parameter of the radial distance, $r=0$, $r=4$ and $r=8$ mm. It can be seen that the U_o and the r don't affect during $\tau=0$ to 0.3 [s]. Figure 11 shows the variation of α with the degree of superheat, ΔT_{SAT} , for $D_o=6.0$ mm and $U_o\approx 62$ m/s as a parameter of the initial heated rod temperature, $T_{s_0}\approx 200$, 400 and 800°C . Also, Figs. 11 (a), (b) and (c) show the relation between α and ΔT_{SAT} for $r=0$, 4 and 8 mm, respectively. It can be recognized again that the values of T_{s_0} and r markedly affect α and ΔT_{SAT} relations from above figures. Further,

the velocity U_0 don't affect α and ΔT_{SAT} relations for $r=0\text{mm}$, and for higher ΔT_{SAT} than 200°C against larger r than 4mm .

5.4 Thermal Shock Fracture Mechanism by Impinging Water Jet

In the previous work (Kiyohashi, et al., 1978, 1980), it has been found that fracturing patterns of heated specimens made of a castable insulating material by impinging water jets varied characteristically with the specimen temperature, T_{s0} . On the surface of the heated specimen struck by the water jet for 10s, a cylindrical hole-shaped cavity with a certain diameter at the stagnation point was observed in both cases of $T_{s0}=400^\circ\text{C}$ and $T_{s0}\geq 800^\circ\text{C}$. A large crater-shaped cavity was observed at $T_{s0}=600^\circ\text{C}$. These phenomena on the heated surface struck by the water jets can be well explained by the heat transfer characteristics obtained. The fracturing mechanism have been described in detail elsewhere (Kiyohashi, et al., 1978, Kiyohashi et al., 1980).

6. CONCLUSIONS

An experimental study has been carried out on clarifying the characteristics of the transient boiling heat transfer to the high speed water jet impinging onto a circular heated rod. The results obtained in this study are summarized as follows : (1) The transient boiling heat transfer phenomena between the hot surface and the impinging high speed water jet are classified according to their characteristics varied with the degree of superheat ΔT_{SAT} on the surface, into two types, that is, a transient boiling system and a nucleate boiling system. (2) The heat transfer coefficient α increases rapidly with increasing impinging time τ for a shorter period than 0.3s , independent of the water jet velocity at nozzle exit U_0 but dependent on the initial surface temperature T_{s0} . However, for the period longer than 0.5s and for larger surface temperatures T_s larger than the saturated temperature of water, U_0 and T_{s0} affect α . (3) The velocity U_0 and nozzle diameter D_0 almost never affect the relations between α and ΔT_{SAT} . (4) For larger ΔT_{SAT} , the α -values rapidly decrease with increasing ΔT_{SAT} but never be affected by the radial distance. (5) For smaller ΔT_{SAT} , the values of α are affected by the radial distance and T_{s0} . (6) The thermal shock fractures, appearing on the hot surface by impingement of the water jets, can be well explained by these heat transfer characteristics.

ACKNOWLEDGMENTS

The authors appreciate the support and encouragement of Professor Masuda, H., Institute of Fluid Science, Tohoku University.

REFERENCES

- Aihara, T., Kim, J.K., Suzuki, K. and Kasahara, K., "Boiling Heat Transfer of a Micro-Impinging Jet of Liquid Nitrogen in a Very Slender Cryoprobe," *Journal of Heat and Mass Transfer*, Vol.36, pp.169-175, 1993.
- Aihara, Y., "Study on Flow around Extremely Supersonic Speed Plane - Background and future -," *Journal of Aeronautics and Space Institute of Japan*, Vol.38, pp.170-176.
- Armstead, H.C.H. and Tester, J.W., "Heat Mining", E. & F.N. SPON, 1987.
- Beck, J.V., Blackwell, B. and St. Clair, C.R., Jr., "Inverse Heat Conduction," A Wiley-Interscience Publication, New York, 1985.
- Burggraf, O.R., "An Exact Solution of the Inverse Problem in Heat Conduction Theory and Applications," *Transactions of the ASME, Journal of Heat Transfer*, Vol.86, pp.373-382, 1964.
- Chandra, S. and Avedisian, C.T., "Observations of Droplet Impingement on a Ceramic Porous Surface," *International Journal of Heat and Mass Transfer*, Vol.35, pp.2377-2388, 1992.
- Fatehi, M. and Kaviany, M., "Analysis of Levitation of Saturated Liquid Droplets on Permeable Surface," *International Journal of Heat and Mass Transfer*, Vol.33, pp.983-994, 1990.
- Kikuchi, A., Tamai, Y., Taniguchi, S., Tadaki, T. and Maeda, S., "Experimental Study on Cooling of Disk by Impinging Jet of Water," *Iron and Steel*, Vol.14, pp. 68-73, 1982.
- Kiyohashi, H., Kyo, M. and Ishihama, W., "Effect of Rock Temperature on the Thermal Fracturing of an Imitation Rock Specimen - Studies on the fracturing of hot dry rocks by high speed water jets -," *Journal of Mining and Mineral Processing Institute of Japan*, Vol. 94, pp. 515-521. 1978.
- Kiyohashi, H., Kyo, Shinkawa, M. and Ishihama, W., "Effects of Rock Temperature and Standoff Distance on Water Jet Drilling Performance for an Imitation Hot Dry Rock," *Technology Reports of Tohoku University*, Vol.45, pp. 137-168, 1980.
- Kiyohashi, H., Kyo, M. and Ishihama, W., "Application Technology of Hot Dry Rocks as Geothermal Energy Resources," *Journal of the Japan Society of Mechanical Engineers*, Vol.84, pp.1363-1369, 1981.
- Kiyohashi, H., "Application of Water Jets to Geothermal Extraction Technology - A technology for drilling and cutting of hot dry rocks and magma-," *Turbomachinery*, Vol. 17, pp. 747-752, 1987.

- Kiyohashi, H., Shinkawa, M., Kyo, M., Sekiguchi, R. and Matsushita, Y.,
 "Transient Boiling Heat Transfer on Hot Materials by Impinging Water Jet
 and the Thermal Shock Fracture," Proceedings of the International Symposi-
 um on Impact Engineering, Vol. 1, pp.400-405, Sendai, Japan, 1992.
- Kunioka, K., Hirata, S., Sugiyama, S. and Kamio, H., "Study on Water Jet
 Cooling of High Temperature Surface," Transactions of the JSME, Vol.45,
 No.390, pp.279-285, 1979.
- Lienhard V, J.H., Liu, X. and Gabour, L.A., "Splattering and Heat Transfer
 during Impingement of a Turbulent Liquid Jet," Transactions of the ASME,
 Journal of Heat Transfer, Vol.114, pp.362-372, 1992.
- Liu, X., Lienhard V, J.H., and Lombara, J.S., "Convective Heat Transfer by
 Impingement of Circular Liquid Jets," Transactions of the ASME, Journal of
 Heat Transfer, Vol.113, pp.571-582, 1991.
- Monde, M., "Critical Heat Flux in Saturated Forced Convection Boiling on a
 Heated Disk with an Impinging Jet", Transactions of the ASME, Journal of
 Heat Transfer, Vol.109, pp.991-996, 1987.
- Shoji, M., "A Study on Inverse Problem of Unsteady Heat Conduction,"
 Transactions of the JSME, Vol.44, No. 381, pp. 1633-1643, 1978.
- Stolz, G., Jr., "Numerical Solutions to an Inverse Problem of Heat Conduction
 for Simple Shapes," Transactions of the ASME, Journal of Heat Transfer,
 Vol.82, pp. 20-26, 1960.
- Sugai, T., "Removal of Kiln Deposit by Super-High Pressure Water Jets,"
 Proceedings of the 29th Symposium on Cement Manufacturing Technique,
 pp.126-128, Osaka, 1972.
- Touloukian, Y.S. and Ho, C.Y., "Specific Heat, Metallic Elements and Alloys,"
 in Thermophysical Properties of Matter TPRC Data Series, Vol. 4,
 Thermophysical Properties Research Center, IFI/PP NWE, 1970.

NOMENCLATURE

a : thermal diffusivity [m^2/s]	T_s : surface temperature [$^{\circ}C$]
c : specific heat [$kJ/(kg \cdot K)$]	T_{SAT} : saturated temperature [$^{\circ}C$]
D_o : nozzle diameter [mm]	T_{so} : initial temperature [$^{\circ}C$]
h : distance [mm]	ΔT : degree of superheat ($=T_s - T_{SAT}$) [$^{\circ}C$]
L : standoff distance [mm]	U_o : water jet velocity at nozzle exit [m/s]
q_r : local heat flux at r [W/m^2]	α : heat transfer coefficient [$W/(m^2 \cdot K)$]
r : radial distance [mm]	λ : thermal conductivity [$W/(m \cdot K)$]
T : temperature [K, $^{\circ}C$]	τ : time [s]
T_L : water jet temperature [$^{\circ}C$]	

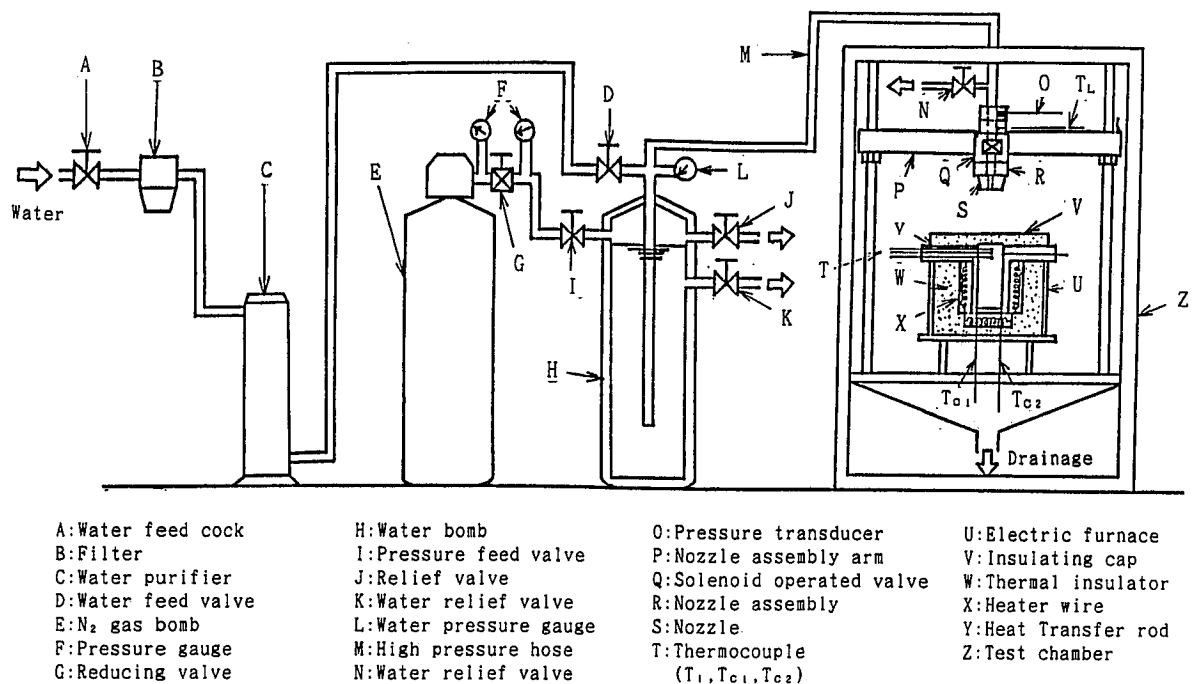


Fig. 1. Schematic diagram of experimental apparatus.

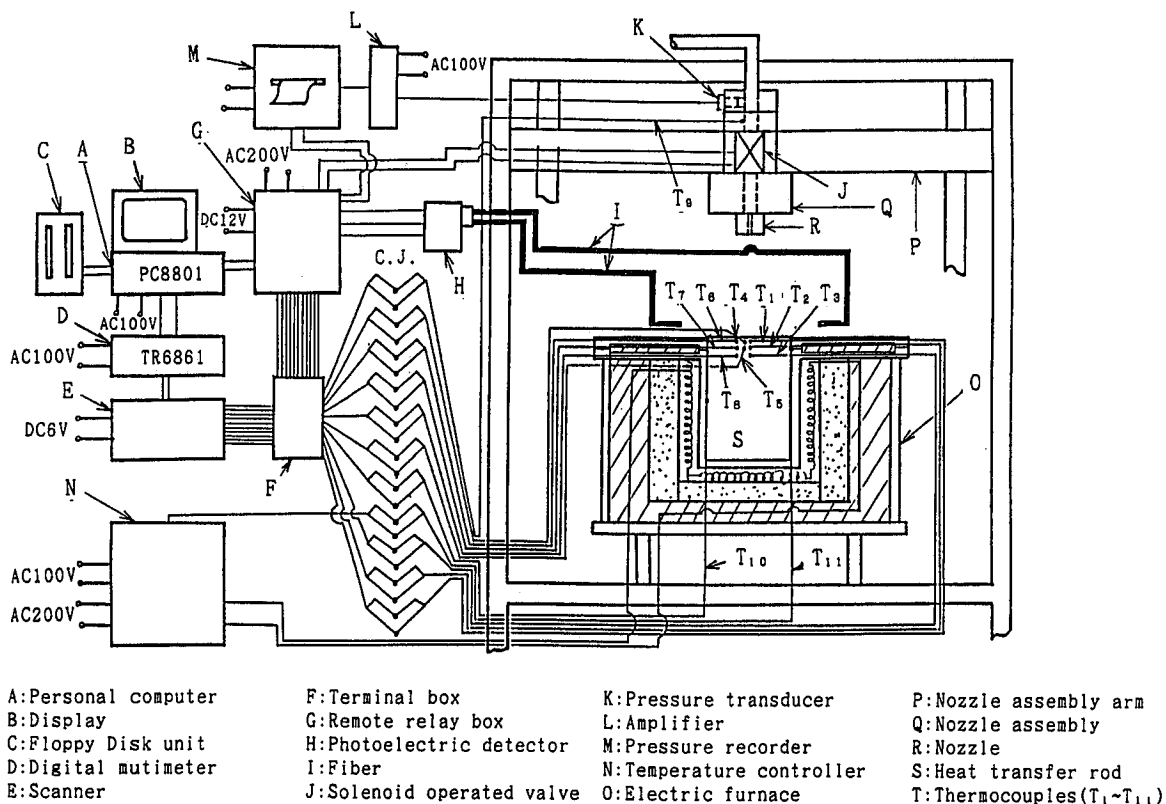


Fig. 2. Systems for data logging and temperature control of the electric furnace.

Table 1. Experimental conditions

D_o [mm]	T_o [°C]	U_o [m/s]	T_L [°C]	L/D_o
4.0	207	31.1	10.9	50
	206	62.5	9.7	
	208	108	9.1	
	397	30.8	13.0	
	400	62.0	9.3	
	401	109	9.4	
6.0	779	31.3	19.9	50
	783	61.8	16.2	
	779	108	13.6	
	203	31.4	13.9	
	191	62.8	14.2	
	192	105	13.0	
6.0	399	32.3	15.7	50
	405	62.8	15.3	
	400	108	15.2	
	757	31.3	20.2	
	768	62.0	17.3	
	772	109	15.8	

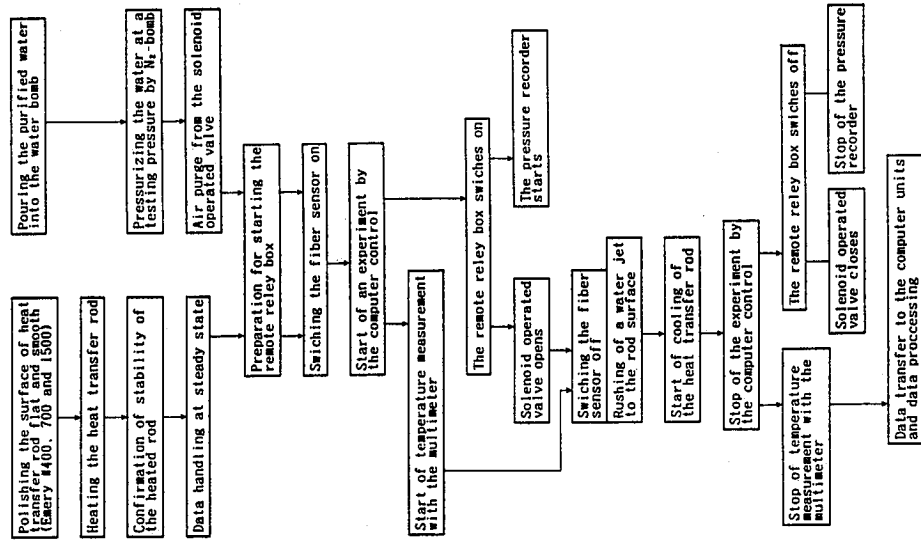


Fig. 6. Flow-chart of the experimental method.

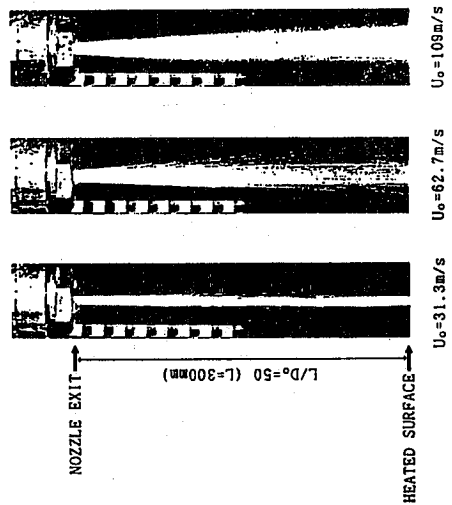


Fig. 7. Configurations of the water jets ($D_o=6.0$ mm).

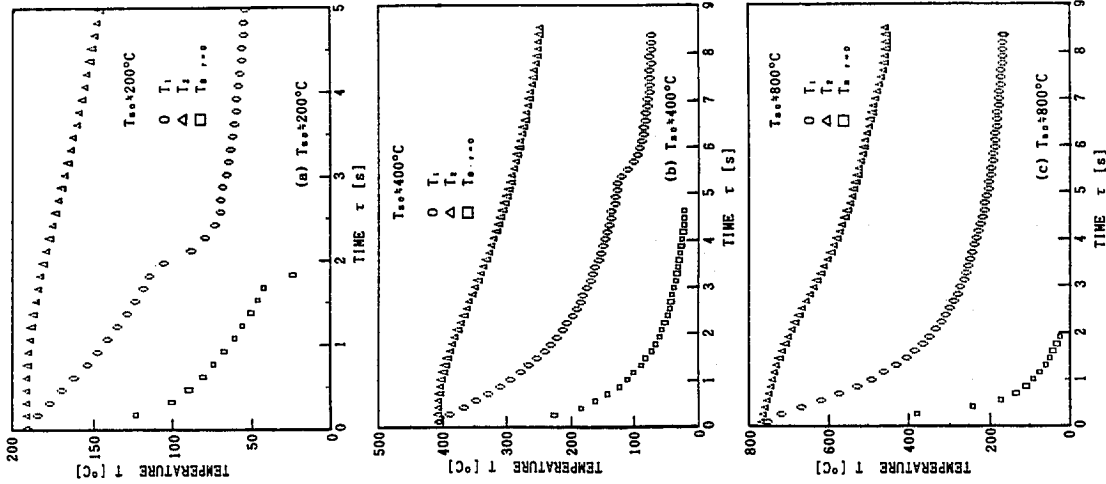


Fig. 8. Temperature histories at the two interior locations and at the stagnation point on the surface of the heated rod in the cases of $D_o=6.0$ mm and $U_o=62.8$ m/s.

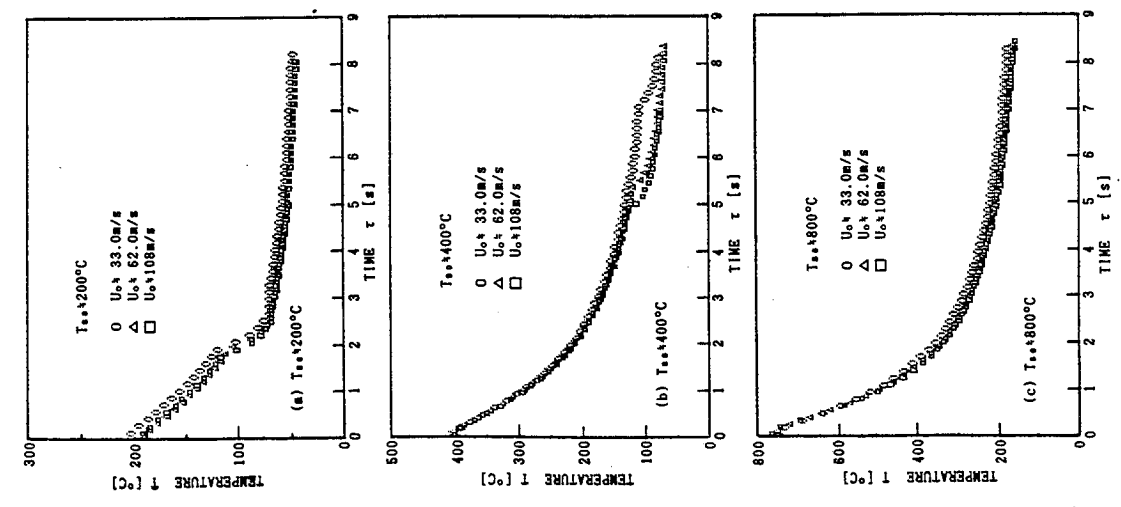


Fig. 9. The temperature histories at the interior location T_1 of the heated rod as a parameter of the jet velocity in the cases of $D_0=6.0\text{mm}$.

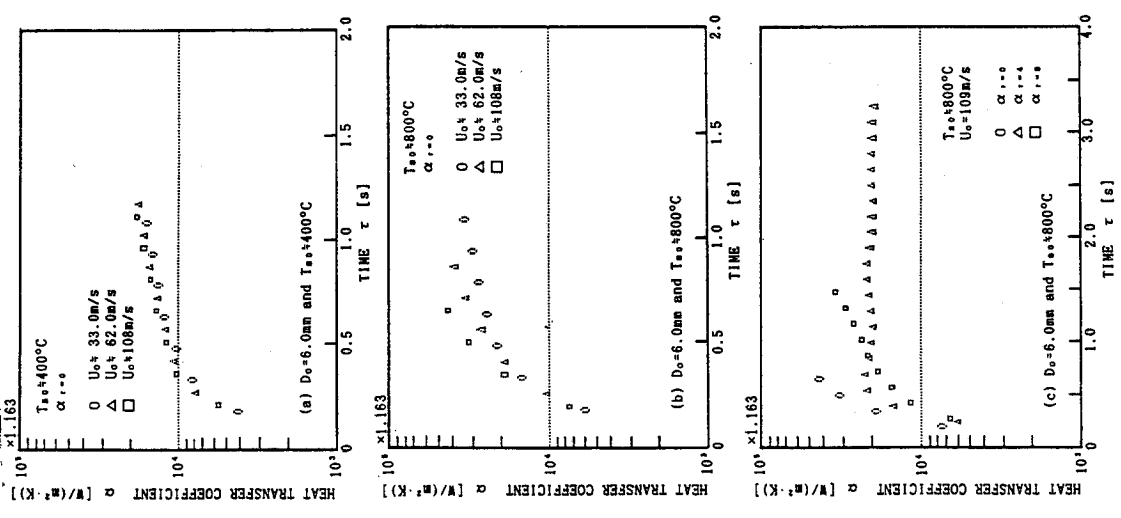


Fig. 10. Variations of the heat transfer coefficients with time in the cases of $D_0=6.0\text{mm}$.

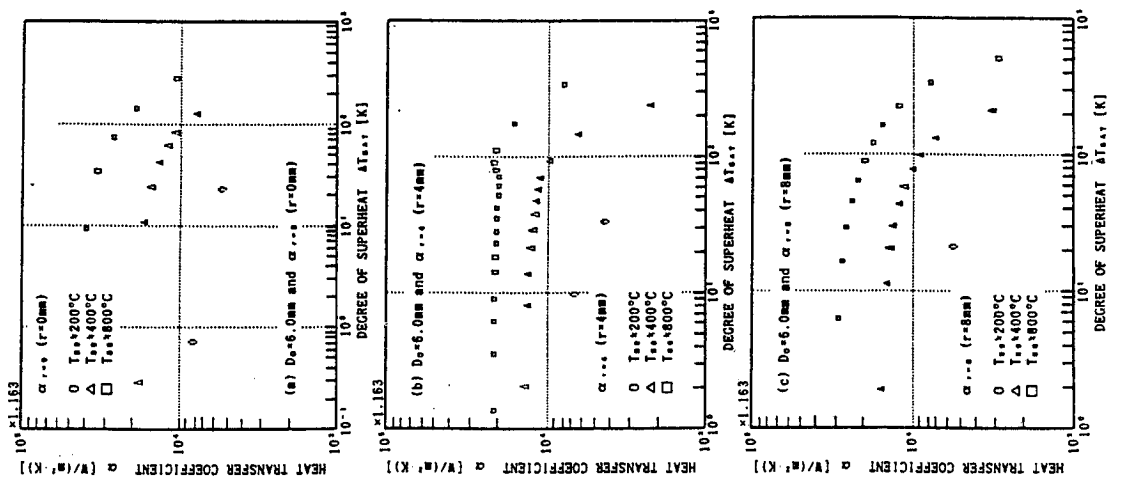


Fig. 11. Variations of the heat transfer coefficients with degree of superheat in the cases of $D_0=6.0\text{mm}$ and $U_0=62.0\text{m/s}$.

PERFORMANCES OF HP FLUID JET TO CUT FOOD PRODUCTS

Claudie MERLE
AQUARESE Industries
Massy, Essonne, France.

Marielle BOUX, Marc SIONNEAU, Jean VASSEUR
Ecole Nationale Supérieure des Industries Agro-Alimentaire (ENSIA)
Massy, Essonne, France.

ABSTRACT

A short synopsis of the applications of water jet cutting in food industry summarizes the main advantages and special conditions of using this technology for these type of products.

Different experiments are conducted to study the hygienic aspects of cutting foods by high pressure water jets. Special recommendations are given for the quality of the water and the ambient air.

Methodologies have been elaborated to study the slicing of bread. Cutting performances are evaluated by 3 paramaters of "lenght of cut" ; a linear model is suggested to correlate these paramaters with the process parameters (d, P, u), and to choose the optimal conditions to get complete cuts. Some experiments have been realised to estimate the moistening pick up and the loss of the material due to the jet.

1. INTRODUCTION.

Cutting is a very important standard unit operation in food processing. It is often indispensable for harvesting and trimming agricultural products before transformation. Also, many products will be conditioned as pre-cut portions. There are even food industries in which the food transformation consists of a sequence of cutting operations (example: slaughter houses).

As canned, frozen and prepackaged food in portioned volumes penetrates the world markets, individual domestic cutting is being shifted to the food processing industry.

In most market studies on applications for the high pressure waterjet cutting process, the food industry is mentioned as a candidate with many opportunities [Lombard ; Heiland et al.- 1990].

2. STATE OF THE ART.

In the early 70, when waterjet cutting installations had reached an industrial standard in other industries, also the food industry became interested in the new technology. However, the first companies involved tried to use a liquid, which would be more compatible with their products than water, for instance vegetable oil or heated cocoa butter for confectionery. Since that time the term "Fluid Jet" should be used rather than the standard term "waterjet".

Today approximately one hundred "high pressure fluid jet installations" worldwide are reported to cut food products; this represents less than 5 % of all the HP fluid jet applications in other industries.

Geographically, the food cutting installations are located: 50 % in the America, 40 % in Europe and 10 % ROW.

The main sectors equipped with fluid jets are the meat and fish portioning and the candy bar and cake cutting.

Slitting and crosscutting of bakery or confectionary goods in many different arrangements make up for 20 % of all food applications. (Fig. 1)

Combined with completely automatic vision-control and weighing systems, the CNC controlled jet cuts fish filets and chicken breast to the gram. (Fig. 2)

15 % of the equipments are used for research in public or private centers. Shield et al. (1973) investigated HP jet for cutting of lettuce stems ; Heiland et al. (1990) proposed to use an automatic controlled HP water jet for excising objectionable material from slices of bone-in beef chuck ; BECKER R. and GRAY G.M. (1992) evaluated cellular damages and consequences on potatoes slices.

3. SPECIAL CONDITIONS FOR THE CHOICE OF EQUIPMENT.

Several mayor criteria have to be evaluated for the choice of the cutting tool.

3.1. Reactions between Tool and Material.

For certain products knives or saws will have to be heated, cooled or vibrated (by ultrasonic waves) in order to avoid sticking and to have a smooth cut.

Very elastic or jelly material will be strained and are deformed after cutting. Hard particulate in a soft matrix can be displaced by the tool and cause holes, crushes or striation.

The fluid jet can solve many of these problems due to its small diameter, concentrated energy and high speed.(up to $4 \cdot 10^8$ J/m³ and 900 m/s)

3.2. Output, loss of material.

For portioning of material containing imperfections or inclusions like bones, fat, parasites the mechanization of the cutting process with knives and saws normally will result in excess loss of material.

The fluid jet is ideally suitable for robotic positioning and CAM nesting programs, due to its omnidirectional feature and instantaneous on/off capability. Thus the waste will be minimized. These are the main arguments presented by Heiland et al (1990), Frigoscandia (1988) and Lumetech (1990).

3.3. Flexibility.

On mechanized production lines, the product mix often changes as to hardness, composition, dimensions or weight. The number and positions of the jets and the cutting parameters can be adapted much easier to changing conditions than any other tool.

3.4. Hygiene.

Food stores require products with a long shelf life. This can only be achieved by a processing under ultra hygienic and germ free conditions. A mechanic tool, once contaminated, will contaminate through its repeated material contact automatically all the product that passes the line. This can result in a large amount of rejects. The fluid jet with its continuous stream and non repeatable surface contact to the material reduces the risk of contamination and the cleaning frequency.

4. STUDY OF HYGIENIC CRITERIA AND CONDITIONS FOR THE FLUID JET.

The possible sources for contamination of the cut product are the following :

- The fluid jet itself.
- The ambient air, which is entrained by the jet.
- The conveyors and other surfaces in contact with, or closed to, the product.
- The product itself.

The experimental study concentrated on the influence of the jet and the ambient air .

4.1. Materials and Methods.

4.1.1. High Pressure Equipment.

A single intensifier pump "Flow International" with a capacity of 3.1 liters per minute at 3 800 bars pressurized one or two stationary nozzles with standard on/off valve. The demineralized tap water was supplied to the pump through a water booster and filtration unit equipped with standard filters down to 0.45 micron. No additives were applied to the water.

4.1.2. Cutting Table.

The sterile material was placed on the sterilized surface of a slitting table, which can be moved at speeds from 0.1 to 50 meters per minute under the stationary jet. The principle of the catcher and its suction device excluded splash back from underneath. The set-up permitted to cut under a hood with ambient air or with a small overpressure of filtered clean air.

4.1.3. Sampling and Measurement of Water Contamination.

Under sterile conditions the water samples were taken:

- at the tap
- after demineralization (by means of cationic and anionic resins).
- after booster and filtration unit.
- at the nozzle exit (the water must be caught in cooled container to avoid heating, due to the dissipation of the jet's energy).

The samples are diluted (from 10^0 to 10^{-5}) or filtered (at $0.45 \mu\text{m}$), depending on the concentration of microorganisms. An inoculated, nutritious matrix PCA (Plate Count Agar, at 15 g/l) enriched with Glucose (2 g/l), serves for the observation and counting of the microbial colonies after 72 hours of incubation at 30 degrees centigrade.

4.1.4. Sampling and Measurement of Air Contamination.

The air samples are captured in Petri dishes, which contain a sterile nutritious matrix PCA, enriched in agar (45g/l) and glucose (2g/l) ". Petri dishes are opened on the slitting table near the material, all along the cutting experiments (Fig. 4), and evaluated after an incubation of 72 hours at 30°C.

4.1.5. The Product to Simulate Food.

Under sterile conditions a cylinder of nutritious material (500 ml) was poured into a mold consisting of a plastic film. The solidifying liquid basically has the same composition as the matrix used for the inoculation : 45 g/l of agar and 2 g/l of glucose. The cylinder was positioned on the slitting table horizontally allowing round slices to be cut (Fig.4).

Using a 0.18 mm diameter nozzle at 380 MPa, the slices were cut at the speed of 5 m/min. ; the stand off distance between the nozzle and the top of the product was minimal (1 to 3 mm).

After cutting, the single slices were removed from the table with the help of sterile pliers and put into a Petri dish and evaluated as above.

4.2. Results and Discussion of Hygienic Conditions.

4.2.1. Water Contamination.

The results are summarized in Fig. 3.

- The demineralization device is a considerable source of water contamination due to the fact that the micro balls of resin can be a nutriment for the bacteria. The discontinuous mode of operation enhances the growth of the germs.

- The standard filtration of 0.45 micron is not sufficient to retain all the microorganisms.

In order to solve the problem there are two suggestions:

- change the sequence of filtration from 10, 1 and 0.45 micron to 5, 3 and 0.2 micron.
- install a closed loop in order to circulate the water constantly in the whole system, even when the high pressure pump runs idle or stops. This closed loop will also serve to regularly sanitize the circuit by steam or by chemicals. Thus no films of germs can develop on the inner walls of the system elements.

- High pressure treatment of the water (in the pump and all tubing), and then the decompression at the nozzle has a real influence on the non-multiplication of the micro-organismes. A 10^2 microbial reduction is obtained with $P = 380 \text{ MPa}$ and $d = 0.18 \text{ mm}$.

Today a lot of researches are done on the influence of the high pressure on the micro-organismes, specially with the objective to find a treatment that eliminates the germs and preserves the special

characteristics of foods (flavor, taste, color, texture) ; this seems to be possible with very high pressure (up to 1000 MPa) when high temperature modifies most of the quality characteristics. Ludwig et al.(1992) and Smelt & Rijke (1992) got 10^2 to 10^5 reductions on *Escherichia coli* during hydrostatic pressure treatment of 5 min at 350MPa.

For the water used as cutting medium, some complementary experiments will be necessary to confirm if the microorganismes are really killed or only inactivated because of the stress of high pressure and decompression treatments. Optimisation of the pressure, the nozzle diameter and other important parameters (like time, temperature, pH, air quality) should be done to control the minimal level of contamination that could be obtained with this process.

Consequently, to be sure of the hygienic quality of the jet, it is recommended to provide a sterilizing filtration system, as describe above.

4.2.2. Air Contamination.

The tests, evaluated in Fig. 5 have been made with ambient air, which always is naturally contaminated with molds, yeast and bacteria. The results presented in Fig. 5 are given in average number of CFU (Colony Forming Unit), observed on one Petri dish and on one agar slice, contaminated during the same experiment.

Part of the germs from the air was found on the surfaces of the cut. The depression created by the high speed of the fluid jet entrains the ambient air into the kerf. It appears that the micro organisms will adhere to the surface of the nutritious material and grow from there.

The consequences from the observations will certainly depend on the biologic properties of the food to be cut and the following steps of processing. For all products which are sensitive to contamination and which will be packed directly after cutting, we suggest to put the cutting station into an enclosed space, where an air quality class 100 and positive pressure can be maintained. (Class 100 : Less than 100 particles larger than 0.5 micron per cubic foot. Generally there will be 1 microorganism per 1000 to 10000 partcles.)

5. CASE STUDY: CUTTING BREAD

5.1. Materials and Methods.

5.1.1. Cutting Equipment.

The basic set-up of high pressure and motion control equipment was the same as for studying the hygienic criteria.

- Maximum pressure $P = 3800$ bar
- Variable cutting speed $u = 0.1$ to 50 m/min.
- Diameters of the nozzle $d = 0.1$ to 0.33 mm

5.1.2. Characteristics of the Bread.

The white bread, which was used for testing, had the French standard dimensions.

- cross section 72×72 mm
- total length 230 mm

The industrial recipe for a shelf life of 6 months includes the following ingredients: wheat powder, water, yeast, milk by products, sugar, animal fat, emulsifiers, Soya lecithin, salt, extract of malt, ascorbic acid, natural tocopherols.

The density of the packaged bread was 0.23 g/cm³ at an average moisture of $H = 31$ % of total weight, equivalent to $X = 0.45$ of the dry mass.

5.1.3. Choice of the parameters.

- Process parameters.

For this first series of experiences, and following the experimental work described by different authors [BECKER - 1992 ; HASHISH & duPLESSIS- 1978 ; HEILAND et al.-1990 ; LOMBARD ; and YAZICI & SUMMERS - 1987], we have chosen only the three fundamental variables to control the process:

- d : internal diameter of the nozzle
- P : water pressure at the exit of the pump
- u : speed of the relative movement between nozzle and material

- Cutting performance.

In literature [HASHISH & duPLESSIS - 1978 ; YAZICI & SUMMERS - 1987], generally the depth of cut in material of unlimited thickness is used to describe the performance of a liquid jet. However, for bread and food in general, this alone is not sufficient to characterize the cutting performance. First of all, food comes in naturally grown dimensions, which are similar, but irregular and macroscopically inhomogeneous. Even, if food is molded into specific shapes, like bread, there may be a crust, which means different hardness on the surface as well as at the entry and exit of the jet, horizontally and vertically. Rather than extrapolating cutting performance from the depth of cut, it is necessary to establish quality parameters of the real product, as it is sold.

The cross section schematically presented in Fig.6 shows an incomplete cut. The uncut areas are due to the deflection of the jet by the crust. The parameters must be adapted to reduce jumps or deflections when the jet passes over the crust or exits.

In order to define and describe the results of cutting bread, three illustrative parameters have been chosen :

- L₁ = depth of cut at the start
- L₂ = depth of cut at the end
- L₃ = the distance between the uncut areas at the bottom of the bread.

These parameters consider the specific inhomogenities and the morphology of bread.

Ten repetitions for each identical experimental configuration have been performed in order to verify the validity of the results.

- Other important features.

In literature, very often the roughness or striation on the surface serves to describe the quality of the cut. Although important for most food as well, the surface quality could be neglected for the tested type of bread.

However, materials with a high porosity, like bread, tend to be considerably moistened by the waterjet. This should be minimized and controlled.

The amount of kerf material, entrained by the jet and flushed into the catcher, has an impact on the economics of the cutting process. Its recuperation and the treatment of the waste water are also a cost factor.

Both, humidity pick up and loss of kerf material were measured by simple weighing , evaporation (105 ° C , 24 h) and calculated mass balance before and after the cut.

- M_L = loss of kerf material in mg per cm²
- M_{WJ} = water deposited to the surface by the jet in mg per cm²

The sum of all slices M_{WJ} - M_L represents the total difference of weight between the loaf of bread before and after cutting.

All measurements must be referred to the created surface in order to be comparable.

5.1.4. Schedule of Experiments.

To characterize the cutting performance, the three control parameters (d,P,u) have been varied according to a decision matrix (Central Composite Experimental Design) ; 16 variations were determined to be sufficient to cover the experimental field.

To evaluate the moistening and the loss of material, only those slices have been chosen, which had been completely cut. Starting from there, d, P and u were changed continuously according to trial and error.

5.2. Results and Discussion.

5.2.1. Cutting Performance.

The results for the 16 experiments were analyzed using the computer program SYSTAT.

For this first step, a linear model of second order were proposed to describe the influence of the variables on the results of cutting.

Three equations are expressed to correlate the jet performances, in terms of L₁, L₂ & L₃, with the process parameters (d, P, u and the linear combinaisons of second order) ; that means 10 coefficients for each 3 models.

The squared multiple regression coefficients of these equations has value of 0.886 to 0.925. The dispersion of the calculated results versus the experimental results is plotted in Fig. 6, and can be evaluated as acceptable. This type of model is simple and suitable for this first study, but other regression models will be considered in the future.

With these equations, the theoretical variations of L₁, L₂ and L₃ versus d and P can be expressed, for different invariable values of u. Some of these 3 dimensional graphes are plotted in contours in the figures 7, 8 and 9.

For the tested type of bread it has been decided, with a safety margin, that the industrial purpose of "**complete cut**" for all the slices, was realised for L₁, L₂ and L₃ superior or equal to 80 mm.

Figures 10, 11 and 12 describe how to manage the 3 process paramaters, d, P u to get complete cuts on L₁, L₂ and L₃.

The curves describing L₁ and L₂ have quite the same shape ; but the cut is harder at the start (L₁) than at the end (L₂). The nozzle diameter seams to have less influence at the bottom cut (L₃) than at the start and end cuts. Consequently, the process paramaters have to be chosen according to the results obtained for the start cut (L₁), which is the limited factor for the complete cut of the slice.

5.2.2. Moistening and Loss of Material.

White bread will pick up moisture from the waterjet and will loose kerf material in the order of :

$$M_{WJ} = 3 \text{ to } 20 \text{ mg / cm}^2 \text{ and } M_L = 3 \text{ to } 8 \text{ mg / cm}^2.$$

For the complete loaf of 23 slices the variation of the results are estimated at :

$$M_{WJ} = 11 \text{ to } 47 \text{ g and } M_L = 8 \text{ to } 18 \text{ g.}$$

Generally the bread gains more water than it looses kerf material. The total change can vary between a loss of 1 g and a gain of 47 g.

The dominating influence on the water pick up is first the pressure P and then the traverse speed u. It seams that minimal moisture pick up can be obtained at P = 3000 to 3500 bars and at u = 20 to 30 m/min.. These values are probably function of the contact time between the water jet and the material, and the ability of this one to absorb water. But those results will be confirmed in the future by complementary tests.

6. CONCLUSIONS

There are many advantages for food industries to use a HP pressure fluid jet systems to cut their products ; specially due to the present preoccupations with hygiene and longer shelf life.

The experiments described above indicates what are the conditions to make with the jet a perfectly clean tool :
- for the cutting media : filtration at 0,2 μ m and regular sanitation of the tubing
- for the ambient air : controlled atmosphere, class 1000 or 100, according to the product.

These operations are quite usual in this type of industry, and will not give any major problems.

With the case study of bread a methology have been elaborated to understand how HP jet cuts this type of product. The values of kerf loss and the moisture pick of the material can be now compared to other cutting tools.

ACKNOWLEDGMENTS

All this research work could not have been done without a complete, profitable and sympathetic collaboration between a University partner, that is ENSIA, and an Industrial partner, that is AQUARESE Industries. Both brought their own competency and materials, to make this technology well adapted to the preoccupations of the food industry : know-how on food science and food process and know-how on high pressure fluid jet.

So the authors wish to acknowledge the staff of ENSIA and AQUARESE for their invaluable assistance with this work.

A very special thank is given to Dr. Uwe EHLBECK, wellknown by a great number of water jet users, for all he did in order that this paper exists for the 7th American Water Jet Conference.

REFERENCES

BECKER R. & GRAY G.M.

"Evaluation of a water jet cutting system for slicing potatoes"
1992 - p. 132 à 137 Journal of food science - Vol 57, N°1

DESIGN SYSTEM Inc.

" A clear cut difference in food processing"
1988 - 4 p.
Publisher : Design System Inc. (USA)

HASHISH M. & duPLESSIS M.P.

"Theoretical and experimental investigation of continuous jet penetration of solids"
Février 1978 - p. 88 à 94
Transaction of ASME, J. engineering for industry - Vol 100

HEILAND W.K., KONSTANCE R.P. & CRAIG J.C , JR

"Robotic high pressure water jet cutting of chuck slices"
1990 - p.131 - 136 Journal of food process engineering 12

LANGEMAN M.

"Jet cutting of candy bars"
1987 - 23 p.

Publisher : Flow International - Kent (USA)

LOMBARD D.B.

"History of waterjet cutting and application the food industry"

25 p.

Publisher : Flow International - Kent (USA)

LUDWIG H., BIELER C., HALLBAUER K. and SCIGALLA W.

" Inactivation of microorganisms by hydrostatic pressure"

in High Pressure and Biotechnology, Proceedings of the First European Seminar on High pressure and Biotechnology

Publisher : INSERM (France) ; Colloque INSERM vol 224 ; pp 25-32, 1992

LUMETECH Ltd

" Automatic trimming machine for fish fillets"

1990 - 6 p.

Publisher : Lumetch Ltd. (Denmark)

SMELT J.P.P., RIJKE G.G.F

" High pressure treatment as a tool for pasteurisation of foods"

in High Pressure and Biotechnology, Proceedings of the First European Seminar on High pressure and Biotechnology

Publisher : INSERM (France) ; Colloque INSERM vol 224 ; pp 361-364, 1992

YAZICI S. & SUMMERS D.A.

"The use of high pressure water jets in cutting foam"

Proceedings of the 4th U.S. Water Jet Conference (Berkeley)

1987 - p. 11 à 18

Publisher : The American society of mechanical engineers (N.Y.)

NOMENCLATURES

d	internal diameter of the nozzle (mm)
L ₁	depth of cut at the start of the product (mm)
L ₂	depth of cut at the end of the product (mm)
L ₃	total of distances between the uncut areas at the bottom of the product (mm)
M _L	loss of kerf material (mg/cm ²)
M _{wj}	water deposited to the cut surface by the jet (mg per cm ²)
P	water pressure at the exit of the HP pump (MPa)
u	traverse speed of the material under the jet (m/min.)

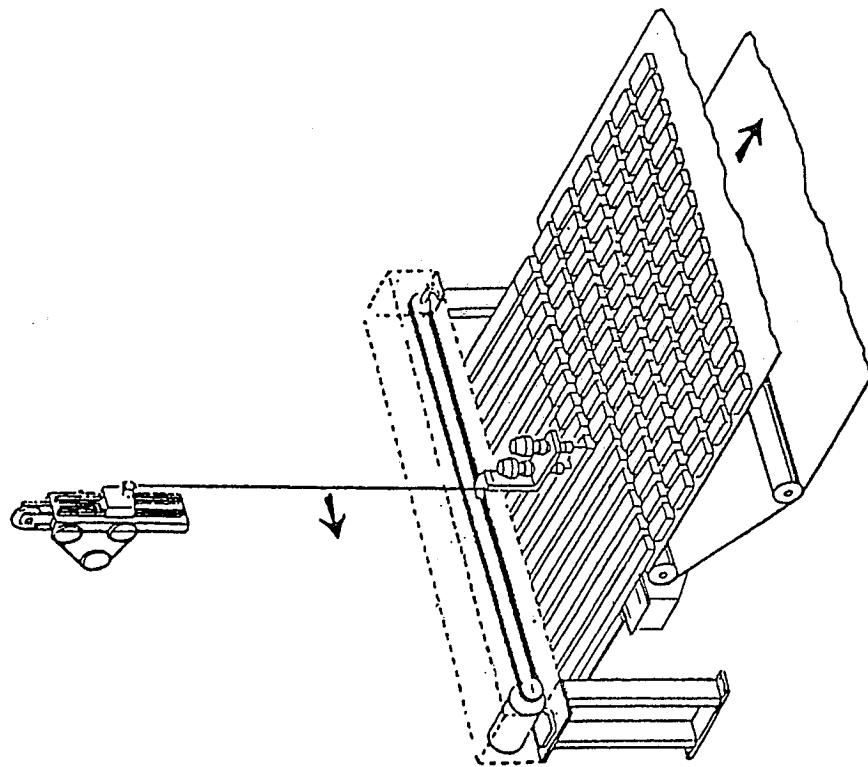


Fig. 1 - Slitting and Crosscutting Table
[LANGEMANN, 1987]

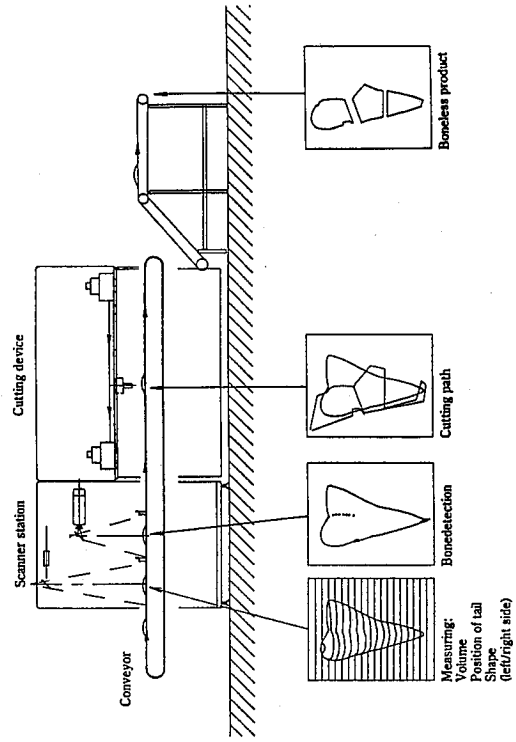
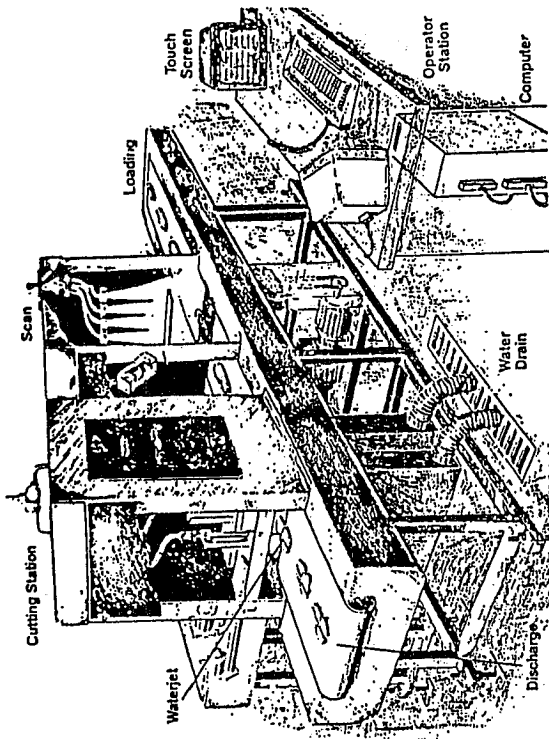


Fig. 2 - Automatic Portioners with Vision System
[DESIGN SYSTEM, 1988] [LUMETECH, 1990]

MAIN HP FLUID JETS CUTTING EQUIPEMENTS, USED IN FOOD INDUSTRY

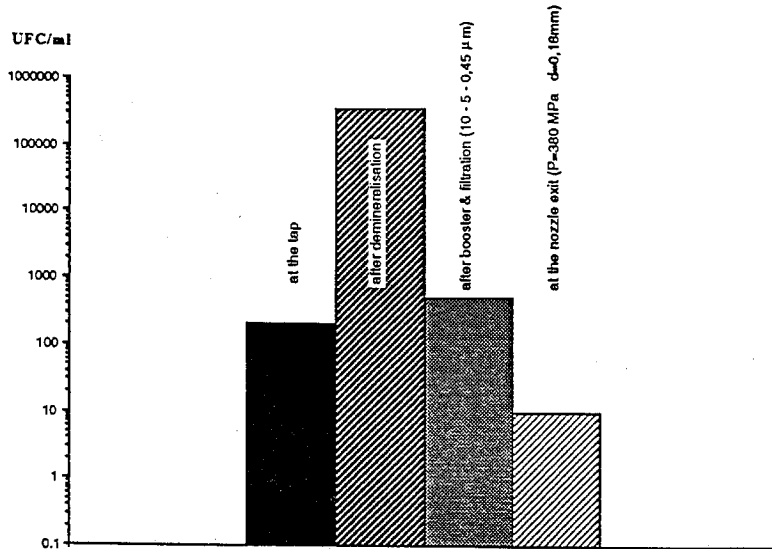


Fig. 3 - Contamination of the Water in the Different Samples

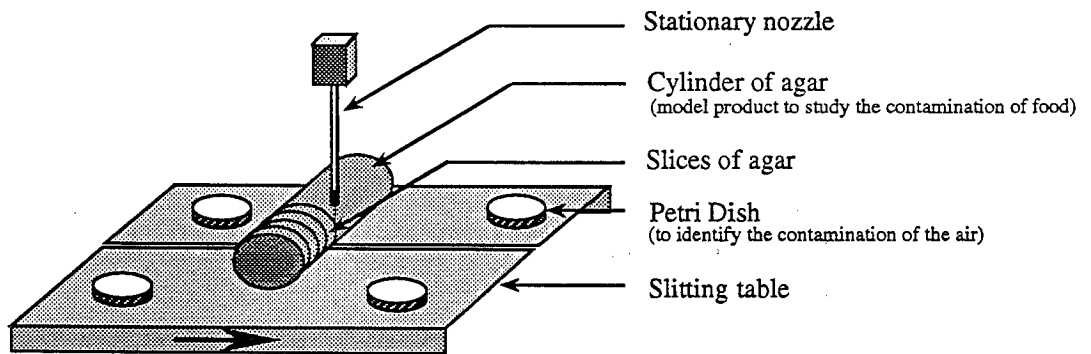


Fig. 4 - Material & Method to study the Contamination Transfers from the Air to the Cut product

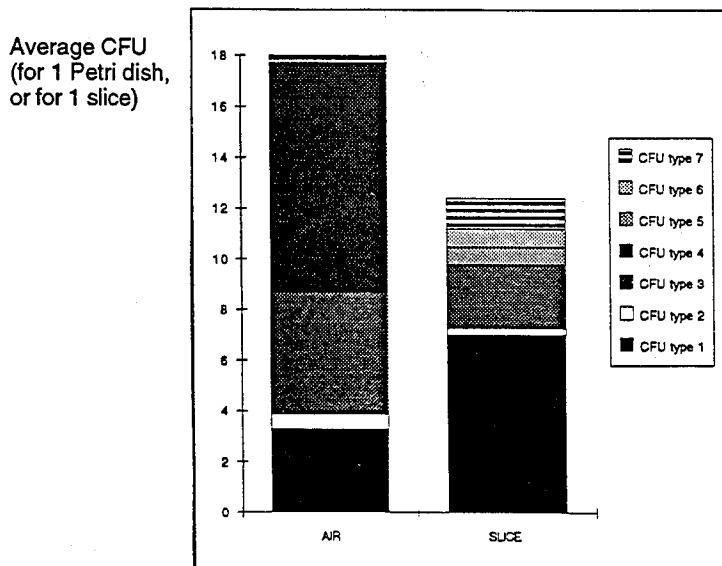


Fig. 5 One Result of the study of Contamination Transfers from the Air to the Agar Slices during Water Jet Cutting

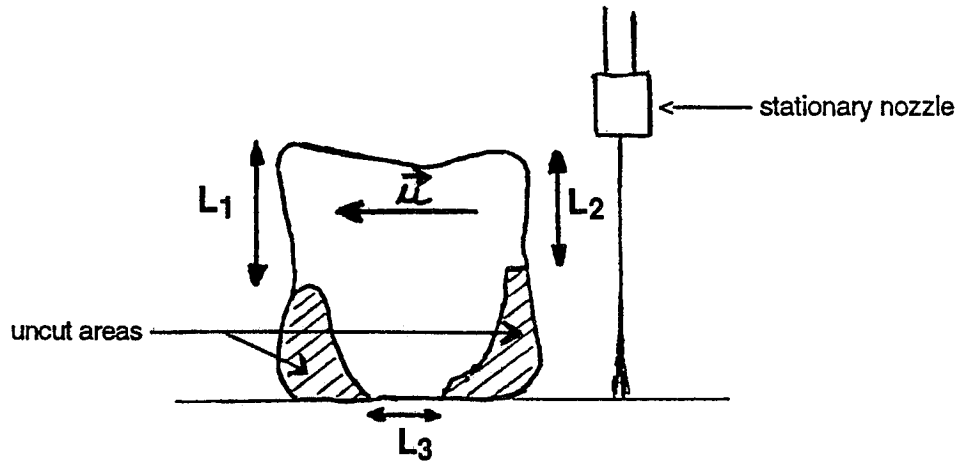


Fig. 6 - Cross section of an incompletely cut slice of bread and presentation of the 3 cutting parameters

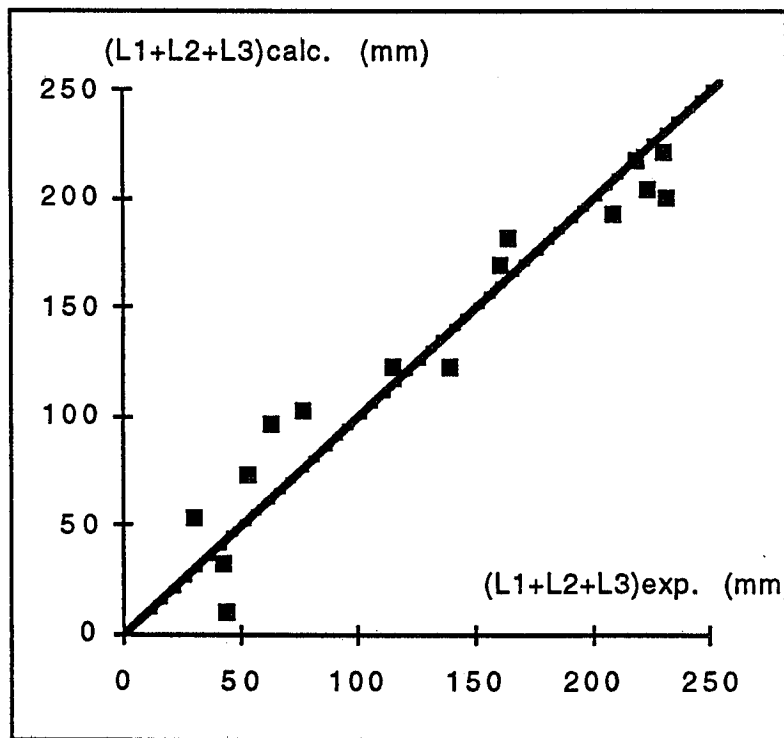


Fig. 7 - Validity of the model in term of dispersion of the calculated results versus experimental results

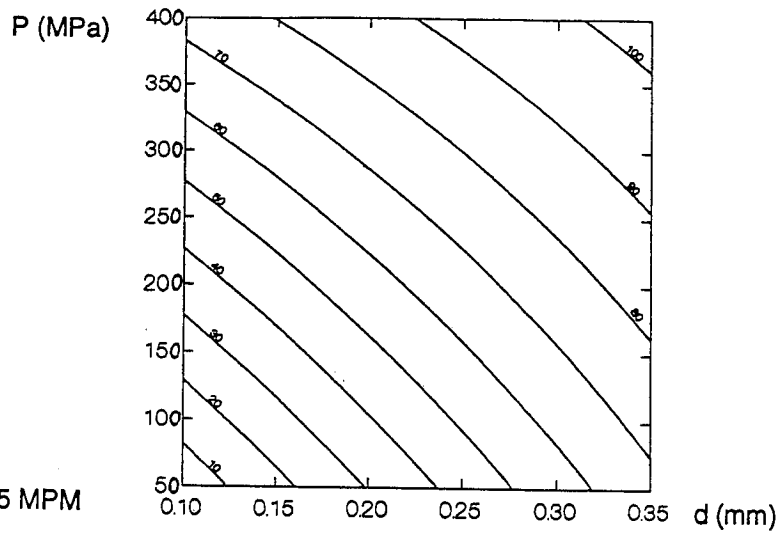


Fig. 8 - $L_1 = f(d,P)$ for $u = 5$ MPM

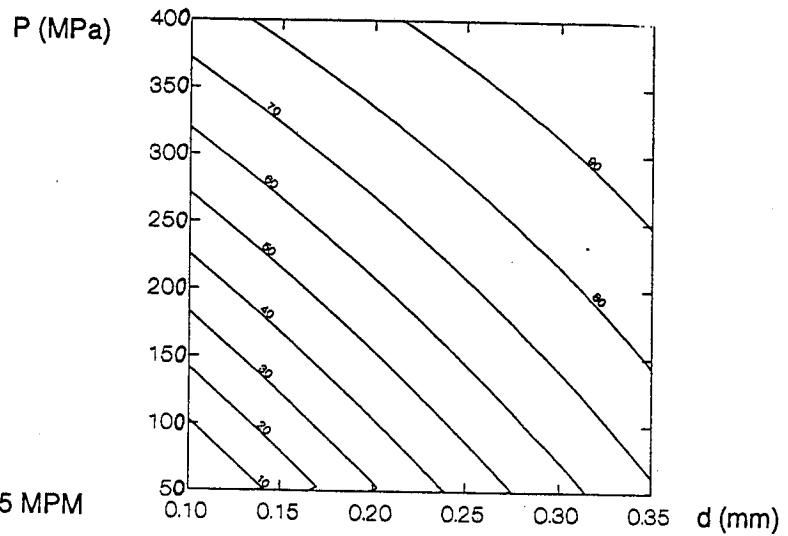


Fig. 9 - $L_2 = f(d,P)$ for $u = 5$ MPM

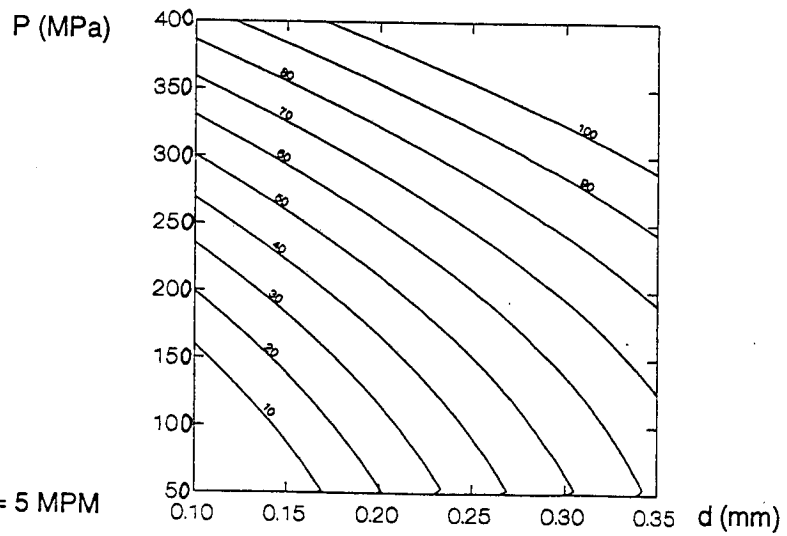


Fig. 10 - $L_3 = f(d,P)$ for $u = 5$ MPM

Calculated variations of the 3 cutting parameters (L_1 , L_2 , L_3) versus nozzle diameter and water pressure for a traverse speed of 5 MPM

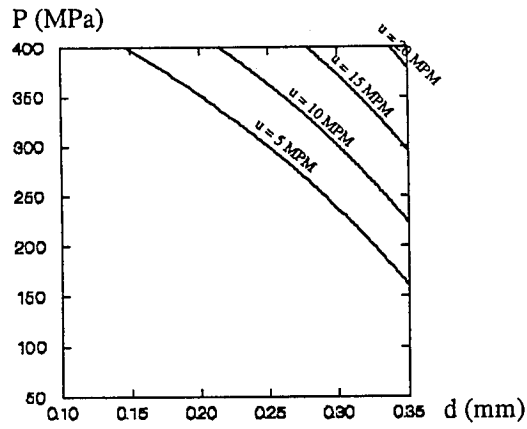


Fig 11. (L1 = 80 mm) = f(d,P,u)

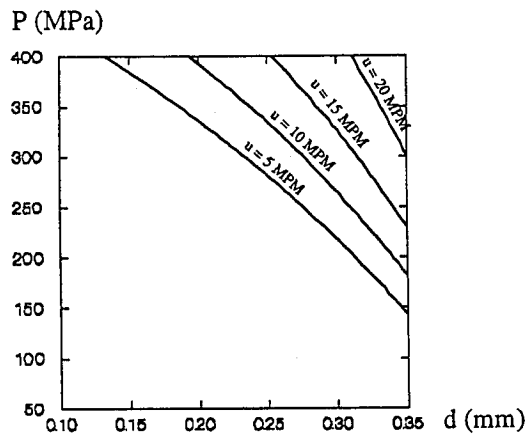


Fig 12. (L2 = 80 mm) = f(d,P,u)

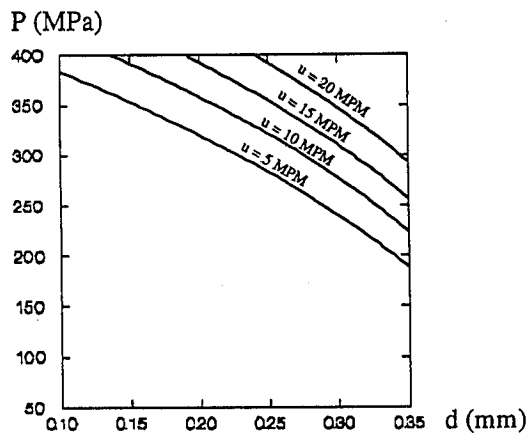


Fig 13. (L3 = 80 mm) = f(d,P,u)

Variation of the Process Parameters d, P, u to get Complete Cuts on L1, L2, L3 for the Tested Bread

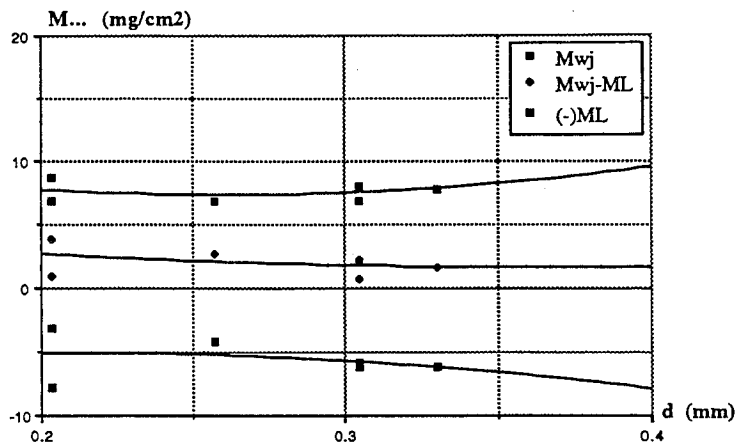


Fig. 14 - Variations of Mw & ML versus d for P = 350 MPa and u = 5 MPM

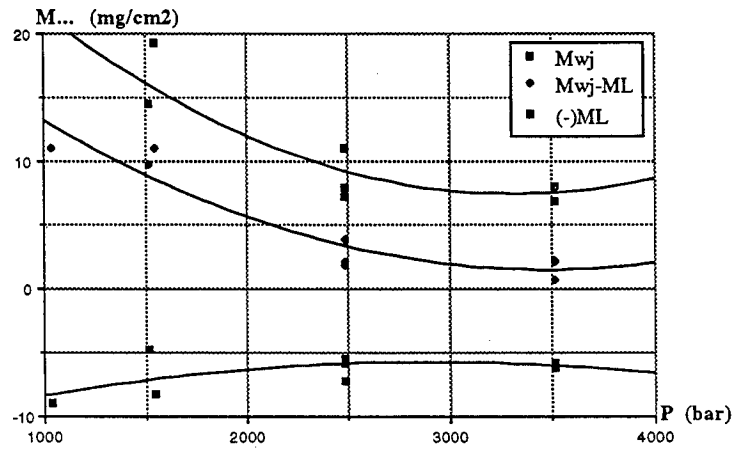


Fig. 15 - Variations of Mw & ML versus P for d = 0.30 mm and u = 5 MPM

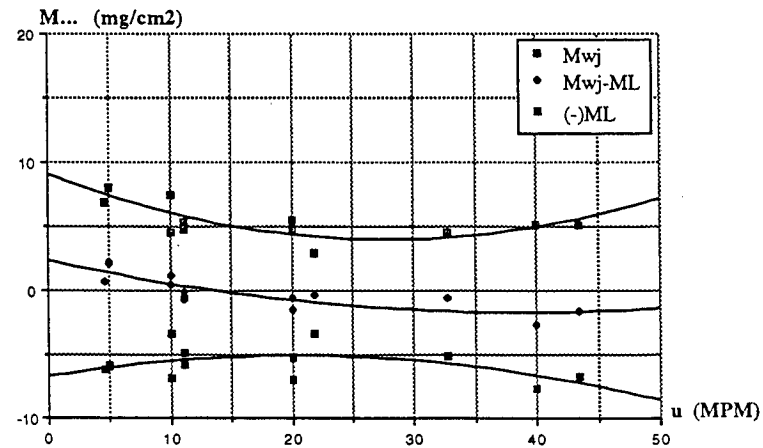


Fig. 16 - Variations of Mw & ML versus u for d = 0.30 mm and P = 350 MPa

A MODEL FOR MILLING WITH ABRASIVE WATER JETS

A. Laurinat, H. Louis, G. Meier-Wiechert
Institut für Werkstoffkunde
Universität Hannover, Hannover, Germany

ABSTRACT

The first part of the paper is concerned with the definition of optimal process parameters to achieve high material removal rates as well as high specific material removal rates in relation to the consumption of power, of abrasive and of water. The definition of optimal parameters has to take into account the specific requirements of milling with abrasive water jets which covers e.g. the necessity to produce kerf profiles with a regular shape. Secondly it is shown that a simple cosine function is suitable to describe a variety of different kerf profiles produced by various parameters. Based on the description of the kerf profile by the cosine function thirdly a model is introduced which allows to predict the depth as well as the width of the kerf in relation to selected parameters. This model is verified for different materials. Finally the superposition of kerf profiles is modelised for both cases total and partial superposition. The accuracy of this model is proofed by milling tests.

1. INTRODUCTION

Abrasive water jets are available since one decade (Hashish, 1982) and mainly used for cutting applications. But abrasive water jets have the opportunity to become a flexible tool for manufacturing allowing milling, turning and piercing operations (Hashish, 1985 and 1992). In case of machining non-rotary-symmetrical parts fig. 1 shows schematically two possible manufacturing strategies. On the left side the final geometry is produced by removing coherent parts of the workpiece. It is obvious that this strategy is only applicable to simple machining tasks but it shows a good ratio of material to be removed by the abrasive water jet to material totally removed from the workpiece. On the right side the geometry of the workpiece is changed by a complete removal of the material due to a multiple-passing operation. Although the ratio mentioned before is more unfavourable in this strategy, which is comparable to conventional NC-milling operations, it allows to machine parts of a more complex geometry. Milling with abrasive water jets can be done on one hand side by using a mask to achieve sharp edged final shapes (Hashish, 1985), but in this case applications are limited to two-dimensional milling operations. On the other hand side the milling operation can be based on a deterministic approach which is subject of this paper. The elements of this approach which were introduced in (Freist et al., 1989) are

- modelling of the interaction between abrasive water jet parameters and the kerf profile
- modelling of the interaction between subsequently superposed kerf profiles.

The combination of both models which is subject of running research work aims at choosing an optimal sequence of operations and at predicting the workpiece geometry at any time during as well as at the end of the machining operation.

2. FACILITIES AND MATERIALS SPECIFICATION

An intensifier with maximum pressure of 400 MPa and maximum flow rate of 4 l/min was used for all tests. The abrasive water jet was generated by a self designed adjustable cutting head. Abrasive used was Olivine AFS 60 with a narrow particle size distribution (60 mass-% in the range of 250-355 μm , 27 mass-% in the range of 180-250 μm , 4 mass-% over and 9 mass-% below these ranges).

The profile was measured by a modified tactile roughness measurement system with a measuring range of ± 5 mm. Data collected was analysed using commercial mathematical software.

Most of the tests were carried out on hardened steel (90MnCrV8, 65 HRC), the validation of the models developed was carried out on austenitic (X5 CrNi 18 9, HRC 28) and ferritic steel (C45, HRC 26).

3. INFLUENCE OF PROCESS PARAMETERS ON MATERIAL REMOVAL RATE

As shown in fig. 2 many parameters influence the performance of the abrasive water jet milling operation. These parameters can be grouped as hydraulic parameters, abrasive parameters as well as abrasive jet generation parameters. The most important parameters of these groups are pressure, nozzle diameter and abrasive mass flow rate which are all faced in this study. Focus diameter as well as focus length are directly related to the nozzle diameter to obtain an optimal acceleration process. In this study the focus diameter is 3 to 4 times the nozzle diameter and the focus length is 45 times the focus diameter. In addition the machining result depends on the working parameters traverse rate, working distance and lateral feed increment.

From a manufacturing orientated point of view a very important requirement of the milling process is to achieve a high rate of volume removal.

Considering firstly a constant nozzle diameter volume removal rate increases with increasing abrasive mass flow rate as well as with increasing pressure. While there is a linear dependence of volume removal rate from the pressure it exist an optimal abrasive mass flow rate for each pressure level due to the momentum transfer capability of the water jet. Optimal feed rate can be expressed by the mass ratio which is defined by the ratio of abrasive mass flow rate to water mass flow. From fig. 3 it can be seen that an average value for the optimal mass ratio is about $R=0.33$ showing the tendency to become smaller for low pressures and greater for high pressures.

Considering secondly the material removal rate for various nozzle diameters and constant mass ratio in each case fig. 4 shows that at the beginning the material removal rate increases linearly with increasing nozzle diameter. If the nozzle diameter exceeds a specific level a significant deviation from the linear behaviour can be obtained due to an increasing damping effect in the kerf caused by the high absolute abrasive flow rates as well as by the increasing depth of kerf.

In relation to the requirements of a specific machining operation the selection of machin-

ing parameters is also influenced e. g. by the consumption of energy, of abrasives and of water to achieve a certain material removal rate. If the material removal rate is for instance related to the abrasive mass flow rate fig. 5 shows that for this specific material removal rate an optimal nozzle diameter in the range of 0.2 to 0.25 mm exists. This range is also valid for the material removal rate in relation to the hydraulic power input. The dependence of the material removal rate in relation to the water flow rate shows qualitatively a similar behaviour as given in fig. 4 due to the fact that water and abrasive mass flow rate are connected by the mass ratio.

From these results it is obvious that it doesn't exist only one optimal combination of parameters but one has to find a compromise between a high absolute material removal rate and high specific material removal rates. Keeping this in mind in this study the pressure was set to 300 MPa, the nozzle diameter to 0.25 mm, the focus diameter to 0.9 mm and the abrasive mass flow rate to 6 g/s ($R=0.25$). The reduction of the mass ratio below the value of $R=0.33$, which leads to a maximum material removal rate, increases the specific material removal rate in relation to the abrasive mass flow rate significantly.

Considering thirdly the influence of the working distance and the traverse rate it can be seen from fig. 6 that the material removal rate increases significantly with decreasing traverse rate if for a given working distance the traverse rate is below a certain value. This critical traverse rate increases with decreasing working distance. Above the critical traverse rate the material removal rate is constant in-between a narrow scattering band and is independent on the working distance. There are two reasons for this behaviour. On one hand side the energy density of the abrasive water jet at the point of impingement increases with the decrease of both parameters working distance as well as traverse rate. On the other hand side there is a transition in the macroscopic material removal process as can be recognised from fig. 7. This transition occurs if the energy density exceeds a critical value. Fig. 7 shows exemplary the kerf profile for a working distance of $s=20$ mm and traverse rates beginning on the left of 200 to 1000 mm/min. An overcritical energy density ($v=200$ mm/min) initiates a cyclic material removal process corresponding to the deformation wear mode observed during cutting operations (Hashish, 1989; Tan, 1986). As long as the energy density is below the critical value the material removal process shows a stationary behaviour producing smooth kerfs. Although the cyclic material removal process enables to achieve high volume removal rates any combinations of parameters causing this are not suitable to the requirements of milling with abrasive water jets. This is because corresponding parameters lead to a highly irregular topography of the bottom of the kerf

which results in a dramatic increase of the surface roughness as can be seen from fig. 8. These irregularities have to be totally avoided at any time of the machining process because they cannot be corrected by following passes.

So in the following chapters only those combinations of parameters are considered which produce smooth kerf profiles.

4. MATHEMATICAL DESCRIPTION OF KERF PROFILE

As stated earlier (Freist et al., 1989) the mathematical description of kerf profiles is one very important element to realise the machining method finally aimed at. To get quantitative information about the kerf profile the following requirements have to be fit:

- good matching concerning the shape of the kerf profile
- good correlation between the process parameters and the coefficients of the mathematical expression describing the characteristics of the kerf profile (e.g. depth of kerf and width of kerf)
- minimal number of coefficients

Among the variety of possibilities which are suitable in general to describe the kerf profile (e.g. fft-analysis and -synthesis with reduced number of coefficients, polynomial of order 4 at least, segments of parabola) a modified cosine function is a very simple function which fits the requirements listed above very well in a wide range of parameters (see also chapter 6.1). The characteristics of the modified cosine function (see fig. 9) are the amplitude Φ and the wave length λ . Using an Cartesian co-ordinate system with the origin in the symmetry plane of the kerf profile and in the unaffected surface of the workpiece the depth of kerf is two times the amplitude

$$k_c = 2 \Phi \quad (1)$$

and the wave length is

$$\lambda = \frac{2 \pi}{b_c} x ; -b_c/2 < x < b_c/2 \quad (2)$$

Looking to the subplots in fig. 10 one can see that the cosine function fails in case of sharp

contoured and deep kerf profiles which are produced for instance using small working distances and relatively low traverse rates. Considering the macroscopic shape matching becomes better the smoother the kerf profile is.

Facing smooth kerf profiles only, fig. 11 shows the good correlation between the depth of kerf k measured with the roughness measurement system and the depth of kerf k_c resulting from the description of the kerf profile using the cosine function. This comparison confirms quantitatively very clearly the qualification of the cosine function to describe the shape of kerf profiles.

5. MODELLING OF WIDTH AND DEPTH OF KERF

As explained in chapter 4 the cosine function is suitable to describe quantitatively the kerf profile for a wide range of parameters. To use the cosine function in a simulation model that means to predict the kerf profile the two characteristics Φ and λ have to be correlated to the process parameters. Based on the results presented in chapter 3 in this study the variable parameters are the traverse rate and the working distance while all the other parameters remain constant. It is obvious that the model introduced below can be extended in principle also on other parameters (Hashish, 1987; Blickwedel et al., 1990).

Considering eq. 2 the wave length of the cosine function can be expressed by means of the width of the kerf b_c . From the tests carried out it was found that there is a linear relationship between the width of the kerf and the working distance which can be expressed by

$$b_c = b_1 s + b_0 \quad (3)$$

For hardened steel (see fig. 12) the coefficients of eq. 3 were found by regression analysis being $b_1 = 0.08$ and $b_0 = 0.918$ respectively.

It can be seen from fig. 12 also that the width of the kerf shows no significant dependency on the traverse rate.

Due to the energy density at the impingement point of the jet the amplitude Φ should show an inverse proportional relationship concerning both the traverse rate as well as the working distance. A simple equation was found which considers these relationships as well as the fact that reducing the traverse rate towards zero will lead to a limited depth of kerf

$$\Phi_{\text{Cal}} = \frac{R_E}{v(c_1 s + c_2)} \quad (4)$$

Due to the calibration of eq. 4 on the hardened steel used in this study the relative erosion resistance is $R_E = 1$ for this material with the coefficients c_i being $c_1 = 0.0002504 \text{ mm}/\text{min}^3$ and $c_2 = 0.002224 \text{ mm}/\text{min}^2$.

Fig. 13 demonstrates the excellent conformity between the amplitude directly resulting from the cosine function Φ and the amplitude Φ_{Cal} which was calculated using eq. 4. The correlation coefficient for this material is $r = 0.997$.

The general validity of the model given by equations 3 and 4 was checked by kerfing austenitic and ferritic steel respectively. Considering eq. 4 it was assumed that only the numerator i.e. the value of the erosion resistance has to be adapted to the properties of different materials. Table 1 summarises the coefficients of eq. 3 and 4 and the corresponding correlation coefficients for all the materials tested. As can be derived from the correlation coefficients the conformity between the values measured and calculated is very high.

6. MODELLING OF THE SUPERPOSITION OF KERF PROFILES

6.1 Theoretical Background

Assuming that the cosine function is suitable to describe the kerf profile mathematically fig. 14 shows which final shape of the machined part is expected if five similar kerf profiles are superposed without and with different lateral feed increments. A most simple machining operation is considered here that means that the moving paths of the cutting head producing the individual kerf profiles shall be parallel to each other as sketched in fig. 2. It is assumed furthermore the validity of a linear superposition model that means that the final shape can be calculated by addition of all local depths of the considered kerf profiles. Then the total superposition ($e=0$) of $N_t=5$ kerf profiles should lead to a final shape which can also be described by a cosine function and which has a depth of five times the depth of the kerf profile. The depth of the final shape in a generalised form is

$$k_A = N_t k_c ; e=0. \quad (5)$$

If the lateral feed increment is increased the final shape depends on the combination of the number of partial superposed kerf profiles N_p and the lateral feed increment. As long as $N_p < b_c / e$ the final shape should remain a cosine function. If $N_p \geq b_c / e$ a flat bottom of the final shape should occur with a depth of

$$k_A = \frac{k_c b_c}{2 e} ; 0 \leq e \leq b_c / 2, N_p \geq b_c / e . \quad (6)$$

If the lateral feed increment is greater than $b_c / 2$ but less than b_c the final shape should show a waviness with a maximum depth of

$$k_A = k_c ; b_c / 2 \leq e \leq b_c . \quad (7)$$

6.2 Validation of a Linear Superposition Model

6.2.1 Total Superposition of Kerf Profiles

Fig. 15 shows the development of the final shape in case of the total superposition of a various number of kerf profiles. Under the chosen parameters the final shape itself is of cosine type up to $N_t=3$. Increasing the number of kerf profiles totally superposed leads to a significant deviation of the final shape from the cosine function. Beside this it is obvious that there is a difference between the depth of the final shape and the predicted depth which increases with increasing number of kerf profiles superposed. Since the active working distance is only influenced marginal with increasing depth of the final shape the main reason for this behaviour is seen in increasing friction losses due to a more and more intensive contact between the abrasive water jet and the profile produced so far.

Both aspects - deviation of the final shape from the cosine function as well as the increasing difference between the depth of the final shape and the predicted depth - become more distinct if kerf profiles with greater depth of kerf are superposed.

So as a pre-conclusion concerning the total superposition of kerf profiles it can be said, that the linear superposition model is valid if relatively flat kerf profiles are superposed and if the final shape produced so far does not exceed a critical state which is mainly characterised by the angle of the flanks of the final shape.

6.2.2 Partial Superposition of Kerf Profiles

Fig. 16 images exemplary the final shape in case of the partial superposition of two kerf profiles with a lateral feed increment of $e = b_c / 4$. The working distance is $s = 40$ mm and the depth of the kerf profile is 0.25, 0.5 and 1.0 mm respectively. The different depths of kerf lead to different angles of the flanks of the kerf profiles. According to the explanation in chapter 6.1 the final shape should be of cosine type, because $N_t = 2 < b_c / e = 4$ is fulfilled. Each subplot shows the final shape (continuous line) and compares it with the result of the prediction based on the superposition of two similar cosine functions (discontinuous line) as well as on the superposition of the two kerf profiles (dotted line). These kerf profiles are also the basis for the matching by the cosine functions. Considering first the upper left subplot it can be seen that there is a good conformity between the final and the predicted shape. If the depth of the kerf is increased as shown in the right subplot a deviation occurs between the final and the predicted shape. As can be seen from the lower subplot this deviation becomes more significant the greater the depth of the kerf profile is.

Increasing the lateral feed increment to $e = b_c / 2$ should result in a final shape with a flat ground because in this case the condition $N_t = 2 \geq b_c / e = 2$ is fulfilled. Facing the upper left subplot in fig. 17 it can be seen that there is a markedly deviation between the final shape and the predicted shape based on the cosine function. But it is important to note that there is no significant difference between the prediction based on the kerf profile and the final shape. The deviation between the predicted shapes is due to a small size mismatching of the lateral parts of the kerf profile by the cosine function. Increasing the depth of the kerf profile does of course not affect the predicted shapes qualitatively but leads to a more and more significant deviation between the final shape and the prediction based on the kerf profile in particular.

As a pre-conclusion concerning the partial superposition of kerf profiles it can be said that the linear superposition model is valid if relatively smooth kerf profiles are superposed. Also in this case deviations occur if the depth of the kerf exceeds a critical level which is defined by the angle of the flank of the profile produced so far.

7. CONCLUSIONS AND OUTLOOK

- Concerning the requirements of the abrasive water jet milling process only those combinations of parameters are acceptable which lead to a smooth and regular kerf

profile.

- To achieve a maximum material removal rate the pressure and the nozzle diameter should both be as high as possible and the abrasive mass flow rate should be about 30 to 35 % of the water mass flow rate.
- Facing the consumables energy, water and abrasive the nozzle diameter should be in the range of 0.20 to 0.25 mm to achieve optimal specific material removal rates.
- The material removal rate can be increased significantly by decreasing the traverse rate as well as the working distance. But in this case the high material removal rates are the result of a cyclic material removal process which has to be avoided because the kerf profiles produced in this case are not suitable for the milling operation. The cyclic process is initiated if for a given combination of the other parameters the combination of the traverse rate and the working distance is below a critical value. If the critical value is exceeded the material removal process becomes stationary and the material removal rate remains unaffected by further increasing of the traverse rate and the working distance.
- Concerning suitable parameter combinations a model for the mathematical description as well as for the prediction of the kerf profile was developed based on a modified cosine function.
- In relation to the description of the kerf profile by a cosine function a theoretical model for the prediction of the final shape as a result of the linear superposition of individual kerf profiles was introduced. The results of tests carried out to verify this model have shown that it is valid in principle if smooth kerf profiles are concerned. The remaining deviations between the predicted and the final shape are due to a slight mismatching of the cosine function in relation to the lateral regions of the kerf profiles.
- In order to improve the accuracy of prediction further work has to be done to find methods to improve the precision of matching. This can be done on one hand side by the modification of the cutting head geometry to achieve a kerf profile which is totally fit by a cosine function. On the other hand side other functions as for instance segments of parabola have to be specified and involved into the introduced models.

8. ACKNOWLEDGMENTS

The authors wish to express their thanks to the "Deutsche Forschungsgemeinschaft" providing financial support to the project "Dreidimensionale Bearbeitung schwerspanbarer Werkstoffe mit Hochdruck-Abrasivstrahlen" where the results are taken from.

9. REFERENCES

- Hashish, M., "Steel cutting with abrasive water jets", Proceedings of the 6th International Symposium on Jet Cutting Technology, pp. 465-488, BHRA Fluid Engineering Center, Cranfield, UK, 1982
- Hashish, M., "Machining with abrasive-waterjets, phase I final report", National Science Foundation, Washington, DC, Grant MEA8460065, 1985
- Hashish, M., "Three-dimensional machining with abrasive-waterjets", Proceedings of the 11th International Symposium on Jet Cutting Technology, pp. 605-620, Kluwer Academic Publishers, Dordrecht, NL, 1992
- Freist, B.; Haferkamp, H.; Laurinat, A. and H. Louis, "Abrasive jet machining of ceramic products", Proceedings of the 5th American Water Jet Conference, pp. 191-204, National Research Council of Canada. U.S. Bureau of Mines, 1989
- Hashish, M., "A model for abrasive-waterjet (AWJ) machining", Journal of Engineering Materials and Technology Vol. 111, pp. 154-162, 1989
- Tan, D. K. M., "A model for the surface finish in abrasive-waterjet cutting", Proceedings of the 8th International Symposium on Jet Cutting Technology, pp. 309-313, BHRA Fluid Engineering Center, Cranfield, UK, 1986
- Hashish, M., "Prediction of depth of cut in abrasive-waterjet (AWJ) machining", in: "Modelling of materials processing", ASME MD-Vol. 3, pp. 65-82, 1987
- Blickwedel, H.; Guo, N. S., Haferkamp, H. and H. Louis, "Prediction of abrasive water jet cutting performance and quality", Proceedings of the 10th International Symposium on Jet Cutting Technology, pp. 163-180, Elsevier Science Publishers Ltd., Barking, UK, 1990

10. NOMENCLATURE

b_c	width of kerf resulting from cosine function	mm
b_1	coefficient of eq. 3	mm
b_0	coefficient of eq. 3	mm
c_1	coefficient of linearisation of eq. 4	min/mm^{4-i}
d_F	focus diameter	mm
d_D	nozzle diameter	mm
e	lateral feed increment	mm

k	depth of kerf profile	mm
k_c	depth of kerf profile resulting from matching by cosine function	mm
k_A	depth of final shape	mm
l_F	focus length	mm
\dot{m}_p	abrasive mass flow rate	g/s
N_p	number of partial superpositions of kerf profiles	--
N_t	number of total superpositions of kerf profiles	--
p	pressure	MPa
Q_Z	material removal rate	mm ³ /min
$Q'_{Z,P}$	specific material removal rate	mm ³ /g
r	correlation coefficient	--
R	mass ratio	
R_E	relative erosion resistance	--
R_Z	roughness	μm
s	working distance	mm
v	traverse rate	mm/min
λ	wave length of cosine function	mm
Φ	amplitude of cosine function	mm
Φ_{Cal}	calculated amplitude resulting from eq. 4	mm
x,y,z	Cartesian co-ordinates	mm

Table 1: Coefficients of eq. 3 and 4

material	90MnCrV8	X5CrNi18 9	C45
R_E	1	1.96	1.78
r	0.997	0.985	0.996
b_1	0.080	0.081	0.075
b_0	0.918	1.027	1.223
r	0.998	0.993	0.993

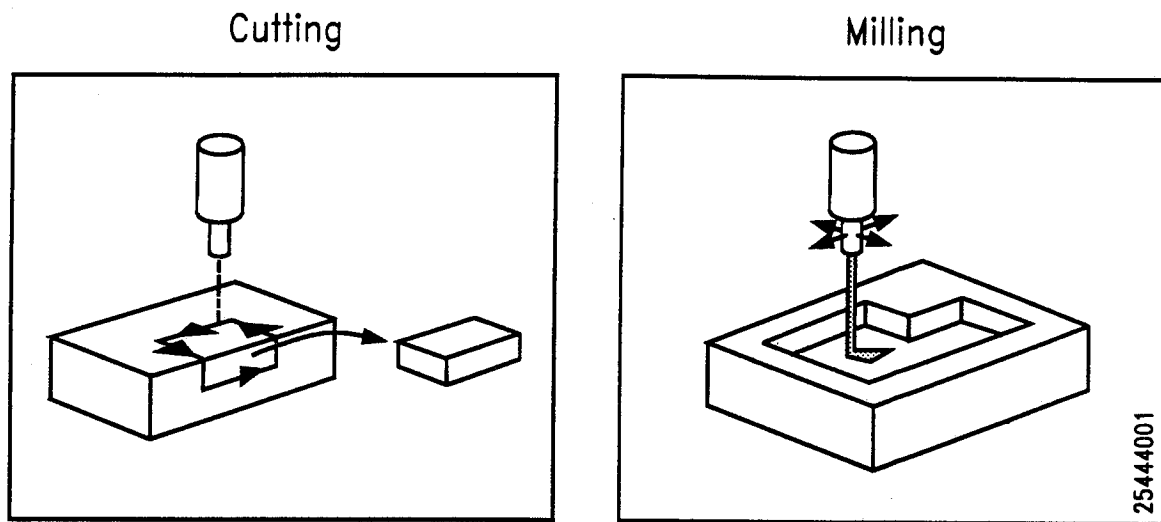


Fig. 1: Possibilities for three-dimensional machining with abrasive water jets

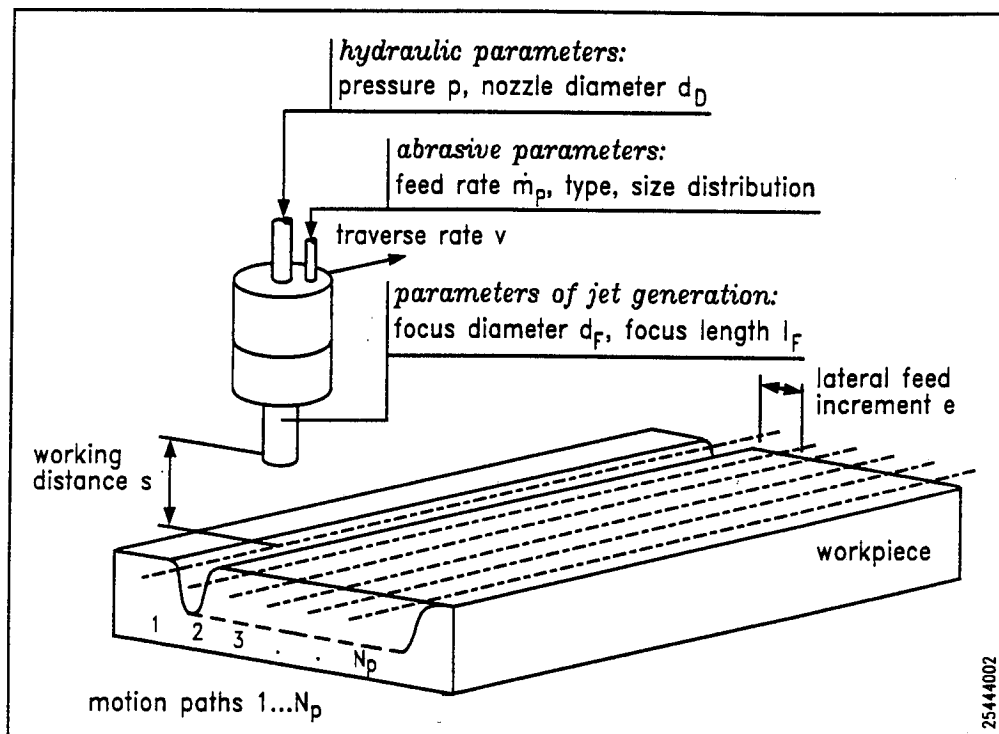


Fig. 2: Strategy for milling with abrasive water jets

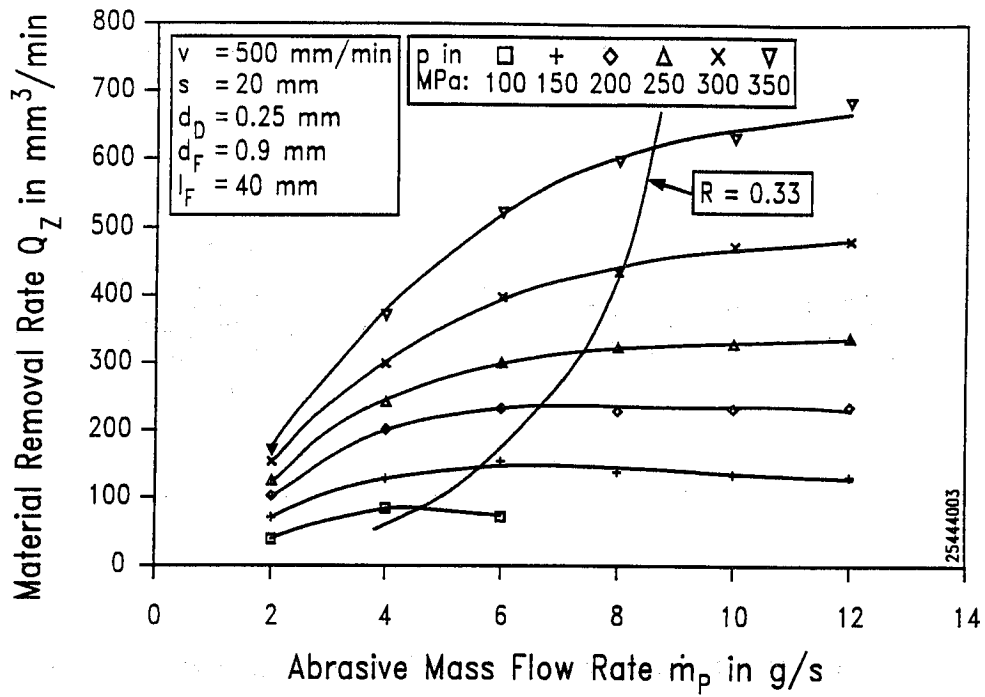


Fig. 3: Material removal rate in relation to abrasive mass flow rate

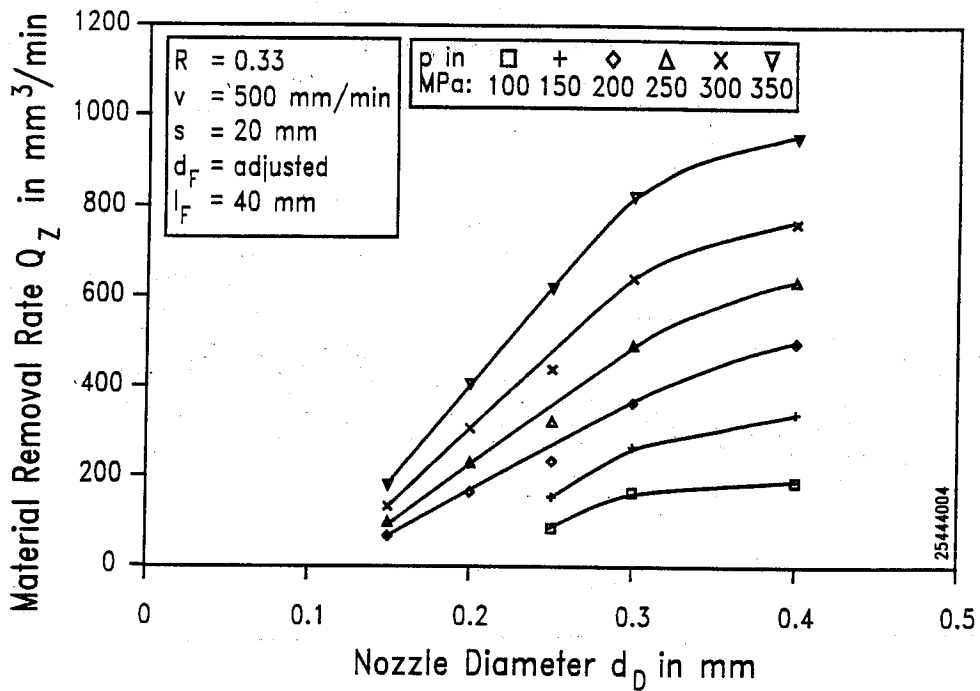


Fig. 4: Material removal rate in relation to nozzle diameter

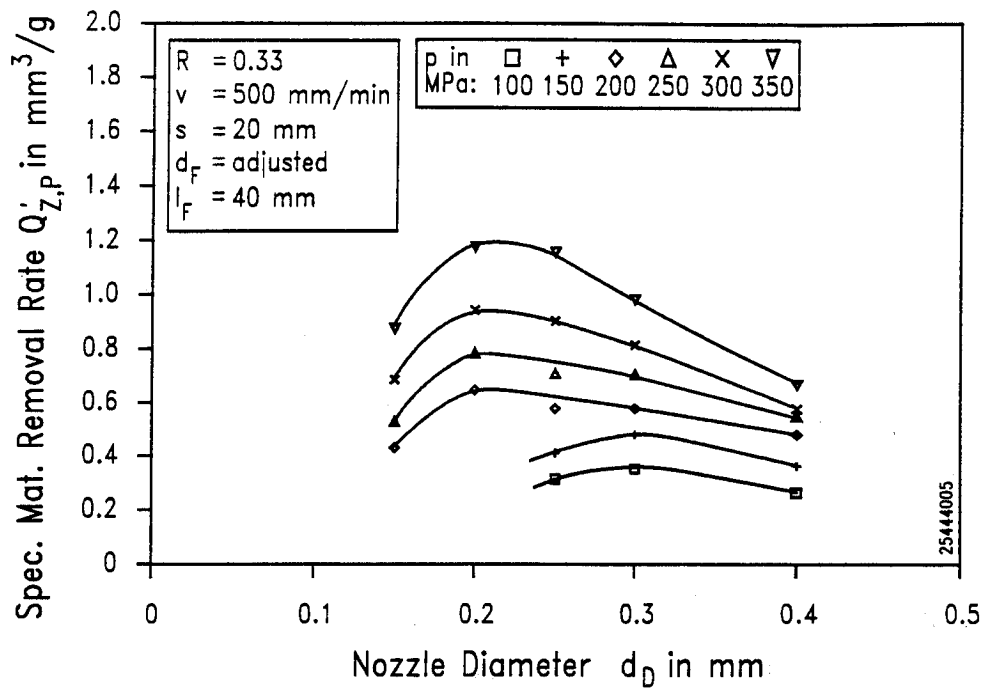


Fig. 5: Specific material removal rate in relation to nozzle diameter

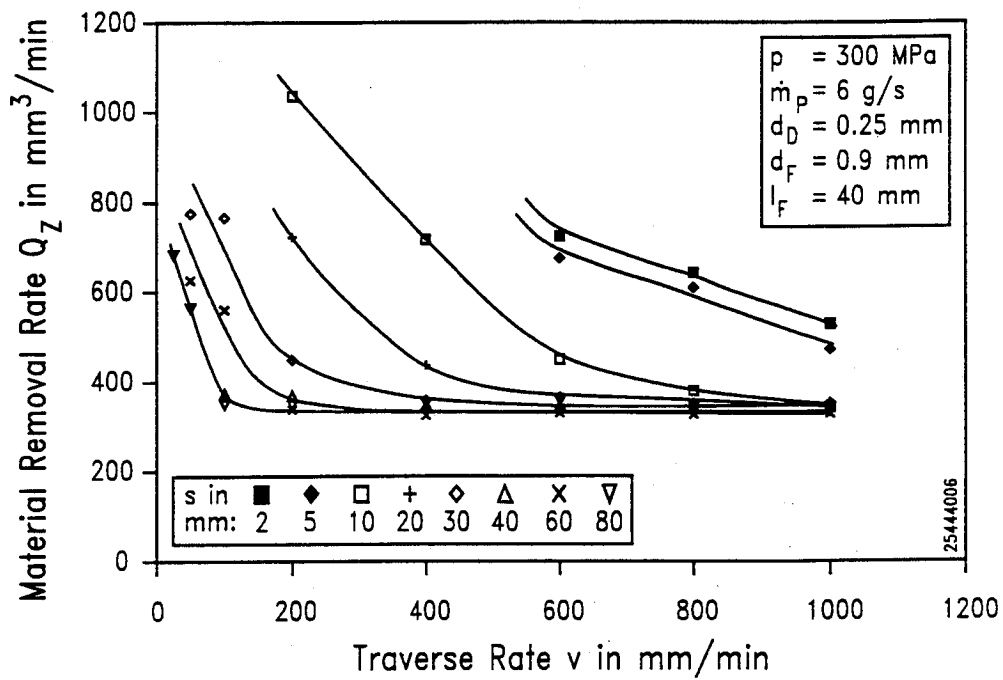


Fig. 6: Material removal rate in relation to traverse rate

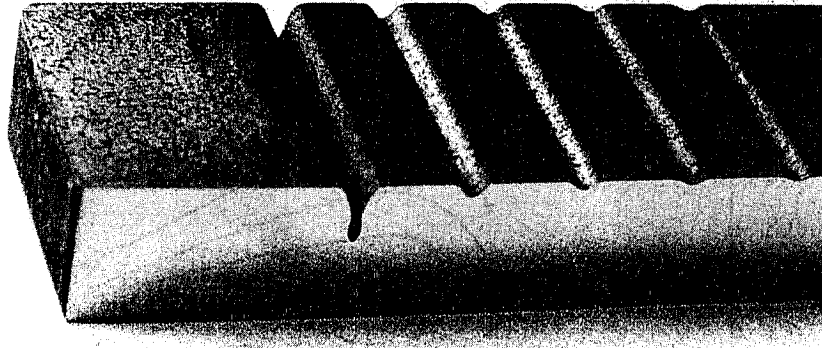


Fig. 7: Kerf profile in relation to traverse rate

$v = 200, 400, 600, 800, 1000 \text{ mm/min}$

$s = 20 \text{ mm}, p = 300 \text{ MPa}, \dot{m}_p = 6 \text{ g/s}, d_D = 0.25 \text{ mm}, d_F = 0.9 \text{ mm}, l_F = 40 \text{ mm}$

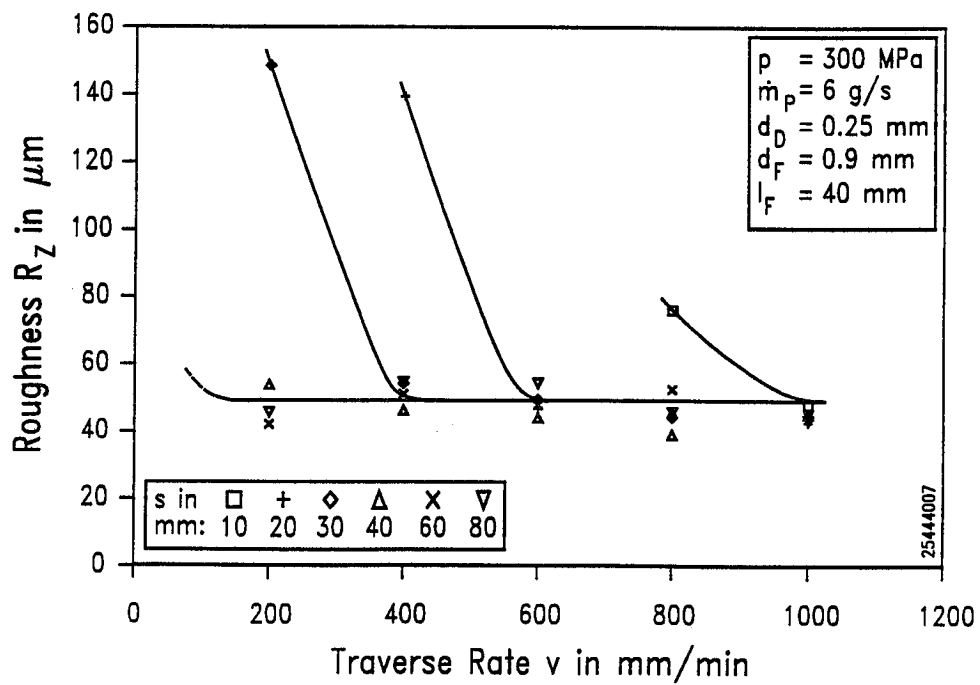


Fig. 8: Roughness in relation to traverse rate

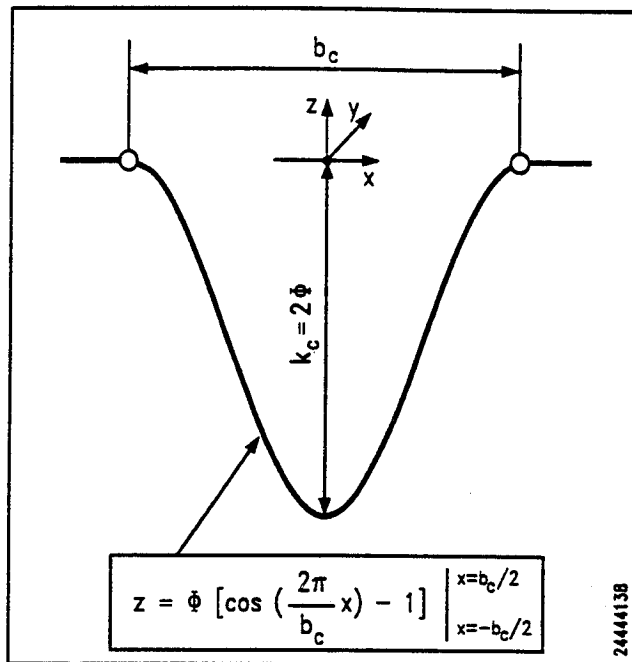


Fig. 9: Description of kerf profile by cosine function

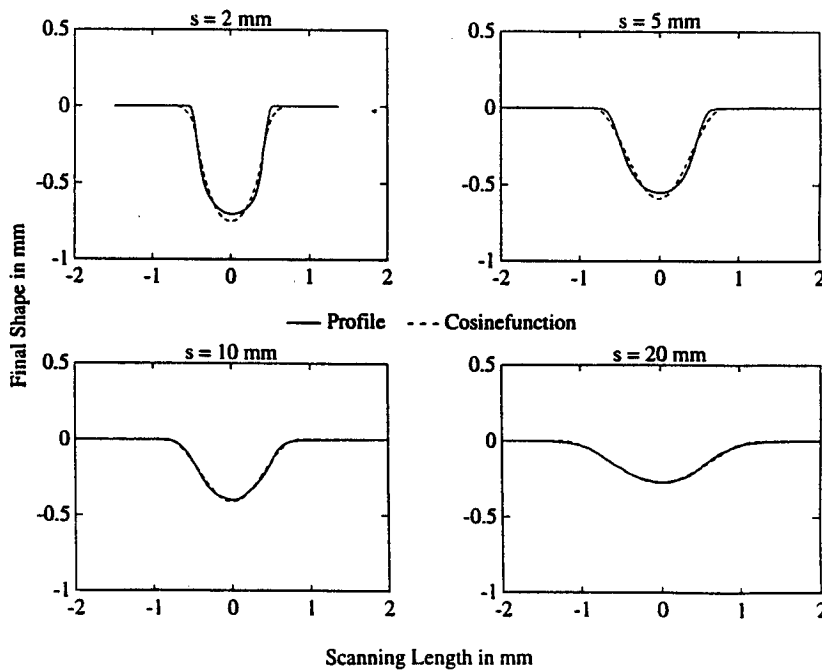


Fig. 10: Influence of working distance on accuracy of matching

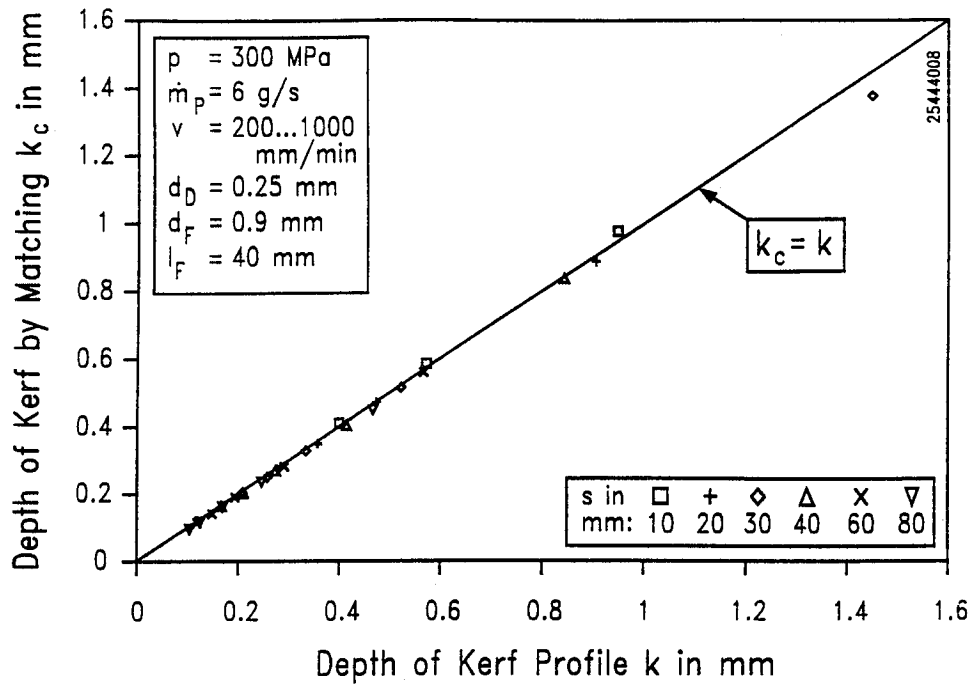


Fig. 11: Depth of kerf profile resulting from matching by cosine function in relation to real depth of kerf profile

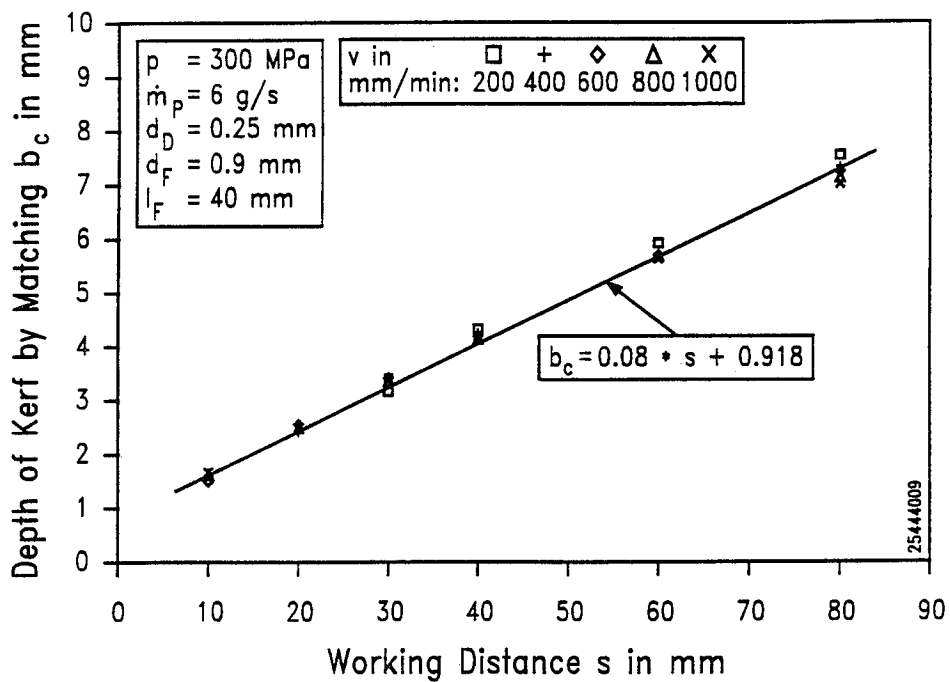


Fig. 12: Width of kerf profile in relation to working distance

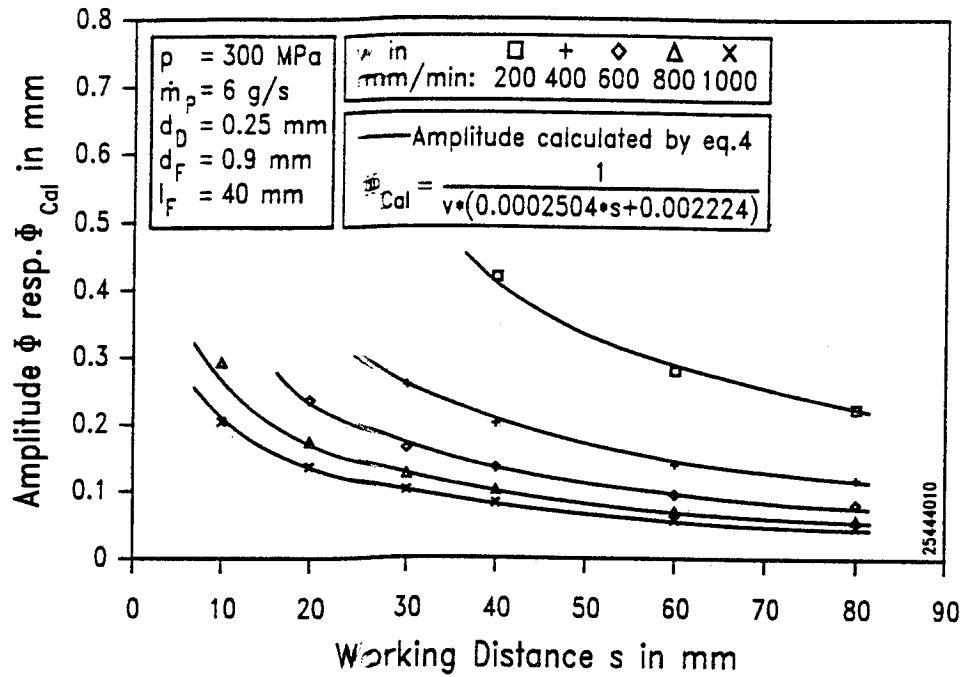


Fig. 13: Amplitude of cosine function in relation to working distance, comparison between amplitude resulting from matching and calculation using eq. 4

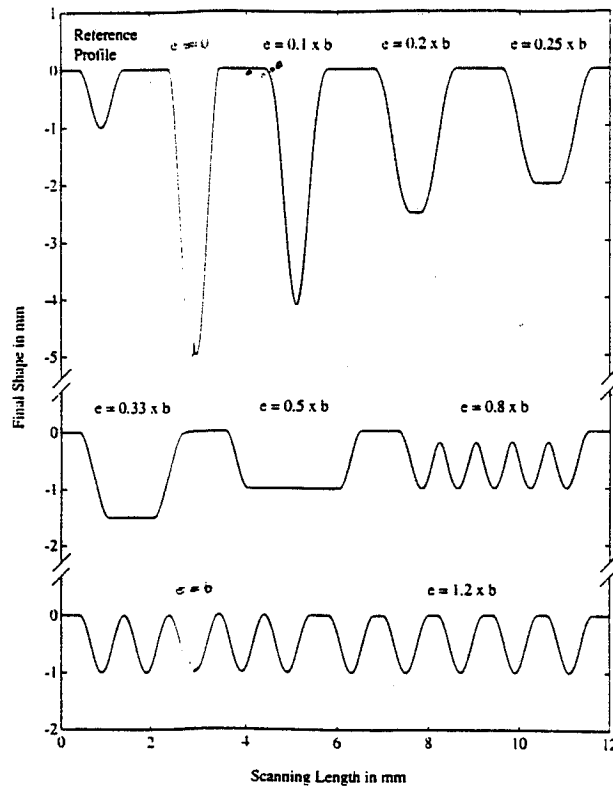


Fig. 14: Influence of lateral feed increment on final shape for the description of kerf profile by cosine function (theoretical)

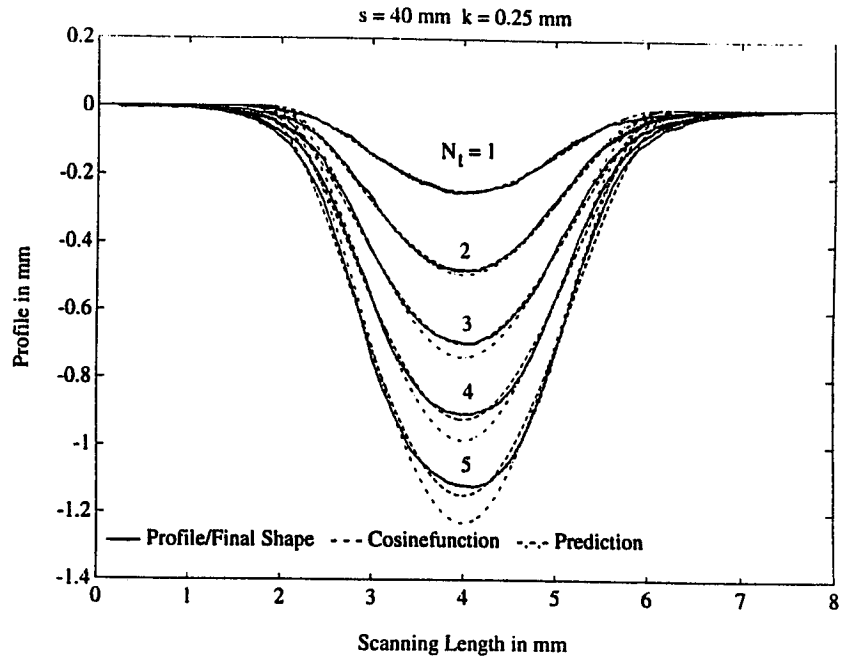


Fig. 15: Influence of number of total superpositions on final shape
 $s = 40$ mm, $v = 655$ mm/min, other parameters see fig. 7

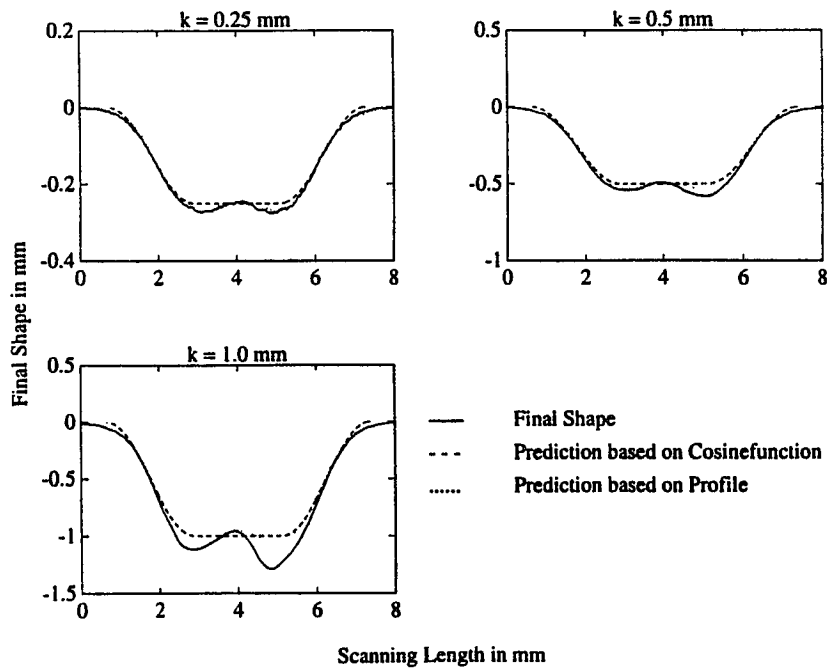
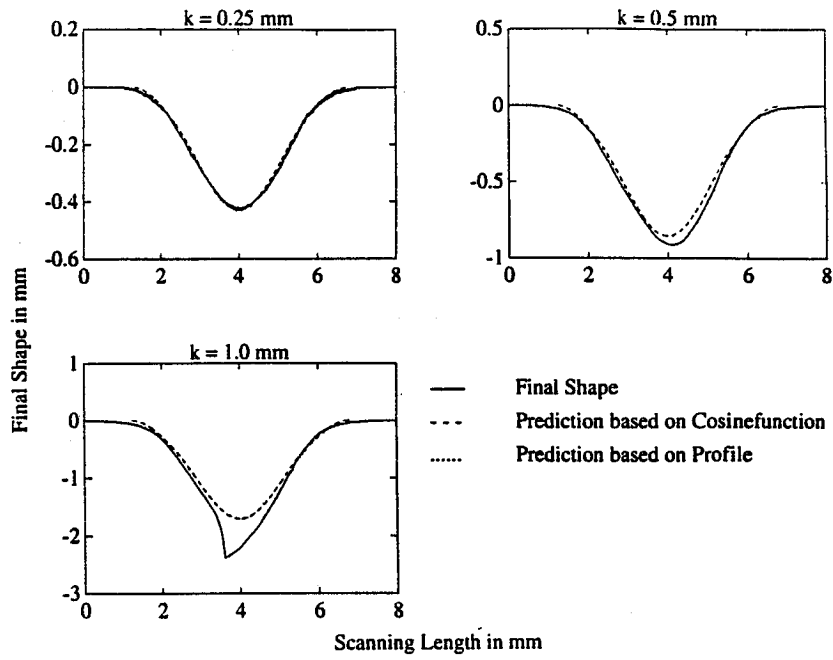


Fig. 16: Influence of number of partial superpositions on final shape, $e = b_c/4$
 $s = 40$ mm, $v =$ adjusted, other parameters see fig. 7



**Fig. 17: Influence of number of partial superpositions on final shape, $e = b_c/2$
 $s = 40$ mm, $v = \text{adjusted}$, $p = 300$ MPa, other parameters see fig. 7**

A TRANSIENT MODEL FOR MATERIAL REMOVAL IN THE ABRASIVE WATERJET MACHINING PROCESS

by

Raju, S.P., and Ramulu, M
Department of Mechanical Engineering, FU - 10
University of Washington
Seattle, Washington 98195

ABSTRACT

A semi-empirical transient numerical model was developed to predict material removal during piercing in the abrasive waterjet machining process. This model is based on an energetic principle, and utilizes the principle of conservation of momentum, to obtain an approximate mean velocity distribution of the slurry within the cavity. A quasi-static penetration process was assumed for the purposes of simplifying the equations that govern the process. It was proven that a model based on a cylindrical cavity could be adapted for the actual "cubic" cavity with ease, by making appropriate transformations. Experimental determination of two empirical constants was involved in the study. The experimental constants, when utilized in the model, predicted reasonably well the jet penetration results.

1.0 Introduction

Abrasive waterjet drilling or piercing involves the normal impact of an abrasive-laden waterjet onto a target material to bring about erosion. This process is a continuous one, and the jet upon penetration, by impact followed by erosion, loses its kinetic power, due to the back-flow of the slurry, resulting in the lowering of the penetration rate with time. The piercing characteristics such as the penetration, the penetration depth, a nature of the kerf etc. are a strong function of the material properties, the slurry characteristics, and the process parameters. Due to a large number of parameters that are involved, which arise out of the nature of interactions between the various phases that are at play, very few transient prediction studies have been reported. Many of these studies are adaptations of earlier theories on particle cutting (Benchaita et al., 1985) or are highly empirical in nature. But however, a considerable amount of experimental work pertaining to penetration has been reported in the literature (Ramulu et al., 1991). The simulation of the transient process of piercing using AWJs, considering the loss of energy due to penetration into the target, has never been attempted before from physical principles.

This paper presents a semi-empirical model for the continuous process of abrasive waterjet piercing by considering the energy loss of the fluid slurry as it tries to penetrate the workpiece. The model is based on an energetic principle, and it utilizes, the principle of conservation of momentum in an effort to solve completely for the penetration rate. A prediction equation is derived assuming two-empirical constants. This equation related very well with the experimentally observed data for abrasive waterjets. The model presented has a very general validity for any kind of a fluid, and hence may be even adapted for pure waterjets.

2.0 Theoretical Analysis

The process of piercing involves normal impact of a high-velocity abrasive-laden slurry onto a target material. The abrasives upon impact bring about failure in the material resulting in erosion and crater formation. The role of water in drilling of hard materials, is assumed to be essentially to help in the transfer of momentum to the abrasive particles in the nozzle. After a cavity is formed, the oncoming slurry upon further bombardment on the material surface creates a new failed surface leading subsequently to erosion. Once the cavity is formed, the oncoming fluid is retarded before impact in the cavity and then turns around and gets accelerated out of the cavity. The velocity of the outgoing slurry is dependent upon the target material removal rate and the velocity of the incoming jet stream. The process of piercing may be modeled by analyzing the retardation of the flow of the slurry into a cavity. For convenience, the cavity will be assumed to be cylindrical, although in reality the cavities formed are far from having straight generatrices and a flat bottom. This assumption considerably reduces the computations involved in the prediction procedure. The slurry will be assumed to be homogenous at points in the fluid and at all times, which means that momentum between the particles and the carrier medium is transferred infinitely fast, and there is perfect mixing. Further it will also be assumed that the two-phase slurry will be in kinematic equilibrium. Energy principles will be utilized to obtain the governing equation of material removal rate. In this section, a quantitative analysis of the process of retardation and acceleration of the slurry along with the material removal rate of the target will be made, in an effort to predict the material removal process.

2.0.1 Governing Equations:

Consider the flow of the abrasive slurry into a cylindrical cavity as shown in Figure 1. The oncoming jet is assumed to have uniform mean velocity of V_j and it will be assumed that the jet does not diverge after it exits the nozzle. This assumption is true only for small standoff distances, because the jet stream doesn't have enough room for mixing with the surrounding medium. The jet stream upon impact creates a damaged surface on the target material and with time will penetrate the cavity by erosion. It will be assumed in this model that the cavity will grow as a cylinder of radius R , inward into the target material.

To determine the penetration depth h and the penetration rate dh/dt , at any time t , momentum and energy conservation principles will have to be invoked. The nature of the velocity distribution within the cavity is essential, for estimating the loss of the piercing power of the abrasive jet with penetration. To obtain the governing equations for the penetration depth and penetration rate, the velocity distribution within the cavity needs to be determined. This can be accomplished by assuming that the piercing process in time is a quasi-static one, and that the velocity distribution one obtains on freezing the phenomenon in time, may be generalized to predict the transient penetration into the target.

To achieve this goal, consider a cylindrical cavity frozen in time with dimensions h and R as shown in Figure 1. Although, Figure 1 does not show the incoming jet stream and the outgoing slurry stream to be rubbing against one another, in practical situations the two fluid streams interact. This interaction causes the incoming jet stream to lose its velocity downward, and the outgoing stream to gain velocity. The figure separating the two streams was drawn merely for convenience of visualizing. To model, the acceleration and deceleration of the slurry in the cavity consider an infinitesimal element (of thickness dy) of the abrasive-laden fluid as shown in Figure 2a. Figure 2a shows an infinitesimal element of the two interacting streams. The incoming stream is of radius r and has a velocity of V_j and the outgoing stream exits the target out of an area equal to $\pi(R^2 - r^2)$ with a velocity V_f . The interaction of the two beams causes a drag force, and for any general flow situation the drag force may be given as:

$$F_d = \frac{1}{2} C_D \rho_s A_s v^2 \quad (1)$$

where C_D is the drag coefficient that needs to be determined from experiments, ρ_s is the density of the slurry, A_s is the area over which the drag force acts, and v is the relative velocity of the fluid.

Although, definite boundaries exist, and boundary or shear layers are formed in the cavity, no boundary layer effects will be assumed in this analysis. Inclusion of these effects make the analysis more cumbersome and hence they will be relegated to a future work. It will be also assumed in this analysis that the outgoing stream exits the cavity with a mean velocity V_f at any y and at $y = h$, the slurry will leave the cavity with a mean velocity V_e .

The deceleration process of the incoming slurry can be analyzed by considering the jet part of the infinitesimal fluid element shown in Figure 2b. Upon traversing a distance " dy ", along the direction of the flow, the velocity of the jet V_j , falls to a lower value, which is caused by the shear force F_d (or drag force), acting on the sides. The decrease in the velocity of the fluid stream may be estimated using Taylor's series, and neglecting higher order terms. This yields a velocity of $V_j - (dV_j/dy)dy$ after the jet has traversed a distance " dy ". Hence using Newton's second law one

can write the following equation for the equilibrium of the jet fluid element:

$$V_j - \frac{dV_j}{dy}dy - V_j = \frac{F_d}{(\dot{m}_a + \dot{m}_w)} \quad (2)$$

or using equation (1), we have,

$$V_j - \frac{dV_j}{dy}dy - V_j = \frac{C_D Q_s (V_j - V_f)^2 (2\pi r) dy}{2(\dot{m}_a + \dot{m}_w)} \quad (3)$$

where, $2\pi r dy$ has been substituted for the area where the drag force acts, and $V_j - V_f$ has been substituted for v . Equation (3) may be simplified, and written as,

$$\frac{dV_j}{dy} = - \frac{C_D Q_s (V_j - V_f)^2 (2\pi r)}{2(\dot{m}_a + \dot{m}_w)} \quad (4)$$

This is the governing equation for the variation of V_j with y . To obtain the governing equation for V_f , certain simplifying assumptions need to be made. These include the assumption of a uniform V_f profile, and the absence of any boundary layer effects. This assumption is valid because, we have been considering the mean velocities and uniform velocity profiles right from the start. Assuming these, one can now consider the outgoing part of the infinitesimal fluid element considered in Figure 2c. Note that, V_f has a direction opposite to that of the incoming stream and it increases from the bottom to the top of the cavity due to acceleration of the fluid. Utilizing again, the concept of the Taylor's series, one obtains the velocity of the outgoing slurry after it has traversed a distance dy as $V_f + (dV_f/dy)dy$ after neglecting the higher order terms. Now if one writes Newton's second law for this element assuming that the mass flow rate of the eroded material is negligible compared to the mass flow rate of the slurry we obtain approximately:

$$V_f + \frac{dV_f}{dy}dy - V_f = \frac{F'_d}{(\dot{m}_a + \dot{m}_w)} \quad (5)$$

or,

$$V_f + \frac{dV_f}{dy}dy - V_f = \frac{C_D Q_s (V_f - V_j)^2 (2\pi r + 2\pi R) dy}{2(\dot{m}_a + \dot{m}_w)} \quad (6)$$

considering the new area where the drag acts as $2\pi(r+R)dy$. The drag coefficient C_D will be assumed the same, and again it is some mean drag coefficient of all the flow situations occurring in the cavity. Equation (6) may be further simplified as:

$$\frac{dV_f}{dy} = \frac{C_D Q_s (V_f - V_j)^2 (2\pi r + 2\pi R)}{2(\dot{m}_a + \dot{m}_w)} \quad (7)$$

Equations (4) and (7) can be used to completely solve for the velocities V_j and V_f in the cavity. However due to the "parabolic" nature of the equations, the boundary conditions are different for each one of them. Hence exact solutions of these equations are essential. Upon dividing equation (7) by equation (4) we obtain,

$$\frac{dV_f}{dV_j} = - \left(1 + \frac{R}{r} \right) \quad (8)$$

Since there will be no slurry exit velocity if there is no jet exit velocity, we can integrate Equation (8) above to obtain:

$$V_f = - \left(1 + \frac{R}{\Gamma} \right) V_j \quad (9)$$

and hence we can write:

$$V_f - V_j = - \left(2 + \frac{R}{\Gamma} \right) V_j \quad (10)$$

Substituting Equation (10) into equation (4) we have,

$$\frac{dV_j}{dy} = - \frac{C_D Q_s \left(2 + \frac{R}{\Gamma} \right)^2 (2\pi r)}{2(\dot{m}_a + \dot{m}_w)} V_j^2 \quad (11)$$

or assuming,

$$k_1 = \frac{C_D Q_s \left(2 + \frac{R}{\Gamma} \right)^2 (2\pi r)}{2(\dot{m}_a + \dot{m}_w)} \quad (12)$$

we can write,

$$\frac{dV_j}{dy} = - k_1 V_j^2 \quad (13)$$

This is a simple ODE which can be integrated when the boundary condition is known. The boundary conditions for V_j from the physics of the problem may be written as:

$$\text{when } y = h, \quad V_j = U \quad (14)$$

Using this boundary condition, one can integrate equation (13) to yield the following:

$$\frac{1}{V_j} - \frac{1}{U} = k_1(y - h) \quad (15)$$

or using the definitions,

$$a = \frac{1}{U} - k_1 h \quad (16)$$

we can write,

$$V_j = \frac{1}{(a + k_1 y)} \quad (17)$$

This equation proves that within the cavity the incoming stream loses its velocity hyperbolically and not linearly as enunciated by Hiemenz (see Schlichting (1960)) for the normal impact of a jet onto a flat plate.

Now substituting equations (17) and (10) into equation (7) we obtain the follow

ing equation for the velocity V_f :

$$\frac{dV_f}{dy} = \frac{C_D Q_s (2 + \frac{R}{r})^2 (2\pi r + 2\pi R)}{2(\dot{m}_a + \dot{m}_w)} \frac{1}{(a + k_1 y)^2} \quad (18)$$

or using the definition,

$$k_2 = \frac{C_D Q_s (2 + \frac{R}{r})^2 (2\pi r + 2\pi R)}{2(\dot{m}_a + \dot{m}_w)} \quad (19)$$

we obtain:

$$\frac{dV_f}{dy} = k_2 \frac{1}{(a + k_1 y)^2} \quad (20)$$

This is also a simple ODE which can be integrated to yield,

$$V_f = -\frac{k_2}{k_1} \frac{1}{(a + k_1 y)} + I \quad (21)$$

where I is a general integration constant. Now again from the physics of the problem, we can write the following approximate boundary condition for V_f for the transient case:

$$\text{when } y = 0, \quad V_f = -\frac{dh}{dt} \quad (22)$$

This boundary condition is approximate, because in a realistic situation, flow bending distorts the actual velocity in the vicinity of the stagnation point.

Using the boundary condition in equation (22), equation (21) may be integrated to yield:

$$V_f = \frac{k_2}{k_1} \left[\frac{1}{a} - \frac{1}{(a + k_1 y)} \right] - \frac{dh}{dt} \quad (23)$$

This equation proves that the exit velocity V_f at any point y depend upon the penetration rate dh/dt , which in turn is dependent upon the target material resistance to penetration. The exit velocity at the mouth of the cavity may be obtained from the condition at $y = h$, which yields the following expression for V_e :

$$V_e = \frac{k_2}{k_1} \left[\frac{1}{a} - \frac{1}{(a + k_1 h)} \right] - \frac{dh}{dt} \quad (24)$$

Since the net energy that has gone into penetrating the material is the difference in the kinetic energies of the incoming and the outgoing streams, and since we assumed the case of erosion predominantly due to the abrasive, we can write the following expression for the net energy that is utilized for piercing as:

$$\dot{E}_{net} = \frac{1}{2} \dot{m}_a (U^2 - V_e^2) \quad (25)$$

If we assume that the volume growth of the cavity is proportional to the rate at which the net energy of the fluid stream is transferred into penetrating the medium (following the

arguments of Bitter (1963)) we can write the following expression for the volume removal rate:

$$\pi R^2 \frac{dh}{dt} \propto \dot{E}_{net} \quad (26)$$

or,

$$\pi R^2 \frac{dh}{dt} = \xi \frac{1}{2} \dot{m}_a (U^2 - V_e^2) \quad (27)$$

where ξ is some empirical constant.

Upon substituting the expression for V_e from equation (24) into the equation (26) above, we get the following equation that governs the penetration of the jet into the target:

$$\frac{dh}{dt} = k_3 (U^2 - [\frac{k_2}{k_1} [\frac{1}{a} - \frac{1}{(a + k_1 h)}] - \frac{dh}{dt}]^2) \quad (28)$$

where,

$$k_3 = \frac{\xi \dot{m}_a}{2\pi R^2} \quad (29)$$

This is the governing equation for the penetration of an abrasive waterjet into a target.

2.0.2 Solution Procedure

The equation (28) derived above, is a nonlinear ordinary differential equation in dh/dt , and hence numerical methods have been resorted to in solving for dh/dt . A combination of Adams method (Piskunov, 1974) and fixed point iteration techniques was used to integrate this equation. The flowchart in Figure 3 describes the solution procedure. It was also found that the solution procedure was very sensitive to the time increment (Δt) used for numerical integration, and hence after trying various time increments, it was found that the solution was stable for all $\Delta t \leq .01$ sec. The solution procedure discussed here assumes that the two empirical constants C_D and ξ are known *a priori*. These constants were found from experiments and the methods utilized to determine them will be discussed next.

3.0 Experimental Work

3.0.1 Penetration studies and Kerf Geometry

Piercing experiments were conducted on transparent polycarbonate specimens at the Waterjet laboratory of the University of Washington. The details of the experimental setup and procedure may be found in Ramulu et al. (1991). The goal of this study was two-fold: 1) To capture the penetration process in time, and 2) To study the kerf geometry. The penetration process was captured using a camera at a speed of 5 frames per second. As expected, the penetration rate is not constant with time. This is attributed to the loss of power of the jet upon penetration.

A detailed study of the geometry of the profiles that were obtained during the

tests was made in a effort to obtain a functional form for the kerf profile. Various regression experiments were performed towards achieving this goal. Figures 4a-f show typical functions that best describe the kerf profiles obtained experimentally. The exponents obtained varied between 2.4-3.6, however to simplify the analysis, a cubic polynomial of the form given below was chosen to best describe the profile geometry:

$$y = \left(\frac{h}{R'}\right)x^3 \quad (30)$$

where h is the depth of the cavity, and R' is the radius of the "cubic" cavity at the crater exit and the coordinate system is shown in the figures. In all the experiments, it was found that the radius R' was more or less constant at all times. It was found to be approximately 1.2 mm (mean value). This value is in accordance with Leach and Walker's (1966) value of 1.3 which can be obtained from the relationship:

$$R' = 2.6 r \quad (31)$$

where r is the radius of the jet stream.

3.0.2 Experimental Determination of R, C_D and ξ

The model proposed in section 2.0 assumed that the cavity was cylindrical in shape. However in view of the experimental evidence showing a cubic polynomial to best represent the functional form of the kerf geometry, a modification of the proposed model needs to be done. To apply the analysis discussed so far, one needs to consider an equivalent cylindrical cavity of radius R that has the same volume and the same depth h as the "cubic" cavity obtained from experiments. Using the functional form of the kerf as given in equation (30), one can obtain the volume of the cavity from calculus (see for eg., Piskunov, 1974) as:

$$V = \frac{3}{5}\pi R'^2 h \quad (32)$$

Now upon equating the two volumes, one obtains the following equation relating R' and R:

$$R = \sqrt{\frac{3}{5}}R' \quad (33)$$

This value of R may be used in equation (28) for predicting the penetration depth h.

As was suggested in section 3.01, experiments were also performed to obtain the penetration depth at various times. The simulation of equation (28) was done so as to best fit the experimentally obtained data for the penetration depth. An initial value of .005 was assumed for the value of C_D as suggested by Wallis (1969), and an initial value of 1 × 10⁻¹¹ was tried for ξ, and then subsequent corrections were made until the model best fitted all the experimental data. Two abrasive sizes were experimented upon, and different values of C_D and ξ were obtained for

the different abrasive sizes. These are given below:

for 50# Garnet	$\xi = 2.5 \times 10^{-11}$	$C_D = .00032$
for 80# Garnet	$\xi = 5.0 \times 10^{-11}$	$C_D = .00051$

4.0 Simulation Results

As discussed above, the values of the empirical constants ξ and C_D were obtained from experimental data. The values presented above are the values that best fit the experimental data. Drilling tests were performed on 20 specimens, for various process conditions. Two abrasive sizes of garnet (#80 and #50) were used to penetrate polycarbonate targets. The model proposed above matched the experimental data a very reasonable degree.

Figures 5a, 5b, and 5c show the model predictions alongside with the experimental data for experiments using #50 garnet at various pressures. For the low pressure case of 117 MPa (Figure 5a), the model overpredicts at large times. However for the cases of supply pressures 193 and 240 MPa, the model predicts very well the experimentally observed data. Figures 6a, 6b, and 6c show the model predictions *versus* the experimental data using a different set of values for the empirical constants, for the #80 garnet abrasive. In the cases of a supply pressure of 117 MPa and 193 MPa, the model overpredicts during initial times, however, at late times, predicts very well the observed data. The comparison is very good in the case of 158 MPa. Results for both abrasive sizes, prove that the penetration into the cavity is not constant in time, but varies nonlinearly, and the penetration rate decreases in time.

These results demonstrate the accuracy of the model for predicting the penetration depth and the penetration rate during abrasive waterjet drilling.

5.0 Conclusions

This study presents a semi-empirical model for the prediction of the transient penetration depth of the jet during abrasive waterjet drilling. The model is based on an energetic principle, and utilizes the principle of conservation of momentum, to obtain an approximate mean velocity distribution within the cavity. A quasi-static penetration process was assumed for the purposes of simplifying the equations that govern the process. It was proven that a model based on a cylindrical cavity could be adapted for the actual "cubic" cavity with ease, by making appropriate transformations. Experimental determination of the two empirical constants involved in the study, suggested that they were more or less constant over a series of experiments under a variety of process conditions. The obtained experimental constants, when utilized in the model, predicted very well the experimentally obtained results for most cases.

Acknowledgements

We sincerely appreciate the financial support of the National Science Foundation, through Grant Number MSS-895864.

References

- Abramovich, G.N., *The Theory of Turbulent Jets*, M.I.T. Press, Cambridge, MA, 1963.
- Benchaita, M.T., "Two-dimensional channel bend of a solid-liquid stream," *Trans. of the CSME*, Vol. 9, No. 2, 1985.
- Bitter, J.G.A., "A study of erosion phenomena - parts I-II," *Wear*, Vol. 6, 1963.
- Hashish, M., and duPlessis, M.P., "Theoretical and Experimental investigation of continuous jet penetration of solids," *Trans. of ASME, J. of Engr. for Ind.*, Feb. 1978.
- Leach, S.J., and Walker, G.L., "The application of high-speed liquid jets to cutting," *Philosophical Transactions of the Royal Society of London*, Vol. 260-A, 1966.
- Piskunov, N., *Differential and Integral Calculus*, MIR Publishers, Moscow, 1974.
- Ramulu, M., Yeh, H., Wong, K.P., and Raju, S.P., "Photoelastic investigation of jet piercing process," 6th American Waterjet Conference held at Houston, Texas, USA, 1991.
- Schlichting, H., *Boundary layer theory*, McGraw-Hill Book Company, Inc., New York, 1960.
- Wallis, G.B., *One-dimensional two-phase flow*, McGraw-Hill Book Company, NY, 1969.
- Wong, K.P., "Photoelastic Investigation of Abrasive Waterjet Machining," Master's Thesis, Department of Mechanical Engineering, University of Washington, Seattle, 1991.

Nomenclature

a	constant of equation (16)
A_s	area affected by drag
C_D	drag coefficient
E_a	abrasive kinetic energy
F_d, F'_d	drag force
h	maximum depth of the cavity
k_1	constant of equation (12)
k_2	constant of equation (19)
k_3	constant of equation (28)
m_a	abrasive mass flow rate
m_w	water mass flow rate
r	radius of the jet
R	radius of the cavity
R	radius of the "cubic" cavity
U	mean jet exit velocity of the abrasive slurry from the nozzle
v	any general velocity
V	volume of the cavity
v_a	abrasive velocity
V_e	mean velocity of the outgoing slurry at the mouth of the cavity
V_f	mean velocity of the outgoing slurry at any point inside the cavity
V_j	mean velocity of the incoming slurry at any point inside the cavity
x, y	radial and axial coordinates of the cavity
ξ	empirical constant of equation (27)
Q_s	density of the slurry

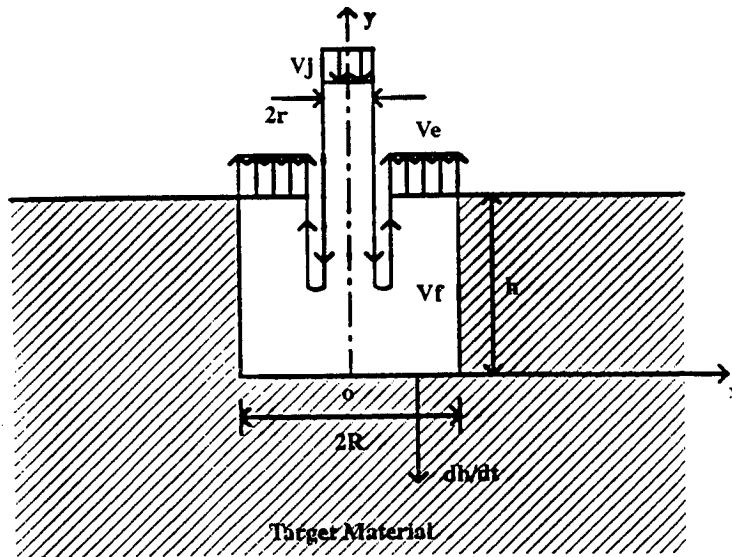
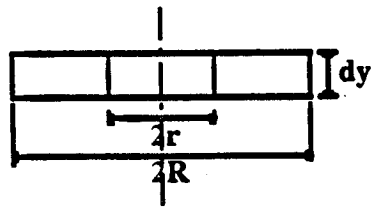
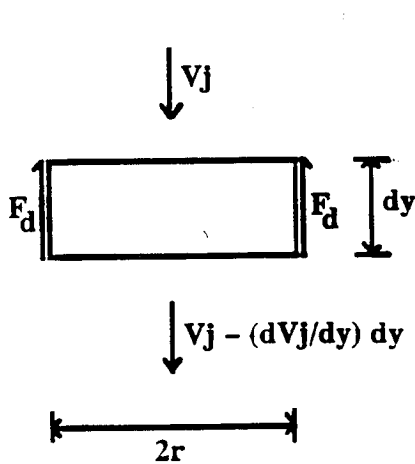


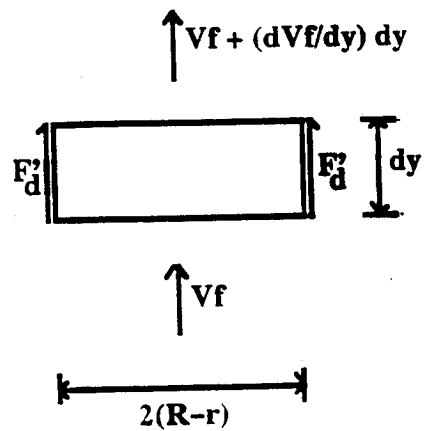
Figure 1. Drilling of a Cylindrical Cavity



(a) The Infinitesimal Fluid Element



(b) The Jet Part of the Stream



(c) The Outgoing Slurry Part of the Stream

Figure 2. A Typical Fluid Element in the Cylindrical Cavity

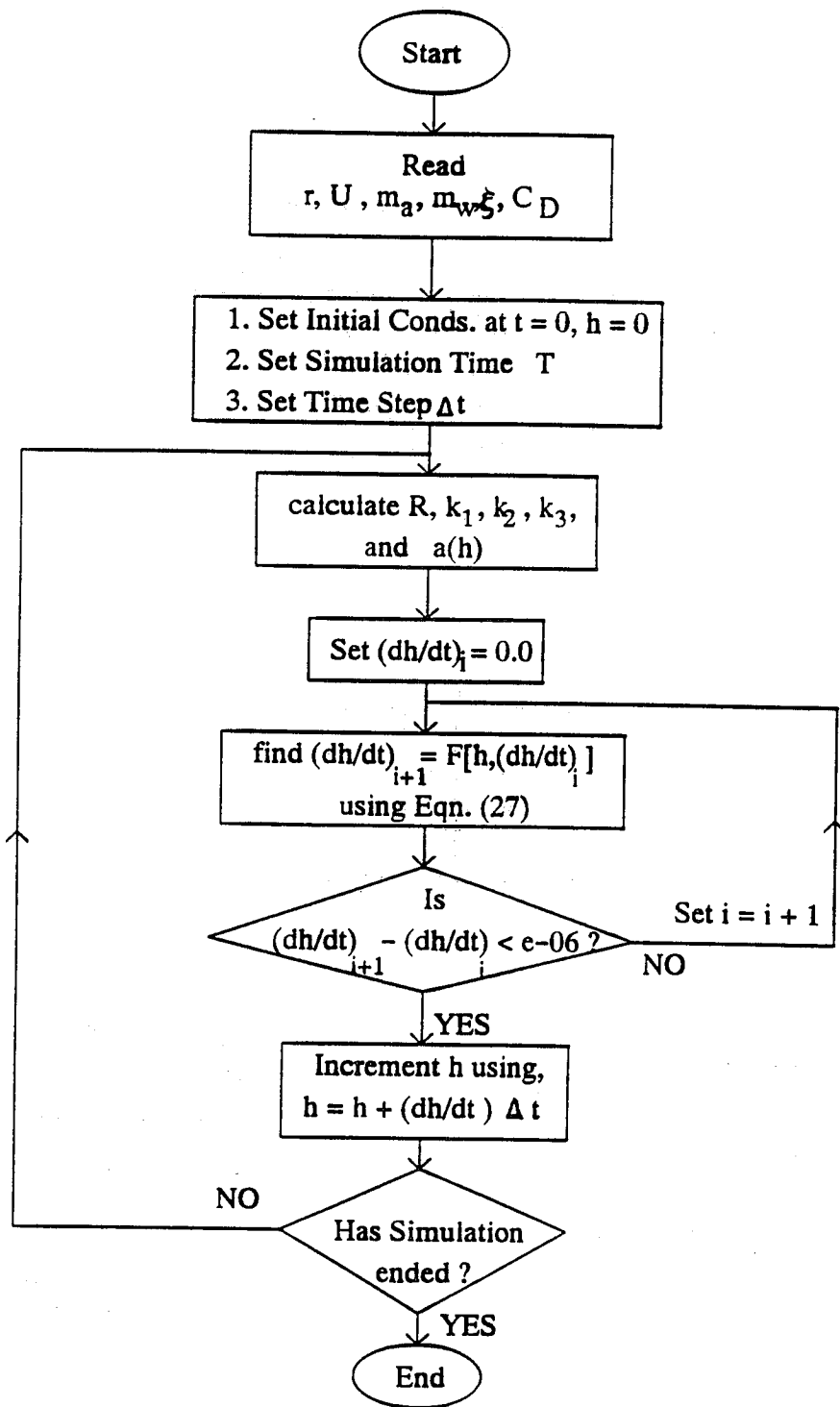


Figure 3. A Flow Chart showing the Solution Procedure

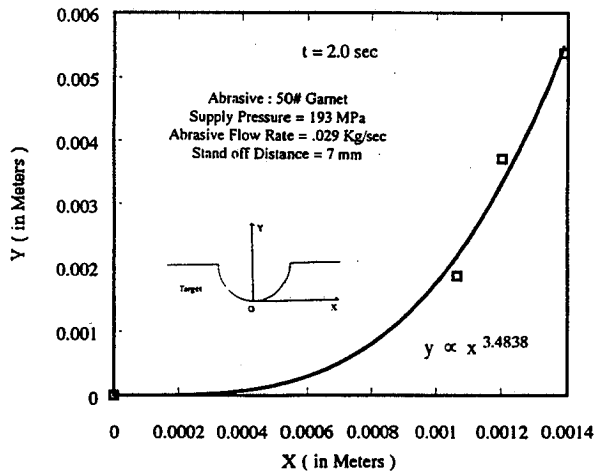
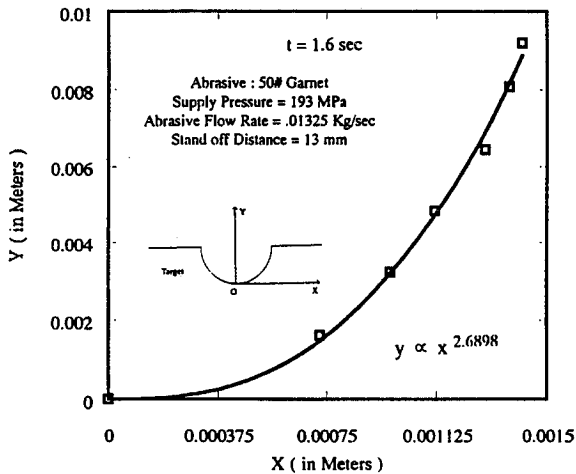
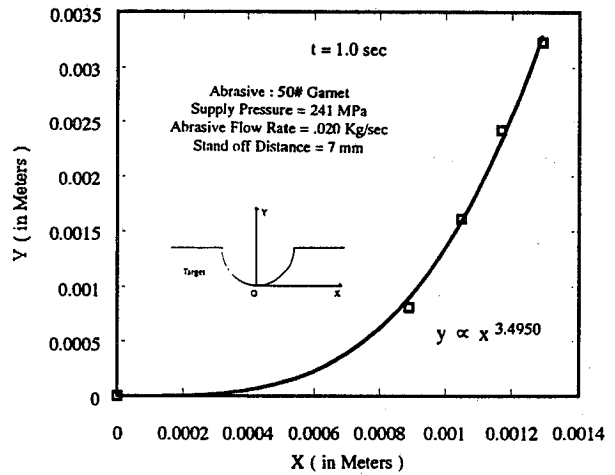
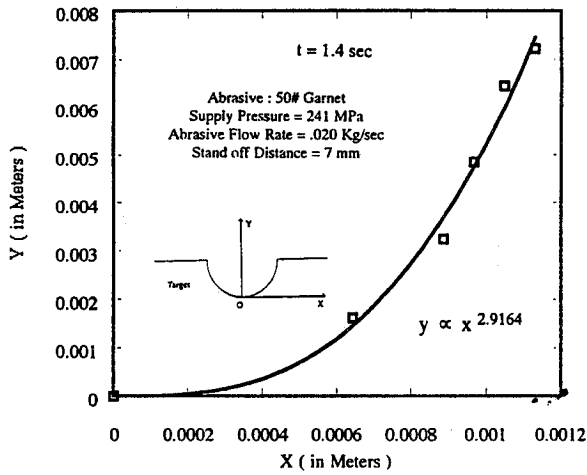
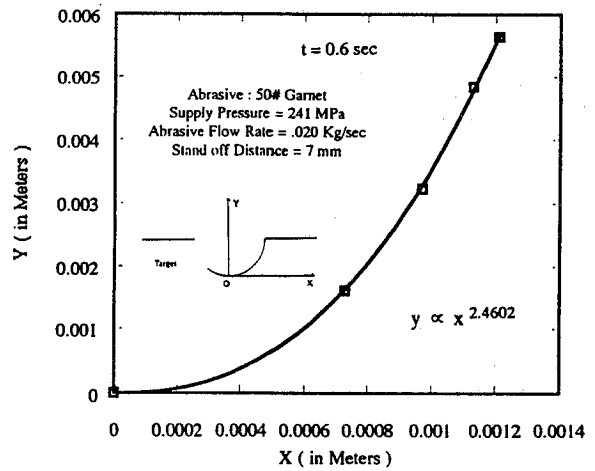
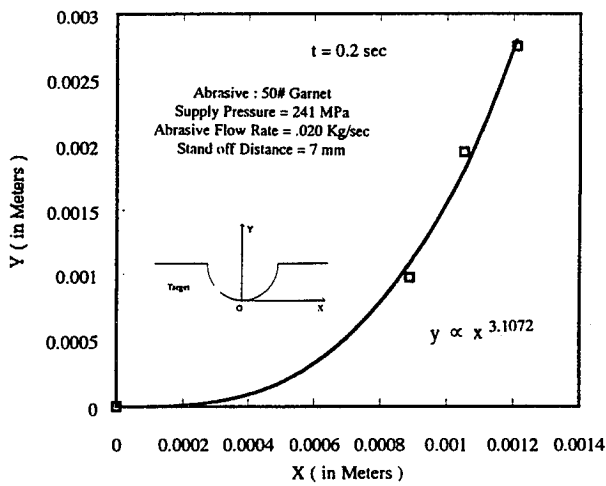
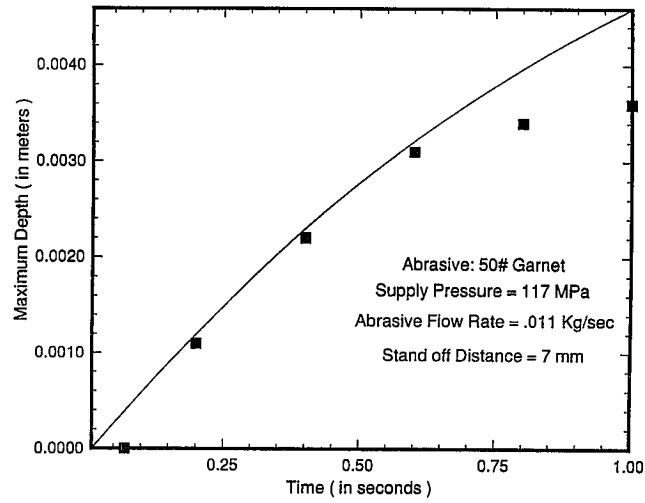
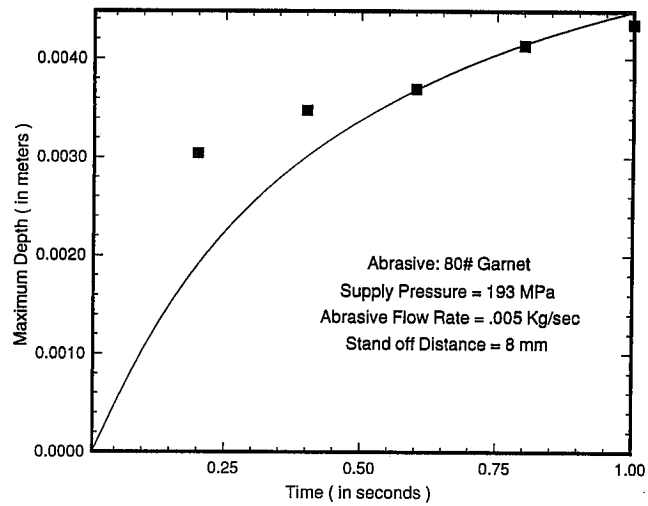


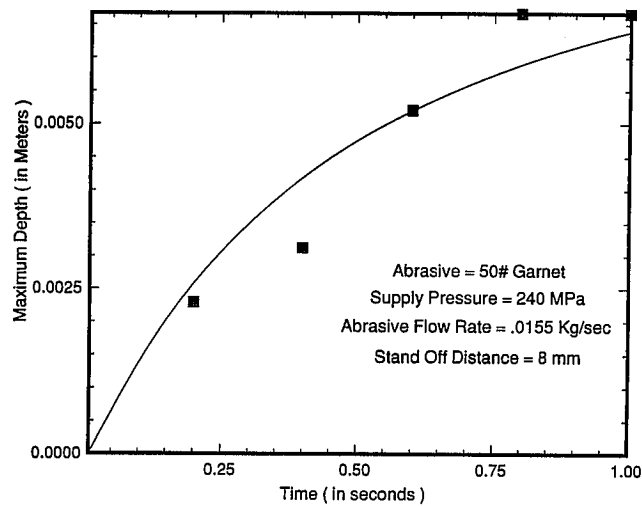
Figure 4. Experimentally Observed Kerf Profiles alongside with the Regressed Equations



(a)

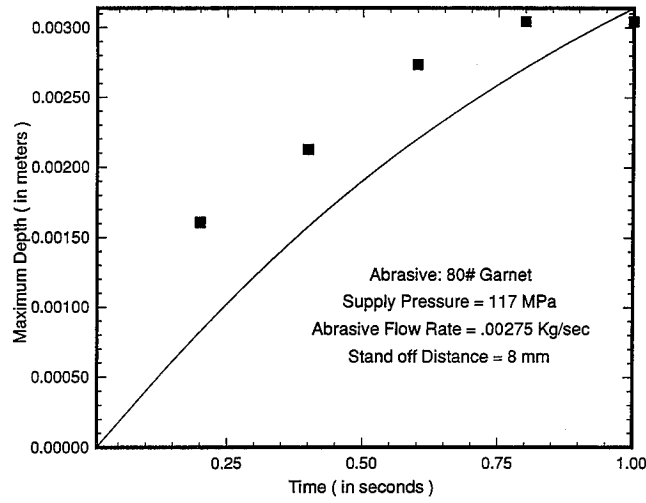


(b)

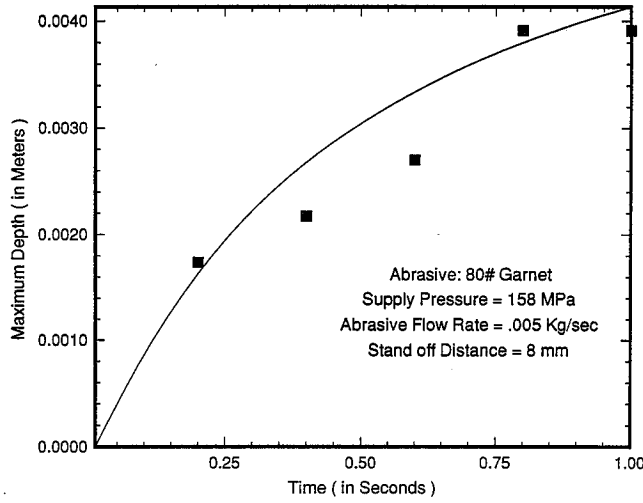


(c)

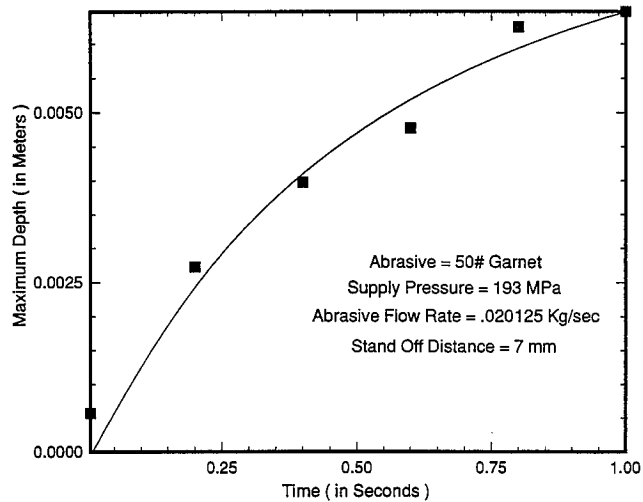
Figure 5. A Comparison of the Proposed Model versus the Experimental Data for 50# Garnet



(a)



(b)



(c)

Figure 6. A Comparison of the Proposed Model versus the Experimental Data for 80# Garnet

ON A SIMPLIFIED MODEL FOR HYDRO ABRASIVE JET MACHINING PREDICTION, CONTROL AND OPTIMIZATION

Edoardo CAPELLO
Research intern, Politecnico di Milano
Milano, Italy

Roberto GROPPETTI
Professor, Università degli Studi di Perugia
Perugia, Italy

ABSTRACT

The prediction of the results of Hydro Abrasive Jet Machining (HAJM) in terms of productivity and quality as cutting feed rate, maximum depth of cut, kerf width and surface roughness by means of a model of the process is the fundamental step towards the prediction, control and optimization of the process, which are the basis for a full exploitation of this machining process. The paper presents, analyses and validates a mathematical model of HAJM, suitable to predict the maximum penetration depth of the jet inside the workpiece. The energetic hypothesis at the basis of this model and the semi empirical approach followed lead to a simplified equation with a reduced number of empirical coefficients. This energetic model has been validated through a set of systematical cutting experiments which have demonstrated, by means of a statistical analysis of the results, its suitability for homogeneous and non-homogeneous materials, with different behaviours as ductile and brittle, as aluminium alloy, glass and fibre reinforced polymer. A good correlation between the model predicted results of the process and the actual ones has been demonstrated by the obtained correlation coefficients. The identified and proposed model, due to its simplicity and completeness, is suitable and can be easily implemented both in off-line programming, planning, optimization and CAD/CAM integration and in on-line control for the Adaptive Control of HAJM process.

1. INTRODUCTION

The prediction of the productivity and quality of Hydro Abrasive Jet Machining (HAJM) (i.e. cutting feed rate, kerf width and surface roughness, etc.) by means of a predictive model of the process, based on a function of process variables and parameters, is the fundamental step towards the control, automation and optimization of the process, which are the basis for a full and effective exploitation of this machining process.

The paper presents, analyses and validates a simplified mathematical model for HAJM, suitable for the prediction of the maximum penetration depth of the jet inside the workpiece for different machining conditions. The major peculiarity of this model is the energetic hypothesis, on which it is based, which leads to a simple equation, with a reduced number of empirical coefficients, easy to be evaluated and implemented. This energetic hypothesis has been verified through a set of experimental cuts, which have demonstrated, by means of a statistical analysis of the results, its validity on different materials, homogeneous and non-homogeneous, with different behaviours as ductile (aluminium alloy), brittle (glass) and composite (Fibre Glass Reinforced Polymer).

Both the simplicity and the completeness of the identified model, that is based at the same time on a reduced number of empirical statistical parameters and on a high number of process variables, that influence the predicted results, allow the implementation of this model both in off-line planning, programming and optimization for CAD/CAM integration of the HAJM process and in on-line Adaptive Control.

Some considerations about the precision required to the mathematical model of the process and its operative use are reported in the following section, before the analysis of the approach followed and the mathematical aspects of model identification.

- a. It has been observed that the influence of focuser wear on the machining result is not negligible because the maximum depth of cut depends on the focuser wear conditions and decreases as wear increases. This reverse relationship is due to the enlargement of the impinging area that involves a decrease of the penetration capability of the jet. The quantitative aspects of this kind of "machining-time depending efficiency" are quite difficult to evaluate; research efforts are in progress in order to obtain a mathematical relationship between focuser wear and process efficiency. Any predictive model of the machining process should take into account the influence of wear when implemented.
- b. Some replications of the experiments have been carried out and have demonstrated a quite wide spectrum of machining results. This is probably due to the lack of control of some factors that slightly influence the machining result, mostly abrasive grain size and distribution, pressure fluctuations, relative assembly position of nozzle and focuser, etc.. These random factors induce some natural variance (experimental error) in the results of the process.
- c. The maximum depth of cut reached by the impinging jet is not constant along the cut. In fact, even if the focuser moves continuously in the feed direction, at the bottom of the kerf the jet feed rate is not constant, due to jet intrinsic instability and deflection, and the erosion capability of the jet seems to follow a periodical modulation which cannot be predicted nor controlled. As known, the depth of cut is not constant and presents sharp peaks and deep valleys. Therefore the real maximum thickness that can be cut is the minimum value of the

peaks of the bottom of the kerf. Thus the entity "maximum penetration depth" is mainly a statistical variable with mean and, above all, variance.

- d. The lower part of the side surface of the kerf is strongly characterized by surface waviness, which should be avoided in most of the practical HAJM applications, selecting suitable machining conditions. Therefore, in many cases the operative machining conditions exceed the critical limit of the through cut/maximum penetration depth for a certain workpiece thickness.

All these considerations show that there is no need to look for an extreme precision of the model, because the results of the process are subject to a natural variance which cannot be easily controlled. On the other side, from the utilization point of view, one of the most interesting aspects of the model is the possibility to predict the maximum depth of cut for any different material. Therefore the equation of a useful model should take into account the material response to HAJM, or a material characteristic parameter, as proposed by Zeng and Kim (1992).

The problem of introducing the material response to HAJM in the model equation has been faced and analysed in the literature by means of two different approaches, respectively of "physical" and "empirical" kind, as discussed by the authors (1992) and by Blickwedel et al. (1990).

The first kind of approach, the "physical" approach, leads to a mathematical relationship accounting for the influence of the different material and abrasive characteristics on the machining results. Even if the cognizance of the phenomena involved is fairly accurate, their complexity involve approximations in the model definition and the dependence of the obtained equations on some statistical parameters. These parameters must be estimated by a regression analysis made on the results of some experimental cuts. Therefore the physical models of HAJM use both "a priori" information about the phenomena involved in the process and "a posteriori" information obtained by a reduced set of cutting experiments. However, these cost and time consuming experiments partially make useless the effort made in the identification of the mathematical relationship between the material characteristics and its behaviour during HAJM. Moreover, the mathematical functions obtained are often very complex and difficult to use in operative conditions, and require the knowledge of some material mechanical characteristics which may not be available.

The second kind of approach, the "empirical" one, is characterized by the definition of a simple mathematical equation correlating the most relevant process variables to the process results. The identification of this kind of function does not require any "a priori" information about the material behaviour when machined by HAJM, but just a general information about the process. In fact, the empirical function can be identified simply by evaluating the trend of the experimental data and the regression function that fits best. These equations generally have a simple mathematical structure but, due to the lack of information about the mechanics of the process, depend on a large number of empirical parameters. These parameters must be determined by a regression analysis on a large number of experimental data.

Both these approaches have some limitations and constraints. The best way to identify a mathematical model is to find a compromise between the two approaches. One can obtain some basic relationships from general considerations about the physics of the process, but the material response to HAJM, or HAJM machinability, has to be introduced by identifying a relationship

between the standard mechanical material characteristics and the statistical parameters of the model, as discussed by Zeng and Kim (1992).

2. MODEL IDENTIFICATION

2.1 Model Definition

In a previous work (1992) the authors have presented and discussed a semi empirical energetic model for HAJM, making reference to the fundamental work done, among the others, by Bitter (1963), Blickwedel et al. (1990), Geskin et al. (1989), Hashish (1984), Matsui et al. (1991), Yanaida and Ohashi (1978), Zeng and Kim (1990-1991). In the following section a simplified model, based on the same semi empirical approach followed for the previous one, is defined and validated. Beside the definition and the validation procedure, some peculiar aspects of this simplified model are analysed.

In order to define a synthetical index of the cutting conditions, as level of pressure, abrasive mass flow rate and feed rate, which could simplify the model of the process, the maximum penetration depth h for different materials, as aluminium alloy, glass and fibre reinforced polymer has been expressed as a function of the energy per unit of length of the impinging jet (see Nomenclature):

$$h = f\left(\frac{dE_j}{dx}\right) = f(\epsilon_j) \quad (1)$$

where the energy per unit of length ϵ_j has been evaluated by the following equation:

$$\epsilon_j = \frac{dE_j}{dx} = \frac{dE_j}{dt} \frac{dt}{dx} = \frac{1}{2 \cdot u} \dot{m}_a \cdot V_j^2 = \frac{1}{2 \cdot u} \dot{m}_a \left(\frac{\dot{m}_w}{\dot{m}_a + \dot{m}_w} \cdot V_w \right)^2 \quad (2)$$

Figures from 1 to 3 show that, even if there is an evident relationship, the experimental data have a great dispersion around the mean value, i.e. for the same ϵ_j level a wide range of experimental penetration depths can be obtained. Due to this dispersion, ϵ_j seems not to be a good synthetical index of the process conditions. After a brief analysis on the level of the different process variables that provide the same ϵ_j level, the reason of the dispersion was identified in the omitted primary nozzle efflux efficiency ξ in the evaluation of the energy of the jet. Therefore, the energy per unit of length has been calculated using the following equation:

$$\epsilon_j = \frac{1}{2 \cdot u} \dot{m}_a \left(\frac{\xi^2 \cdot \dot{m}_w}{\dot{m}_a + \xi \cdot \dot{m}_w} V_w \right)^2 \quad (3)$$

where ξ has been evaluated through a set of experimental measurements of the efflux flow rate of different primary nozzles. The mean value is $\xi = 0.65$. Replacing this value into the former equation, the penetration depth as a function of the energy per unit of length (figures from 4 to 6) demonstrates a strong concentration of the data around the mean value, that is they lay on a curve

that characterises the material behaviour when machined by HAJM. Therefore the ϵ_j energy per unit of length can be used as a synthetical index of the process condition, as it synthetically accounts for the influence of the most significative process variables (pressure, abrasive flow rate and feed rate).

The equation of the machinability characteristic curve of the material behaviour can be obtained by means of an analysis of the relationship between the volume removal rate and the energy of the abrasive flow. In fact, the primary role in material erosion is played by the abrasive flow, while water is the accelerating mean of the particles that play a minor role in the erosion process. The hypothesis of the existence of a relationship between the kinetic energy of a single particle and the volume of removed material has been verified and accepted by many authors (Bitter (1963), Blickwedel (1990), Zeng and Kim (1990)); as discussed previously by the authors (1992), as first order approximation, this relationship is supposed to be linear:

$$\delta V_p = k_s \cdot e_p \quad (4)$$

where k_s is a factor related to material characteristics, abrasive characteristics, and impact parameters. For limited flow rates the volume eroded by an abrasive flow is the sum of the volumes eroded by single particles: the finite removed volume δV_p can be replaced by the elementary removed volume dV and the finite kinetic energy of the particle can be replaced by the elementary energy of the abrasive flow involved in the erosion:

$$dV = k_f \cdot dE_a \quad (5)$$

This equation, dividing both sides by dt , formulates the proportionality between the volume removal rate and the power of abrasive flow involved in the erosion process:

$$\frac{dV}{dt} = k_f \frac{dE_a}{dt} \quad (6)$$

The energy involved in the erosion process is somehow related to the energy of the impinging jet, whose value depends on the process variables:

$$E_a = \eta(z) \cdot E_j \quad (7)$$

where $\eta(z)$ is a decreasing function of the kerf depth z . The influence of $\eta(z)$ can be seen in figures from 4 to 6: the gradient of the curve diminishes as the energy increase, especially for deep cuts. The $\eta(z)$ function accounts for the energy losses inside the kerf which dissipate the jet energy and for the deflection of the penetrating jet, which causes a decrease in the jet erosion efficiency. The energy dissipation and the jet erosion efficiency of the penetrating jet are complex phenomena that have not been completely investigated and understood yet. Therefore a simple $\eta(z)$ function cannot be easily identified by means of a physical analysis of the process; $\eta(z)$ can be identified by choosing the empirical equation that fits the experimental data best. Among the many functions investigated, the best results have been obtained using the following expression:

$$\eta(z) = \frac{1}{(1+z)^\gamma} \quad (8)$$

which satisfies the fundamental conditions:

$$\eta(0) = 1$$

$$\frac{d\eta}{dz} < 0$$

where γ is an empirical parameter that influences the slope of the curve. Substituting equation (7) and (8) in equation (6) one obtains the following equation:

$$\frac{dV}{dt} = \frac{dx \cdot dy \cdot dz}{dt} = \frac{\mu}{(1+z)^\gamma} \frac{dE_i(x,y)}{dt} \quad (9)$$

where x , y and z are the co-ordinates referred to the three orthogonal axes that originate from the intersection of the jet axis and the workpiece impinging surface. For a generic point P of the impinging surface, equation (9) can be rewritten in the following form:

$$\frac{dz(x,y,z)}{dt} = \frac{\mu}{(1+z)^\gamma} \frac{dE_i(x,y)}{dx \cdot dy \cdot dt} \quad (10)$$

The left term of this equation is the penetration rate of the jet inside the workpiece, the right term is the kinetic energy delivered to the workpiece per unit of time and area. As discussed by the authors (1992), this energy is not constant across the jet cross section because of the different speed and mass flow rates of the particles. Nevertheless, for simplicity's sake, this energy per unit of time and area can be supposed to be constant over the jet cross section and the Spatial Density of Power Distribution (SDPD) function can be supposed to be cylindrical instead of "bell shaped", as illustrated by the authors (1992). The level of the jet power distribution solely depends on the value of the process variables:

$$\frac{dz(z)}{dt} = \frac{\mu}{(1+z)^\gamma} \frac{dE_i}{dx \cdot dy \cdot dt} = \frac{\mu}{(1+z)^\gamma} \frac{W_i}{dx \cdot dy} = \frac{\mu}{(1+z)^\gamma} w_j \quad (11)$$

where

$$w_j = \frac{W_i}{dx \cdot dy} = 2 \frac{\dot{m}_a \cdot V_j^2}{\pi \cdot d_j^2} \quad (12)$$

represents the SDPD. Considering that the nozzle moves at a feed rate u , equation (11) can be rewritten as:

$$(1+z)^\gamma dz = \mu \frac{\dot{m}_a \cdot V_j^2}{u \cdot d_j^2} dx \quad (13)$$

The left side of this equation can be integrated from 0 to the maximum reached depth h , the right side from 0 to the maximum x displacement, that is d_j .

$$\int_0^h (1+z)^\gamma dz = \int_0^{d_j} \mu \frac{\dot{m}_a \cdot V_j^2}{u \cdot d_j^2} dx \quad (14)$$

obtaining:

$$h = \left[1 + \mu \cdot (1+\gamma) \frac{\dot{m}_a \cdot V_j^2}{u \cdot d_j} \right]^{\frac{1}{1+\gamma}} - 1 \quad (15)$$

This equation (15) can be expressed directly in terms of process variables, where V_j and \dot{m}_w can be made explicit also in terms of water supply pressure P and primary nozzle diameter or water jet diameter d_w :

$$h = \left[1 + \mu \cdot (1+\gamma) \frac{\dot{m}_a}{u \cdot d_j} \frac{k' \cdot P \cdot d_w^4}{(\dot{m}_a + k'' \cdot P^{1/2} \cdot d_w^2)^2} \right]^{\frac{1}{1+\gamma}} - 1 \quad (16)$$

where k' and k'' are constant values, dependent on the efflux and energy transformation efficiencies of the ejecting system and independent on the interaction of the jet with the workpiece material. Equations (15) and (16) relate the maximum penetration depth of the jet inside the workpiece to the most relevant process variables and the two empirical parameters μ and γ to be evaluated as explained in the following section.

The structure of these equations is fairly simple and can be easily implemented and used in operative conditions. The equation (15) can be considered as a simplified expression of the former final equation presented by the authors (1992), which can be used to evaluate the geometry of the kerf in the h - y plane as a function of the process variables and parameters and the two integrals of the SDPD on respect to the jet cross section and to the cordal length of the cross section border at the y distance from the jet axis.

The model proposed is based on a mathematical representation of the real process. Differences between the modelled situation and the real one can be found in two different aspects:

- a. The hydro-abrasive jet is represented as a deflectionless energetic flow. In the real process the jet deflects while it penetrates into the machined material. The indefinite integration of equation (12) cannot be used to predict the shape of the erosion front of the cut.
- b. The jet geometry is considered as a constant cylindrical jet. In the real process the jet widens as the distance covered by the jet increases: the jet diameter d_j is not constant but increases as standoff distance increases. Therefore the model cannot predict changes in the maximum penetration depth due to variations of standoff distance. This distance has to be held constant during operation.

2.2 Parameter Analysis

The maximum penetration depth h inside the workpiece, calculated by means of the final equation of the model, depends not only on the level of the most relevant process variables, respectively abrasive mass flow rate m_a , abrasive flow velocity V_j , that depends on the water efflux velocity and on the ratio of water mass flow rate and the total mass flow rate (see equation (2)), feed rate u , focuser diameter d_j , but also on the value of the two statistical parameters μ and γ . These parameters have to be evaluated by a regression on a set of experimental data.

The first parameter μ is related to the proportionality factor between volume removal rate and energy of the jet per time unit. It depends both on material and on abrasive characteristics and it can be considered as a "machinability parameter". This result is in accordance with the results proposed by Zeng and Kim (1992). The sensitivity of the maximum penetration depth to this parameter is very high: its value deeply influences the precision of the prediction.

The second parameter γ represents the energy losses and the global efficiency inside the kerf. Like the first parameter μ , it should depend both on material and on abrasive characteristics but, due to the relatively low sensitivity of the predicted result to it, the value of γ can be estimated once for all on a wide spectrum of material and abrasives, and can be considered as a constant of the HAJM process/system, as explained later.

3. EXPERIMENTS DESCRIPTION

3.1 Experimental Set-up and Plan

In order to verify the hypotheses stated and to validate the proposed model, some kerfing experiments have been carried out on three different materials. The kerfing experiments were executed by means of a HAJM CNC machining cell developed in co-operation with SOITAAB s.a.s., Milano (Italy) and of a high pressure intensifier system supplied by UHDE GmbH, Werk Hagen (Germany) previously presented by one of the author and Comi (1991) and by the authors (1992).

Kerfing experiments have been carried out on three distinct materials with different mechanical and physical characteristics: aluminium alloy 6061-T6 as representative of ductile materials, glass as representative of brittle materials and Fibre Glass Reinforced Polymer - FGRP as representative of non homogeneous composite materials.

The cutting conditions were identified in order to cut a "standard" thickness for each material: maximum penetration depths range from 8 to 65 mm for aluminium alloy, from 2 to 28 mm for glass and from 2 to 24 mm for FGRP. Pressure level range from 150 to 350 MPa, abrasive flow rates range from 3.3 to 10 g/s, feed rates range from 1.25 to 33.3 mm/s. All the other process parameters have been held constant (primary nozzle diameter $d_w = 0.25$ mm, focuser diameter $d_f = 1$ mm, length $l_j = 40$ mm).

3.2 Measurements of Process Results

The maximum depth of cut has been measured by means of a comparator. Four measurements have been made for each cut and the mean of them was taken as the maximum penetration depth. The four data were also utilized to evaluate the standard deviation of the measurement and, because of its high level in respect to other random factors, was used as a rough estimation of the experimental error.

4. RESULTS ANALYSIS AND DISCUSSION

The kerfing data have been used for a non-linear regression analysis in the two parameters μ and γ of the model. In order to execute this non-linear regression, the algorithm of Levenberg Marquardt reported by Press et al. (1988) has been implemented. The aim of the analysis was to validate the proposed model and to determine if it is possible to reduce the number of the statistical parameters without decreasing the precision of the prediction. Three analysis have been carried out on sets of homogeneous data obtained from the three different materials.

Table 1 reports the correlation coefficients and the values of the parameters of the best fits; figures from 7 to 9 are the comparative charts between predicted and real process results. The numerical values reported in Table 1 and 2 are calculated using the SI standard measurement units. Both charts and correlation coefficients show a good correlation between predictions and actual results of the process for all the materials investigated. Moreover, the covariance matrixes show a good reliability of the estimate of the parameters. Therefore, the regression analysis, through the experimental plan and the data collection, has validated the hypotheses stated during the model definition.

The analysis of the covariance matrixes of the parameters have demonstrated the possibility of ulteriorly reduce the number of model parameters. In fact, the relatively low sensitivity of the prediction to the value of γ and the restricted range of regression values obtained for this parameter allow the definition of a constant of the HAJM process/system. The value of γ can be determined once for all by a regression on sets of data obtained from kerfing experiments on materials with very different mechanical and physical characteristics. When this value has been determined, any new material can be characterized only by the μ -parameter.

The value of the γ constant has been determined simply by calculating the weighted mean of the singles γ obtained from the three regressions. In order to reduce the decrease of the value of the correlation coefficients ρ^2 and of the precision of the model prediction, the inverse of the diagonals of the covariance matrixes of the parameter estimates have been used as weights.

Therefore the weights account for the different sensitivity of the prediction to the variation of the γ value.

The regression analysis has been performed again. The value of γ has been fixed to the mean value 22.8 and only the value of μ was estimated. The three values obtained and the new values of ρ^2 are reported in Table 2. Their values show that it is possible to hold the γ -parameter constant without an appreciable decrease of the precision of the model prediction.

The parameter μ characterizes the material behaviour when machined by HAJM. This parameter can be defined as a machinability parameter and has to be estimated for every unknown material that has to be machined. The value of the parameter μ can be determined in two ways. The first requires the execution of experimental cuts, the measurement of kerf characteristics, the organization of data and the regression analysis. The second requires the definition of a relationship between the value of μ and some standard mechanical characteristics of the machined material i.e. hardness, Young modulus, etc.. The definition of this relationship is still matter of research.

5. CONCLUSIONS

- a. A model based on the energy per unit of length delivered to the workpiece by the abrasive flow has to account for the primary nozzle efflux efficiency. In fact, the experimental data obtained on three materials with very different characteristics, when plotted as a function of the energy per unit of length, show a reduced dispersion around the mean value when this efficiency is introduced in the energy estimation. In this way the energy per unit of length delivered to the workpiece can be used as a synthetical index of the process conditions (pressure level, abrasive flow rate and feed rate).
- b. The hypotheses stated in the model definition have been validated experimentally and the model proposed in this paper has shown a fairly good correlation between real and predicted results of the process.
- c. The number of statistical parameters of the model can be reduced if the value of γ is set to a mean value and hold constant during the regression analysis. The mean value has to be determined with regressions on an extensive experimental plan on materials with different characteristics. In order to maintain a high level of precision, the weighted mean operation has to be used where weights are the inverse of the diagonals of the covariance matrixes of the parameter estimate.
- d. The characterisation of the material behaviour when machined by HAJM depends on the parameter μ . This "machinability parameter" is different for each couple machined material/abrasive used.
- e. The model accounts for the influence on the machining results of the most relevant process variables. Therefore, the completeness and the simplicity of the model allow its use in a wide range of applications, ranging from on-line control and Adaptive Control Constrain (ACC), where a model of the process is fundamental for on-line identification and for the respect of the controlled variable set points, to off-line CAD/CAM integration, programming, planning and optimization of the process, where the predicted depth of cut is one of the constraints that must be satisfied by the optimum process condition of multi-objective optimization model, as discussed by one of the authors and Comi (1991).

ACKNOWLEDGMENTS

This work was carried out with the funding of the Italian MURST (Ministry of University and Scientific and Technological Research) and CNR (National Research Council). The Authors are grateful to UHDE GmbH - Werk Hagen (Germany), SOITAAB s.a.s - Ronco Briantino, Milano (Italy), OSAI A-B S.p.A. - Ivrea, Torino (Italy) for their support.

The experimental facilities were partially supplied within commodatum contracts between Politecnico di Milano - Dipartimento di Meccanica and UHDE GmbH, and SOITAAB s.a.s..

REFERENCES

- Bitter, J.G.A., "A Study of Erosion Phenomena - Part I," *Wear*, vol. 6, pp.5-21, 1963.
- Bitter, J.G.A., "A Study of Erosion Phenomena - Part II," *Wear*, vol. 6, pp.169-190, 1963.
- Blickwedel, H.; Guo, N.S.; Haferkamp, H.; Louis, H., "Prediction of Abrasive Jet Cutting Efficiency and Quality," *Proceedings of the 10th International Symposium on Jet Cutting Technology*, BHRG, 1990.
- E. Capello, R. Groppetti, "On an Energetic Semi-Empirical Model of Hydro Abrasive Jet Material Removal Mechanism for Control and Optimization," *Proceedings of the 11th International Symposium on Jet Cutting Technology*, BHRG, 1992.
- Geskin, E.S., Chen, W.L., Chen, S.S., Hu, F., Khan, M.E.U., Kim, S., Singh, P., Ferguson, R., "Investigation of Anatomy of Abrasive Waterjets," *Proceedings of the 5th Waterjet Technology Conference*, WJTA, 1989.
- Groppetti, R., Comi, G.E., "Contribution to Computer Control and Optimization of Hydro-Abrasive Jet Machining Process," *Proceedings of the International Conference on Computers in Industry*, ASME, 1991.
- Hashish, M., "On the Modeling of Abrasive-Waterjets Cutting," *Proceedings of the 7th International Symposium on Jet Cutting Technology*, BHRA, 1984.
- Hu, F., Yang, Y.; Geskin, E.S.; Chung, Y., "Characterization of Material Removal in the Course of Abrasive Waterjets Machining," *Proceedings of the 6th American Water Jet Conference*, 1991.
- Matsui, S., Matsumura, H., Ikemoto, Y., Kumon, Y., Shimizu, H., "Prediction Equations for Depth of Cut made by Abrasive Water Jets," *6th American Water Jet Conference*, 1991.
- Matsui, S., Matsumura, H., Ikemoto, Y., Shimizu, H., Takada, I., "High precision Cutting Method For Metallic Materials By Abrasive Water Jet," *6th American Water Jet Conference*, 1991.
- Press, W.H., Flannery, B.P., Teukolsky, S.A., Vetterling, W.T., "Numerical Recipes, the Art of Scientific Computing," *Cambridge University Press*, 1988.
- Vajapee, S., "Understanding the Mechanism of Waterjet Cutting," *Manufacturing Engineering*, 1988.
- Yanaida, K., Ohashi, A., "Flow Characteristics of Water Jets in Air," *Proceedings of the 4th International Symposium on Jet Cutting Technology*, 1978.
- Zeng, J., Kim, T.J., "A Study of Brittle Erosion Mechanism Applied to Abrasive Waterjet Process," *Proceedingd of the 10th International Symposium on Jet Cutting Technology*, 1990.
- Zeng, J., Heines R., Kim, T.J., "Characterization of Energy Dissipation Phenomenon in Abrasive Waterjet Cutting," *Proceedings of the 6th American Water Jet Conference*, 1991.
- Zeng, J., Kim, T.J., "Development of an Abrasive Waterjet Kerf Cutting Model for Brittle Materials," *Proceedings of the 11th International Symposium on Jet Cutting Technology*, BHRG, 1992.

NOMENCLATURE

d_j	Abrasive flow diameter (focuser diameter)
d_w	Water jet diameter (primary nozzle diameter)
e_p	Kinetic energy of a particle
E_a	Kinetic energy involved in the material removal mechanism
E_j	Kinetic energy of the abrasive flow
h	Maximum penetration depth
\dot{m}_a	Abrasive mass flow rate
\dot{m}_w	Water mass flow rate
P	Water supply pressure
u	Feed rate
V	Removed material volume
V_j	Abrasive flow velocity
V_w	Water efflux velocity
x	Feed displacement
y	Distance from the jet axis in the direction perpendicular to the feed rate
z	Current kerf depth
w_j	Spatial Distribution of Power Density (SDPD)
W_j	Power of the abrasive flow
δv_p	Material removed volume by a single particle
ϵ_j	Abrasive flow energy per unit of length
γ	Parameter accounting for the energy loss inside the kerf
$\eta(z)$	Characterizing function of the energy loss inside the kerf
μ	Proportionality parameter between the volume removal rate and the jet energy per time unit
ξ	Efflux efficiency

Table 1

Correlation coefficient ρ^2 and estimated parameters for different materials

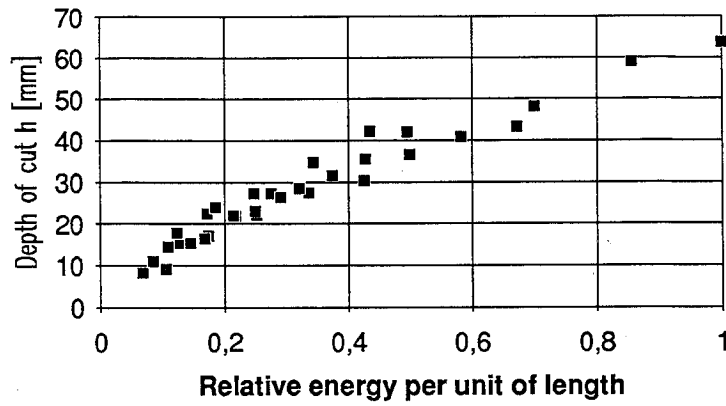
MACHINED MATERIAL			
	Aluminium Alloy	Glass	FGRP
$\mu =$	8.609 10 ⁻¹¹	3.377 10 ⁻¹⁰	2.874 10 ⁻¹⁰
$\gamma =$	22	31.3	36.5
$\rho^2 =$	0.974	0.974	0.966

Table 2

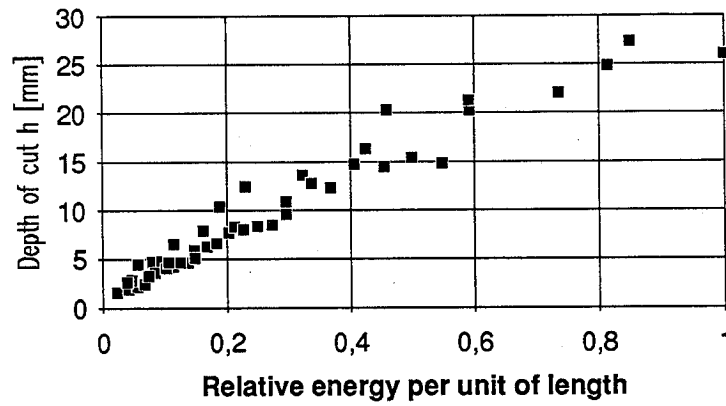
**Correlation coefficient ρ^2 and estimated parameter for different materials
(γ constant).**

MACHINED MATERIAL			
	Aluminium Alloy	Glass	FGRP
$\mu =$	8.752 10 ⁻¹¹	3.115 10 ⁻¹⁰	2.595 10 ⁻¹⁰
$\gamma =$	22.8	22.8	22.8
$\rho^2 =$	0.973	0.972	0.961

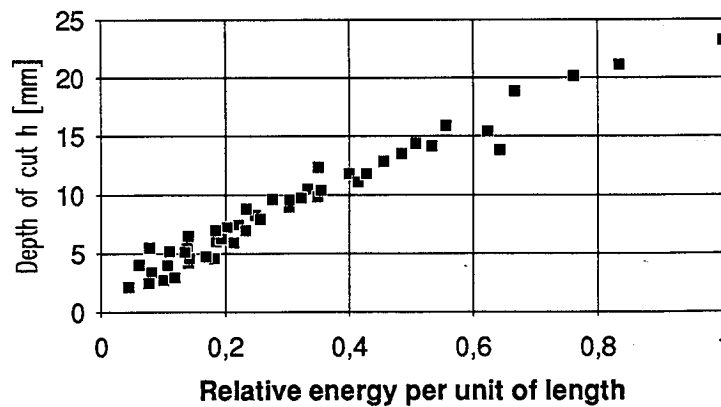
Aluminium alloy



Glass

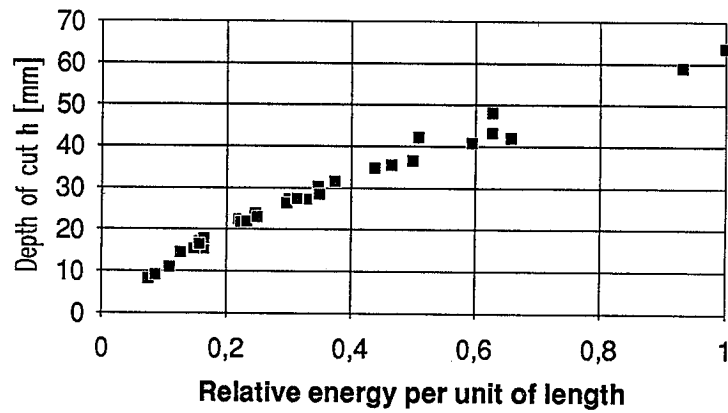


FGRP

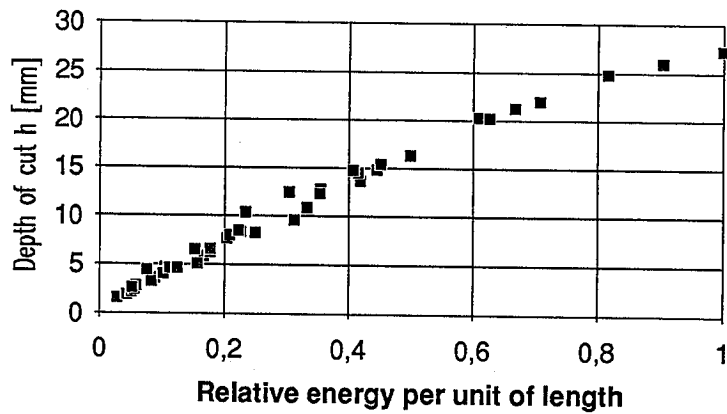


Figures 1, 2, 3
Diagrams of the $h=f(\epsilon_p)$ function without considering the efflux efficiency ξ .

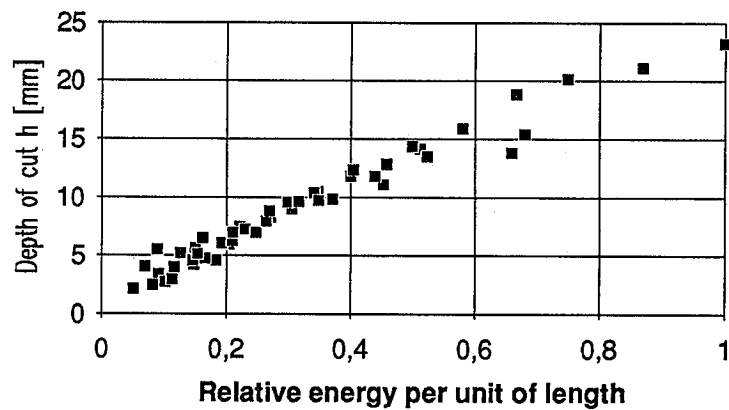
Aluminium alloy



Glass



FGRP



Figures 4, 5, 6

Diagrams of the $h=f(\epsilon_r)$ function considering the efflux efficiency ξ .

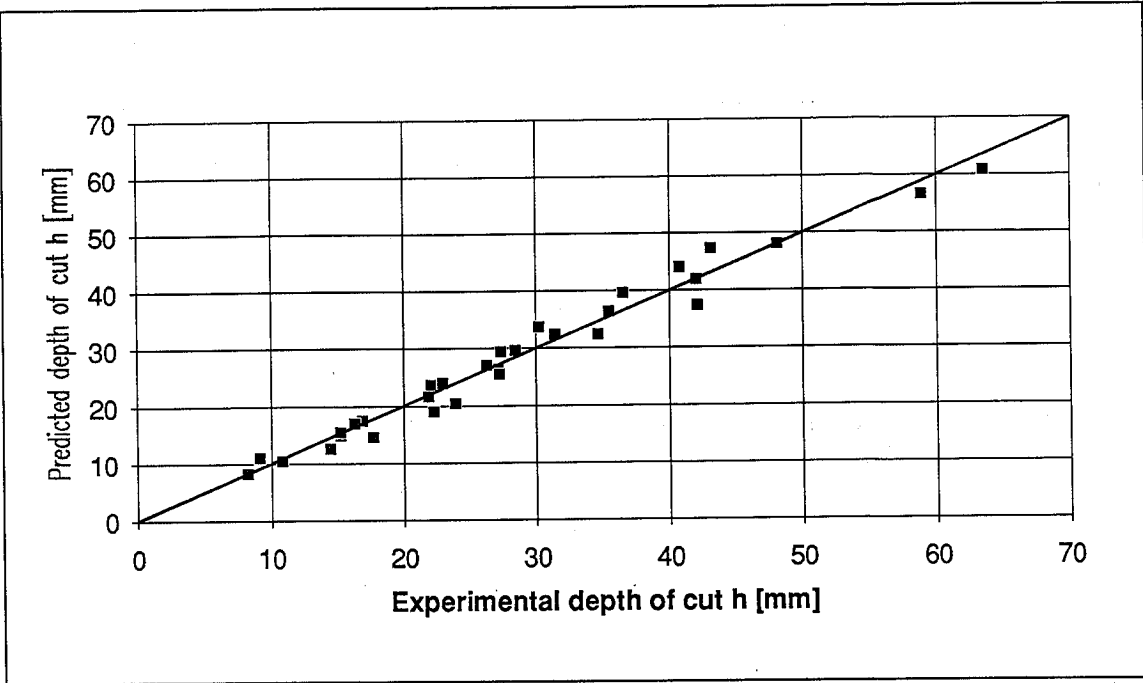


Figure 7
Comparative chart between predicted and experimental kerf depth for aluminium alloy.

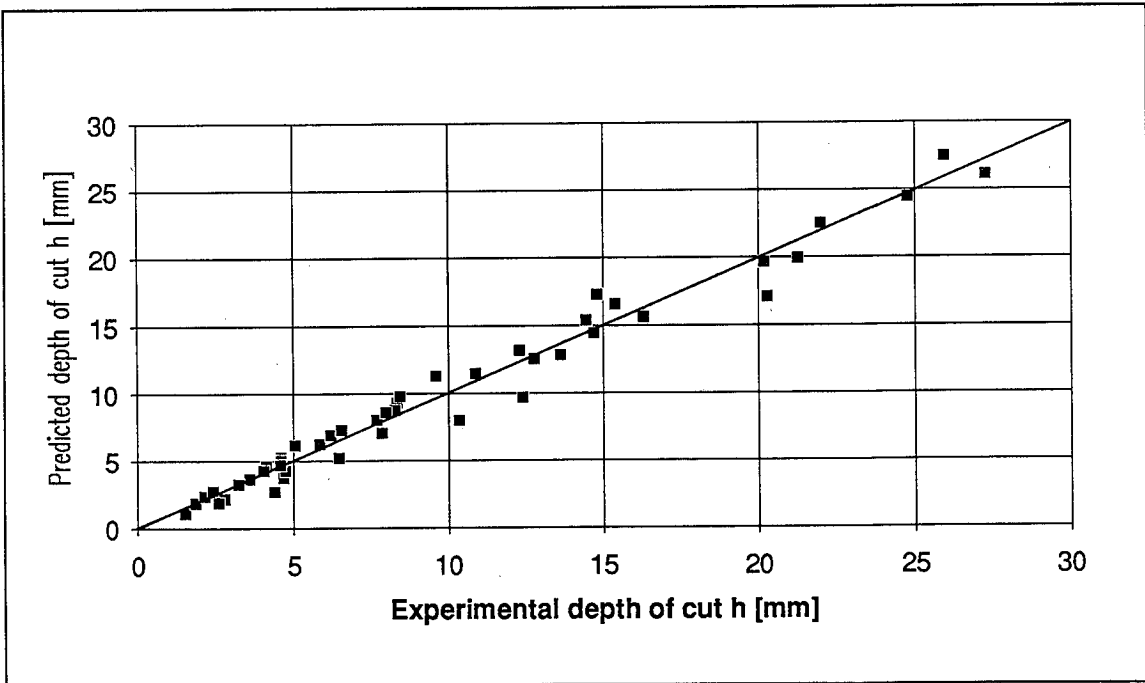


Figure 8
Comparative chart between predicted and experimental kerf depth for glass.

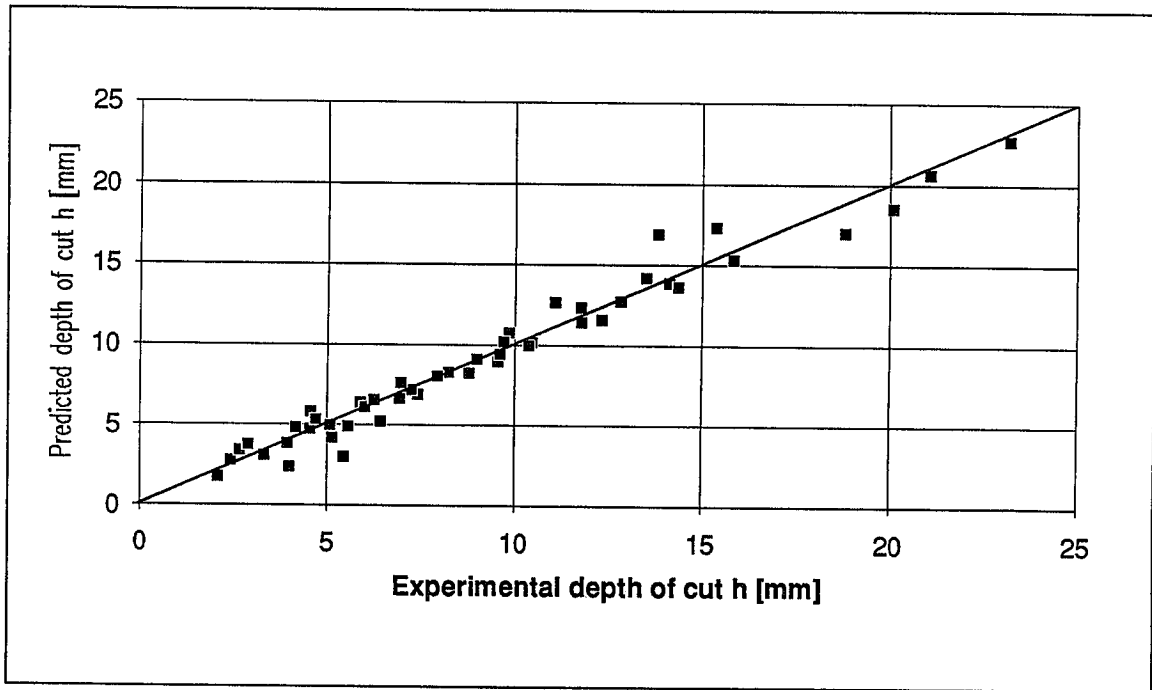


Figure 9
Comparative chart between predicted and experimental kerf depth for FGRP.

**PARAMETER PREDICTION AND COST ANALYSIS IN
ABRASIVE WATERJET CUTTING OPERATIONS**

Jiyue Zeng* and Thomas J. Kim
University of Rhode Island
Kingston, RI 02881
U.S.A.

ABSTRACT

Machinability of engineering materials by an abrasive waterjet was previously quantified in terms of "Machinability Number". Using "Machinability Number" as a material parameter, a previously derived equation for abrasive waterjet cutting is applied to predict the cutting speed as well as other process parameters. The predicted cutting speed is then applied in a cost analysis procedure to make a cost prediction.

*Present Address: Ingersoll-Rand Waterjet Cutting Systems
23629 Industrial Park Drive, Farmington Hills, MI 48335, U.S.A.

1. INTRODUCTION

The objective of an abrasive waterjet (AWJ) cutting operation is to remove material at a high rate while maintaining a reasonable accuracy and a quality surface finish. Recent advances in high pressure intensifier technology have made AWJ a more reliable, versatile and low cost non-traditional machining tool. With improved cutting accuracy and speed, AWJ cutting has now emerged as a viable precision machining technology as laser, EDM and other traditional and non-traditional machining methods. A better understanding of AWJ material removal mechanisms and its performance has greatly enhanced the application of this erosion based technology. However, compared to the advance in hardware development, software development lags behind. Boosting software development in AWJ technology is the primary goal of this paper. Our recent studies (Zeng and Kim, 1992b; Zeng et al., 1992) have established a link between our previously derived theoretical models for AWJ material removal and quantitative evaluation of AWJ machinability. This paper will continue this effort and extend it to a complete parameter prediction and cost analysis method.

2. CUTTING SPEED PREDICTION

It is generally understood that in abrasive waterjet cutting processes the total depth of cut can be divided into two distinct zones due to different modes of abrasive/target interaction. In the upper zone, material is removed by abrasive particles impacting at shallow angles. In the lower zone, sequential steps are formed which lead to large angle impacts. A modeling study (Hashish, 1984) characterized the upper zone as a cutting wear zone and the lower one a deformation wear zone. In this study, Finnie's microcutting model (Finnie, 1958) and Bitter's deformation wear model (Bitter, 1963a and 1963b), respectively, were used to evaluate the material removal in the cutting wear and deformation wear. A global cutting equation was then derived for AWJ cutting of ductile materials. More recently, Hashish (1987) improved Finnie's model by incorporating the effects of particle size and shape which resulted in a change in the particle velocity exponent from 2 to 2.5. This provides better correlation with experimental results. Hashish (1989) also obtained a modified version of the kerf cutting equation in terms of non-dimensional process parameters. A good correlation between the modified equation and cutting experiments with various metal samples was reported.

A kerf cutting model has been derived for AWJ cutting of brittle materials by the authors (Zeng and Kim, 1992b). By examining the kerf cutting front with a scanning electron microscope, it was observed that material removal in the kerf cutting operation is due primarily to

impacts of abrasive particles at glancing angles. By equating the material removal on the cutting front to the accumulated volume of microcutting by individual abrasive particles entrained in the jet, the equation for depth of cut is derived as:

$$h = \frac{f(\theta_c) \left(\frac{\dot{m}}{m}\right) V}{Du} \quad (1)$$

where u is the traverse speed, D is the focusing nozzle diameter, V represents the volume removal by a single abrasive particle, m is the mass of an abrasive particle, \dot{m} is the mass abrasive flow rate, θ_c is the critical jet exit angle, defined as the angle of slope at the bottom of the cutting front as the maximum depth of cut is reached. The function $f(\theta_c)$ is defined by:

$$f(\theta_c) = \frac{2 \tan^2 \theta_c}{\ln\left(\frac{1 + \sin \theta_c}{\cos \theta_c}\right) \left[\frac{\tan \theta_c}{\cos \theta_c} + \ln\left(\frac{1 + \sin \theta_c}{\cos \theta_c}\right) \right]} \quad (2)$$

Since θ_c is usually less than 50 degrees (Zeng et al., 1991), it has been shown that for $0 < \theta_c < 50^\circ$, $f(\theta_c)$ is approximately equal to one (with variation less than 2%).

The volume removal V is derived from a modeling study of brittle material removal by a single particle (Zeng and Kim, 1992a) as:

$$V = \left(\frac{\eta C_v C_y}{1 + R} \right)^2 \frac{C_e \dot{m} P_w}{\rho_w} \left(\frac{f_w \beta a \sigma_f \alpha^2}{3 \gamma E} + \frac{\alpha}{\sigma_f} \right) \quad (3)$$

where η is the momentum transfer efficiency, C_v the orifice efficiency, C_y the compressibility coefficient, R the abrasive/water mass flow ratio, C_e the coefficient of impact efficiency, P_w the water pressure, ρ_w the water density, α the impact angle, f_w the fraction of effective stress wave energy, β a function of the Poisson's Ratio of the target material, a the grain size, σ_f the flow stress, γ the fracture energy, and E the elastic modulus of target material. The equation for the depth of cut can then be expressed as:

$$h = \left(\frac{\eta C_v C_y}{1 + R} \right)^2 \frac{C_e \dot{m} P_w}{\rho_w Du} \left(\frac{f_w \beta a \sigma_f \alpha^2}{3 \gamma E} + \frac{\alpha}{\sigma_f} \right) \quad (4)$$

Although Equation (3) is applicable for brittle materials, the validity of Equation (4) can generally be extended to ductile materials. The reason is that the brittle material removal model expressed by Equation (3) includes both brittle fracture and plastic flow as the material removal mechanisms. The component of material removal due to plastic flow, which depends on material ductility, is evaluated with Finnie's model (Finnie, 1958; Finnie and McFadden, 1978) and reflected by the second term in Equations (3) and (4). If the fracture toughness γ is very large, the first term becomes negligible and Equation (4) can be used as a model for ductile materials.

Examination of Equation (4) enables us to define a single parameter which characterizes the overall material erosion resistance, called 'Erosion Resistance', R_e ,

$$R_e = \frac{1}{\frac{f_w \beta a \sigma_f \alpha^2}{3\gamma E} + \frac{\alpha}{\sigma_f}} \quad (5)$$

The value of R_e can be estimated using Equation (5) or determined experimentally by conducting an AWJ kerf cutting test and using the following inverse relation:

$$R_e = \left(\frac{\eta C_v C_y}{1 + R} \right)^2 \frac{C_e \dot{m} P_w}{\rho_w D u h} \quad (6)$$

The inverse of R_e represents the machinability of target material in an AWJ cutting process.

Although Equation (4) has a reasonable correlation with experimental results, its accuracy is not sufficient for parameter prediction. To obtain an applicable model, an empirical equation is proposed using a parameter structure similar to that of Equation (4). The effect of each parameter on the depth of cut is represented in exponential given as

$$h = \frac{n_0 P_w^{n_1} \dot{m}_w^{n_2} \dot{m}^{n_3}}{D^{n_4} u^{n_5}} \quad (7)$$

where $n_0, n_1, n_2, n_3, n_4, n_5$ are determined from regression analysis.

To determine these coefficients, a large number of AWJ kerf cutting tests have been conducted to generate the data trends of depth of cuts in terms of the five major process parameters: water pressure (P_w), water flow rate (\dot{m}_w), focusing nozzle diameter (D), traverse speed (u) and abrasive flow rate (\dot{m}). While the target material evaluated is primarily Aluminum 6061-T6, other materials such as nylon, granite, stainless steel (316L) and alumina ceramics (AD 99.5) are also tested.

A computer program is written to perform the regression analysis. The following regression coefficients are obtained: $n_0 = 0.0234$, $n_1 = 1.25$, $n_2 = 0.687$, $n_3 = 0.343$, $n_4 = 0.618$, $n_5 = 0.866$. The correlation coefficient is 0.954 and the determination coefficient is 0.911. The correlation between the model and the test data associated with Al 6061-T6 is shown graphically in Figure 1.

To evaluate the validity of Equation (7) for target materials other than 6061-T6, the data from the five different workpiece materials are normalized and compared with the normalized values from Equation (7) in Figures 2 - 6. A similarity among these data trends is generally observed. Therefore, Equation (7) can be applied to other engineering materials if an appropriate material characteristic parameter is included. This material characteristic parameter is defined as 'Machinability Number', N_m , which resembles the coefficient n_0 or the inverse of the 'Erosion Resistance' R_e . It has a unique value for a given workpiece material. The value of a material's 'Machinability Number', N_m , is determined experimentally with a standardized AWJ kerf cutting test and the following relation:

$$h = \frac{N_m P_w^{1.25} \dot{m}_w^{0.687} \dot{m}^{0.343}}{C D^{0.618} u^{0.866}} \quad (8)$$

where the constant C is a scale factor chosen to give N_m values within a preferred range. Since the 'Machinability Number' N_m is designated to be dimensionless, the constant C has a nominal unit to balance the dimension. The values of C are given for the following two unit systems:

<u>Parameter</u>	<u>Metric System</u>	<u>Inch System</u>
Depth of cut, h	mm	inch
Nozzle diameter, d_j	mm	inch
Traverse speed, u	mm/s	inch/min
Water pressure, P_w	mpa	kpsi
Water flow rate, \dot{m}_w	lpm(litre/minute)	gpm(gallon/minute)
Abrasive flow rate, \dot{m}	g/s	lb/min
C	8800	14071

The establishment of an AWJ cutting database requires that the 'Machinability Numbers' for all available engineering materials be determined. As a preliminary attempt, a total of 27 materials are selected from the entire spectrum of engineering materials, varying from very soft to extremely hard materials. Like all of the other material constants (e.g., tensile strength, fracture toughness, etc.), variation of the 'Machinability Number' within a reasonable range should be

expected for any engineering material. Calculated from the data of a total of 249 cutting tests on Al 6061-T6 with variation in water pressure, nozzle size, cutting speed, abrasive flow rate and water flow rate, the value of the "Machinability Number" for Al 6061-T6 varies within $\pm 10\%$ for 61% of the data and $\pm 20\%$ for 90% of the data. Granted that a standardized set of process parameters be used, the error will be less than $\pm 10\%$. Since such a standardization is not yet available, a practical method is used in this study. Three test cuts with varied parameter settings were made. The average value of N_m determined from Equation (8) and the parameter settings from these three cutting tests are regarded as an estimate of the true value of N_m . They are listed in Figure 7.

The machinability number can be used in various abrasive waterjet machining applications. One of the most important applications is in the selection of optional AWJ process parameters for kerf cutting. When the workpiece material and thickness are known and the preset values of water pressure, orifice/nozzle size, abrasive flow rate are used, the traverse speed can then be predicted using the following equation:

$$u = \left(\frac{N_m P_w^{1.25} \dot{m}_w^{0.687} \dot{m}^{0.343}}{CqhD^{0.618}} \right)^{1.15} \quad (9)$$

where q is a quality level parameter. The value of q can be chosen between 1 and 5, depending on the desired quality level. The quality level of $q = 1$ is referred to a separation cut in which the jet is just capable to separate the workpiece. Rough striation marks are visible at the lower portion of the kerf for a separation cut. Examination of the kerf surface of a separation cut revealed that striation marks are initiated at about 1/3 of the total workpiece thickness (measured from the top). Therefore, to estimate the traverse speed required for a striation-free cut, 3 times of the workpiece thickness should be substituted into Equation (9) for the value of h , i.e. $q = 3$. The values of q for five different quality levels are defined as follows:

Quality Levels	Description
$q = 1$	Criteria for separation cuts. Usually, $q > 1.2$ should be used.
$q = 2$	Rough surface finish with striation marks at the lower half surface.
$q = 3$	Smooth/rough transition criteria. Slight striation marks may appear.
$q = 4$	Striation free for most of engineering materials.
$q = 5$	Very smooth surface finish.

It should be noted that selection of a higher quality level results in slower cutting speeds, thereby increasing operating cost. The quality level parameter introduced in this study is merely a useful tool for practical AWJ cutting operations.

Using these parameter settings: water pressure 242 mpa (35 kpsi), water flow rate 3.32 lpm (0.877 gpm) (i.e. orifice diameter 0.381 mm(0.015")), nozzle diameter 1.016 mm(0.040") and abrasive (garnet) flow rate 7.56 g/s(1 lb/min), the following two test cuts serve as examples of applying Equation (9):

(1) Cutting a 12 mm thick ceramic (AD 94) plate: As shown in Figure 7, the value of N_m for AD 94 is 17.3. The traverse speed is determined with Equation (9) to be 0.69 mm/s for a separation cut and 0.19 mm/s for a smooth cut(quality level = 3). The results of the cuts are shown in Figure 8(a).

(2) Cutting an unidentified steel plate with a thickness of 26.8 mm: The workpiece material is suspected to be some kind of stainless steel. Thus, the appropriate N_m is estimated to be 82. Equation (9) yields a 1.63 mm/s traverse speed for a separation cut and 0.46 mm/s for a smooth cut. These cuts are also very close to estimated quality as shown in Figure 8 (b).

Equation (9) does not include the effects of stand-off distance, abrasive type and abrasive size. As a general trend, the depth of cut is reduced as the stand-off distance increases. However, variation of the stand-off within a small distance, say, 3 mm, does not cause any significant changes in the depth of cut. Similarly, as indicated by Hashish (1986), variation of abrasive size within the ordinary range (mesh 50 - 150) has little effect on the attainable maximum traverse speed.

The abrasive type is an important parameter. Different types of abrasive may result in substantial difference in depth of cut. The derived model does not incorporate this effect because the effect of abrasive type on the material removal mechanism is not well understood. Equation (9) can be modified slightly by multiplying N_m by an abrasive constant to account for different kinds of abrasive. The abrasive constant can be determined using the following procedure: (1) Conduct a few cutting tests with the given abrasive type; (2) Calculate the value of N_m using Equation (8); (3) Divide the new value of N_m by that given in Figure 7, yielding the abrasive constant for this specific abrasive; (5) Multiply N_m by the abrasive constant in Equations (8) and (9). Since certain types of abrasive behave very differently when cutting different materials (e.g. aluminum oxide), this abrasive constant may need to be determined on an individual base for a particular workpiece material.

3. COST PREDICTION

Cost effectiveness of AWJ cutting operations is always the key factor in determining its viability. Although some examples of cost analysis have been given by Hashish (1991, Houston), a more thorough evaluation method is still in need.

Actual cost composition of an abrasive waterjet cutting operation could be fairly complicated. This study does not attempt to cover every aspect of AWJ cutting cost. Cost factors such as depreciation, income tax, risk, and many more are not included. The focus of analysis is placed on the major cost factors. The approach used here is to determine the hourly cost for operating an abrasive waterjet system. Based on the parameter prediction as discussed in the previous section, cost for cutting a specific workpiece can be evaluated.

To determine the hourly cost for operating an abrasive waterjet system, the following cost components are considered:

(1) Machine Hourly Cost (C_{mh})

It is assumed that capital investment in an abrasive waterjet cutting system is C_m U.S. dollars (\$), the service life of such a system is n years with h_y work hours per year, the salvage value by the end of n years is zero, the rate of return is i (%). Using the uniform annual cost method (Groover, 1980), the annual machine cost (C_{my}) can be calculated by:

$$C_{my} = \frac{i(1+i)^n C_m}{(1+i)^n - 1} \quad (\$ \text{ per year}) \quad (10)$$

Then the machine hourly cost can be determined by:

$$C_{mh} = \frac{C_{my}}{h_y} = \frac{i(1+i)^n C_m}{[(1+i)^n - 1]h_y} \quad (\$ \text{ per hour}) \quad (11)$$

(2) Labor Hourly Cost (C_{lh})

This component of cost analysis includes the wages paid to operate the abrasive waterjet cutting system, fringe benefits and supervision. Assuming the annual salary of the operator to be O_y (\$), the fringe benefit equivalent to be F_y (\$) and the supervision equivalent is S_y (\$), the labor hourly cost can be determined as:

$$C_{lh} = \frac{O_y + F_y + S_y}{h_y} \quad (\$ \text{ per hour}) \quad (12)$$

(3) Material Hourly Cost (C_{th})

Considering abrasive costs C_a (\$/kg), an abrasive flow rate of \dot{m} (g/s) will generate hourly cost of $3.6\dot{m}C_a$. Similarly, water hourly cost is $60\dot{m}_w C_w$, where C_w is the cost of water (\$/litre) and \dot{m}_w is the water flow rate of \dot{m} (lpm). Assuming that an abrasive waterjet nozzle costs C_n (\$) and its service life is L_n (hr), the hourly cost of nozzle is C_n/L_n . Similarly, the hourly cost of the waterjet orifice is C_o/L_o , where C_o stands for the cost of an orifice (\$) and L_o stands for its service life (hr). Considering a downtime rate of T_d (%), the hourly cost of materials is calculated by:

$$C_{th} = (3.6\dot{m}C_a + 60\dot{m}_w C_w + \frac{C_n}{L_n} + \frac{C_o}{L_o})(1 - T_d) \quad (\$ \text{ per hour}) \quad (13)$$

(4) Power Hourly Cost (C_{ph})

If the electric power costs C_p (\$/kwh), an abrasive waterjet system of P (kw) will cost PC_p per hour. Considering the downtime rate, the hourly cost of power is:

$$C_{ph} = PC_p(1 - T_d) \quad (\$ \text{ per hour}) \quad (14)$$

(5) Hourly Cost of Maintenance and Disposal (C_{dh})

It is assumed that the maintenance costs C_{mt} dollars for every h_{mt} machine hours and disposal work costs C_{dp} dollars for every h_{dp} machine hours. Therefore, the hourly cost of maintenance and disposal is calculated by:

$$C_{dh} = \frac{C_{mt}}{h_{mt}} + \frac{C_{dp}}{h_{dp}} \quad (\$ \text{ per hour}) \quad (15)$$

By combining all of these cost components, the total hourly cost (C_h) for operating an abrasive waterjet cutting system is:

$$C_h = C_{mh} + C_{lh} + C_{th} + C_{ph} + C_{dh} \quad (\$ \text{ per hour}) \quad (16)$$

The cost for cutting unit length of workpiece (C_l) can be determined by:

$$C_l = \frac{C_h}{u} = C_h \left(\frac{Cq h D^{0.618}}{N_m P_w^{1.25} \dot{m}_w^{0.687} \dot{m}^{0.343}} \right)^{1.15} \quad (\$ \text{ per unit length}) \quad (17)$$

Here is an example:

A turnkey two- or three-axis NC-controlled AWJ shapecutting system with a 60 hp intensifier pump is estimated to cost \$ 200,000. Its service life is assumed to be 5 years with 2088 work hours per year (one shift). If a rate-of-return of 15% is applied, the machine hourly cost can be calculated with Equation (10) to be \$ 28.57. It is assumed that the annual salary of the operator is \$ 25,000, the fringe benefit is 20% and the supervision is 30% of the salary. Therefore, the labor hourly cost is calculated to be \$ 17.96. The costs for abrasive and water are assumed to be \$ 0.66 per kg and \$ 0.005 per litre, respectively. The abrasive and water flow rates are assumed to be 7.56 g/s and 3.32 lpm, respectively. A composite WC nozzle costs \$ 200 and lasts approximately 50 hours. A sapphire orifice costs \$ 25 and lasts about 100 hours. Considering a downtime rate of 10%, the total hourly cost for materials is \$ 20.89. Assuming that power costs \$ 0.09 per kwh, a 60 hp (44.7 kwh) system yields an hourly cost of \$ 3.62. It is assumed that maintenance costs \$1/h and disposal \$.5/h. Therefore, the total hourly cost obtained is \$ 72.54.

For a workpiece of 25.4 mm (1") thick stainless steel plate ($N_m = 82$) and the parameter settings of water pressure 242 mpa (35 kpsi), water flow rate 3.32 lpm (0.877 gpm) (i.e. orifice diameter 0.381 mm(0.015")), nozzle diameter 1.016 mm(0.040") and abrasive (garnet) flow rate 7.56 g/s(1 lb/min), and a quality level of 3 is expected, the cutting speed is predicted to be 0.474 mm/s(1.12 inch/min). The estimated cost for cutting this workpiece will be \$ 0.43 per cm (\$ 1.08 per inch).

4. CONCLUSIONS

A method for AWJ kerf cutting parameter prediction was described. The use of this method makes the cutting speed prediction more realistic. Application of the predicted cutting speed in the cost analysis formulation leads to cost prediction.

REFERENCES

Bitter, J.G.A., "A Study of Erosion Phenomena --- Part I," *Wear*, Vol. 6, pp. 5-21, 1963a.

Bitter, J.G.A., "A Study of Erosion Phenomena --- Part II," *Wear*, Vol. 6, pp. 169-190, 1963b.

Finnie, I., "The Mechanism of Erosion of Ductile Metals," *Proceedings of the 3rd National Congress of Applied Mechanics*, pp. 527-532, ASME, 1958.

Finnie, I. and McFadden, D.H., "On the Velocity Dependence of the Erosion of Ductile Metals by Solid Particles at Low Angles of Incidence," *Wear*, Vol. 48, pp. 181-190, 1978.

Groover, Mikell P., *Automation, Production Systems, and Computer-Aided Manufacturing*, Prentice-Hall, Englewood Cliffs, New Jersey, 1980.

Hashish, M., "On the Modeling of Abrasive Waterjet Cutting," *Proceedings of the 7th International Symposium on Jet Cutting Technology*, Paper E1, 1984.

Hashish, M., "Aspects of Abrasive-Waterjet (AWJ) Performance Optimization," *Proceedings of the 8th International Symposium on Jet Cutting Technology*, pp. 297-308, BHRA, Durham, England, 1986.

Hashish, M., "An Improved Model of Erosion by Solid Particle Impact," *Proceedings of the 7th International Conference on Erosion by Liquid and Solid Impact*, Cambridge, UK, Paper 66, 1987.

Hashish, M., "Visualization of the Abrasive-Waterjet Cutting Process," *Experimental Mechanics*, June, pp. 159-169, 1988.

Hashish, M., "A Model for Abrasive-Waterjet(AWJ) Machining," *Journal of Engineering Materials and Technology*, Vol. 111, pp 154-162, 1989.

Hashish, M., "Cutting with High-Pressure Abrasive Suspension Jets," *Proceedings of the 6th American Water Jet Conference*, pp. 439-455, Houston, August 24-27, 1991.

Zeng, J., Heines, R., and Kim, T.J., "Characterization of Energy Dissipation Phenomenon in abrasive waterjet cutting," *Proceedings of the 6th American Water Jet Conference*, pp. 163-177, Houston, U.S.A., 1991.

Zeng, J. and Kim, T.J., "An Elasto-Plastic Model of Brittle Material Removal in Abrasive Waterjet Cutting Processes," submitted for publication in *Journal of Engineering Materials and Technology*, 1992a.

Zeng, J. and Kim, T. J., "Development of an Abrasive Waterjet Kerf Cutting Model for Brittle Materials". *Proceedings of the 11th International Conference on Jet Cutting Technology*, pp. 483-501, St. Andrews, Scotland, 1992b.

Zeng, J., Kim, T. J., and Wallace, R. J., "Quantitative Evaluation of Machinability in Abrasive Waterjet Machining". *Proceedings of the Winter Annual Meeting of ASME ---- Precision Machining: Technology and Machine Development and Improvement*, PED-Vol. 58, pp. 169-179, Anaheim, 1992.

NOMENCLATURE

a	grain size		
C	scale factor		
C_a	abrasive costs (\$/lb)		
C_{dh}	hourly cost of maintenance and disposal		
C_{dp}	disposal work cost for every h_{dp} machine hours		
C_e	coefficient of impact efficiency		
C_h	total hourly cost for operating an abrasive waterjet cutting system		
C_l	cost for cutting unit length of workpiece		
C_{lh}	labor hourly cost		
C_m	capital investment in an abrasive waterjet cutting system		
C_{mh}	machine hourly cost		
C_{mt}	maintenance cost for every h_{mt} machine hours		
C_{my}	annual machine cost		
C_n	abrasive waterjet nozzle cost		
C_o	orifice cost		
C_p	electric power cost		
C_{ph}	power hourly cost		
C_{th}	hourly cost of consumable materials		
C_v	orifice efficiency		
C_y	compressibility coefficient		
C_w	cost of water		
D	focusing nozzle diameter		
E	elastic modulus of target material.		
F_y	fringe benefit of the operator		
f_w	fraction of effective stress wave energy		
h	depth of cut		
h_{dp}	machine hours between disposal		
			services
		h_{mt}	machine hours between maintenance services
		h_y	work hour per year
		i	rate of return (%)
		L_n	nozzle service life
		L_o	orifice service life
		m	mass of an abrasive particle
		\dot{m}	mass abrasive flow rate
		\dot{m}_w	water flow rate
		n	service life (the number of years) of an abrasive waterjet cutting system
		$n_0, n_1, n_2, n_3, n_4, n_5$	regression coefficients
		N_m	'Machinability Number'
		O_y	annual salary of operator
		P	power of machine
		P_w	water pressure
		q	quality level parameter
		R	abrasive/water mass flow ratio
		R_e	'Erosion Resistance'
		S_y	supervision cost
		T_d	machine downtime rate (%)
		u	traverse speed
		V	volume removal by a single abrasive particle
		α	impact angle
		β	a function of Poisson's Ratio of the target material
		γ	fracture energy
		η	momentum transfer efficiency
		θ_c	critical jet exit angle
		ρ_w	water density
		σ_f	flow stress of workpiece material

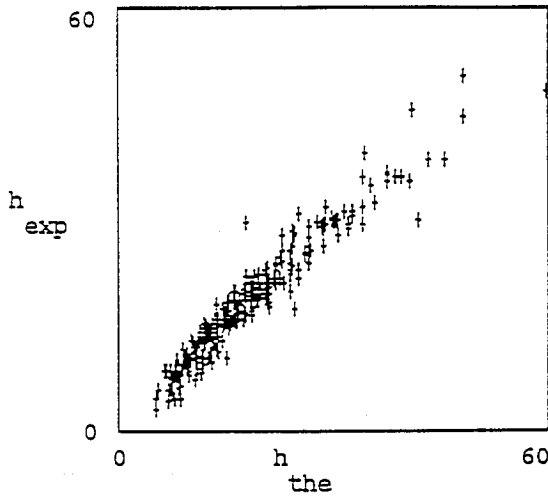


Figure 1 Correlation between the predicted depth of cut from the empirical model and the measured values from experiments.
 (h_{exp} --- measured depth of cut; h_{the} --- predicted depth of cut)

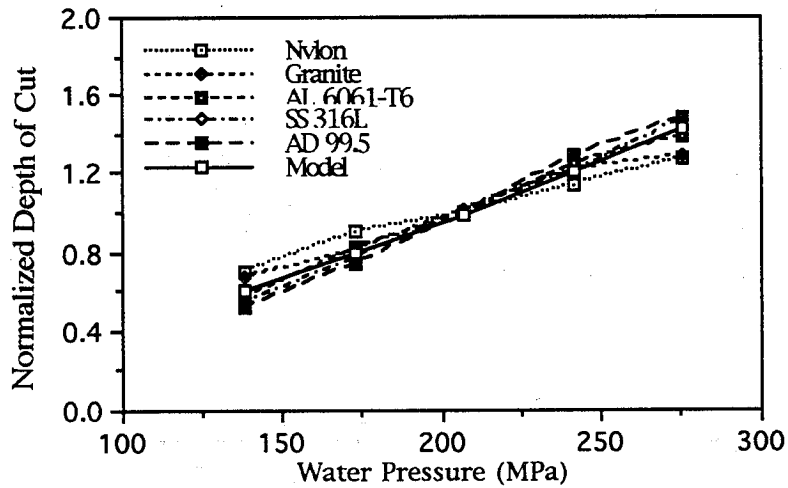


Figure 2 Normalized depth of cut verse water pressure for different target materials

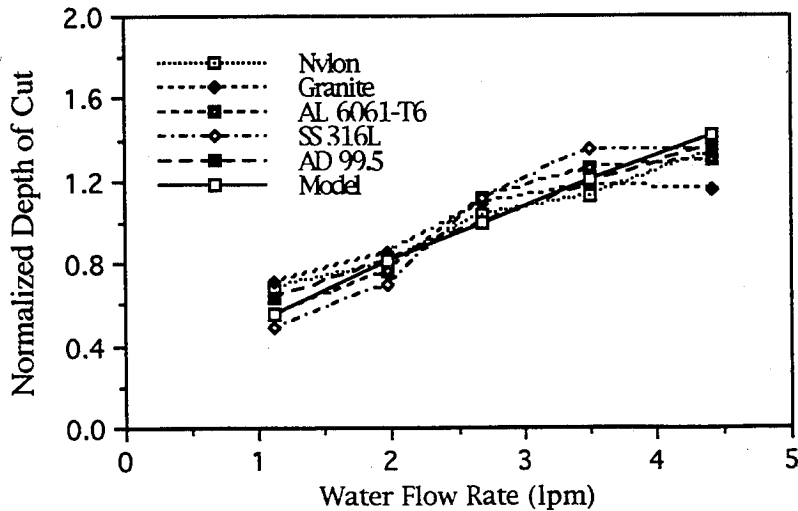


Figure 3 Normalized depth of cut verse water flow rate for different target materials

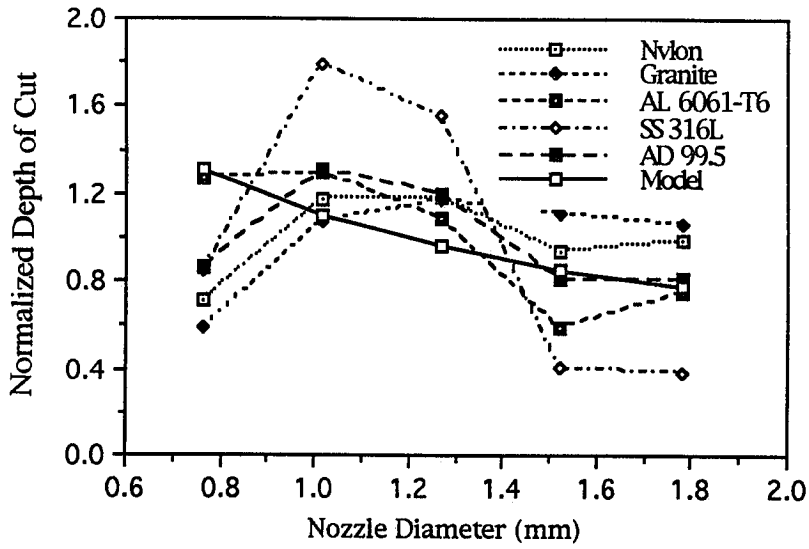


Figure 4 Normalized depth of cut versus nozzle diameter for different target materials

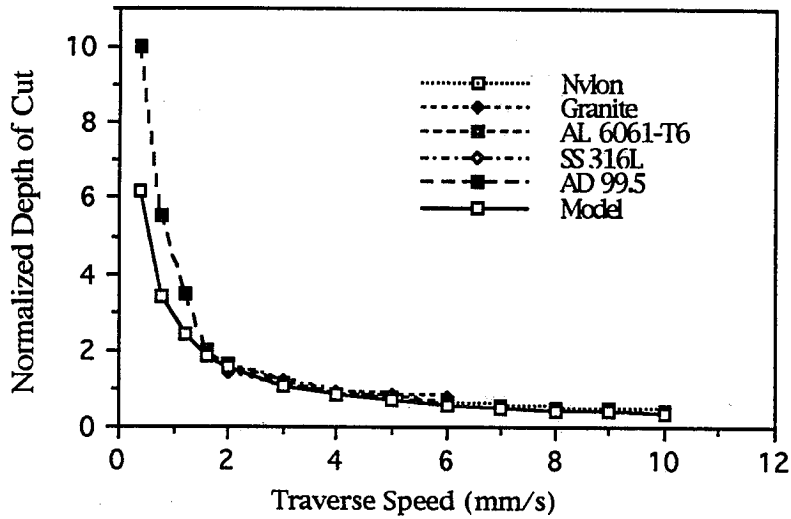


Figure 5 Normalized depth of cut versus traverse speed for different target materials

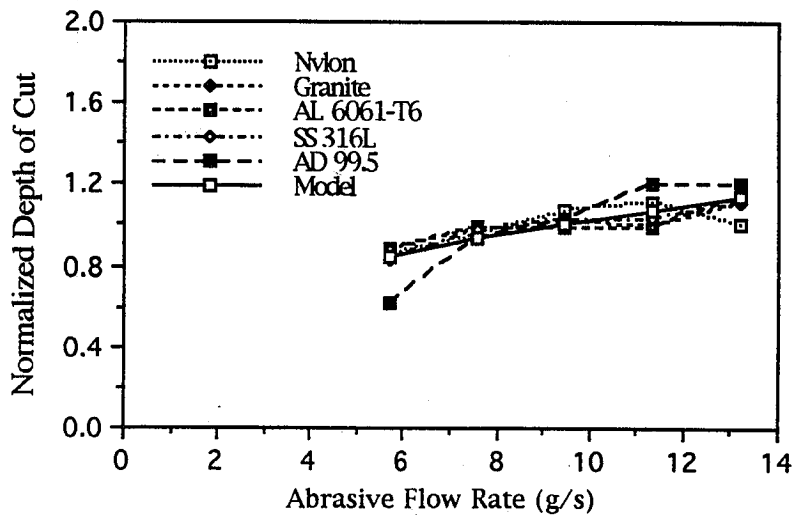


Figure 6 Normalized depth of cut versus abrasive flow rate for different target materials

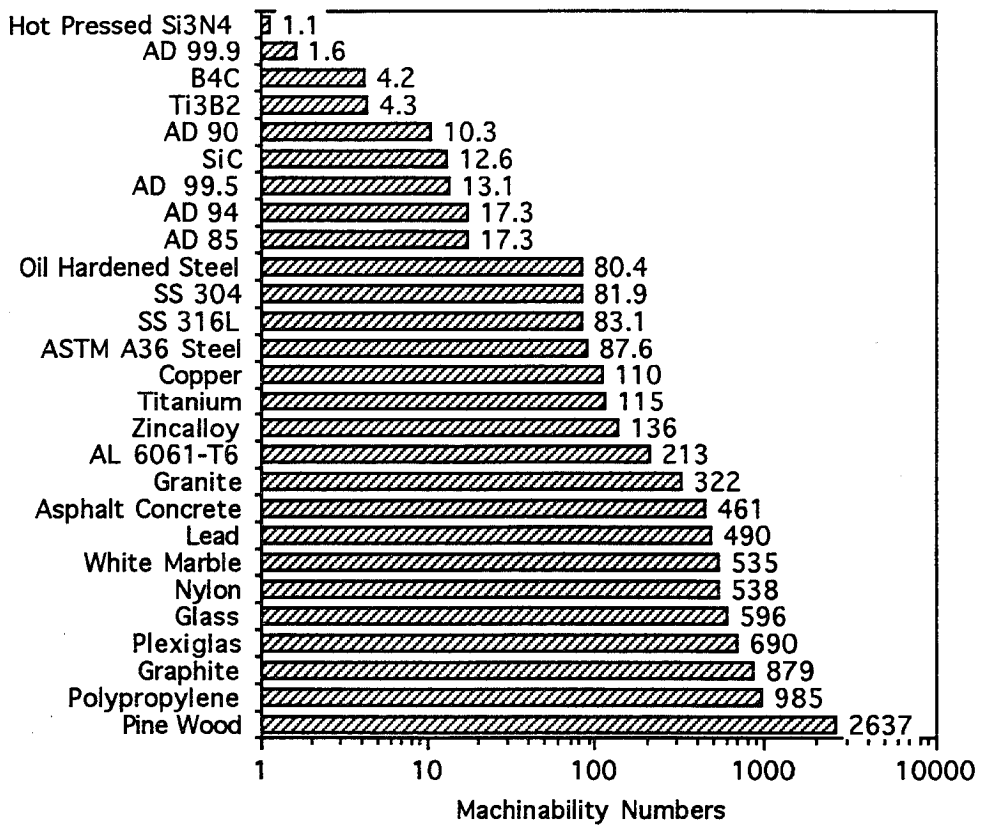


Figure 7 Machinability numbers of various engineering materials.

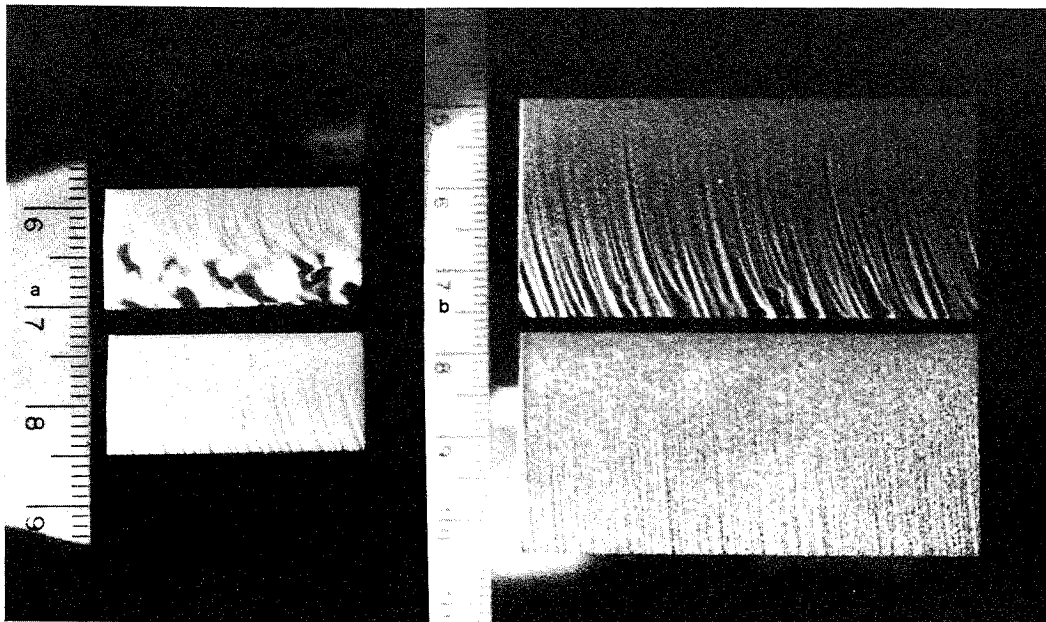


Figure 8 Cut surfaces of (a) AD 94 (left) and (b) steel (right) plates.

COST OPTIMIZATION OF ABRASIVE WATERJET CUTTING SYSTEMS

Pawan J. Singh and Jose Munoz
Ingersoll-Rand Waterjet Cutting Systems
23629 Industrial Park Drive
Farmington Hills, MI 48335, USA

ABSTRACT

The paper enumerates several types of costs involved in the operation of a waterjet system. Since many operation parameters are involved in waterjet cutting, selection of an optimum set of parameters offers opportunity for significant cost savings. The paper relates costs to operation parameters and shows that seemingly complex optimization problem can be simplified to a single parameter function through local optimization. Through an example, it is shown cost optimization can save anywhere from 10 to 30% in total operating costs. The paper also presents a cost computation model that can be applied to any waterjet system and virtually any material to be cut.

1. INTRODUCTION

As waterjet cutting has progressed from a novel, enabling technology to an established, practical process, its future depends on its economics relative to other traditional and non-traditional cutting processes. Unfortunately, good economic analysis of the process has been lacking since such analysis is neither simple nor straight forward. In some applications, the economics of waterjet cutting is so superior as not to even merit a detailed analysis. An example of such application is abrasive waterjet cutting of titanium parts for the aircraft industry. However, waterjet has already been employed in many of such clearly superior applications. For the growth of waterjet cutting to continue, the equipment sellers will have to demonstrate the process's economic superiority over competing processes. Fortunately, waterjet cutting does offer economic advantages in many cases and a clear economic analysis can be beneficial to both the buyers and sellers of the equipment.

Three factors make economic analysis of the waterjet cutting process somewhat difficult: a) same cutting results can be achieved by many different combinations of cutting parameters; b) the process's flexibility, its ability to cut different profiles without hardware changes, is hard to value in most cases; c) different customers have different objectives and they may value various attributes differently. Thus, a good economic analysis model should account for these three factors.

A simple cost analysis that computes various costs of system operation is relatively straight forward and has been outlined by Zeng and Kim (1993), among others. This kind of analysis avoids the issue of optimization except on an ad-hoc basis. The optimization, whether reflected in the demand for cost minimization or maximum throughput, presents a potential for significant savings over the cutting system's life. It also helps determine the system configuration, operation parameters, and mode of operation. However, several requirements as follows must be met for meaningful optimization:

- Optimization objective must be defined clearly. A typical objective may be to cut a well-defined production load with a defined quality of cut. The quality is usually defined by maximum roughness of the cut surface and by limits on dimensional tolerance. For fibrous materials, another criterion may be the absence of fiber separation.
- Limiting conditions must be defined. Such conditions may include a limit on number of work shifts, a limit on initial investment and a limit on the range of materials to be cut.
- Since the system may not be able to meet the demand either due to a breakdown or for several other reasons, an opportunity cost for such failures must be defined. In many cases, the opportunity cost may become the dominant criterion in selection or definition of the system.

- Costs are defined in various ways by various businesses. Engineers, for example, want to focus on operating costs; accountants want to address burdened costs; and business managers want to know after-tax costs that can be translated into net cash flow for making business decisions. Without a proper definition of cost, cost optimization would be meaningless.

This paper addresses all of the above issues and presents a blueprint for conducting economic analysis for individual transactions. Based on typical component and investment costs, the paper, through case studies, provides relative magnitude of various costs and shows how these computations can be used to optimize investment decisions. While the concepts presented here can be applied both to water and abrasive waterjet cutting, we will focus on the latter.

2. COST ANALYSIS - TWO PERSPECTIVES

Cost analysis and cost optimization are often interpreted differently by various organizations and sometimes differently by individuals in the same organization. This is why different companies may claim their products as offering the best cost performance for the same application although their operating costs and equipment prices may be quite different.

We here take two perspectives of cost analysis: first, an accounting perspective, according to which costs are defined by standard cost accounting policies and often known as burdened costs; second, a business economics perspective, in which the focus is on return on investment. The two views, although not mutually exclusive, play differently in practice. Particularly, the business perspective accounts for alternative investments, tax policies, opportunity costs and in its most refined versions for flexibility. While flexibility is the hardest to evaluate in hard numbers, it is also sometimes the most important benefit of investment in flexible automation equipment like waterjet. Other potentially large benefits of waterjet system are material savings, reduced secondary processing and improved environment.

3. COST COMPUTATION AND OPTIMIZATION: ACCOUNTING PERSPECTIVE

Here, costs can be divided in three main components:

- Operating costs
- Labor costs including burden
- Capital costs reflected by depreciation or amortization

Each of these costs can be controlled through efficient operation and investment, although we would assume that the labor cost rate is a reflection of the local labor market conditions and is unaffected by the investment decisions. The costs are

computed for a complete waterjet system that includes three main components: intensifier, cutting nozzle system including abrasive delivery system if applicable, and motion control system.

Several benchmarks can be used to compare costs across various investment decisions. Examples include total cost per hour of operation, total annual cost of operation and cost per unit of production. The most meaningful cost benchmark for waterjet cutting is cost per centimeter of cut (CPCC), since it incorporates cutting characteristics of the waterjet system. The cutting speed depends on the type of material to be cut and several system parameters. For example, the cutting speed can be enhanced by using larger diameter nozzle and the use of more abrasive. However, with the increase in cutting speed, operating costs and even investment costs are likely to increase, often disproportionately.

3.1 Operating Costs

Operating costs can be classified as:

Cost of power:	C_p
Cost of cutting water:	C_w
Cost of cooling water:	C_{cw}
Cost of abrasive:	C_a
Cost of focusing tube:	C_f
Cost of nozzle assembly:	C_n
Cost of maintenance:	C_m

These costs, based on per hour of operation, can be related to system parameters such as system pressure (P) and nozzle diameter (d_n). In particular:

$$Q = 1.479 d_n^2 P^{0.5} \quad (1)$$

$$KW = 0.0455 d_n^2 P^{1.5} \quad (2)$$

where Q is cutting water flow rate in l/m and KW is intensifier power input in kilowatts. The units of P and d_n are MPa and mm respectively. Equations (1) and (2) include estimates for hydraulic and motor efficiencies.

The selection of nozzle size plays a key role in the selection of other parameters. First, it has an influence on the intensifier specifications that must satisfy equations (1) and (2). Second, abrasive flow rate, focusing tube size and maintenance costs are greatly influenced by the nozzle diameter.

We can compute various operating costs as follows.

$$C_p = c_p \text{ KW} \quad (3)$$

$$C_w = 60 c_w (Q + Q_{cw}); Q_{cw} = K_{cw} \text{ KW}; K_{cw} = 0.19 \text{ to } 0.30 \quad (4)$$

$$C_a = 60 c_a m_a \quad ; m_a = K_a Q; K_a = 0.13 \text{ to } 0.20 \quad (5)$$

$$C_f = c_f / L_f \quad ; L_f = L_{f,ref} / K_a^{0.25}; L_{f,ref} = 80 - 120 \text{ hours} \quad (6)$$

$$C_n = c_n / L_n \quad ; L_n = 40 \text{ to } 100 \text{ hours for sapphire nozzle,} \quad (7)$$

500 to 1000 hours for diamond nozzle

$$C_{m,i} = \sum_i c_{m,i} / L_{m,i}; L_{m,i} = L_{m,i,ref} Q_{ref} / Q \quad (8)$$

In the above equations, c_p , c_w , c_a , c_f , c_n , $c_{m,i}$ are cost of power (\$/kwh), cost of water including disposal costs (\$/liter), cost of abrasive including disposal costs (\$/kg), cost of focusing tube (\$), cost of nozzle (\$) and cost of maintenance including labor costs for the i th item, i standing for a counter for the various replacement parts and maintenance services (\$), respectively. m_a is abrasive flow rate in kg/min. L_f , L_n , $L_{m,i}$ are lives in operating hours of focusing tube, nozzle and i th maintenance item, respectively. The subscript ref in Equation 8 stands for a reference value for which the maintenance costs $c_{m,i}$ are specified. Equations (3) to (8) express relationships among unit costs and cost per hour of operation. The specified range of coefficients K_a , K_{cw} , $L_{f,ref}$ and L_n is based on experience. In the absence of prior experience, an average of the range limits can be used for economic assessment.

3.2 Labor Costs

This may seem to be the easiest cost to quantify but the wages and benefits are only one component of the burdened labor cost. Traditional cost accounting has lumped all manufacturing costs except materials in one pool and then distributed these costs in proportion to the total labor hours as a so-called burden. This practice may have had relevance in pre-automation era when the labor costs constituted a significant portion of the total costs. However, now, in most large-scale manufacturing processes, labor costs constitute less than 10% of the total costs. Cost accountants recommend using the new activity-based accounting for automated processes in which the costs for a particular process account for only the activities necessary for that process. Despite some shift to this new approach, cost burdening still remains the most popular form of cost accounting in the manufacturing industry.

$$C_l = c_l (1+k_l) (1+b_l) \quad (9)$$

where C_l is cost of labor per hour of operation, c_l is cost of wages per hour of labor for all employees working on the system, b_l is the fractional burden rate and k_l is the amount of average idle system time per hour of operation for any reason. Such reasons

may include maintenance, start up, material loading and unloading and recreational time breaks. We recommend that burden costs, b_j , include the costs of those activities directly attributable to the waterjet system. Burden costs should not include capital investment costs in the form of depreciation or lease costs.

3.3 Capital Investment Costs

Capital investment cost includes waterjet system cost, installation cost, cost of tooling and recommended on-hand spare parts, and start-up costs. The capital cost should be amortized over the expected life of the equipment or the related project at the current finance rate (not expected rate of return on investment). The project life should be used for amortization when no other use of the equipment can be seen at this time. In all cases, the salvage value of the equipment at the end of amortized life, R , should be used. If the equipment is leased, lease costs should be used. Since the capital costs should be amortized continuously, it is preferable to use monthly amortization. In the following equation, n is the number of months and i is the monthly interest rate (annual rate/12).

$$c_e = (P_s - R/k^n) (k^{n-1} i / (k^n - 1)); k = 1 + i \quad (10)$$

$$C_e = c_e / L_e; L_e = N_e k_e$$

where c_e , C_e are the amortized cost per month and the capitalized cost of equipment per hour of operation, respectively, L_e is the average number of hours the equipment is in operation per month, N_e is the number of hours the equipment is available and k_e is the fraction of the available time the equipment is in operation.

3.4 Total Cost

The above costs can be added to give cost per hour of operation, as follows:

$$C_o = C_p + C_w + C_a + C_f + C_n + C_m + C_l + C_e \quad (11)$$

While these costs may provide an estimate of operating costs before the system purchase or provide accounting costs after the purchase for cost monitoring or job pricing, the key cost function, as mentioned earlier, is the cost of material cut per unit cm (CCPC). To determine CCPC, one must know the cutting speed which is hard to determine without experiments. Fortunately, after years of research and experimentation, several researchers have come up with theoretical or regression-based relationships that can be used to give reasonable estimates of cutting speeds for various materials and operating conditions. A caveat: these relationships should be carefully used within the recommended parameter range, and do not expect average accuracy of less than 20%. However, that is much improvement over other alternatives of extrapolation and guesstimates. Most manufacturers have built large data bases of

materials and cutting speeds but the data still covers discrete points in a multidimensional parameter space whose complete coverage is economically unfeasible. The best solution is to make sure that the mathematical relationship is consistent with test data within a certain accuracy range.

4. CUTTING SPEED COMPUTATION

Several researchers, among them Hashish (1989), Matsui et al (1991), Bickwedel (1990), have presented models for the cut depth or cutting speed prediction. We follow the model of Zeng and Kim (1993) which is based on the modeling of cutting process to formulate a dimensional relationship and the use of test data regression to determine power constants in the relationship.

$$u = \frac{(N P^{1.25} Q^{0.687} m_a^{0.343})^{1.15}}{(K q H d_f^{0.618})^{1.15}} \quad (12)$$

where u = cutting speed (mm/sec)
 d_f = focusing tube diameter (mm)
 H = workpiece thickness (mm)
 q = Quality level
 N = Machinability number of workpiece material
 K = 3352

The quality level is an empirical index, defined as follows: $q = 1$ for separation cut (material separates but the surface is very rough), $q = 2$ for rough surface finish (maximum surface roughness > 350 microinch; typically, striations over more than half the thickness), $q = 3$ for striation-free surface; $q = 5$ for best-possible finish. Surface finish in waterjet cutting depends on several factors and can vary widely (see Singh et al (1991)). Machinability number, N , is another empirical index derived by Zeng and Kim (1993) from extensive testing. The machinability number reflects the material's resistance to separation and is a function of material properties such as hardness and fracture resistance. Values of N for some common materials are as follows:

M2 Tool Steel:	72
SS 304 HRAP:	86
Ti-6Al-4V:	98
C10100 CR Cu:	110
Al 6061-T6:	218
Glass:	339
Carnico Marble:	413
Plexiglass:	486

Some of these machinability numbers have been updated since Zeng and Kim's study and are based on latest data. For materials not listed here, a user can determine the machinability number from Equation (12) by running at least three tests and averaging the computed values. Estimated standard error over the whole spectrum of materials is 12%. For relative comparisons, the error is significantly lower.

Equation (12) is valid in a wide range of parameters as long as the value of these parameters stays within the realm of normally acceptable operation. For example, cutting speed always increases with the abrasive flow rate in (12); however, in practice, beyond a certain flow rate, the abrasive-jet mixture begins to get over saturated, resulting in reduced cutting speed. One would not want to operate the system in this over saturated range anyhow. The recommended range of validity for (12) is as follows: Pressure: 240 to 375 MPa; $d_n = 0.18$ to 0.45 mm; $d_f/d_n = 2.5$ to 4.5 ; $m_a/\rho Q = 0.12$ to 0.25 , where ρ is water density in kg/l.

The true measure of system efficiency, cost per cm of cut, is given by:

$$CCPC = 10 C_o / (60 u k_{cf})$$

where k_{cf} is the contour factor which accounts for the necessary slow down of the system during turns. k_{cf} is defined as the ratio of time to make a contoured cut to the time required to make a cut of the same length as the circumference of the contoured cut. Since virtually all of the waterjet cuts are contoured cuts, k_{cf} is an important factor in cost evaluation.

5. SYSTEM OPTIMIZATION

We consider optimization here as a problem of cost minimization for a specified production run, with a specified cut quality. Two issues arise here: production capacity and operating costs. While these two issues may seem unrelated, they are, in fact, closely intertwined. The cutting speed at which the cost is minimized may not be fast enough to make the production. On the other hand, the best way to minimize the cost may not be to increase the cutting speed but to increase system availability through overtime or another shift, or through adding another cutting head to the system, or through purchasing another system. These are not idle academic questions, since the cost of inefficient decisions can run into hundreds of thousands of dollars. In this section, we will attempt to provide some guidelines on the optimization of system operation and system capacity. We will do it through an example, using typical costs for various cost components.

The key parameter that controls cutting speed is nozzle diameter or indirectly the cutting water flow rate. The other two parameters that greatly influence the speed are system pressure and abrasive flow rate (for abrasive jet cutting). However, optimum values of these parameters are not totally independent. Optimum system pressure is a function of the material to be cut. Most metals are best cut in the 300 - 360 Mpa

pressure range and most brittle materials are cut in the 275 - 310 MPa range. Optimum abrasive flow rate can be related to cutting water flow rate, as indicated earlier. Even the maintenance and capital equipment costs can be related to nozzle diameter. With a larger nozzle, the flow rate increases and the intensifier cycles faster to meet the demand. The life of major maintenance items in the intensifier such as seals, check valves and filters is or should be measured in number of cycles, not hours. Also, with a larger nozzle, the intensifier HP increases as a square of the nozzle diameter.

Local suboptimization of various variables, as indicated above, then simplifies the global optimization problem by reducing the number of true variables to only one, nozzle diameter. When considering a total system, a few other variables such as the number of nozzles on one cutting head or the number of independent heads in one system also need to be considered. However, these variables mainly affect the production capacity constraints and can be easily handled within the problem's scope.

In our cost minimization example, we will treat nozzle diameter as a discrete variable, select recommended values of other parameters based on the nozzle diameter, and use representative cost values to develop a cost model for cutting one inch thick stainless steel. This model will then be used to make some general observations on the system operation. The selected values are as follows:

$$d_n = 0.254, 0.279, 0.305, 0.330, 0.356 \text{ mm}$$

$$d_f = 0.76 \text{ mm if } d_n = 0.254 \\ = 1.09 \text{ mm if } d_n > 0.254; \text{ these values are based on commercially available sizes.}$$

$$m_a = 0.34 \text{ Kg if } d_n < 0.254 \\ = 0.34 (d_n/0.254)^2 \text{ Kg if } d_n > 0.254$$

$$c_p = 0.08 \text{ \$/kwh; } c_w = 0.004 \text{ \$/l; } c_a = 0.77 \text{ \$/Kg}$$

$$c_f = 235 \text{ \$; } L_f = 100 \text{ hr; } C_f = c_f / L_f$$

$$c_n = 550 \text{ \$ if } d_n < 0.254 ; \quad L_n = 500 \text{ hr; } C_n = 1.1 \text{ \$/hr} \\ = 800 \text{ \$ if } d_n > 0.254; \quad L_n = 500 \text{ hr; } C_n = 1.6 \text{ \$/hr}$$

$$C_m = 1.1 (d_n/0.254)^2 \text{ \$/hr}$$

$$c_e = 135,000 \text{ \$ if } d_n \leq 0.279 \\ = 170,000 \text{ \$ if } d_n > 0.279; \text{ the additional cost reflects the cost of another intensifier.}$$

$$R = 0.2 c_e; \quad i = 0.0833; \quad n = 60$$

The above costs are typical or national average costs and reflect current market conditions. The focus here is on optimization relative to system operation parameters. The optimization is not significantly influenced by small variations in absolute costs. The maintenance costs are composed of intensifier and system maintenance, including labor costs incurred during maintenance.

We apply the above cost model to two case studies: a) cutting of 25.4 mm thick Ti-6Al-4Vd with a striation-free cut surface ($q=3$) and minor contouring ($k_{cf}=0.9$). This might be an application for cutting large titanium parts for aircraft industry. b) cutting of 12.7 mm thick glass with slightly rough finish ($q=2$) and significant contouring ($k_{cf}=0.7$).

6. RESULTS AND DISCUSSION

Table 1 shows total operating costs per hour and cost per cm of cut for five nozzle diameters varying from 0.254 to 0.356 mm. In addition, for each material, two cases, one with one cutting nozzle and the other with two cutting nozzles, are considered. The number of cutting nozzle assemblies mounted on a single head is a significant parameter since it allows double the production capacity without any increase in labor and capital amortization costs, with some limitations. The main limitation is that both assemblies must be cutting identical parts which is not a significant limitation in production environment where multiple parts need to be cut. Furthermore, when only one part needs to be cut, one or more of the assemblies can be turned off and the rest of the assemblies can be fitted with larger nozzles appropriate to the optimum configuration. The other limitation is the flow capacity of the intensifier. However, within the capacity of a given intensifier, several options are possible. For example, with an intensifier rated at 37.5 kw, one can use two 0.254 mm diameter nozzles, one 0.356 mm diameter nozzle, or any other combination such that the sum of the square of the nozzle diameters is less than 0.13 mm^2 . It is also possible to use independently controlled multiple heads but the choice adds significantly to complexity and cost of such systems, and the benefits are negated to much extent by the additional cost. Within the constraints of intensifier capacity and system design and stability, there is no limit to the number of nozzles that can be mounted on one head.

Figure 1 shows the cost of cut per cm for cutting 25.4 mm thick titanium as a function of diameter nozzle. The cost goes down with the diameter except for 0.279 mm diameter nozzle. This anomaly is caused by our violation of suboptimization condition and a reflection of commercial reality. The long life focusing tube is available in discrete sizes and we have used the appropriate next available size. Ignoring this one data point, larger nozzles produce higher cutting speed. While the operating costs go up in near proportion to the flow, the labor costs and capital amortization costs per hour remain virtually fixed. In the present example, we have assumed the burdened labor costs, including idle time costs, to be \$36/hour. Combined with \$20-25/hour capital amortization cost, the operating costs are only about 30% of the total costs. Thus, it is more economical to use larger nozzle when using only one cutting nozzle

assembly. The use of larger nozzle does require additional initial capital investment. Significantly, the cost difference between the best selection and the worst selection is over 25%.

Looking at Table 1, the optimum choice, with the intensifier power rating limited to 37 kw, is to use two smaller nozzles and achieve 10% further cost reduction when both nozzles can be effectively used. The capital investment costs are about the same in both cases. In this analysis, we have accounted for additional cost of wear components, maintenance and material loading time with the use of multiple nozzles. Multiple cutting nozzles of smaller diameter offer a better choice in cutting efficiency, cost effectiveness and flexibility. For metals, our experience is that smaller nozzles produce better quality cut surface. This improvement needs to be quantified and is an area of future research.

Figure 2 shows the relationship between cutting speed and nozzle diameter for cutting 12.7 mm thick glass, using one cutting nozzle. Cutting of glass and the associated cost structure follow exactly the same pattern as discussed above for titanium. Table 1 provides details of various costs and cutting speeds for one and two nozzle cases. It is significant that the cost per cm of contour cutting 12.7 mm thick glass can be as little as 2 cents.

While we have shown results of only one and two nozzle systems, same trend will be observed with the use of even more nozzles.

7. CONCLUSIONS

Significant cost savings are available to the waterjet system users through optimization of system configuration and operation parameters. In particular:

- At first sight, cost optimization problem seems hopelessly complex, since the number of parameters affecting cost structure is extremely large. However, by using local suboptimization, the problem can be greatly simplified. It is shown that optimization can be conducted with only one parameter, nozzle diameter.
- Smaller nozzles are more efficient in cutting, i.e., the length of material cut per unit of input power is higher with smaller nozzles. However, larger nozzles are more cost efficient since their use produces higher throughput which reduces labor, capital and total costs.
- Multiple head systems offer flexibility and lower overall operating costs, since by using smaller nozzles they combine the higher cutting efficiency of smaller nozzles with higher throughput of multiple heads. When cutting one-of-a-kind piece, larger nozzle on a single head can be used to maintain cost advantage. The flexibility in the use of single or multiple heads according to production demand almost always

lowers the total operating costs relative to single-head systems. The additional capital and operating costs with multiple heads are not significant.

- Waterjet cutting can be extremely cost competitive for cutting certain materials. For example, the cost of contour cutting of 12.7 mm thick glass is about 2 cents per cm.
- Careful cost analysis and cost optimization can save 10 to 30% of total cost of the waterjet system operation.

8. ACKNOWLEDGMENTS

The authors are grateful to the management of Ingersoll-Rand for the permission to publish this paper. They are particularly thankful to Jiyue Zeng for help in the preparation of this manuscript, for conducting tests on which some of the authors' recommendations rest and for reviewing this paper.

9. REFERENCES

Bickwedel, H., Guo, N. S., Haferkamp, H. and Louis, H., " Prediction of Abrasive Jet Cutting Performance and Quality," Proceedings of the 10th International Conference on Jet Cutting Technology, pp 163-179, Elsevier Science Publishers Ltd, 1990.

Hashish, M., " A Model for Abrasive Waterjet (AWJ) Machining," Journal of Engineering Materials and Technology, Vol. 111, pp 154-162, 1989.

Matsui, S., Matsumura, H., Ikemoto, Y., Kumon, Y. and Shimzu, H., " Prediction Equations for Depth of Cut Made by Abrasive Water Jet," Proceedings of the 6th American Waterjet Conference, pp 31-42, Water Jet Technology Association, St. Louis, Missouri, 1991.

Singh, P. J., Chen, W. L., and Munoz, J., "Comprehensive Evaluation of Abrasive Waterjet Cut Surface Quality," Proceedings of the 6th American Waterjet Conference, pp 139-162, Water Jet Technology Association, St. Louis, Missouri, 1991.

Zeng, J. and Kim, T. J., " Parameter Prediction and Cost Analysis in Abrasive Waterjet Cutting Operations," To be presented at the 7th American Water Jet Conference, Water Jet Technology Association, St. Louis, Missouri, 1993.

TABLE 1

Mat.	depth mm	No. of nozzles	Nozzle dia mm	Opr. Cost (\$)	Total cst (\$)	Contour Factor	cut speed cm/min	cost of cut/cm	Capital Inv.(K\$)	Input pwr kw
Ti	25.4	1	0.254	23.7	86.1	0.9	4.01	0.398	135	16.9
			0.279	28.4	91.8	0.9	3.89	0.437	135	20.5
			0.305	33.1	102.4	0.9	4.78	0.396	170	24.4
			0.330	38.2	108.5	0.9	5.78	0.347	170	28.6
			0.356	43.6	114.9	0.9	6.89	0.309	170	33.2
Ti	25.4	2	0.254	47.6	110.4	0.9	8.02	0.255	175	33.8
			0.279	57.1	120.4	0.9	7.79	0.286	175	41
			0.305	66.4	135.3	0.9	9.57	0.262	210	48.8
			0.330	76.6	146	0.9	11.56	0.234	210	57.2
			0.356	87.6	157.4	0.9	13.78	0.211	210	66.4
Glass	12.7	1	0.254	23.7	86.1	0.7	59.13	0.0347	135	16.9
			0.279	28.4	91.8	0.7	57.38	0.0381	135	20.5
			0.305	33.1	102.4	0.7	70.51	0.0346	170	24.4
			0.330	38.2	108.5	0.7	85.22	0.0303	170	28.6
			0.356	43.6	114.9	0.7	101.60	0.0269	170	33.2
Glass	12.7	2	0.254	47.6	110.4	0.7	118.26	0.0222	175	33.8
			0.279	57.1	120.4	0.7	114.76	0.0250	175	41
			0.305	66.4	135.3	0.7	141.02	0.0228	210	48.8
			0.330	76.6	146	0.7	170.43	0.0204	210	57.2
			0.356	87.6	157.4	0.7	203.20	0.0184	210	66.4

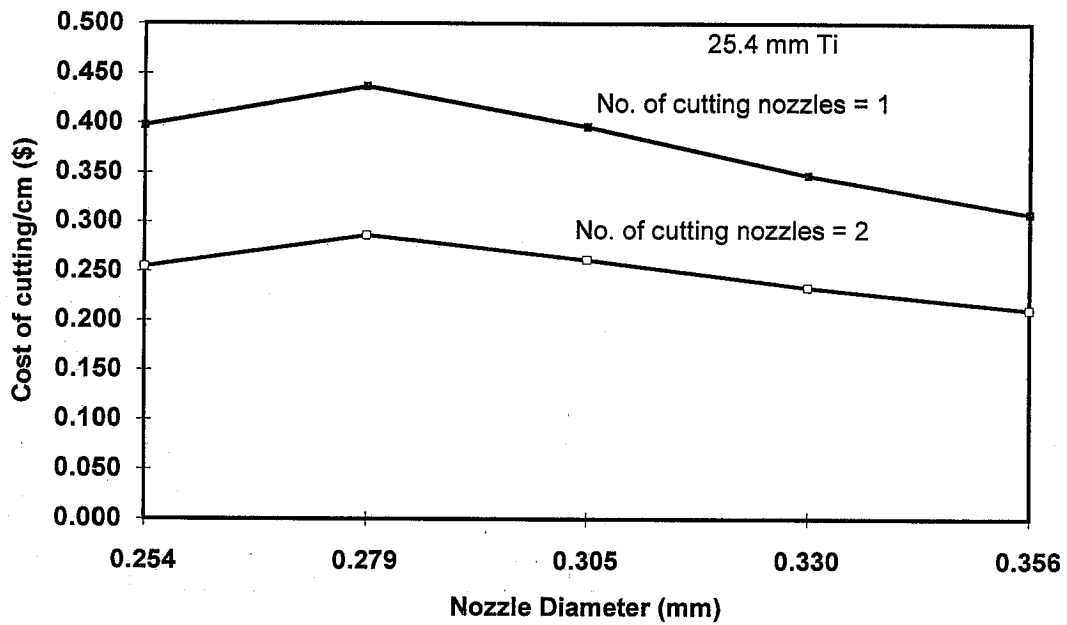


Figure 1: Cost of cutting 25.4 mm titanium as a function of nozzle diameter and number of cutting nozzles. Note that the power input with two cutting nozzles is double that for one cutting nozzle.

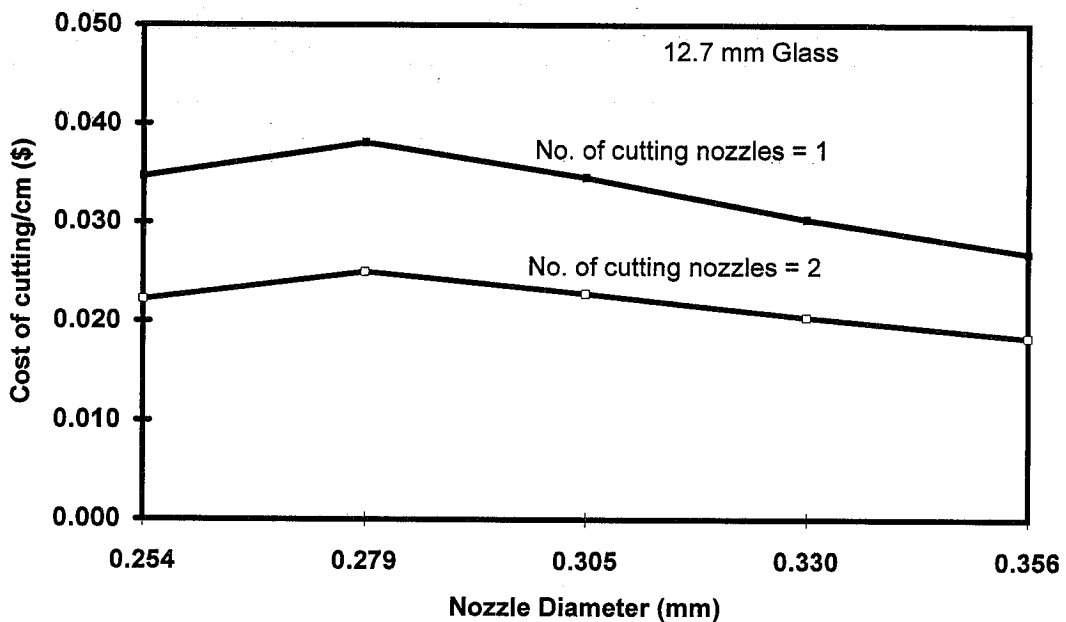


Figure 2: Cost of cutting 12.7 mm glass as a function of nozzle diameter and number of cutting nozzles.

PREDICTION MODELS FOR AWJ MACHINING OPERATIONS

Mohamed Hashish
QUEST Integrated, Inc.
Kent, Washington, U.S.A.

ABSTRACT

This paper presents physical models for cutting rate, surface waviness, milling, drilling, lathe slotting, and turning with abrasive-waterjets (AWJs). The similarities and differences among the different machining processes are illustrated using these prediction models. All the models are based on simple erosion theories. Examples and observations supporting model hypotheses are also presented. Areas for model improvement are recommended.

INTRODUCTION

The kinematic interaction of the abrasive-waterjet (AWJ) as a cutting beam with the workpiece material can result in several machining effects. Obvious examples include cutting, turning, milling, and drilling. Figure 1 shows a sequence of operations for the machining of a complex three-dimensional part by controlling the beam/workpiece manipulation parameters relative to each other. Table 1 shows more details on relevant process parameters for several machining operations. In all of these operations, whether the machined part is simple or complex, the dynamics of the material removal process is essentially the same. Dynamic control of the process parameters also adds flexibility to allow the production of even more complex geometries. For example, hole geometry can be altered significantly by dynamic manipulation of the jet pressure during piercing. Again, the dynamics of the process is still essentially the same.

The various machining operations result in different materials removal rates. These differences, which are largely used to classify the processes, could be caused by several factors. The most obvious such factor is the relative speed of the AWJ with respect to the workpiece. The effect of the return flow during piercing is another factor that quantitatively affects the dynamics of the process.

In this paper, we present several equations for cutting, milling, and turning that are based on a simple model developed by Finnie (1958) and Bitter (1963) and adapted by Hashish (1984) for AWJ cutting. The derivation of the models is not presented here, but references are provided. The goal of this paper is to provide the reader with a simple set of equations that can be used for quick analyses. Prior to presenting the machining equations, a general set of jet flow equations is presented.

GENERAL

In AWJs, an exchange of momentum occurs between the high-velocity waterjet mass flow rate (m_w) and the abrasive flow rate (m_a). The abrasive particle velocity (V_a) can be related to the waterjet velocity (V_j) as follows:

$$V_a = \eta \frac{V_j}{1 + (m_a/m_w)} \quad (1)$$

where η is a momentum transfer efficiency that was found to be around 80%.

The waterjet velocity and water flow rate can each be related to the pressure (P) by the simple Bernoulli equation:

$$V_j = C_v (2P/\rho_w)^{1/2} \quad (2)$$

$$m_w = C_d \frac{\pi}{4} d_n^2 (2P/\rho_w)^{1/2} \quad (3)$$

where ρ_w is the water density and C_v and C_d are, respectively, the velocity and discharge coefficients of the waterjet orifice, whose diameter is d_n . These coefficients are typically 0.98 and 0.7, respectively.

LINEAR CUTTING

To observe the interaction between the AWJ and the workpiece, high-speed movies were made of the jet/material interface during cutting in transparent material (Hashish, 1988). It was observed that a steady-

state interface exists at the top of the kerf to a depth h_c . Below h_c , a step(s) forms in the material and appears to move under the impact of the jet until it reaches the final depth (h). This step progression process is illustrated in Figure 2, which is a series of pictures of the jet/material interface. The kerf curvature at depth h_c changes suddenly, marking a transition from cutting wear mode to deformation wear mode (Hashish, 1988).

Figure 3 shows a schematic illustrating the different cutting zones. The zone up to depth h_c is referred to as the cutting wear zone, as termed by Bitter (1963) for shallow angle impact. In this zone, material removal occurs primarily by particle impacts at shallow angles. The step formation zone below h_c is termed the deformation wear zone, where impacts at large angles cause material removal. Another marked difference between these two zones of cutting is that cutting wear is a steady-state process in which the material removal rate equals the jet material displacement rate by traversal. When this condition terminates at depth h_c , the jet penetrates the material by removing a step at a decreasing rate as the depth increases.

Proceeding with simple mathematical derivation and based on Hashish's (1987) particle erosion model, Hashish (1989) expressed h_c as

$$h_c = \frac{cd_j}{2.5} \left(\frac{14m_a}{\pi u d_j^2 \rho_a} \right)^{2.5} \frac{V_a}{V_i} \quad (4)$$

where c represents the portion of the abrasives used for cutting. Inclusion of a threshold velocity below which all deformations are elastic, as in Bitter (1963), can be incorporated by replacing V_a with $(V_a - V_c)$ where V_c is the critical velocity. The intrinsic velocity (V_i) combines both particle and material characteristics and may be used as an erosion condition for erosion characterization. It is expressed as

$$V_i = \left(\frac{3\sigma_f R_f^3}{\rho_a} \right)^{1/2} \quad (5)$$

where R_f is a particle roundness factor defined by

$$R_f = \frac{d_c}{d_p} \quad (6)$$

The equation for deformation wear depth (h_d) was also derived by Hashish (1989) based on Bitter's (1963) equation for erosion by solid particle impact at large angles. This equation is

$$h_d = \frac{1}{\frac{\pi d_j \sigma_f}{2(1-c)m_a(V_a - V_c)} + \frac{C_f}{d_j} \frac{V_a}{V_a - V_c}} \quad (7)$$

Then, the total depth of cut (h) is the sum of h_c and h_d .

It should be noted that at high traverse rates no steady zone (h_c) will be established. In this case, all the cutting action will belong to the deformation wear zone, and its attributes will cover the entire cut surface. The critical rate at which this transition occurs is related to the critical angle (α_c) of erosion by particle impact. This angle can be considered a material characteristic whose dependence on other material properties is rather complex and is beyond the scope of discussion in this paper.

The critical traverse rate can be determined from

$$u_c = \frac{14m_a}{\pi\rho_a d_j^2} \left(\frac{\alpha_c V_a}{V_i} \right)^{2.5} \quad (8)$$

SURFACE WAVINESS

The hypothesis of the waviness model is that the jet/material interface is not steady. A step of material moves under the jet until it reaches the bottom of the sample at time t . During this time the jet traverses a distance x , as shown in Figure 4 where the AWJ moves from centerpoint A to B. The ridge C is observed as a striation (waviness mark) of depth R_w . The illustration in Figure 4 shows the geometry at the bottom of the cut; part of ridge C is removed due to the jet trailback and side deflections, which distort this ideal geometry. From Figure 4, we can write

$$\frac{2R_w}{d_j} = 1 - \left[1 - (x/d_j)^2 \right]^{1/2} \quad (9)$$

If we assume that all the material in the zone beyond h_c is removed through deformation wear at 90° impact angles, then we can use Bitter's (1963) equation to express the volume removal rate \dot{v} , which can also be expressed as

$$\dot{v} = \frac{\pi}{4} d_j^2 \frac{\partial h}{\partial t} \quad (10)$$

where d_j is the local AWJ diameter or cutting width at depth h , which will be assumed constant. The distance was derived based on the above as follows:

$$x = \frac{\pi \varepsilon d_j (h - h_c) u}{2 m_a V_a^2} \quad (11)$$

Using this value for x in Equation (9), the following equation is obtained:

$$\frac{2R_w}{d_j} = 1 - \left\{ 1 - (\pi/4)^2 \left[\frac{d_j (h - h_c) u}{0.5 m_a V_a^2 / \varepsilon} \right]^2 \right\}^{1/2} \quad (12)$$

This equation needs to be further developed to include kerf width variations as a function of depth of cut. Further discussion can be found in Hashish (1992).

MILLING

The milling process generally involves traversing the jet many times over the area to be milled. During a single "sweep" over an area, due to the width of the swath of the jet and the overlap at the edge of each swath, the jet may cut over some zones more than once. Because of the high traverse rates used in milling, no cutting wear mode will be encountered, and the depth of milling per pass can be determined from Equation (7). The depth of milling will vary along the direction of the cross feed due to this difference in

exposure time (or number of passes) resulting in "lay" on the surface. For a general case with a non-dimensional overlap number (O_n) the number of sweeps can be expressed mathematically as

$$N_p = \text{INT}(O_n) + 1 \quad (13)$$

Assuming that the standoff distance does not affect the depth of milling per pass, the average depth of milling per sweep is derived as

$$h_{av} = \frac{\text{INT}(O_n) + 1}{\frac{\pi d_j \sigma_f u}{2m_a(V_a - V_c)^2} + \frac{C_f V_a}{d_j V_a - V_c}} \quad (14)$$

The above equation can further be simplified by neglecting $V_c \ll V_j$ for soft materials and setting $C_f = 0$, as the depth of milling per pass is very small. The resulting simplified equation is

$$h_{av} = [\text{INT}(O_n) + 1] \frac{2m_a V_a^2}{\pi d_j \sigma_f u} \quad (15)$$

The cross-feed rate is implicitly expressed in the lateral feed increment in the above equation.

LATHE SLOTTING

The simplest case of turning is when no motion is imparted to the AWJ nozzle. Such interaction results in the formation of a circumferential groove around the workpiece periphery. This is termed a "lathe slotting" operation.

As the workpiece rotates under the cutting jet, the penetration results in a change in the radius (r) and the angle of impact (α). At any time, the impact angle is given by (see Figure 5)

$$\alpha = \cos^{-1}[(r_i - \delta)/r] \quad (16)$$

Thus, the slotting operation is an unsteady process with an angle of impact that is greatest at the time $t = 0$ and decreases gradually until at some other time t it becomes zero, at which time r is also equal to the difference between the initial radius (r_i) and the turning depth of cut (δ).

The rate of radius change is

$$\frac{dr}{dt} = -\frac{\dot{v}}{2\pi r d_j} \quad (17)$$

where t is the time and the slot width is assumed to be equal to the AWJ diameter (d_j). For large angles of impact, \dot{v} is given by Finnie as

$$\dot{v} = \frac{\cos^2 \alpha m_a V_a^2}{6 \sigma_f \psi} \quad (18)$$

From these equations, the following expression for the turned radius (r) versus time (t) can be derived:

$$r = \left[r_i^4 - \frac{m_a V_a (r_i - \delta)^2}{3\pi\sigma_f \psi d_j^2} t \right]^{1/4} \quad r \leq (r_i - \delta) \quad (19)$$

TURNING

In a recent study of turning with AWJs, Ansari and Hashish (1992) found the following:

- The material removal for the range of traverse speeds and depths commonly encountered in AWJ turning takes place at the "face", rather than the circumference, of the workpiece (the face refers to the plane transverse to the rotational axis of the workpiece).
- No significant deflection of the AWJ occurs in the radial direction at the material removal site.
- The axial deflection of the AWJ changes cyclically.

The problem of turning is to determine the final diameter (d_f) as a function of AWJ and turning parameters. As the AWJ nozzle traverses in the axial direction at a speed u , a step starts to form beyond a steady-state zone at the location where the material removal rate is zero. However, during the same time the workpiece undergoes angular displacement. On the next time step, a step is formed in the workpiece, and the AWJ impacts the step at an angle of 90° , thereby removing it (Figure 6). The maximum step width is equal to the axial distance traversed during one workpiece revolution. Determination of the final workpiece diameter (d_f) is based on the above hypothesis for the formation of steps in AWJ turning.

The relationship between the penetration depth and workpiece radius can be expressed (Ansari and Hashish, 1992) as

$$\frac{dr}{dh} = \frac{h - (2r_i \delta - \delta^2)^{1/2}}{\left[r_i^2 - 2h(2r_i \delta - \delta^2)^{1/2} - h^2 \right]^{1/2}} \quad (20)$$

The volume removal rate can also be written as

$$d\dot{v} = -2\pi r u dr \quad (21)$$

From the above equations we get

$$d\dot{v} = -2\pi r \left[h - (2r_i \delta - \delta^2)^{1/2} \right] dh \quad (22)$$

Using a simplified form of Finnie's (1958) theory of erosion, the following expression results for h_c where α becomes zero at the end of the shallow angle impact zone:

$$h_c^2 - 2(2r_i \delta - \delta^2)^{1/2} h_c + \frac{V_j^2 m_a}{\pi u \sigma_f \psi K} [\sin(2\alpha_t)] = 0 \quad (23)$$

This equation is quadratic in h_c and can be solved numerically. The angle α_p , which is the deflection angle at the top of the cut, was derived as

$$\alpha_t = \frac{2\pi u (2r_i \delta - \delta^2)^{1/2} \sigma_f \psi K d_j}{V_j^2 m_a [\sin(2\alpha_t)]} \quad (24)$$

Similar to linear cutting, a critical traverse rate (u_c) should exist beyond which no steady-state turning can be achieved. This can be determined from the above equation by substituting α_c instead of α_t ; α_c is an angle related to the material characteristics.

For the case of deformation wear, whereby the steps are cut, the volume removal rate is

$$\dot{v} = -(u/N) 2\pi r \frac{dr}{dt} \quad (25)$$

Using Equations (25) and (20), the volume removal rate can be written in terms of the penetration depth (h), which upon simplification becomes

$$\dot{v} = \frac{-2\pi u}{N} \left[h - (2r_i \delta - \delta^2)^{1/2} \right] \frac{dh}{dt} \quad (26)$$

For abrasive particles impacting the step in the kerf at angles of 90° , Bitter's (1963) model under normal impact is expressed as

$$\dot{v} = \frac{m_a (V_j - V_c)^2}{2\sigma_f} \quad (27)$$

The above two equations can be used to yield the depth for deformation wear turning (h_d) as

$$(h_d - h_c)^2 - 2(h_d - h_c)(2r_i \delta - \delta^2)^{1/2} + \frac{m_a d_j (V_j - V_c)^2}{4\pi^2 \sigma_f r_i u} = 0 \quad (28)$$

To determine the final radius (or diameter) of the specimen, the following equation is used:

$$r = \left\{ (r_i - \delta)^2 + \left[(2r_i \delta - \delta^2)^{1/2} - h \right]^2 \right\}^{1/2} \quad (29)$$

DRILLING

In piercing with AWJs (see Figure 7), an abrasive particle is subjected to hydrodynamic drag that becomes significant due to the return flow. The momentum balance for an abrasive particle is

$$m_p V_a \frac{dV_a}{dh} = -0.5 C_f \rho_w A_p (V_w - V_a)^2 \quad (30)$$

where m_p is the mass of the abrasive particle and A_p is the cross-sectional area of the abrasive particle. The velocity of the particle (V_a) as a function of the depth of cut (h) can be determined from this equation after expressing the return velocity (V_w) using the continuity equation. The coefficient of drag (C_p) can be

determined experimentally to account for the three-phase condition. The density of the return fluid (ρ_w) may also be determined by considering it as a mixture of water and air.

The penetration rate can be determined from erosion theories. Hashish (1987) developed the following equation for erosion at shallow angles:

$$\dot{v} = 0.564 \left(\frac{m_a \rho_a^{0.25} V_a^{2.5}}{\sigma_f^{1.25} R_f^{0.75}} \right) \sin 2\alpha \sqrt{\sin \alpha} \quad (31)$$

This equation can be used to determine the effect of the return flow while piercing and the effect of jets after piercing. No further work has been done on the modeling of the hole drilling process.

CONCLUSIONS

This paper presented several physical models to predict AWJ machining results. Significant efforts are still needed to model the different attributes of AWJ machining, such as surface characteristics, kerf geometry, kerf width, and hole shape. Quantitative volume removal rate models based on erosion theories, however, are reasonably well developed and can be adapted to develop further models.

ACKNOWLEDGMENTS

The work presented in this paper has been extracted from several different projects supported by the National Science Foundation and the Department of the Army under the Small Business Innovation Research (SBIR) program. The support of Flow International Corporation in preparing this paper is most appreciated.

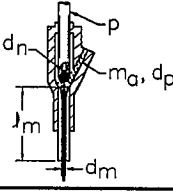
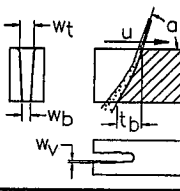
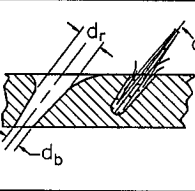
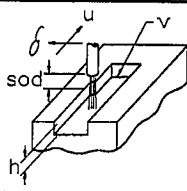
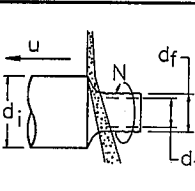
REFERENCES

- Ansari, A. I., and Hashish, M., "On the Modeling of Abrasive Waterjet Turning," Jet Cutting Technology, 11th International Conference, BHR Group, St. Andrews, Scotland, September 8-10, 1992.
- Bitter, J. G. A., "A Study of Erosion Phenomena: Part I," *Wear*, Vol. 6, pp. 5-21, 1963.
- Finnie, I., "The Mechanism of Erosion of Ductile Metals," *Proceedings of the 3rd National Congress on Applied Mechanics*, ASME, 1958.
- Hashish, M., "Abrasive-Waterjet Cutting Studies," *Proceedings of the 11th Conference on Production Research and Technology*, National Science Foundation, Carnegie-Mellon University, Pittsburgh, Pennsylvania, pp. 101-111, May 21-23, 1984.
- Hashish, M., "An Improved Model of Erosion by Solid Particle Impact," *Proceedings of the 7th International Conference on Erosion by Liquid and Solid Impact (ELSI)*, Cambridge, UK, pp. 66-1 to 66-9, 1987.
- Hashish, M., "Visualization of the Abrasive-Waterjet Cutting Process," *Experimental Mechanics*, June, pp. 159-169, 1988.
- Hashish, M., "A Model of Abrasive-Waterjet Machining," ASME Transactions, *Journal of Engineering Materials and Technology*, Vol. 111, pp. 154-162, 1989.
- Hashish, M., "On the Modeling of Surface Waviness Produced by Abrasive-Waterjets," International Symposium on Waterjet Cutting, 1992.

NOMENCLATURE

A_p	cross-sectional area of particle	R_w	waviness
C_d	discharge coefficient	r	radius
C_f	coefficient of drag	r_i	initial radius
C_v	velocity coefficient	t	time
c	portion of abrasives used for cutting	u	traverse rate
d_c	effective particle tip diameter	u_c	critical traverse rate
d_f	final turned diameter	V_a	abrasive particle velocity
d_j	AWJ diameter	V_c	critical velocity
d_m	diameter of mixing tube	V_i	intrinsic velocity
d_n	waterjet orifice diameter	V_j	waterjet velocity
d_p	average diameter of abrasive particle	V_w	water velocity
h	depth	\dot{v}	volume removal rate
h_{av}	average depth of milling per sweep	x	distance
h_c	steady-state or cutting wear zone depth	α	impact angle
h_d	deformation wear zone depth	α_c	critical impact angle
K	constant	α_o	angle related to material characteristics
l_m	length of mixing tube	α_t	deflection angle at top of cut
m_a	abrasive mass flow rate	δ	depth of cut in turning
m_p	mass of abrasive particle	ε	deformation wear specific energy
m_w	mass flow rate of waterjet	η	mixing efficiency
N	rotational speed	ρ_a	abrasive density
N_p	number of passes	ρ_w	density of water
O_n	overlap number	σ_f	material resistance to erosion
P	pressure	ψ	ratio of particle chip contact length to particle penetration
R_f	particle roundness factor		

Table 1. AWJ Machining Process Parameters

AWJ Parameters	Machining Parameters			
	Linear Cutting	Drilling	Milling	Turning
				
Pressure Waterjet Diameter Mixing Tube Length Mixing Tube Diameter Abrasive Material Abrasive Size Abrasive Flow Rate Abrasive Condition	Angle Standoff Distance Traverse Rate Number of Passes Material Thickness	Angle Standoff Distance Dwell Time Pressure Profile Material Thickness	Traverse Rate Lateral Increment Number of Passes Number of Sweeps	Rotational Speed Direction of Rotation Angle Traverse Rate Initial Diameter Final Diameter Depth of Cut
	Machining Requirements (Dependent Variables)			
	Traverse Rate Surface Finish Width of Cut	Diameter Drilling Time Hole Shape	Volume Removal Rate Depth Control	Turned Diameter Surface Finish Machining Time

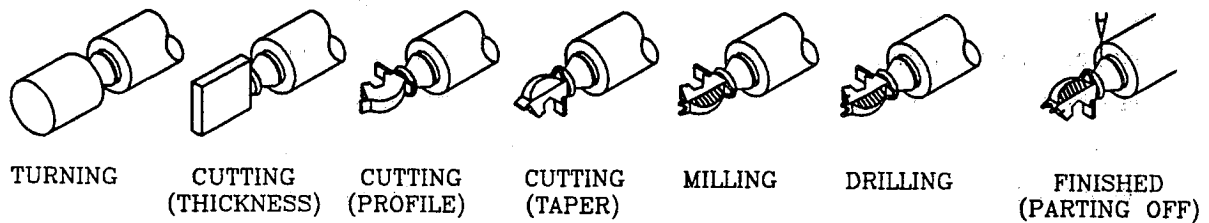


Figure 1. Example Sequence for Complex Three-Dimensional Machining with an AWJ

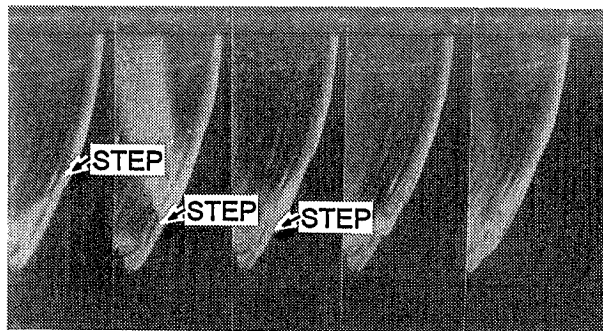


Figure 2. Progression of Steps Under AWJ Impact

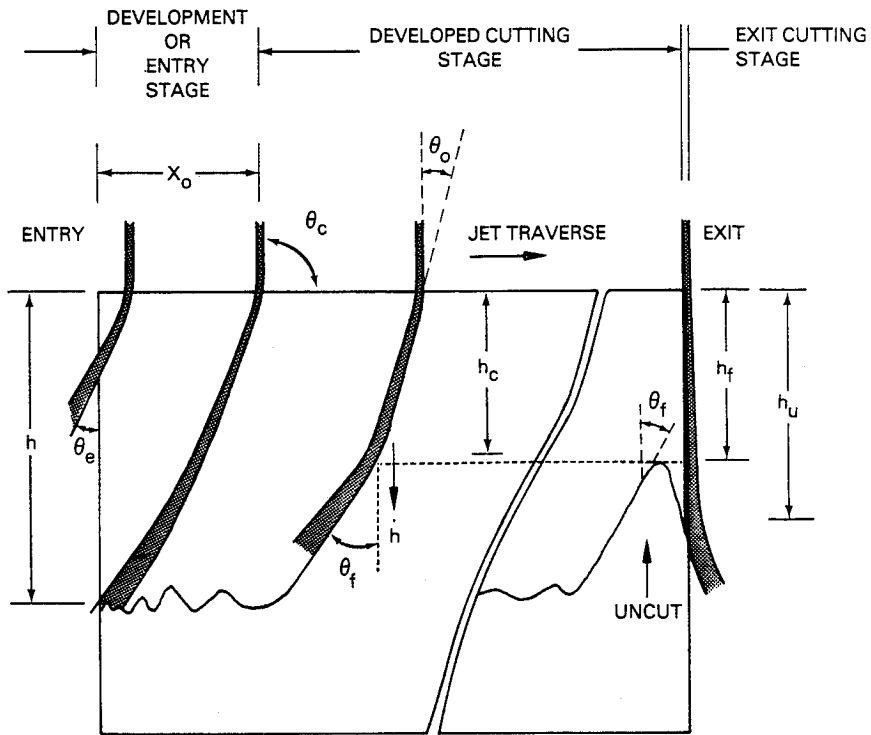


Figure 3. Different Zones of the Jet/Material Interface

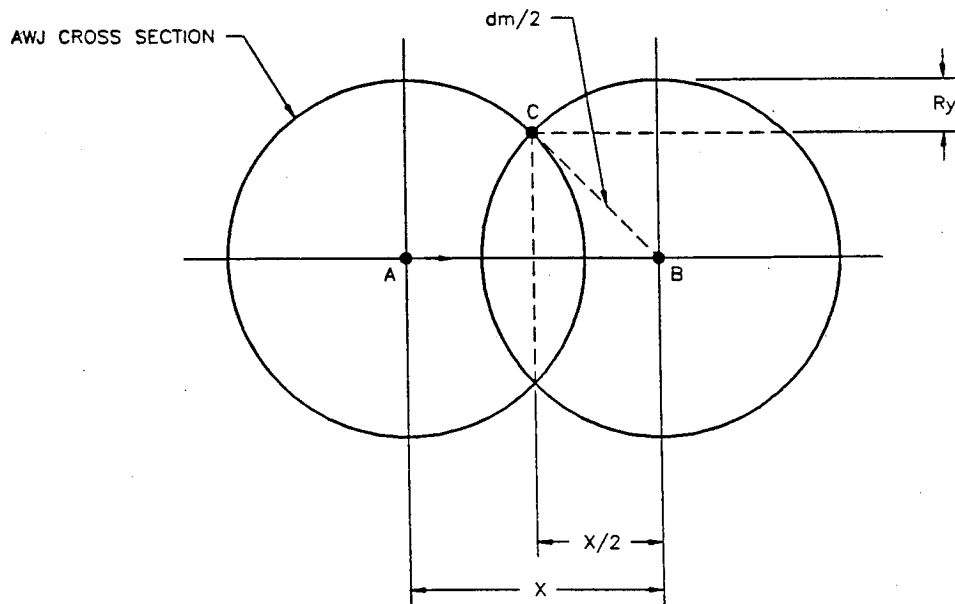


Figure 4. Idealized Geometry for Waviness Modeling

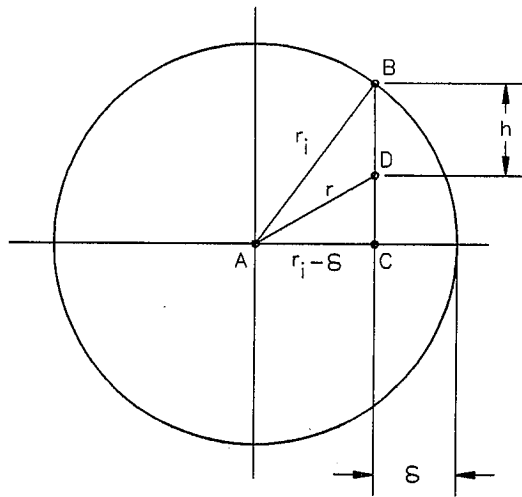


Figure 5. Relationship Between AWJ Penetration Depth and Workpiece Radius

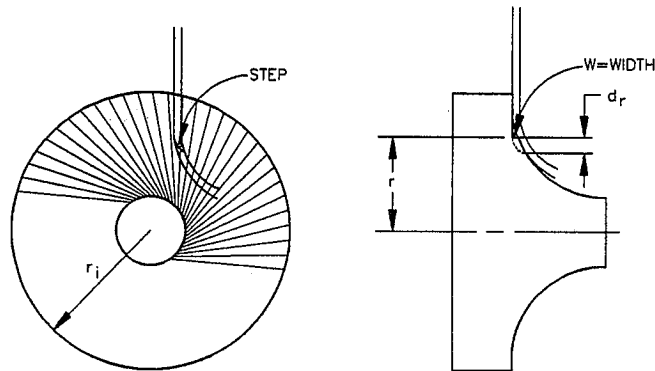


Figure 6. Schematic Representation of Step Formation in AWJ Turning

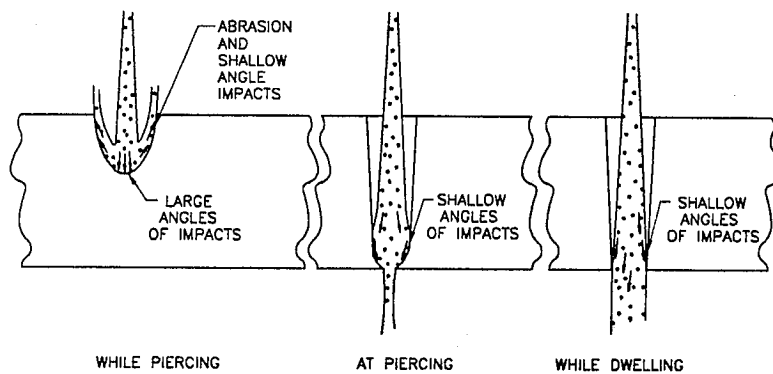


Figure 7. Drilling with an AWJ

DETECTION OF ABRASIVE WATERJET NOZZLE WEAR USING ACOUSTIC SIGNATURE ANALYSIS

Kovacevic, R., Wang, L. and Zhang, Y. M.
Center for Robotics and Manufacturing Systems
Department of Mechanical Engineering
University of Kentucky
Lexington, Kentucky 40506

ABSTRACT

One of the most critical parts that influences the technical and economical performance of an abrasive waterjet (AWJ) cutting system is the AWJ nozzle. Sensing AWJ nozzle wear is a key aspect in producing high-quality parts on a fully automated AWJ system. In this paper, an approach for on-line sensing nozzle wear is proposed, based on monitoring the acoustic signals generated by the abrasive waterjet. The sound produced by the flow of the waterjet and abrasive waterjet is measured for various AWJ nozzle diameters and nozzle lengths during cutting through material and without cutting. It was shown that the amplitude of the spectrum has a high sensitivity to a small variation of the nozzle exit geometry for each analyzed case. A time-series analysis technique is used to model the acoustic signals. The results show that there is a strong correlation between the nozzle wear and the ARMA model coefficients.

1. INTRODUCTION

The AWJ nozzle acts mainly to focus the spreading jet and accelerate the abrasive particles which do not penetrate the jet stream. The increased wear of the AWJ nozzle makes the clearance between waterjet and AWJ nozzle larger. Obviously, the larger the diameter of the AWJ nozzle's outlet, the lower the transverse particle velocity. The result of this is incomplete mixing of the abrasive particles with the waterjet, which will cause a reduction in cutting ability and tend to produce unacceptable manufacturing quality. It is evident that the outlet of the AWJ nozzle determines the final shape of the abrasive waterjet and its cutting performances. The change rate of the inside diameter at the nozzle outlet is used to quantify the nozzle wear.

Computer control makes AWJ cutting a prime candidate for application in flexible manufacturing systems. Automated equipment must have the ability to detect nozzle wear early before final results exceed acceptable limits. However, currently there is no reliable wear sensing system available. A number of approaches have been investigated. Generally speaking, the methods that could be used to detect AWJ nozzle wear can be categorized as either direct or indirect. Direct methods make an assessment of nozzle wear by either measuring the inside diameter (ID) of the nozzle at its tip, or measuring the material loss of the nozzle by radiometric techniques. Two direct sensing units have been proposed to measure the AWJ nozzle inside diameter (Kovacevic, 1988 and 1991). One of proposed direct sensing units is based on a conductive loop which is embedded in the tip of the nozzle where it is exposed to effects of erosion and abrasive wear. The predetermined threshold of the AWJ nozzle inside diameter will be detected by this sensor. The other direct sensing system consists of wear sensor probes and a digital logic unit connected to the PC. The wearable probes are placed on the ceramic plate and are divided into four quadrants with a hole in the center having a diameter equal to the inside diameter of the new AWJ nozzle. Unfortunately, these approaches cannot be successfully used for on-line monitoring the increase in the AWJ nozzle inside diameter (ID). The indirect methods are promising approaches for on-line sensing of nozzle wear and compensation for the increase in the nozzle ID. Indirect methods are based on the measurement of some parameters that are correlated to the AWJ nozzle wear such as the change of the stream diameter at the nozzle exit, or the change of the workpiece normal force generated by the impacting jet, vibration, sound, etc.

The abrasive waterjet diameter can be directly monitored and measured by a solid-state CCD matrix or linear-array camera, and the actual diameter of the AWJ nozzle can be linked to the abrasive waterjet diameter. The proposed abrasive waterjet diameter monitoring system (Kovacevic, 1991) based on the machine-vision system consists of three main components: a CCD matrix-array camera, a frame grabber, and a PC. The measurement of the abrasive waterjet diameter is performed periodically.

Recently, a number of experiments (Kovacevic et al., 1989, 1990, 1991) have proven that the workpiece normal force generated by an abrasive waterjet can be used as an indicator of nozzle wear. With an increase of the nozzle inside diameter, the workpiece normal force will increase, keeping all other cutting variables constant, and thus wear can be monitored from an early stage. Besides the change of the workpiece normal force level, its signal characteristics are also expected to change with an increase in the nozzle wear. It was shown that nozzle wear in the cutting through and milling operation with abrasive waterjet can be detected and monitored by analyzing the dynamic portion, i.e., the A.C. component, of the workpiece normal force signal generated by the impacting abrasive waterjet. For the in-process sensing of the diameter, the model parameters can be updated adaptive.

Mechanical vibration and acoustic analysis have found extensive use in fault detection lately. The sensors that are used for measuring acoustic signals are not expensive and can easily be mounted at a desired location. Pattern-recognition analysis of sound radiation was

developed as a basis for monitoring the metal-cutting process (Traeisi and Kannatey-Asibu, 1991). Using the resubstitution method, signals coming from sharp and worn tools were easily distinguished. In order to monitor tool flank wear, an experimental program (Sadat and Raman, 1987) was designed using low frequency noise spectra resulting from the rubbing action of the tool and workpiece. In addition to mechanical acoustics, some papers deal with the fluid acoustics. In fact, measurement and theory of the high-speed jet noise have been investigated in aerodynamics for many years. The predictions of the theory are in good agreement with experimental work (Lush, 1971). In order to control the process of laser grooving, acoustic sensing was used (Chryssolouris et al., 1991). The acoustic signal is emitted from the impinging gas jet on the erosion front. Correlations between resonant frequency and hole, kerf or groove geometry were found. An automatic remote detection of nozzle wear in plasma cutting torches has been investigated (Braeuel et al., 1987). It was found that the amplitude and spectral structure of the resonant tone are extremely sensitive to any changes in the orifice geometry. The acoustic technique also has been proposed to analyze the state of the AWJ cutting in inaccessible environments like the deep-sea (Louis and Meier, 1991).

The idea of using an acoustic sensing method to detect nozzle wear is based on the hypothesis that a change in the AWJ nozzle inside diameter affects the flow of the waterjet and thus influences the level of noise.

2. EXPERIMENTAL SETUP

A commercial abrasive water-jet cutting system is used to conduct the experiments. The principle of this system can be illustrated by Fig. 1. In this system, an intensifier pump is connected to the abrasive waterjet cutting head which consists of a sapphire orifice, an abrasive waterjet nozzle, and a mixing chamber. The position of the cutting head is controlled by a CNC controlled positioning table.

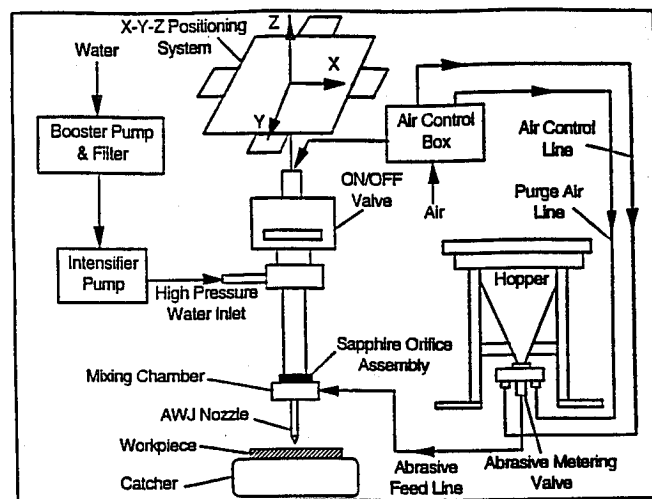


Fig 1. Schematic of abrasive waterjet cutting system

In order to investigate the correlation between the nozzle diameter and the generated level of noise, a number of diameters for two different nozzle lengths are considered (see Table 1) while other parameters, are kept constant throughout this study (see Table 2). A 6.35 mm condenser microphone (B & K 4135) is employed to measure the acoustic signal. The microphone is aimed at the nozzle's output from a distance of 10 cm away. During the cutting operation the microphone travels with the cutting head in order to maintain a fixed distance from the nozzle exit. In addition the atmospheric pressure is measured at regular intervals during testing and frequent checks are made on the microphone calibration using a B & K pistonphone (type 4220). The block diagram of this experimental setup is shown in Fig. 2.

Table 1. Parameters for Test Nozzles

(mm) \ no.	1	2	3	4	5	6
AWJ nozzle length	76.20	76.20	88.90	88.90	88.90	76.20
nozzle inside diameter	1.02	1.14	1.27	1.40	1.52	1.80

Table 2. Constant Process Parameters for AWJ Cutting

waterjet pressure (P)	- 275 MPa
waterjet orifice size (d_n)	- 0.254 mm
stand-off distance (SOD)	- 6.00 mm
abrasive type	- garnet
abrasive size (d_p)	- 80 mesh (0.180 mm)
traverse speed (u)	- 0.85 mm/s
jet angle (α_c)	- 90°
abrasive flow rate (M_a)	- 6.05 g/s

A 386 Compar/PC data acquisition system (Wavepak ver 2.42 software with the hardware board from Computational System Inc.) is used to collect and process the data. Wavepak consists of two IBM PC compatible expansion boards and a custom software package that is designed to allow an IBM PC to act as a dual-channel FFT signal analyzer which controls data analysis and displays graphics.

In order to minimize the measure error caused by the reflection noise, an acoustic foam is utilized to cover the stand and supporting structure. The signal is preamplified before it is sent to the PC. The amplified signal is fed into a single channel spectrum analyzer, which analyzes the signal using fast Fourier transform and displays the signal spectrum. A frequency range from 0 to 40kHz is scanned. Sampling time for a single sweep of the frequency range is 10 ms. For each diameter, two sets of data are acquired in order to test signal repeatability.

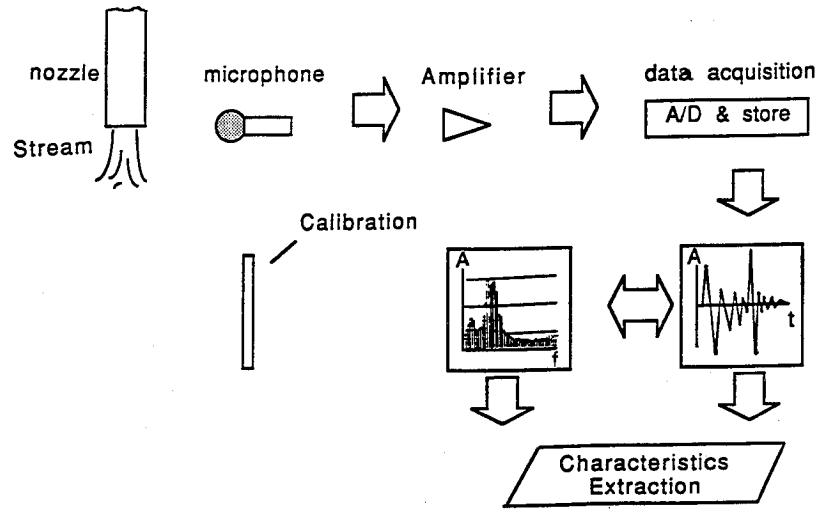


Fig 2. Acoustic analysis system of an AWJ cutting system

3. RESULTS AND DISCUSSION

In order to analyze the relationship between the nozzle inside diameter and the generated acoustic signal, the experiments are performed under two different conditions: 1. when only pure water is forced through the AWJ nozzle, and 2. when a mixture of water and abrasive is forced through the AWJ nozzle. In the case of abrasive waterjet, the level of noise is monitored during the cutting through the workpiece and without cutting.

In the case of cutting through the workpiece, we found that the acoustic signals originated from two sources. One is generated at the nozzle exit, and the other at the workpiece during the cutting operation. Obviously, the acoustic coming from the nozzle exit is our concern. We expected the nozzle wear will cause a change in the level of acoustics. Also, the different flow media (pure water and mixture of water and abrasive particles) will cause different acoustic characteristics.

An analysis of the findings for the three different conditions is given below. It is evident that the different conditions will generate a different pattern of acoustic signals. The aim of this analysis is to investigate under which conditions the acoustic signal will give the most accurate information about AWJ nozzle wear.

3.1 Waterjet: For the single phase flow jet, the far-field intensity, I , may be written in dimensional form as follows (Lush, 1971):

$$I \sim \frac{\rho_m^2 V_j^8 D^2}{\rho_0 a_0^5 R^2} \frac{D(\theta)}{(1-M_c \cos\theta)^5} \quad (1)$$

where V_j is the jet velocity, D is the nozzle inside diameter and R is the distance from the jet to the observer. The sound power may be obtained using the following expression:

$$P \sim \frac{\rho_0 V_j^8 D^2}{a_0^5} \frac{1+M_c^2}{(1-M_c^2)^4} \quad (2)$$

It is evident from Eq. 2 that the sound power increases with the eighth power of the jet velocity and the second power of the jet nozzle inside diameter. It is known that the jet exit velocity varies directly with the square root of pressure. For a given pressure, the velocity is assumed to be constant. By keeping AWJ cutting conditions constant, it is expected that the power of acoustic will only depend on the nozzle ID. It is certain that the sound power is very sensitive to the nozzle geometry change, i.e. nozzle wear.

Fig. 3 shows the result of the sound measurement when ID = 1.40 mm. It found that the flow of the waterjet becomes turbulent due to the high speed and pressure. The spectral components of the sound signal are used to qualitatively estimate the intensity of the AWJ nozzle wear. Initially, a single-phase flow is considered for purpose of simplicity. Fig. 4 and Fig 5 show the acoustic spectra for a waterjet without abrasive and for the two different nozzle lengths (76.2 mm and 88.9 mm). The results show that with an increase of the nozzle inside diameter, the acoustic signal has the same frequency pattern for a given length of nozzle, while the acoustic power shows an evident increase.

3.2 Waterjet With Abrasive: It is known that three phases (water, air and abrasive) exist in the abrasive waterjet. The interaction between turbulent fluid flow and the particles will raise the turbulence due to wake shedding. On the other hand, the effects of particles on continuous phase turbulent properties are limited to wave numbers (Hetsroni, 1985). The kinetic energy of the turbulence is somewhat higher in the two-phase jet, as compared to the single-phase one. Figs. 6 and 7 show the acoustic spectra for the case of the abrasive waterjet without cutting the workpiece for two different nozzle lengths. All other parameters are the same as in the previous experiments. Although, the patterns of spectra for the different diameters in the low frequency range (below 20 kHz) cannot be easily distinguished, in the high frequency range (over 20 kHz) it can be seen that the amplitude of the spectra pattern strongly depends on the nozzle inside diameter. The fluid flow mixed with abrasive is more chaotic than the case of water only due to the influence of the abrasive action. The acoustic signals seem to be less dependent on the nozzle wear. Fortunately, this kind of influence only acts in the low frequency range (below 20 kHz). Thus, the nozzle wear can still be recognized by the amplitude of spectra in the high frequency range.

3.3 Cutting Operation: In order to monitor the AWJ nozzle wear on-line using acoustic signature analysis, all acoustic sources during the workpiece cutting must be considered. Figs. 8 and 9 show the acoustic spectra generated during the AWJ cutting operation using different nozzle inside-diameters and lengths. A workpiece of cross-section 50.8 mm x 76.2 mm made of aluminum 6061 is used in the cutting through experiment. In comparison with the cases of no cutting operation (sec. 3.1 and 3.2), in cutting operation the acoustic increases dramatically due to the addition of the acoustic source generated by the erosion of the workpiece. From obtained results, it is evident we can still easily distinguish the different AWJ nozzle inside diameter by the amplitudes of spectra.

To summarize the above three cases, we found that the amplitude of the spectra at high frequency range over 20kHz is a good indicator for monitoring the nozzle wear. The ideal monitoring of the AWJ nozzle wear will be during the actual cutting. However, acoustic generated during the cutting depends on the workpiece material and the selected operation method (cutting through or grooving) besides the cutting parameters. In the case of using only waterjet, as mentioned earlier, only the AWJ nozzle ID will affect the acoustic signal. But this approach for monitoring the nozzle wear is inconvenient for the AWJ operation because of switching on/off the flow of abrasive. Among the analyzed cases, the abrasive waterjet nozzle wear can best be monitored when a mixture of water and abrasive is forced through the nozzle without cutting the workpiece. It is shown that the signal spectra strongly depends on the nozzle wear in the high frequency range. Monitoring the acoustic signal could be performed in a very short period of time by moving the cutting head away from the workpiece to the corner of the worktable, where the AWJ nozzle wear monitoring system is set.

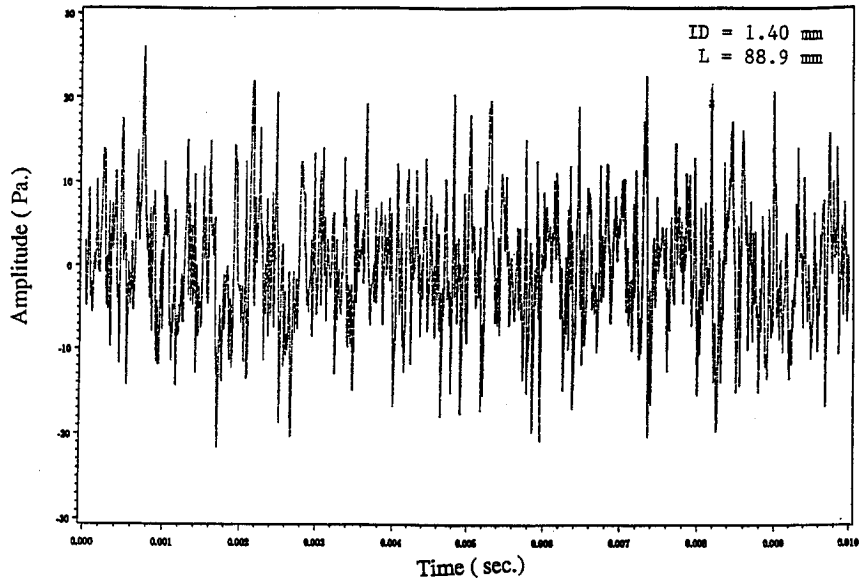


Fig 3. Acoustic signal for only water

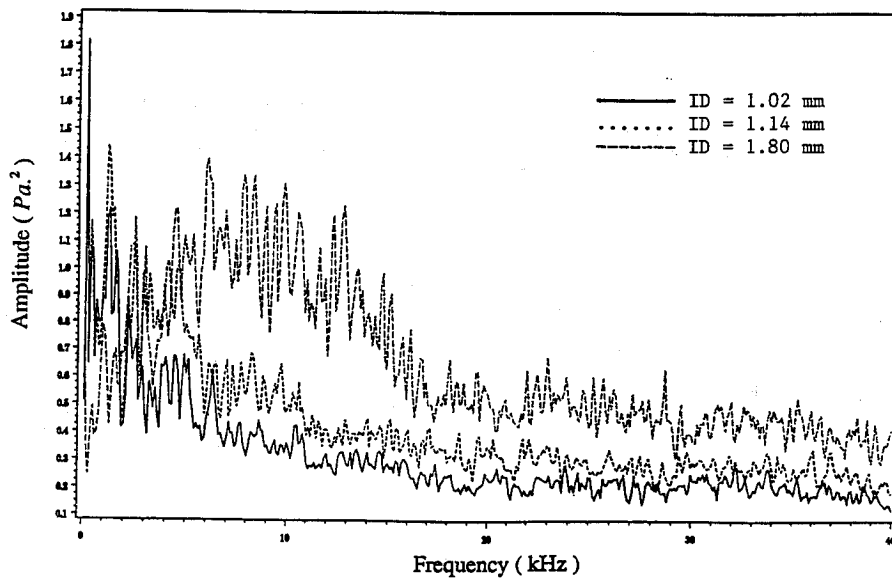


Fig. 4. Power spectrum of acoustic signal for only water (L=76.2 mm)

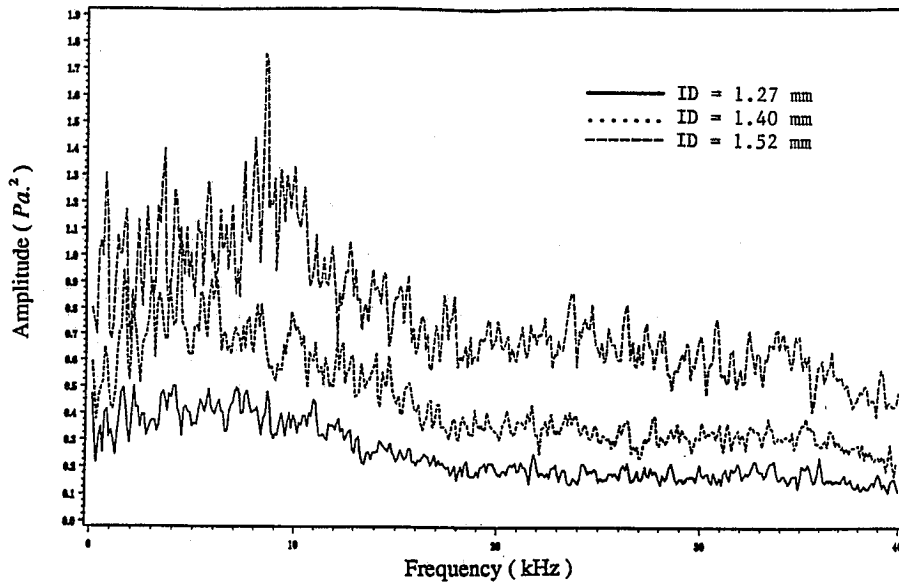


Fig. 5. Power spectrum of acoustic signal for only water ($L=88.9$ mm)

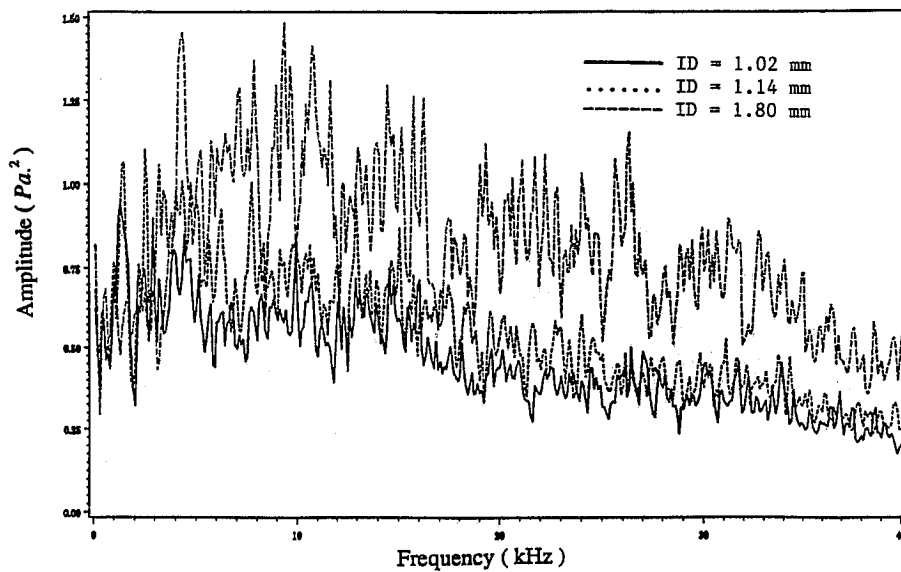


Fig. 6. Power spectrum of acoustic signal for water and abrasive ($L=76.2$ mm)

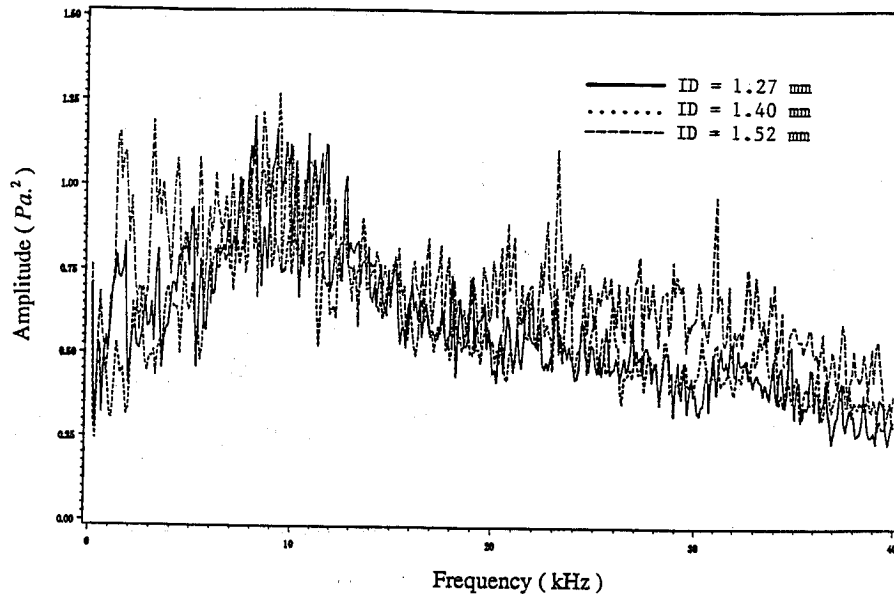


Fig. 7. Power spectrum of acoustic signal for water and abrasive (L=88.9 mm)

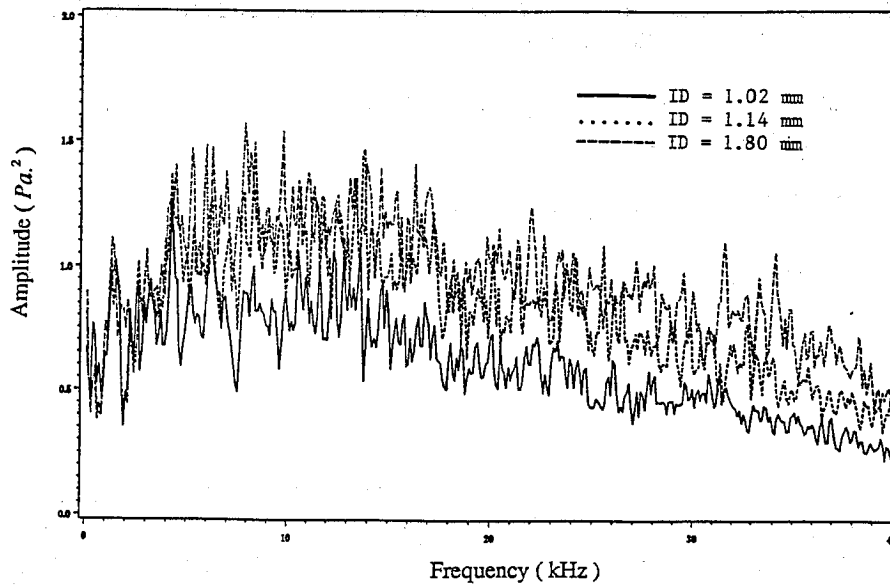


Fig. 8. Power spectrum of acoustic signal for AWJ cutting operation (L=76.2 mm)

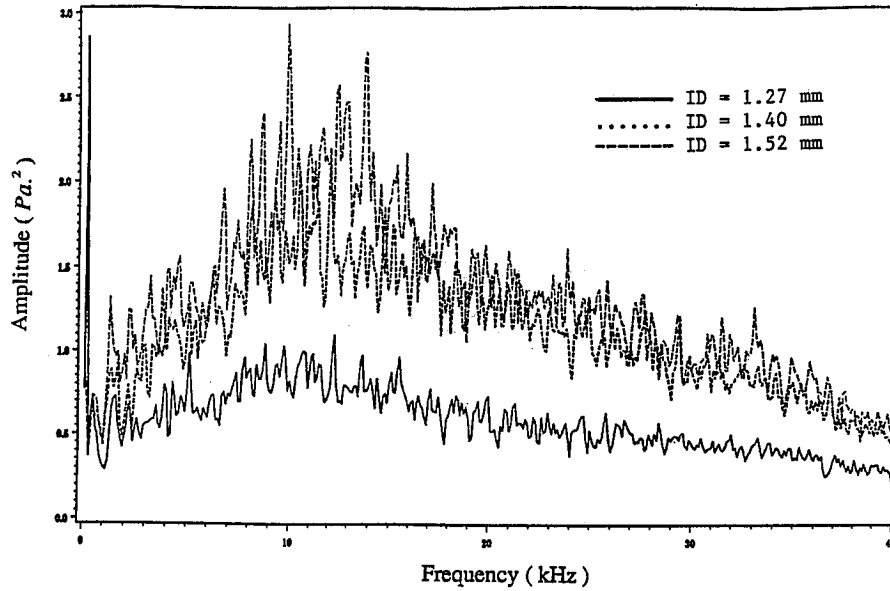


Fig. 9. Power spectrum of acoustic signal for AWJ cutting operation (L=88.9 mm)

4. ARMA MODEL ANALYSIS

The FFT based spectral analysis has been employed to study the relationship between the spectrum and the nozzle inside-diameter in the previous section. However, in order to investigate the underlying characteristics behind the AWJ nozzle wear process, a model describing the acoustic signal will be helpful. Thus, in this section, the ARMA modeling is addressed for the measured acoustic signals.

4.1 ARMA Modeling: Assume that y_t 's ($t=1,2,\dots,N$) are the measured sound signals. Its ARMA (n,m) model can be described:

$$y_t - \phi_1 y_{t-1} - \phi_2 y_{t-2} \dots - \phi_n y_{t-n} = \epsilon_t - \theta_1 \epsilon_{t-1} - \theta_2 \epsilon_{t-2} \dots - \theta_m \epsilon_{t-m}$$

where $\phi_1, \phi_2, \dots, \phi_n$ and $\theta_1, \theta_2, \dots, \theta_m$ are the ARMA coefficients, and $\epsilon_t \sim N(0, \sigma^2)$ is the white noise.

It can be shown that the ARMA model coefficients $\phi_j (j=1, \dots, n)$ and $\theta_j (j=1, \dots, m)$ are determined by the cutting parameters: the waterjet pressure, abrasive flow rate, AWJ nozzle inside-diameter, etc. In our case, however, all the other parameters have been kept constant except the AWJ nozzle diameter. Thus, the variation of the ARMA model coefficients will be influenced by the nozzle diameter. The nozzle wear, therefore, can be detected by the on-line identified ARMA coefficients.

4.2 Order Selection: The order selection is a fundamental step in identification of ARMA models. Numerous approaches have been proposed to select the order of an ARMA model. However, each approach associated with a specific point of view. The full description of model has not found yet. In this work, spectrum is of concern. So far, a few criteria have been designed for the application of spectral estimation. In order to obtain all appropriate ARMA model orders, a spectrum-oriented order selection criterion is proposed based on the concept of Model Spectral Distance MSD (Kovacevic and Zhang, 1992). A model selected by one criterion may not be selected by the other one. Thus, application-oriented optimal orders should be more suitable than the consistent orders in the special application.

Suppose that y_t can be described by a stationary-invertible autoregressive moving-average model:

$$\phi(B)y_t = \theta(B)\varepsilon_t \quad (3)$$

where ϕ_j ($j=1, \dots, p$) and θ_j ($j=1, \dots, q$) are real. The power spectral density of y_t can be written as:

$$p(\omega) = |H(\omega)|^2 \sigma_\varepsilon^2 \quad (4)$$

where

$$H(\omega) = \frac{1}{\sqrt{2\pi}} \frac{\theta(e^{-i\omega})}{\phi(e^{-i\omega})} \equiv \frac{1}{\sqrt{2\pi}} \frac{c(\omega) + i d(\omega)}{a(\omega) + i b(\omega)} \quad (5)$$

Consider $H^{(2)}(\omega)$ and $H^{(1)}(\omega)$, Let

$$d^2(H^{(2)}(\omega) \rightarrow H^{(1)}(\omega)) \equiv \left| \frac{H^{(1)}(\omega) - H^{(2)}(\omega)}{H^{(1)}(\omega)} \right|^2 \quad (6)$$

Thus, we define $D(H^{(2)} - H^{(1)})$ as the model spectral distance (MSD) from $H^{(2)}$ to $H^{(1)}$.

$$D(H^{(2)} \rightarrow H^{(1)}) = \sqrt{\frac{1}{2\pi} \int_{-\pi}^{\pi} |d|^2 d\omega} \quad (7)$$

The MSD is regarded as a measure of the difference between two given models in the foregoing discussion. It may be employed to measure the parameter estimation accuracy. Thus, it can be shown that:

$$D^2(\hat{H} \rightarrow H) = \frac{1}{2\pi} \int_{-\pi}^{\pi} \left| \frac{\Delta \hat{\theta}(e^{-j\omega})}{\hat{\theta}(e^{-j\omega})} - \frac{\Delta \hat{\phi}(e^{-j\omega})}{\hat{\phi}(e^{-j\omega})} \right|^2 d\omega \quad (6)$$

$$D(\hat{H}) = E(D(\hat{H} \rightarrow H)) \quad (7)$$

The Model Spectral Distance Criterion (MSDC) tends to select an optimal model which produces the minimum spectral estimate error among possible models. The significance of order increase will be determined through a comparison of possible accuracy improvement and loss. Assume that $ARMA(p+\Delta p, q+\Delta q)$ ($\Delta p \geq 0, \Delta q \geq 0$) is a higher order ARMA model than $ARMA(p, q)$. The MSD from $ARMA(p, q)$ to $ARMA(p+\Delta p, q+\Delta q)$ can be considered as possible accuracy improvement. On the other hand, the contribution of parameter estimation to the modeling error will increase. If possible error increase is larger than the possible accuracy improvement the order increase will not be proper. Otherwise, the order increase is proper.

In this paper, we selected the $ARMA(n, n-1)$ model to model the acoustic signature of the waterjet and abrasive waterjet by using the MSDC method. Three different data sets corresponding to three different inside-diameters were calculated for each case. The identified models are listed in Tables 3 and 4, respectively. It can be seen that $ARMA(4,3)$ has been frequently selected. The coefficients of the $ARMA(4,3)$ model appear in Table 5.

Table 3. Order Determination for only water

Transfer trial	(1,0) - (2,1)	(2,1) - (3,2)	(3,2) - (4,3)	(4,3) -(5,4)
$D^2_H - D^2_L$	0.0029	0.0034	0.0070	0.00904
Distance	7.4450	0.9432	0.7381	0.01919
Significance	Yes	Yes	Yes	No

* L = 88.90 mm, ID = 1.40 mm

Table 4. Order Determination for water with abrasive

Transfer trial	(1,0) - (2,1)	(2,1) - (3,2)	(3,2) - (4,3)	(4,3) -(5,4)
$D^2_H - D^2_L$	0.0031	0.00524	0.0058	0.00795
Distance	11.220	0.20710	0.6141	0.01250
Significance	Yes	Yes	Yes	No

* L = 88.90 mm, ID = 1.40 mm

Table 5. Coefficients of the $ARMA(4,3)$ model (L=88.90 mm)

coef. \ ID	only water(mm)			water & abrasive(mm)		
	1.27	1.40	1.52	1.27	1.40	1.52
AR1	0.200	0.269	0.379	0.283	0.315	0.448
AR2	0.222	0.167	0.377	0.174	0.177	-0.212
AR3	0.312	0.321	0.335	0.150	0.210	0.109
AR4	-0.310	-0.266	-0.219	-0.351	-0.292	-0.146
MA1	-1.169	-1.413	-0.879	-1.037	-1.015	-0.536
MA2	0.126	-0.014	0.803	0.441	0.570	0.319
MA3	0.407	0.426	0.772	0.580	0.640	-0.111

4.3 Coefficient Indicator: Theoretically, a full description of the AWJ nozzle wear through acoustic signature needs all the coefficients included in the ARMA model. However, it is shown by this study that the change in the AWJ nozzle inside-diameter can be sufficiently described by the coefficient locus on the $\phi_1-\phi_4$ plane. Fig. 10 depicts the loci associated with the experiments. It can be seen that the 2-D coefficient loci clearly express the different nozzle wear conditions with respect to the different coefficients. Thus, a suitable technique for monitoring the nozzle wear under given cutting conditions can be obtained. Also, it can be seen in Fig. 10 that although the two loci corresponding to the case of waterjet experiments and the case of abrasive waterjet experiments are similar, a shift exists between these two loci. In fact, the abrasive may focus from one eddy to another because of the inertia and cross trajectories effect. Hence, the resulting acoustic signal will be different as already shown in section 3.2.

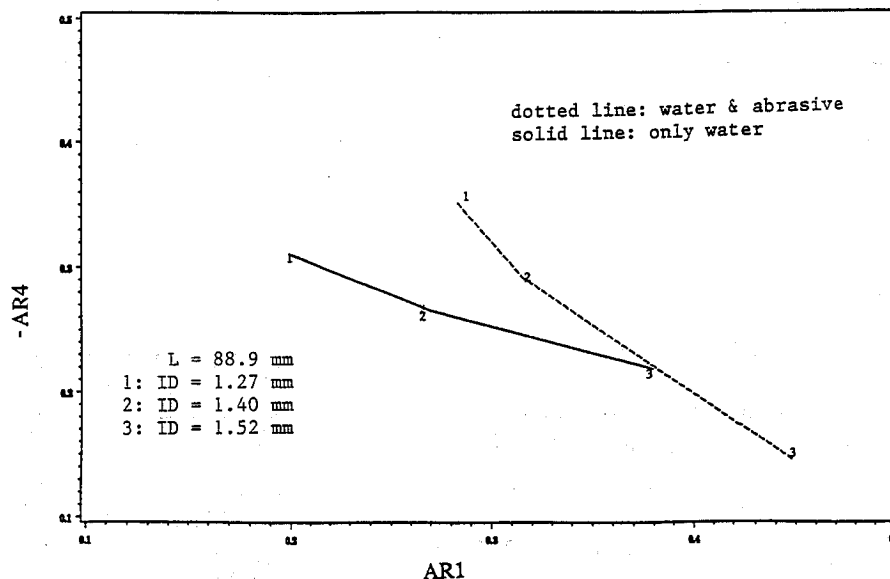


Fig. 10. 2-D (AR1,AR2) plane for ARMA(4,3) model

5. CONCLUSIONS

Through the experimental study it was shown that the acoustic signal could be successfully applied in monitoring the AWJ nozzle wear. From the results of the tests and conducted signal processing, it is proven that the amplitude of acoustic spectra could be used for on-line monitoring of AWJ nozzle wear. The following conclusions can be drawn:

1. The spectra of the acoustic signal has a high sensitivity to a small variation of the nozzle inside diameter. Under each investigated condition, the patterns of the spectra are the same during the increase of the nozzle inside diameter. However, the amplitudes of the acoustic signal are different and they can be used for on-line monitoring of the AWJ nozzle wear.
2. The abrasive added to the waterjet made the acoustic signal larger and more complex than that produced by the single-phase flow. This influence is present only in the low frequency range. Also, the results show that the length of the focussing tube is an influencing factor for the acoustic signals.
3. Three sets of acoustic signals (pure water, mixture of abrasive particles and water with and

without cutting through the waterjet) are acquired. Among the analyzed cases, the abrasive waterjet nozzle wear can best be monitored when a mixture of water and abrasive is forced through the nozzle without cutting the workpiece.

4. The ARMA model order was selected using the MSDC method. An optimal model which produces the minimum spectral estimate error among possible models is selected. ARMA (4,3) is chosen as the most desired form.

5. A time-series analysis shows that there is a strong correlation between the nozzle wear and the values of the ARMA(4,3) model coefficient (AR1, AR4). Based on the coefficients of the ARMA model, it is possible to on-line monitor the nozzle wear even in the early stage.

ACKNOWLEDGEMENT

Authors are grateful to Dr. A. F. Seybert and Mr. A. R. Mohanty for their help in this study. The financial support of the Center for Robotics and Manufacturing Systems, University of Kentucky and support in equipment from Flow International, Inc., Kent, WA are greatly appreciated.

REFERENCES

- [1] Kovacevic, R., 1988, " Sensor for detecting the nozzle wear in abrasive waterjet cutting systems ", Invention Disclosure, Syracuse University, Syracuse, NY, March
- [2] Kovacevic, R., 1991, " A new sensing system to monitor abrasive waterjet nozzle wear ", Journal of Materials Processing Technology, 28(1991), pp. 117-125.
- [3] Kovacevic, R., 1991, " Development of opto-electronic sensor for monitoring the abrasive waterjet nozzle wear ", The ASME's 1991 Winter Annual Meeting, Symposium on Sensors, Controls, and Quality Issues in Manufacturing, Dec.1-6, Atlanta, Go.
- [4] Kovacevic, R. and Evizi, M., 1990, " Nozzle wear detection in abrasive waterjet cutting systems ", Materials Evaluation, 48, March, pp.348-353
- [5] Kovacevic, R., 1989, " Nozzle wear sensing in turning operation with abrasive waterjets ", The SME's Nontraditional Machining Conference " Nontrad for the 90's ", Oct. 30-Nov. 2, Orlando, FL
- [6] Kovacevic, R. and Chen, G., 1989, " A workpiece reactive force as a parameter for monitoring the nozzle wear in turning operation by abrasive waterjet ", The ASME's 1989 Winter Annual Meeting- The High Energy Beam Manufacturing Technology Session, Dec. 14-17 San Francisco, CA
- [7] Kovacevic, R., 1991, " Detection of abrasive waterjet nozzle wear by using time series modeling technique ", NAMRI Transactions, May, pp. 96-100.
- [8] Kovacevic, R., 1990, " Estimation of nozzle wear under varying cutting condition ", The ASME's 1990 Winter Annual Meeting, Symposium on Monitoring and Control for Manufacturing Processes: Sensors and Signal Processing, Nov. 25-30, Dallas, TX, pp.9-16
- [9] Traeisi, E. and Kannatey-Asibu, Jr. H., 1991, " Pattern-recognition Analysis of Sound Radiation in Metal Cutting ", Int. Journal of Manufacturing Technology, pp. 220.
- [10] Sadat, A. B. and Raman, S., 1987, " Detection of Tool Flank Wear Using Acoustic Signature Analysis ", Wear, Vol. 115, pp. 265.
- [11] Lush, P. A., 1971, " Measurements of Subsonic Jet Noise and Comparison with Theory ", Journal of Fluid Mech., Vol. 46, part 3, pp. 477.

- [12] Chryssolouris, G., Sheng, P, and Alvensleben, F., 1991, " Process Control of Laser Grooving Using Acoustic Sensing ", Journal of Engineering for Industry, TRANS. of ASME, Vol 113, pp. 268.
- [13] Braeuel, M., Nadeau, F. and Bayoumi, M., 1987, " The Nozzle of Plasma Cutting Torches ", IEEE TRANS. on Ultrasonics, Ferroelectrics, and Frequency Control, Vol. UFFC-34, No. 2, March.
- [14] Louis, H. and Meier, G., 1991, " Methods of Process Control for Abrasive Water Jets ", 6th American Water Jet Conference, Paper No. 32, August 24, Houston, Texas.
- [15] Hetsroni, G., " Particle- Turbulence, Interaction ", Journal of Engineering for Industry, TRANS. of ASME, Vol 11, No. 1, Feb.
- [16] Kovacevic, R. and Zhang, Y., 1992, " Identification of Surface Characteristics from Large Samples ", Proceedings Part C, Journal of Mechanical Engineering Science, Vol. 206.

ENHANCING THE PERFORMANCE OF CAVITATING WATER JETS

M.M. Vijay^{*}, S.G. Hu^{**} and M.K.Y. Lai^{*}

^{*}Institute for Engineering in the Canadian Environment
National Research Council of Canada
Ottawa, Ontario, Canada, K1A 0R6

^{**}Department of Power Engineering
Shanghai Institute of Mechanical Engineering
Shanghai, 200093, P.R. China
(Guest Scientist at the National Research Council of Canada)

ABSTRACT

The mechanism of high speed cavitating jets, emerging in air or artificially and fully submerged environments, is not well understood. This explains why they are not as popular as other types of jets (for example, abrasive-entrained water jets) for practical applications. The structure of cavitating flows is highly complex and small changes in the governing variables appear to deteriorate their performance significantly. Experimental results and analytical results from the computational fluid dynamics analysis of the high speed water flows are presented which show that it is possible to enhance the performance by artificial submergence. Nozzle configurations which facilitate artificial submergence are described and the factors which influence their performance are discussed.

1. INTRODUCTION

A study of the literature (only a selected few references are cited due to limited length of the paper) shows that there is a great deal of interest in cavitating water jets. The principle of cavitating jets and their characteristics have been expounded by a number of investigators (Conn & Johnson, 1980; Johnson, et al., 1972; Lai, et al., 1991; Lichtarowicz, 1974; Shimizu & Yamaguchi, 1988; Vickers, et al., 1980; Vijay, 1987, Vijay, et al., 1990). Despite the profuse evidence on the potential of cavitating jets for multiplicity of applications, for example, drilling of rocks (Bardin & Cholet, 1988; Cholet & Bardin, 1984), cutting and fragmentation of coal, rock or metals (Conn & Rudy, 1976; Johnson, et al., 1972; Mazurkiewicz & Summers, 1982; Vijay & Brierley, 1979, Vijay, 1991; Vijay, et al., 1992) and cleaning (Vickers & Houlston, 1978; Vickers, et al., 1980), their industrial uses are not widespread. The reasons for this are: (i) the prevalent notion that cavitating jets are useful only under fully submerged environment, (ii) their peak performance occurs almost at a fixed standoff distance and is quite sensitive to slight changes in the geometric (the diversity in the nozzle designs reported in the literature is truly confusing) and operating variables (Vijay, 1987; Vijay et al., 1990, 1992) and (iii) the flow structure is highly complex and therefore, the mechanism of cavitation bubble (**vaporous, not gaseous**) inception, growth and collapse (related to performance) is not well understood (see, for example, Chahine, et al., 1984; Lai, et al., 1991, Shimizu & Yamaguchi, 1988). In this paper experimental results are presented to show that it is possible to enhance the performance of cavitating water jets by artificial submergence. The purpose of artificial submergence, as opposed to full submergence, is to confine, transport and focus cavitation bubbles, generated by any type of nozzle, on to the target material being processed. A preliminary CFD (computational fluid dynamics) analysis of the high speed coaxial flows associated with artificial submergence is also included to support this view. Details on some of the topics (for instance, CFD) discussed in this paper can be found in the publications by Lai, et al., 1991, Vijay, 1987 and Vijay, et al., 1990 & 1992.

2. EXPERIMENTAL PROGRAM

2.1 Background

A high speed water jet issuing from any type of nozzle under fully submerged environment will generate cavitation in the turbulent mixing shear layers (Conn & Johnson, 1980; Lai, et al., 1991; Shimizu & Yamaguchi, 1988). This is termed "**natural cavitation**" in this paper. In contradistinction, the term "**forced cavitation**", refers to cavitation bubbles produced by external excitement of a jet (This is beyond the scope of this paper. See Hawrylewicz, et al., 1986; Puchala & Vijay, 1984). Although a plethora of nozzle designs (Bardin & Cholet, 1988; Chahine, et al., 1984; Erdmann-Jesnitzer, et al., 1978; Johnson, et al., 1972; Lichtarowicz, 1974; Vickers & Houlston, 1978; Vijay, et al., 1990 & 1992) has been investigated to improve the performance of natural cavitating jets, the limitations alluded to above still remain. Also, intentional control of the intensity of natural cavitation (defined, for example, as number of bubbles per unit area of the jet) is not possible except, somewhat by varying the pump or the ambient pressure. Preliminary study conducted in the laboratory (Vijay, et al., 1992; see also Vickers, et al.,

1980) showed that it is possible to enhance the performance significantly by artificial submergence of the jet. However, the study also indicated that in order to achieve optimum nozzle configurations, it is important to understand the patterns of the highly complex coaxial flows. The objective of the work reported in this paper was to investigate the influence of some of the relevant variables on nozzle performance.

2.2 Nozzle and Artificial Submergence Configurations

Although a number of nozzle configurations, shown in Fig. 1 (for specifications, see Table 1), are under thorough investigation in the laboratory (for details see Vijay, et al., 1990; Vijay, et al., 1992), those of considerable interest are designated as #17 to #22. These are simply the modified versions of the centre-body nozzle designated as #3 to #5, except that the centre-body now incorporates orifices of different geometries. The principle of operation of the configurations #17 to 22 is based on the observations that (i) centre-body nozzle cavitates both in air and under fully submerged environment (Vijay, et al., 1990) and (ii) the outer annular stream not only provides the required artificial submergence for the cavitation bubbles, but also encourages further cavitation inception in the highly turbulent shear layers between the two streams. An additional advantage is that the source of water for artificial submergence is from the same pump used for generating the high speed jet, a definite advantage over the two separate sources used by Vickers, et al., 1980 and Vijay & Brierley, 1979. Also, in configurations #20 to #22, it is possible to incorporate swirling devices (turning vanes as described by Johnson, et al., 1972) in the central orifice to induce vortices in the central jet to intensify cavitation. However, the following points should be noted with regard to these configurations:

- The optimization (from the standpoint of peak performance) of these configurations requires a thorough understanding of the effect of the variables indicated in the figure { L , L' , D , d_c (diameter of the orifice in the centre-body), etc} on the complex fluid dynamics of the high speed flows. As shown in Fig. 2, the discharge coefficients of the nozzles decrease considerably as the basic centre-body configuration is changed to other forms. This is acceptable provided the losses thus incurred enhance the formation of cavitation in the jet.

In order to simulate the influence of several of the variables (L , L' , etc) on cavitating flows, experiments and the CFD analysis were conducted using a simple configuration shown in Fig. 3. In this arrangement, a high pressure nozzle ($d = 1.78$ mm) was located in a plexiglass tube which terminated in a nozzle of larger diameter. Tap water at varying flow rates was supplied to the plexiglass tube for artificial submergence of the high speed jet. Ambient pressure measured just upstream of the larger nozzle was close to atmospheric pressure.

3. RESULTS AND DISCUSSION

3.1 Fully Submerged Water Jets

A series of systematic tests was first conducted under fully submerged environment using

geometrically similar conical entry nozzles for the purpose of comparing data obtained in different environments and to deal with some of the perplexing questions or prevalent misconceptions. For instance, visualization studies have shown that the pattern of cavitating jet is quite sensitive to slight alterations in the cavitation number (Vijay, 1987). Does this influence its cutting ability? In Fig. 4, mass losses (taken as a measure of performance) of aluminum samples exposed to the jet are plotted against the standoff distance with the depth of water (h) over the sample as a parameter ($0.00298 < \sigma < 0.00306$; $\sigma = \text{global cavitation number} \approx P_a / \Delta P$ where $\Delta P = P_n - P_a$). A small increase in the cavitation number ($\approx 2.5\%$) due to an increase in the water level, decreases the erosion (mass loss) by about 11%. Although trivial in many situations, this can be quite significant in applications such as oil well cleaning or drilling. Note that the peak performance occurs almost at a fixed standoff distance ($S/d \approx 28$).

Other observations for the fully submerged case are:

Figure 5: It has been a common practice in cavitation work to test the same sample several times (Lichtarowicz, 1974). For example, to study the effect of time of exposure, the same sample is exposed to the jet for different durations, noting the mass loss after each successive test. The authors, on the other hand, used a new sample in each test, because they felt that repeated use of the same sample is perhaps inappropriate (jet in each successive test impinges on the sample already weakened in a previous test). In order to verify if the method of testing has any bearing on the results, tests were conducted in both modes at the optimum standoff distance noted above ($S/d \approx 28$). The close agreement between the two sets of results shown in Fig. 5 indicates that the two modes of testing are equally valid. This observation is quite important from the standpoint of comparing results from different sources. The figure also shows that the rate of mass loss is much higher at the optimum than other standoff distances.

Figures 6 & 7: The data in these figures show that an increase in the pressure or the nozzle diameter does not improve the performance with respect to standoff distance. That is, although mass loss increases with the increase in pressure or the nozzle diameter, the maximum performance still occurs at a fixed standoff distance.

Figures 8 & 9: These figures show the effect of increasing the hydraulic power ($H_p = 13$ and 21 kW; Fig. 8) or the flow rate ($Q_n = 36$ and 43 litre/min; Fig. 9) on performance. The combination of nozzle diameters and pressures indicated in the figures were chosen to maintain constant hydraulic power or flow rate. Contrary to the prevalent belief, note that there is no improvement with respect to the standoff distance in both cases. Also, data in Fig. 8 seem to indicate that there is an optimum nozzle diameter (1.98 mm) for given hydraulic power. For a given flow rate (Fig. 9), on the other hand, increasing the pressure appears to enhance the performance.

In summary, peak performance of fully submerged cavitating jets occurs at a fixed but short standoff distances ($15 < S/d < 30$, depending on the magnitude of operating variables). In situations where full submergence is readily available and this constraint is not severe, cavitating jets are highly beneficial (see also Vijay, et al., 1990, 1992).

3.2 Artificially Submerged Water Jets

3.2.1 Experimental Results

Variables of interest in the investigation were: diameters of the high speed water jet nozzle and the nozzle for artificial submergence (d , D ; Fig. 3), relative distance between the exit planes of the two nozzles ($H = 0$ when the inner nozzle is flush with the outer one and downstream distance is taken as negative), nozzle pressure ($P_n = \text{constant} = 34.5$ MPa in this paper), rates of flow in the inner and outer nozzles (Q_n , Q_w), standoff distance (S , measured from the exit plane of the outer nozzle) and the time of exposure (T) of the sample. Although not reported in this paper, the external profile of the inner nozzle and the inner profile of the outer nozzle will have significant influence on the performance (see Vickers, et al., 1980. This is the only publication where artificial submergence is reported in great detail).

Figure 10: In this figure mass loss results are plotted against S/d with Q_w as a parameter. The main function of the outer flow is to fully submerge the high speed jet and to promote the development of shear layers. For instance, if D is too large compared to d , Q_w should be increased so that there is no void (air) between the two streams. The data clearly show that in order to extend the effectiveness of the cavitating jet to large standoff distances ($S/d \approx 60$), and for the given value of $D = 11$ mm, the magnitude of Q_w should be in the neighbourhood of 31 litre/min, which is slightly lower than Q_n (≈ 36 litre/min at 34.5 MPa). This information is quite useful in designing nozzles of the type designated as #17 to #22 in Fig. 1. Also, erosion starts to increase at $S/d \approx 15$. This indicates that shear between the two streams (for the given value of $H = 7$ mm) starts to develop at this point. Cavitation, which develops in these shear layers (see CFD analysis results presented below in Section 3.2.2), appears to persist to a large standoff distance ($S/d \approx 90$). Thus, artificial submergence certainly seems to overcome one of the limitations of full submergence.

Figure 11: The effect of the outer nozzle diameter (D) on mass loss is indicated in this figure. Data obtained under fully submerged condition are plotted for comparison. It is immediately obvious that performance of cavitating jets developed under artificial submergence is far superior to that developed under full submergence. This is because under artificial submergence, it is possible to generate cavitation bubbles gradually and to transport them to the target material. Under full submergence, on the other hand, the bubbles disperse rapidly and collapse prematurely before reaching the target (see Vijay, et al., 1990). Another important observation from this figure is that there is an optimum outer diameter ($D = 11$ mm for the given values of other parameters) below or above which the performance deteriorates. As the values of D increase, the performance, as anticipated, approaches that of full submergence. When the values of D decrease below 11mm, the interaction between the two streams will probably lead to the formation of scattered droplets or even spray.

Figure 12: The effect of H (location of the high pressure water nozzle in the plexiglass tube) and the standoff distance on the mass loss is depicted in this figure. There is some

inconsistency in the results with respect to the effect of H. The observation that the maximum mass losses occur only at H = 7 mm is difficult to explain. In any case, the magnitude of H does have a significant influence on the performance.

Figure 13: Data plotted in this figure were obtained to compare the performance of cavitating and noncavitating jets. Another important objective was to prove that artificial submergence does not always generate slugs or droplets of water (a prevalent misconception). It is clear from the observed trends of data that the mechanism of erosion of each type of jet configuration ('in air', 'artificially submerged' and 'fully submerged') should be quite different. For example, for the case of a water jet emerging in air, the cross-sectional area of the jet increases with standoff distance and eventually breaks up into droplets (for details see Vickers, et al., 1980; Vijay, et al., 1990). Therefore, the observed increase in mass loss at large standoff distances for this configuration is due to the combined effect of both factors. Since the overall shapes of the erosion curves for the artificially and fully submerged jets are similar, it can be concluded that contribution to enhanced performance (increased mass loss) under artificial submergence, for the appropriate nozzle configuration, is from the collapse of cavitation bubbles generated in the shear layers of the two mixing streams. This will become more clear from the CFD results presented in the following section.

3.2.2 CFD Analytical Results

Due to limited length of the paper, it is not possible to delve into details of the CFD analysis. The methodology used in the analysis is reported by Lai, et al., 1991. To demonstrate the complexity of the fluid dynamics of coaxial flows, the distributions of turbulent kinetic energy (which arises due to Reynolds stresses and contributes to the development of cavitation, see Lai, et al., 1991) and local cavitation numbers are depicted in Figs. 14 and 15 for the two cases of interest in this study. For inception, the value of local cavitation number is slightly less than zero. The degree or intensity of cavitation is indicated by the negative values of σ' (local cavitation number).

Figure 14: The CFD results depicted in this figure correspond to the experimental results plotted in Fig. 12, that is, for $D = 11$ mm and $H = -3.5$ to 10.5 mm (note: turbulence kinetic energy is not shown for $H = +7$ and 10.5 mm). The results show that the low pressure region, indicated by the negative values of σ' , is located within the turbulent boundary layer between the two streams and in the boundary layer between the jet development and entrainment regions. The results clearly show that the extent of the cavitation region is highly dependent on the location of the inner nozzle in the plexiglass tube. Consider, for instance, the cases for $H = -3.5$ and 0 mm. Here the low pressure region starts right inside the plexiglass tube in the annular area between the inner nozzle and the tube. Immediately downstream of the tube exit cavitating zone is exposed to the surrounding air and therefore will not contribute to erosion of the samples. Cavitation may persist near the jet axis. Although this observation is not sufficient to fully explain the trend of the data for $H = -3.5$ or 0 mm, (Fig. 12), it does show that these values of H are not favourable for producing cavitation. Examination of the contours in Figs. 14F, G & H appears to suggest that an optimum value for H exists for which performance of cavitation

will be maximum. Notice, for instance, when $H = +7$ mm, cavitation is confined within the elongated conical zone inside the jet development region (the line for $\sigma' = 0$ is the water layer between the surrounding air and the cavitation zone).

Figure 15: The contour lines shown in this figure were obtained for $D = 18$ mm, but the outer flow (Q_w) was increased to 72 litre/min to make sure that the jet remains fully submerged. Although no experimental data were obtained for this condition, the contours do indicate that the cavitation zone is well confined within the jet development region. Once again, the cavitation zone is well developed for the case where the high pressure water nozzle is located inside the tube.

In summary, the CFD analysis confirms that it is possible to enhance the performance of cavitating jets by artificial submergence. It is now being used to analyze the flows in nozzles of the type designated as #17 to #22 in Fig. 1.

4. CONCLUSIONS

The conclusions from the results reported in this paper are:

- The usefulness of fully submerged cavitating jets is limited because the peak performance occurs almost at a fixed and short standoff distance. Increasing the pressure, flow rate or the hydraulic power does not improve this limitation. Where this is acceptable cavitating jets can be put to good use;
- The performance of artificially submerged cavitating jets operating at identical conditions surpasses that of fully submerged or noncavitating jets;
- Artificially submerged cavitating jets appear to have a great potential for a wide variety of applications. Enhancement of the performance depends a great deal on the nozzle configuration. Further work is therefore required for optimizing the nozzle configurations. CFD analysis is a valuable tool for this purpose.

5. ACKNOWLEDGMENTS

The authors are grateful to Mr. N. Paquette, Technical Officer for the Water Jet Project, for his technical assistance. Thanks are also due to Miss. K.E. Smith, Department of Mathematics and Statistics, Carleton University, Ottawa, for the computer plots shown in Figs. 14 and 15.

6. REFERENCES

- Bardin, C., and Cholet, H., "Assistance for deep drilling by cavitation damage", Proceedings of the 9th International Symposium on Jet Cutting Technology, pp. 611-628, BHRA, Cranfield, Bedford, England, 1988.
- Chahine, G.L., Genoux, P.F., and H.L. Liu, "Flow visualization of numerical simulation of

- cavitating self-oscillating jets", Proceedings of the 7th International Symposium on Jet Cutting Technology, Paper A2, pp. 13-32, BHRA, Cranfield, Bedford, England, 1984.
- Cholet, H.J., and Bardin, C.A., "Jet-assisted oil drilling", Proceedings of the 7th International Symposium on Jet Cutting Technology, Paper A3, pp. 33-50, BHRA, Cranfield, Bedford, England, 1984.
- Conn, A.F., and Johnson, V.E., "The fluid dynamics of submerged cavitating jet cutting", Proceedings of the 5th International Symposium on Jet Cutting Technology, Paper A1, pp. 1-14, BHRA, Cranfield, Bedford, England, 1980.
- Conn, A.F., and Rudy, S.L., "Cutting coal with the cavijet cavitating water jet method", Proceedings of the 3rd International Symposium on Jet Cutting Technology, Paper D8, pp. X41-49, BHRA, Cranfield, Bedford, England, 1976.
- Erdmann-Jesnitzer, F., Louis, H., and Hassan, A.M., "A study of the effect of nozzle configuration on the performance of submerged water jets", Proceedings of the 3rd International Symposium on Jet Cutting Technology, Paper A2, pp. 21-38, BHRA, Cranfield, Bedford, England, 1978.
- Hawrylewicz, B.M., Puchala, R.J., and Vijay, M.M., "Generation of pulsed or cavitating jets by electric discharges in high speed continuous water jets", Proceedings of the 8th International Symposium on Jet Cutting Technology, Paper 36, pp. 345-352, BHRA, Cranfield, Bedford, England, 1986.
- Johnson, V.E., Kohl, R.E., Thiruvengadam, A., and Conn, A.F., "Tunnelling, fracturing, drilling and mining with high speed water jets utilizing cavitation damage", Proceedings of the 1st International Symposium on Jet Cutting Technology, Paper A3, pp. 37-55, BHRA, Cranfield, Bedford, England, 1972.
- Johnson, V.E., Conn, A.F., Lindenmuth, W.T., Chahine, G.L., and Frederick, G.S., "Self-resonating cavitating jets", Proceedings of the 6th International Symposium on Jet Cutting Technology, Paper A1, pp. 1-25, BHRA, Cranfield, Bedford, England, 1982.
- Lai, M.K.Y., Vijay, M.M., and Zou, C., "Computational fluid dynamics analysis of submerged cavitating water jets", Proceedings of the 6th American Water Jet Conference, pp. 411-426, Water Jet Technology Association, St. Louis, Missouri, USA, 1991.
- Lichtarowicz, A., "Experiments with cavitating jets", Proceedings of the 2nd International Symposium on Jet Cutting Technology, Paper D1, pp. 1-6, BHRA, Cranfield, Bedford, England, 1974.
- Mazurkiewicz, M., and Summers, D.A., "The enhancement of cavitation damage and its use in rock disintegration", Proceedings of the 6th International Symposium on Jet

- Cutting Technology, Paper A2, pp. 27-38, BHRA, Cranfield, Bedford, England, 1982.
- Puchala, R.J., and Vijay, M.M., "Study of an ultrasonically generated cavitating or interrupted jet: aspects of design", Proceedings of the 7th International Symposium on Jet Cutting Technology, Paper B2, pp. 69-82, BHRA, Cranfield, Bedford, England, 1984.
- Shimizu, S., and Yamaguchi, A., "Structure of cavitating jets and its effects on erosion", Proceedings of the 9th International Symposium on Jet Cutting Technology, Paper A1, pp. 1-12, BHRA, Cranfield, Bedford, England, 1988.
- Vickers, G.W., and Houlston, R., "Surface cleaning using water-jet cavitation and droplet erosion", Proceedings of the 4th International Symposium on Jet Cutting Technology, Paper H1, pp. 1-18, BHRA, Cranfield, Bedford, England, 1978.
- Vickers, G.W., Harrison, P.W., and Houlston, R., "Extending the range of cavitation cleaning jets", Proceedings of the 5th International Symposium on Jet Cutting Technology, Paper J1, pp. 403-412, BHRA, Cranfield, Bedford, England, 1980.
- Vijay, M.M., and Brierley, W.H., "A study of erosion by high pressure cavitating and noncavitating water jets", Proceedings of the Conference on Erosion: Prevention and Useful Applications, pp. 512-529, ASTM STP 664, American Society for Testing and Materials, New York, USA, 1979.
- Vijay, M.M., "Some aspects of high speed cavitating water jets", Proceedings of the International Water jet Symposium (Beijing, China), pp. 2:59-74, Colorado School of Mines, Golden, Colorado, USA, 1987.
- Vijay, M.M., Zou, C., and Tavoularis, S., "A study of the characteristics of cavitating water jets by photography and erosion", Proceedings of the 10th International Symposium on Jet Cutting Technology, Chapter 3, pp. 37-67, Elsevier Applied Science, London, England, 1990.
- Vijay, M.M., "Comparison of the performance of high-speed abrasive-entrained, cavitating and plain water jets for selective mining applications", Proceedings of the 6th American Water Jet Conference, pp. 195-212, Water Jet Technology Association, St. Louis, Missouri, USA, 1991.
- Vijay, M.M., Remisz, J., Tavoularis, S., Zou, C., and Hu, S.G., "A study of the practicality of cavitating water jets", Proceedings of the 11th International Symposium on Jet Cutting Technology, pp. 75-99, Kluwer Academic Publishers, London, England, 1992.

8. NOMENCLATURE

- d Nozzle orifice diameter (mm)
- d_c Diameter of the orifice in the centre-body (inner orifice, see Fig. 1)

- D Diameter of the exit hole of the plexiglass tube (mm)
 d_e Equivalent nozzle orifice diameter (mm)
 E_v Specific energy (J/cm³ or MJ/m³)
h Depth of water over the sample submerged in a tank of water (mm)
H Distance between the exit planes of the nozzle and the plexiglass tube (mm)
 H_p Hydraulic power (kW)
k Turbulence kinetic energy
 P_a Ambient pressure (MPa)
 P_n Pump pressure (MPa)
 Q_n Flow rate of water through the high pressure nozzle (litre/min)
 Q_w Flow rate of water through the plexiglass tube (litre/min)
S Standoff distance (m)
T Time of exposure of the sample to the jet (min)
 σ Global cavitation number
 σ' Local cavitation number

Table 1. Design specifications of basic nozzle configurations shown in Fig. 1

Nozzle #	1	13	2	3	4	5	6*	12*
d (mm)	1.78	1.60	1.78	1.78	1.78	1.78	3.05	3.05
d_e (mm)	1.78	1.60	1.78	1.78	1.78	1.78	1.78	1.78
d'							1.59	1.59
L/d_e	2.0	2.0	2.0	2.0	2.0	2.0	2.0	2.0
α	20°	20°	180°	20°	20°	20°	20°	20°
L' (mm)				23.8	28.2	32.7		
L''							0.0	30.5
θ								5°

* For the specifications of nozzles 4B to 4F see Vijay, et al., 1990 (designated as #7 to #11).

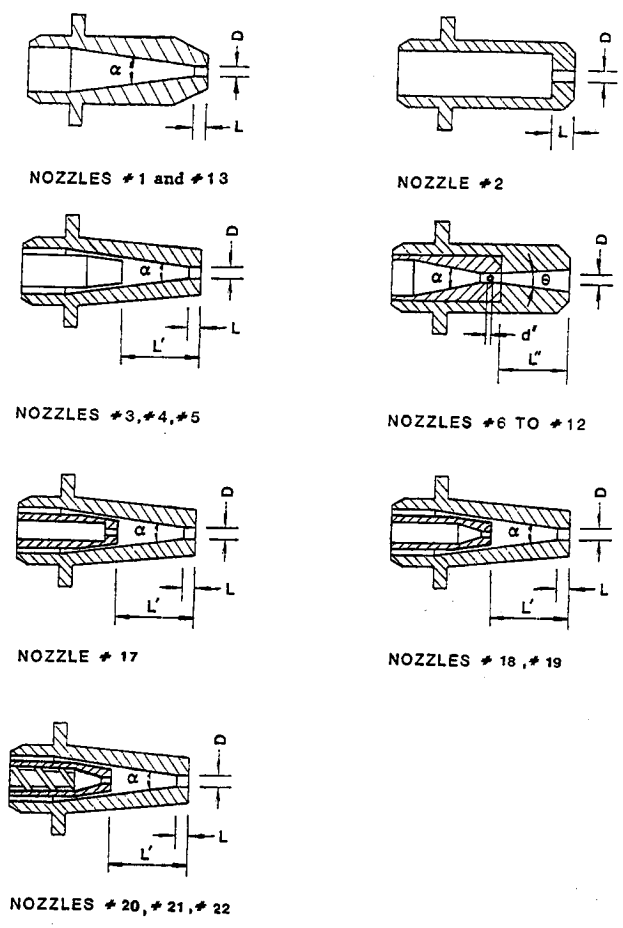


Fig. 1 Schematics of the nozzles under study (See Table 1).

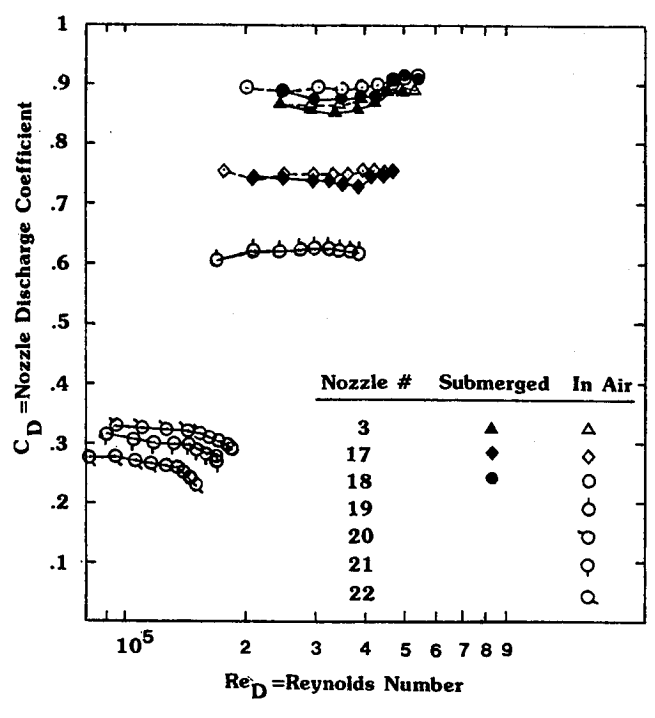


Fig. 2 Plot of nozzle discharge coefficients against Reynolds number.

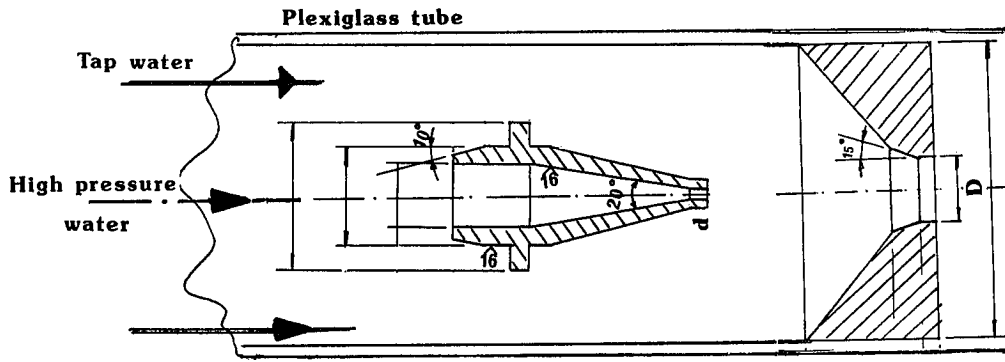


Fig. 3 A schematic of the arrangement for artificial submergence of nozzles

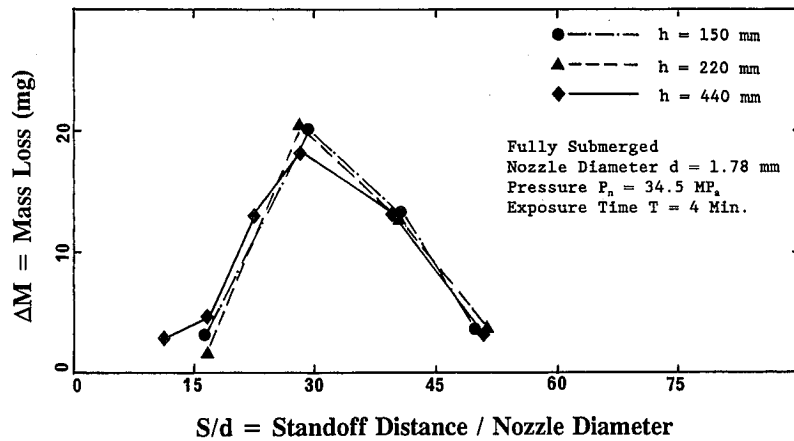


Fig. 4 Plot showing the effect of h (depth of water over the sample) and S/d on mass loss

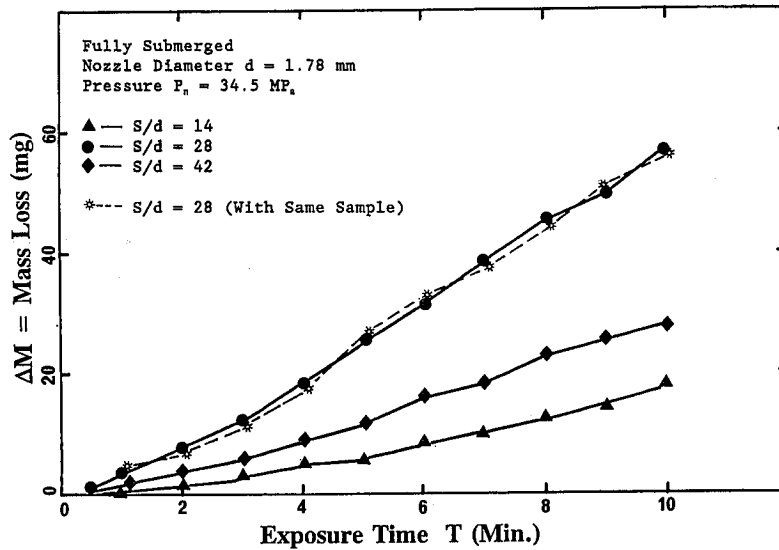


Fig. 5 Plot showing the effect of time of exposure (T) and the method of testing on the mass loss

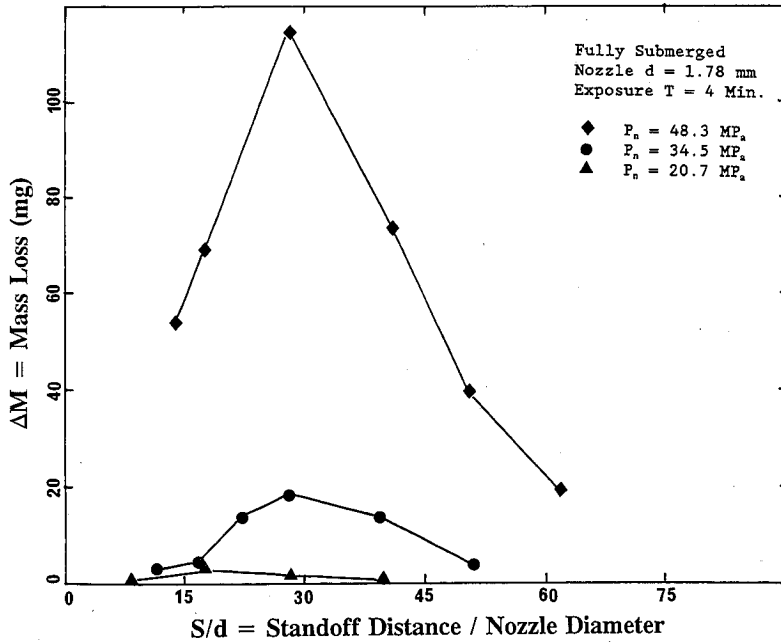


Fig. 6 Plot showing the effect of S/d and nozzle pressure (P_n) on mass loss for 1.78 mm nozzle

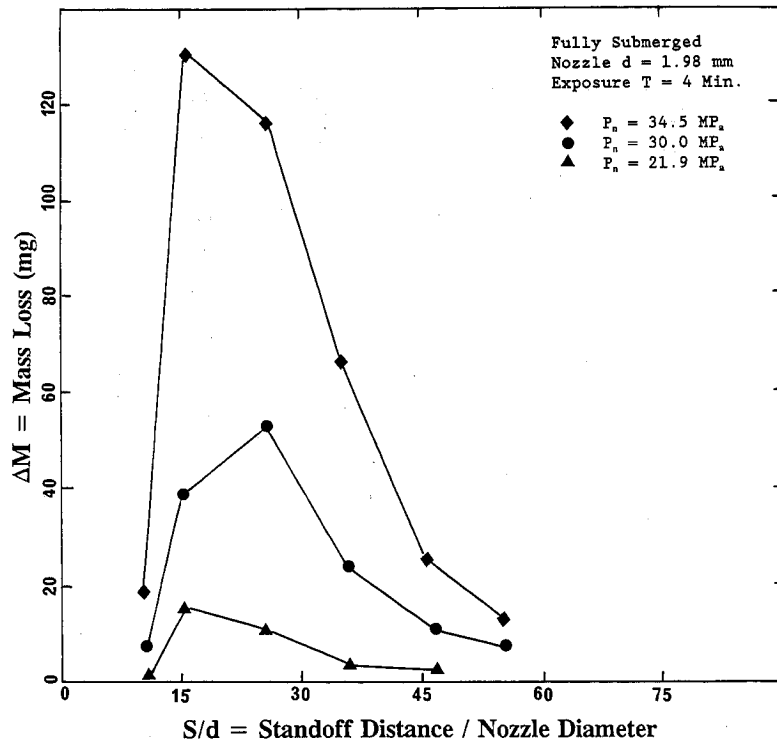


Fig. 7 Plot showing the effect of S/d and nozzle pressure (P_n) on mass loss for 1.98 mm nozzle

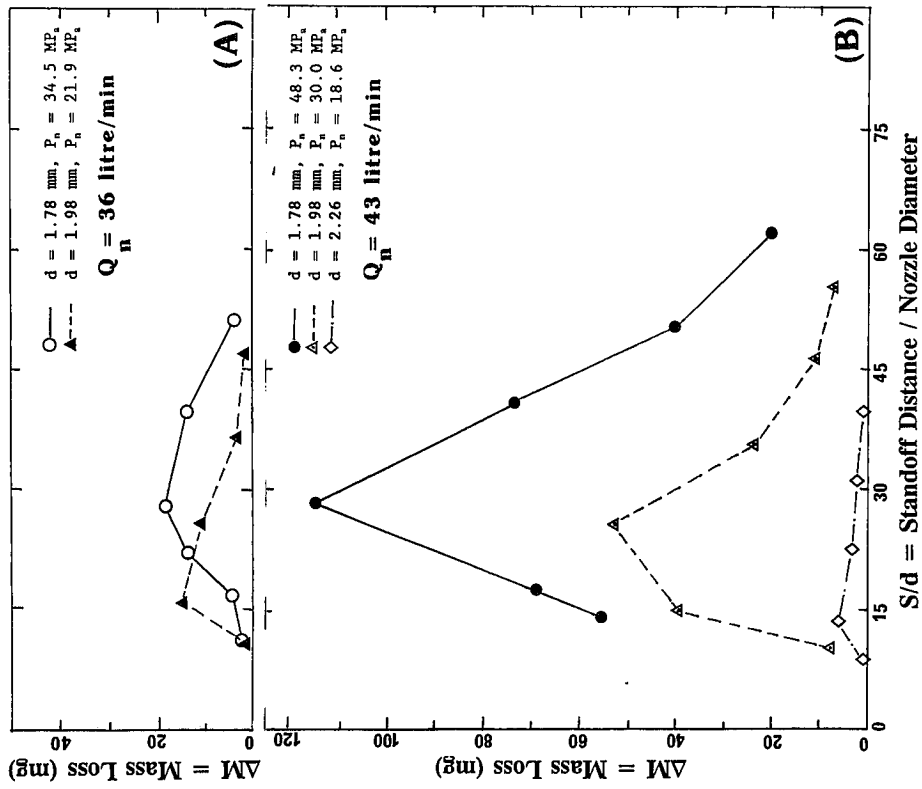


Fig. 9 Plot showing the effect of S/d and nozzle flow rate (a) 36 litre/min, (b) 43 litre/min (obtained by a combination of nozzle pressures and diameters as indicated) on mass loss.

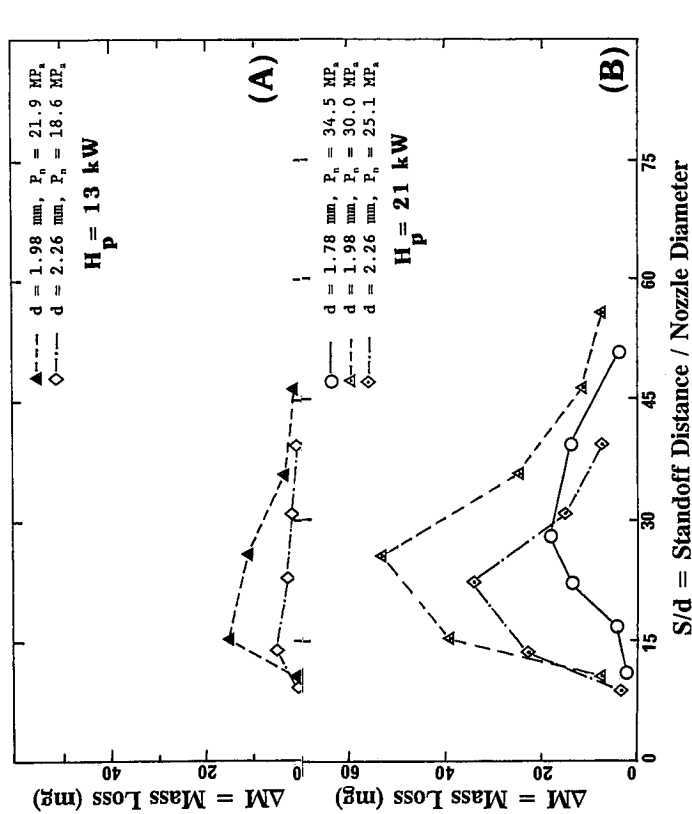


Fig. 8 Plot showing the effect of S/d and hydraulic power (a) 13 kW, (b) 21 kW (obtained by a combination of nozzle pressures and diameters as indicated) on mass loss.

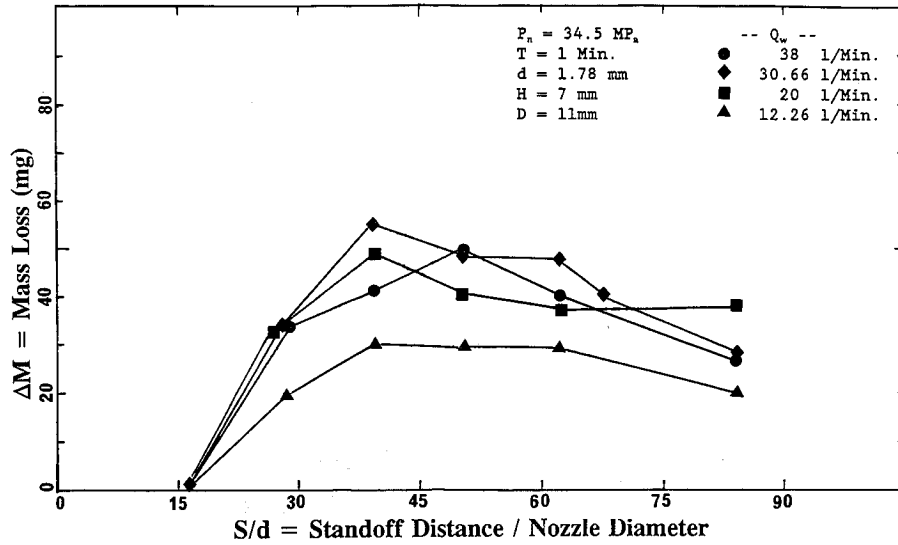


Fig. 10 Plot showing the effect of S/d and the flow rate in the plexiglass tube (Q_w) on mass loss

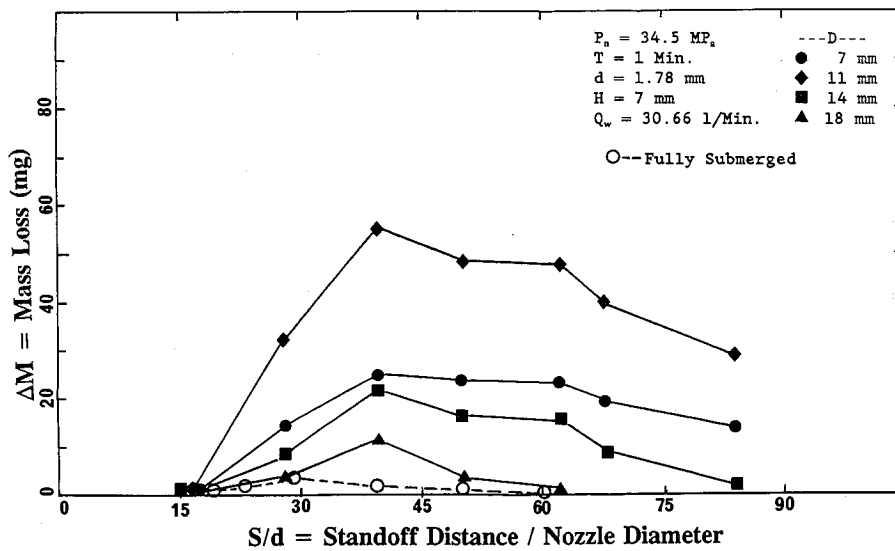


Fig. 11 Plot showing the effect of S/d and the outer nozzle diameter (D) on mass loss

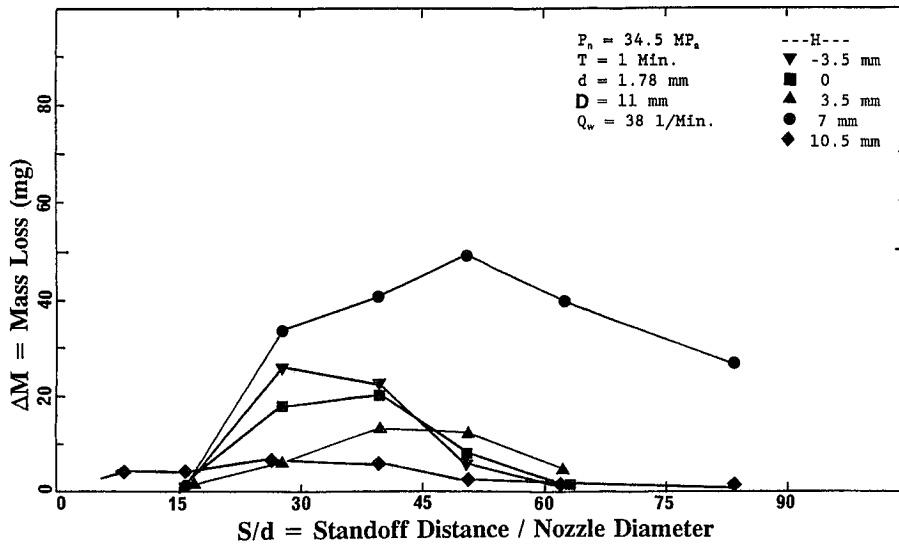


Fig. 12 Plot showing the effect of S/d and the distance between the inner and outer nozzles (H) on mass loss

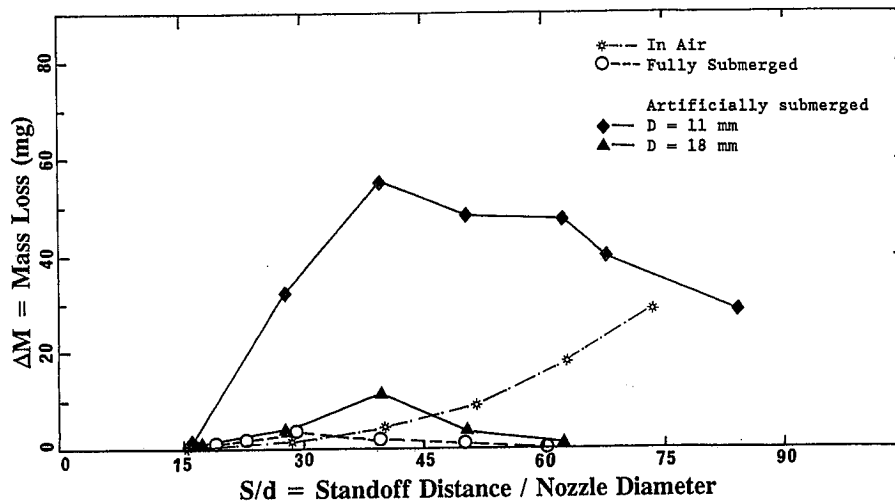


Fig. 13 Comparison of the performance of artificially and fully submerged cavitating and noncavitating (jet in air) water jets

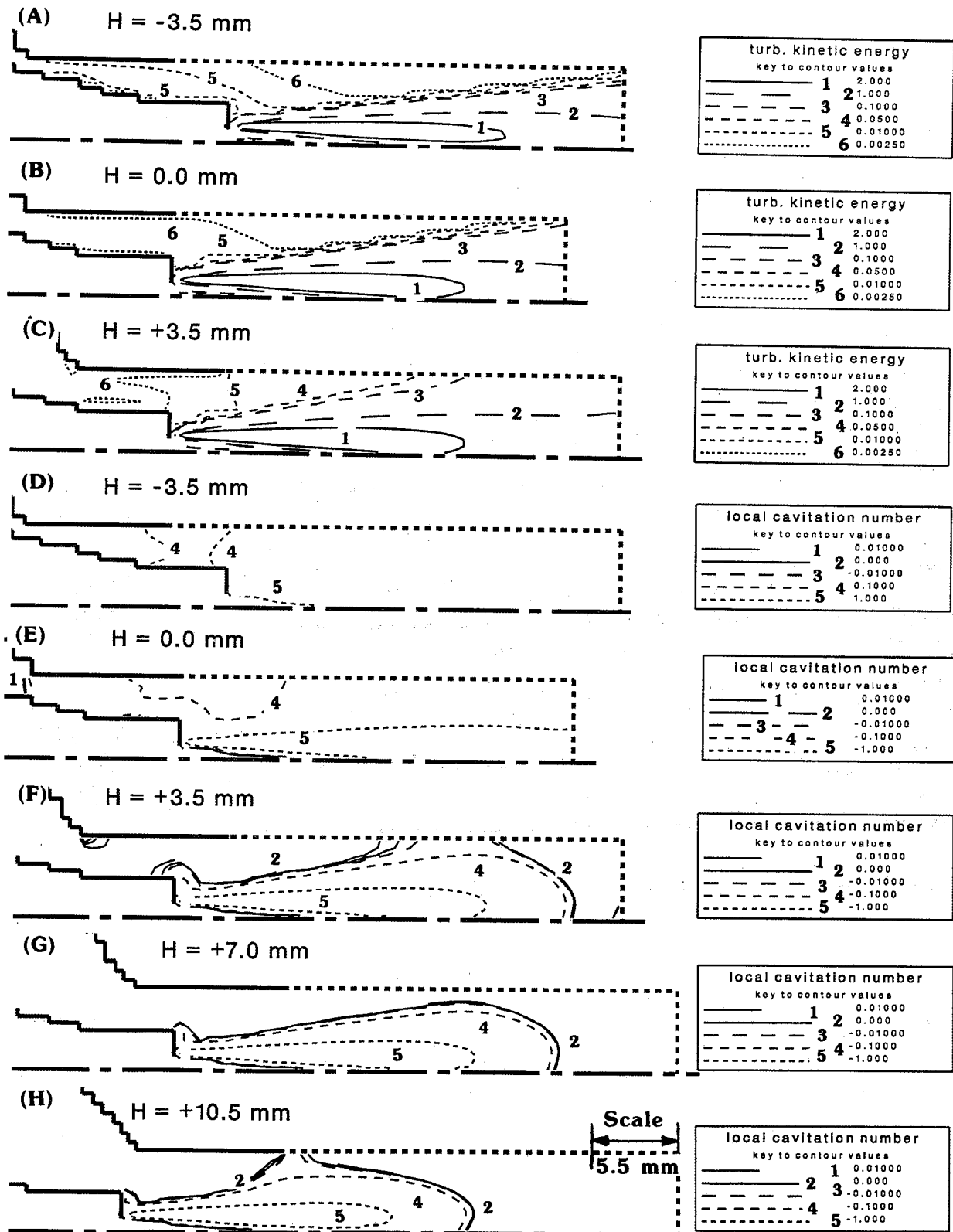
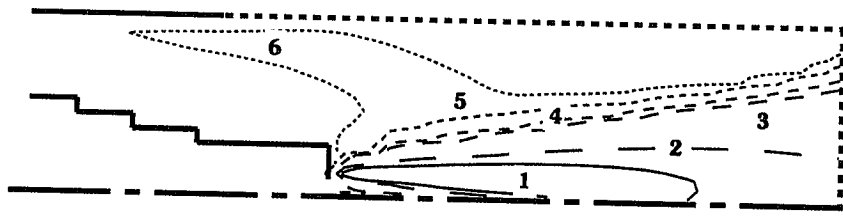


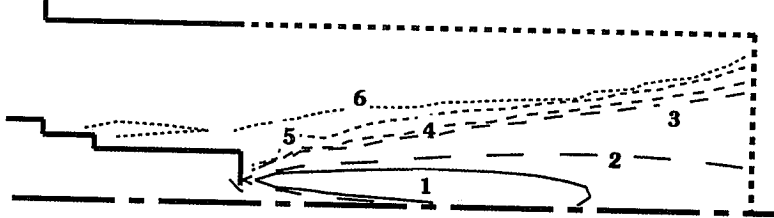
Fig. 14 Distribution of turbulence kinetic energy (k) and local cavitation number (σ') predicted by CFD analysis for the experimental conditions shown in Fig. 12.
 $P_n = 34.5$ MPa, $d = 1.78$ mm, $D = 11$ mm, $Q_w = 38$ litre/min

(A) CONFIGURATION #2 (H = -5.3 mm)



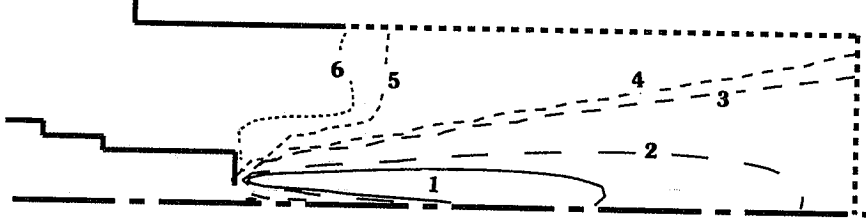
turb. kinetic energy	
key to contour values	
1	2.000
2	1.000
3	0.1000
4	0.0500
5	0.01000
6	0.00250

(B) CONFIGURATION #1 (H = 0.0 mm)



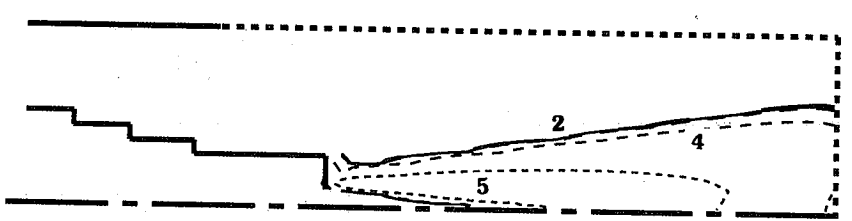
turb. kinetic energy	
key to contour values	
1	2.000
2	1.000
3	0.1000
4	0.0500
5	0.01000
6	0.00250

(C) CONFIGURATION #3 (H = +5.3 mm)



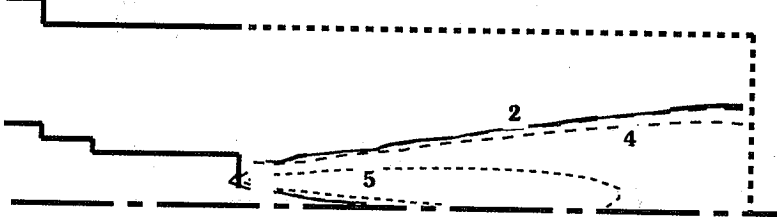
turb. kinetic energy	
key to contour values	
1	2.000
2	1.000
3	0.1000
4	0.0500
5	0.01000
6	0.00250

(D) CONFIGURATION #2 (H = -5.3 mm)



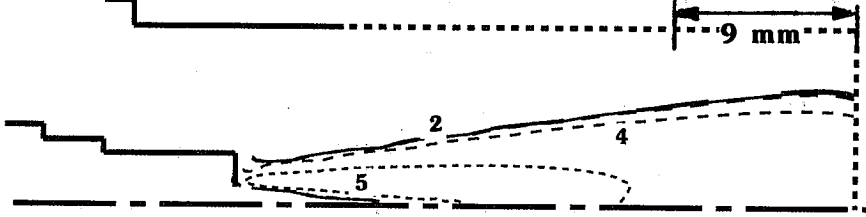
local cavitation number	
key to contour values	
1	0.01000
2	0.000
3	-0.01000
4	-0.1000
5	-1.000

(E) CONFIGURATION #1 (H = 0.0 mm)



local cavitation number	
key to contour values	
1	0.01000
2	0.000
3	-0.01000
4	-0.1000
5	-1.000

(F) CONFIGURATION #3 (H = +5.3 mm)



local cavitation number	
key to contour values	
1	0.01000
2	0.000
3	-0.01000
4	-0.1000
5	-1.000

Fig. 15 Distribution of turbulence kinetic energy (k) and local cavitation number (σ') predicted by CFD analysis for the conditions indicated below.

$D = 18 \text{ mm}$, $P_n = 34.5 \text{ MPa}$, $d = 1.78 \text{ mm}$, $Q_w = 72 \text{ litre/min}$

The Influence of Ambient Pressure and Nozzle Shape on Submerged Water Jet Velocity and Spreading

Kenneth M. Kalumuck, Georges L. Chahine, and Gary S. Frederick

DYNAFLOW, Inc.
7210 Pindell School Rd.
Fulton MD 20759

Abstract

Submerged jet flow data are typically based on noncavitating conditions. However, it is expected that cavitation would extract energy from the flow and affect jet mixing and spreading. To investigate the effect of the presence and the amount of cavitation on jet behavior, experiments were run in which the cavitation number was varied by changing the ambient pressure for a fixed value of the jet discharge velocity. A range of conditions from no cavitation to developed cavitation was covered. Jet flow dispersion patterns were made visible by dye injection. Centerline jet velocities were measured as a function of distance from the nozzle with a pitot tube at distances up to 140 nozzle diameters.

Three nozzle shapes were compared at a fixed nozzle pressure drop and ambient pressure. Results showed slower velocity decay with downstream distance for a contoured nozzle compared to conical and straight sided nozzles.

Increasing amounts of cavitation in the jet flow was found to increase jet spreading and decrease jet velocity at a given distance downstream thus reducing standoff distance at which the jet is effective. These results underline the importance of conducting tests at cavitation numbers comparable to those expected in practice. They also suggest that, for a fixed discharge velocity, jet performance would be degraded at shallower depths and improve at greater depths (until cavitation is suppressed). At a fixed ambient pressure, an increase in the nozzle discharge velocity may not improve results as much as expected due to an increase in the amount of cavitation.

1 Experimental Setup

Experiments were conducted in DYNAFLOW's High Pressure Cell (HPC) capable of ambient pressures up to 20.7 MPa (3000 psi). A sketch of the HPC is presented in Figure 1. The HPC is a cylindrical pressure vessel with inside dimensions of approximately 24 cm (9.5 inch) diameter and 71 cm (28 inch) length with three quartz view ports circumferentially spaced and located near its mid length. Constructed for studies of deep hole drilling with cavitating jets, it includes a rotating fixture in which rocks are placed and rotated for cutting beneath the jet. Ambient pressure is adjusted and maintained by a choke plate which acts as a back pressure valve in the outflow line. The jet flow is driven by a Weatherford five piston positive displacement pump capable of up to 76 liters/min (20 gpm) at 69 MPa (10,000 psi). More details of the experimental setup and the work conducted can be found in Kalumuck et al. (1991).

Three different jet nozzle designs were utilized. The first employed a smooth contoured contraction from the upstream diameter to the orifice to preclude separation. The second design consisted of a 45 degree conical section followed by a straight section. Design 3 was an 18 degree conical nozzle. The nozzles were machined from 316 Stainless Steel pipe plugs with an orifice of 2.69 mm (0.106 in). Great care was taken in the fabrication to obtain smooth inner walls. The nozzles were mounted in-line to sections of stainless steel tubing that were inserted into the HPC feed tube.

1.1 Scaling

In many applications, it is desirable to maximize the "reach" or the downstream distance at which the jet can maintain a desired velocity or stagnation pressure. In many cases, controlled scale model experiments can be conducted to investigate the influence of different design and operating conditions on jet "reach". For proper scaling of the jet velocity versus distance relation and thus jet "reach", the nozzle shape should be identical to the full scale nozzle but reduced or increased in size by the scale factor. Other quantities must then be properly scaled. The basic scaling law to employ is the turbulent jet velocity decay relation (Rajaratnam, 1976):

$$\frac{u}{U_0} = C \frac{d_0}{x}, \quad (1)$$

where $C = 6.3$ in the absence of cavitation for a circular turbulent jet of initial diameter d_0 and velocity U_0 , and u is the centerline jet velocity at a distance x downstream of the nozzle.

The other important factor is the Cavitation Number, σ , given by:

$$\sigma = \frac{P_a - P_v}{\Delta P} \quad (2)$$

Here, ΔP is the pressure drop across the nozzle, P_a the ambient pressure, and P_v the vapor pressure of the liquid. The cavitation number must be approximately the same in the model and full scale systems for cavitation effects to be properly accounted for. Matching of the Reynolds Number is less important if the flow is highly turbulent in both model and full scale.

The pressure drop across the nozzle, ΔP , is taken to be the difference between the measured pressures in the line immediately upstream of the HPC and the ambient cell pressure. The discharge coefficient, C_d , is related to the volumetric flow rate, Q , the jet velocity at the nozzle exit, U_0 , and the nozzle orifice diameter, d_0 , by:

$$C_d = \frac{Q}{\frac{\pi}{4} d_0^2 U_0} \quad (3)$$

The jet velocity is related to ΔP , and the liquid density ρ by

$$U_0 = \sqrt{\frac{2\Delta P}{\rho}} \quad (4)$$

Combining these, the discharge coefficient is found from the measured pressure drop and flow rate:

$$C_d = \frac{Q}{\sqrt{\Delta P}} \sqrt{\frac{\rho}{2}} \frac{4}{\pi d_0^2} \quad (5)$$

The jet velocity at a given downstream location, x , can be related to the jet pressure and flow rate by combining expressions (1,3,4) above to obtain

$$u \sim \frac{1}{x} \left(\frac{Q}{C_d} \right)^{0.5} (\Delta P)^{0.25} \quad (6)$$

Thus it can be seen that for the same pumping power (given by the product of pressure and flow rate), greater downstream velocities can be attained by increasing the flow rate (by increasing the jet diameter) than by increasing the nozzle pressure drop. An increase in the nozzle pressure drop is shown below to result, under certain conditions, in an increase in jet cavitation which decreases downstream velocities below those given by the idealized relations above.

1.2 Jet Flow Visualization and Velocity Measurements

Two types of tests were conducted: jet flow pattern visualization and jet velocity measurement downstream of the nozzle. The tests were conducted at two discharge velocities – 36 and 200 m/s – at varying ambient pressures up to 9.3 Mpa (1350 psi). These jet velocities correspond to pressure drops across the nozzle, ΔP , of 0.66 and 20 MPa (95 and 2900 psi).

The jet flow dispersion patterns were made visible by injection of a red dye into the feed pipe upstream of the nozzle. The dye injection system used in these tests consisted of a 0.5 liter stainless steel sample cylinder used as a dye reservoir, filled with red dye, and connected by pipe tee's in parallel with the main nozzle feed pipe just upstream of the entrance to the high pressure cell. Regulating valves were employed at the dye reservoir inlet and outlet and a ball valve in the main line between the reservoir inlet and outlet was used to adjust the main line pressure drop to enhance the flow through the dye reservoir.

Using a Cannon Hi 8 Digital Video Camera and back lighting with a strobe light through a view port, video recordings were made of the jet flows made visible with dye injections. The strobe flash had a duration of 50 microseconds. Individual frames could then be taken from the video using a 35 mm camera and 21 inch color video monitor. The HPC quartz window view ports are 3.8 cm in diameter. However, due to the jet being at a distance from the back lit view port, the area of illumination has a diameter of approximately 3.3. To observe different jet downstream locations, the nozzle was moved relative to the view port. At approximately 30 orifice diameters, the jet flow had spread to cover the entire field of view, and thus useful pattern visualization could be obtained only at distances less than this. High speed movies at frame rates from 3000 to 5000 frames per second were also taken with a Hycam II 16 mm high speed camera with back and side lighting.

Measurements of jet velocity were made using a pitot tube mounted to an arm that could be rotated and translated from outside the cell. The 0.3175 cm (1/8 in.) O.D. pitot tube was fitted with copper tubes which ran through the cell lid to a Pace P7D Transducer. Three interchangeable transducers were used having different maximum ranges (0.069, 0.69, and 1.7 MPa) (10, 100, and 250 psi). A CD-10 carrier demodulator signal conditioning unit and digital voltmeter were employed in conjunction with the transducers. The transducers were calibrated against a Heise Precision Pressure Gage.

Readings of jet centerline velocity as a function of distance from the jet were obtained by adjusting both the height of the nozzle and the position of the pitot tube. Care was taken to align the pitot tube along the jet axis. In addition, the pitot tube was

rotated across the jet to find the peak velocity at a given distance from the nozzle – which corresponds to the jet centerline velocity. Measurements were made at distances up to $x = 38$ cm ($x/d_0 \approx 140$).

2 Nozzle Shape Effects

Measured centerline jet velocities for the three nozzle types are presented in Figures 2 and 3 for the case of a 200 m/s discharge velocity at an ambient pressure of 4.8 MPa (700 psi) at distances from the nozzle of up to 140 orifice diameters. Results are shown for 2 copies of the contoured design and one nozzle fabricated for each of the other two designs. The small differences in the performance of the nozzles 1-I and 1-II is likely due to machining imprecisions. Although the differences in downstream velocities for the three shapes are not large, they can be significant if one wishes to maximize the “reach” of the jet - i.e., the distance at which some threshold velocity or stagnation pressure (proportional to the square of the velocity) is achieved.

Design 1 provides the highest downstream velocities, particularly at large downstream distances. Design 3 (conical) is as good or better near the nozzle but results in a jet velocity of only 0.85 that of nozzle 1-I at 105 orifice diameters downstream (corresponding to a stagnation pressure of only 0.72 that of 1-I). Given the flatness of the velocity vs. distance curves at large downstream distances, these differences could translate into significant differences in jet “reach”. Nozzle 2 produced the lowest velocities near the nozzle. Its relative performance improved somewhat further downstream.

The contoured nozzle design was selected for evaluation of the effects of ambient pressure variation presented in the next section.

3 Cavitation Number Effects

Classical submerged jet flow data (e.g. Rajaratnam, 1976) are typically based on non-cavitating jet flows. However, cavitation will be present in the jet flow for conditions at which the cavitation number, σ , defined above in equation (2), is below approximately 0.5.

In order to investigate the effect that the presence and the amount of cavitation has on the behavior of the jet and on the downstream jet velocity, a series of experiments were run in which the cavitation number was varied by changing the ambient pressure in the cell for a fixed value of the jet discharge velocity (nozzle pressure drop). Ambient pressures, and thus σ , were selected such that the range of conditions from no cavitation to large amounts of cavitation was covered. This range of conditions at which to conduct

the tests were selected by visually observing the amount of cavitation in the jet as the ambient pressure was varied.

Figure 4 presents photographs of the effect of cavitation number variation on dye visualizations of the jet flows taken from videos over a range of σ for the case of $\Delta P = 20$ MPa (2900 psi) corresponding to $U_0 = 200$ m/s. Results at ambient pressures of 2.1, 4.8, and 9.3 MPa (300, 700, and 1350 psi) corresponding to $\sigma = 0.1, 0.24,$ and $0.47,$ respectively, are shown. Shown for each case are views at two locations – the left edge of the view port is at the nozzle in the left frame and at 5.1 cm downstream in the right frame. The two frames for a given case were taken from a different experimental run at the same conditions. It should also be noted that these are views taken at a particular instant of time, and although the turbulent jet is steady in the mean, the instantaneous location of the turbulent structures - and thus the dye edge - varies in time (as was observed from the high speed movies and the videos).

The case of $P_a = 9.3$ MPa (1350 psi) is approximately at cavitation inception, and negligible cavitation is observed. Moderate cavitation, within a few diameters of the nozzle, can be observed at a cavitation number of 0.24. Significant amounts of cavitation persisting more than 12 diameters downstream can be observed in the jet flow for $\sigma = 0.1.$

The effect on jet velocity is shown in Figures 5 and 6 which compare the measured velocities for these three cases. Figure 6 presents the data of Figure 5 normalized by the measured velocity for the case of $P_a = 4.8$ MPa (700 psi). At $P_a = 2.1$ MPa (300 psi), the increased cavitation is seen to decrease the downstream jet velocity by approximately 5-12 % relative to the case of $P_a = 4.8$ MPa (700 psi). Similarly, suppression of cavitation by raising the ambient pressure to 9.3 MPa (1350 psi) is seen to increase the downstream jet velocity by approximately 8-12 % over the $P_a = 4.8$ MPa case. (One measured point, at $x/d_0 = 85,$ does not follow this trend and is believed to be an experimental error).

The measured discharge coefficients are also affected by the cavitation number. For $P_a = 4.8$ MPa, $C_d = 0.98.$ At an ambient pressure of 2.1 MPa, C_d drops to 0.94 while at $P_a = 9.3$ MPa, C_d was measured to be 1.03. This value larger than 1.0 could be due to the jet attaching slightly to the outside of the nozzle, thus effectively increasing the orifice size or to a combination of measurement uncertainties or both. The trend of decreasing discharge coefficients with increasing amounts of cavitation (decreasing σ), however, is clear, and is supported by the velocity measurements discussed above.

An analysis of the spreading angle of the jets was conducted. Due to the unsteady movement of the dye edge by the turbulence, different instantaneous views of the jet

will yield different angles. Thus an approximate average of the position of the dye edge was measured to estimate the spread angles. These estimates were made at a number of locations and for a number of different frames. The spread angle is defined to be that between one side of the jet and the other. Thus angles with respect to the center line are half these.

The jet spreading angle was found to increase with decreasing ambient pressure or cavitation number (11.3, 12.2, and 13 degrees for $P_a = 9.3, 4.8,$ and 2.1 MPa, respectively) which is consistent with the velocity and discharge coefficient behavior.

For $\Delta P = 0.66$ MPa (95 psi) ($U_0 = 36$ m/s), $\sigma = 7.5$ (well above cavitation inception) and there is no cavitation at $P_a = 4.8$ MPa. The ambient pressure was reduced to the lowest possible in our cell - 34 KPa above atmospheric ($\sigma = 0.21$). Only light cavitation was observed. Thus, for $U_0 = 36$ m/s, little influence of the ambient pressure was observed. This is consistent with the jet velocity measurements presented in Figure 7, where the effect of the reduced ambient pressure is seen to insignificantly change the measured jet velocities. There was also no measurable variation in discharge coefficient between the two cases.

The results of jet velocities, spreading angles, and discharge coefficients all point to poorer jet performance with increased amounts of cavitation (decreasing σ) at 200 m/s discharge velocity. This underlines the importance of conducting tests at cavitation numbers comparable to those expected for the full scale application. It also suggests that, for a fixed discharge velocity, jet performance would be expected to degrade at shallower depths and improve to some degree at greater depths (until cavitation is suppressed). Similarly, at a fixed ambient pressure, an increase in the nozzle discharge velocity may not improve results as much as expected due to an increase in the amount of cavitation. This suggests that to increase the standoff distance at which a jet is effective, it is better to increase the flow rate through the use of larger nozzle diameters rather than to increase the jet velocity with a higher pressure drop across the nozzle which will decrease the cavitation number.

4 Conclusions

A contoured nozzle shape was shown to result in larger downstream velocities than either a conical or a combined conical/straight design when operated at the same pressure drop and flow rate. The effect of variation of the cavitation number in submerged jet flows by varying the ambient pressure was seen to be significant when cavitation occurred. Relative to the case of $\sigma = 0.24$, (4.8 MPa or 700 psi ambient pressure), raising the ambient pressure to 9.3 MPa (1350 psi) resulting in $\sigma \approx 0.5$, prevented cavitation and

resulted in an increase in measured downstream velocity of approximately 10 %. A reduction in ambient pressure to 2.1 MPa (300 psi) corresponding to $\sigma \approx 0.1$ resulted in a comparable decrease of approximately 10 % in jet velocity (below that of the case for $\sigma = 0.24$). Discharge coefficients were seen to decrease and jet spread angles to increase with increasing cavitation (decreasing ambient pressure). Thus increased amounts of cavitation are seen to decrease downstream jet velocity which would likely decrease jet effectiveness, particularly at large standoffs, in any application where jet velocity or stagnation pressure are important. This is important to keep in mind when considering operating at significantly different depths and/or jet velocities. It also highlights the need to perform testing at cavitation numbers comparable to those expected in the actual full scale application.

5 Acknowledgements

The results presented here are based on work supported by Imperial Oil Resources Limited.

6 References

Kalumuck, K. M. and Chahine, G. L., and Frederick, G. S. "Small Scale Experimental Evaluation of Submerged Water Jet Nozzles," DYNAFLOW, Inc., Technical Report 91014-1, December 1991.

Rajaratnam, N., "Developments in Water Science 5: Turbulent Jets," Elsevier, Amsterdam, 1976.

7 Nomenclature

C_d , discharge coefficient defined in equation (3)

P_a , ambient pressure

P_v , vapor pressure of the liquid

ΔP , nozzle pressure drop

x , distance from orifice along jet centerline

u , jet centerline velocity in x direction

U_0 , average jet velocity at orifice

ρ , liquid density

σ , cavitation number defined in equation (2)

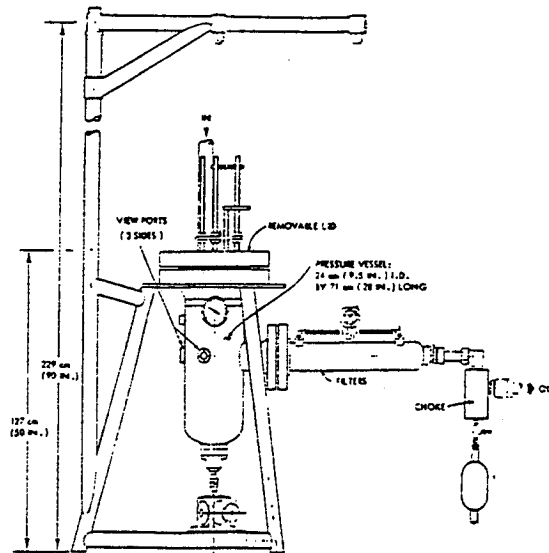


FIGURE 1. HIGH PRESSURE CELL (HPC) FOR JET TESTING AND EXPERIMENTATION AT ELEVATED AMBIENT PRESSURES UP TO 20.7 MPa (3,000psi).

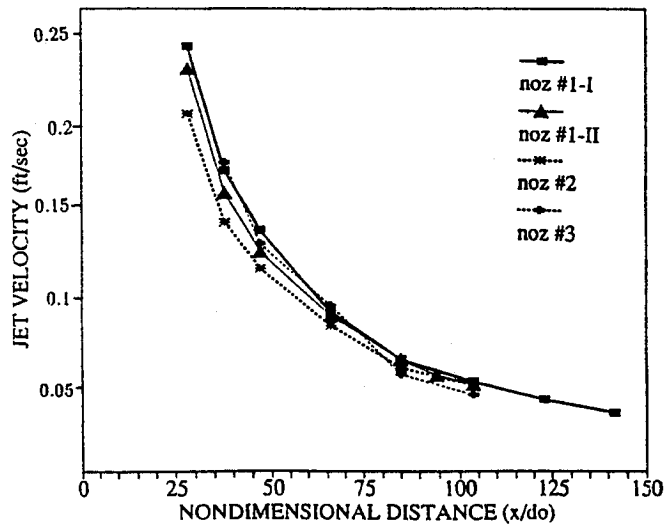


FIGURE 2. INFLUENCE OF NOZZLE SHAPE ON MEASURED JET VELOCITIES, $U_0 = 200m/s$, $P_a = 4.8MP_a$ (700psi)

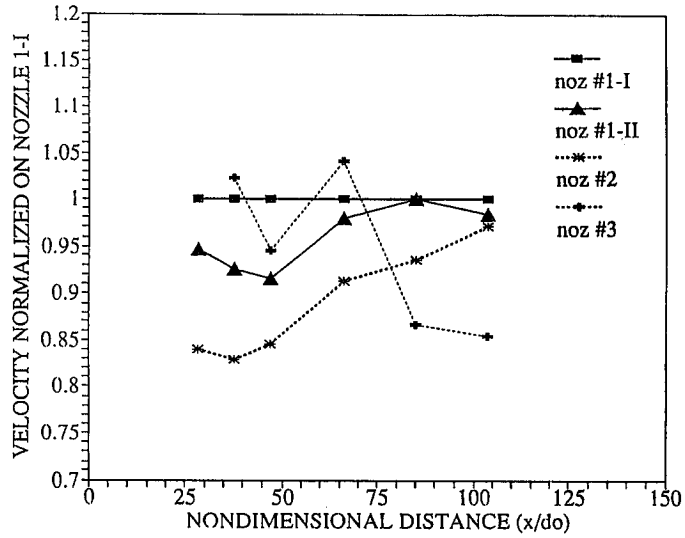


FIGURE 3. INFLUENCE OF NOZZLE SHAPE ON NORMALIZED JET VELOCITIES, $U_0 = 200 \text{ m/s}$, $P_a = 4.8 \text{ MPa}$ (700 psi).

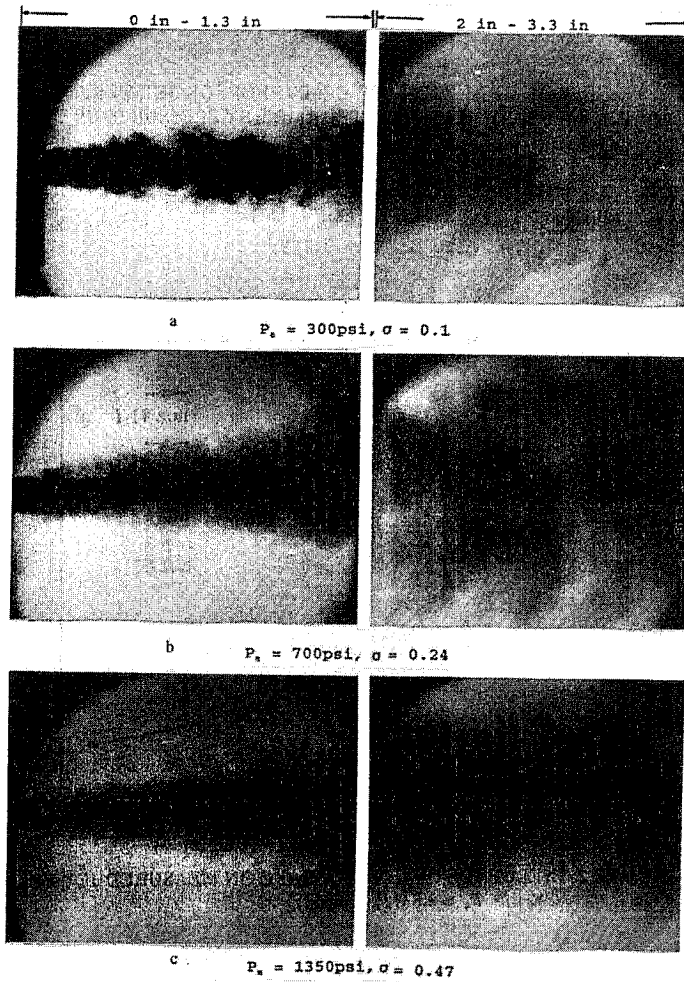


FIGURE 4. EFFECT OF CAVITATION NUMBER VARIATION ON JET FLOW VISUALIZED WITH DYE. NOZZLE AT LEFT EDGE OF PHOTO. $U_0 = 200 \text{ m/s}$. a) LARGE AMOUNT OF CAVITATION AT $\sigma = 0.1$. b) MODERATE CAVITATION NEAR NOZZLE AT $\sigma = 0.24$ c) NEGLIGIBLE CAVITATION AT INCIPITION.

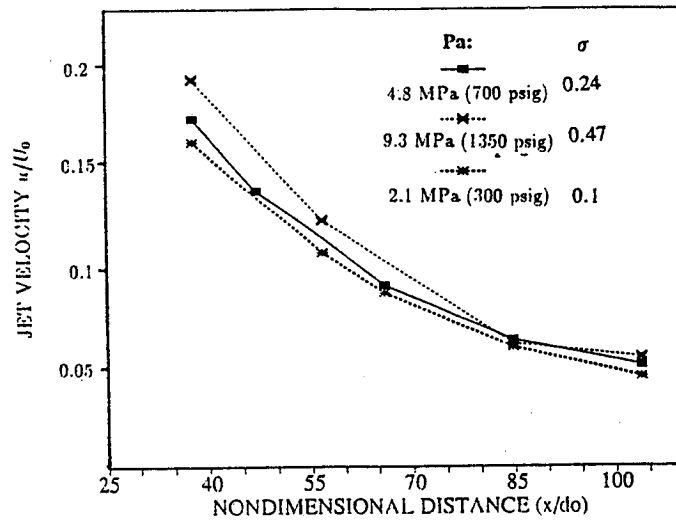


FIGURE 5. THE INFLUENCE OF VARYING AMOUNTS OF CAVITATION ON MEASURED DOWNSTREAM CENTERLINE JET VELOCITIES OBTAINED BY VARYING P_a . $U_0 = 200 \text{ m/s}$. P_a FOR INCEPTION $\approx 9.3 \text{ MPa}$ (1,350 psi).

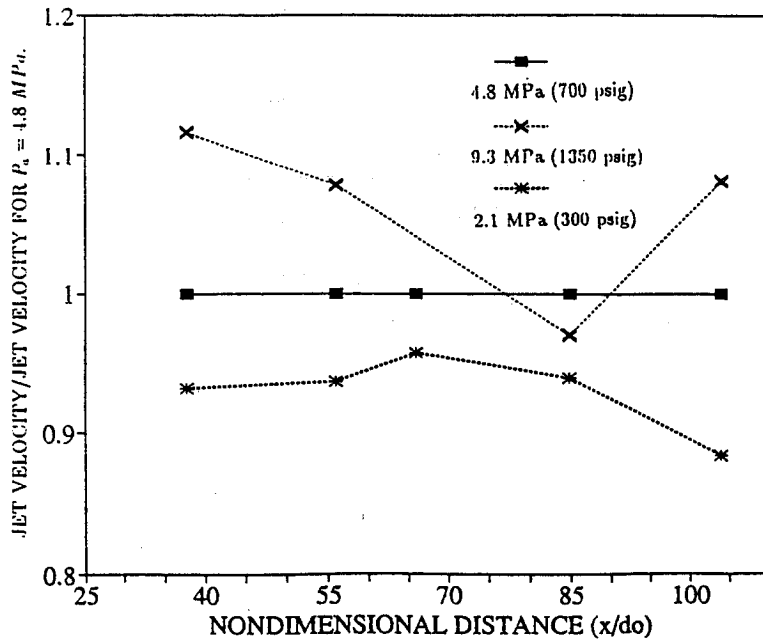


FIGURE 6. THE INFLUENCE OF VARYING AMOUNTS OF CAVITATION ON MEASURED DOWNSTREAM CENTERLINE JET VELOCITIES. $U_0 = 200 \text{ m/s}$. DATA OF FIGURE 5 NORMALIZED ON CASE FOR $P_a = 4.8 \text{ MPa}$.

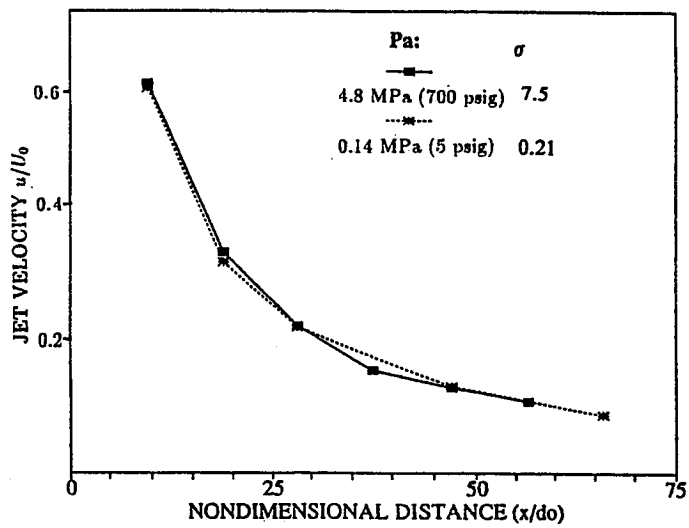


FIGURE 7. MEASURED DOWNSTREAM JET CENTERLINE VELOCITIES FOR $U_0 = 36 \text{ m/s}$ SHOWING NEGLIGIBLE EFFECT OF AMBIENT PRESSURE CHANGE FOR THIS LOW SPEED JET.

EXAMINATION OF THE RANGE OF JET ACTION IN AN AQUEOUS MEDIUM

A. Kalukiewicz
University of Mining and Metallurgy
Kraków, Poland

ABSTRACT

In this paper results of the research into the variations of the dynamic force of a water jet of the pressure up to 200 MPa and 1 mm diameter have been presented. The jet is forced into an aqueous medium of the pressure from 0 to 1 MPa. The distance of the nozzle operating in the air or under water at the pressure of 0.005 MPa and 1 MPa from the measuring point have been changed. The effect of the jet under the water has been also tested on concrete blocks.

1. INTRODUCTION

In a large number of countries, in which the mining industry is meaningfully developed, scientific researches into new, unconventional methods of extracting coal and cohesive rock are carried out. This brings about the necessity of looking for new constructional solutions of mining machines and equipment.

This kind of research is also carried out at the University of Mining and Metallurgy in Cracow in close co-operation with the mining industry. The research concentrates on hydraulic or hydromechanical mining with high-pressure water jets up to 250 MPa. These techniques find application in building arm-roadheaders or full-face machines and equipment for driving galleries, cross-cuts, tunnels and shaft. These new generation machines of high mining efficiency will improve working conditions, protect the environment in the working place and safeguard it against the explosions of methane and coal dust.

In previous years research into cutting and mining rock with water jets operating in the air was made at the University of Mining and Metallurgy in Cracow, Poland. Results of those investigations were presented in (Kalukiewicz, 1985, Klich, 1989, Jarno, 1992).

In the mining industry there are numerous situations where water jets should be used for mining or for aiding mining operations in aqueous media. Therefore, it is necessary to get well acquainted with the phenomena connected with the action of high-pressure water jets operating under the surface of water.

2. TEST STAND

A stand for testing the action of an immersed jet is based on the device constructed at the University of Mining and Metallurgy in Cracow for examining hydraulic mining. A diagram of the device has been shown in Fig. 1.

The device consists of:

- a feeding station (Fig. 2) of the power $N = 90$ kW, delivery $q = 238$ l/min, pressure $p = 20$ MPa,
- a hydromonitor (Fig. 3) in which three intensifiers forming pressure converters with the ratio 1:10 are fed with oil from the low pressure side,
- a water container (Fig. 4) having the height $h = 1$ m, the diameter $D = 1$ m, and enduring pressure $p_n = 1$ MPa.

The container is equipped with a system measuring and controlling internal pressure during the forcing of water into it from the nozzle.

Inside the container, it is possible to fix and shift rock samples or a jet dynamic forces sensor.

Testing of dynamic forces of a jet in an aqueous medium causes a series of technical inconveniences. The sensor must resist an aqueous surrounding under a considerable outer pressure, in the medium where high energetic turbulent and cavitation disturbances occur.

Because of the above, sensors of strong and firm construction are preferable. But this, in consequence, is contrary to the requirement of high sensitivity.

As in previous experiments and investigations with water jets operating in the air, measurement were made using strain gauges (Fig. 5). Fig. 6 shows a sensor fixed in the container in the jet axis. In the feeding station an oil pressure sensor of the range 0÷20 MPa is used. A similar sensor is installed on the feeder conduit of the hydromonitor rotations motor.

The measurement results were recorded and processed by an IBM computer furnished with a suitable software.

The testing was made in three series:

- in the air,
- in water at the pressure of 0.005 MPa,
- in water at the pressure of 1 MPa.

To enable the comparison, it was established that:

- the pressure of water jet $p = 200$ MPa,
- the nozzle diameter $d = 1$ mm,
- the distance of the nozzle from the sensor $l = 20 + x \times 50$ mm, where $x = 1 \div 10$,
- rotations of the hydromonitor $n = 6$ s⁻¹.

During the first series of the experiments, dynamic forces of the jets operating in the air were measured. The measurements were started with the maximum bringing together of the force sensor and the nozzle (20 mm). During the next measurements the distance of the sensor from the nozzle was increased until it reached 520 mm.

Exemplary records of the dynamic force of the jet and feeding pressures are shown in Fig. 7. Acting in a similar way, the values of the forces and pressures of the jet operating under water, as well as under water and under the pressure of the water surrounding the jet $p_w = 1$ MPa were recorded.

The curves denoting the forces and pressures presented as examples were prepared for the distance of the nozzle from the sensor equalling 70 mm, and for that equal up to 520 mm respectively.

Fig. 8 presents diagrams of the variations of the jet dynamic force in dependence on the distance of the nozzle from the measuring point within the range of 20 up to 520 mm. Analyzing the variation of the dependencies obtained from the measurements in can be seen that dynamic forces acting on the sensor increase more considerably when the jet operates under the water surface than when it is used in the air. It is worth noticing that

there exists a certain concurrence of the above dependencies and the results of cutting concrete under water (Fig. 9) where for the assumed parameters deeper incisions were made under water. When concrete is cut under water, the effect of this incision is obtained only where the jet core operates. The effect of the dispersed jet on concrete and the influence of the cavitation phenomena is quite unimportant in a short time.

The considerable increase of the jet dynamic forces under water results from the summing up of the action of the jet core and the dispersed jet whose velocity is much smaller but its diameter mass grows quickly. When the sensor has quite a considerable surface ($\varnothing = 90$ mm), a rapid increase of the force is recorded within the distance range to 120 mm, followed by its decrease when the greater and greater part of the dispersed jet by-passes the measuring area of the force sensor.

3. CONCLUSIONS

The investigations carried out show that it is possible to apply effectively jet cutting under water. The research can be also helpful at designing machines mining rock hydraulically or using jet aided conventional tools.

To determine the distribution of water velocities in the plane perpendicular to the jet axis, a point wise measuring sensor should be applied. The sensor should be movable in three directions in the water space, and each shift should be measured. Such investigations are being prepared.

REFERENCES

- Jarno L., Kalukiewicz A., Klich A.: „Possibility of using cutting technology in Polish mining industry”. *Kluwer Academic Publishers Jet Cutting Technology*, Dordrecht – Boston – London, 1992.
- Klich A., Kalukiewicz A., Kotwica K.: „Prace nad zbudowaniem polskiego kombajnu pełnoprzekrojowego”. *Zeszyty Naukowe AGH*, Nr 1256, Mechanika z. 17, pp. 77-93, Cracow, Poland, 1989.
- Kalukiewicz A., Klich A.: „Versuchsergebnisse an einer Hochdruckwasserstrahlanlage für Stein- und Kohlegewinnung”. *Hydromechanisation 4*, Karl-Marx-Stadt, DDR, 1985.
- Klich A., Kalukiewicz A.: „High-Pressure Water Jet as a Cutting Tool”. *5th American Jet Conference*, VIII, pp. 141-155, Toronto, Canada, 1989.
- Klich A., Kalukiewicz A.: „Investigation On Water Jet Cutting of Concrete in Water Surroundings”. *6th American Jet Conference*, VII, pp. 371-380, Houston, Texas, USA, 1991.

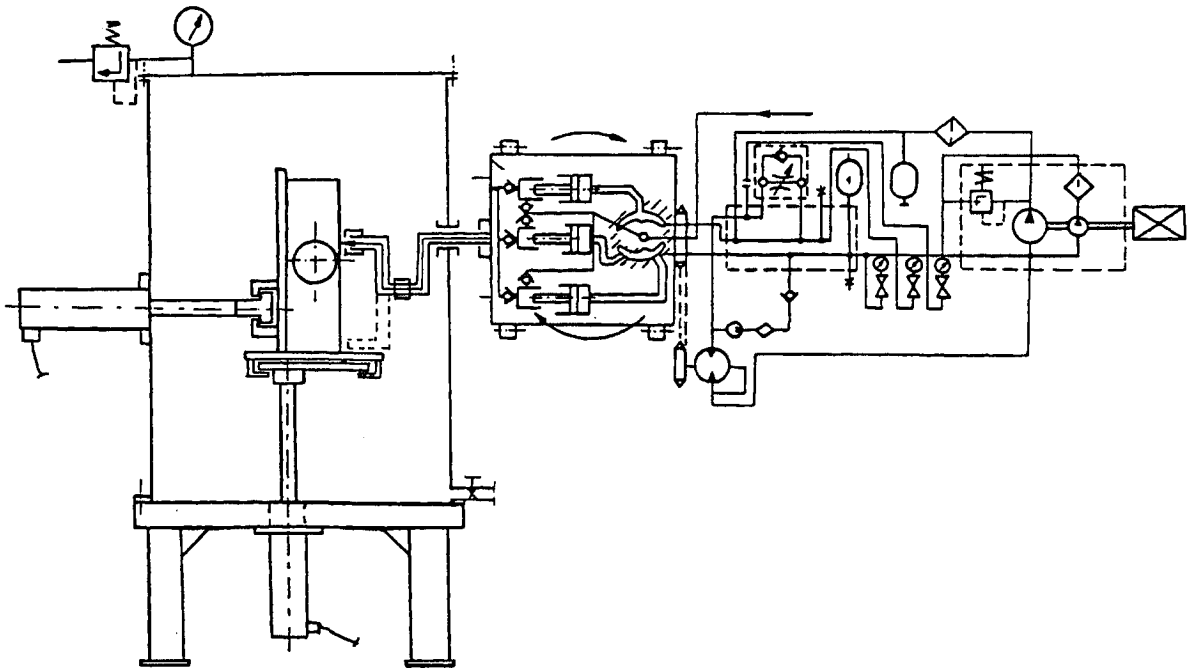


Fig. 1. Diagram of the stand for testing the jet action under water.

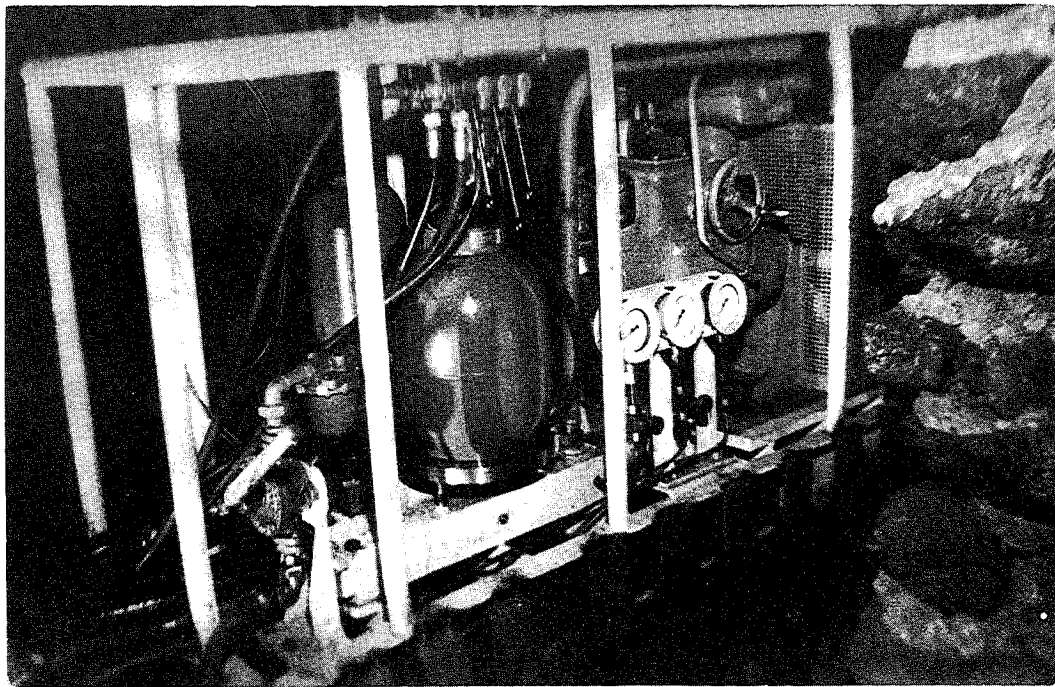


Fig. 2. Feeding station (90 kW, 238 l/min, 20 MPa).

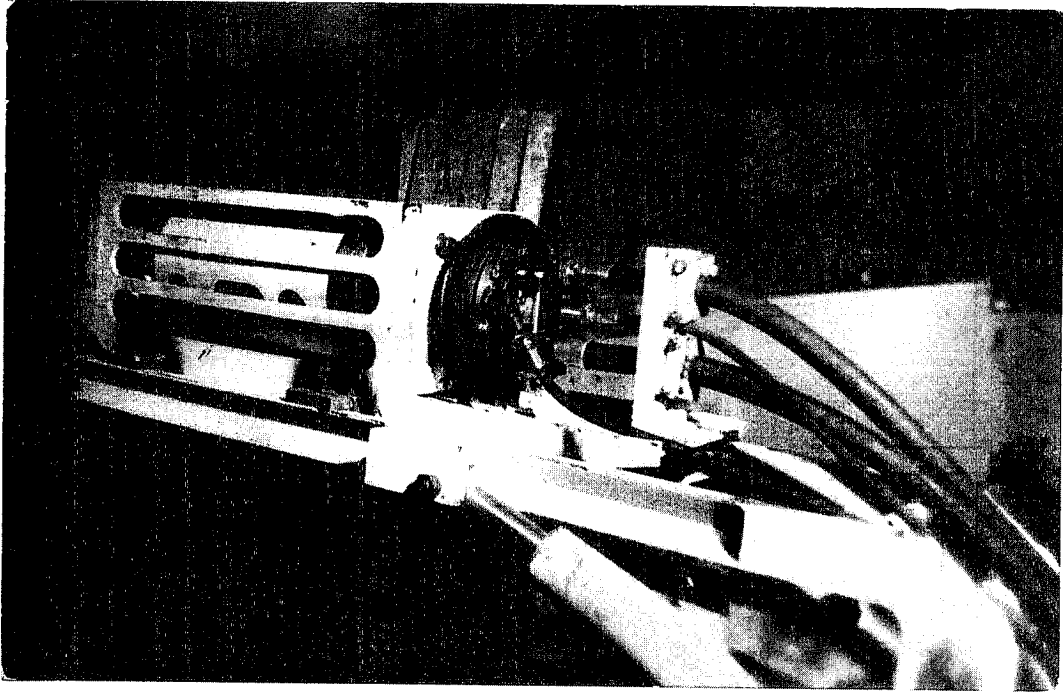


Fig. 3. Hydromonitor with three intensifiers pressure conversion 20/200 MPa.

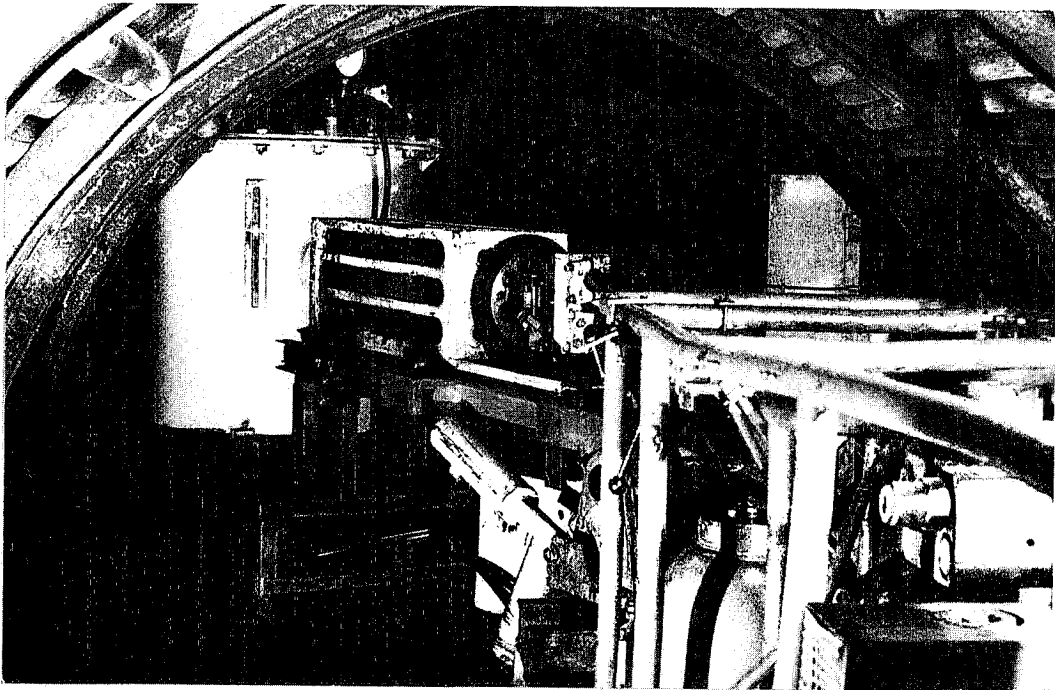


Fig. 4. Water container $h = 1$ m, $D = 1$ m, maximum internal pressure 1 MPa.

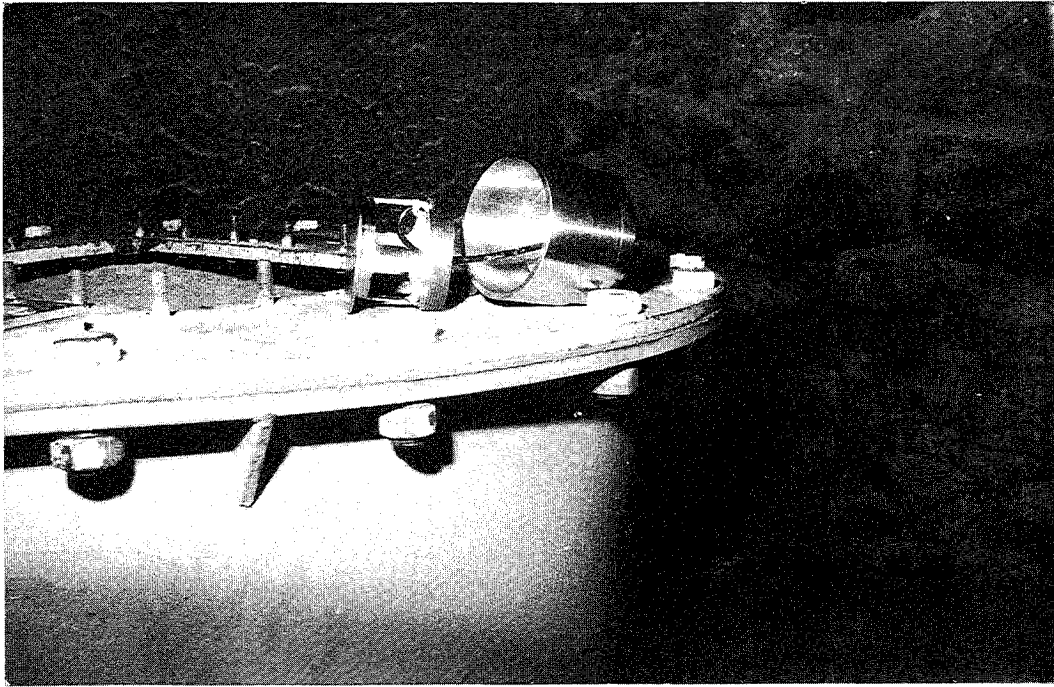


Fig. 5. Strain gauge for measuring the jet dynamic force.

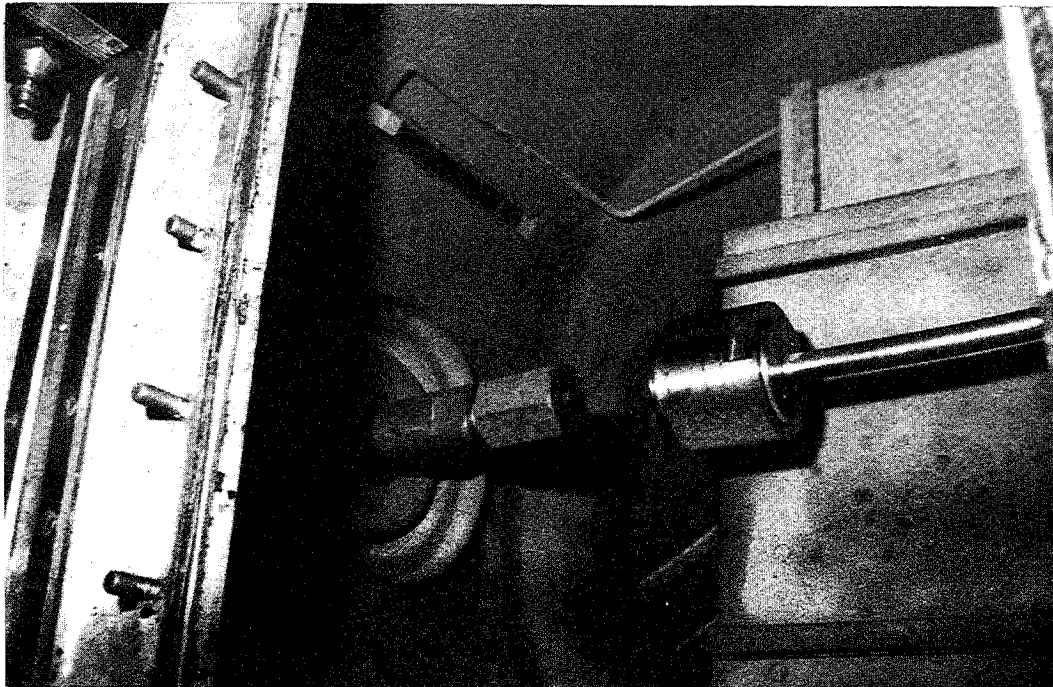


Fig. 6. View of the dynamic force sensor fixed in the container.

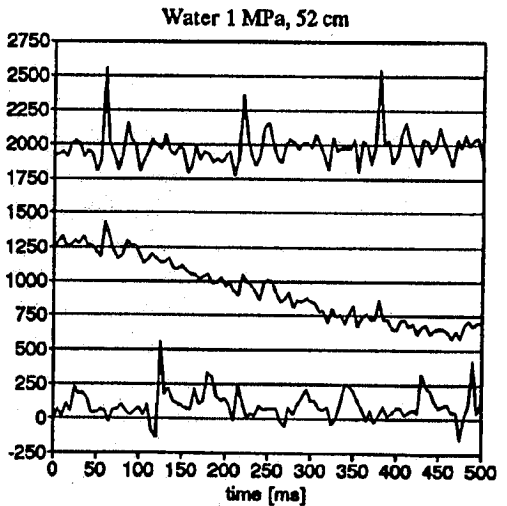
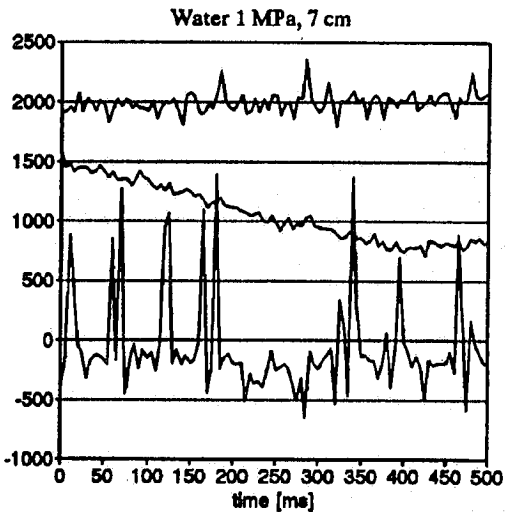
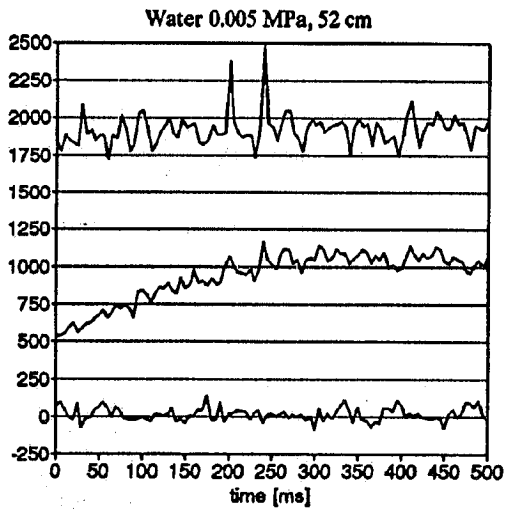
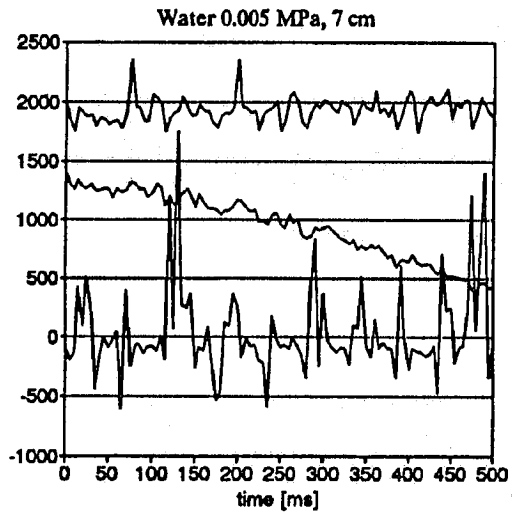
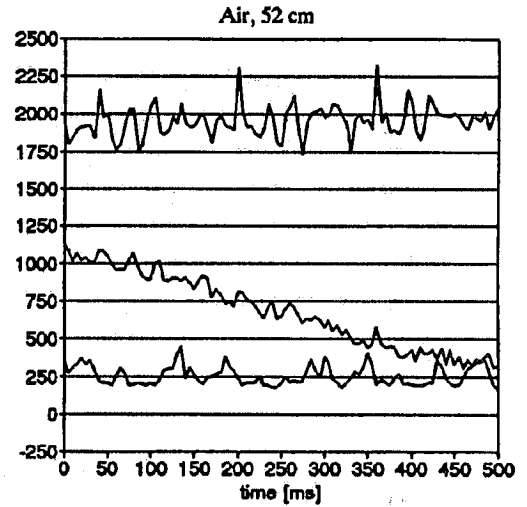
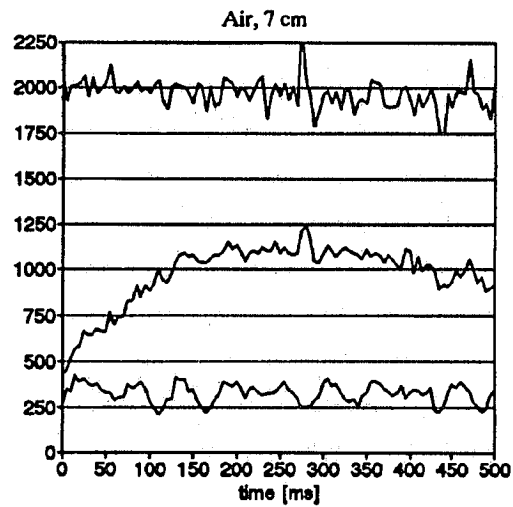


Fig. 7. Records of the jet dynamic force (the lowest line on each diagram) and the feeding pressure for the distance of the sensor from the nozzle 7 and 52 cm.

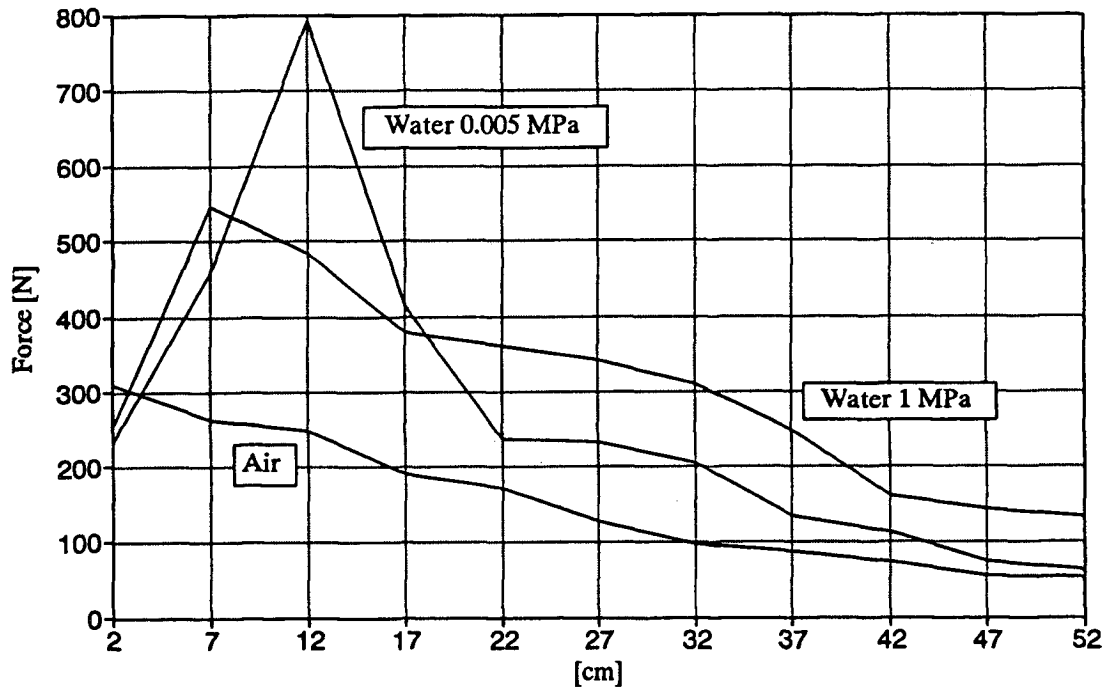


Fig. 8. Dependence of the jet dynamic force variations on the distance of the nozzle from the measuring point within the range 0÷520 mm

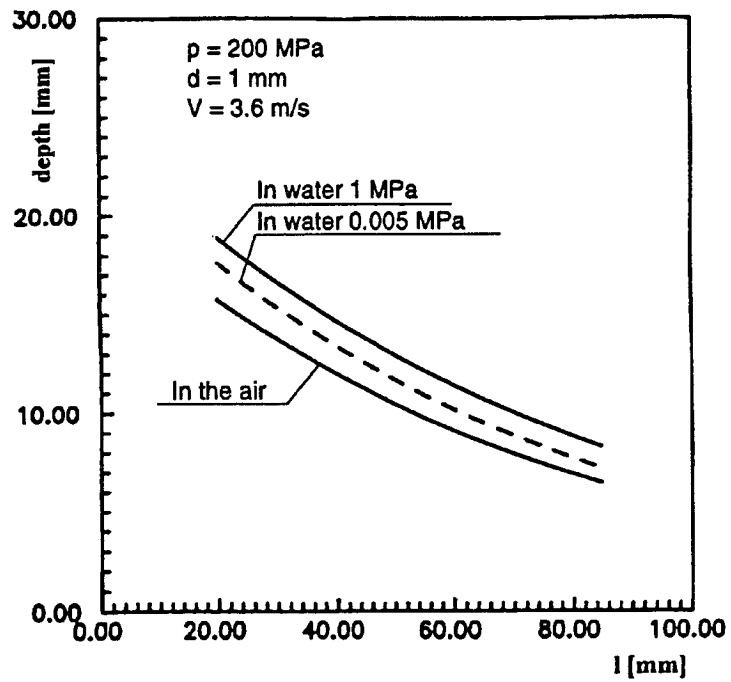


Fig. 9. Depth of cutting concrete (compressive strenght $\sigma = 9.3$ MPa).

A NUMERICAL INVESTIGATION OF TURBULENT BEHAVIORS OF WATER FLOW INSIDE NOZZLE

M. E. H. Khan and E. S. Geskin
Department of Mechanical and Industrial Engineering
New Jersey Institute of Technology
Newark, New Jersey, U.S.A.

ABSTRACT

In this research a computational approach is employed for the prediction of dynamic behavior of high pressure turbulent water flow inside of various sapphire nozzles. The analysis is based on the numerical solution of conservation equations of continuity and momentum as well as equations of turbulent kinetic energy (k) and energy dissipation (ϵ). A finite element package, FIDAP is used to solve these equations for 2-dimensional axisymmetric flow. The investigation provides a complete picture of velocity and pressure fields as well as dissipation of turbulent kinetic energy inside of the nozzle. The analysis reveals flow separation (formation of "cat's eye") and cavitation which in turn provides vital information for nozzle design. The computational results conform with our experimental results. An attempt is made to compare the obtained data with available literature information and a good agreement has been found.

1. INTRODUCTION

High pressure water jets have been used in coal mines and other industries where fire hazard becomes common due to frictional heating. When cutting, drilling or turning operation is carried out, the object is to attain maximum pressure as well as minimizing jet dispersion. Again cavijet and pulsed jet have been used widely in the industry due to their high destructive nature. In order to achieve high pressure and velocity of the jet in the jet- workpiece interaction zone and to understand the mechanism of jet integration, dissipation of turbulent kinetic energy and formation of cavities and pulse require through investigation of flow inside and outside of the nozzles.

There has been a limited works in jet analysis and a very few works in flow inside nozzles found in the papers. Leach et al. (1966) suggested few nozzle shapes and carried out an investigation to quantify the jet pressure on target material. Several of their nozzle shapes gave maximum pressure on target was half the pump pressure at about 350 nozzle diameters away. Shavlovsky (1972) studied the dynamics and structure of fine continuous jets at different pressures. From his experimental analysis, he noticed that the nozzle having a cone with cylindrical end section is better than any other form of the nozzle and optimum length of the cylindrical section is four times the nozzle exit diameter. Davies et al. (1980) presented some experimental results for three different nozzles and observed that tapered nozzles produce the most coherent jets and higher pressure at target plate. They noticed that significant deceleration only begins when the jets start to break into discrete packets of water.

A computational approach was developed by Lai et al. (1991) for the investigation of cavitating submerged jets. They designed several nozzles and found a center body insert into a conical nozzle produced enhance cavitation. A few more papers on jet behaviors, its pressure, velocity distribution and disintegration in the air are found in the work of Dunne et al. (1954), Semerchan et al. (1958), Yanaida (1974), Edwards et al. (1982) and Chen et al. (1990). Their investigation mostly confined in the jet characteristics and did not consider the flow configuration inside nozzle.

Few papers are found on the effect of diverging angle to flow. Tropea et al. (1989) used different diffusers angles and found a great influence of angle on flow separation and production of turbulence. Habib et al. (1982) developed a numerical method of calculating the properties of axisymmetric swirling and nonswirling turbulent recirculating flows in wide-angle diffusers.

All of the above investigations provide partial information of the dynamics of fluid flow inside the nozzles in the case of water jet machining. Therefore, a model which accurately determines the velocity, pressure and turbulence both inside and outside of the nozzle is highly desired. In this investigation, several nozzles were used for flow simulation using a k- ϵ turbulence model. A computational approach was developed for 2-dimensional axisymmetric flow applying finite element discretization of the flow domain by using FIDAP code. The effects of nozzles shapes and geometry on flow were analyzed. Numerical results are compared with experimental data of the authors as well as the measurements data of other researchers. The paper ends with the suggestion of better nozzles in water jet machining.

2. NUMERICAL APPROACH

With reference to the Fig. 1 for axisymmetric 2-dimensional flow simulation, the governing equations for a steady incompressible, isothermal flow without body forces, including a two-equations turbulence model (k-ε) can be written as follows:

$$\text{Continuity:} \quad u_{i,j} = 0 \quad (1)$$

$$\text{Momentum:} \quad \rho u_j u_{i,j} = -p_{,i} + [\mu(u_{i,j} + u_{j,i}) - \overline{\rho u'_i u'_j}]_{,j} \quad (2)$$

where the viscosity is defined as

$$\mu = \mu_0 + \mu_t \quad (3)$$

The eddy viscosity is computed by Kolmogorov-Prandtl equation

$$\mu_t = \rho c_\mu k^2 / \varepsilon \quad (4)$$

By algebraic manipulation of Navier Stokes equations (Launder and Spalding, 1974), the semiempirical transport equations for k and ε have the form as follows:

$$\rho u_j k_{,j} = \left(\frac{\mu_t}{\sigma_k} k_{,j} \right)_{,j} + \rho G - \rho \varepsilon \quad (5)$$

$$\rho u_j \varepsilon_{,j} = \left(\frac{\mu_t}{\sigma_\varepsilon} \varepsilon_{,j} \right)_{,j} + c_1 \rho \frac{\varepsilon}{k} G - c_2 \rho \frac{\varepsilon^2}{k} \quad (6)$$

where G, the shear generation term which is the production of turbulent energy from interaction between mean flow patterns and turbulence field. In k-ε model, G is defined as

$$\rho G = \mu_t (u_{i,j} + u_{j,i}) u_{i,j} \quad (7)$$

The empirical constants in equations (5) and (6) are taken by the following recommended values $c_\mu=0.09$, $\sigma_k=1.00$, $\sigma_\varepsilon=1.30$, $c_1=1.44$ and $c_2=1.92$.

A perturbed system of equations is used to solve the above equations where the continuity requirement is weakened by replacing

$$u_{i,i} = -\zeta p \quad (8)$$

Here the penalty parameter, ζ is typically equal to 10^{-6} . This approach eliminates the dependent variable p , which is then recovered by post-processing from the velocity field by the equation

$$p = -(1/\zeta)u_{i,i} \quad (9)$$

2.1 Boundary Conditions and Solution Procedure

The domain (Fig. 1) over which the equations have to be solved is that enclosed by the inlet and the outlet sections, the axis of symmetry, and the wall. At the inlet section, the water is taken to have uniform velocity which is computed from constant volume flow rate. At the inlet, k and ε were prescribed by the following equations obtained from Rodi (1980) and FIDAP (1991) for this flow condition

$$k = I \frac{u^2}{100} \quad (10)$$

$$\varepsilon = \frac{k^{1.5}}{l} \quad (11)$$

where I , the turbulence intensity was equal to 10 and l , characteristics eddy length was taken 5 % of the inlet radius. The arbitrary nature of turbulence has weak influence on numerical predictions of the flow field, as also was found in Khan and Geskin (1992). At the outlet, all the variables were constrained to have zero gradients in the axial direction, while at the axis of symmetry, the gradients are set to be zero in the radial direction. No slip boundary conditions and zero gradient of turbulence energy were prescribed on the solid wall.

The above equations (1), (2), (5) and (6) with the preceding boundary conditions were solved by a finite element technique. 2-dimensional quadrilateral finite elements have been used in fluid domain and 2-dimensional boundary elements have been used at the wall. The solution procedure was based on FIDAP code used for turbulence modeling. The numerical solution was converged when the sum of the normalized residuals of each variable had fallen below 0.0001.

3. EXPERIMENTAL APPARATUS AND PROCEDURE

The experimental investigation of velocity measurement was carried out in the work cell of Ingersoll Rand's 5-axis water jet machine. The supply pressure was maintained 330.7 MPa and flow rate was 1.65 lit/min. A back scattered laser transit anemometer with 15 mw He-Ne laser as a light source was used to measure the velocity of the jet. The experimental details was described in Chen and Geskin (1990). A Photec 16 mm rotating prism camera with a speed of 8000 frames/sec was used with back scattered light to do filming of high speed jet.

4. RESULTS AND DISCUSSION

The computational analysis has been performed for different converging angles of the nozzles and also the effect of orifice length was studied. The Figs. 2-3 show the contour plots of streamline and turbulent kinetic energy for two extreme converging angles. It reveals that 90° converging angle produced circulation before the entry of the orifice. The turbulent kinetic energy mostly dissipated near to the wall. In Fig.4, the axial velocity distribution for three different converging angles are presented. The formation of circulation in 90° converging resulted in higher exit velocity whereas 10° and 60° gave similar velocity distribution. In Fig. 5, the effect of orifice length on velocity distribution is presented. It is noticed that velocity decreases with the increase of length and found optimum length in between 4~10 times of orifice diameter as also noticed by Shavlovsky (1972). The conventional nozzles (nz2 in Figs. 6-7) used in the experiments are also employed for computational analysis. Figs. 6-7 present the flow pattern and the turbulent energy distribution inside the nozzle. The flow forms circulation after the expansion from orifice and it is separated from the wall. Turbulent kinetic energy is mostly dissipated in the orifice. From the streamline contour plot it is clear that the core of the flow is primarily determined by the orifice diameter. Again this result agrees with our high speed filming of the jet where core is extended to the downstream with a diameter approximately equal to the orifice diameter (Khan et al., 1992). The axial velocity distribution for two different orifices is depicted in Fig. 8. The centerline velocity reached to the peak in the entrance of the orifice and then it maintained almost constant value in the orifice section. Due to the diverging section of the nozzle, energy dissipated rapidly which caused reduction of velocity as also conforms with Habib et al. (1982). In Fig. 9, the contour plots of streamline, velocity vector, pressure and kinetic energy for nz3 are depicted. The maximum pressure is achieved at the entry of the orifice. The two steps diverging section generates vigorous flow separation which forms pulse jet. The centerline velocity distribution is similar to nz2 (Fig.10).

The nozzle exit kinetic energy of the flow is compared in Figs. 11-12. For nz1, the spatial velocity distribution is uniform and there is no flow separation in the orifice (Fig. 11) and it implies that flow speels out as a normal conventional jet. In Fig.12, a comparison is shown with computational and experimental results. The LTA velocity measurement right at the exit of the nozzle was performed for the nozzle type nz2. During experiment it could not be possible to record data for wider jet because of diffused and droplet zone of the jet. Both experimental and computational results around the centerline of the flow conform with each other. In this figure, the flatten portion of the curves is close to the orifice diameter of the nozzle. It is the part of the jet having concentrated energy assumed to be the core of the jet.

5. CONCLUSIONS

A computational technique is developed for the analysis of 2-dimensional axisymmetric turbulent flow inside the nozzle using finite element code FIDAP. The numerical prediction of the flow inside nozzle with the k- ϵ turbulence model compares generally well with the experiments. The results show that converging nozzles produce concentrated high energy jet whereas the nozzle with diverging section produce cavijet. Converging nozzle with 5~10 times orifice diameter produce

high energy jet. Flow is separated in the the conventional nozzle and form circulation which in turn produces pulse jet. The core of the jet generates from the orifice. The nozzle exit velocity is compared with experimental results and found agreement.

ACKNOWLEDGEMENTS

This work was supported by NSF grant number DMC 8810639 and the Center of Manufacturing Systems, New Jersey Institute of Technology. The support from Pittsburgh Super Computer C90 for computation was also appreciated.

REFERENCES

- Chen, W. L., and Geskin, E. S., "Measurement of the Velocity of Abrasive Water Jet by the use of Laser Transit Anemometer," *Proceedings of the 10th International Symposium on Jet Cutting Technology*, pp. B4-1 - B4-22, BHRA Fluid Engineering, Cranford, Bedford, UK, 1990.
- Davies, T. W., Metcalfe, R. A., and Jackson, M. K., "The Anatomy and Impact Characteristics of Large Scale Water Jets," *Proceedings of the 5th International Symposium on Jet Cutting Technology*, pp. 15-32, BHRA Fluid Engineering, Cranford, Bedford, UK, 1980.
- Dunne, B., and Cassen, B., "Some Phenomena Associated with Supersonic Liquid Jets," *Journal of Applied Physics*, Vol. 25, No. 5, pp. 569-572, 1954.
- Edwards, D. G., Smith, R. M., and Farmer, G., "The Coherence of Impulsive Water Jets," *Proceedings of the 8th International Symposium on Jet Cutting Technology*, pp. C4-123 - C4-140, BHRA Fluid Engineering, Cranfield, Bedford, England, 1982.
- FIDAP Manual, *Fluid Dynamics International, Illinois*, Vol. 6, 1991.
- Habib, M. A., and Whitelaw, J. H., "The Calculation of Turbulent Flow in Wide-Angle Diffusers," *Numerical Heat Transfer*, Vol. 5, pp. 145-164, 1982.
- Khan, M. E. H., and Geskin, E. S. "Investigation of Formation and Development of Highly Turbulent Water Jet," *Proceedings of the 3rd Pacific Rim International Conference on Water Jet Technology*, pp. 59-78, 1992.
- Lauder, B. E., and Spalding, D. B., "The Numerical Computation of Turbulent Flow," *Computer Methods in Applied Mechanics and Engineering*, 3, 269, 1974.
- Lai, M. K. Y., Vijay, M. M., and Zou, C., "Computational Fluid Dynamics Analysis of Submerged Cavitating water Jets," *Proceedings of the 6th American water Jet Conference*, pp. 411-426, Water Jet Technology Association, St. Louis, Missouri, 1991.
- Leach, S. J., and Walker, G. L., "The Application of High Speed Liquid Jets to Cutting," *Phil. Trans. Royal Soc.*, Vol. 260, pp. 295-315, 1966.

Rodi, W., "Turbulence Models and Their Applications in Hydraulics," *International Association for Hydraulic Research*, The Netherland, 1980.

Semerchan, A. A., Vereshchagin, L. F., and Filler, F. M., "Distribution of Momentum in a Continuous Liquid Jet of Supersonic Velocity," *Sov. Phys. - Tech. Phys.*, Vol. 3, No. 9, pp. 1894-1903, Sept. 1958.

Shavlovsky, D. S., "Hydrodynamics of High Pressure Fine Continuous Jets," *Proceedings of the 1st International Symposium on Jet Cutting Technology*, pp. A6-81-A6-92, BHRA Fluid Engineering, Cranfield, Bedford, England, 1972.

Tropea, C., Weiser, N., and Nitsche, W., "Experimental Investigation of the Flow through Axisymmetric Expansions," *Transactions of the ASME, Journal of Fluids Engineering*, Vol. 111, pp. 464-471, December, 1989.

Yanaida, K., "Flow Characteristics of Water Jets," *Proceedings of the 2nd International Symposium on Jet Cutting Technology*, pp. A2-19 - A2-32, BHRA Fluid Engineering, Cranfield, Bedford, England, 1974.

NOMENCLATURE

k	turbulent kinetic energy
l	eddy length
P	stagnation water pressure
p	static water pressure
r	radius of the nozzle
t	time
u	axial velocity
u_i ($i=1,2$)	eulerian fluid velocity vector

Greek Symbols

δ_{ij} ($i,j=1,2$)	Kronecker delta
ε	turbulence dissipation
μ	dynamic viscosity
μ_0	laminar viscosity
μ_t	eddy viscosity
ν	kinematic viscosity
ρ	density
σ_{ij} ($i,j=1,2$)	stress tensor

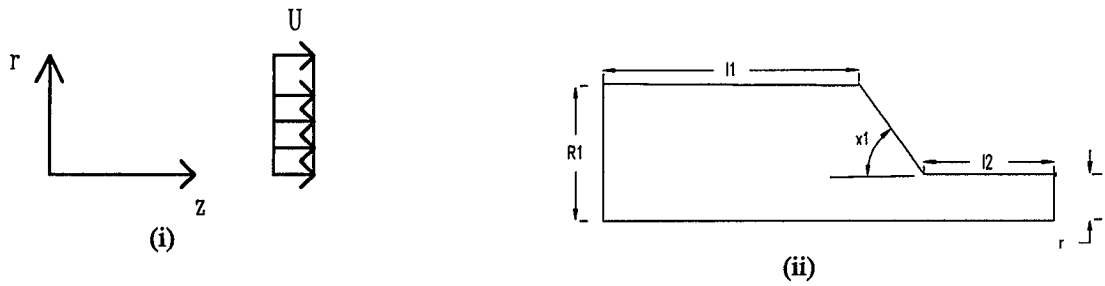


Fig. 1(a): (i) The coordinate system and inlet velocity profile (ii) Nozzle type nz1, (unit: mm) $l_1=15.98$, $l_2=2.55$, $R_1=1.598$, $r=0.127$. Three different converging angles ($x_1=10^0, 60^0, 90^0$) has been used.

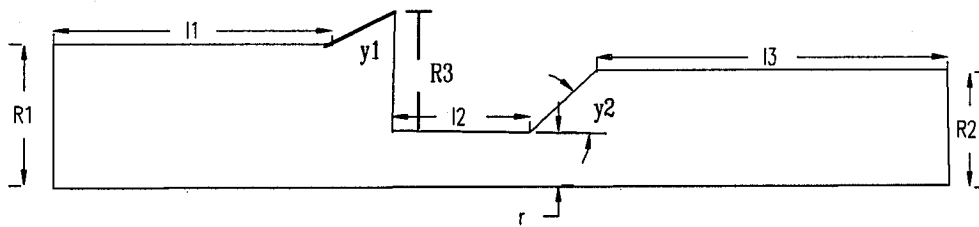


Fig. 1(b): Nozzle type nz2, (unit: mm) $R_1=1.598$, $R_2=0.762$. $y_1=y_2=30^0$. For nz2-I, $l_1=2.54$, $l_2=1.30$, $l_3=8.31$, $r=0.127$, $R_3=2.003$ and for nz2-II, $l_1=25.6$, $l_2=1.30$, $l_3=8.31$, $r=0.089$, $R_3=2.004$

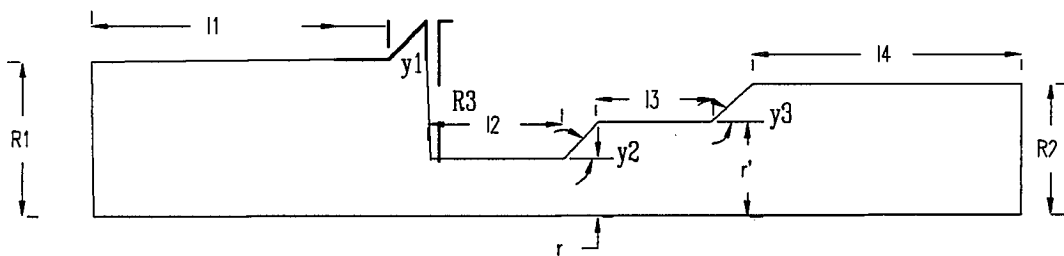


Fig. 1(c): Nozzle type nz3, (unit: mm) $l_1=2.54$, $l_2=1.08$, $l_3=1.51$, $l_4=7.6$, $R_1=1.6$, $R_3=2.003$, $r=0.127$, $r'=0.292$, $R_2=0.793$, Angles $y_1=30^0$, $y_2=y_3=60^0$.

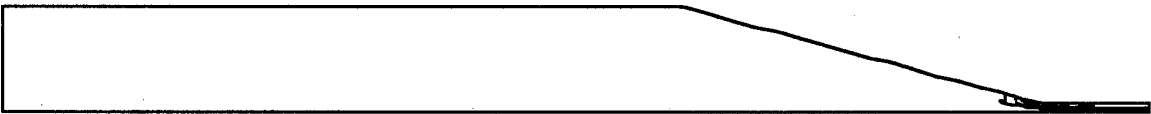


(a) $\Psi = 0.0 \sim 29.3$

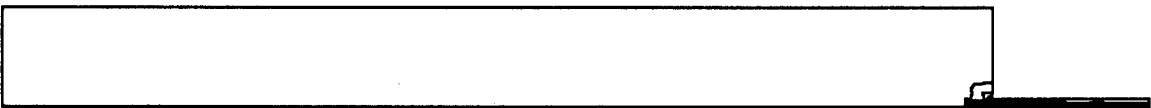


(b) $\Psi = -2.0 \sim 30.9$

Fig. 2: Stream line contour plots for nz1 with converging angles
(a) $\alpha = 10^\circ$ and (b) $\alpha = 90^\circ$



(a) $k = 141 \sim 0.141e9 \text{ cm}^2/\text{s}^2$



(b) $k = 160 \sim 0.16e9 \text{ cm}^2/\text{s}^2$

Fig.3 Kinetic energy contour plots for nz1 with converging angles
(a) $\alpha = 10^\circ$ and (b) $\alpha = 90^\circ$

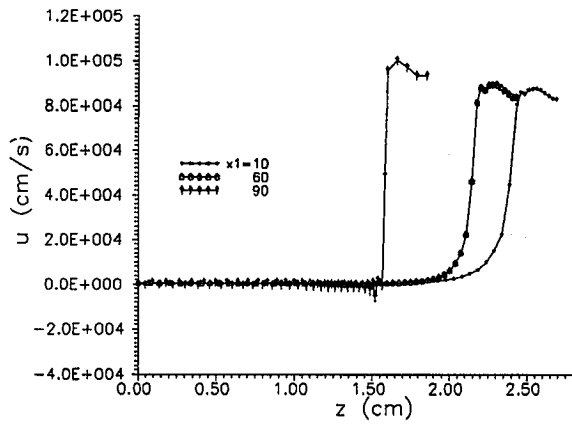


Fig.4 Axial velocity distribution along the centerline for nz1 with same l2

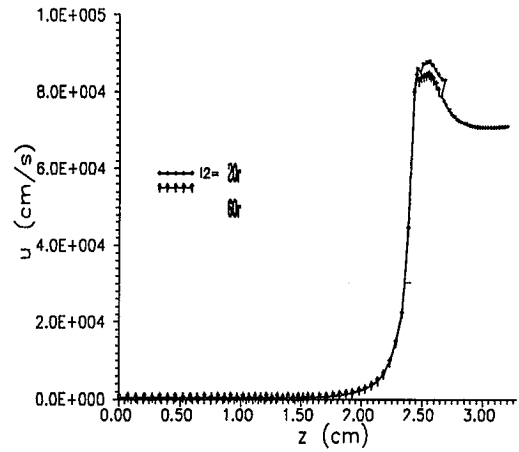
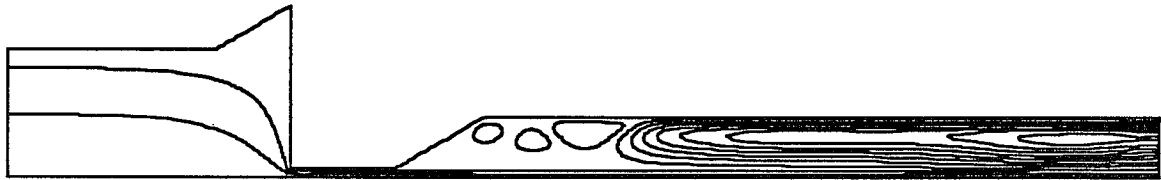
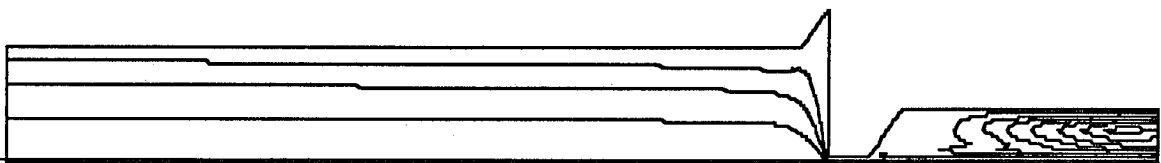


Fig. 5 Centerline velocity distribution for nz1 with converging angle $x_1=10^0$

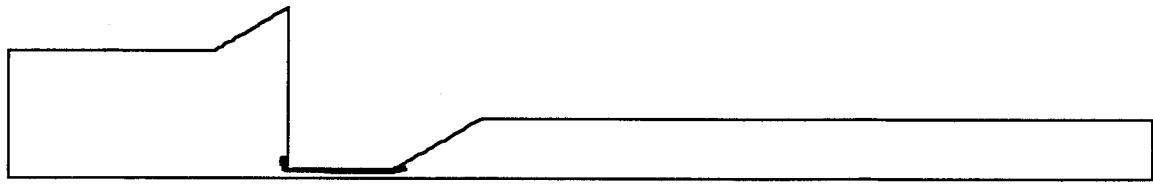


(a) $\Psi = 0.0 \sim 112.5$

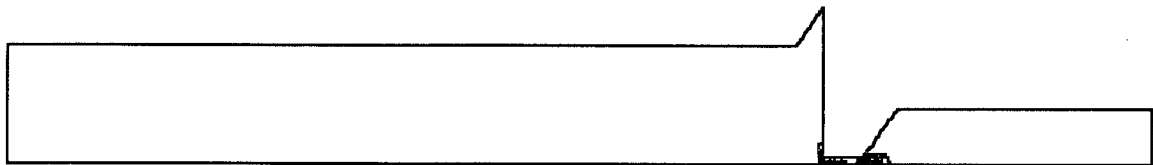


(b) $\Psi = 0.0 \sim 103$

Fig.6 Streamline contour plots for nz2 with orifice radius
(a) $r=0.127$ and (b) $r=0.089$ mm respectively.

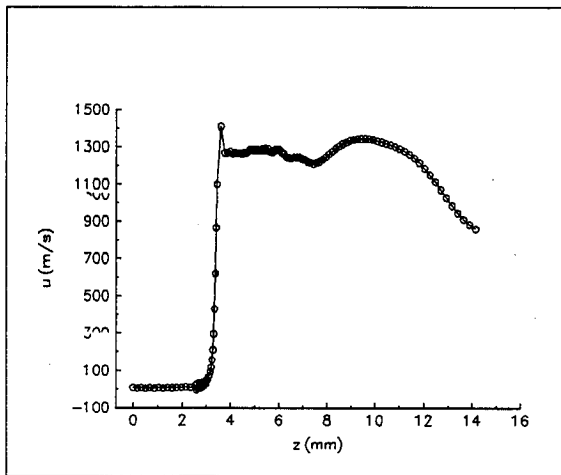


(a) $k=800 \sim 0.96e9 \text{ cm}^2/\text{s}^2$

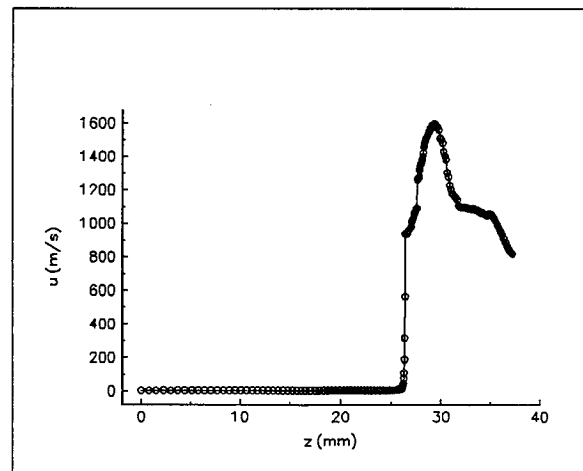


(b) $k=925 \sim 0.926e9 \text{ cm}^2/\text{s}^2$

Fig.7 Kinetic energy contour plots for nz2 with orifice radius
(a) $r=0.127$ and (b) $r=0.089$ mm respectively.

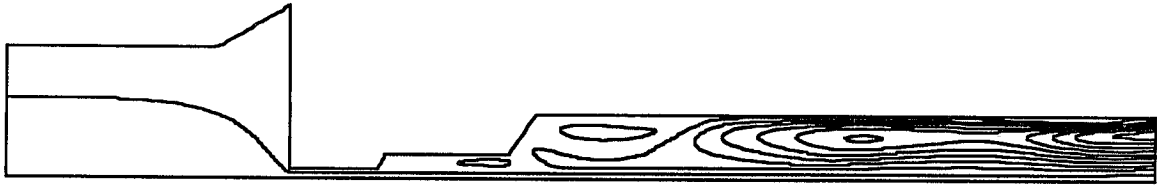


(a)

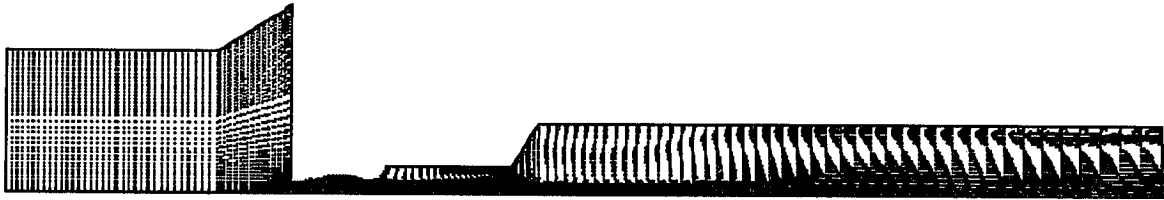


(b)

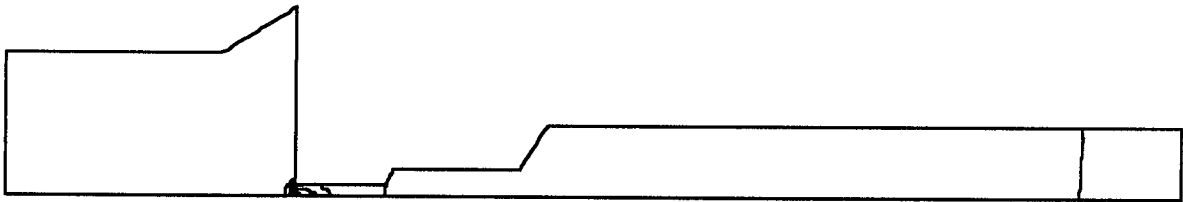
Fig.8 Centerline velocity distribution for the nz2 with orifice radius
(a) $r=0.127$ mm and (b) $r=0.089$ mm respectively



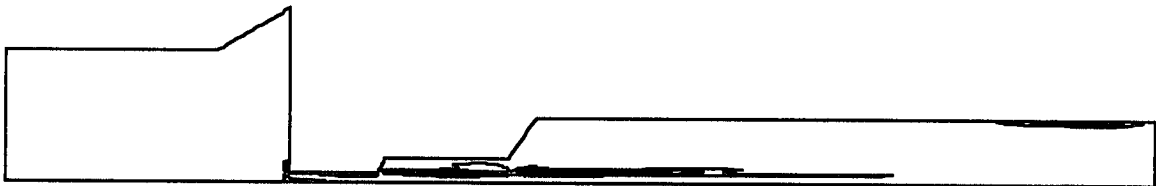
(a) $\Psi = 0.0 \sim 360$



(b) Velocity vector $V = 157 \sim 1250$ m/s



(c) $p = 0.679e7 \sim 0.103e11$ gm/cm-s²



(d) $k = 86 \sim 0.86e8$ cm²/s²

Fig. 9 Contour plots: (a) streamline (b) velocity vector, (c) pressure and (d) turbulent kinetic energy for nz3

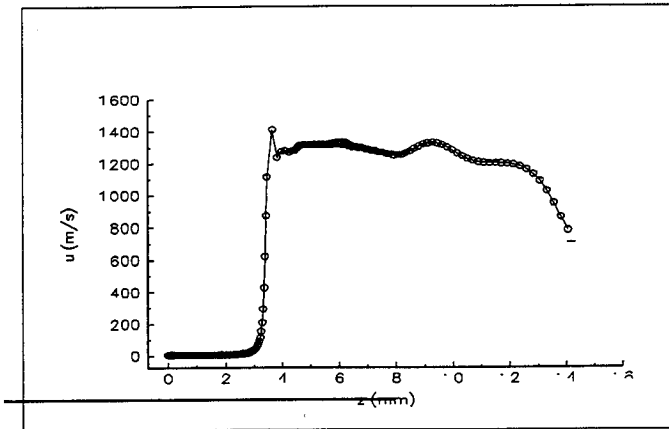


Fig. 10 Centerline velocity distribution for nz3

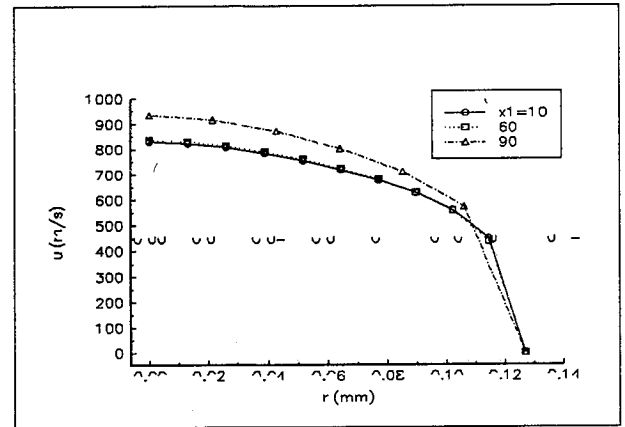


Fig. 11 Transversal velocity distribution for nz1 exit with same l2

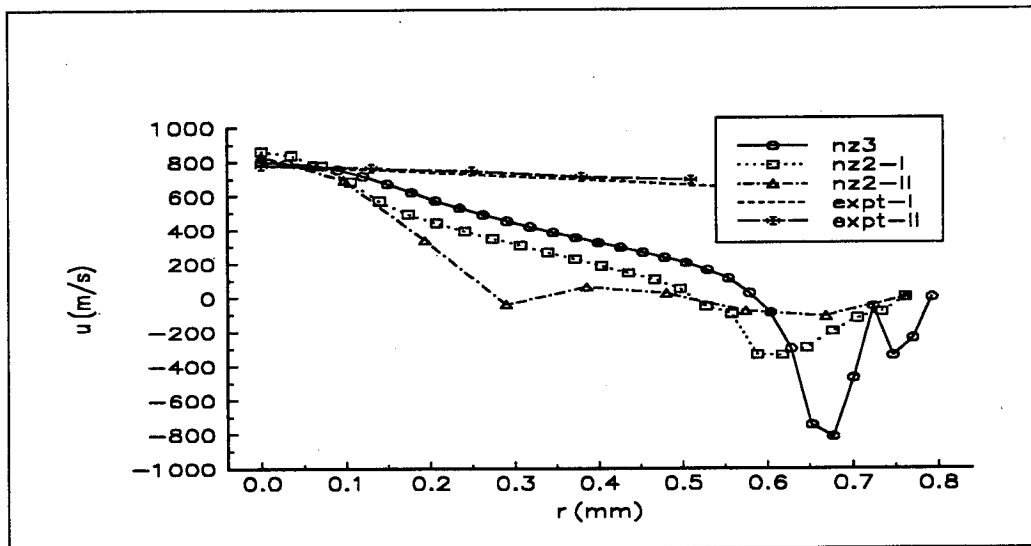


Fig. 12 Comparison of transversal velocity distribution at the exit of the nozzle
 nz2-I ($r=0.127$ mm), nz2-II ($r=0.089$ mm)
 expt-I (LTA measurement of nz2-I)
 expt-II (LTA measurement of nz2-II)

**MATHEMATICAL MODELING OF THE ACCELERATING
PROCESS OF PARTICLES IN DIA-JET**

Chuwen Guo, Dazhong Cheng, Linsheng Liu
China University of Mining & Technology
Xuzhou, Jiangsu, P.R.C.

ABSTRACT

Based on the theory of two-phase flow, the paper analyses the accelerating process of particles in a DIA-Jet system. A mathematical model is established and solved by numerical method. A function called the Distance Function is put forward. This function is very important in the accelerating process. Experimental results indicate that the most important parameter in cutting is the velocity of particles. At the end, the paper summarizes the accelerating mechanism of particles in DIA-Jet, which will give instruction to the designing of nozzles.

1.0 INTRODUCTION

The technology of abrasive water jet (AWJ) has been studied as early as in 1970's. During the last decade, AWJ has become a powerful cutting tool due to the development of ultra-high pressure intensifiers. It can be used to cut various materials, such as steel, ceramics and composite materials.

Generally, cutting with AWJ needs a pressure of about 200MPa. For so high a pressure, the cutting cost is increased and the reliability of the cutting system is lowered. In 1986 Fairhurst[1] presented the first paper on Direct Injection Abrasive Waterjet (DIA-Jet). From then on, researchers all over the world were very interested in the new kind of AWJ. They began to study DIA-Jet in succession. AWJ technology has been lead to a new developing stage after the appearance of DIA-Jet.

Compared with traditional AWJ, DIA-Jet has a lot of unique advantages. For instance, the working pressure can be largely lowered, sometimes it is only 1/20 of the pressure required by AWJ. The study results from Hashish[2] indicate that the effects of various cutting parameters on the cutting effect of AWJ can be considered to be the effects of these parameters on the kinetic energy of the abrasive particles. Based on the experimental results, E. Nadeau[3] points out that the erosion rate of materials with AWJ is directly proportional to the square of the abrasive velocity.

As can be seen from the above, the velocity of abrasive particles plays a very important role in cutting with AWJ. In order to study this velocity, we establish a mathematical model and carry out some cutting experiments.

2.0 MATHEMATICAL MODEL

In a DIA-Jet system, abrasive and water are ejected out from the same nozzle. So that the structure of its nozzle is basically the same as that of pure water jet, as shown in Figure 1.

The abrasive is directly mixed into the high pressure pipes from the storage tank. When the abrasive arrives at the entrance of the nozzle, the abrasive and water come into an equilibrium stage because the distance between the tank and the nozzle is relatively short and the velocity of water in the pipe is low. The abrasive is mainly accelerated within the conical section and the cylindrical section of the nozzle.

Usually, the size of abrasive particles often used in DIA-Jet cutting system is about 30 ~ 100 meshes, the volume friction of abrasive is no more than 15%. So that the solid phase can not be treated as a kind of pseudo-fluid. This paper will discuss the movement of a single particle to obtain the mechanism of abrasive accelerating.

Particles with the same size have the same dynamic feature, the possibility of direct collision is less. However, there still exist influences between particles due to the large rear flow scope of a particle. As approximation, it is assumed that

1. Particles are even spheres.
2. Interaction between particles are neglected.

Assuming that the flow field within a nozzle is approximately one dimensional. According to the theory of two-phase flow, the motion equation of a particle is

$$\frac{du_p}{dt} = \frac{3c_D \cdot \beta}{4\alpha \cdot d_p} (u - u_p)^2 + \frac{3\beta}{2\alpha} \cdot \frac{du}{dt} \quad (1)$$

Where, u — the velocity of water

u_p — the velocity of particles

ρ — the density of water

ρ_p — the density of particles

d_p — diameter of a particle

$\beta = \rho / \rho_p$, $\alpha = 1 + \beta / 2$

c_D — drag coefficient

Since the flow is constant, equation (1) can be rewritten as

$$\frac{du_p}{dx} = \frac{3C_D \cdot \beta}{4\alpha \cdot d_p} \cdot \frac{(u - u_p)^2}{u_p} + \frac{3\beta}{2\alpha} \cdot \frac{du}{dx} \quad (2)$$

Once the water velocity is given, equation (2) can be solved to get the velocity of particles. The continuity equation of the mixture of water and abrasive is

$$\frac{\partial[(\rho j \cdot u + \rho_p (1 - j)u_p) \cdot A]}{\partial x} = 0 \quad (3)$$

In the equation (3), water voidage f has the following relation with the volume fraction of abrasive ϕ :

$$j = \frac{(1 - \phi)u_p}{\phi u + (1 - \phi)u_p} \quad (4)$$

The initial condition is $X=0$, $u=u_p=u_0$, $A=\pi R^2$. R is the inlet radius of nozzle, u_0 is the corresponding water velocity.

From equation (4) and (5), we obtain

$$\frac{A \cdot u \cdot u_p}{\phi \cdot u + (1 - \phi)u_p} = \pi R^2 \cdot u \quad (6)$$

In the conical section, the area A of the cross section is

$$A = \pi (R - X \tan \theta)^2 \quad (7)$$

where, θ is half of the convergent angle of the nozzle.

Equation (2) and (6) are solved by Euler Method. Table 1 is the results calculated with $\rho_p=2400\text{kg/m}^3$, $d_p=0.165\text{mm}$, $R=8\text{mm}$, outlet radius of nozzle $r=1\text{mm}$.

It can be seen from Table 1 that the convergent angle has little effects on the acceleration of the particles.

In the cylindrical section, water velocity is considered to be even, therefore equation (2) is simplified as

$$u_p \frac{du_p}{dx} = \frac{3\beta C_D}{4\alpha \cdot d_p} (u_1 - u_p)^2 \quad (8)$$

where, u_1 is the velocity of water.

By solving equation (8), we get

$$\frac{1}{1 - u_p / u_1} + \ln(1 - u_p / u_1) = \frac{3\beta C_D}{4\alpha} \cdot \frac{x}{d_p} + C \quad (9)$$

Assuming the velocity of particles at the entrance of the cylindrical section is u_{p0} . Introduce a function $f(u)$:

$$f(u) = 1/(1-u) + \ln(1-u) \quad (10)$$

Then

$$x = \frac{4\alpha}{3\beta C_D} \cdot d_p \cdot [f(u_p / u_1) - f(u_{p0} / u_1)] \quad (11)$$

Equation (11) gives the relation between the dimensionless velocity u_p/u_1 and moving distance X of a particle. It indicates that the distance X is determined by the function $f(u)$. Therefore, we called the function $f(u)$ the Distance Function. In order to have a good comprehension in the accelerating process of particles, the value of the Distance Function is listed in Table 2.

3.0 CUTTING EXPERIMENTAL

From the calculation results, it is clear that the velocity of particles is determined by the velocity of water. Cutting experiments are carried out to show the importance of the particle velocity.

The experimental parameters are as follows:

Working pressure:	17MPa
Flow rate of abrasive:	3.8kg/min
Cutting speed:	0.6m/min
Off distance:	10mm
Material cut:	Marble
Diameter of nozzle:	1.6, 2.2, 2.8mm

Figure 2 and Figure 3 give the experimental results. It can be seen, that the cutting depth does not increase much when the diameter of nozzles becomes larger. On the other hand, the energy consumed increases rapidly. That is say, the cutting ability of DIA-Jet mainly depends on the velocity of abrasive. While the flow rate of water has little effects on the cutting results.

4.0 CONCLUSION

Based on the analysis and calculated results, the abrasive accelerating mechanism of DIA-Jet is summed up as follows:

- (a) The abrasive and water are at an equilibrium state within the high pressure pipe. The difference between their velocities is zero.
- (b) In the conical section of a nozzle, the convergent angle has no important effects on the accelerating process of the abrasive. Particle velocity at the end of this section is only about 50% of the water velocity.
- (c) In the cylindrical section, particles are accelerated slowly due to their higher initial velocity. In the example of this paper, a distance of 5.3mm is needed to accelerate a particle from 0.5 (nondimensional velocity) to 0.8, while 31.8mm is needed from 0.5 to 0.95. According to the value listed in Table 2, the nondimensional velocity of abrasive at the outlet of the nozzle is about 0.95. Velocity higher than 0.95 requires much longer cylindrical section.

5.0 REFERENCES

- [1] R. M. Fairhurst, "DIAJET A New Abrasive Waterjet Cutting Technique," Proceedings of the 8th Inter. Sym. on Jet Cutting Tech., Durham, England, 1986.
- [2] Hashish, "A Modeling Study of Metal Cutting With Abrasive Waterjet," Journal of Eng. Materials & Tech., 1984.
- [3] E. Nadeau, "Prediction and Role of Abrasive Velocity in AWJ Cutting," Inter. Journal of Waterjet Tech., Vol. 1, No. 3, 1991.

Table 1 Comparison of Particle Velocity And Water Velocity

Convergent Angle	15		30		45		60	
Nozzle Legth	26		12		7		4	
x/l	u_p/u_o	u_p/u	u_p/u_o	u_p/u	u_p/u_o	u_p/u	u_p/u_o	u_p/u
0	1	1	1	1	1	1	1	1
0.1	1.10	0.91	1.10	0.91	1.10	0.91	1.10	0.91
0.2	1.26	0.85	1.25	0.84	1.24	0.83	1.24	0.83
0.3	1.52	0.81	1.47	0.78	1.45	0.77	1.44	0.77
0.4	1.91	0.79	1.82	0.75	1.77	0.73	1.74	0.71
0.5	2.51	0.78	2.36	0.72	2.27	0.69	2.20	0.67
0.55	2.92	0.76	2.74	0.71	2.62	0.68	2.53	0.65
0.6	3.45	0.76	3.22	0.70	3.07	0.67	2.95	0.64
0.65	4.41	0.75	3.85	0.69	3.66	0.65	3.50	0.62
0.70	5.05	0.74	4.69	0.68	4.45	0.64	4.24	0.61
0.75	6.31	0.72	5.85	0.66	5.53	0.62	5.25	0.58
0.80	8.12	0.71	7.50	0.65	7.08	0.61	6.71	0.57
0.85	10.34	0.69	9.98	0.62	9.40	0.58	8.89	0.55
0.90	15.23	0.66	13.96	0.60	13.12	0.56	12.38	0.52
0.95	23.0	0.62	20.93	0.56	19.96	0.52	18.47	0.48
1.0	38.58	0.57	34.88	0.51	32.56	0.47	30.57	0.43

Table 2 Value of the Distance Function

u_p/u_1	0.1	0.2	0.3	0.4	0.5	0.6	0.7	0.75	0.80	0.85	0.90	0.95	0.98
$f(u_p/u_1)$	1.11	1.25	1.43	1.67	2	2.5	3.33	4	5	6.67	10	20	46

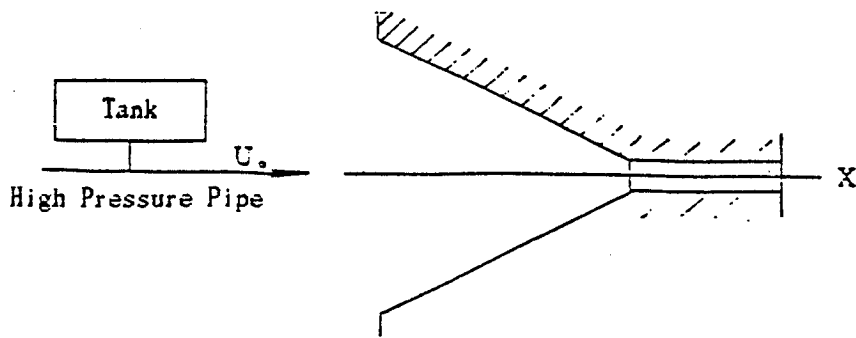


Fig.1 DIA-Jet Nozzle Structure

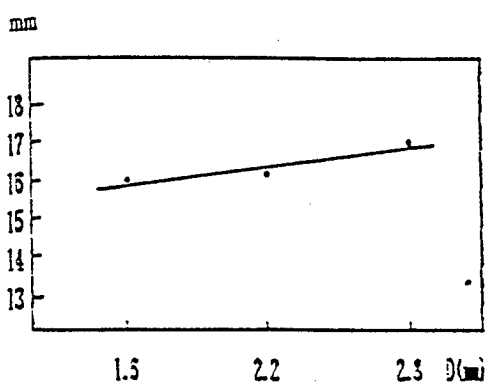


Fig.2 Cutting Depth With Different Nozzle Diameters

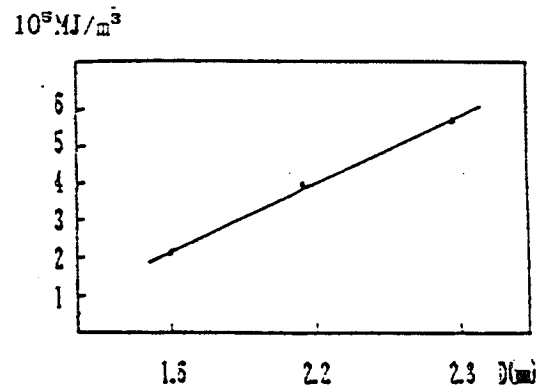


Fig.3 Energy Consumed With Different Nozzle Diameters

STUDY ON A DIRECT INJECTION ABRASIVE JET SYSTEM

You Ming-qing, Zhang Hai, Chai Zi-Pu
Jiaozuo Mining Institute
Jiaozuo City, Henan Province, China

Cheng Da-zhong
Mining University of China
Xuzhou City, Jiangsu Province, China

ABSTRACT

In the Direct Injection Abrasive Jet (DIAJET) system, flow conditions in every part except in the nozzle do not depend on the absolute pressure, but are only affected by the total flow rate of water and the geometrical parameters of the components. This is also verified in our experiment. So lower pressure can be used in studying the abrasive feeding system.

In order to investigate the process of abrasive feeding, an abrasive tank and several pipes are made of transparent plexiglass. It is understood that there are two kinds of flow in the tank. One is that abrasive and water flows down together just like a kind of slurry. The other is that abrasive particles drop down and the water permeates up. They influence the process and the rate of abrasive feeding in various degrees in different structure of Abrasive Feeding System.

In this paper, the feasibility, stability, evenness and abrasive rate's controlling of abrasive feeding proceeding have been researched thoroughly. A new system of DIAJET has been designed, and some experiment results have been described.

1.0 INTRODUCTION

Abrasive water-jet which is formed by high velocity waterjet entraining abrasive, has been widely used in various fields. However the efficient of abrasive waterjet is not very high, because it is difficult for abrasive particle to go into the central region of jet and to be accelerated to high velocity. Recently, the premixing abrasive water jet, which is also called DIAJET, increases the capability of abrasive jet. In DIAJET system, abrasive particles are carried into high pressure water before the formation of high velocity jet, and are accelerated together with water in the nozzle, forming a kind of slurry jet. So the velocity of abrasive is approximately the same as the water in the DIAJET, and much higher than that in abrasive water jet. According to our lab experiment, the DIAJET can cut steel, rock, concrete and other materials successfully at pressure of 10-15 MPa.

But there are two problems which still confine the application of DIAJET. The first is the nozzle's wearing, the second is choking and unevenness in the feeding process of abrasive. In this paper, the results of studying on abrasive feeding system are described. There are four main points as follow:

- (a) Feasibility: The abrasive feeding system transport abrasive continuously and without choking.
- (b) Stability or repeatability: The process and the rate of abrasive feeding keep the same in various experiments. The results of test can be controlled, and are not random.
- (c) Evenness: The rate of abrasive feeding is constant in the whole process of an experiment.
- (d) Flow control: The rate of abrasive feeding can be controlled. The regulating method must be accurate and easy.

2.0 METHOD OF STUDY AND EXPERIMENTAL APPARATUS

In the DIAJET system, the abrasive tank which is closed holds the pressure as same as the whole system. Flow conditions, in every part except nozzle, do not depend on the absolute pressure and are only affected by the total rate of water and geometrical parameters of the components from which the pressure loss and the velocity in every part can be determined. In other words, if we do not consider the flow field in the nozzle, but the process of abrasive feeding only, we need not take the absolute pressure in the DIAJET system into account. That is, if we increase the pump pressure only, the rate of abrasive feeding will keep the same.

This is very important to research the process of abrasive feeding. The flow conditions at very low pressure of 0.2-0.5 MPa can be used to simulate the flow at high pressure.

In order to investigate the process of abrasive feeding, the abrasive tank, caliber 140 mm, and some pipes are made of transparent plexiglass. Besides that, another abrasive tank, caliber 200 mm and height 1000 mm, is made of steel which can be working at pressures up to 35 MPa.

Figure 1 includes diagrams of two kinds of DIAJET systems used in our experiment. The difference between system A and B is the structure of abrasive feeding. Figure 1A shows the system generally used in recent application. High pressure water flows into the tank from the top. Figure 1B is the new system, in which there is no water flowing into the tank, but flowing into a small mixing chamber beneath the tank.

The abrasive water jet is collected with many buckets at regular intervals, 15 or 20 seconds, and then the water and abrasive are weighed separately. The accuracy of time measuring is 0.5 second and the accuracy of weighing is 0.05 kilogram.

3.0 CHOKING IN THE PROCESS OF ABRASIVE FEEDING

In the application of DIAJET, it must be ensured that the abrasive feeding is continuous and does not choke in the pipes. But choking happened from time to time in our initial tests. And no doubt, some of them can be dredged with high pressure water; but others can not be. Afterwards, a series of tests was carried out to investigate the problem of choking. It has been understood that there are three kinds of choking occurring at different times in the operation.

3.1 Choking at the beginning

When the flow velocity in the pipes of DIAJET system is too slow to transport abrasive fed from abrasive tank efficiently, the abrasive will deposit in the pipes due to gravity. If the pipes connecting abrasive tank and nozzle are quite short and horizontal, the flow can be maintained transporting little abrasive, or become discontinuous. The reason is that the deposited abrasive makes the pipe's section smaller and the velocity of water in pipe is increased. However, in many cases, the deposited abrasive will get more and more, and sooner or later, all pipe connecting nozzle and tank will be choked completely, and it will be very difficult to dredge.

This kind of choking usually occurs when the operating parameters like water pressure or nozzle diameter are changed in experiment that may cause total rate of water flow decreasing. But in practical application of DIAJET, the pump will operate at its rated conditions, the diameter of pipes should be choiced to make the flow velocity in pipes be 2.5 ~ 4 M/sec in order to transport abrasive efficiently.

3.2 Choking in the operating process

If there are other materials or large size abrasive in the pipes, the outlet of nozzle will be plugged up fully or partly. In the later case, the rate of flow will decrease with the decreasing of effective area of nozzle outlet, which may cause choking in the pipes, that has been reviewed above. And it is more difficult to be dredged.

According to the test result, the diameter of abrasive particles is better to be 1/3 less than nozzle's diameter, and the larger the abrasive is, the faster the nozzle wears.

If the diameter of rubber hose is small or its position not suitable, the velocity of abrasive particles in the hose will be high enough to wear its inner face, and produce some rubber slices. These rubber slices are the major source of the special materials which cause the choking in DIAJET system.

3.3 Choking after operating pause

In the operating process of DIAJET, there are two ways to get a pause. One is to close valve downstream of the abrasive tank. The other is to shut valve upstream of the tank or to stop the pump directly. The latter is often used for defensing the valve against wearing. Sometimes choking appears when DIAJET system reoperates after the pause.

According to the observation to the flow conditions in abrasive tank and pipes which are transparent, it is easy to know that the choking results from the air in the tank.

4.0 EFFECT OF AIR IN THE ABRASIVE TANK ON ABRASIVE FEEDING

Air is often carried into abrasive tank when abrasive is filled, and it will be compressed from an atmosphere to the pump pressure at the beginning. During the time water flows into the tank from the bottom, and the abrasive be pushed up as a solid cylinder. There are four layers in the abrasive tank, from top to bottom, that is air, water, abrasive, and slurry in which there is a little suspensive abrasive particles. And it is found that there is little abrasive and even nothing spurting out in the jet at the initial time of operating.

After the pump stopped, the air in the tank will expand, releasing its energy as a new pressure source for abrasive fed continually, but in pipe there is no water from pump to transport the abrasive from tank. The flow conditions in the pipes connecting tank and nozzle are shown in Figure 2.

When the pump stopped, pressure in pipes will decrease. But the air in abrasive tank still holds higher pressure. So abrasive slurry with little water rushes into the pipe due to the pressure difference between top and bottom of abrasive tank. At the same time, the air expands and the pressure decreases.

The velocity in the pipe gets slower and slower, so the abrasive in the pipe deposit, (a). The deposit-bed reduces the pipe's section of efficient flowing area, thus slurry can still flow at quite big velocity to transport abrasive above the deposit-bed. When slurry reaches the front point of deposit-bed, it will deposit as the velocity becomes slower. So deposit-bed gets longer and longer (b), and the resistance gets bigger and bigger.

However pressure in the tank is decreasing continually along with abrasive feeding out. In the end abrasive above deposit-bed will drop down, and the pipe is choked. This process moves in the opposite direction of slurry flowing, towards the tank (c).

After that, the abrasive in the pipe is pushed forward by the pressure air, from tank to nozzle, one section after one section (d). And the whole abrasive deposited in pipe will move at the same velocity (e). But it can not be maintained for a long time.

The pressure is decreasing, but the flow resistance is increasing. At last, the moving abrasive will stop, step by step, along the opposite direction of moving (f). No doubt, the air in the tank still holds a little pressure.

As has been reviewed above, the processes of (c), (d) and (f) result in abrasive pressing and make the choking more and more seriously.

The choking can be dredged with high pressure water from pump. But if the pressure is not high enough, choking not only can not be dredged, but also get more seriously. And the way to dredge abrasive choking with high pressure water will induce dangerous wear of nozzle.

5.0 INSTABILITY IN THE PROCESS OF ABRASIVE FEEDING

It is called instability phenomena that different results are obtained in a series of tests carried out at the same conditions, which is also called irrepeatability. In the experiments of DIAJET cutting, this phenomena used to occur. The dispersive cutting depths at the same operating parameters result from the instability in the process of abrasive feeding.

There is always random space among abrasive particles in the tank. To make things worse, it influences the rate and process of abrasive feeding directly. The larger the space among abrasive particles, the less the flow resistance and the more the abrasive feeding rate. If the abrasive in the tank gets hardened and impervious, there is no abrasive spurting out from nozzle in the initial time.

There are many factors which influence the space among abrasive particles in the tank, including the way of filling abrasive into tank, the time between abrasive filling and spurty, and the environmental disturbance on the abrasive tank.

6.0 EVENNESS OF ABRASIVE FEEDING

It is most important but very difficult for a DIAJET system to feed abrasive evenly. There are two kinds of unevenness. One is fluctuation due to the oscillating of pipes or the pulsing of water flow. The other is long-term unevenness which is induced by the decreasing of abrasive amount in the tank as abrasive jet spurts out.

To solve this problem, we first investigate the flow conditions in the tank. There are two kinds of flow:

- (A) Abrasive and water among abrasive particles flow down together just like slurry or a special kind of fluid.
- (B) Abrasive drops down due to gravity and meanwhile water permeates up through the space among abrasive particles.

These two kinds flow influence the process and the rate of abrasive feeding in varying degrees on different structure of abrasive feeding system.

In the system of Figure 1A, the flow in abrasive tank mainly belongs to the kind A given above, and in quasi-steady condition, there are:

$$q = q_1 + q_2$$

$$P_A + q_1^2 / 2\rho + (\rho^* - \rho)gH = P_B + q_1^2 / 2\rho^* + \Delta P_1 + kH$$

$$P_A + q_2^2 / 2\rho = P_B + q_2^2 / 2\rho + \Delta P_2$$

ρ	density of water
ρ^*	density of slurry
P	pressure
ΔP	pressure loss
H	height of abrasive in the tank
kH	pressure loss of abrasive in the tank

For quartz sand used in our experiment, $\rho^* = 1.5\rho$, hence

$$q_1^2 / 6\rho = \Delta P_1 - \Delta P_2 + (k - \rho g / 2)H$$

The coefficient of pressure loss varies with flow rate, it is smaller than $pg/2$ when q_1 is not much larger. So that, the lower the height of abrasive is, the larger the flow rate q_1 is.

In the initial time, there is much abrasive which need to be accelerated, so the increasing of q_1 is confined. After that flow rate q_1 will increase rapidly as shown in Figure 3.

It is also easy to understand the effect of total amount of abrasive in tank on the feeding abrasive rate. In Figure 3 two curves corresponding to the total amounts of abrasive 8 kg and 14 kg respectively are given. The abrasive is quartz sand.

In a word, this kind of DIAJET system in which high pressure water flows into from the top of the tank can not feed abrasive evenly. This conclusion comes from both analysis and experiment.

It is Figure 1B, the new system, that is recommended in this paper. In this system, there is no pressure water flowing into the abrasive tank. So the flow in the tank are only abrasive particles dropping down and water permeating up, which can be clearly observed through the transparent tank and pipes in our experiments.

The permeating velocity of water is mainly determined with pressure gradient which is

$$(\rho^*g_{ll} - \rho g_{ll})/H = (\rho^* - \rho)g$$

It has nothing to do with H, the height of abrasive in the tank. And the volume rate of water permeating up just equals to that of abrasive dropping down. In Figure 4, two curves with \bigcirc and \triangle correspond the abrasive rate of quartz sand and corundum respectively which is obtained using plexiglass tank and the throttle valve being whole open. When the throttle valve is altered, the abrasive feeding rate will vary. However, apart from the initial process of abrasive accelerating and air, if there is, compressing, the flow rate of abrasive is still a constant. That is Figure 5, using abrasive of quartz sand.

7.0 FLOW-REGULATING IN DIAJET SYSTEM

As has been said above, the abrasive feeding is related to the total water flow rate and the structure of the system. Moreover it has been found in our experiment using the steel tank that the relationship between abrasive and water flow rate is in proportion, that is Figure 6. The results in Figure 6 are obtained in various pressure, water flow rate and nozzle's diameters. In other words, in abrasive water jet the density of abrasive, the ratio of abrasive to water weight, which is dimensionless, is a constant as long as the DIAJET system is not changed. When the DIAJET system or throttle valve, for example is changed, the density of abrasive will change as well. It is shown in Figure 7.

Generally speaking, the best way to adjust abrasive feeding rate is to use a throttle changing the flow rate of water flowing into the mixing chamber beneath the abrasive tank. When the open area of the throttle valve is regulated, the density of abrasive in the DIAJET system will keep a constant whatever the pressure and water flow rate is. But it must be remembered that the total amount of abrasive is related to the water flow late, not a constant.

It can also be seen in Figure 6 and Figure 7 that the pressure in the DIAJET system does not affect the abrasive feeding rate, or the density of abrasive in DIAJET which can be seen clearly in Figure 8.

It must be said that the abrasive feeding rate is affected by the size or diameter of abrasive particles, as well as the type of abrasive which has shown in Figure 4. For example, the weight density of abrasive in DIAJET is 13% when the sand quartz is 50~80 mesh, and it will become to 15% when the sand quartz is 28 ~ 40 mesh.

8.0 CONCLUSION

1. Flowing conditions in abrasive feeding system of DIAJET does not depend on the absolute pressure, so the researching can be underway at lower pressure.
2. There are three kinds of choking in the DIAJET system. One of them occurs after pause of abrasive water jet spurting, which results from the air in the abrasive tank. And the air will also cause less abrasive spurting at the initial time of operating. The way to dredge abrasive choking with high pressure water jet will induce serious wearing of nozzle.
3. Space among abrasive particles in the tank influences the process and rate of abrasive feeding directly, and causes the instability or irrepeatability of experimental results.
4. There are two kinds of flow in abrasive tank. One is that abrasive and water flow down together just like a kind of slurry. The other is that the abrasive particles drop down and the water permeates up.
5. DIAJET system in which high pressure water flows into the tank from its top can not feed abrasive evenly.
6. The new DIAJET system recommended in this paper can feed abrasive stability and evenness, and the density of abrasive in the abrasive jet keep the same when the water pressure and flow rate are varying. The density of abrasive can be adjusted easily.

9.0 ACKNOWLEDGEMENT

The authors are pleased to acknowledge the valuable help given by Prof. Cui Moshen and Engineer Ren Baocai and Yu Naiyin.

10.0 REFERENCES

1. You Ming-qing, Cui Mo-shen, "Study On The Mechanism Of Abrasive Water Jet", 9th International Symposium on Water Jet Cutting Technology, 1988.
2. Zhang Hai etc, "Effect Of Air In Abrasive Tank On The Process Of Abrasive Feeding" (Chinese), Journal of High Pressure Water Jet, 1992.9.
3. Cui Mo-shen etc, "Study On The Abrasive Feeding System Of DIAJET", 3rd Pacific Rim International Conference on Water Jet Technology, Tainan, Taiwan, China. Nov. 30-Dec. 2, 1992.

This work is aided financially from
National Natural Science Research Fund Foundation of China

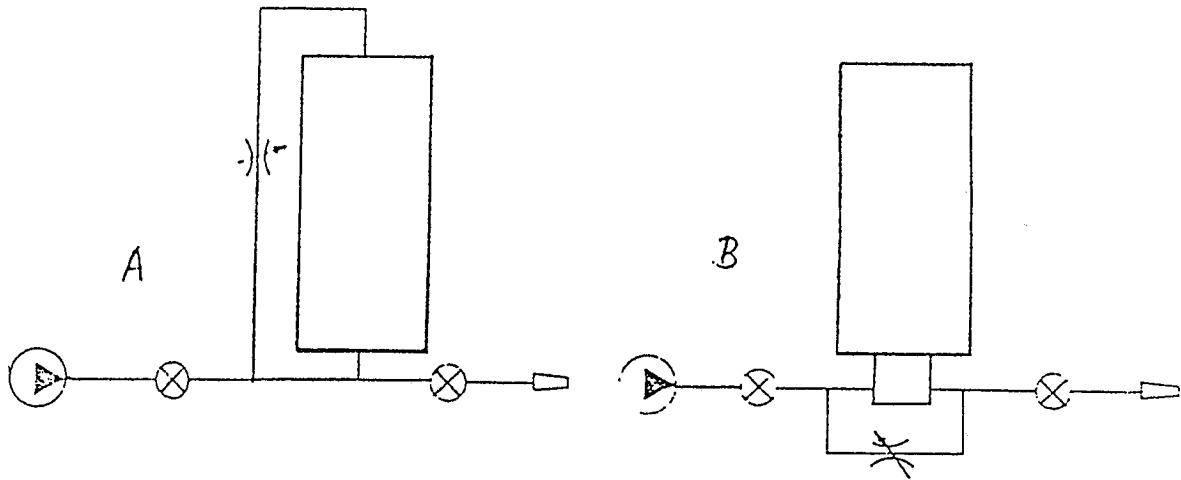


Fig. 1 Diagrams of DIAJET system

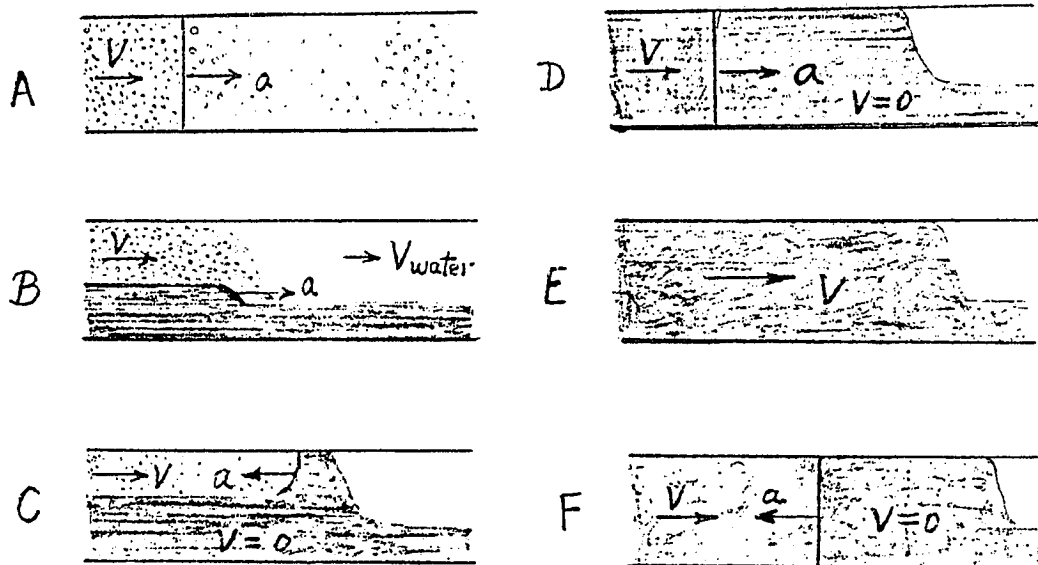


Fig. 2 Choking process in pipes

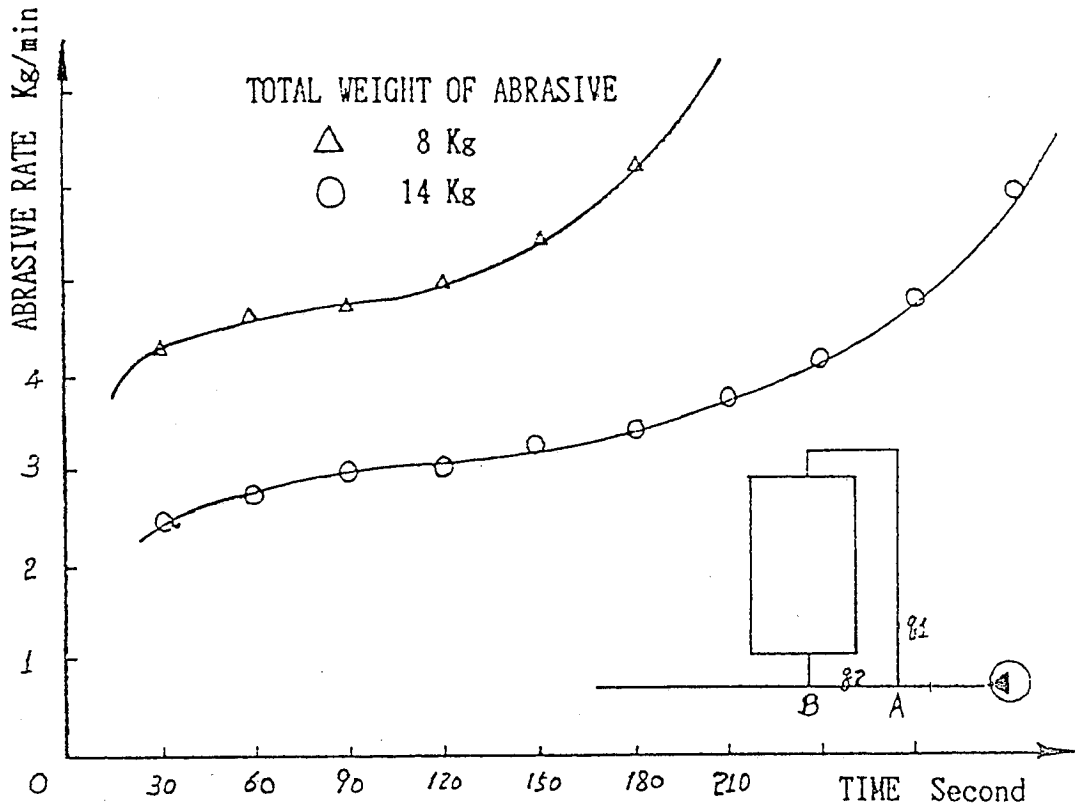


Fig. 3 Unevenness of abrasive feeding in system A

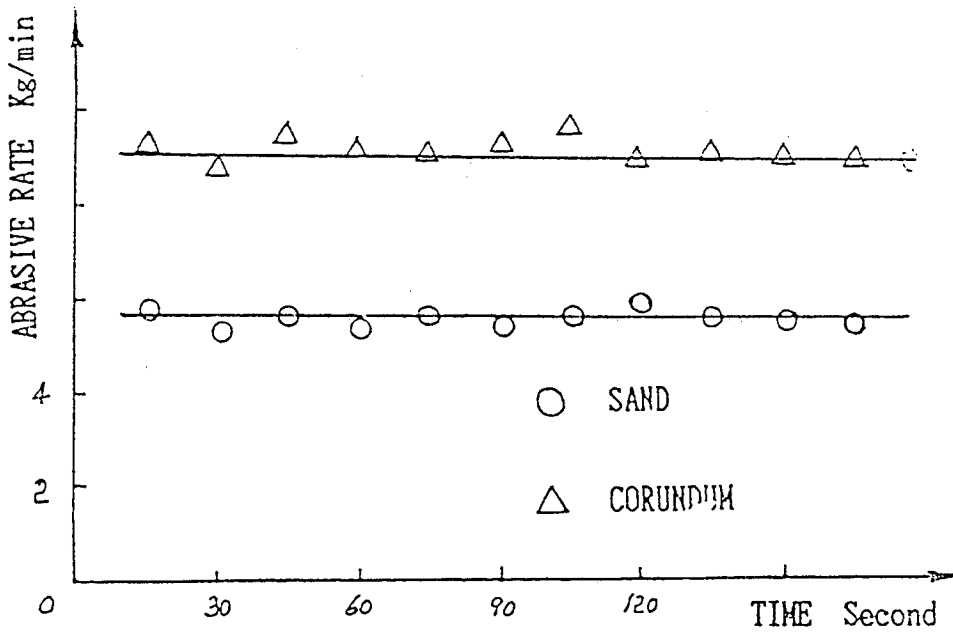


Fig. 4 Evenness of abrasive feeding in system B

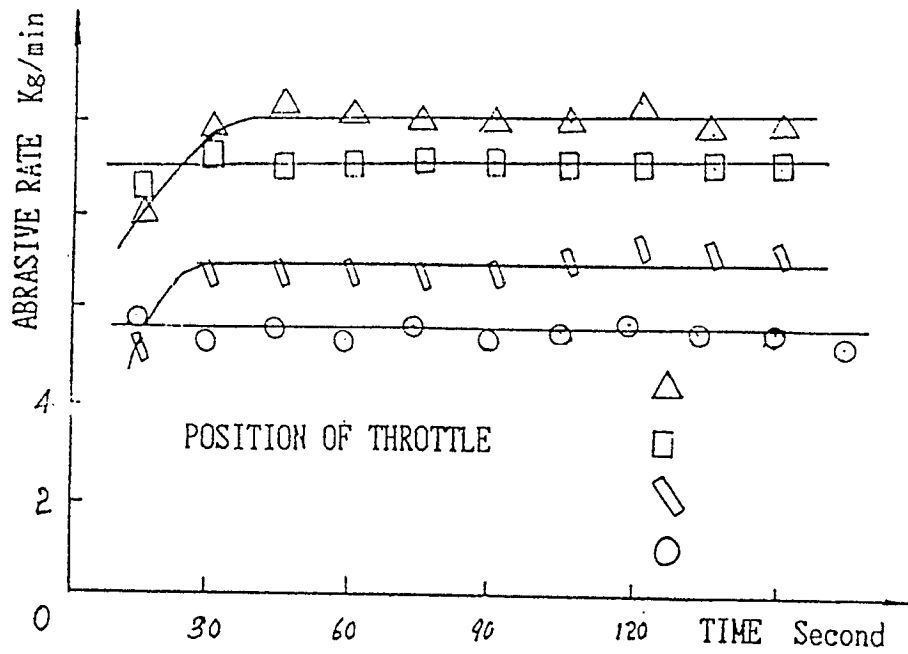


Fig. 5 Evenness of abrasive feeding in system B

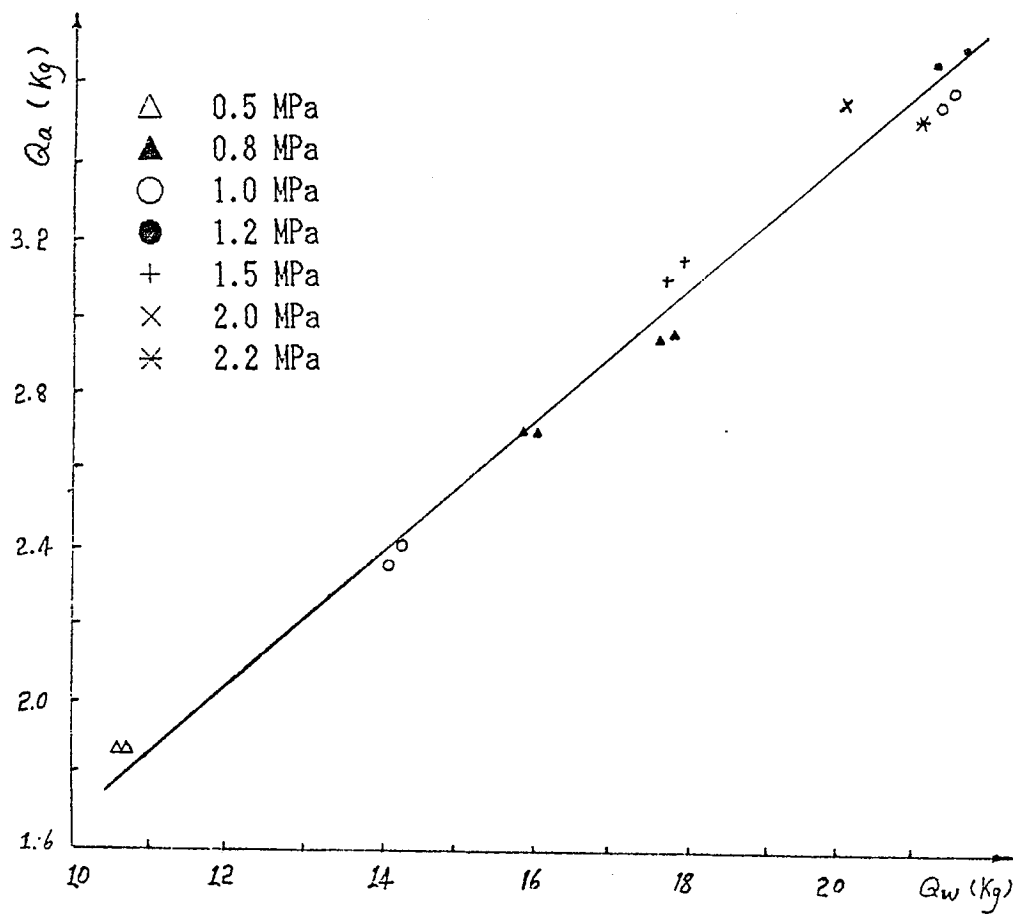


Fig. 6 Relation between abrasive feeding rate and total water flow rate

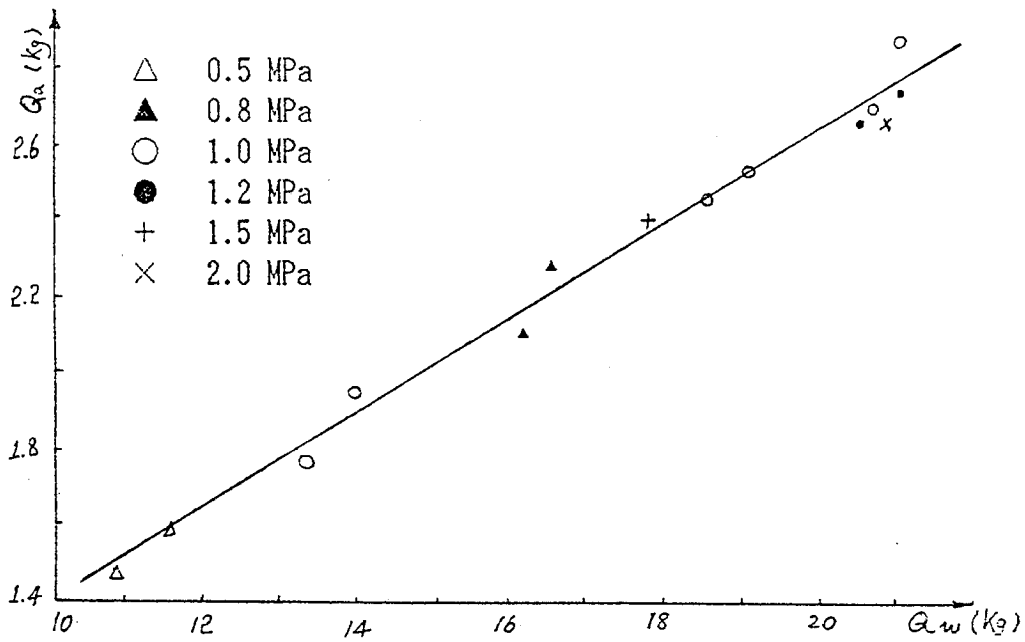


Fig. 7 Relation between abrasive feeding rate and total water flow rate

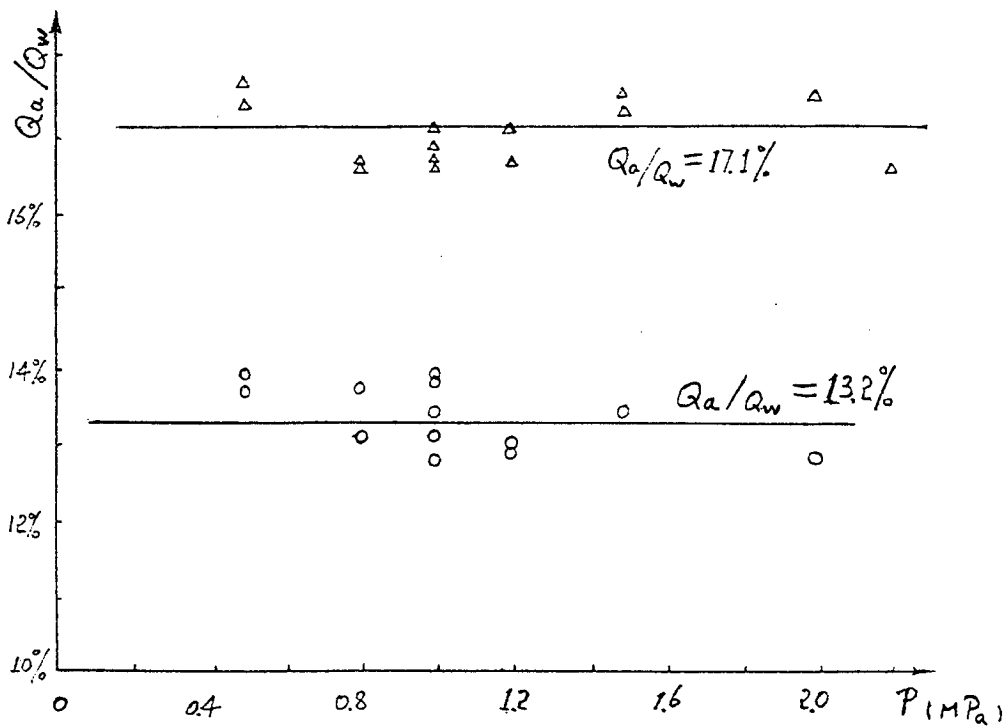


Fig. 8 Relation between abrasive density and pressure

FATIGUE STRENGTH OF STEEL IN HIGH PRESSURE WATER

W.A. Lees
Rogan and Shanley, Inc.
Houston, Texas, U.S.A.

F. Zacharias, P.S.J. Crofton
Imperial College
London, England

ABSTRACT

Designing to avoid fatigue failure in high pressure water jetting equipment is a major concern both for manufacturers and users, but has been hampered by lack of relevant material fatigue data and uncertain design techniques. Experimental data on the transverse (across-the-grain) fatigue limits of some steels in a high pressure water environment is presented.

1. INTRODUCTION

Corrosion Fatigue is the term used to describe the phenomenon of cracking (including both initiation and growth) in metals under the combined actions of a fluctuating or cyclic stress and a corrosive environment. In this definition, the word "combined" is highly relevant, since it has been shown by many investigators that neither cyclic stress in an inert medium nor environmental attack applied separately produce the same damaging results as the simultaneous action. That is, a pre-corroded specimen does not necessarily show appreciable reduction in fatigue life, nor does pre-fatiguing in air increase the corrosion rate of metals. The majority of observed fatigue failures are, in fact, corrosion fatigue failures, since only fatigue occurring in an absolute vacuum can be termed as "pure" fatigue. For example, it has been shown that for many metals, relatively innocuous environments such as the normal atmospheric gases contribute quite strongly to an increase in fatigue crack propagation rate, without producing visible corrosion [Shim and Wei, 1983].

Corrosion fatigue should not be confused with stress corrosion cracking. All metals which are susceptible to corrosion are susceptible to corrosion fatigue in any corrosive environment. Stress corrosion cracking on the other hand, is suffered only by alloys in very specific environments, and is normally associated with loading under static tension rather than dynamic loading. It should be noted, however, that the application of cyclic stress to a component nominally under stress corrosion cracking conditions may induce corrosion fatigue cracking behavior [Duquette, 1972]. Corrosion fatigue is one of the most common modes of fracture in service, frequently involving advanced engineering structures or components, the total failure of which can have serious implications for safety, quite apart from the economic losses. A major concern in the design of metal structures is the ability of component parts to maintain their integrity when subjected to a combination of fluctuating loads and an active chemical environment. The nature of the loading and the type and degree of interaction with the environment varies from application to application, so that it is difficult to lay down general design principles and detailed data has to be obtained by laboratory testing [Knott, 1983].

This investigation specifically concerns steels traditionally used in the manufacture of high pressure pumps. Many high pressure pumps and related components are required to operate with water as the pressurizing medium in water jet cleaning and cutting applications. The internal water pressure in such pumps is cyclic with a frequency of around 5 Hz, with the pressure varying in the range of a few thousand psi up to 60,000 psi, depending on the application. The combination of these factors whilst the pump is in use, i.e. cyclic stresses and pressurized water, often results in corrosion fatigue failures [Körner and Crofton, 1980]. In this type of situation, design must be based on the avoidance of fatigue failure or the minimisation of the effects of such a failure.

Martensitic precipitation hardening stainless steels such as 17-4 PH, 15-5 PH, 13-8 PH and austenitic stainless steels such as AISI 316, and A 286 are commonly specified for these applications, but the selection of these steels is based solely on their ambient pressure corrosion resistance. In order to provide some justification for the use of high strength steels it is necessary that an improvement in corrosion fatigue strength can be demonstrated and quantified experimentally in comparison with less highly alloyed steel, when subjected to water at high pressure.

2. OBJECTIVES

The major objectives of this investigation are:

1. To design and develop an experimental apparatus in which high cyclic life fatigue tests can be carried out, whilst the specimen is subjected to a hydrostatic water pressure.
2. To generate experimental data to determine if the corrosion fatigue strength of stainless steels is markedly superior to that of conventional steels in high pressure water.

3. TEST SYSTEM REQUIREMENTS

The test system [Crofton and Movahed, 1987] as originally conceived was required to be capable of applying a static force of 250 kN (56,000 lb) or a dynamic force of 100 kN (22,500 lb) at 10 Hz to a specimen of engineering material, which was simultaneously exposed to a hydrostatic pressure of up to 7,000 bar (100,000 psi).

3.1 Experimental Apparatus

3.1.1 Pressure Vessel/Seal Arrangements:

The pressure vessel shell is a crossed bored cylinder machined from a length of cold reduced, thick walled tubing of AISI 4340 electroslag remelt steel. The vessel has been autofrettaged to approximately 70% of the wall thickness. Screwed end caps retain identical end plugs, which carry both the static vessel seal, made at the bore of the vessel, and the more critical dynamic seal arrangement.

Figure 1 shows the general arrangement and dimensions of the pressure vessel and the associated sealing plugs and end caps. The more important seal arrangement is that for the dynamic seals, which must remain pressure tight for long periods during the high cyclic life tests. Also the frictional characteristics of the dynamic seals should remain essentially constant during each test. The seals used are a commercially available variant of a conventional elastomeric lip seal containing a concentrically embedded 'O' ring in the pressure side. A hard polyamide ring immediately behind each seal is a light push fit between the seal recess and the loading rod. This ring acts as an effective load distributor rather than as a true anti-extrusion ring. This latter function is provided by inner and outer chamfer rings of beryllium copper which in turn are supported by a maraging steel back-up ring. Alignment of the loading and compensating rods is ensured by the use of bronze guide bushes on both sides of each dynamic seal. These bushes are a light press fit into the end plugs. A sectional view of an end plug and detail of the seal arrangement is shown in Figure 2.

3.1.2 Pressurizing System

The pressurizing system consists of a high pressure air-driven pump, a pressure transducer and a digital volt meter (DVM) to facilitate direct pressure reading, and a pressure release valve. The pump is driven by 7 bar (100 psi) compressed air from the laboratory air supply and can provide oil or water at up to 5,000 bar (70,000 psi). High pressure oil from the outlet of the pump is fed to the pressure vessel through stainless steel, large diameter ratio high pressure tubing. Pressure in the system is maintained at the required level by adjusting the air regulator valve on the pump. This system was capable of maintaining pressure within 2 % of the required level. External trips are also incorporated in the system to stop the test in the event of pressure dropping below the control level.

3.2 Load Control Unit

3.2.1 Loading Train

The dimension of the specimens (radiused hour glass type) is to some extent a compromise, determined by the size of the loading train arrangement, the amount of travel and load capacity available from the servo-hydraulic machine which provides the external loading. Specimens are gripped by means of screw threads: one end of the specimen screws into the end of the compensating rod (upper rod) and the other end screws directly into the bottom of the half yoke. The free end of the half yoke is fixed to the upper end plug by two small cap screws.

The compensating rod (upper rod) and the loading rod (lower rod) are connected together by a full yoke. Both yokes and rods are made from maraging steel, heat treated to a 0.2 % proof stress of 1200 MPa (175,000 psi). The loading rod connects via a flange arrangement to the ram of a servo-hydraulic machine which provides loads of up to 250 kN (56,000 lb). When the ram of the machine is displaced upwards, the loading rod and hence the full yoke and compensating rod are also displaced upwards. This displacement strains the specimen and hence generate a tensile load, the reaction of the load being transmitted through the half yoke. The half yoke is used as the internal load cell, measuring load on the specimen directly, using strain gauges bonded to the yoke. Eight strain gauges arranged in a full bridge configuration are used to form the load measuring transducer. All strain gauges are located within the pressurized system, so minimizing inaccuracies due to different temperatures. Stainless steel clad mineral insulated cable was used as the basis for the lead-through to connect the individual leads from the internal load cell on the high pressure side to the external load measuring instrumentation on the atmospheric side. The four conductor cable is brazed into a tapered, maraging steel bush which is lapped to give an intimate fit in a supporting plug of the same material.

3.2.2 Control System

The servo-hydraulic machine used is a 250 kN (56,000 lb) load capacity DARTEC capable of being controlled in load, displacement and external function mode by a feed-back signal in a closed loop control system. The load measure system comprises a connection to the internal load cell (half yoke) via an amplifier and a GOULD 1604 20 MHz digital oscilloscope. The machine load control is adjusted by the level of the external load to give the required internal load (set load) on the specimen. The voltage output of the internal load cell was calibrated against the machine load cell for different frequencies (1-10Hz), under static/cyclic loading and with/without high pressure water. No effect was observed when changing the frequency but a different calibration resulted when the vessel was pressurized under static or cyclic loading. It was found that the increased seal friction with the system pressurized reduced the transmitted load by about 10 %. After an initial settling period no further adjustment of the applied load was required to maintain constant test conditions.

4. EXPERIMENTAL PROCEDURE

4.1 Material

Three different steels were used in the course of this investigation:-

Mild Steel BS 970 Grade 070 M20 (equivalent to AISI 1021 or DIN 1.0402);

Austenitic Stainless Steel BS 316 S 16 (equivalent to AISI 316 or DIN 1.4401);

Martensitic Precipitation Hardening Stainless Steel CARPENTER 450 (equivalent to DIN 1.4568).

The mild steel was included in this investigation as an example of a C-Mn steel with a ferritic-pearlitic

microstructure [Brandes and Brook, 1992]. The tensile strength of the mild steel is relatively low and in comparison with the other investigated steels it is highly susceptible to corrosion. The mild steel therefore represents a baseline for comparison of the other steels tested.

Austenitic stainless steel type 316 is an '18-8' chromium nickel steel modified by the addition of molybdenum, which greatly increases the corrosion resistance as well as improving physical properties at elevated temperatures [CJA S.Steels, 1991]. It is non-magnetic in the annealed condition and not hardenable by heat treatment. Both hardness and strength are increased by cold working.

Martensitic precipitation hardening stainless steel such as CARPENTER 450 [Carpenter Tech., 1992] is an alloy of importance to designers because of its combination of high strength and hardness, excellent corrosion resistance and easy heat treatment. The normal hardening treatment requires heating to about 480°C (900°F) followed by air cooling. This low temperature procedure virtually eliminating scaling and distortion. Additional features of this alloy are its high resistance to crack propagation and relatively good transverse properties.

As supplied from the mill in the solution annealed condition, CARPENTER 450 can be heat treated at different temperatures to develop a wide range of mechanical properties. In critical applications the steel is invariably used in the precipitation hardened condition, such as the H900 condition which implies precipitation hardening at a temperature of 482°C (900°F) for four hours. Therefore in this investigation the CARPENTER 450 specimens were heat treated to this condition. Tables 1 and 2 show the chemical composition and the mechanical properties of the three steels investigated.

4.2 Specimen Geometry

Radiused hour glass specimens were used for the corrosion fatigue tests, to the dimension shown in Figure 3.

The specimens were secured in the loading train by means of screw threads. One end of the specimen screws directly into the bottom of the half yoke (9/16" UNF thread), and the other end screws into the end of the compensating rod (upper rod M12 thread). The threads at both ends of the specimen were produced by thread rolling rather than thread cutting to induce residual compressive stresses in the thread roots by which the fatigue strength in this relatively critical part of the specimen geometry is maximized [Metals Handbook, 1978].

4.3 Specimen Orientation

In common with almost all steels ductility may be appreciably lower in the transverse direction compared to the ductility in the longitudinal direction, parallel to rolling. This is due to the grain structure and the inclusions of the steels being elongated in the working direction [Samuels, 1988]. All specimens were prepared with their longitudinal axis normal to the original bar stock axis, i.e. transverse to the rolling direction. This particular orientation was chosen to best simulate the stress conditions in high pressure pump components where the alternating hoop stresses is the controlling stress. Fatigue specimens were machined from 4" to 6" bar stock of each steel. After turning and machining on a CNC lathe, the specimens were polished using 1200 grade emery cloth.

4.4 Test Parameters

Many engineering structures and components such as high pressure pumps, rotating shafts, vehicles etc are subjected to cyclic loading, and often fail at stresses levels that are far below the tensile strength, this phenomenon being generally known as fatigue. In addition the corrosion fatigue, the behavior of steels

is influenced by many other variables such as mean stress level, stress range, environment, surface finish, and metallurgical factors. In the case of fatigue in a corrosive environment the time for which the steel is exposed to the cyclic stress must also be considered [Nagasaki et al., 1972]. In high pressure pump components, such as pump barrels and heads, repeated tensile stresses are generated by the pulsating internal water pressure of the pump. Therefore in these experiments the specimens were also subjected to repeated tension loading [Troost, 1989].

4.4.1 Frequency / Waveform

From a practical point of view, the effects of frequency and waveform on corrosion fatigue behavior are not easily quantified. It is well known that the fatigue endurance of a steel in an aggressive environment, compared to the endurance measured in air, is frequency dependent. A steady increase in crack growth rate per cycle (da/dN) with decreasing frequency is often reported in the literature [Panasyuk and Romaniv, 1983]. Therefore, the results of accelerated corrosion fatigue tests must be treated with caution. In these tests the specimens were subjected to a sinusoidal repeated tensile loading at a frequency of between 5 and 10 Hz, which is a typical range of frequencies used in high pressure pumps.

4.4.2 Environment / High Pressure

The effect of environment on the corrosion fatigue endurance of a steel is known to be considerable. For example, fatigue lives are longer for tests carried out in vacuum, and the normal fatigue limit observed for a low carbon steel tested in air is absent if the steel is tested in a corrosive medium [Knott, 1983]. This is understandable because under the influence of the environment, the deterioration or damage of the steel increases with time; therefore the likelihood of failure will also increase with time. Initially steel specimens were tested in air, to determine the fatigue limit, which could be used as a basis for comparison with the results for specimens tested in both water and high pressure water. The second series of tests was carried out by exposing further specimens to fatigue loading whilst the specimen was immersed in distilled water at atmospheric pressure. Finally all of the steels were fatigue tested in the pressure vessel to determine the effect of water under hydrostatic pressure of 2,000 bar (29,000 psi) on the fatigue endurance of the steel.

To ensure reproducibility of frictional conditions in the loading train the pressure vessel was pressurized with hydraulic oil. A flexible PVC sleeve filled with distilled water and closed at both ends with metal wire was placed around the gauge length of each specimen in order to subject the specimen to the corrosive environment. Several preliminary experiments under pressurized conditions were carried out to ensure that this method of introducing the environment remained leak free over an extended period. Distilled water (i.e. partially deoxygenated) rather than tap water was used as the aggressive environment, so as to further enhance the reproducibility of results. The hydrostatic pressure of the water was set at 2,000 bar (29,000 psi), since many high pressure pumps operate with discharge pressures of this order.

4.5 Determination of the Fatigue Limit

Corrosion fatigue is a generic term that describes the response of a material to the combined actions of cyclic loading and corrosive environments. For a particular frequency (which to a large extent determines the time the crack is exposed to the environment), the material response can be measured in terms of either the number of stress cycles to produce failure, N_f , or the rate of fatigue crack growth per cycle, da/dN , under given loading conditions [Speidel and Wei, 1972]. In this investigation, the emphasis has been placed on the long life behavior of different steels in the pressurized medium of distilled water, therefore curves (alternating stress amplitude versus log number of cycles to failure) are used to present the test results.

5. RESULTS

Previous crack growth studies have shown a wide range of environmental effects with both reductions and dramatic accelerations in crack growth rate, resulting in different numbers of cycles to failure. Therefore it is recognized that because fatigue is primarily a surface initiation and crack growth phenomenon, the environment in contact with the surface nearly always plays a role in enhancing or retarding the dislocation-controlled fatigue process operating in the material. In this investigation the effects upon corrosion fatigue of a pressurized environment (distilled water) were examined.

It is difficult to define "baseline" fatigue properties for a material which give crack initiation time, crack growth rate and endurance at a given stress level with no significant effect from the environment. Several studies show that reversibility of the fatigue process can only occur in hard vacuum. In other words, when the operation of a mechanism is affected by environmental attack, then all data are truly relative [Tomkins, 1979].

5.1 Tensile Tests

A brief examination of the schematic stress strain curves for the three different steels is presented in Figure 4. The mild and the austenitic steels show typical ductile behavior with a large elongation and a tensile strength of about 410 MPa (59,000 psi) and 790 MPa (114,500 psi) respectively. The martensitic steel has a much higher yield stress and the highest tensile strength of about 1,050 MPa (152,000 psi).

5.2 Corrosion Fatigue Tests

Analyzing the S_a-N_f curves, it will be noted that the data is scattered. This is due to fluctuations in crack initiation life caused by the fact that the crack initiation occurs in one or more favorably oriented grains. Therefore the initiation time is influenced by localized micro-discontinuities which differ from grain to grain and so from specimen to specimen.

Having achieved the result of no failure, the test was reproduced at a lower alternating stress amplitude in order to verify the result. The tests were regarded as complete after about six million cycles in air and in water after about eight million cycles, when no failure had occurred. As regards the tests in air it is clear that the fatigue limit of the steel was reached (knee of S_a-N_f curve). For the tests in a corrosive environment the deterioration continues throughout the lifetime of the steel but with laboratory tests a sensible end must be defined.

5.2.1 Mild Steel

The first material to be considered is mild steel, Figure 5. In air it was found that the fatigue limit was about ± 160 MPa ($\pm 23,200$ psi). This compares with the result in water at 8 Hz of ± 105 MPa (15,225 psi), which is 35 % lower than in air. Several tests were also carried out in water at 5 Hz. Whilst the number of cycles to failure was not significantly different from the tests carried out at 8 Hz, it was noted that they all occurred at the lower end of the data range, i.e. at lower alternating stress amplitudes. The tests in high pressure water at 8 Hz resulted in an endurance limit of ± 130 MPa (18,850 psi). This is a decrease of 19 % from the results in air but all of these data are at a higher level than those found in unpressurised water.

5.2.2 Austenitic Steel

The results from the tests in air with austenitic steel show a fatigue limit of ± 220 MPa ($\pm 31,900$ psi), Figure 6. In water at 8 Hz a fatigue endurance of ± 205 MPa ($\pm 29,725$) was found, and in high pressure an endurance limit of ± 195 MPa (28,275 psi) is estimated. There is only a marginal difference in the results in air compared with those in water and in high pressure water.

5.2.3 Martensitic Steel

Martensitic steel when tested in air showed a fatigue limit at about ± 390 MPa ($\pm 56,550$ psi), Figure 7. However, the differences in results between fatigue endurance in water and high pressure water are more marked than for the austenitic steel. This is shown by the endurance limit in water which is ± 300 MPa ($\pm 43,500$ psi), 23 % smaller than in air, and in high pressure water which is ± 310 MPa ($\pm 44,950$ psi), 20 % smaller than in air.

6. DISCUSSION

Various mechanisms have been proposed to explain enhanced crack growth resulting from the presence of a corrosive environment during cycling loading, and these are not essentially different from those used in explaining stress corrosion. Thus, localized plastic deformation arising from cyclic loading has been suggested:

- as causing the disruption of otherwise protective surface films which then enhances electrochemical activity,
- by sustaining a selective corrosion tendency for the material in question to corrode in a transgranular or intergranular manner,
- of facilitating the ingress of hydrogen to lower grain boundary surface energy and promote crack growth and even of lowering the energy requirements for cracking by aiding adsorption of specific species.

These are very similar to the models proposed to explain the mechanism of stress corrosion cracking. The logical conclusion that stress corrosion and corrosion fatigue are possibly the same mode of failure is tempting. However the environmental conditions under which corrosion fatigue occurs are much more extensive than those that promote stress corrosion, i.e. the enhancement of crack growth during cyclic fatigue loading can occur in environments that will not promote stress corrosion in the same alloy. Thus attempts to rationalize the effects of environments in corrosion fatigue are not likely to be successful. Some environments that are markedly corrosive to a particular metal have little or no effect on fatigue behavior, whereas others that are not corrosive to unstressed metal significantly influence fatigue failure. Similarly, corrosion pits, produced by pre-exposure or during cyclic loading, may have damaging effects or be without influence. Suggestions by various investigators that corrosion fatigue results from stress intensification at the bases of corrosion pits also provides little hope of rationalizing the effect of environmental influence upon fatigue because marked environmental effects have been observed in systems that do not exhibit corrosion pitting. Nevertheless some theories/models such as [Frost and Pook, 1973 and Williams, 1973] have been developed through the use of fracture mechanics.

It is therefore probable that the rationalization of environmental effects in relation to corrosion fatigue will not occur soon. The specificity that is an important part of the environmental aspects of stress corrosion cracking does not apply to corrosion fatigue to such a degree, and it seems likely that the explanation of

environmental effects on fatigue crack propagation will involve a variety of mechanisms. This can be seen by considering the possible roles for corrosion in the initiation and propagation stages of cracking [Parkins, 1983].

The mechanism of corrosion fatigue failure consists essentially of three stages; crack initiation, sub-critical crack growth and failure. The initiation of fatigue cracks at initially plain surfaces may take up as much as 90 % of the total life in the absence of any environmental influence, but corrosion reactions may reduce this proportion of the life to less than 10 %.

6.1 Initiation

In service situations the ability to initiate cracks under cyclic loading often determines the integrity of a structure or component. Few sharp cracks exist at a surface and these must be nucleated rapidly by dislocation processes involving reversed slip at a defect or stress raiser (e.g. inclusions, near welds). The action of these processes produces microcracks which in some alloys can occur within 1 % of the final endurance while in others, notably planar slip alloys, they can take up most of the life. The fatigue strength of a material can often be thought of as a crack initiation limit below which dislocation structures which create surface cracks cannot form. However, just as surface roughening by machining or fretting can produce effective small stress raisers for crack initiation, corrosion attack at a surface can produce pits or cracks along grain boundaries or dislocation channels by preferential attack. Thus, the corrosion process can radically reduce fatigue strength by enhancing crack initiation at stress concentration sites.

6.2 Crack Growth

In many structures and components cracks can initiate rapidly at stress raisers or pre-existing defects, with the result that component life is dominated by crack growth. Crack growth studies have shown how cracks grow at various stages of their development, which can be seen schematically across a section following surface initiation in Figure 8. Three stages of crack growth have been identified. The first is an extension of the crack initiation process by dislocation movement within a surface grain, usually termed as stage I growth. This is followed by a second growth phase (stage II) normal to the maximum applied tensile stress. This stage is often characterized by the appearance of striations on the fracture surfaces. Finally crack growth occurs by a third stage (stage III) in which material inhomogeneities such as inclusions or precipitates initiate hole formation ahead of the crack which contributes directly to crack advance by microvoid coalescence. Decohesion of these particles ahead of the crack leads to subsequent hole growth during crack opening and linkage into advancing crack. Stage III is terminated by unstable crack advance [Tomkins, 1979].

In general the effect of an environment is most likely to be confined to stage II crack growth since there is little or no time for an environment to have any effect when stage III conditions are reached. However, even under stage II crack growth conditions the effect of an environment is likely to be highly frequency dependent since the environment transport to the crack tip or adsorption rate becomes the limiting factor. In this regard the effect of an environment on crack growth rate is very similar to the effects noted for stress corrosion cracking. Low cyclic loading frequencies implying longer contact times will tend to enhance crack growth rates and vice versa.

7. CONCLUSIONS

The principal aim of this project was to investigate the effect of pressurized water on the fatigue endurance of steels subjected to repeated tension fatigue loading.

The main conclusions to be drawn from this investigation can be summarized as follows:

- 1) The fatigue limits in air of the steels tested compared to their tensile strength are as expected. The fatigue endurances for the tests in water at atmospheric pressure and under high pressure vary significantly depending on the particular environmental behavior of each steel.
- 2) For the mild steel the number and size of corrosion pits which develop, and the ensuing corrosive reactions in these pits, are the main factors influencing the initiation and propagation of cracks. These effects result in markedly reduced fatigue endurance in unpressurised water (± 105 MPa, $\pm 15,225$ psi) compared to that in air (± 160 MPa, $\pm 23,200$ psi). The unexpected and relatively high fatigue endurance limit found for mild steel in high pressure water (± 130 MPa, $\pm 18,850$ psi) is probably due to the smaller amount of water /dissolved oxygen in the closed sleeve around the specimen inside the pressure vessel. This would seem to indicate that the corrosion potential of the water is more significant than the effects of the high pressure.
- 3) The results from the fatigue tests with the austenitic steel specimens show only a marginal difference in fatigue endurances in air compared to those in water both at atmospheric pressure and under high pressure. The insensitivity of the austenitic stainless steel to aqueous corrosion is confirmed, i.e. no signs of corrosion occurred. Inspection of the fatigue crack initiation sites by scanning electron microscopy indicates that no defect controlled initiation was obvious. Thus, the fatigue failures of the austenitic steel specimens can only be presumed to be a dislocation controlled process.
- 4) The martensitic precipitation hardening stainless steel demonstrated the highest fatigue endurance of the investigated steels under the various environmental conditions (between ± 390 MPa in air and ± 310 MPa ($\pm 56,550$ and $44,950$ psi) in high pressure water). For this steel, the fatigue failures in high pressure water were of great interest, because this steel is the steel predominantly used in the manufacture of high pressure pumps. Inspection of the fracture by the scanning electron microscope reveals in almost every case inclusions lying at or near the surface as the cause of initiation. The notch effect due to the inclusions together with superimposed hydrostatic pressure causes stress concentration at these points which weakens the steel. This is in contrast to the failures in air where no specific type of origin could be identified.

ACKNOWLEDGMENTS

The authors gratefully acknowledge the support of Polyflex Schwarz GmbH of Germany, and Rogan and Shanley, Inc. of Houston Texas, USA.

REFERENCES

- Barson, J.M. "Effect of Cyclic Stress Form on Corrosion Fatigue Crack Propagation below K_{ISSC} in a High Yield Strength Steel",
In: NACE-2, National Association of Corrosion Engineers, Houston, Texas, USA, 1972, pp. 424
- Brandes, E.A., Brook, G.B. Smithells Metals Reference Book, 7th ed.,
Butterworth-Heinemann Ltd., Oxford, England, 1992
- Crofton, P.S.J., Movahed, M.
"Development of a Testing System for Fatigue Tests under Hydrostatic Pressure",
Internal Report of Imperial College, London, England, 1987
- Crofton, P.S.J.-"The Fatigue Limit of Thick-Walled Steel Cylinders",
In: Fatigue Thresholds: Fundamentals and Engineering Applications, Engineering Materials Advisory Services Ltd., Warely, England, 1982, pp. 1033
- Duquette, D.J. "A Review of Aqueous Corrosion Fatigue",
In: NACE-2, National Association of Corrosion Engineers, Houston, Texas, USA, 1972, pp. 12
- Fenner, R.T. "Mechanics of Solids",
Blackwell Scientific Publications, England, 1989
- Frost, N.E., Pook, L.P. "A Fatigue Crack Growth Theory",
International Journal of Fracture, Vol. 9, 1973, pp. 53
- Körner, J.P., Crofton, P.S.J.
"Entwicklung und Konstruktion eines Druckübersetzers für den Dauerbetrieb bei Drücken über 3000 bar", Chemie-Technik, 9. Jahrgang (1980) Nr. 11, pp. 561
- Knott, J.F. "Effects of Environment on Crack Growth under Monotonic and Cyclic Loading",
In: Corrosion Fatigue, R.N. Parkins and Y.M. Kolotyrkin (eds.), The Metals Society, London, England, 1983, pp.9
- Metals Handbook, vol. 1: Properties and Selections of Irons and Steels,
American Society for Metals, Metals Park, Ohio, USA, 1978
- Nagasaki, R. et al "Corrosion Fatigue of A-302B Steel in High Temp. Water",
In: NACE-2, National Association of Corrosion Engineers, Houston, Texas, USA, 1972, pp. 439
- Panasyuk, V.V., Romaniv, O.N. "Mechanics of Corrosion Fatigue",
In: Corrosion Fatigue, R.N. Parkins and Y.M. Kolotyrkin (eds.), The Metals Society, London, England, 1983, pp.24
- Parkins, R.N. "Aqueous Environmental Influences in Corrosion Fatigue",
In: Corrosion Fatigue, R.N. Parkins and Y.M. Kolotyrkin (eds.), The Metals Society, London, England, 1983, pp.36

Product Data: CARPENTER 450 (17-4 PH), Carpenter Technology Corporation, Houston, Texas, USA, 1992

Product Information: Type 316 S 16,
CJA Stainless Steels Ltd, Thames Ditton, Surrey, England, 1991

Pugh, H.L.I.D. "Mechanical Behavior of Solids at High Pressure",
Proc 6th AIRAPT Conf., Plenum Press, New York, USA, 1979, pp. 583

Samuels, L.E. Metals Engineering: A Technical Guide,
ASM International, Metals Park, Ohio, USA, 1988

Shim, G., Wei, R.P. "Fracture Mechanics and Corrosion Fatigue",
In: Corrosion Fatigue: Mechanics, Metallurgy, Electrochemistry and Engineering, ASTM STP 801,
T.W. Crooker and B.N. Leis (eds.), American Society for Testing and Materials, USA, 1983, pp. 5

Speidel, M.O., Wei, R.P. "Phenomenological Aspects of Corrosion Fatigue",
In: NACE-2, National Association of Corrosion Engineers, Houston, Texas, USA, 1972, pp. 379

Tomkins, B. "Role of Mechanics in Corrosion Fatigue",
Metal Science, July 1979, pp. 387

Troost, A. Einführung in die Allgemeine Werkstoffkunde Metallischer
Werkstoffe, Bibliographisches Institut, Mannheim/Wien/Zürich, 1989

Williams, D.P. "A New Criterion for Failure of Materials by Environment-Induced Cracking",
International Journal of Fracture, Vol. 9, 1973, pp. 63

NOMENCLATURE

n	Cyclic Loading Frequency
S_{mean}	Mean Stress
S_a	Alternating Stress Amplitude
N_f	Number of Cycles to Failure
a	Crack Length
N	Number of Cycles Applied
da/dN	Crack Growth Rate

TABLES

Table 2: Chemical Composition in Weight %

Type of steel	Mild	Austenitic	Martensitic
C	0.16/0.24 *	0.046	0.03
Cr	-	18.05	15.0
Ni	-	10.92	6.75
Mo	-	2.23	0.77
Mn	0.5/0.9 *	1.3	0.35
Si	0.05/0.35 *	0.44	0.34
Cu	-	0.13	1.53
P	0.05 max	0.033	0.026
S	0.05 max	0.016	0.003
Cb	-	-	0.63
Cb + Ti	-	-	0.65
* min/max values			

Table 3: Mechanical Properties

Type of Steel	Mild	Austenitic	Martensitic
Yield Stress [MPa] [psi]	235 34,075	530 76,850	1,002 145,290
Tensile Strength [MPa] [psi]	410 59,450	700 101,500	1,082 156,890
Elongation on 5D [%]	38	62	20
Hardness, Hv Approx. Conversions	140 --	200 190 Brinell	390 40 Rc

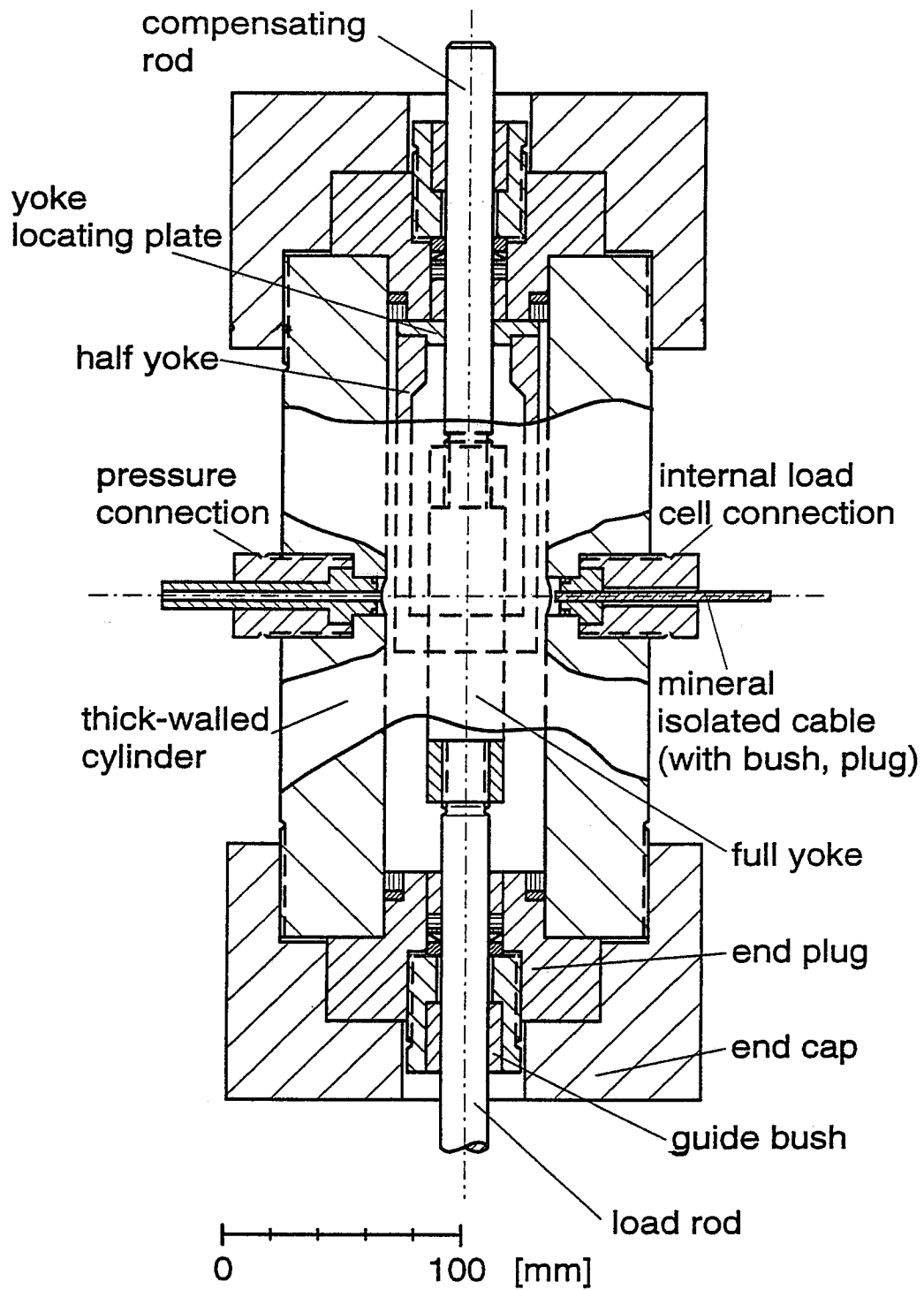


Figure 1. General Arrangement of Test Chamber

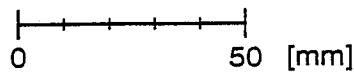
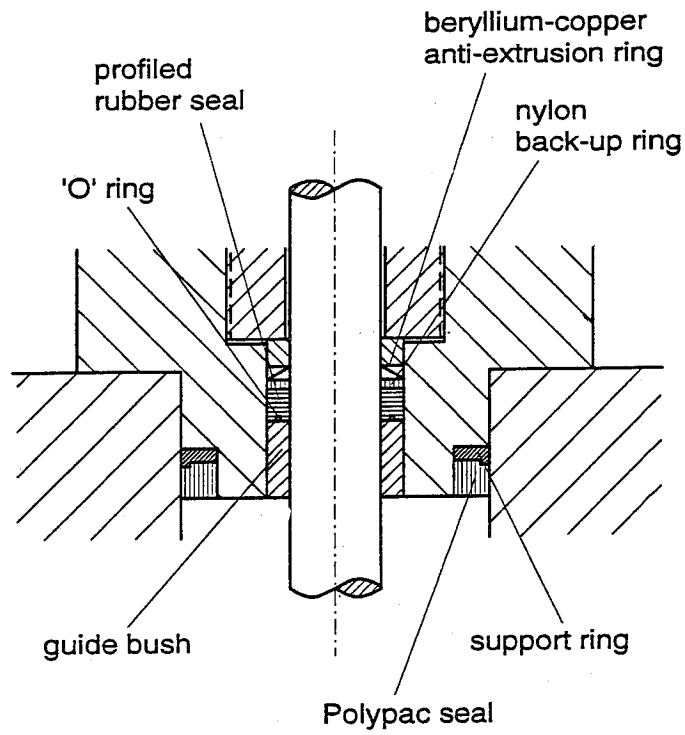


Figure 2. Arrangement of Dynamic Seals

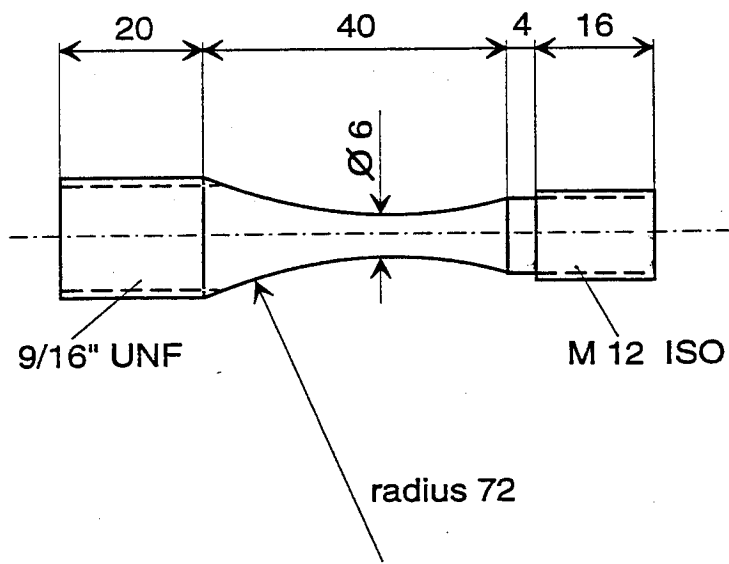


Figure 3. Specimen Geometry (in mm)

- A** Mild Steel
- B** Austenitic Stainless Steel
- C** Martensitic Precipitation-Hardening Stainless Steel

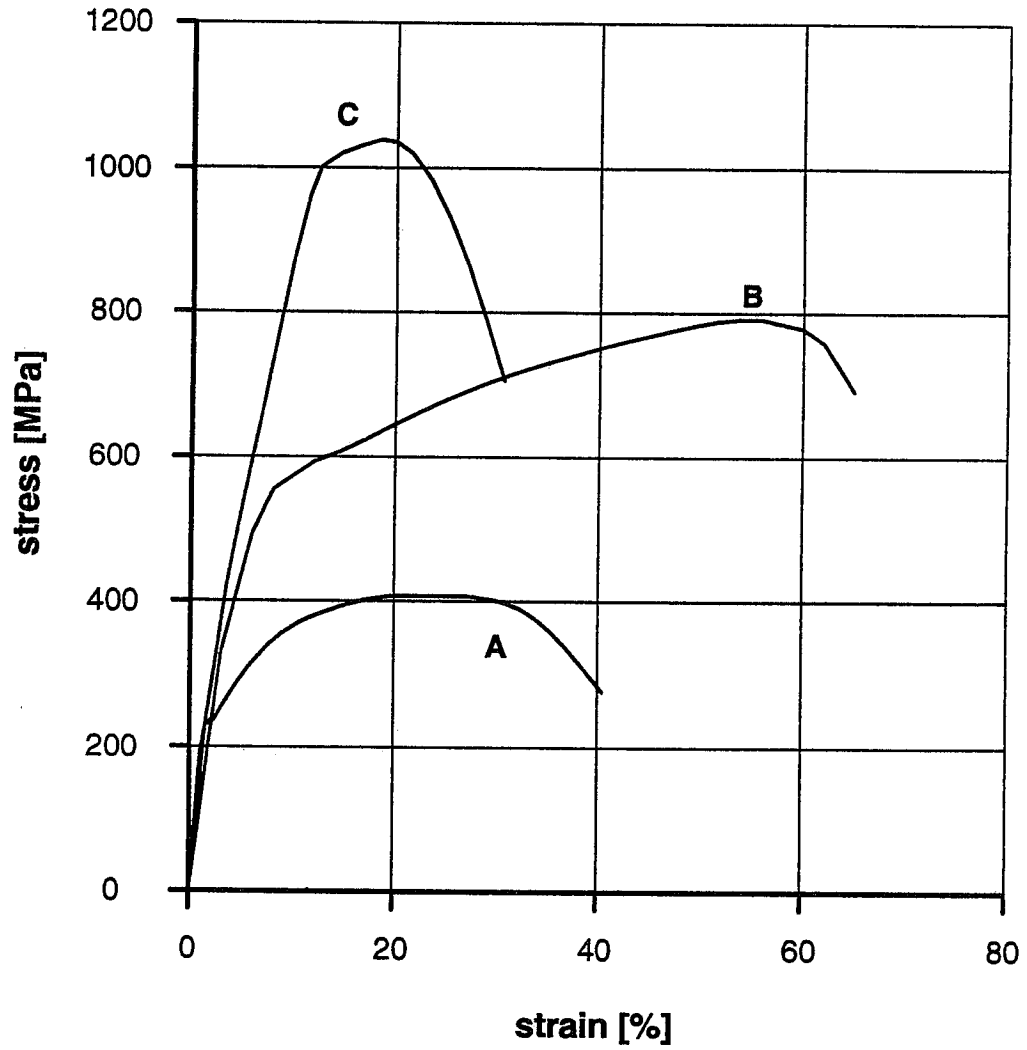


Figure 4. Load - Extension Curves

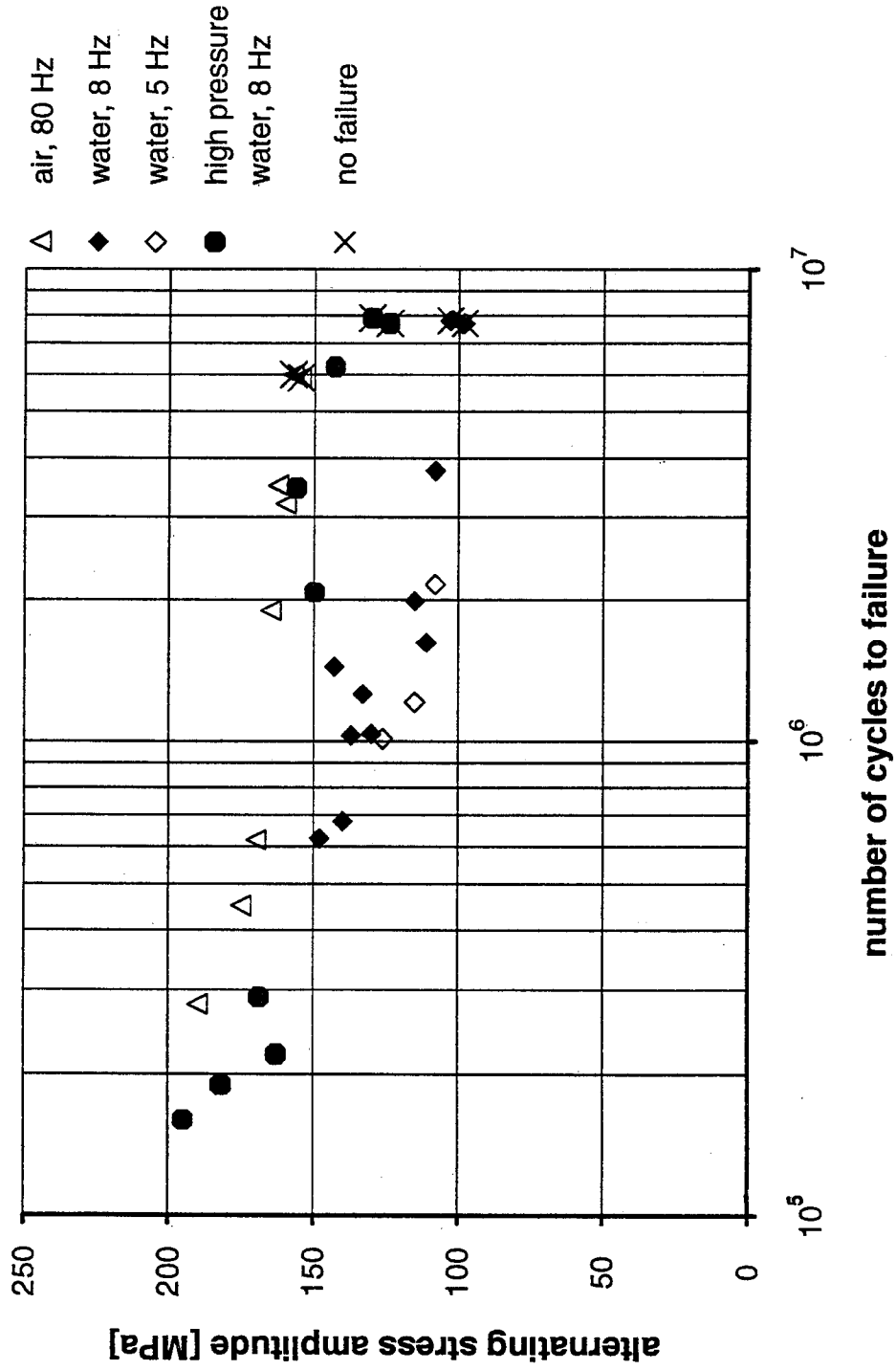


Figure 5. Fatigue Curve for Mild Steel

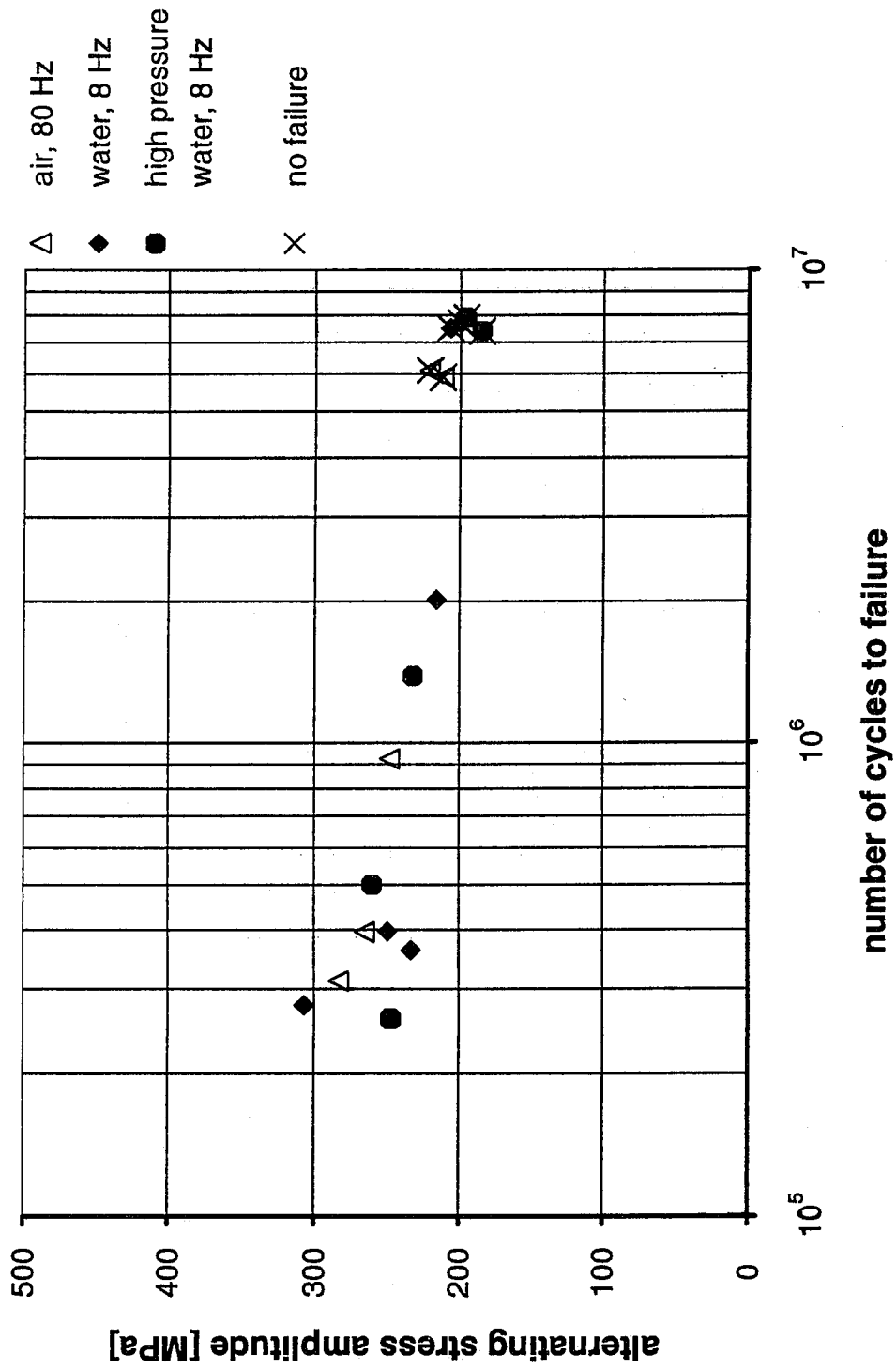


Figure 6. Fatigue Curve for Austenitic Steel

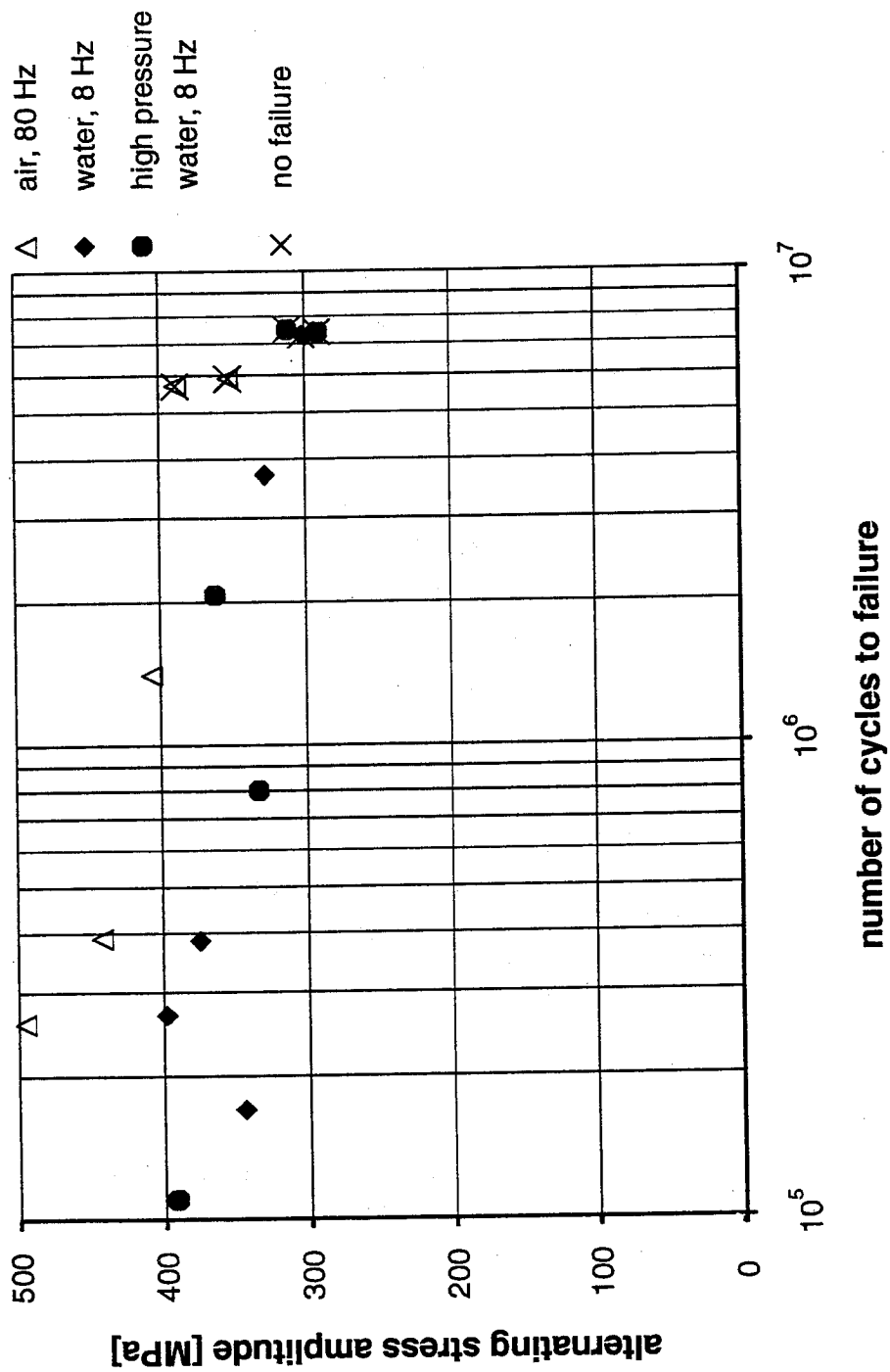
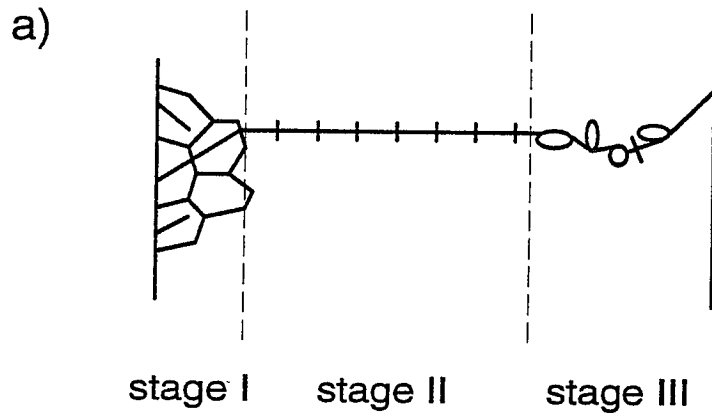
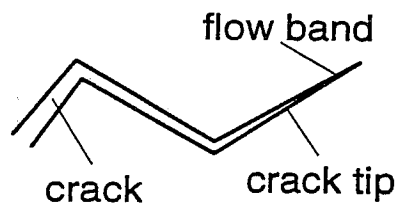


Figure 7. Fatigue Curve for Martensitic Steel

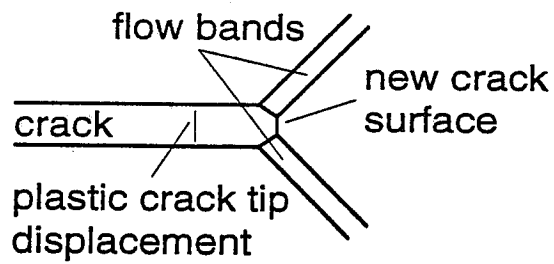


b)

stage I:



stage II:



stage III:

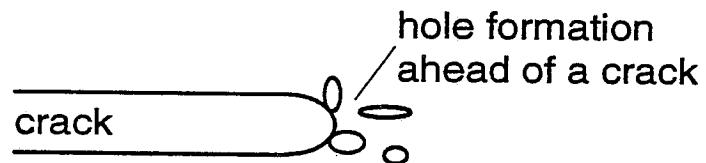


Figure 8. Stages of Fatigue Crack Growth

PRESSURE FLUCTUATION AND OPERATING EFFICIENCY OF INTENSIFIER PUMPS

Eric J. Chalmers
Jet Edge, Inc.
Minneapolis, Minnesota USA

Abstract

The pressure fluctuation of 30, 56 and 112 kW(40, 75 and 150 horsepower) pumps, utilizing double acting intensifiers with an attenuator for suppression of pressure fluctuation, was measured. The measurements were made at operating pressures in excess of 345 mPa(50,000 psi) and flow rates at close to the pumps maximum rated output. Measurements comparing the effect of attenuator volume on pressure fluctuation showed that the fluctuation increased at volumes less than 1638 ml(100 in³). The pressure fluctuation was 2.5% - 5.4%, depending on pump size and number of intensifiers, with an attenuator volume of 2130ml(130 in³). Nozzle power and input power to the pump's motor were measured and compared as the flow rate and pressure were changed. With an intensifier pump incorporating a pressure compensated variable displacement hydraulic pump, the overall efficiency was a constant value of 60% at nozzle output powers greater than 40% of the pump's maximum achievable output power.

1.0 Introduction

Applications that include waterjet cutting, abrasive-waterjet cutting and waterjet cleaning require ultra-high pressure pumps that are optimized for performance, reliability, efficiency and safety. Pumps that generate working pressures in excess of 207 mPa(30,000 psi) can be either intensifier-based or direct-drive, positive displacement (PD) crankshaft types. Positive displacement pumps are not commonly used at these pressures due to their limited flexibility responding to the varying demands of pressure and flow rate. By far, intensifiers are the preferred method to generate higher pressures .

Intensifiers operate on the principle of conservation of hydraulic energy. A low pressure , high flow hydraulic region acts on a piston of large area. A large force is generated, which in turn acts on a small plunger area, creating a much higher pressure. An exchange of energy is made where low pressure, high flow hydraulic fluid is converted to high pressure, low flow water. The ratio of the low pressure piston area to the high pressure plunger area is called the intensification ratio. For most intensifier pumps, the ratio is between 12:1 and 20:1. Using these ratios a hydraulic system, operating at 21mPa(3000 psi), can generate pressures of up to 414 mPa(60,000 psi) on the water side. Most ultra-high pressure pumps use double-acting intensifiers to generate output flow. In some cases, single acting intensifiers are used. Both types create ultra-high pressure essentially the same way but they minimize output pressure fluctuation differently.

Pressure fluctuation must be minimized to assure that all components exposed to the ultra-high pressure perform as well as possible. Excessive fluctuation can lead to premature wear and fatigue failure of components such as tubing, valves and orifices. It can also affect the consistency of the cutting stream and the accuracy and quality of the cut. The level of fluctuation is determined by the hydraulic system, intensifier shift valves, and the content of the high pressure side of the intensifier pump.

The operating efficiency of the intensifier pump determines the electrical and cooling water consumption which influences the cost of operation. The type of hydraulic system that the pump employs and the components used directly control the efficiency of the unit at full rated power and at partial power. The hydraulic system can be either pressure compensated by using a variable displacement hydraulic pump or it can be fixed displacement. Both approaches can yield the same efficiency at full output flow, but intensifiers pumps generally do not operate at full flow. The specific application determines the flow rate as controlled by the orifice size and operating pressure and whether the cutting head is on or off. At partial output, or deadhead condition, the pressure compensated

system will change its power requirement in response to the load, whereas a fixed displacement pump will consume a constant amount of power as the flow demand changes. Intensifier pumps that incorporate pressure compensated hydraulic pumps offer the best efficiency throughout their operating range.

2.0 Intensifier Pump General Description

The performance and efficiency of an intensifier pump is largely governed by the fluid power components. Figure 1 shows a simplified hydraulic schematic for a typical intensifier pump. The fluid power system consists of two halves: low pressure hydraulic and high pressure water. The schematic shows the hydraulic side as including a pressure compensated variable displacement(PCVD) pump, accumulator, directional valve, heat exchanger, and filtration. The hydraulic system must be highly responsive to meet the varying demand of the reciprocating intensifier, and maintain smooth output pressure. Fixed displacement hydraulic pumps, such as gear pumps, are less expensive and have been used instead of PCVD pumps, but they have a higher cost of operation.

The high pressure side of an intensifier pump normally consists of single or multiple intensifiers. The schematic shows one double acting intensifier. The output from the intensifier passes through the attenuator which dampens the pulsations caused by the intensifier's shifting. Intensifier pumps can also be constructed using multiple single acting intensifiers.

3.0 Intensifier Comparison

Intensifier pumps for waterjet applications must have minimal output pressure fluctuation. This has been accomplished in two different ways by using either multiple single acting intensifiers or one or more double acting intensifiers with an attenuator.

3.1 Single acting intensifier pumps normally use two hydraulic cylinders, one of which is on the power stroke while the other is either retracting or in position to stroke. Pressure fluctuations are limited by the fact that at any given time one of the two actuators is generating pressurized water. In theory, this approach should yield zero pressure variation, but in practice the actual fluctuation is greater than with double acting intensifiers when comparing similar sized pumps. The fluctuation has been measured at 4.6% on a 18.6 kW(25 horsepower) pump at a peak operating pressure of 350 mPa(50,750 psi) with a 25 mm(.010") orifice by Singh and Benson(1991).

3.2 Double acting intensifiers generate high pressure water in both stroke directions. The hydraulic piston has a plunger connected to either side. As it strokes, creating pressure and output flow in one direction, the opposite side is

in its suction stroke. When the piston reaches the end of its stroke, the directional valve is shifted. The output pressure decays due to the response time of the valve and the plunger stroke required to compress the water to the output pressure. At 393 mPa(57,000 psi), water is compressed to 87%(given in Marks' Handbook) of its original volume. When the water pressure in the high pressure cylinder equals the pump's output pressure, the high pressure check valve opens. The shift dwell time and responsiveness of the hydraulic system are primarily responsible for the pressure fluctuation of intensifier pumps. Pumps that have multiple intensifiers have slightly greater fluctuation than single intensifier pumps because of increased dynamic interaction between the hydraulic system and the intensifiers.

To maintain flow during the intensifier reversal, it is necessary to have an accumulator, normally called an attenuator. This is simply a pressure vessel that is installed in-line with the output of the intensifier. It uses the compressibility of the water, acting as a spring, to minimize pressure fluctuation of the pump's output. The internal volume of the attenuator is sized to provide an acceptable amount of fluctuation while keeping its size and cost reasonable.

Pressure fluctuation measurements were taken of three intensifier pumps using a GP:50 Ltd. Model 212 pressure transducer and a Graphtec Corp. Model WR7700 Thermal Arraycorder. The pump model's performance ratings are shown in table 1.

Table 1

Model Number	Motor Size kW(hp)	No. of Intens	Maximum working pressure mPa(ksi)	Max Flow @ MWP lpm (gpm)
57-40	30(40)	1	393(57)	3(0.8)
57-75	56(75)	2	393(57)	6(1.6)
57-150	112(150)	2	379(55)	11(2.9)

Figures 2,3 and 4 show the pressure fluctuation for pump models 57-40, 57-75, and 57-150 respectively. Each reading is taken at near each model's maximum output flow and pressure. The 57-40 is a single intensifier pump and has a pressure fluctuation of only 2.5%. Models 57-75 and 57-150 are dual intensifier pumps and have a pressure fluctuation of 5.2% and 5.4% respectively.

The amount of pressure fluctuation that a double acting type intensifier pump with an attenuator generates is significantly less than a comparable single acting type pump.

4.0 Attenuator Volume

The fluctuation values cited in figures 2-4 were based on a standard attenuator with a volume of 2130 ml(130 in³). Other attenuators of lesser volume were tested in a 57-75 pump. These results are shown in figure 5.

The fluctuation of the 0.45 mm(.018 in) orifice running off of two intensifiers is slightly less than the 0.30 mm(.012 in) orifice with one intensifier. When a pump is operating at close to maximum displacement, the fluctuation is reduced. The amount of pressure variation increases at an attenuator volume of less than 1639ml(100 in³).

The attenuator offers another benefit besides dampening the pump's output pressure. Two 0.45 micron cartridge filters inside the attenuator trap any particulates generated upstream such as from seals or check valves. The attenuator filtration makes the use of in-line filters unnecessary.

High pressure in-line filters are made from sintered metal. To minimize pressure drop, the filter size is normally 5 micron or coarser. They are susceptible to fatigue rupture caused by water hammer from the cutting head valve. The coarse level of filtration will shorten orifice life. Should the element rupture, the orifice will require replacement and the valve seat could be damaged.

The attenuator capacity has been carefully sized to minimize pressure fluctuation and provide for a high level of filtration of the water for cutting.

5.0 Pump Efficiency

Pump efficiency is largely a function of the hydraulic system design and the components of that system. Most intensifier pumps, rated for working pressures of over 345mPa(50,000 psi), have efficiencies of .6 to .7 based on the output power of the motor at full load. The efficiency of the intensifier pump at less than full load is largely controlled by the type of hydraulic pump employed. The hydraulic pump can either be fixed or variable displacement.

5.1 Fixed displacement pumps generate a constant output flow at a given motor speed. A relief valve sets the pressure. Excess flow such as dead-heading during valve closure or undersized orifice flow is dissipated as heat. For example, if the pump is running at maximum flow and pressure, and the cutting head valve is closed, all of the pump's output power passes across the relief valve. Although no nozzle horsepower is created, the intensifier consumes the same amount electricity. In addition, the lost power is converted into heat which must be cooled by the heat exchanger and leads to excessive cooling water usage. Fixed

displacement hydraulic pumps may be used in intensifier pumps because they are inexpensive, but they cause high operational costs.

5.2 Pressure compensated variable displacement(PCVD) pumps vary hydraulic output flow in response to the load. If the cutting head valve closes, the pump swashplate will go to zero displacement while maintaining static pressure.

To determine the operating efficiency of a PCVD intensifier pump, a 57-40 was tested with .23mm(.009 in), .28mm(.011 in) and .33mm(.013 in) orifices at pressures of 393mPa(57,000psi), 345mPa(50,000psi), 276mPa(40,000psi) and 207mPa(30,000psi).

Power in was found by measuring the input voltage and current . Input power can then be calculated for three phase power.

$$P_{in}(kW) = \text{Volts} \times \text{Amps} \times \text{Power Factor} \times 1.73 / 1000$$

Power out, or nozzle power, was found by measuring the output flow and pressure. Output power can then be calculated.

$$P_{out}(kW) = \text{Flow}(lpm) \times \text{Pressure}(mPa) / 60$$

Operating efficiency can then be determined.

$$\text{eff} = P_{out}/P_{in}$$

Figure 6 shows required input power and operating efficiency at the various nozzle output powers. The input power increases in relation to nozzle power. The efficiency is constant at a value of about 0.6 when the nozzle power exceeds 40% of the maximum pump output power.

The pump uses a "high efficiency" electric motor with an average efficiency of 0.9. The pump efficiency based on the rated motor output power of 30 kW(40 horsepower) is $0.6/0.9 = 0.67$ at full output power.

Figure 7 shows P_{in} vs P_{out} if the 57-40 were equipped with a fixed displacement(FD) pump with the same efficiency as the PCVD pump. The graph shows that with a fixed displacement pump, as the demand for flow decreases, the input power remains constant at a given pressure set point. At maximum output flow the FD pump's efficiency is the same as the PCVD pump. As the demand for flow is reduced, the efficiency is reduced.

6.0 Conclusions

Ultra-high pressure pumps incorporating double acting intensifiers in conjunction with an attenuator provide for lower output pressure fluctuation than other types of intensifiers. Although many aspects of the intensifier pump contribute, the attenuator volume ultimately controls the range of fluctuation. Using an attenuator with a capacity of 2130 ml(130 in³), the pressure varied by 2.5% with a 30kW(40 horsepower) single intensifier pump. Larger dual intensifier pumps had pressure fluctuation of up to 5.4%. The larger pumps have an increased but still acceptable fluctuation level because of the interaction between dual intensifiers and the larger displacement hydraulic pump. A significant added benefit of the attenuator is that it contains filtration, replacing the need for in-line high pressure filters.

Intensifiers that are powered by pressure compensated variable displacement hydraulic pumps are more efficient than those with a fixed displacement pump when operated at less than the maximum rated flow. Overall pump efficiency was determined to be a constant value of about 0.6 within the top 60% of the pump's power range. PCVD equipped intensifier pumps generally require power in proportion to the demand. This results in lower cooling water and electrical power usage.

7.0 Acknowledgements

The author thanks Dave LaFavor and Rich Trombley of Jet Edge, Inc. for their effort and contributions.

8.0 References

1. Singh, P. and Benson, D., "Development of Phased Intensifier for Waterjet Cutting", presented at the 11th International Conference on Jet Cutting Technology, pg 314, Kluwer Academic Publishers, 1992.

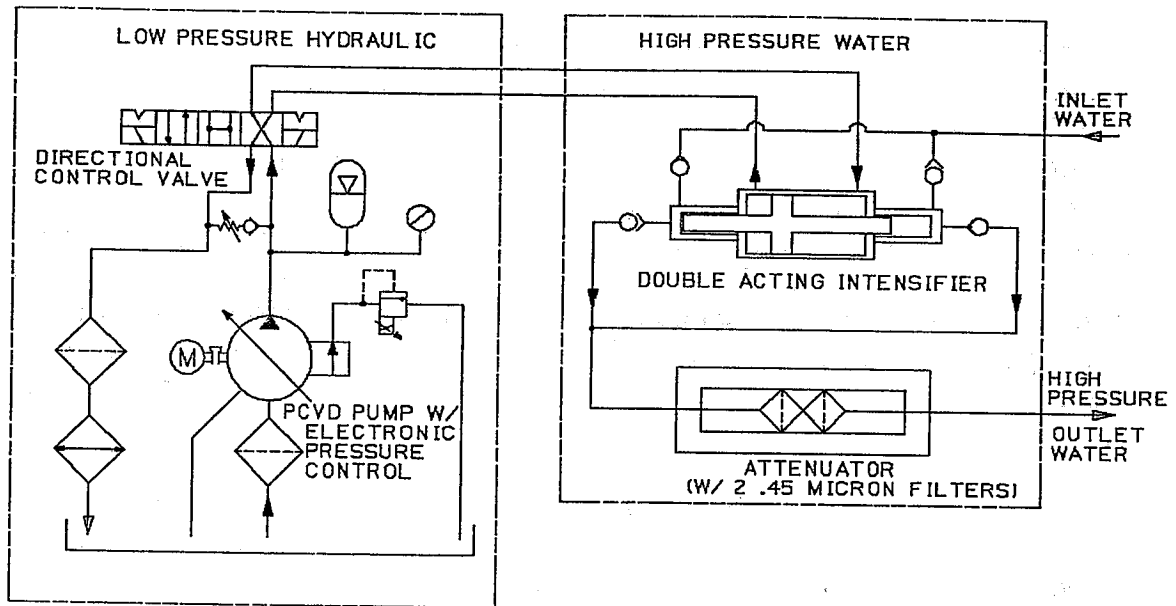
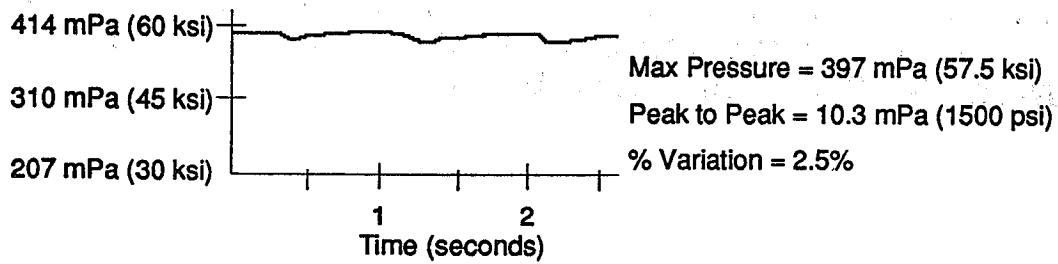


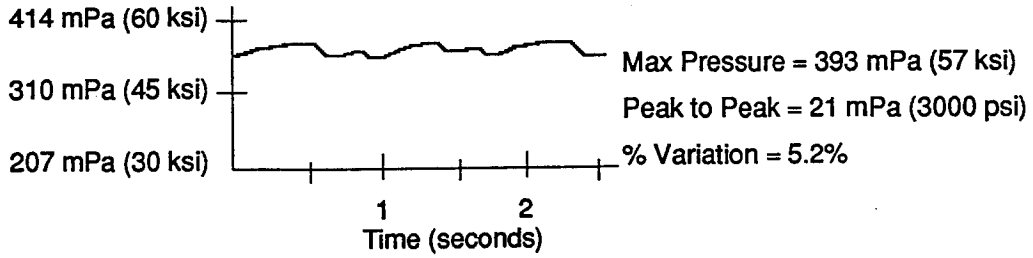
Figure 1. Simplified Hydraulic Schematic for an Intensifier Pump



57-40 Pump

2.3 lpm (0.6 gpm) Measured Flow Rate

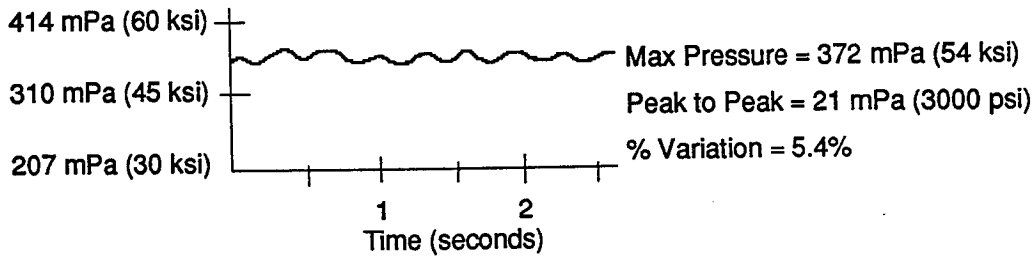
Figure 2 Pressure Fluctuation of 30kW(40 Hp) Intensifier Pump



57-75 Pump

6.0 lpm (1.6 gpm) Measured Flow Rate

Figure 3. Pressure Fluctuation for 56kW(75Hp) Intensifier Pump



57-150 Pump

10.2 lpm (2.7 gpm) Measured Flow Rate

Figure 4 . Pressure Fluctuation for 112kW(150Hp) Intensifier Pump

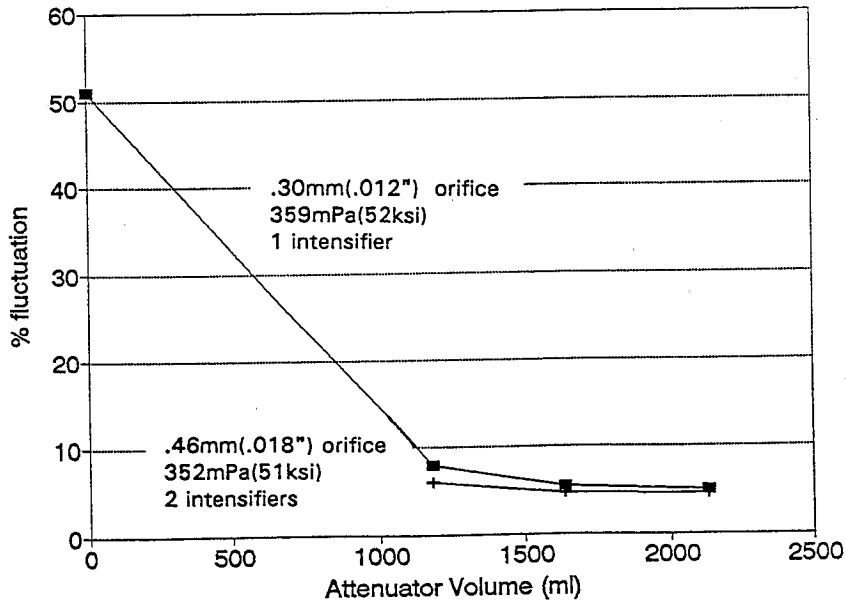


Figure 5. Effect of Attenuator Volume on Pressure Fluctuation

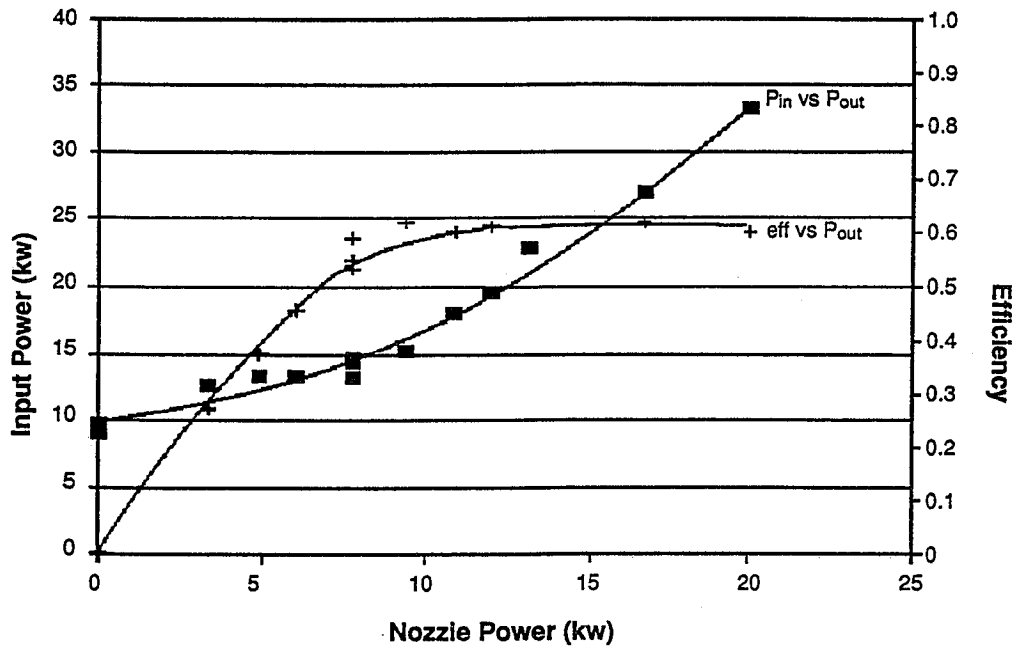


Figure 6. Power Requirement and Efficiency for a 30kW(40Hp) Intensifier Pump using a PCVD Hydraulic Pump.

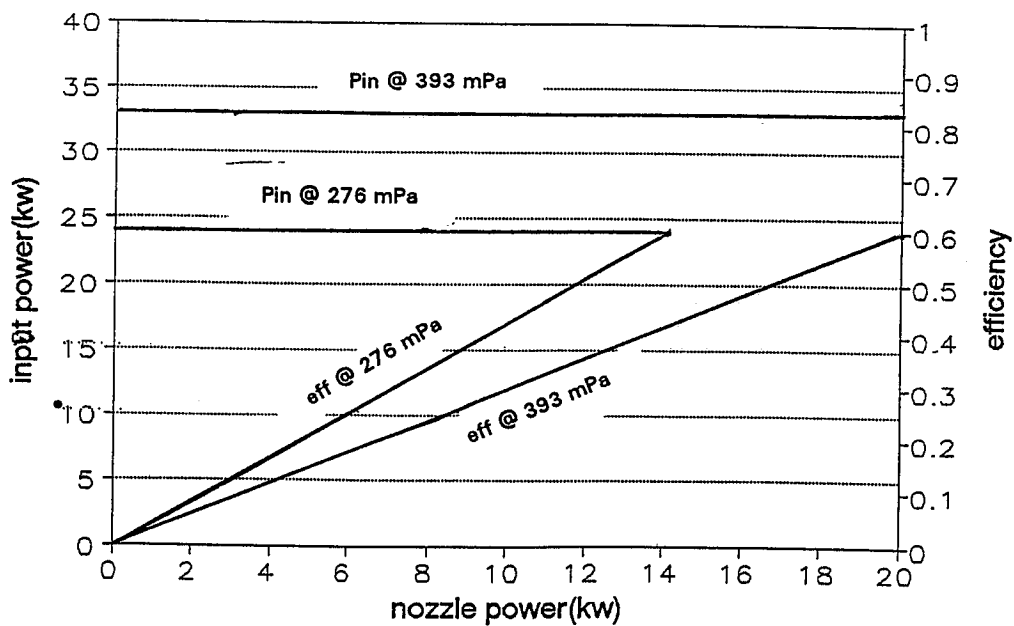


Figure 7. Power Requirement and Efficiency for a 30kW(40Hp) Intensifier Pump Using a Fixed Displacement Hydraulic Pump.

**SIMULATION AND CONTROL OF DISCHARGE PRESSURE FLUCTUATION OF
ULTRA HIGH PRESSURE WATERJET PUMP**

Fang Hu and Jason Robertson
HYDRO-PAC, INC.
Fairview, Pennsylvania, U.S.A

ABSTRACT

This paper presents the investigation results of the discharge pressure fluctuation of an ultra high pressure waterjet pump. A new method is introduced to simulate the discharge pressure fluctuation by using a personal computer. Factors influencing the pressure fluctuation and several control methods are also studied.

1. INTRODUCTION

All ultra high pressure waterjet pumps consist of a double acting reciprocation intensifier, a hydraulic pump package and a high pressure attenuator. Fig.1 shows a typical schematic design of an ultra high pressure waterjet pump. The principle of this type of pump is that low pressure hydraulic oil is alternately applied to each side of a large piston causing it to move back and forth. The movement of the large piston drives a small diameter piston which acts against water in the small high pressure cylinder. Because of the piston's area ratio, low pressure hydraulic oil, acting at the large piston side will generate very high water pressure at the small piston side. Due to the reciprocating nature of intensifiers, discharge pressure fluctuation occurs at each cycle. Since ultra high pressure is involved, this variation results in stress reversals which causes pump component fatigue failure.

The discharge pressure fluctuation phenomena has been investigated by several researchers (R. A. Tikhomirov et. al. [1] and Romeo Susan-Resiga [2]). Although the mathematical models have been documented, none of these models can be used directly to simulate the discharge pressure fluctuation based on the waterjet pump parameters, orifice diameter, and the volume of the attenuator. In order to control the discharge pressure fluctuation of a waterjet pump, a model and several computer programs were developed by Hydro-Pac's engineer. By using the computer programs, people can predict the pressure drop for their waterjet pump or select the size of the attenuator for certain pressure fluctuation requirements.

2. THE INVESTIGATION OF THE DISCHARGE PRESSURE FLUCTUATION PHENOMENA OF THE ULTRA HIGH PRESSURE WATERJET PUMP

Figure 2 shows a typical ultra high pressure waterjet pump discharge pressure curve and a hydraulic pressure curve at normal operating conditions. It is clearly shown that the waterjet pump discharge pressure fluctuation is caused by the shifting of the intensifier. At the end of the stroke, it takes a certain time (T_s) for the directional control valve to shift and to let the intensifier reverse its direction. After the intensifier is reversed, it also takes certain time (T_c) to compress the water inside the other side of the high pressure cylinder to a certain pressure. During this period of time ($T_d = T_s + T_c$), both discharge check valves of the pump are closed because of the differential pressure. There is no output from the intensifier and the output of the waterjet pump is actually provided by the attenuator installed. Because the high pressure attenuator is a storage chamber of compressed water, pump discharge pressure is decreasing during this period of time until one of discharge check valves is reopened.

It is obvious that the pressure fluctuation process of the waterjet pump consists of two independent processes. One is a "depressurization process", which represents how the water pressure inside the attenuator drops in a certain time. This process can be defined as a function of pressure and time, which is affected by the size of the attenuator and diameter of orifice. Another process is called a "pressurization process", which represents how the water pressure inside the high pressure cylinder rises from inlet pressure.

This process can also be defined as a function of pressure and time, which is controlled by the volume of the high pressure cylinder and speed of the piston.

Figure 3 shows a model simulating the pressure fluctuation of the waterjet pump. In this model, "depressurization process" and "pressurization process" are presented respectively by two functions which are generated by using two computer programs. By solving those functions, it is very easy to calculate the pressure fluctuation ($dp = P_{max} - P_{min}$) of the waterjet pump.

3. SIMULATION OF THE DEPRESSURIZATION PROCESS

After the intensifier reverses its direction, all discharge check valves are closed. The attenuator provides continuous water flow to the nozzle. The water depressurization process is controlled by three factors: maximum water pressure, size of the attenuator, and orifice diameter. The first two factors determine how much water is stored inside the attenuator. The orifice diameter governs how fast the water is discharged. In order to simulate the depressurization process, we have to find the relationship between water compressibility and water pressure, as well as, the water discharge rate through the orifice.

Fortunately, these relationships have been studied and documented in various papers or books. The relationship of the water compressibility and pressure is presented in Figure 4. This relationship can be presented by two empirical equations, 1 and 2.

$$(1) K(P) = a_0 + a_1 * P + a_2 * P^2 + a_3 * P^3 + a_4 * P^4 + a_5 * P^5$$

$$(2) P(K) = b_0 + b_1 * K + b_2 * K^2 + b_3 * K^3 + b_4 * K^4 + b_5 * K^5$$

K is the compressibility of water, which is defined by equation 3. P presents water pressure.

$$(3) K = \frac{V_w - V_a}{V_a} \quad \begin{array}{l} V_w: \text{volume of water stored inside} \\ \text{the vessel at certain pressure} \\ V_a: \text{internal volume of the vessel} \end{array}$$

The water discharge rate through the orifice (dn) is presented by equation 4.

$$(4) Q(dn, P) = C_d * \frac{\pi}{4} * dn^2 * \sqrt{\frac{P}{\text{water_density}(P)}}$$

The amount of water discharged through the orifice at a certain time (dt) can be calculated by equation 5.

$$(5) dV = Q(dn, P) * dt$$

Based on these equations, a computer program was written to simulate the water depressurization process. Figure 5 is the flow chart for this program.

A test is designed to verify the result of this program. The main part of the test is to use a pressure transducer to get the pressure signal near the orifice versus time. The attenuator is only a high pressure water source to the orifice. Figures 6 - 9 are comparisons of the results of the tests and calculations. From these results, it is clearly shown that the computer program accurately models the water depressurization process.

4. SIMULATION OF THE PRESSURIZATION PROCESS

The pressurization process starts at the end of the stroke of the intensifier and finishes when the water pressure inside high pressure cylinder is high enough to reopen the discharge check valve. This process is controlled by the shifting time of the directional control valve, internal volume of the high pressure cylinder, and speed of the piston. The shifting time of the directional control valve is given by the valve manufacturer most of time. The shifting time is defined as T_s in this paper. The internal volume of the high pressure cylinder is calculated by equation 6 and the speed of the piston is calculated by equation 7.

$$(6) V_i = \frac{\pi}{4} * d_z^2 * L_s + V_{end}$$

d_z : plunger diameter
 L_s : length of stroke
 V_{end} : volume of end space

$$(7) \text{Speed} = \frac{4 * Q_{hyd}}{\pi * (D^2 - d^2)}$$

Q_{hyd} : hydraulic pump flowrate
 D : hydraulic piston diameter
 d : rod diameter

Based on equations 2, 3, 6, and 7, a computer program was written to simulate the water pressurization process. Figure 10 is the flow chart for this program. A test was carried out to measure the water pressure inside the high pressure cylinder versus time. Figure 11 is comparison of the results of test and calculation. It clearly shows that the computer program accurately models the water pressurization process.

5. FACTORS INFLUENCING THE PRESSURE FLUCTUATION AND CONTROL METHODS

After the pressure fluctuation simulation model was successfully established, predicting the pressure drop for a waterjet pump became very easy. This model shows that there are four key factors affecting the pressure fluctuation of the waterjet pump at a certain pressure and orifice diameter. They are: the size of the attenuator, the shifting time of the directional control valve, the internal volume of high pressure cylinder, and the speed of the hydraulic piston. Figure 12 shows how these four factors affect the pressure fluctuation. In order to control the pressure fluctuation of the waterjet pump with single intensifier, these four factors have to be selected properly based on some rules of thumb:

- A. Increasing the size of the attenuator will reduce the pressure fluctuation of the waterjet pump. Because all current attenuators used for the waterjet pump are only a simple high pressure vessel, to increase the size of the attenuator unlimitedly will also increase the cost. It is necessary to design a low cost, high efficiency attenuator in the future.
- B. In order to reduce the pressure fluctuation of the waterjet pump, it is necessary to let the intensifier reverse its direction at the end of the stroke as quickly as possible. Using a fast shifting directional control valve is one of the methods.
- C. After the intensifier reverses its direction, it is important to let the intensifier move as quickly as possible in order to compress the water to a certain pressure level in a short period of time. The hydraulic pump flowrate, the design of the hydraulic circuit, and internal volume of the high pressure cylinder are factors that have to be considered here.
- D. Other arrangements involving multiple intensifiers can also reduce the pressure drop. However, these add cost and complexity. This model does not cover these but could easily be extended to cover these.

6. CONCLUSION

A model has been developed to simulate discharge pressure fluctuating in waterjet intensifier pumps. By using this model, it is very easy to predict the pressure fluctuation for a waterjet pump system or to select the proper size of the attenuator for a certain pressure fluctuation requirement.

REFERENCES

- [1] R. A. Tikhomirov, et al.: "HIGH-PRESSURE JETCUTTING", 1992, pp. 121-129.
- [2] R. Susan-Resiga, "Attenuator's Volume Influence on High Pressure's Pulsations in a Jet Cutting Unit", Proceedings of the 11th International Conference on Jet Cutting Technology, pp. 37-45, BHR Group Ltd, St Andrews, Scotland, 1992.

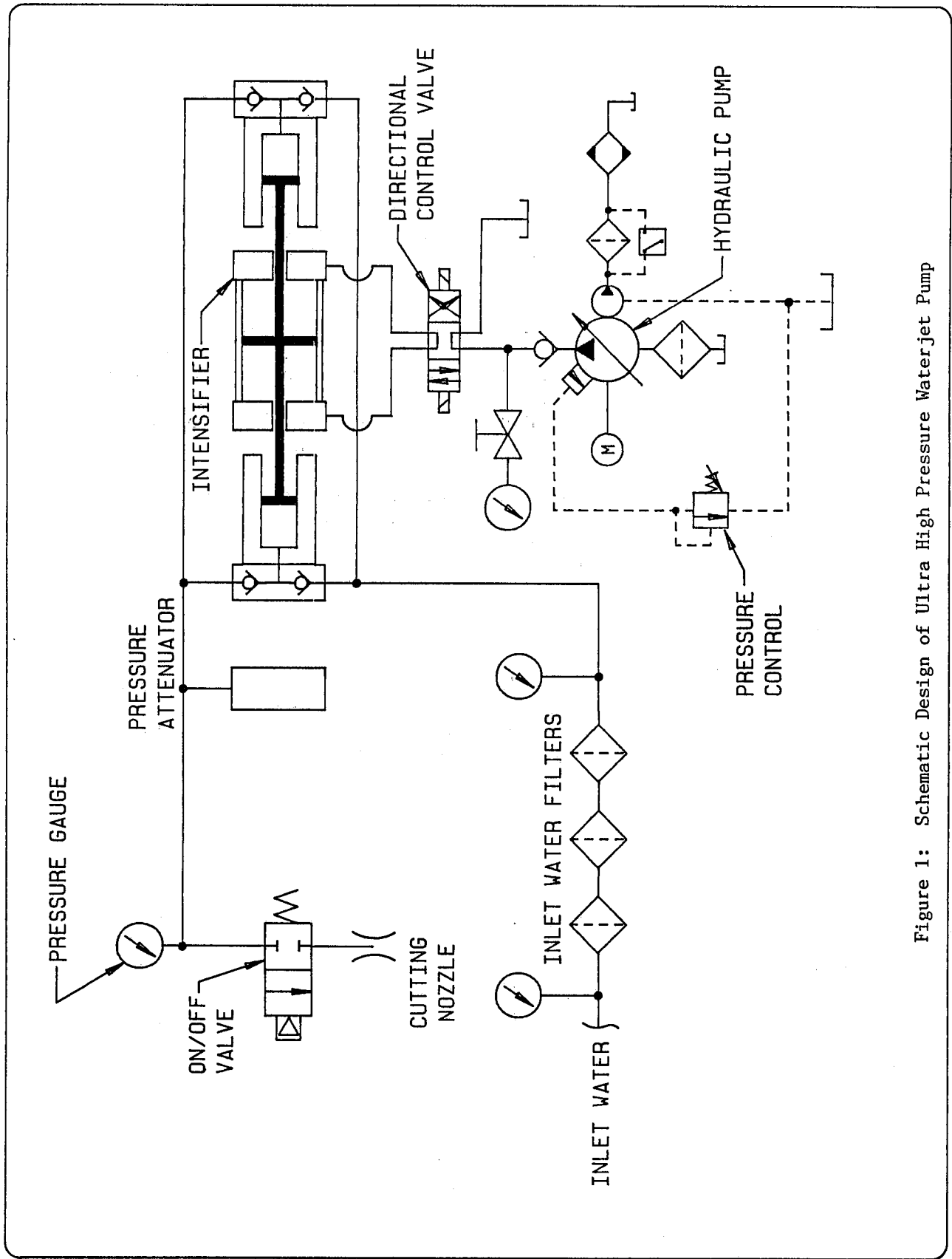


Figure 1: Schematic Design of Ultra High Pressure Waterjet Pump

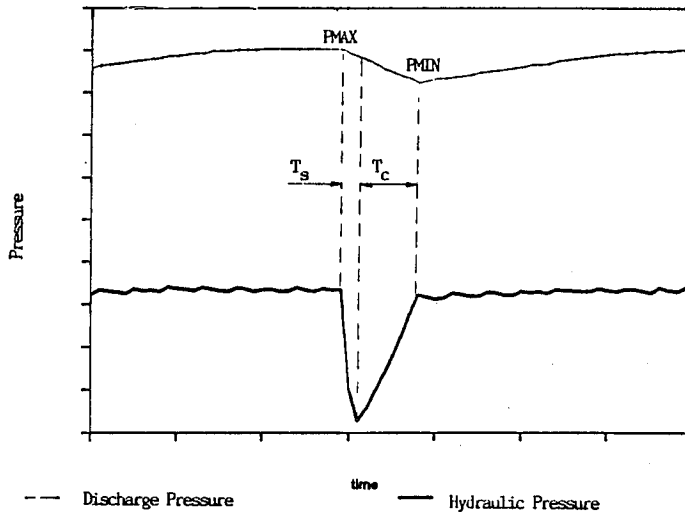
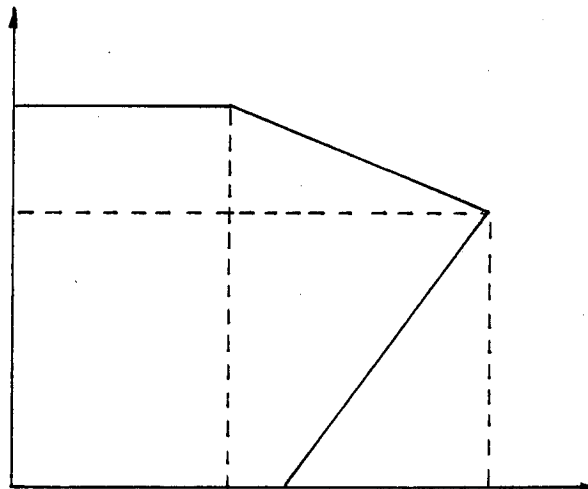
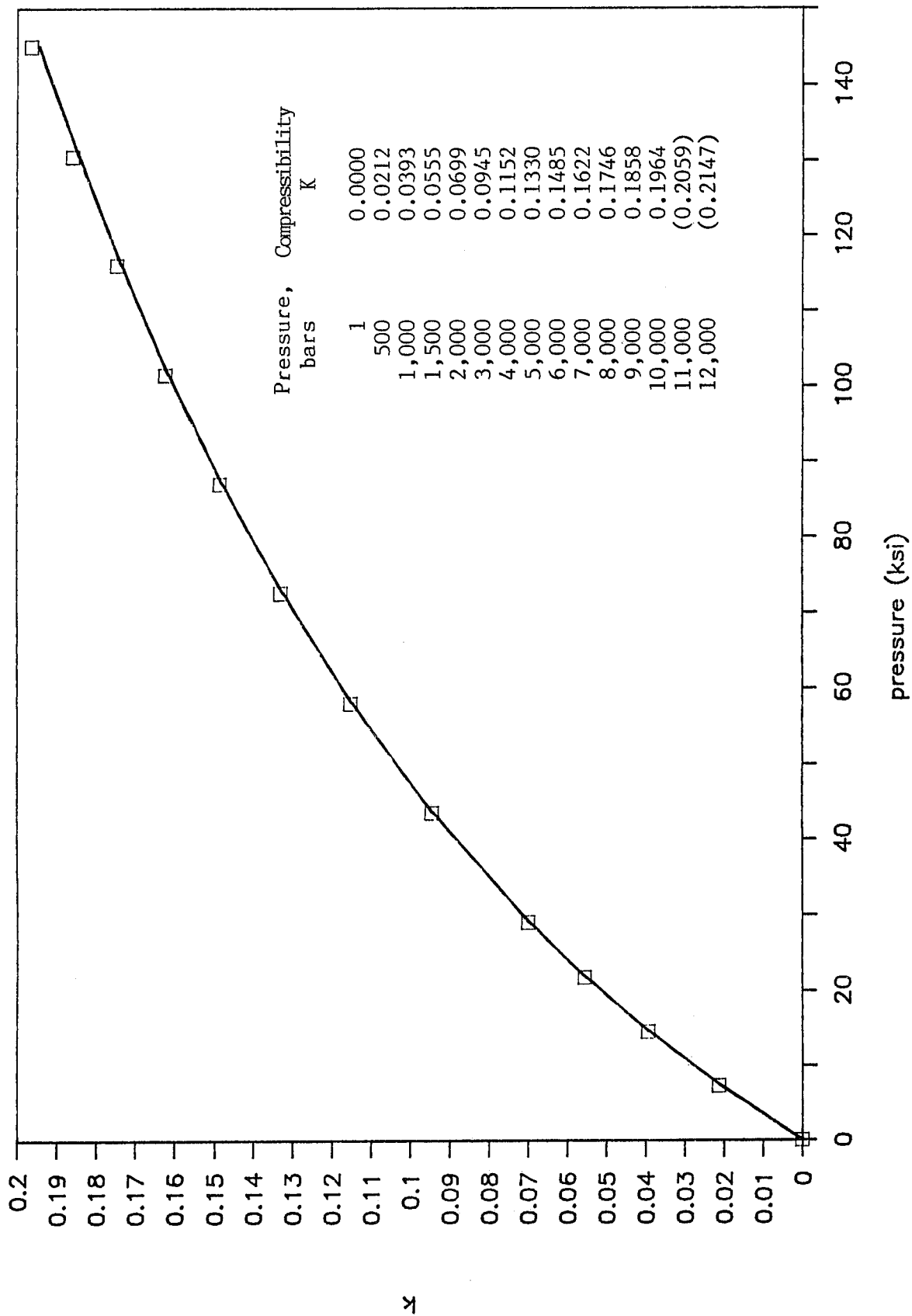


Figure 2: Pressure Curve of Waterjet Pump



- P_{MAX}: Maximum Water Pressure
- P_{MIN}: Minimum Water Pressure
- P_{INLET}: Inlet Water Pressure
- T_s: Directional Value Shifting Time
- T_c: Water Pressurization Time
- P_a = f₁(T): "Depressurization Process"
- P_i = f₂(T): "Pressurization Process"

Figure 3: Model of Pressure Fluctuation



From D. M. Newitt, "The Design of High Pressure Plant and the Properties of Fluids at High Pressures," Oxford University Press, New York, 1940; data from Adams, Am. J. Sci., 35:1 (1938).

Figure 4: Water Compressibility at 25 C.

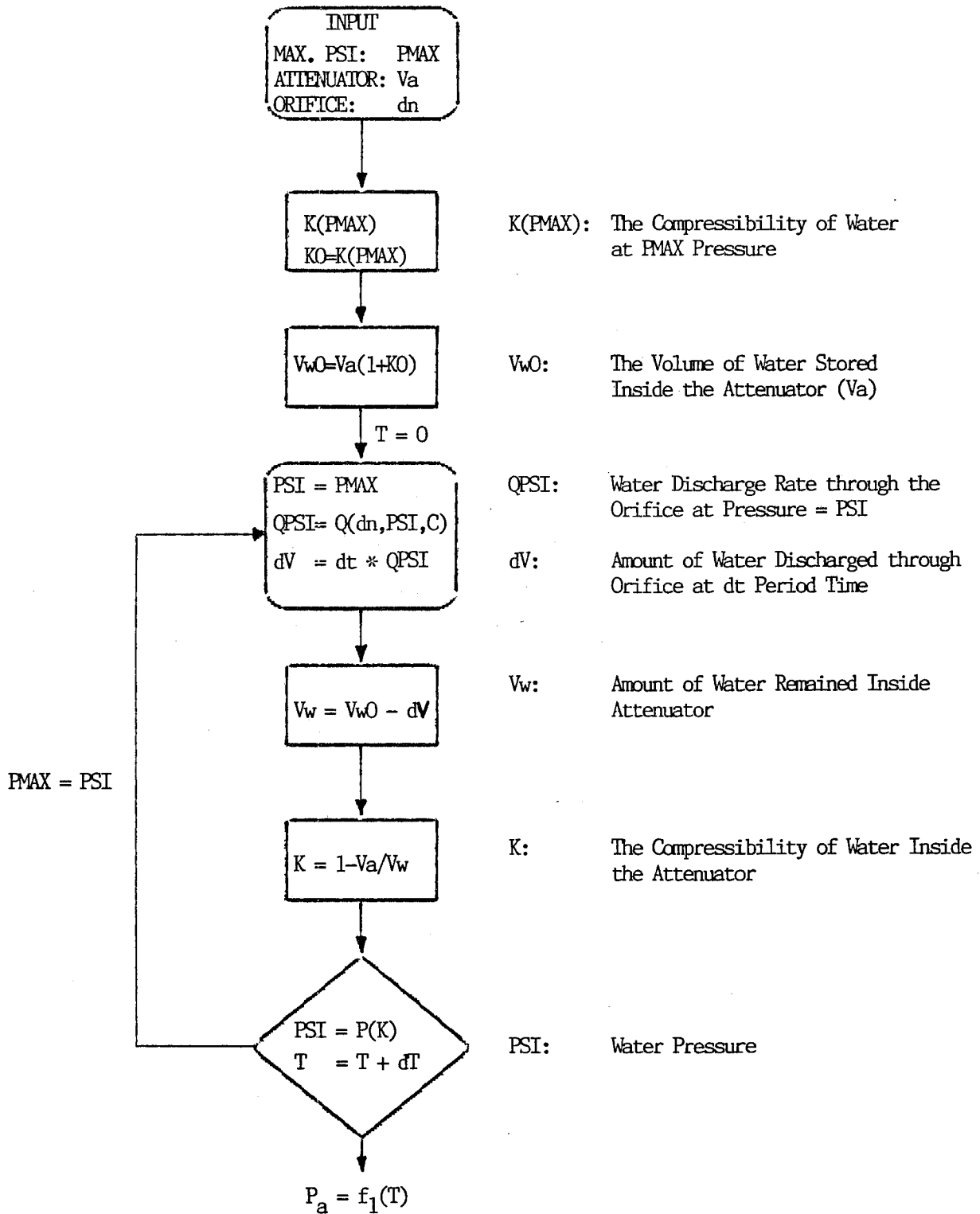


Figure 5: Flow Chart for Program "DEPSI"

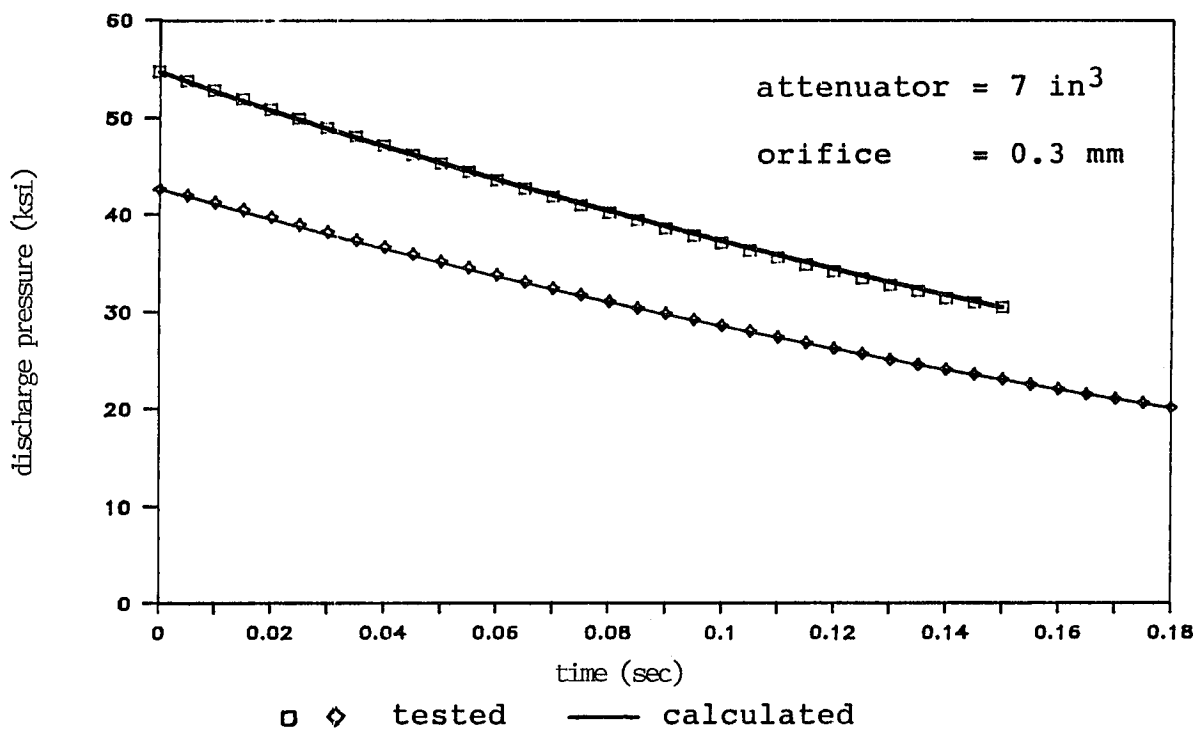


Figure 6: Discharge Pressure vs. Time

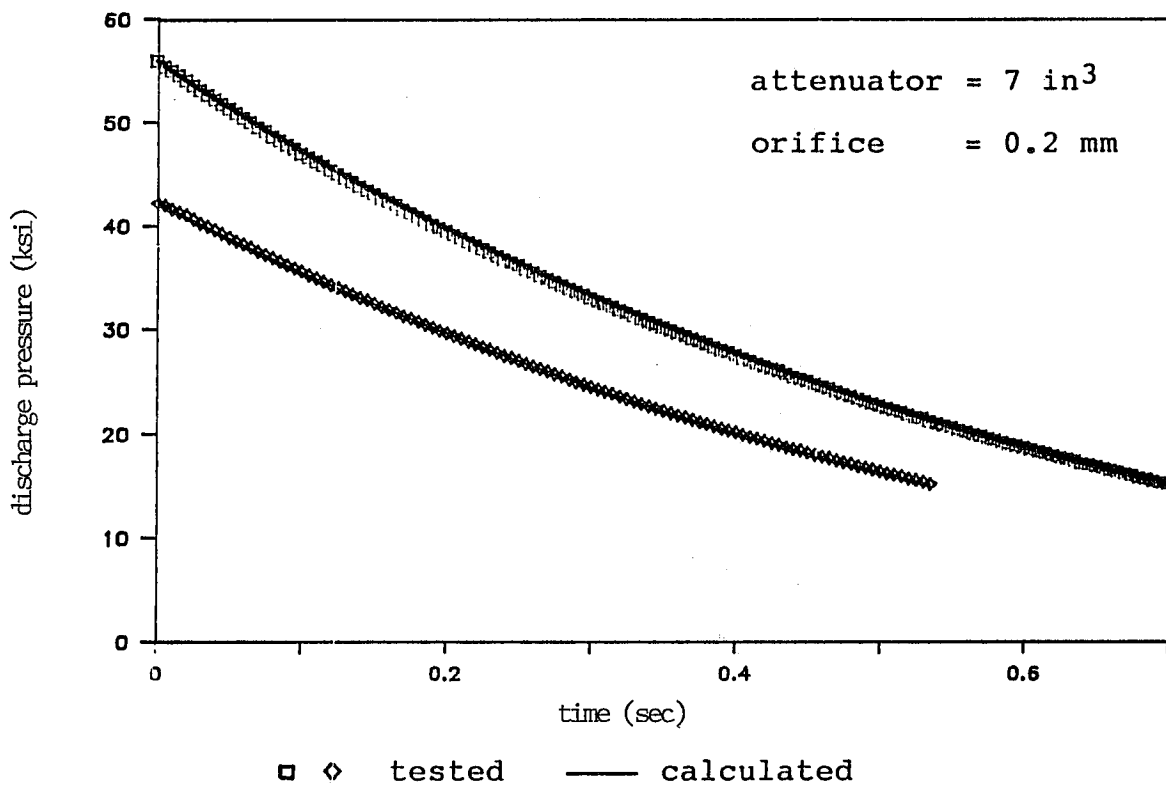


Figure 7: Discharge Pressure vs. Time

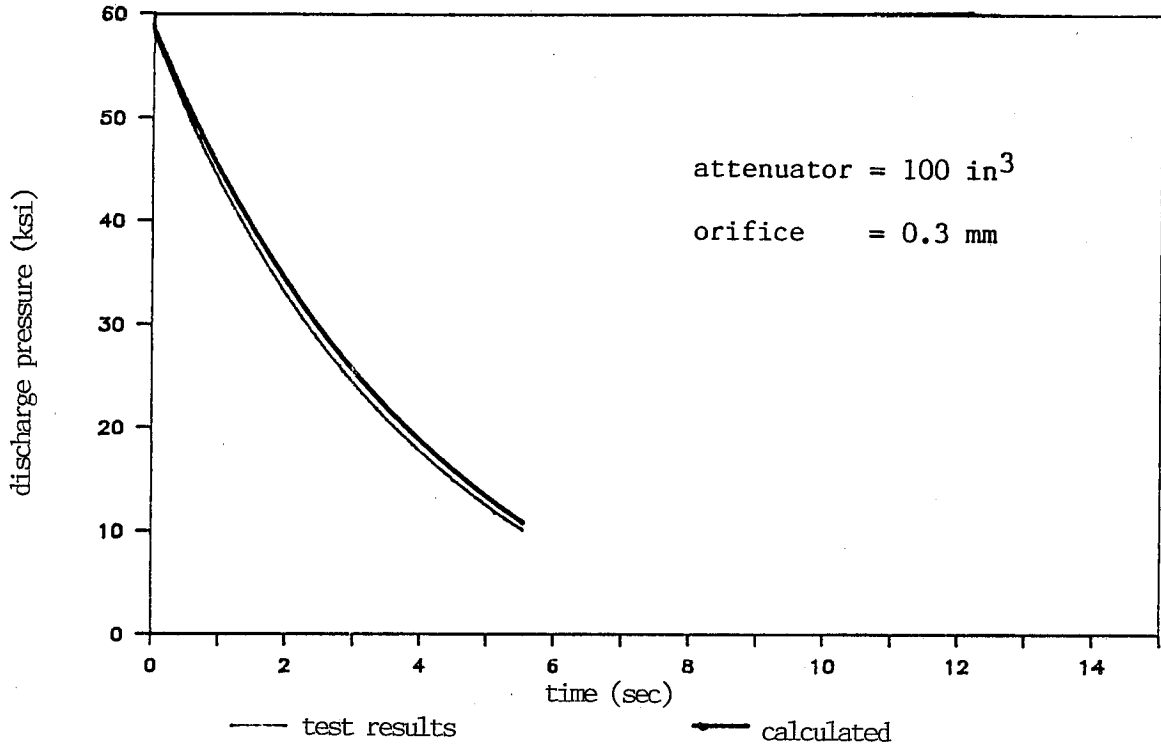


Figure 8: Discharge Pressure vs Time

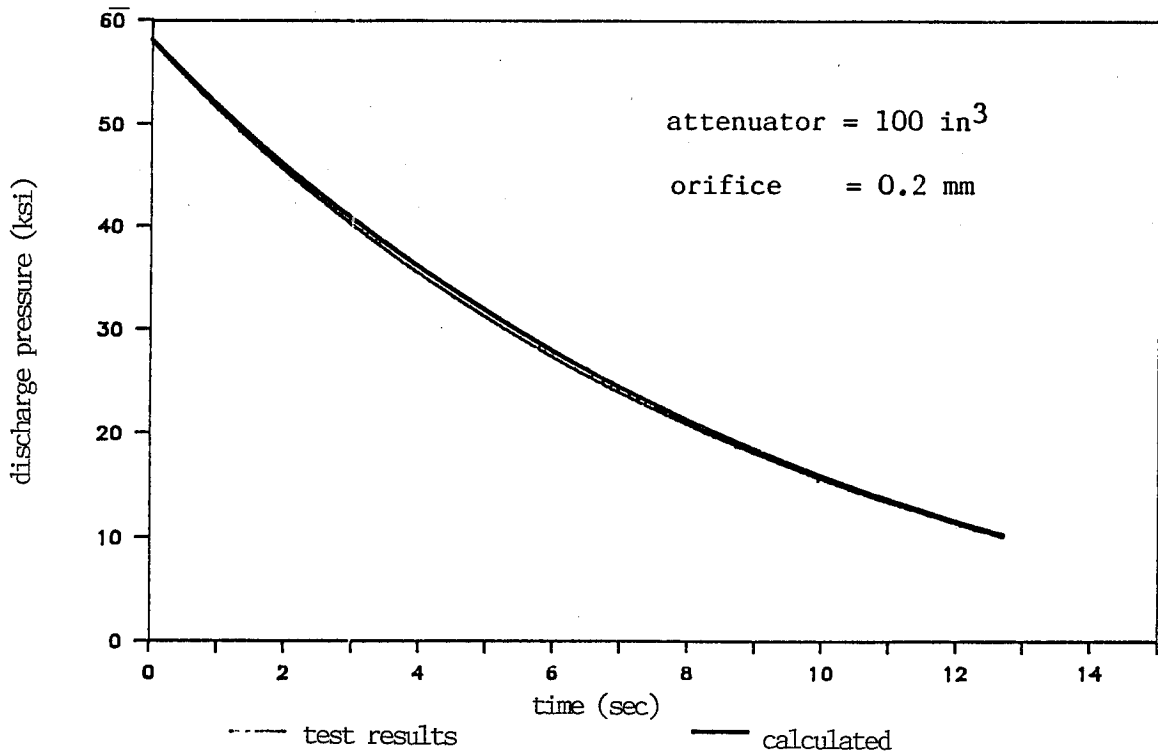


Figure 9: Discharge Pressure vs Time

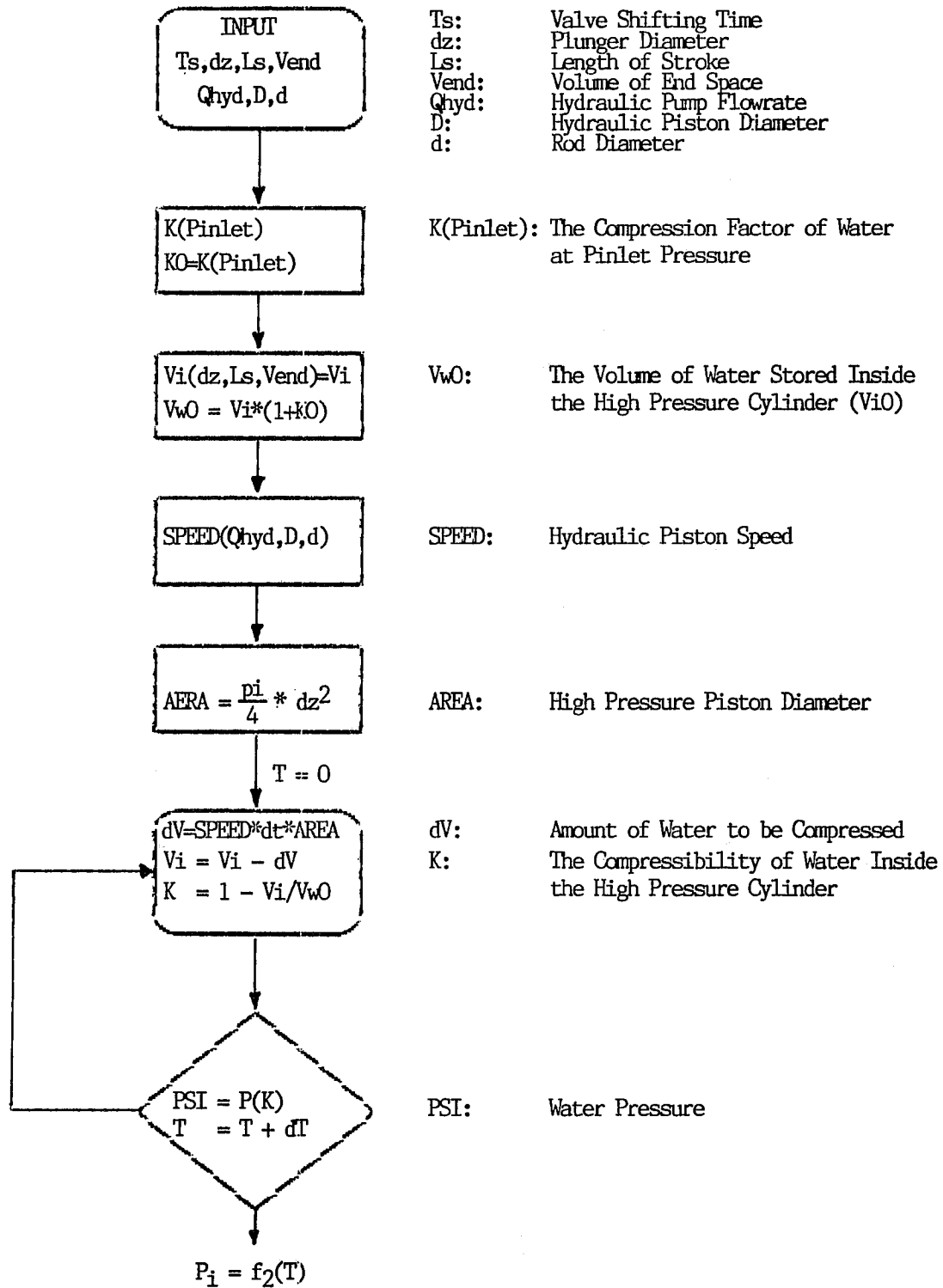


Figure 10: Flow Chart for Program "PSI"

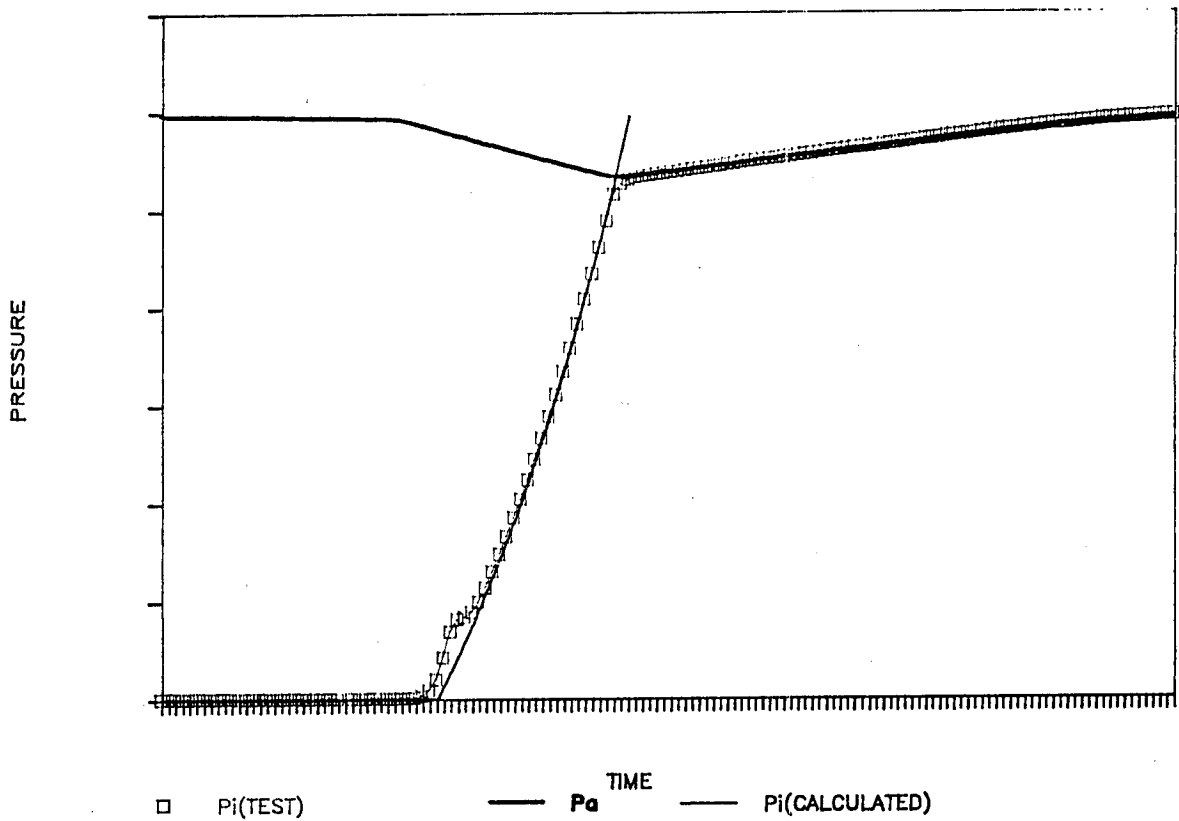


Figure 11: Water Pressure Inside The HP Cylinder

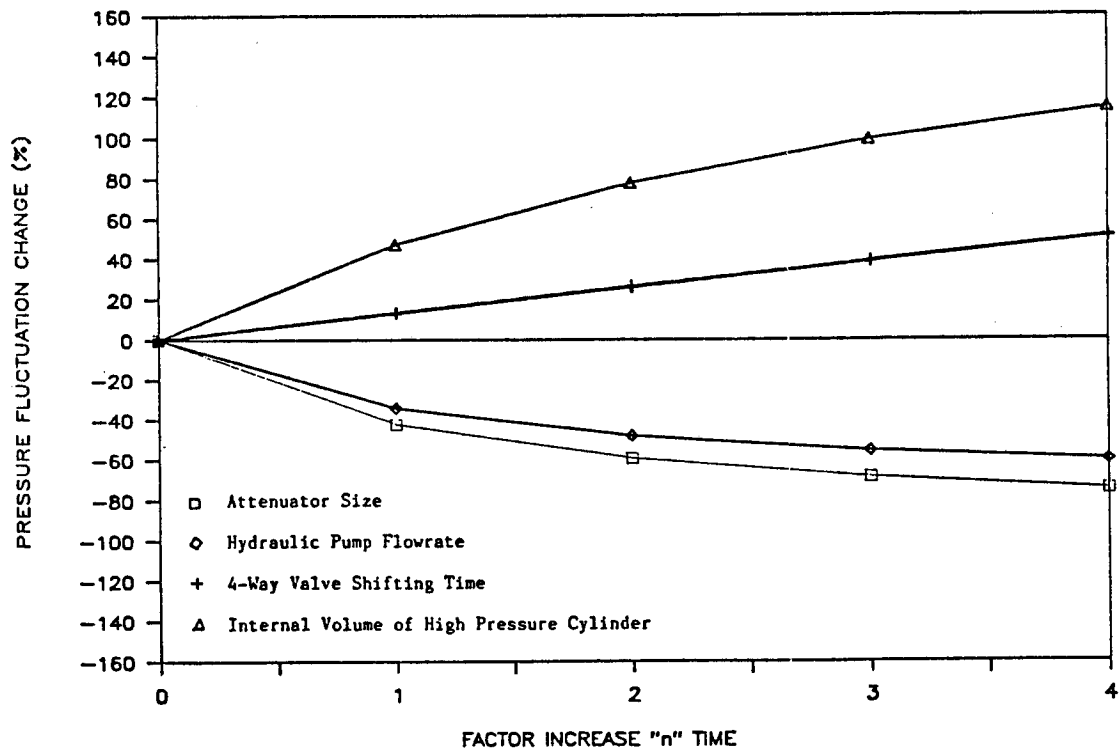


Figure 12: Factors Influencing Pressure Fluctuation

Advances in Direct-Drive Pump Technology Brings the Competitive Edge Back to Ultrahigh-Pressure Waterjets

Terry D. Alkire, Director
Environmental Applications Division

Flow International Corporation
Kent, Washington
U.S.A.

ABSTRACT

Increasing environmental restrictions have created a renewed interest in the use of ultrahigh-pressure (UHP) equipment for industrial cleaning and cutting applications. In an effort to respond to this demand, leading manufacturers of UHP pumps have recently introduced a new generation of direct-drive UHP pumps that are more efficient, economical and easier to service than today's intensifier-based systems. This presentation will discuss the recent advancements in direct-drive UHP pump technology, and focus on the advantages of direct-drive ultrahigh-pressure pumps over hydraulic-based intensifier pumps.

INTRODUCTION

Ultrahigh-Pressure in the Industrial Cutting and Cleaning Market

Ultrahigh-pressure waterjet technology was first introduced into the industrial cleaning market in the early 1980s. The adaptation of this technology can in many ways be seen as a response to the demand for a cleaner, more environmentally friendly way of dealing with the problems of the industrial cleaning market.

The term ultrahigh-pressure (UHP) when used with waterjets is technically defined as those pumps having a working pressure in excess of 28,000 pounds per square inch (psi). With the advancement of technology, the term UHP has generally become accepted today as those pumps with an operating pressure ranging from 36,000 psi to 55,000 psi.

The process involves the focusing of highly pressurized water through a small orifice thus forming a cohesive stream of water. Hand-held applications are normally limited to pressures of 40,000 psi and below. If 55,000 psi is needed, the cutting or cleaning tool is normally robotically controlled. The target materials are removed by the pure energy generated by the waterjet stream which moves at speeds of 2,280 to 2,860 feet per second.

The difference between traditional 10,000 and 20,000 psi waterblasting pumps and ultrahigh-pressure pumps is not unlike the difference between a modern attack fighter and a heavy bomber. UHP waterjets are very precise. Using extremely low volumes of water (2 to 7 gallons per minute), they accomplish their mission by striking their target with a highly focused beam of energy. Waterblaster pumps, on the other hand, saturate their target by delivering a high volume (15 to 250 gpm) of energy over a wider target area.

UHP waterjet machines have become the standard method of choice for a specific number of industrial cleaning applications: Tube bundle/heat exchanger cleaning of extra-tough materials (mechanically controlled, some hand-held), surface preparation (normally hand-held), coating removal (normally hand-held), and abrasivejet (cold) cutting (mechanically controlled).

The reasons that UHP water is the "tool of choice" over traditional cleaning and surface preparation methods such as solvents, acid, sandblasting, heat and high-volume waterblasting are:

- > **Low volume of effluent:** A relatively low amount of water is required in proportion to the volume of material to be removed.
- > **Easy separation of material:** In most cases, simple settling tanks will separate the water from the paint or other substance removed.
- > **No toxic or hazardous wastes:** Besides the material being removed, UHP waterjets produce no toxic, hazardous, or flammable substances that require special handling.
- > **No sand or dust:** Sandblasting requires large volumes of material to be disposed of, particularly where used on modern paint systems. Also, it is difficult to separate the sand from the material removed, and airborne dust and silt can cause numerous problems.
- > **Improved operator safety and health:** Because ultrahigh-pressure water produces no dust or other toxic chemicals, the process alleviates workers' exposure to toxic materials. Due

to the significantly lower volumes of water generated, UHP hand tools are much easier to handle than the high-volume, high-thrust tools typically used with waterblasters.

Intensifier Pumps Open the UHP Cleaning Market

Until recently, the only commercially available ultrahigh-pressure waterjet pumps were hydraulically actuated intensifier pumps (See Figure 1). Since their introduction some 20 years ago, intensifier pumps have been well accepted into a wide variety of industrial cutting and cleaning applications.

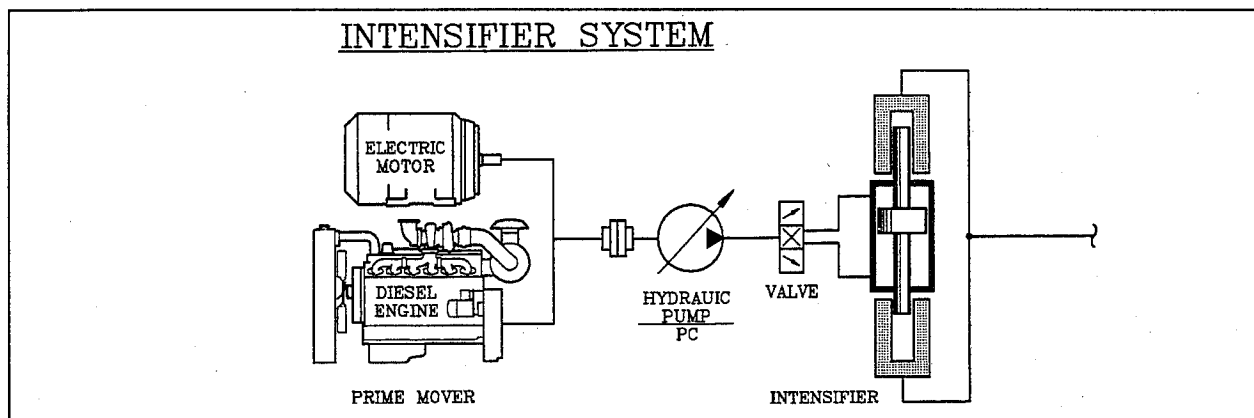


Figure 1: Hydraulic-Based UHP Intensifier Pump

The most common application for intensifier-based UHP waterjet pumps has been in permanent factory cutting installations. These pumps have proven to be quite reliable in well controlled factory environments. Where good water quality is available and routine maintenance can be scheduled under relatively clean conditions, these pumps are often found working around the clock. In the field however, the situation is quite different.

The performance record of intensifier pumps in field cleaning applications has been less than perfect. Equipment used by industrial service contractors is routinely exposed to the extremes of weather and temperature. Clean facilities for maintenance rarely exist under field operating conditions. Contractors are often supplied with dirty or caustic water sources. The combination of these conditions is a formidable challenge for any type of industrial field machinery. Due to the advanced technology used in intensifier pumps, they are particularly susceptible to failures caused by any one or all of the conditions listed above.

High Operating Costs Limit the Use of UHP Equipment

Despite the many advantages offered by UHP waterjets, the actual implementation of this technology into industrial cleaning applications has remained somewhat limited. The reason for this limitation is based primarily on economic reasons.

Ultrahigh-pressure intensifier pumps and their accessories have had high purchase prices and relatively expensive operating costs. The higher cost of operation has limited the use of UHP equipment to a specific number of problems that could only be solved by using pressures in excess of 30,000 psi.

In order to remain competitive, the majority of industrial service contractors continue to use conventional lower pressure / higher volume 10,000 and 20,000 psi waterblaster pumps.

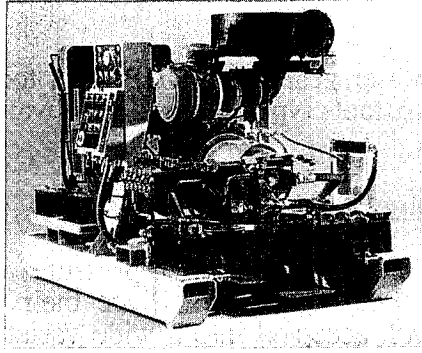


Figure 2: The HUSKY Pump

These pumps are often used in jobs where UHP waterjets could do the same job faster and with less generated waste, but their higher operating costs result in non-competitive bids from the equipment owners.

New Environmental Pressures Open the Door to UHP

Due to a more aggressive enforcement policy by the Environmental Protection Agency (EPA) and other related governmental agencies, many new restrictions are being placed on traditional methods used for industrial cleaning and surface-preparation work. The use of chemicals in stripping lead paint, for example, has come under intense scrutiny. In many areas of the country, open-air sandblasting, when not heavily restricted, is altogether banned. Regardless of the method being used, acid stripping, bicarbonate of soda, sandblasting, shot peening, or low-pressure / high-volume waterblasters, the trend toward containment of cleaning media, recycling of grit or water and a reduction of waste generation is the same throughout the country.

The problems encountered by today's industrial service contractor lie not so much with the method of coating removal, but rather with the amount of waste that is generated during the process. In some geographic locations, the cost of disposal now routinely equals or exceeds removal costs.

In an effort to respond to this demand, many leading pump manufacturers, both UHP and traditional waterblasters, have charged their design teams with developing a new generation of direct-drive ultrahigh-pressure pump that will be more efficient, economical and easier to maintain than intensifier-based systems.

New Direct-Drive Technology Leads the Way

In the development of UHP direct-drive pumps, the emphasis is on combining the reliability and ease of service of triplex-plunger pumps with the pressures of UHP intensifier pumps. With operating pressures ranging from 30,000 psi to 40,000 psi, many of these new pumps have already been introduced into the market.

Several well-known low-pressure / high-volume waterblaster pump manufacturers have recently introduced 30,000 psi direct-drive units. In addition, a large Houston-based, industrial service company is also using a direct-drive 35,000 psi pump which they developed and are manufacturing for their own proprietary use.

One of the most technically advanced direct-drive UHP pumps to be introduced into the industrial service market comes from a leading manufacturer of intensifier equipment, Seattle-based Flow International Corporation. Known as the HUSKY (see Figure 2), this new pump produces 6.5 gpm at 40,000 psi working pressure.

The Challenge of Direct-Drive Pumps at Ultrahigh Pressures

Two fundamental approaches may be taken when designing a UHP direct-drive pump. One approach is to simply take the existing 20,000 psi pump and modify the components so that they will withstand the greater operating pressures. This approach generally takes the standard operating conditions found in 10,000 and 20,000 psi pumps and increases the wall thickness and size of the components in order to withstand the higher operating pressures.

Because traditional waterblaster pump bodies are designed with low-pressure / high-volume operational characteristics, the larger size of the pump components limits the speed at which the pumps can operate. Since the majority of prime movers, either diesel or electric, turn at relatively high revolutions per minute (rpm), the waterblaster style of pump normally requires some type of gear reduction between the engine and the pump (see Figure 3). The average working cycle of these pumps is 400 to 600 rpm. The design criteria for bringing a waterblaster pump up to ultrahigh operating pressures is basically: the slower the rpm and the higher the pressure, the larger the size of the pump components.

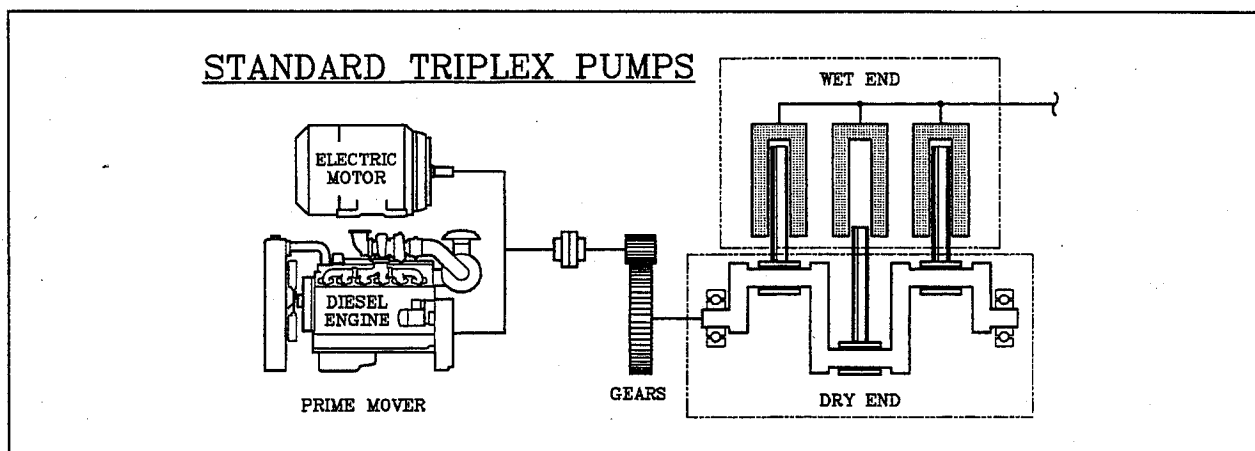


Figure 3: Standard Triplex Pump with Gear Reduction

Another challenge faced by waterblasting pumps at ultrahigh pressures is the design of the high-pressure seals. Most 10,000 and 20,000 psi triplex pumps are equipped with a multi-element packing or seal. The design of the packing becomes even more complicated when dealing with pressures greater than 28,000 psi (see Figure 4).

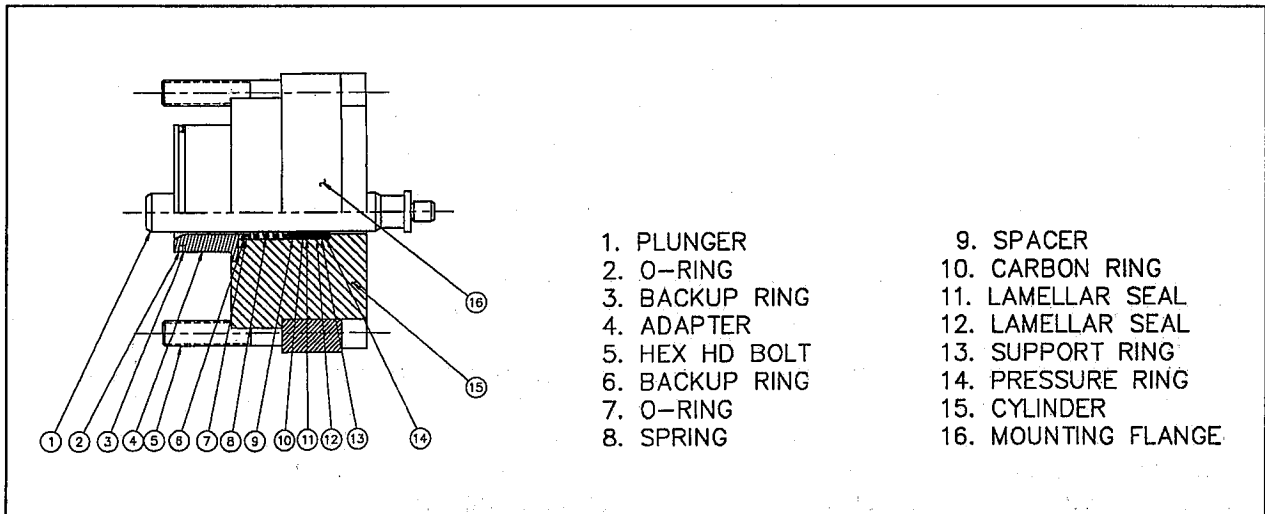


Figure 4: Standard Waterblaster Packing Design

Small Components Allow for High RPM Operation

In the case of the HUSKY, thousands of hours of testing of high rpm pumps was successfully combined with an in-depth knowledge of ultrahigh-pressure materials and components. This combination of technologies led to a patent pending-design which has allowed the HUSKY to have relatively small high-pressure components.

The HUSKY's small-diameter plungers make it possible to operate at much higher rpms than waterblaster pumps are able to handle. It can easily operate at the 1700 to 2100 rpm level found in most prime movers. The ability to run at high rpm means that the pump may be directly coupled to the prime mover, thus eliminating the need for any type of gear reduction (see Figure 5).

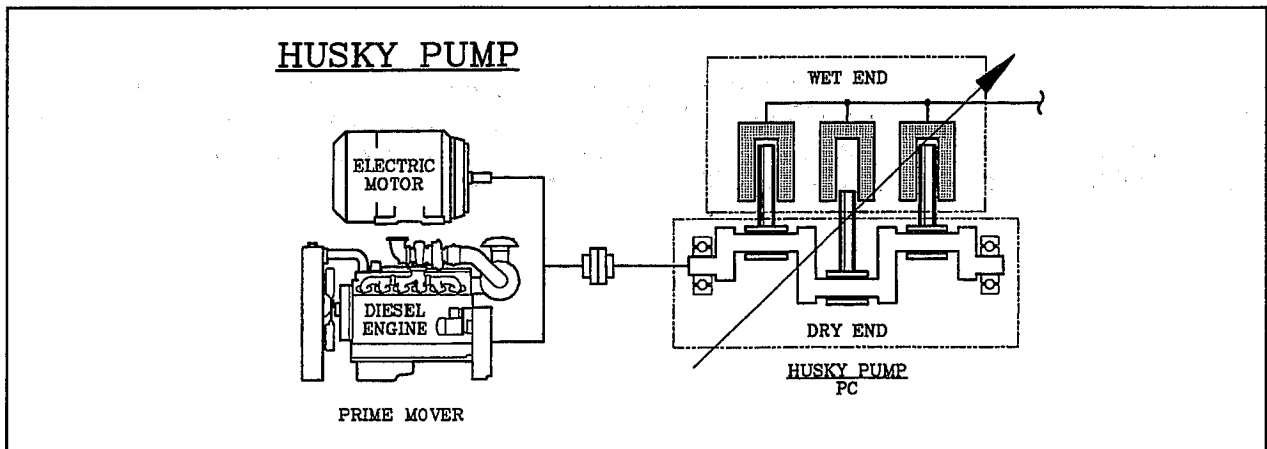


Figure 5: Direct-Drive HUSKY

The high-pressure seal design of the HUSKY pump takes full advantage of the small plunger diameter and the ability to control the length of the plunger stroke. The seals in the HUSKY are very similar to the elastomer and polymer combinations found in the high-pressure seal design of most ultrahigh-pressure intensifier pumps.

The check valve of the HUSKY is sealed with a simple metal to metal seal that eliminates the possibility of extrusion or erosion. The plunger seal or "dynamic" seal is made of a polymeric material and is located at the back end of the plunger. (See Figure 6).

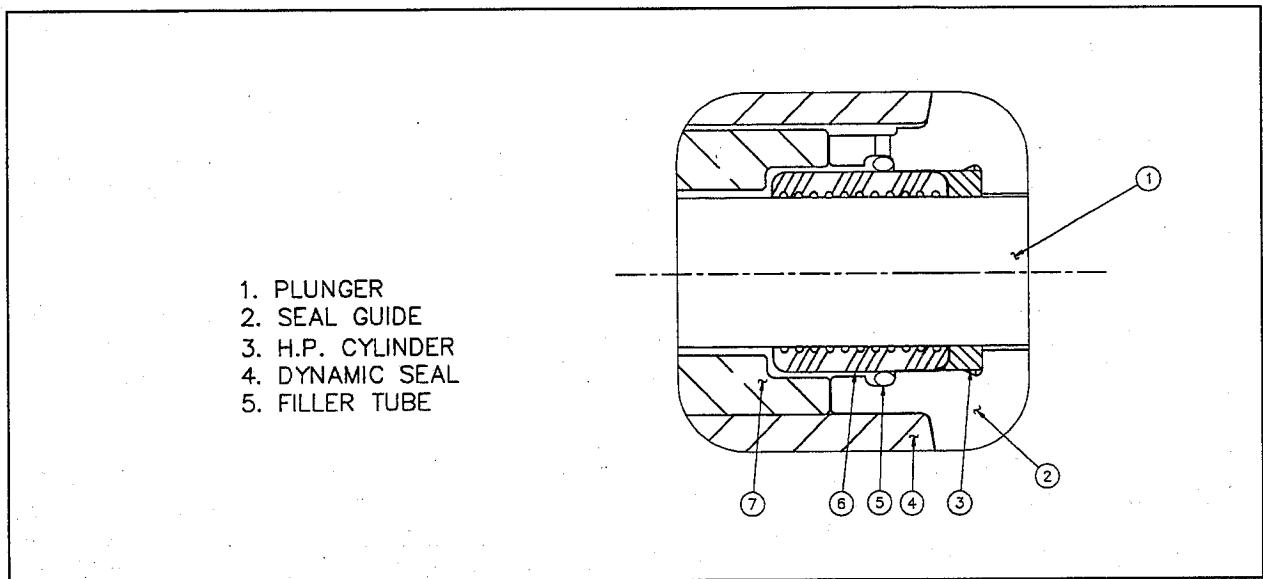


Figure 6: HUSKY Seal Design

The simplified seal design and the smaller size of the high-pressure components directly increase ease of maintenance. The pump's three cylinders may be serviced independently. All major components (such as the end caps, high-pressure cylinders and check valves) can be easily handled by a service technician without the need for mechanical lifting devices. Complete high-pressure seal change on all three cylinders can be performed in about 15 minutes.

Pressure Compensation, a Leap Forward in Direct-Drive Pumps

The feature that most distinguishes the HUSKY pump from the group of modified medium-pressure triplex plunger pumps is its unique pressure-compensation system.

Pressure compensation as it is applied to pumping technology basically means that the output flow rate of the pump will be adjusted to maintain a given constant pressure. When dealing with ultrahigh-pressure pumps, pressure compensation may also be defined as volume control. In order to have pressure compensation it is first necessary to sense a given pressure and then have the pump respond to it. The latter is especially critical when running multiple tools with numerous on/off functions.

In the case of hydraulic-actuated intensifier pumps, the pressure compensation system is based on sensing and adjusting hydraulic oil pressure. During compensation, hydraulic oil pressure is sensed and once regulated, acts upon the swash plate of the hydraulic pump thus changing its displacement. The change in the volume of hydraulic fluid to the intensifier lowers the stroke rate of the intensifier. The reduced stroke rate in turn lowers the output volume of water while maintaining the preset working pressure.

If an intensifier pump is placed in an idle or dead-head mode (where working pressure is maintained but the output flow is stopped) the pressure compensation mechanism will adjust the displacement of the hydraulic pump. Hydraulic fluid will be delivered to the intensifiers so that the high-pressure plungers will only move enough to make up for any leakage of water past the high-pressure seals.

The fact that positive-displacement pumps do not have a hydraulic circuit to control makes the challenge of pressure compensation much more difficult. In the case of the HUSKY, instead of adjusting the output displacement of the pump, a mechanical device is used to prevent the pumping of the fluid which is charged on the inlet plunger stroke.

The pressure compensation device of the HUSKY is a patent-pending mechanism that allows the pump to deliver only the required amount of pressurized water. The amount of water is determined by the pressure setting of the pump and the size and number of orifices at the tool-point.

The pressure-compensation device of the HUSKY works by adjusting volume to maintain pressure. Working pressure is defined by the amount of flow through a nozzle, much like an electrical current through a resistor that establishes a certain voltage. Just as the current through a resistor may be changed to maintain a voltage drop, in the HUSKY the flow through an output nozzle is adjusted in order to maintain a constant pressure.

In order to illustrate this concept, let us assume that an operator is using a HUSKY pump which has an output flow rate of 6.5 gpm @ 40,000 for a hand-held cleaning job. The operator has loaded the hand tool with a nozzle combination which allows 5 gpm of flow. The question is: What happens to the other 1.5 gpm of flow?

The HUSKY has a built-in mechanism which is designed to sense the output pressure. If the operating pressure of the pump has been set at 40,000 psi, it will try to force all 6.5 gpm of water through the output nozzles which are set at 5 gpm. Since not all of the output flow is able to exit the nozzles, the pressure will start to increase. As soon as the pressure starts to rise, the pump immediately senses it and begins to compensate by holding the inlet check valve open as described above.

The water that is in excess of the set discharge rate determined by the output nozzle size is recirculated through the pump's internal plumbing system. It is important here to note that no water is discharged in this process.

If for any reason the pressure compensation mechanism of the HUSKY should fail to react to a pressure build-up, the pump is equipped with a resettable pop-off valve. This valve will automatically open if the pressure exceeds a given level. The valve is easily reset by lowering the pressure of the pump back to idle pressure (approximately 10,000 psi). Once idle pressure is reached, the valve automatically resets and the pump may be brought back up to full operating pressure.

Unloader Valves the Only Alternative to Pressure Compensation

All hydraulic-powered intensifier pumps have pressure compensation systems based on the control of the hydraulic pump as described above. The HUSKY is the only ultrahigh-pressure direct-drive positive displacement pump available with full internal pressure compensation. The majority of 30,000 psi direct-drive pumps have dealt with the problem of pressure compensation by developing various types of pressure by-pass valves.

Also known as dump valves or unloader valves, these units are fairly complex in design. Valves of this type are used regularly with lower pressure pumping equipment. Unloader valves are a high maintenance item even when used with 5,000 psi pressure washers. When pressure losses occur during operation, operators are often tempted to adjust the unloader valve rather than fix the real problem (worn packings or nozzles). Improper adjustments, poor maintenance and excessive wear of by-pass valves can create significant safety problems.

Ultrahigh-pressure positive-displacement pumps that do not have internal pressure-compensation require the use of very complex pressure by-pass valves. Because of extremely high operating pressures and relatively large output volumes the unloader valves for these pumps are often quite massive in size. The seats of these ultrahigh-pressure dump valves are subject to extreme erosion and washout problems causing them to be a high maintenance item.

Environmentally Friendly Closed Loop Cooling System

Many of the new direct-drive pumps address the need to limit the amount of cooling water required by typical intensifier pumps. In some models of intensifier units, up to 6 gallons of water per minute may be run through the pump and subsequently dumped for cooling requirements. In most of the new direct-drive UHP pumps, the cooling systems are closed-loop.

In the case of the HUSKY, the cooling system has been made to operate in a closed-loop zero-discharge mode. The crankcase lubrication oil is cooled on the pump by means of a forced air heat exchanger mounted in front of the radiator. The cooling water of the pump is recirculated through the high pressure heads and only leaves the pump when it is discharged through the nozzles for cleaning and cutting purposes (see Figure 7).

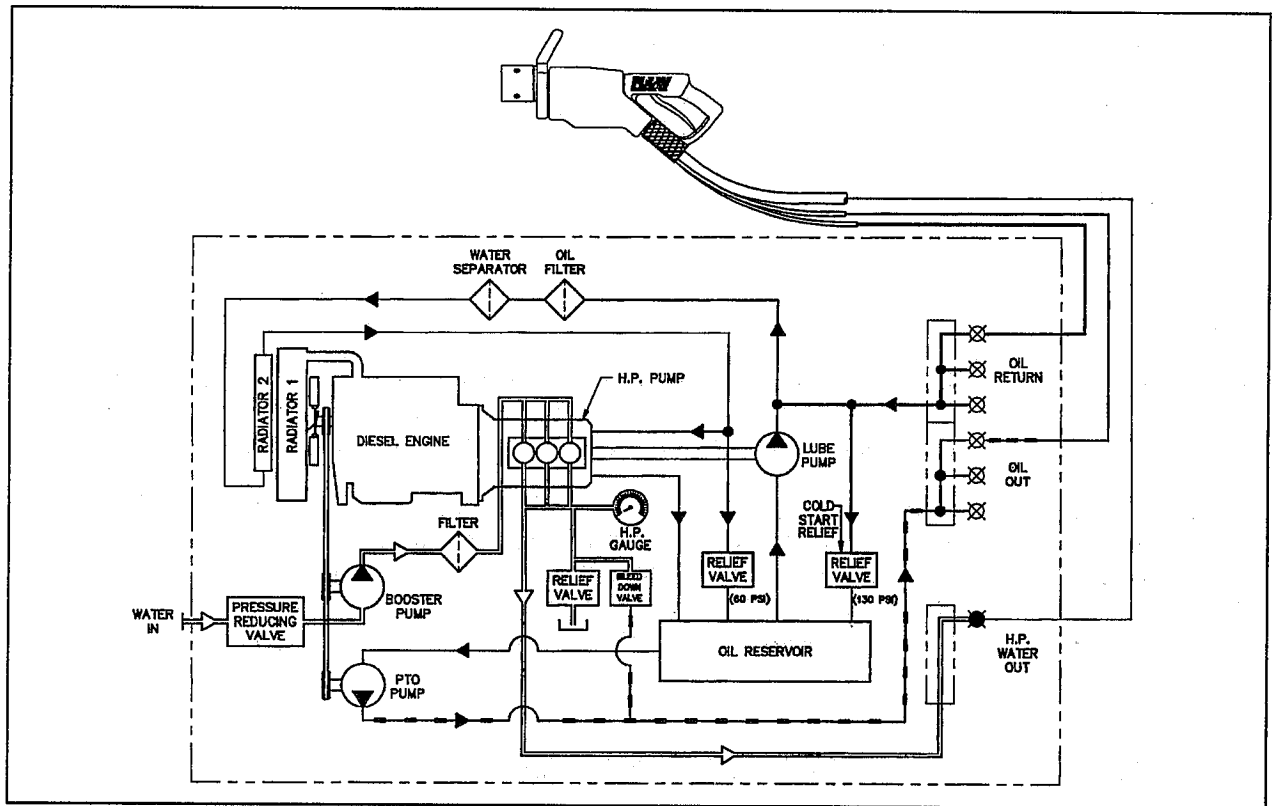


Figure 7: HUSKY Operation Schematic

Efficiency of Operation

Although positive-displacement ultrahigh-pressure pumps have only been on the open market for little more than a year, they are rapidly becoming the new industry standard for mobile cleaning applications. The primary reason for this rapid acceptance is their simple design and ease of maintenance. With the elimination of the entire hydraulic power circuit, these pumps are cheaper to operate and easier to repair than intensifier pumps. For the owners of these new UHP plunger pumps reduced down-time and lower operating costs translate directly into higher profits.

Another important reason that positive-displacement pumps are being readily accepted by industrial cleaning contractors is the absolute increase in efficiency of operation that they offer. Due to energy loss through the hydraulic loop, the average intensifier pump has an overall efficiency level of 60 to 65 percent. Positive-displacement pumps produce an impressive efficiency rating of 90 to 95 percent.

Efficiency can be expressed in several ways. A direct benefit will be a significant fuel savings realized when operating a direct-drive pump versus an intensifier pump. Of greater importance to the operator are larger output flow rates and higher nozzle horsepower.

For industrial cleaning contractors, nozzle horsepower directly impacts surface cleaning and coating removal rates. The greater the nozzle horsepower, the faster, thicker and harder the type of material that can be removed.

Table 1 compares nozzle horsepower for several of the leading commercially available UHP pumps both positive-displacement and intensifier-based units. As indicated in the chart, nozzle horsepower is determined by multiplying operating pressure in psi by the output flow rate in gpm and dividing the product by a coefficient of 1714. The resulting number is the actual horsepower being generated at the nozzle.

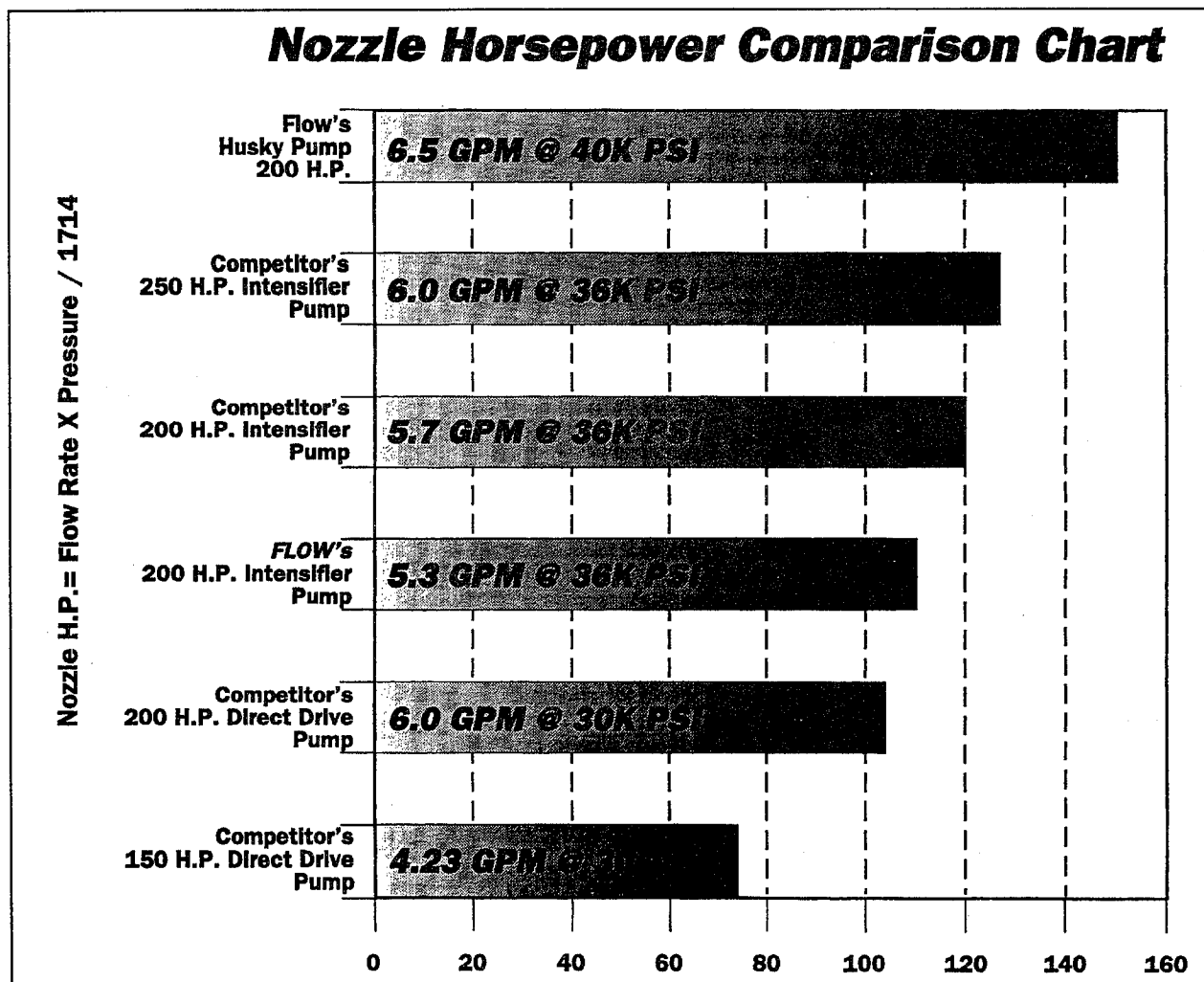


Table 1: Nozzle Horsepower Comparison Chart

Greater Efficiency & Increased Flow Rates Open New Applications for Ultrahigh-Pressure Waterjets

New applications for UHP waterjets are opening up because of improved efficiency and relatively large increases in output flow rates of ultrahigh-pressure positive-displacement pumps like the HUSKY.

The combination of higher water volume with greater nozzle horsepower makes these pumps well-suited for use with multiple hand-held tools as well as large-volume robotic cleaning heads.

Faster removal rates combined with stricter environmental regulations are making UHP waterjets one of the key methods currently being evaluated in each of the following applications:

- > Nuclear decontamination and decommissioning
- > Lead-based paint abatement
- > Automotive paint booth cleaning
- > Large surface coating removal (such as ships & aircraft)
- > Factory cleaning applications to replace solvents

Conclusion - UHP Direct-Drive Pumps are Here to Stay

Much work remains to be done to complete the introduction of these new ultrahigh-pressure direct-drive pumps into these and other new application areas. Manufacturers must prove to their potential customers that positive-displacement pumps are both reliable and cost effective to operate at ultrahigh pressures.

In addition to proving the reliability of the pumps themselves, proper accessories and equipment must be developed for use with these new pumps. New lightweight UHP hand tools must be introduced as well as flexible high-pressure hose capable of withstanding ever-increasing working pressures.

As new types of tools and robotics are perfected for field use, the acceptance of UHP waterjet technology will continue to expand into new application areas.

Under the new administration, environmental regulations are expected to become much more strict. This fact combined with the greater efficiency and ease of operation of ultrahigh-pressure direct-drive pumps will guarantee that this new technology will be accepted as the preferred method of industrial cleaning and coating removal in a wide variety of industries and applications.

ABRASIVES: THEIR CHARACTERISTICS AND EFFECT ON WATERJET CUTTING

John L. Ohman
Barton Mines Corporation
North Creek, New York

ABSTRACT

There are several industrial abrasives available in the market today. Each abrasive has certain key characteristics that determine its performance in industrial applications. These characteristics also effect the performance and cost of operating an abrasive waterjet. A simple equation can be used to calculate the cost of cutting an inch of material by incorporating both abrasive cost and performance.

1. GENERAL ABRASIVE APPLICATIONS

While abrasive waterjet cutting is a relatively new technology, abrasives have been used in industry for a long time. Below are some examples.

Sand blasters use loose abrasives including sand, slag, garnet and steel shot to clean metal structures that are coated with rust or paint. This is a relatively low-tech application where product purity and consistency in sizing are not critical to performance. In fact, having a wide range of grain sizes in a blasting abrasive may aid the cleaning process. Large particles cut through the thickest and heaviest rust while the finer grains scour the pitted metal surface. Recent health and environmental regulations have focused attention on dust generation, free silica content and other possible contaminants. This puts pressure on abrasive suppliers to sell safe, clean abrasives.

Bonded abrasives are used to grind wood or metal. Abrasives like garnet or aluminum oxide are mixed into resin or urethane and molded into the shape of a wheel or block.

Coated abrasives, or sandpaper, is perhaps the best known abrasive use. Silicon carbide, aluminum oxide, garnet and other ceramic abrasives are glued to flexible paper or cloth. Abrasive sizing is critical since an oversized particle will scratch the surface being sanded. An undersize particle does no work at all. See figure 1a. Abrasive characteristics like durability and sharpness also help determine sandpaper's performance. In the woodworking and metalworking industries, the amount of work accomplished by a belt of sandpaper is closely monitored and its performance is compared to its cost. A three dollar belt that sands 100 pieces is better than a one dollar belt that sands 25 pieces.

Micro-abrasives are used in wet slurries to grind and polish glass, paint and metal. See figure 1b. Particle sizing is again critical since oversized particles produce scratches. This "high-tech" application requires extremely high quality abrasive powders that are difficult to produce.

In addition to abrasive waterjet cutting, these are some of the most common industrial abrasive applications.

2. ABRASIVE PRODUCTION

Natural abrasives are often mined from river beds or sand deposits. These "alluvial" abrasives have been exposed to centuries of erosion and have a round to sub-rounded particle shape. See figure 2.

In some cases, abrasives like the garnet from North Creek, New York are found in hard rock deposits. In this case, blasting and crushing are required to liberate the mineral. The resulting particle shape is sharp and irregular. See figure 3.

Once the rock or sand is taken from the ground, the next step is to remove impurities which may range from 10% - 90% of the original ore. This is an important step since the product's purity will effect its performance. Also, impurities such as free silica are a health hazard.

The mineral must then be sized. This is a multiple step process where metal screens are used to remove fine and oversized particles.

Man-made abrasives like aluminum oxide and silicon carbide are produced specifically for abrasive applications. The method of production is electro-fusion. Other "man-made" abrasives are the by-products of other production processes. Copper slag for instance is the dross or waste from the copper smelting process. Glass cullet is often ground from rejected pieces of a glass plant.

3. ABRASIVE PARAMETERS THAT EFFECT WATERJET CUTTING

The type of abrasive used in a waterjet can have a large impact on its cutting performance. Described below are several characteristics, natural and man-made, that effect abrasive performance in waterjet cutting. Generalizations can be made about the effect of each characteristic, but these assume that the rest of the waterjet is working well. If there are other problems such as insufficient pressure, improper nozzle alignment, etc., the full benefit of an abrasive will not be realized. We have also found that as operator skill increases with time, the differences between abrasives may become more evident. Finally, the more difficult the cut, the more important abrasive selection becomes.

3.1 Natural Characteristics.

There are several natural characteristics that determine an abrasives effectiveness in waterjet cutting. Some of the most common abrasives and their natural characteristics are listed below:

	Mohs Hardness	Specific Gravity	Particle Shape
Almandite Hard Rock Garnet	8 +	4.0	Sharp/angular
Almandite Alluvial Garnet	7.5	3.9-4.1	Sub-rounded
Olivine	5.5	2.6	Sub-rounded
Slag	6-7	3.2	Angular
Glass Beads	6.0	2.5	Round
Glass Cullet	6.0	2.5	Angular

3.1.1. Hardness

Harder abrasives often cut faster and deeper. They may also have less break down in the mixing chamber.

3.1.2. Particle shape

Sharp, angular abrasives cut more efficiently than rounded grains, particularly on difficult or thick materials. See figures 2 and 3 again. It is believed that the sharp edges penetrate and shear better than the alluvial sands.

3.1.3. Specific gravity

A heavier particle traveling at the same speed will transfer more energy to the surface and therefore cut quicker.

3.2 Man-made Characteristics

Other abrasive characteristics are the result of the production process. These include:

3.2.1. Purity

Normally impurities reduce the effectiveness of an abrasive. For instance, silica and hornblend are softer and lighter than garnet. A garnet abrasive that has significant quantities of these minerals will not cut as quickly.

3.2.2. Particle Size

With the correct nozzle and pressure, a coarser abrasive (50 mesh for example) will cut faster when speed is the primary consideration. On the other hand, a finer abrasive produces better surface finish. When cutting glass, for instance, a 120 mesh reduces microfracturing. The 80 mesh, however, seems to be a happy medium and is the most popular grade.

3.2.3. Particle Sizing

a. Screen and particle size

Mesh size is defined by the number of holes per square inch. See figure 4. A series of screens are used to progressively narrow down the particle size distribution for a given grade. An 80 mesh water jet abrasive is therefore really a range of sizes. See figure 5. For instance, an abrasive producer could decide to bag everything that falls through a 40 mesh screen and that does not pass through a 120 mesh screen. That manufacturer could label this product "80 mesh." The narrower the range, however, the better the abrasive is for waterjet cutting.

b. Bricks

This is an abrasive term for oversized particles. These "bricks" will cause the nozzle to clog and/or sputter simply because they do not fit through the nozzle opening or because they bind up with other large particles. A general rule of thumb is that the largest particles should be less than half the size of the nozzle.

c. Fines

The removal of fines from a waterjet abrasive is critical. Fines and dust can cause clogging in the abrasive feed tube and in the nozzle. The operator must then take the time to clean the nozzle or in some cases incur the cost of replacing it. Also, when initiating a cut, fines may temporarily clog the nozzle at low pressure but then let go as the water pressure builds. This causes an abrupt blast and may damage the surface of the material being cut.

d. Consistency in distribution and range

Different size particles will cut at different speeds. It is therefore helpful to have consistent particle size distribution for even cutting performance from week to week. A good waterjet abrasive will have consistency both in its distribution (ratio of large to small particles) and its range (the outer size limits at both the fine and coarse ends). See figure to illustrate this point.

3.2.4. Product Modification

In some industrial applications, a product modification such as surface treatment enhances an abrasives performance. In waterjet cutting, heat treatment or tempering improved abrasive performance particularly when cutting the harder metals.

4. IMPACT OF ABRASIVE SELECTION

The quality of an abrasive can effect the performance of an abrasive waterjet in a number of ways. These include:

4.1 Abrasive Feed Rate

The more effective an abrasive is, the less will be required per minute to cut. If less is consumed, less will have to be purchased, transported, cleaned up, and disposed of.

4.2 Cutting Speed

To put it simply, a more aggressive abrasive cuts faster.

4.3 Finish

A better abrasive can improve the taper and edge quality. This is especially important when cutting thick materials.

4.4 Kerf Width and Nesting

If a finer cut is achieved with an abrasive, the parts can be nested closer together and material is saved.

4.5 Component Wear

Poor grading will often accelerate nozzle wear. A more aggressive abrasive may also produce faster nozzle wear, although this is generally outweighed by increased production.

4.6 Reject Rates

Poor surface finish or clogging may require a piece be recut.

Cost ...

5. COST

Both the price per pound and the cutting performance of an abrasive effect the cost of operating an abrasive waterjet. Higher quality abrasives generally cost more because extra effort has gone into producing and refining the product. The additional cost must be weighed against the abrasives performance.

In any production process the most important measurement is the final cost of producing one unit. This can be measured by dividing the total cost of production by output.

$$\frac{\text{Total Cost}}{\text{Output}} = \$ / \text{unit produced}$$

In waterjet cutting, we can define production as inches cut and measure the cost of cutting one inch . Therefore:

$$\frac{\text{Total waterjet operating cost}}{\text{inches per hour}} = \$ / \text{inch cut}$$

Total abrasive cost is determined by cost per pound and the amount of abrasive consumed in one minute.

$$(\$/\text{lb})(\text{lbs/minute})(60) = \text{abrasive cost per hour}$$

Therefore an equation calculating waterjet cost would look something like this:

$$\frac{(\text{lbs/hr})(\$/\text{lb}) + \text{equip} + \text{labor} + \text{consumables} + \text{disposal}}{\text{inches cut per hour}} = \$/\text{inch cut}$$

In the field, waterjet performance varies from installation to installation due to the many variables involved. The operator can plug in numbers into this equation based on his own testing and costs and then determine which abrasive is best in that particular application.

For the sake of illustration, I have assumed those other costs equal \$32 and then compared a low cost, low performance abrasive with a higher cost, high performance abrasive. (See below) The cut rates are similar to those that might be experienced when cutting 1 1/2 inch thick stainless steel.

Example #1:

$$\frac{(60 \text{ lbs/hr})(\$.15/\text{lb}) + \$32/\text{hr}}{.8 \text{ in/min} * 60} = \$.85/\text{inch}$$

Example #2:

$$\frac{(45 \text{ lbs/hr})(\$.40/\text{lb}) + \$32/\text{hr}}{1.25 \text{ inch/min} * 60} = \$.67/\text{inch}$$

In these examples, a very low cost abrasive successfully cuts the metal but the higher cost, higher performance abrasive saves a considerable amount of money by its superior performance. The illustration argues that cutting speed is the most important consideration when selecting an abrasive. Abrasive performance has a greater effect on the final unit cost (that is, the cost of cutting one inch) than does its cost per pound.

5.1 Limitations

This equation is a useful tool for determining the cost of cutting with a waterjet and using a particular abrasive. However, it may not account for several important factors including:

- reject rates
- down time due to abrasive
- kerf width
- surface finish
- health/environmental hazards.

6. CONCLUSION

There are a number of variables to consider when selecting an abrasive. The most important is the abrasive's effect on the cost of producing one unit, or cutting one inch. This can only be determined through experimentation and calculation of the waterjets total costs. Then the cost of the abrasive can be weighed against its performance and the most cost effective abrasive media can be selected.

Other Abrasive Applications

Diagram of a Coated Abrasive (Sandpaper) Product

Single Layer

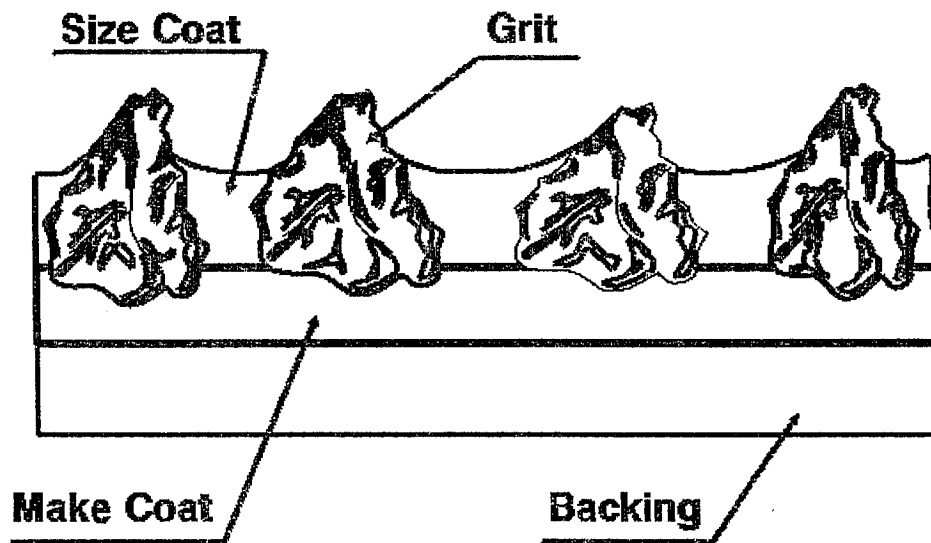


Figure 1a

Cross Section of Workpieces Being Lapped

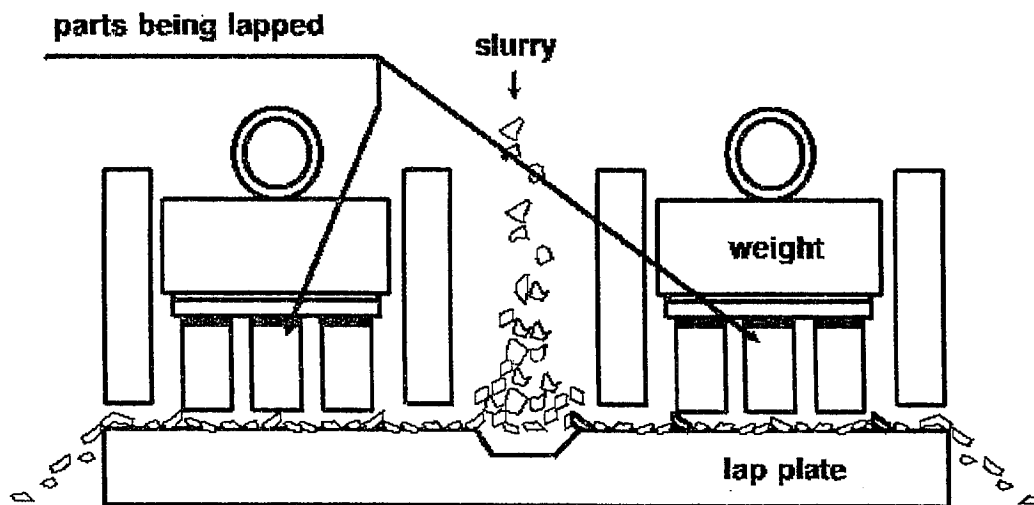


Figure 1b

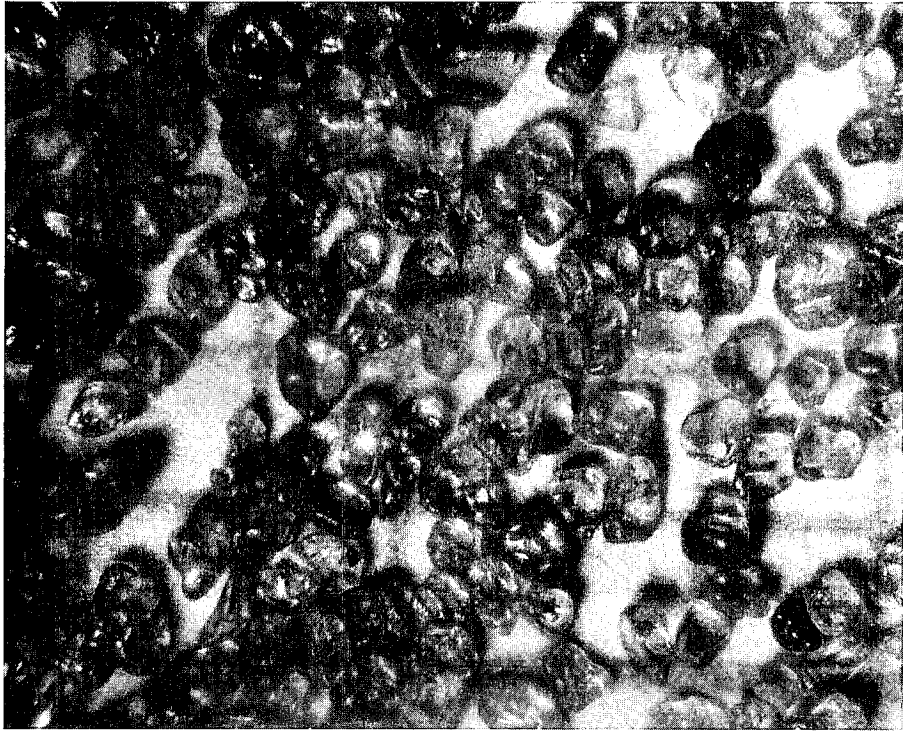


Figure 2



Figure 3

MESH SIZE = # of Openings Per Square Inch

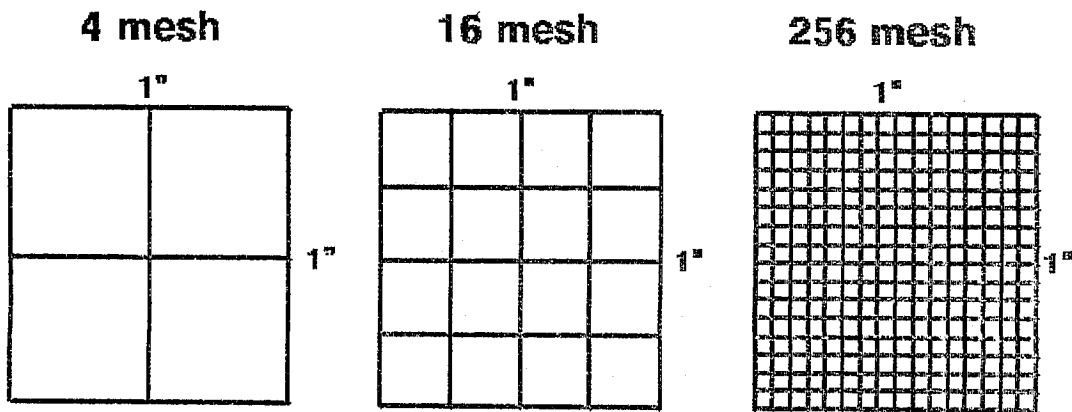


Figure 4

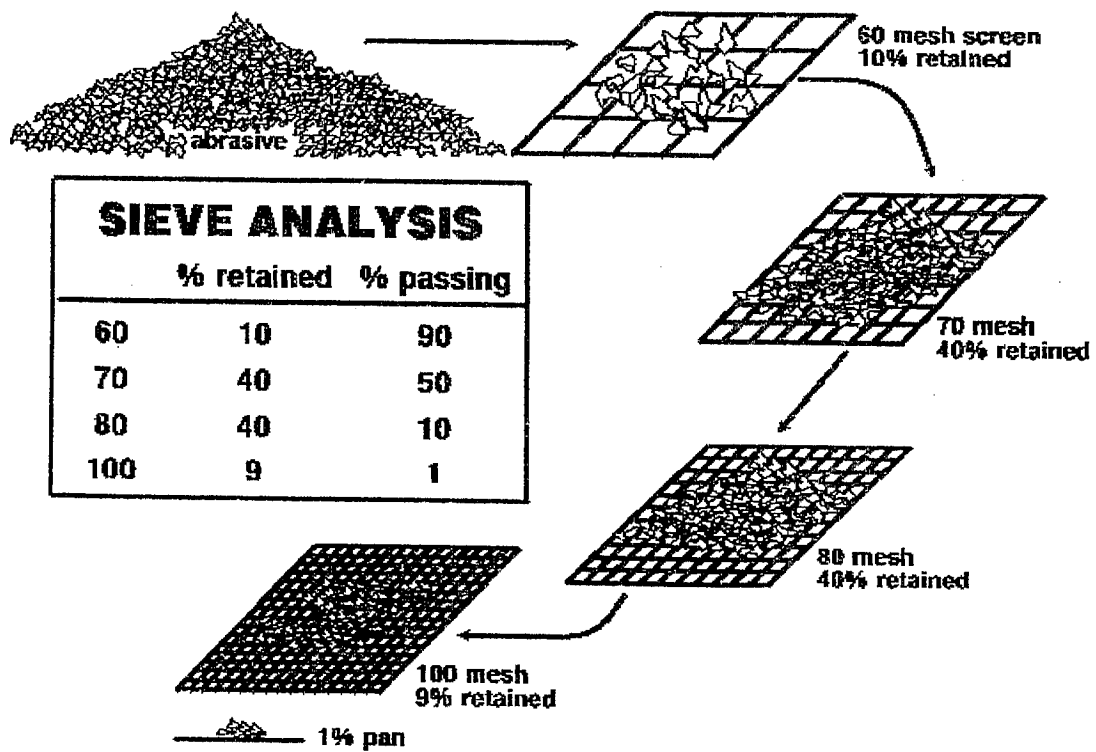


Figure 5

Particle Size Distribution

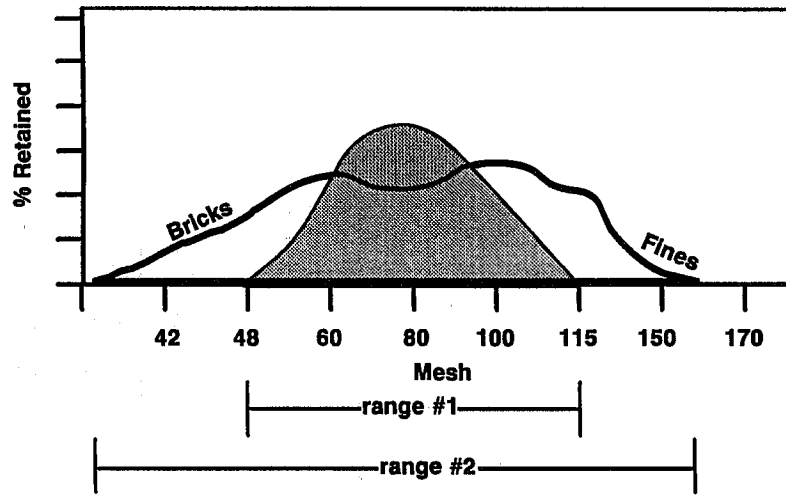


Figure 6

INFLUENCE OF PROPERTIES OF GARNET ON CUTTING PROCESS

J. Vašek, P. Martinec, J. Foldyna, L. Hlaváč
Institute of Geonics (formerly Mining Institute), Academy of Sciences of the Czech Republic
Ostrava-Poruba, Czech Republic

ABSTRACT

Available types of garnet abrasives differ from each other in mineralogical properties, grain shape, portion of defective grains and method of treatment. Abrasive grains are characterized by chemical composition, texture and type of defects, elastic properties, grain shape, density, grain size distribution and content of garnet.

Experimental results and the influence of material and morphological characteristics of different mineral types of garnet on cutting performance are discussed.

1. INTRODUCTION

Garnets are frequently rock-forming minerals. They tend to accumulate in rocks where they form the primary deposits of garnets, or in river and beach sands where they form the secondary deposits as part of heavy minerals. Garnets are very important naturally occurring minerals that are, after processing, widely used as abrasives for numerous applications such as the polishing of materials. However, since 1983 when abrasive waterjet (AWJ) technology was introduced commercially, garnet has been increasingly used as an abrasive material in AWJ applications. Substantial advances have been made in understanding the AWJ cutting process since then. Nevertheless, further investigation into the influence of abrasive material properties on cutting performance is still needed. Hopefully, new insights into the AWJ cutting process may be obtained and better efficiency realized.

Abrasive materials used in AWJ are commonly characterized by their basic parameters such as chemical composition, density, hardness, grain size, and grain shape or "sharpness" (see, e.g., Nakaya et al. (1984), Baumann et al. (1986), Matsumoto et al. (1988), Hashish (1988), Guo et al. (1992), Foldyna (1992)). It may at first seem logical to assume that small variations in the physical characteristics of the abrasive material will not greatly influence the cutting results. However, a detailed analysis of the published results shows that differences in cutting efficiency using various abrasives may indeed be quite significant, though differences in the basic parameters of each respective abrasive material may be quite minimal.

Martinec (1992) suggested that the knowledge of elastic parameters (bulk modulus, shear modulus, elastic modulus), lattice constants, and microhardness of abrasive grains can be very useful in predicting the cutting performance of AWJ using a physical model of the process. As it is very difficult to find elastic constants determined using very small monocrystals of minerals, the elastic parameters, density and lattice constant of garnet end-members are presented in Tables 1 and 2. The elastic parameters and lattice constant for a given garnet mixture can be then determined from corresponding values for end-members of garnets by means of a regression analysis (Babuška et al., 1978) with respect to the chemical composition and cell parameter a_0 of a particular garnet sample. Corresponding values of the microhardness of garnet grains having similar molar composition to ideal garnet end-members were measured using the Vickers method and the values are displayed in Table 3.

To verify the assumption that the mineralogical properties of abrasive grains may influence the cutting performance of AWJ, an extensive experimental program was performed in the Rock disintegration laboratory of the Institute of Geonics (formerly Mining Institute).

2. EXPERIMENTAL PROCEDURE AND MATERIALS

2.1 Abrasive Materials

Several kinds of garnet minerals obtained from natural deposits were prepared for experiments. The experimentation was focused primarily on the most common garnet minerals, namely: almandine, grossular and andradite. These garnet minerals belong to two main groups in the garnet family according to the following classification:

Pyrope-spessartine group

pyrope	$\text{Mg}_3\text{Al}_2(\text{SiO}_4)_3$
almandine	$\text{Fe}_3\text{Al}_2(\text{SiO}_4)_3$
spessartine	$\text{Mn}_3\text{Al}_2(\text{SiO}_4)_3$

Grossulare-uvarovite group

grossulare	$\text{Ca}_3\text{Al}_2(\text{SiO}_4)_3$
andradite	$\text{Ca}_3\text{Fe}_2(\text{SiO}_4)_3$
uvarovite	$\text{Ca}_3\text{Cr}_2(\text{SiO}_4)_3$

These natural abrasive materials of high purity were acquired by grinding, mass separation and sieving. Seven specimens of garnet minerals suitable for the experimentation were obtained. No special treatment or improvement of their properties was done. These garnet specimens contained a large number of different types of naturally occurring defects.

For comparison of cutting efficiency with other laboratories and other types of abrasive material, commercial garnet was also used (mixture of Barton HP 50 and HP 80, marked almandine B). This garnet is specially processed and treated for high purity and low content of defects.

The specimens of garnets used in the experiments were marked as follows:

- almandine B; commercial product,
- almandine M; source: garnet-mica schists; natural material,
- almandine K; source: garnet-biotite gneiss; natural material,
- almandine G (mixture of garnets with dominant content of almandine type); source: the heavy mineral fractions from river sediments; natural material,
- grossulare Z (variant hessonite); source: contact of granite and crystalline limestones; natural material,
- andradite V (with different grain sizes); source: garnet-pyroxene-magnetite skarns; natural material.

The specimen marked almandine G is an example of a typical garnet material with natural treatment of defects.

Basic mineralogical and physical parameters of all garnet specimens used in the experimentation are presented in Table 4, and the proportion of typical grain shapes in studied specimens can be seen in Figure 1.

2.2 Experimental Procedure

Experiments were performed according to the methodology suggested by Foldyna & Martinec (1992), with the notable exception that the jet parameters were maintained constant during all tests. Jet parameters were set as follows:

- water pressure: 300 MPa,
- water nozzle diameter: ≈ 0.325 mm (0.013 in),
- abrasive mass rate: 0.25 kg per minute,
- standoff distance: 10 mm,
- traverse velocity: 60 mm per minute.

Basic schematic of the experimental setup is presented in Figure 2. Both cuts through the target materials and slot cutting of the target materials were performed and roughness of the freshly created surface and the depth of cut were respectively measured. To establish changes in the particle size distribution and shape characteristics of garnet grains during cutting process, samples of the garnet specimens were taken after passing through the focusing nozzle. During testing, the used abrasives, particles of target material and water were collected.

Figure 3 shows a schematic of the catcher used to obtain the abrasive mixture after each test run where the target material was cut through. Before each cut, the collecting vessel was refilled by water to attenuate the jet energy so as to protect the bottom of the catcher against damage. The content of the vessel was poured into a sedimenting tumbler after each cut. The vessel was then cleaned and prepared for another cut.

During slot cutting, the mixture of abrasive material, water and target material fragments was collected by a special container situated along the target material. Again, the contents of the container were poured into a sedimenting tumbler after each cut, and the container was then cleaned and prepared for another cut.

Collected samples of the abrasive and target material mixture were then dried. The abrasive particles were separated from the target material. Subsequently, changes in the physical characteristics of the abrasive grains and of the fragments of the target material were evaluated.

Because processing of the abrasive samples and evaluation of their characteristics is time consuming, only the results related to the depth of cut in slot cutting were available for this paper. The rest of the results will be presented at the International Conference Geomechanics 93.

2.3 Target Materials

During the experimentation, three types of rocks (sandstone, granite, skarn) and a sample of steel were used as target materials. Basic dimensions, physical and mechanical properties of the target materials are given in Table 5. Size of the target material samples was limited by the dimensions of the experimental apparatus. As such, the maximum possible thickness and width of a sample was 120 mm and 60 mm respectively.

3. DISCUSSION OF EXPERIMENTAL RESULTS

Although the mineralogical and physical parameters of different end-members from the garnet family and garnet specimens used in tests are very similar (see Tables 1, 2, 3 and 4), the depths of cut achieved with individual garnet specimens were very different at the same target material (see Figure 4). The fact that the best cutting performance was achieved using Almandine B, was expected as this garnet specimen is specially treated and processed. However, differences in cutting performance of natural garnet minerals are much higher than would correspond to differences in their mineralogical and physical properties. Additionally, these differences seem to be independent at mineral type of garnet.

The only parameter in which natural garnet minerals differed from each other significantly was the content of damaged grains (i.e., grains with inclusions or cracks). Accordingly, the results obtained using natural garnet minerals were sorted with respect to content of damaged grains, and compared to the depth of cuts obtained using Almandine B (see Figure 5). Figure 5 seems to indicate a strong relation between cutting performance and content of damaged grains in the garnet specimen. It leads to a possible conclusion that the amount of damaged grains may represent one of the key parameters in predicting the cutting performance of a particular abrasive material. Unfortunately, this assumption cannot be verified at present using published results as defect factors have not yet been taken into account by other authors.

It is of interest to note that the natural garnet specimen marked as Almandine K was nearly as effective in terms of cutting performance as the commercial garnet specimen Almandine B (from 92% to 96% for all target materials). This observation would seem to indicate that treatment and processing of these natural garnets can improve their cutting performance up to a level comparable with Almandine B.

As is also evident from Figure 5, the results obtained using Almandine M, Almandine G, Andradite V-A and Andradite V-B on different target materials are very inconsistent. The reason for this inconsistency may be explained by the examination of the samples of abrasive particles and fragments of target material collected during the experiments.

Preliminary results from a micropetrography analysis of abrasive material acquired after passing through the focusing nozzle seem to show that changes in both grain shape and grain size distribution had occurred. That is, the abrasive material reaching the target surface is substantially different from the original one at the abrasive input. A physical model describing the processes taking place during jet/abrasive particle interactions in a mixing chamber and a focusing nozzle with respect to particle damage probabilities has been prepared and will be presented at the International Conference Geomechanics 93 (Hlaváč, 1993).

4. CONCLUSION

With regards to the results from this study, micropetrography research currently being done, and prepared physical models, the authors propose the following theory that the unexpected behaviour of the garnet minerals used in this study may be caused by:

- defects in the abrasive mineral grains (inclusions, cracks),
- plastic deformation zones and local stress concentration areas and dislocations in the structure of garnets,
- sharpness of grains, amount of thin shard-like grains.

According to this theory, the elimination of all influences unfavourable for particle stability is necessary for better cutting performance using garnet abrasives. Cutting properties of natural garnets separated from rocks may be improved by intensive mechanical crushing and sorting. The elimination of structural defects is possible by using thermal or radiation treatment. Subsequent separation and sorting of garnet grains may also be very important. Garnet minerals from the secondary deposits show only mechanical defects that are caused by natural processes associated

with sedimentary transport and sorting of minerals by their density and morphology during mineral transport.

The authors also propose that standardization of abrasive materials research is needed so that the comparison of experimental results will be more readily possible.

5. ACKNOWLEDGMENT

This work is supported by the Grant Agency of the Czech Academy of Sciences under grants No. 31 654 and No. 31 655. Authors are very grateful for this support.

6. REFERENCES

- Babuška, V., Fiala, J., Kumazawa, M., Ohno, K., and Sumino, Y., "Elastic properties of garnet solid-solution series," *Physics of Earth and Planetary Interiors*, 16, pp. 157-176, 1978.
- Baumann, L., Boeing, R., and Hessling, M., "Fundamental investigations into the improvement of waterjet performance by the use of abrasive additives," *Proceedings of the 8th International Symposium on Jet Cutting Technology*, Paper 28, pp. 277-286, BHRA, Cranfield, Bedford, England, 1986.
- Foldyna, J., "Experimental research of rock and similar materials cutting using high pressure water jet," *Proceedings of the International Conference Geomechanics 91*, pp. 331-340, Balkema, Rotterdam, Netherlands, 1992.
- Foldyna, J., and Martinec, P., "Abrasive material in the process of AWJ cutting," *Proceedings of the 11th International Symposium on Jet Cutting Technology*, pp. 135-147, Kluwer Academic Publishers, Dordrecht, Netherlands, 1992.
- Guo, N.S., Louis, H., Meier, G., and Ohlsen, J., "Recycling capacity of abrasives in abrasive water jet cutting," *Proceedings of the 11th International Symposium on Jet Cutting Technology*, pp. 503-523, Kluwer Academic Publishers, Dordrecht, Netherlands, 1992.
- Hashish, M., "Data trends in abrasive water jet machining," *Proceedings of the Conference Automated Water-jet Cutting Processes*, Detroit, Michigan, U.S.A., 1988.
- Hlaváč, L., "Physical model of jet-abrasive interaction," *will be presented at the International Conference Geomechanics 93*, Hradec/Ostrava, Czech Republic, 1993.
- Martinec, P., "Mineralogical properties of abrasive minerals and their role in the water jet cutting process," *Proceedings of the International Conference Geomechanics 91*, pp. 353-362, Balkema, Rotterdam, Netherlands, 1992.
- Matsumoto, K., Arasawa, H., and Yamaguchi, S., "A study of the effect of abrasive material on cutting with abrasive water-jet," *Proceedings of the 9th International Symposium on Jet Cutting Technology*, Paper E4, pp. 255-269, BHRA, Cranfield, Bedford, England, 1988.

Nakaya, M., Kitagawa, T. and Satake, S., "Concrete cutting with abrasive waterjet," *Proceedings of the 7th International Symposium on Jet Cutting Technology*, Paper E3, pp. 281-292, BHRA, Cranfield, Bedford, England, 1984.

Table 1. Density and elastic properties of end-members of garnets (Babuška et al., 1978).

	Density [kg m ⁻³]	Bulk modulus K ₀ [GPa]	Shear constant C _s [GPa]	Poisson's ratio [-]
Almandine	4325 (4)	177.9 (0.8)	98.1 (0.5)	0.270 (0.1)
Spessartine	4189 (4)	174.2 (0.9)	96.4 (0.4)	0.270 (0.1)
Pyrope	3553 (4)	173.0 (0.9)	92.5 (0.4)	0.274 (0.1)
Grossulare	3607 (4)	169.1 (0.8)	110.6 (0.4)	0.243 (0.1)
Andradite	3810 (8)	137.9 (1.7)	97.9 (0.7)	0.236 (0.3)

Table 2. Lattice constant and cell volume of end-members of garnets (Babuška et al., 1978).

	Lattice constant a ₀ [Å]	Cell volume V _a [Å ³]
Almandine	11.522 (0.006)	1529.62
Spessartine	11.613 (0.005)	1566.15
Pyrope	11.457 (0.005)	1503.88
Grossulare	11.867 (0.005)	1671.18
Andradite	12.091 (0.009)	1767.61

Table 3. Microhardness (Vickers: 200 g) of the end-members of garnets (measured in the Institute of Geonics).

	Microhardness H _v [kN mm ⁻²]
Almandine	12.42 - 12.65
Spessartine	not determined
Pyrope	11.50 - 12.20
Grossulare (var. Hessonite)	11.10 - 11.90
Andradite	11.42 - 12.09

Table 4. Basic mineralogical and physical parameters of garnet samples

Sample:	Almandine				Grossular	Andradite		
	B	M	K	G		V-A	V-B	V-C
Lattice constant a_0 [µm]	11541 (7)	11547 (7)	11537 (8)		11846 (51)	12046 (8)		
Damaged grains [%]	≈ 5	≈ 60	≈ 15	≈ 60	≈ 30	≈ 90	≈ 80	≈ 90
Density [kg m ⁻³]	4114	4114	4056	3987	3576 (6)	3856 (4)		
Grain size [mm]	0.12-0.35	0.12-0.35	0.12-0.35	0.12-0.35	0.12-0.35	0.12-0.20	0.20-0.35	0.12-0.35
Morphology of grains	$F_{\text{ROUND}}^*)$	0.66 (7)	0.69 (7)	0.66 (7)	0.71 (8)	0.67 (5)	0.68 (9)	0.65 (9)
	$F_{\text{SPHERE}}^{**)}$	0.65 (12)	0.67 (12)	0.66 (13)	0.70 (9)	0.65 (6)	0.68 (12)	0.68 (11)
Grain shapes	Fig. 1a)	Fig. 1b)	Fig. 1c)	Fig. 1d)	Fig. 1e)	Fig. 1f)	Fig. 1g)	Fig. 1h)
Hardness (Mohs)	7.5	7 - 7.5	7 - 7.5	6.5 - 7.5	7	7	7	7
Microhardness (Vickers) 20g [kN mm ⁻²]	12.5-15.6	13.0-15.1	12.3-14.9	not determined	11.0-12.0	11.44		
Symmetry	cubic							
Type of imperfections	cracks irregular, conchoidal type							
Purity [%]	99	97	97	83	98	95	96	96

*) F_{ROUND} = roundness shape factor. The values of this parameter range between close to 0 for very elongated or rough objects and

$$\text{close to 1 for circular objects. } F_{\text{ROUND}} = \frac{4 \cdot \pi \cdot \text{AREA}}{\text{PERIMETER}^2}$$

**) F_{SPHERE} = sphericity shape factor: $F_{\text{SPHERE}} = \frac{D_{\text{MIN}}}{D_{\text{MAX}}}$

Table 5. Basic physical and mechanical properties of the target materials

Sample	Sandstone	Granite	Skarn	Steel
Medium (min - max) grain size [mm]	0.26 (0.1 - 2.836)	0.09 (0.04 - 0.56)	0.30 (0.15 - 0.60)	--
Density [kg m ⁻³]	2666 - 2603	2660 - 2646	2773 - 2666	8050
Porosity [%]	1.81 - 1.30	1.30	not determined	--
Compressive strength [MPa]	153 - 144	150 - 143	112 - 92	
Yield strength [MPa]	--	--	--	720 - 600
Tensile strength [MPa]	8.5 - 10.5	9.4	24.8 - 10.6	340 - 300
Young's modulus [GPa]	26.1 - 22.6	30.7	44.7 - 35.5	190 - 215
Poisson's ratio	0.18 - 0.24	0.20	0.26 - 0.17	0.30
Compressive strength ratio of dry and water saturated samples	0.79	0.96	not determined	--
Abradability [cm ³ /cm ²]	0.26	0.20	0.36	--
Wave propagation speed [m s ⁻¹]	--	--	--	5000
Rock forming minerals	quartz 70%, micas 8%, carbonates 10%, rock fragments 10%, feldspars 2%	quartz 53%, micas 12%, feldspars 35%	quartz 51%, amphiboles, pyroxenes 41%, carbonates 3%, feldspars 5%	--
Dimensions of samples (thickness x width) [mm]				
Slot cutting	120 x 60	120 x 60	120 x 60	60 x 60
Cuts through	25 x 60	22 x 60	26 x 60	8 x 60

Note: Sandstone samples are used as a reference material in the Rock disintegration laboratory of the Institute of Geonics.

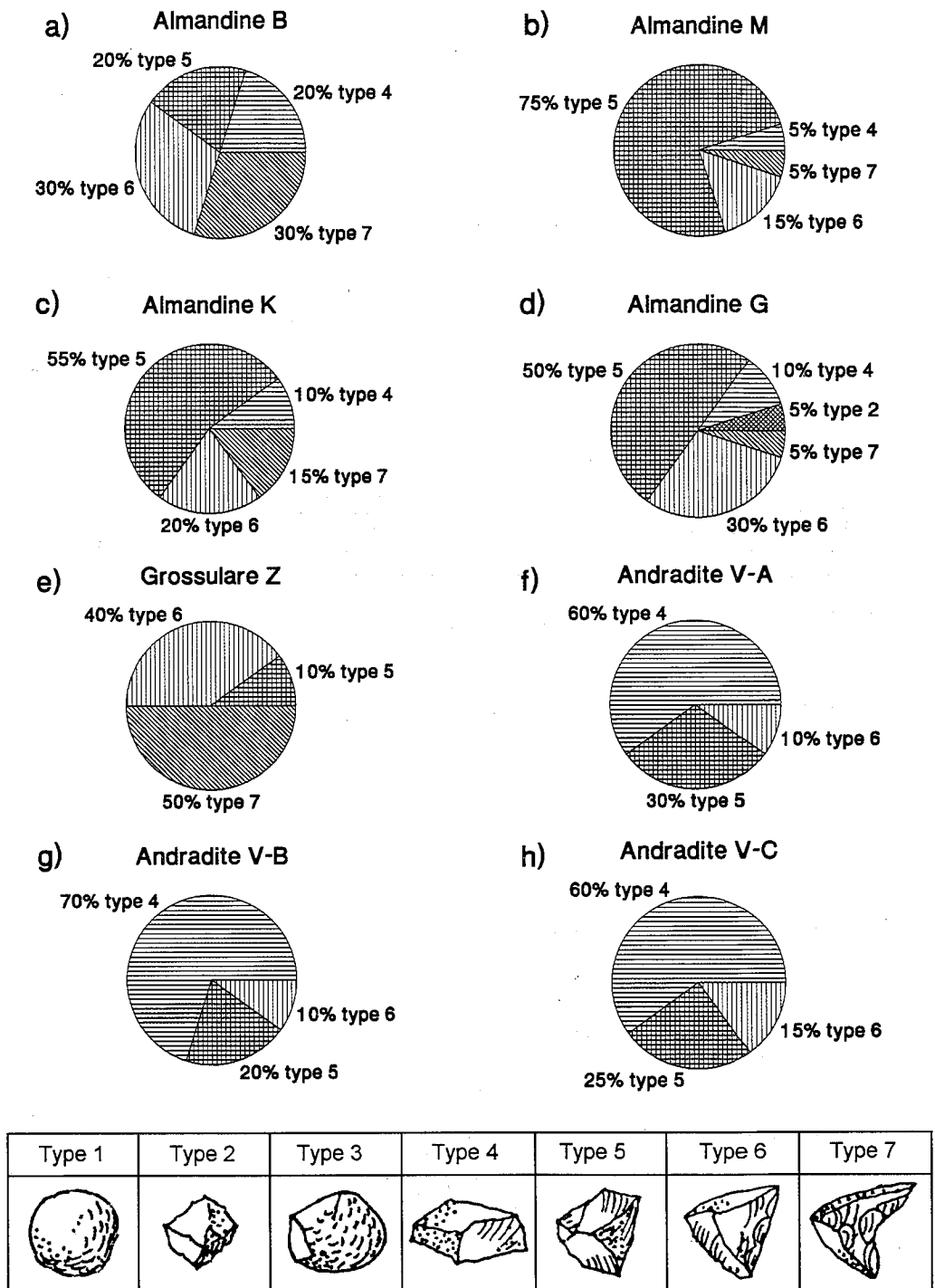


Figure 1. Proportion of each individual grain shape in tested garnet specimens.

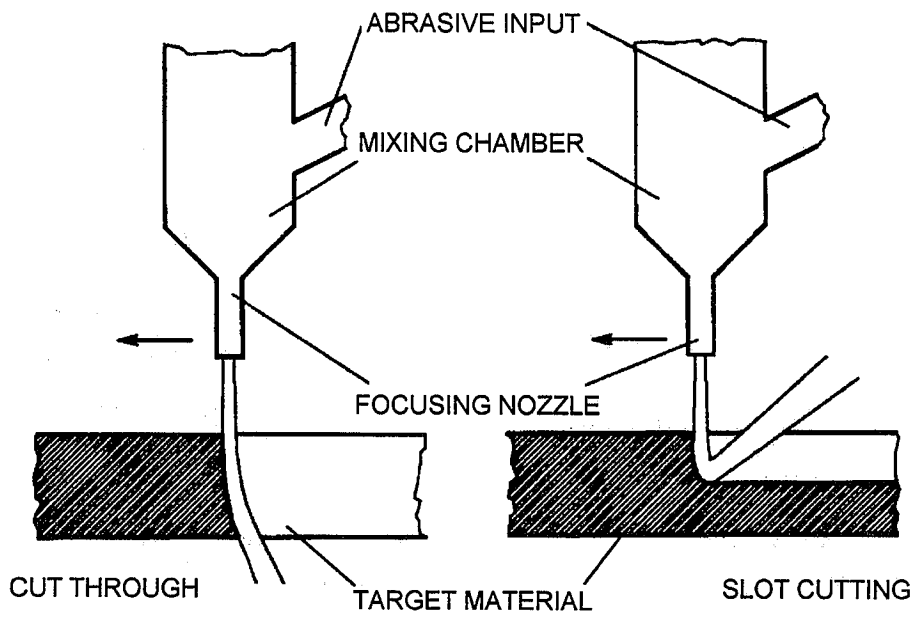


Figure 2. Basic schematic of the experimental setup

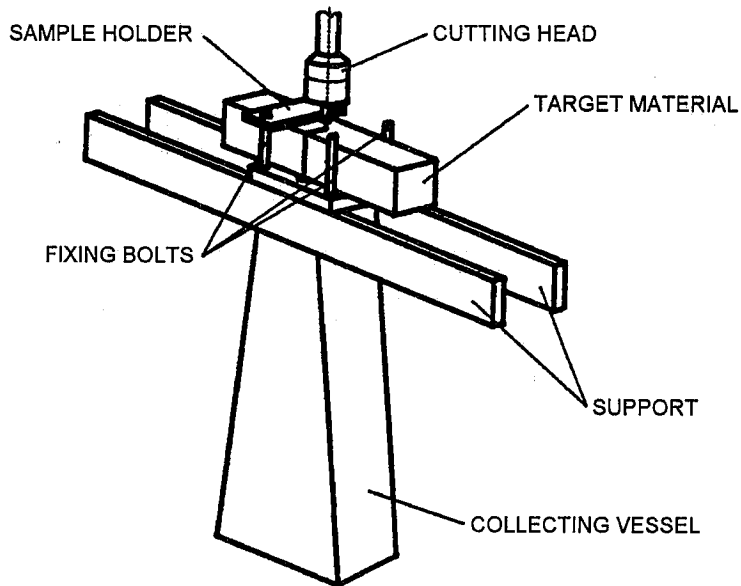


Figure 3. Schematic of the abrasive material catcher.

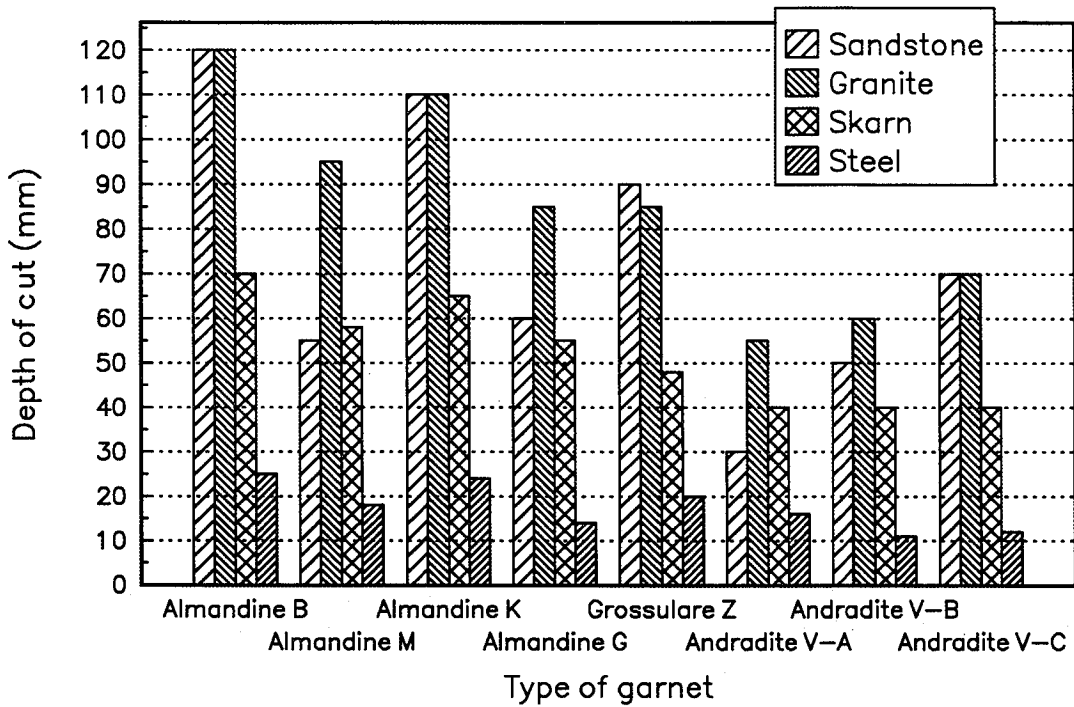


Figure 4. Depth of cut obtained using various garnet specimens on different target materials.

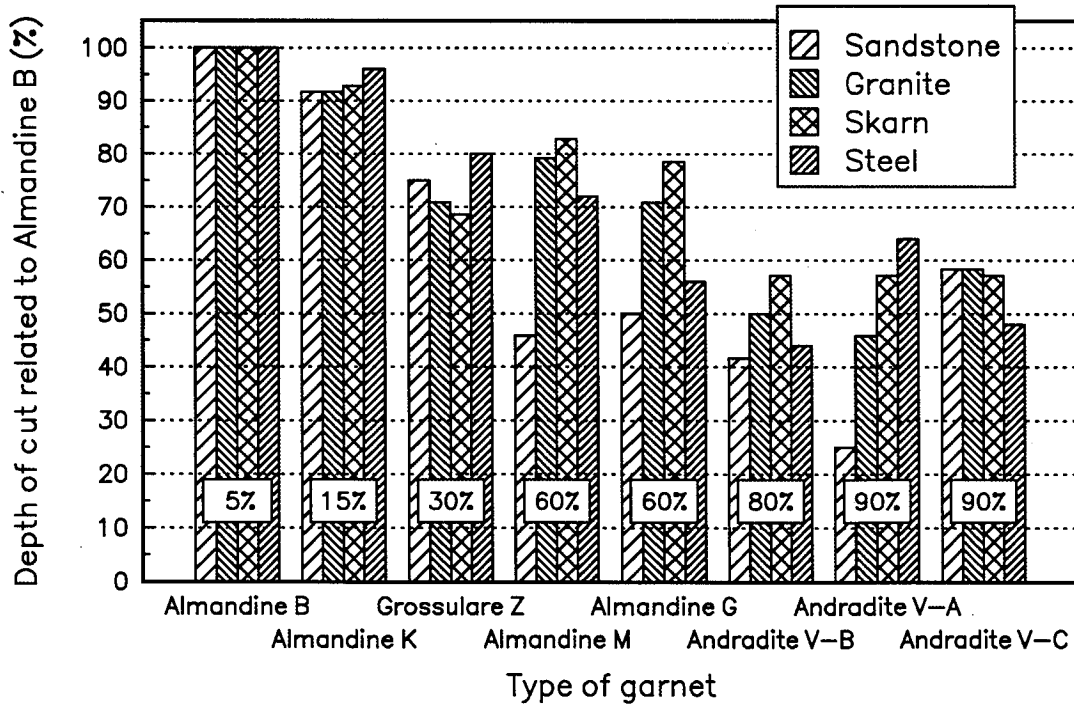


Figure 5. Cutting performance of natural garnet specimens as compared to Almandine B. (Percentages within figure indicate content of damaged grains.)

WATER TREATMENT METHODOLOGIES USED TO MEET STANDARDS FOR DISCHARGE OR REUSE IN WATER JET APPLICATIONS

Michael D. Hanrahan
Advanced Water Systems, Inc.
Woodinville, Washington, U.S.A.

ABSTRACT

In the past, water jet waste streams have not posed nearly the problem they now represent. The advent of ever increasing antipollution legislation, coupled with overloading of municipal waste treatment capabilities, now makes wastewater treatment a critical part of system design, sales and operation.

In addition to providing waterjet equipment that performs to design standards, the water jetting industry must now consider what happens to the water after it has done its work. If wastewater is to be recirculated as supply water in a true closed-loop zero-discharge system, treatment requirements become even more critical.

Depending on the level of wastewater treatment required, design considerations address a variety of water contaminants. Water treatment systems incorporate mechanical, chemical and electrochemical filtration technologies. Results from field testing with several water jetting systems in different applications have established standards and methods to tailor the equipment to individual facility requirements for discharge standards, or closed-loop re-use with zero discharge.

1. INTRODUCTION

Recent legislation at both the federal and state levels (see 40 CFR, 425-699), coupled with worldwide efforts to conserve water resources, has increased pressure on industry to limit use and discharge of water. As standards for discharge become more stringent, the factors of onsite wastewater treatment become critical to the design, sale and operation of water jet equipment.

In many applications, untreated wastewater discharge results in surcharges levied by local municipalities that represent a substantial increase in operating costs. Many large industries, cognizant of the costs associated with use and discharge of water, have instituted resource use guidelines that are geared to cost savings through conservation.

An ever growing number of federal, state and local agencies are performing onsite standards testing to insure the each waste stream within a facility conforms to standards, rather than point of discharge evaluation that was common in the past.

Given the foregoing, it becomes readily apparent that the water jet industry must seek methods and measures to address the myriad problems of waste stream management. These measures must include treatment and potential re-use where practical.

It is the purpose of this paper to outline major considerations for the establishment of design criteria in conjunction with common methods utilized to satisfy discharge standards contained in 40 CFR, 100-149 and effluent guidelines in 40 CFR, 425-699.

While not addressed specifically, long term considerations due to RCRA, must also be part and parcel of design parameters, in order to minimize exposure under this act. Waste must be minimized and produced in a form that is readily managed.

2. ESTABLISHING DESIGN CRITERIA

2.1 Primary Considerations

2.1.1 Jet Pump Feedwater Specifications

Feed pump requirements must include water quality standards for TDS (total dissolved solids), TSS (suspended solids, including particulate size and distribution), hardness, pH and corrosivity to insure maximum durability of seats, seals, orifices and check valves. These standards will vary with materials and operating pressures.

2.1.2 Flow and Volume Requirements

Operating flow requirements must include cycle time and reserve capacities, as well as sumps, associated piping and pump volute volumes to allow adequate time for "batch treat" filtration units to complete processing and come to "stand by" status.

2.1.3 Make-Up Water Quality

Loss and make-up requirements must be determined, along with make-up water profile (lab analysis) to define contaminant level effect on "clean water" supplied to the jet pump. In many instances a municipal supply water contains levels of silica, salts and calcium that must be reduced before use in a water jetting application.

2.1.4 Cost Efficiency

A review of state and local discharge standards and rates (including surcharges) will assist in determination of treatment costs efficiency as it relates to straight discharge, treatment for discharge or treatment for recirculation.

2.1.5 Discharge

Under existing guidelines, it is seldom practical to utilize straight discharge. High TSS contaminants encountered in cutting, milling and stripping operations generally will be above acceptable guidelines. Abrasive entrainment compounds the problem.

2.1.6 Treat and Discharge

Depending on the materials processed by water jet, it is sometimes more practical to treat for discharge than to recirculate in a zero discharge function. Items to consider include: discharge rates (billing), potential surcharges, materials processed and their solubility, which will affect the BOD (biological oxygen demand) and COD (chemical oxygen demand) of the waste stream, the TDS, TSS and pH.

Each effect must be considered and addressed individually and collectively when evaluating cost comparisons. Effects on existing permits, if any, must be identified. In many instances, partial re-use may be more viable than full discharge.

2.1.7 Zero Discharge

Zero discharge full recirculation systems have a definite advantage over partial or full discharge systems. The primary advantage is that a zero discharge installation has no impact on existing discharge permits. If properly managed, zero discharge systems avoid exposure to EPA and state DOE noncompliance citations, which can be very costly for firms with a history of noncompliance. Zero discharge also avoids the costs associated with surcharges, reduces supply water costs and, on metered systems, avoids standard sewage multipliers in most areas.

2.2 Secondary Considerations

After determining the effect of material processing on the water profile (i.e., solubility, TSS, TDS, BOD, COD and pH), then a review of state and local codes will identify specific areas for reduction (straight discharge and partial re-use systems).

Care must be taken to insure that any discharge from the water jetting operation does not exceed permit standards or volumes.

It is recommended that a complete review of plant engineering standards be instituted prior to design planning.

The availability of power (type and amperage) and other services (water, compressed air, drains) must be ascertained. Reporting function and integrated monitors must be specified, along with the availability of reporting loops and signal requirements (i.e., interface).

3. METHODS

3.1 Suspended Solids

Depending on factors in the wastewater profile, preferred methods of treatment will vary. Level of effect desired will also represent a determining factor. As a rule of thumb "staged" treatment is usually more effective and less maintenance intensive than "brute force" methods. Water treatment is generally a series of trade-offs. Anything added to water for a desired effect will ultimately require another process for removal or handling. This is more pronounced as the requirement for product purity increases.

In wastewater treatment, especially high TSS, time is an ally. Since most suspended solids will, over time, precipitate or float due to specific gravity above or below that of water, retention time and careful placement of staged overflows will effect substantial changes in TSS levels. This effect can be enhanced by the addition of non-soluble floccing agents. A number of polymeric agents, both cationic and anionic, are available to the process engineer.

Secondary treatment of high TSS can be effected through simple filtration. A test of particulate spread will indicate surface area requirements, staging necessities and micron sizes required.

Other effective methods of reducing high TSS include clarifuge, centrifuge, belt filtration, filter press and self-cleaning screens in a variety of configurations.

3.2 Dissolved Solids

Once the problem of high TSS is resolved, TDS must be addressed. A laboratory analysis of the make-up water and wastewater is critical. It is only through the determination of component structure that proper treatment methods can be identified.

It is impossible to address all of the compounds soluble in an aqueous waste stream. We will address those most commonly found in water jet operations, which include:

1. Metals
2. Organics
3. Nitrates
4. Sulphates
5. Phosphates
6. Silica
7. Calcium carbonate
8. Bicarb

Metals and organics can be effectively reduced by oxidative reduction, i.e., packed column, O₂ and O₃ injection. Biological components also react readily with the atomic oxygen, or may be controlled by ultraviolet (UV) radiation (Carrigan, 1990).

As discussed by Gottlieb (1990), nitrates, sulphates and phosphates will readily combine with free H₂ with an associated drop in pH, i.e. electrolytic H₂ generation or cation ion exchange resin in the H₂ form. A strong acid exchange resin also acts as an effective dealkalizer, reducing calcium carbonate and bicarbs.

Silica reacts readily with strong base anionic exchange resins (an adjunct effect of these resins is the removal of weakly ionized acids). Additionally, these resins will remove anionic metallic complexes.

To accomplish the best possible balance with specific waste stream components, it is advisable to consult with an experienced resin designer early in the design process.

4. CONCLUSIONS

4.1 Process Sequence

If, after evaluation of plant operations, permits and discharge guidelines, waste treatment is indicated, then the sequence should be as follows:

1. Gross solids reduction
2. Primary filtration
3. Oxidative reduction
4. Secondary (finite) filtration
5. Polish
6. pH adjustment

4.2 Application

This sequence, or a portion of this sequence, will apply regardless of the ultimate disposition of the waste stream. As an example, zero discharge water jet filtration units designed by Advanced Water Systems (see Figure 1) typically flow from the waste sump through a clarifuge to remove gross solids, thence to a series of overflow / underflow clarifiers to allow further natural precipitation of solids, thence through a 5 micron belt filter, thence into a recirculating filter tank utilizing 0.5 micron bag filters in conjunction with an electrolytic precipitator that boosts dissolved oxygen levels to at least 120% of saturation (organic reduction and oxidative reduction of metals). A byproduct of this function is molecular hydrogen (see 3.2).

4.3 Flexibility

The clarified water (0 - 1 NTU) is then delivered back to the water jet pump via polishing GAC and ion exchange columns designed specifically for the application. The water produced by this process typically has a resistivity of 2 to 10 megohms / cm (laboratory grade). A metering valve drawing clarified water from the bag filter assembly is adjusted to bypass the ion exchange columns to allow "dialing in" a TDS of 12 - 30 mg/L (PPM), since the water from the ion exchange column assembly is too clean, hence too aggressive.

The advantages of this type system design is that regardless of the intended disposition of the wastewater, the sequence of processing insures conformity to standards and guidelines.

5. REFERENCES

- Carrigan, P., "Water Disinfection Using Ultraviolet Technology," *Technical Papers of the Water Quality Association Annual Convention*, pp. 68-73, 1990.
- Gottlieb, M.C., "Fundamentals of Ion Exchange," *Technical Papers of the Water Quality Association Annual Convention*, pp. 87-115, 1990.

6. NOMENCLATURE

BOD (Biological Oxygen Demand): The amount of oxygen required to oxidize biological contaminants in water.

COD (Chemical Oxygen Demand): The amount of oxygen required to oxidize chemical contaminants in water.

DEIONIZED WATER: Water which has had all ionic impurities removed by the ion exchange process.

ELECTROLYSIS: The passage of an electrical current through an electrolyte solution. This process will dissociate certain compounds into elemental forms, e.g., O₂ and H₂ from H₂O. water.

GAC (Granular Activated Carbon): A form of elemental carbon whose particles have a large surface area with high adsorptive qualities, used to remove numerous toxic organic compounds from water. Primary forms consist of bituminous coal and coconut husk.

HARDNESS: The amount of calcium and magnesium in the water in grains per gallon (expressed as calcium carbonate). A grain is equal to 17.1 mg/L of calcium and magnesium.

MECHANICAL FILTRATION: The process of removing suspended particles from water by straining action. The finest mechanical filter can remove material as small as 0.1 micron.

NTU (nephelometric turbidity unit): A measure of water turbidity by light scatter caused by particulate load.

ORGANICS: Any compound whose chemical structure is based on carbon (all living organisms are organic).

O₂ (oxygen): Molecular oxygen consisting of two atoms of oxygen. This is a stable form of oxygen effective in oxidative reduction of contaminants in wastewater.

O₃ (ozone): An unstable oxygen-based compound created by a high voltage discharge, which adds one atom of oxygen to an oxygen molecule. Used to disinfect water, it is toxic and highly corrosive in appreciable quantities.

pH: The acidity / alkalinity of a substance. The common pH scale ranges from 0 to 14, with 0 being most acid and 14 being most alkaline. A pH of 7.0 is generally considered to be neutral.

RCRA (Federal Resource Conservation and Recovery Act): Regulates hazardous waste from "cradle to grave," including generators, transporters and treatment, storage and disposal facilities.

TDS (Total Dissolved Solids): The quantity of solids in an aqueous solution, measured in milligrams or micrograms per liter.

TSS (Total Suspended Solids): The quantity of solid contaminants (particulates) suspended in water, measured in milligrams per liter or parts per million (PPM).

UV (ultraviolet): Visible radiation beyond the violet band but less than 4000 angstroms. It is used to disinfect water by locally destroying bacteria.

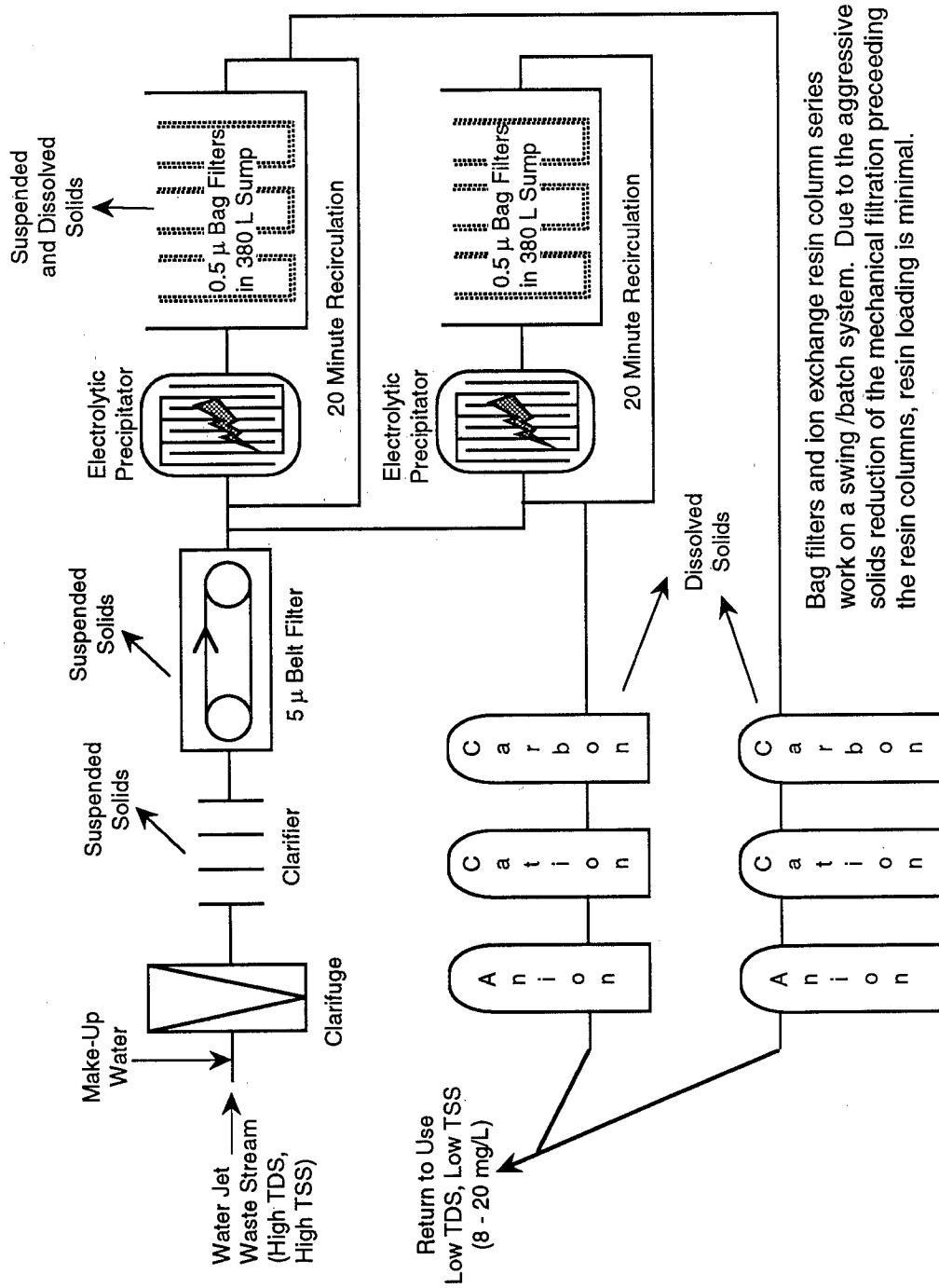


Figure 1. Advanced Water Systems, Inc. Zero Discharge Process Flow Sequence

WATER SOLUBLE ABRASIVES

Dr. M.J. Woodward
Vice President Aqua-Dyne Inc.
Houston, Texas, U.S.A.

ABSTRACT

Water soluble abrasives are finding increased applications when used in conjunction with high pressure water jets. This paper reports on the development of these abrasives and presents an overview of the successful applications obtained so far as well as suggestions for future uses. The paper also describes experimental studies that have been conducted to determine the effect of stand-off distance, pump pressure and flow and abrasive consumption rate upon the performance of these materials.

1. INTRODUCTION

Water soluble abrasives used in conjunction with high pressure water jets have been finding an increasing number of applications since their introduction into the market place in the mid 1980's. The technology permits cleaning many structures which by more traditional methods would be either comparatively expensive or impossible to achieve. Examples of some of the applications to date have been:

- The removal of paint from aircraft frames which cannot be safely performed by sandblasting due to the damage caused and typically can no longer be performed by chemical stripping, due to the toxicity of the stripping agents.
- The removal of graffiti from buildings, bridges, subway cars etc. where dry sandblasting also causes damage to the underlying structures & chemical stripping again causes problems with the toxicity of the stripping agents.

A potential future application is the stripping of lead based paints from bridges where the blast media dissolve in the water, making separation of the paint from the blast media a matter of simple filtration.

When accelerated by high pressure water jets the rate at which water-soluble media perform is dependent upon many factors including the material being removed, the type of media, the water pressure and flow rate, the nozzle design, the stand off distance etc. To the author's knowledge no technical information on these various parameters has been published with respect to water soluble abrasives nor indeed for non-soluble materials. The studies described were conducted in an attempt to gain some insight into the importance of those parameters.

2. TEST PROCEDURE

Identical sections of painted aluminum siding 2.30m long x 0.09m wide were blasted by a hand held control gun until all visible traces of paint had been removed & the time required for this operation recorded. The samples were blasted under varying conditions in order to determine the effect of jet pressure, jet flow & abrasive consumption. The jet pressure was recorded from a glycerine filled pressure gage, jet flow by discharging the jet into a calibrated container for 1 minute & the abrasive flow by removing the abrasive from a plastic hopper & measuring the weight before & after 1 minute of operation.

3. RESULTS

3.1 Jet Pressure

The effect of jet pressure between 41.34 Bar and 895.70 Bar (600 psi and 13000 psi) on the production rate was examined. During this series of tests the following conditions were maintained:

- Water Flow : 5.68 Lpm (1.5 gpm)
- Abrasive Feed : 1.36 Kg/minute (3 lb/minute)
- Abrasive Type : Aqua-Dyne "Blast-It" blast media.

In the range of pressures analyzed once the "threshold pressure" had been exceeded the cleaning rate, as can be seen in Figure (1) is approximately linear with pressure.

3.2 Water Jet Flow

The effect of water flow between 4.92 Lpm and 22.33 Lpm (1.3 gpm and 5.9 gpm) on the production rate was examined. During this series of tests the following conditions were maintained:

- Water pressure : 689 Bar (10,000 psi)
- Abrasive Feed rate : 1.36 Kg/minute (3 lb/minute)
- Abrasive Type : Aqua-Dyne "Blast-It" blast media

In the range of flows analyzed the cleaning rate as can be seen in Figure (2) appears to vary as to the square root of water flow.

3.3 Abrasive Feed Rate

The effect of abrasive feed rate between 0.45 Kg and 4.54 Kg (1 lb/min and 10 lb/min) on the production rate was examined. During this series of tests the following conditions were maintained:

- Water pressure : 689 Bar (10,000 psi)
- Water flow : 14.01 Lpm (3.7 gpm)
- Abrasive Type : Aqua-Dyne "Blast-It" blast media.

As can be seen from Figure (3) there is only a marginal increase in production as the media flow rate is increased and in fact, after an approximate feed rate of 3.63 kilo/min. (8 lb/min.) was obtained the production rate declined, due to an inability of the nozzle assembly to "accept" these high feed rates.

4. DISCUSSION OF RESULTS

From the results of the tests performed it would seem reasonable to suggest that the cleaning rate is related to the jet pressure & flow in the following manners:

- Cleaning Rate $KP\sqrt{Q}$

5. CONCLUSION

Due to the fact that for the foreseeable future the majority of the applications for water soluble media cleaning will involve the use of manually controlled jetting guns and that the reactive force of a jet is $0.052\sqrt{PQ}$ (DeBusk et al 1987), it would seem reasonable to operate units at higher water pressures and lower water flows with minimal abrasive consumption: this will lead to a rapid, cost effective, less fatiguing cleaning system.

6. ACKNOWLEDGEMENTS

The author would like to acknowledge the kind assistance and help of:
Mr. Kevin Hill, Lab technician, Aqua-Dyne Inc., Mr. Richard Valdez, Marketing Manager Aqua-Dyne, Inc., Miss Julie Forister, Technical Writer, Aqua-Dyne, Inc.

7. REFERENCES

DeBusk, P., Evans, R., Evers, J., Pater, L., Raether, R., Reichman, J., Summers, D., Wang, F.D., Wolgamott, J., Woodward, M.J., and Zublin, C., "Recommended Practices for the use of Manually Operated High Pressure Water Jetting Equipment", "Recommended Practices for the use of Manually Operated High Pressure Water Jetting Equipment", Water Jet Technology Association, St. Louis, Missouri, 1987.

Woodward, M.J., "The Development of a High Production Abrasive Water Jet Nozzle System," Proceedings of the 4th American Water Jet Conference, pp. 137-146, Water Jet Technology Association, St. Louis, Missouri, 1987

8. NOMENCLATURE

P = Pressure
K = Constant
Q = Flow

Figure 1 PRODUCTION RATE vs JET PRESSURE

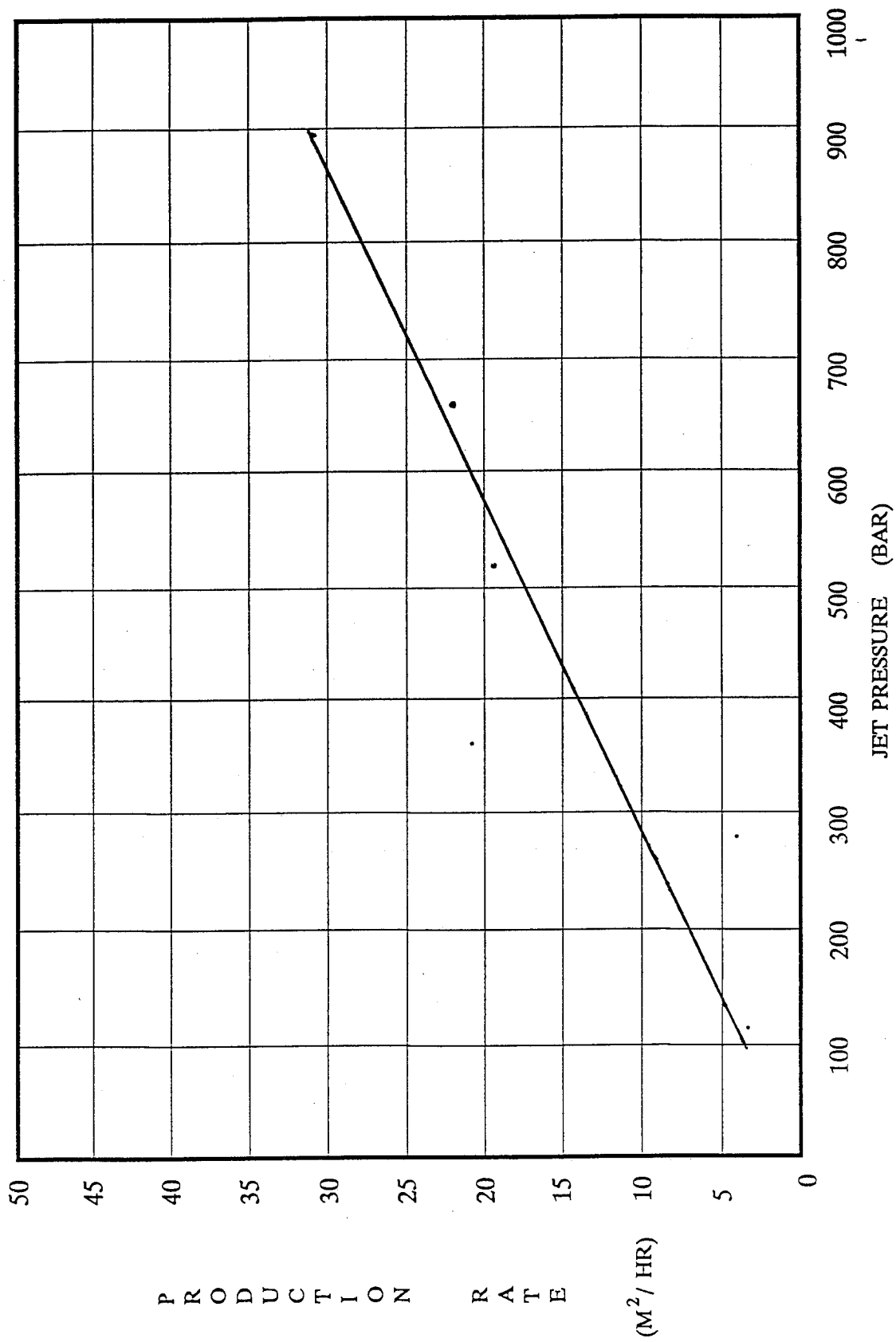


Figure 2 PRODUCTION RATE vs JET FLOW

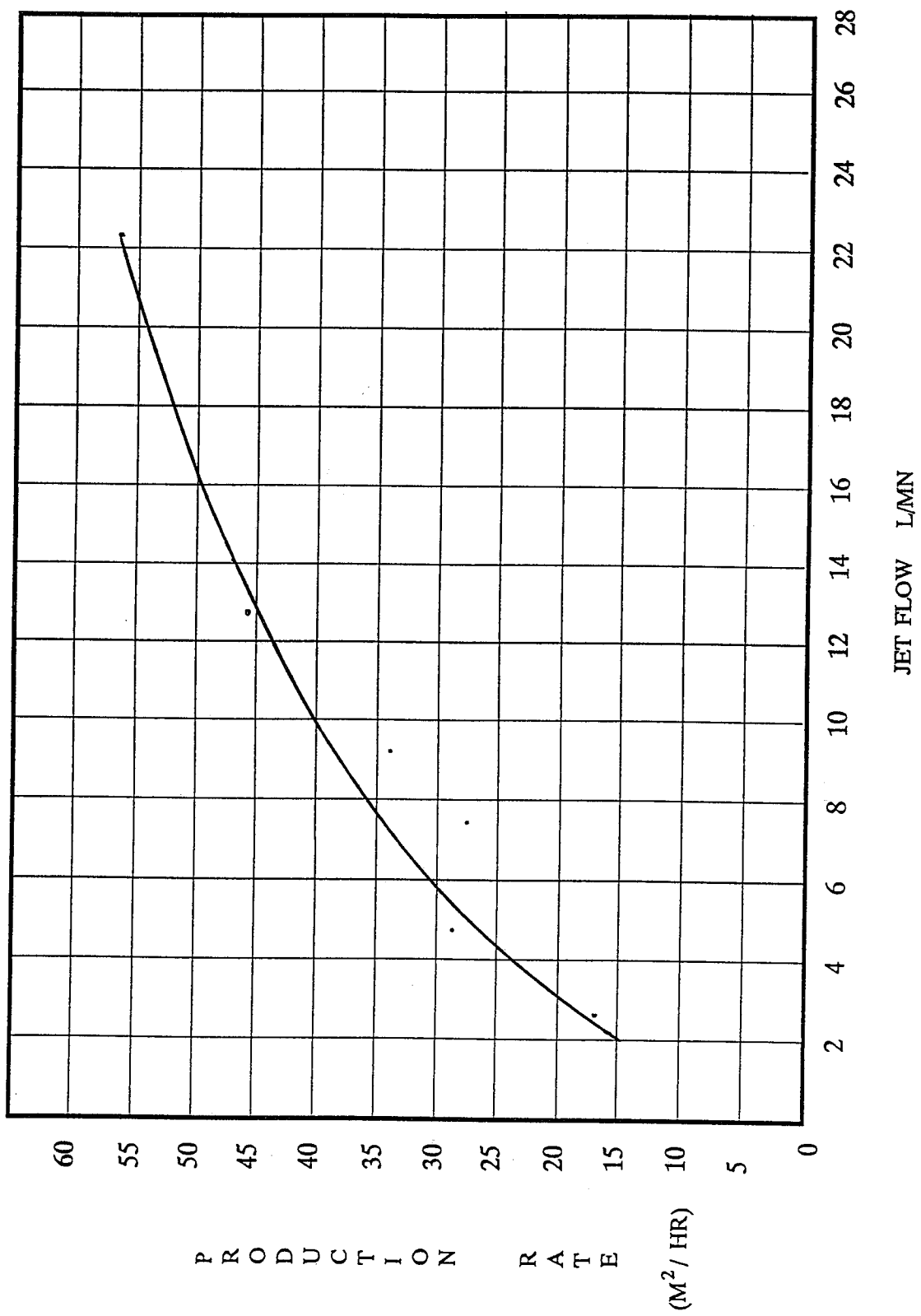
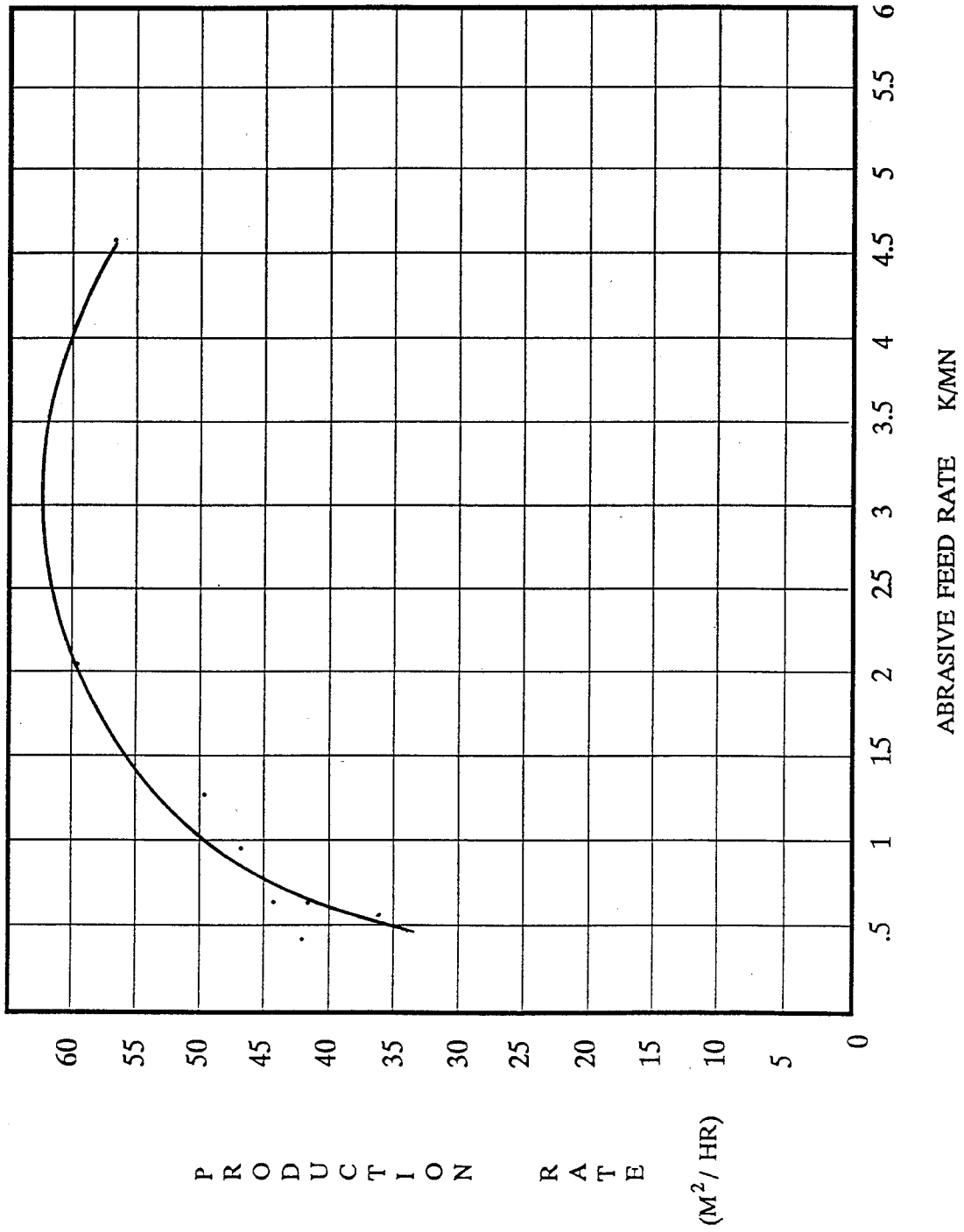


Figure 3 PRODUCTION RATE vs ABRASIVE FEED RATE



PREWEAKENING OF HARD ROCKS WITH WATER JETS

M.M. Vijay

Institute for Engineering in the Canadian Environment
National Research Council of Canada
Ottawa, Ontario, Canada, K1A 0R6

J. Remisz*

Applied Fluid Mechanics Inc.
301 - 4 Goldfinch Court
Willowdale, Ontario, Canada, M2R 2C3

*Guest Scientist at the National Research Council of Canada.

ABSTRACT

A new concept is emerging in the mining industry with regard to processing of hard metallic mineral bearing rock materials. The concept involves the use of pure water jets for preweakening of extremely hard rock formations well ahead of mechanical tools. The purpose, as in the past, is to assist the continuous mining machines to improve their reliability, productivity, safety and life. The basic idea, in contrast to the conventional water jet assist (WJA) methods, is to use water jets to inflict and propagate micro or macro fractures below the rock face. To be economical, the water jet technique employed should meet certain requirements. For instance, the pressure and hydraulic power should not exceed 140 MPa and 150 kW (per jet) respectively.

In this paper an attempt is made to explain the concept of preweakening and the techniques that could be used to evaluate the extent of preweakening below the surface. Limited experiments were conducted using continuous, cavitating (emerging in air or with full or artificial submergence) and interrupted (pulsed) water jets on hard rock samples occurring in Canadian mines. It is shown that pulsed water jets have a good potential for preweakening of hard rocks.

1. INTRODUCTION

A major experimental program is in progress in the laboratory the primary objective of which is to augment the performance of continuous mining machines by preweakening hard rock formation (metallic mineral bearing and waste material) well ahead of the advance of the machine. The concept of "preweakening" as defined in the present study is radically different from the way described by Geier and Hood (1987), and perhaps others (Baumann & Henneke, 1980; Baumann & Koppers, 1982; Fowell, 1992; Frank, et al., 1972; Henneke & Baumann, 1978; Hood, et al., 1991; Hoshino, et al., 1972; Kogelmann, et al., 1989; Kuzmich, et al., 1982; Nikonov & Goldin, 1972; Ohga, et al., 1992; Plumpton & Tomlin, 1982; Summers & Henry, 1972; Vijay & Yan, 1988; Wang, et al., 1976). This can best be explained using Fig. 1 where metallic samples exposed to cavitating jets emerging in air (A) and in fully submerged environment (B) are depicted (Vijay & Brierley, 1981; Vijay, et al., 1990). In Fig. 1(A) the sample is completely penetrated ($\Delta m =$ mass loss of sample > 350 mg), with the damage confined to a small area around the point of jet impingement. In Fig. 1(B), on the other hand, the material is not penetrated ($\Delta m \approx 0$). However, the sample (diameter ≈ 38 mm) is severely deformed and the entire surface is pitted with the imploding cavitation bubbles generated in the shear layers of the impinging submerged jet. Fig. 1(C) shows the severity of the damage below the surface in a sample of copper (more appropriate to simulate hard rocks). Grain deformation and abundant micro cracks through and around the grain boundaries were observed up to a depth of $300 \mu\text{m}$ below the surface. Measurement of the microhardness (a measure of the mechanical strength of the material) indicated that the sample had sustained considerable damage. Thus, although the material was not cut by the jet, it had deteriorated over a large extent, and it is in this context that preweakening is defined in this paper. In other words, preweakening means the initiation and propagation of cracks and micro cracks over a large extent below the surface, leading to considerable loss in the material integrity. From the standpoint of improving the performance of continuous mining machines, removal of material by water jets will be beneficial, but not essential. For a given set of jet and operating parameters, the higher the extent of damage below the surface, the more attractive is the technique for hard rock mining applications. Advantages of preweakening achieved in this manner are discussed below.

2. ADVANTAGES OF PREWEAKENING

Continuous mining machines for processing hard rocks are nothing more than special versions of the currently existing roadheaders or tunnelling machines. For example, a typical machine could be a modified version of the 2.65 m Wirth Tunnel Boring Machine (TBM) as described by Henneke and Baumann (1978). The sample references cited in this paper were chosen deliberately to emphasize that, over a span of two decades, the initial intense worldwide interest in the use of water jets for assisting mechanical cutting machines (Frank, et al., 1972; Hoshino, et al., 1972; Moodie & Artingstall, 1972; Nikonov & Goldin, 1972; Wang, et al., 1976; Henneke & Baumann, 1978) or assisting water jets by mechanical cutters (Vijay & Yan, 1988) has dwindled steadily and now one finds only sporadic references to this work (Kogelmann, et al., 1989; Hood, et al., 1991; Ohga, et al., 1992). As pointed out by Hood, et al., (1991) and Fowell (1992), despite all the

purported benefits of water jet assist, commercial machines, particularly for hard rock mining, are non-existent. The reasons for this are as follows:

- Most of the investigations have been concerned with assisting coal cutting machines only (Fowell, 1992);
- Investigations on hard rocks are very limited and often the term "hard" is used erroneously {for instance, Indiana limestone and some type of granites (Barre granite) are definitely not hard}. Furthermore, connoting the term "hard" to high compressive strength of rocks is not appropriate (see for example, results reported on Aberdeen granite and Carrara marble by Moodie and Artingstall, 1972). The rock material occurring in the Canadian mines (and some other countries), particularly the waste material (for example, gneiss), are extremely difficult to cut with water jets even at pressures and flow rates as high as 140 MPa and 80 litre/min respectively (Vijay & Grattan-Bellew, 1985; Vijay & Yan, 1988; Vijay, 1991; Vijay & Grattan-Bellew, 1991; Vijay, et al., 1992b). Therefore, there is no guarantee that the machines built, based on the results observed on materials such as Indiana limestone, will work effectively on these types of rock;
- In most of the water jet assisted machines (roadheaders or TBMs), the benefits of water jets are achieved generally by associating a water jet nozzle with each of the mechanical tools (point cutters, drag bits or disc cutters) employed. Depending on the pressure and flow, the water jets either cool, lubricate, reduce fire hazards and suppress the dust levels (to date these are the major benefits) or, reduce the normal (thrust) and cutting forces of the tools, by pre-kerfing narrow and shallow slots (this is "preweakening" as defined by Geier & Hood, 1987) on the face of the formation. Used in this manner, the number of nozzles and hydraulic power required to achieve any benefit will depend on the size and type of machine. For example, in the Wirth TBM investigated by Henneke & Baumann (1978), a special cutter head was designed with 14 double-ring disc-roller cutters and 100 water nozzles (diameter < 0.25 mm) concentrated in five different blocks. Maximum pressure, flow and hydraulic power employed were 400 MPa, 120 litre/min and 1000 kW respectively (see also Wang, et al., 1976). Apart from the cost, the reliability of the machine becomes highly questionable when such large number of nozzles are employed. A recent report by Ohga, et al., (1992) supports this view. Their observations, based on the experience gained by testing a roadheader in a coal mine in Japan over an extended period of four years, were: (i) frequent breakdowns, (ii) lack of parts or long waiting periods to obtain replacement parts, (iii) problems relating to transportation of the machine due to heavy weight and (iv) relatively short life of parts.
- There is no consensus of opinion with regard to the disposition of the nozzle with respect to the mechanical tool or the magnitudes of pressure and flow for improving the effectiveness of the hybrid machines (Hood, et al., 1991; Fowell, 1992). All types of configurations have been reported, namely, behind, in front, through the tool, etc. In the new machine developed by Ohga, et al., (1992), the nozzles were placed behind the mechanical bits in the cutting head.

The purpose of this cursory review of the literature is to indicate why the use of water jet assisted hybrid systems is not as widespread as initially hoped. The disadvantages alluded to above can be eliminated if "preweakening" as defined in this paper is achieved. The most important advantages will be:

- The number of water nozzles can be reduced and their dispositions in the cutter head will not be critical;
- There will be a great reduction in the normal and cutting forces. As a matter of fact, cutting forces will be minimal because the mechanical bits will be essentially scouring the material preweakened by water jets (this is "mechanically assisted water jet cutting"). This in turn should reduce the normal forces substantially (reduction by about 70% of the values reported in the literature is not unrealistic);
- The magnitude of pressure will not exceed 140 MPa; however, the magnitudes of the total flow rate or the hydraulic power will depend on the type of jet (continuous or discontinuous) employed for massive preweakening. Discontinuous (cavitating and pulsed) water jets will require less power (Atanov, 1982; Bresee, et al., 1972, Cooley, 1972; Edwards, et al., 1982; Johnson, et al., 1972 & 1982; Labus, 1982 & 1991; Mazurkiewicz & Summers, 1982; Moodie & Artingstall, 1972; Nebeker, 1987; Singh, et al., 1972; Vijay, 1991; Vijay, et al., 1992b);
- Significant reductions in the size and weight of the continuous mining machines can be realized making them commercially attractive.

The purpose of the investigation in progress in the laboratory is to critically examine the potential of continuous and discontinuous (cavitating and pulsed) water jets for preweakening of hard rocks. The constraints on the water jet techniques are:

- Maximum Pump pressure (P): 140 MPa
- Maximum Hydraulic power per jet (H_p): 150 kW
- Traverse speed of nozzle (V_{tr}): 0.005 - 0.05 m/s
- Standoff distance (S): 0.025 - 0.25 m
- Preferred depth of weakening: 0.1 m
- No abrasives in the water

3. EXPERIMENTAL PROGRAM

3.1 Background

Over a period of several years considerable work has been done in the laboratory on drilling and slotting of the hard rock samples received from the Canadian mining companies (Vijay & Grattan-Bellew, 1985; Vijay & Yan, 1988; Vijay, 1991; Vijay & Grattan-Bellew, 1991). The experimental results obtained in these investigations have shown that these rock formations require very high pressure and hydraulic power for drilling and slotting. For example, magnitudes of specific energy obtained in drilling Barre

granite and Inco samples at a pressure of 69 MPa ($H_p \approx 58$ kW) were of the order of 10^4 and 10^6 J/cm³ respectively (Vijay & Grattan-Bellew, 1985), well over the values achievable with the conventional techniques such as percussive drilling ($\approx 10^3$ J/cm³). For this reason, there is no incentive for using water jets for drilling or slotting alone. However, there is considerable interest in the use of water jets for preweakening (as defined here) of rocks, provided the above stated specifications are satisfied.

The material properties of the type of rock samples occurring in the Canadian mines are described in detail in the publications cited above. For the sake of clarity some properties are listed in Table 1. They are characterized essentially by low porosity and permeability, the grain sizes varying from almost 0 to 1000 μ m (Vijay & Grattan-Bellew, 1991).

The ultimate goal of the program is to design a simple, practical, reliable and economically viable water jet system for incorporation into the continuous mining machines. Since these rocks are difficult to cut with continuous water jets, the purpose is to investigate the potential of discontinuous (cavitating and pulsed) water jets for preweakening. The emphasis is on generating discontinuous jets by modulating continuous water jets for the simple reason that highly reliable and relatively inexpensive pumps are readily available to produce pressures and flows in the range stated above. The concept of modulation is clear from Fig. 2, where a nozzle device with an ultrasonic wave generator is shown (Vijay, 1992). Depending on the nozzle design, the high frequency waves can be used to modulate a continuous stream of water to produce either forced cavitating or pulsed (percussive according to Nebeker, 1987) water jets. The purpose of the initial phase of the project, discussed in this paper, was however to acquire data on these rocks with continuous, natural cavitating and interrupted water jets (see below) and to compare their relative performance for preweakening.

3.2 Assessment of Preweakening

Quantitative assessment of the extent of preweakening achieved is key to the adoption of a particular type of water jet technique for continuous mining. Several methods are possible some of which are listed below:

- The usual method of measuring the dimensions or volume of the kerfs cut with water jets, and using these raw data to estimate the values of specific energy (E_v = energy input/volume of material removed) or specific kerfing energy $\{E_k$ = energy input/area of the kerf (= depth X length of the kerf)}. Although it is a convenient and direct method, for obvious reasons, it is not a true measure of the extent of weakening;
- Qualitative observation from the top to bottom of the cores taken from the pristine and water jet treated (in the vicinity of the kerfs) rock samples for evidence of cracks;
- Petrographic examination of the thin sections taken from the rock samples for evidence of the initiation and propagation of cracks or microfractures;
- Measurement of the speed or attenuation of the ultrasonic pulses transmitted through

the water jet treated sample from the top to the bottom surface. Changes in these parameters are an indication of weakening;

- Measurement of the tensile strength of 12.7 mm discs cut from the top to the bottom of cores taken from the pristine and water jet treated samples. Any reduction in the tensile strength of the water jet treated discs is an indication of weakening;
- Subjecting the pristine and water jet treated samples to mechanical disc or drag cutters and measuring the values of cutting and normal forces. The degree of reduction in the magnitude of these forces is a true measure of the extent of weakening.

Although all of these methods are presently under investigation, for illustrating the concept of preweakening, only the first two methods are reported in this paper.

3.3 Cavitating Water Jets

The characteristics of cavitating water jets and their use for a variety of applications have been investigated by several investigators (Johnson et al., 1972 & 1982; Mazurkiewicz & Summers, 1982, Vijay & Brierley, 1981; Vijay, et al., 1990; Vijay, 1991; Vijay, et al., 1992a). However, it should be pointed out that these are natural cavitating jets, the cavitation bubbles arising essentially in the shear layers of a fully submerged high speed water jet (see Vijay, et al., 1992a). It is obvious that one cannot use cavitation in this form for continuous mining. However, it is possible to artificially submerge the nozzles or even develop nozzles capable of generating cavitating jets in air (Vijay, et al., 1990, 1992a). In order to evaluate the potential of cavitating jets for preweakening, a series of 17 nozzle arrangements (in air, fully and artificially submerged environments) was investigated in the laboratory. The basic configurations of the nozzles are shown in Fig. 3 (A, B, C & D) and artificial submergence was obtained by inserting the nozzles in a plexiglass tube (Fig. 3E). A detailed treatment on the characteristics of cavitation generated by these nozzles and the factors that influence their performance are given by Vijay, et al., (1990, 1992a) and are not discussed further here.

3.4 Pulsed Jets

There is abundant evidence in the literature on the destructive power of pulsed jets produced by cannon type of devices (essentially eject periodically single large slugs of water) for fragmentation of rocks (Atanov, 1982; Bresee, et al., 1972; Cooley, 1972; Edwards, et al., 1982; Frank, et al., 1972; Labus, 1982 & 1991; Moodie & Artingstall, 1972; Singh, et al., 1972; Watson, et al., 1982). However, these pulse producing devices, apart from being very large and heavy (Labus, 1991), have a number of other disadvantages (for instance, filling the nozzle with water after each shot is a serious problem) which renders them unsuitable for incorporation into the continuous mining machines. Pulsed jets (variously called "percussive", "interrupted", etc) produced, on the other hand, by modulating a continuous stream of water, although less effective compared to single pulse devices (Labus, 1991), are highly attractive from this standpoint.

Various methods are available for achieving pulsed jets in this manner (Nebeker, 1987).

Since the main objective in the initial phase of the program was to acquire data on the mining samples, interrupted jets were produced by placing a rotating perforated disc downstream of a nozzle. Details on the method, the drawbacks (for instance, these are not truly pulsed jets) of the technique and the experimental results have already been reported by Vijay, et al., (1992b). Only sample results are presented in this paper.

4. DISCUSSION

4.1 Cavitating Water Jets

As stated above, an attempt was made to assess preweakening by (i) measuring the dimensions of the kerfs or estimating the specific kerfing energy (E_k) and (ii) visual observation of the cores taken from the samples. It should be pointed out that it was not possible to achieve a systematic set of data due to (i) lack of adequate good samples, (ii) excessive variation in the material properties (the rock samples were highly heterogeneous) and (iii) frequent premature disintegration of the samples while testing (Figs. 4A, C & D), particularly in those cases where they were not imbedded in concrete. Furthermore, the kerfs were mostly irregular (see test #16 in Fig. 4A) and were accompanied by considerable spalling. For comparison, kerfs made in Barre granite with fully submerged and continuous jets are shown in Fig. 4B. These factors prevented accurate measurement of slot dimensions, accounting for the wide scatter in the results, shown in Fig. 5 for Falconbridge rock samples only. Contrary to the observations made on the metallic samples (Vijay, et al., 1990), the performance of the centre body (#3A) was found to be poor compared to the simple conical nozzle (#1A) and the nozzle with the pin (#4A). There are many explanations for this observed behaviour, the most relevant one being that the configuration (Fig. 3E) used for artificial submergence was not optimized. As shown in the work reported by Vijay et al., (1992a), apart from the geometrical parameters of the nozzles, configurational factors such as the distance between the exit planes of the nozzle and the surrounding tube, and the ratio d/D have considerable influence on the performance of artificially submerged cavitating water jets. While further work on hard rocks with optimized nozzle systems is highly desirable, it is important to note that quantitative assessment of preweakening in terms of the slot dimensions (or E_k) alone is not sufficient (see Section 4.3).

4.2 Pulsed (Interrupted) Water Jets

As stated above, a few selected results are depicted in Figs. 6 and 7 for A-Quartzite and Noranda samples respectively. The main observations from these figures are:

- Although data were obtained with the interrupted jets, it can be stated with some confidence that pulsed jets, generated by modulating continuous water jets, have a good potential for preweakening.
- The degree of improvement is highly dependent on the rock fabric. Therefore, any

attempt to optimize the water jet techniques for preweakening should be based on the rock structures similar to or harder than that of Noranda (Fig. 7);

- Pulsed jets seem to retain their effectiveness over a large range of standoff distances ($S/d \approx 70$) compared to natural cavitating jets ($S/d \approx 15$, Vijay et al., 1990) and hence are more attractive for continuous mining applications.

4.3 Qualitative Assessment of Preweakening

Qualitative assessment of preweakening was made by comparing the cores taken from the pristine and water jet treated rock samples. The extent of surface damage suffered by the samples was generally of the type shown in Fig. 8 for the Inco sample. The cores taken from the water jet treated Inco samples are shown in Fig. 9 and those from Falconbridge and Noranda samples in Figs. 10A and 10B respectively. Cores taken from the pristine samples were not damaged and were used for measuring the mechanical properties and petrographic study. It is clear that there is some evidence that cavitating and pulsed jets could inflict fractures over a fairly large area and to a considerable depth below the kerfs (continuous jets mostly made narrow slots). However, these observations should be corroborated by using more reliable quantitative assessment techniques (Section 3.2). In any case, if cavitating or pulsed water jets can accomplish preweakening to the extent indicated in these figures, then one can envisage a whole new range of applications for water jets in cleaning, mining and tunnelling industries.

5. CONCLUSIONS

The principal objective of this paper was to define a new concept of "preweakening" of hard rock formations which is radically different from the one reported in the literature. A selected few preliminary results obtained on preweakening of several type of mining rock samples (metallic ore bearing and waste material) with continuous, cavitating and interrupted jets were included to explain the concept. Although these results are interesting and highly encouraging, further work is required (i) to quantify "preweakening", (ii) to optimize cavitating nozzle configurations and (iii) to generate well defined (shape, size, frequency, etc) pulsed jets.

A thorough investigation, using the nozzle device shown in Fig. 2 and other techniques, is currently in progress in the laboratory to accomplish these requirements.

6.0 ACKNOWLEDGMENTS

The authors are grateful to HDRK Mining Research Ltd., Oakville, Ontario, Canada for the partial funding provided for this project. Special thanks to Mr. D.K. Sarin, Senior Advisor, Inco Limited, Thompson, Manitoba, Canada and Mr. K.E. Mathews, Director of HDRK. It is a pleasure to acknowledge Mr. N. Paquette, Technical Officer on Water Jet Project for coordinating all the activities related to this investigation. Rock samples were received from the member companies of HDRK.

7. REFERENCES

- Atanov, G.A., "Interior ballistics of impulsive water jet", Proceedings of the 6th International Symposium on Jet Cutting Technology, Paper C5, pp. 141-159, BHRA, Cranfield, Bedford, England, 1982.
- Baumann, L., and Henneke, J., "Attempt of technical-economical optimization of high-pressure jet assistance for tunnelling machines", Proceedings of the 5th International Symposium on Jet Cutting Technology, Paper C4, pp. 119-139, BHRA, Cranfield, Bedford, England, 1980.
- Baumann, L., and Koppers, M., "State of investigations on high-performance water jet assisted road profile cutting technology", Proceedings of the 6th International Symposium on Jet Cutting Technology, Paper 2, pp. 283-300, BHRA, Cranfield, Bedford, England, 1982.
- Bresee, J.C., Cristy, G.A., and McClain, W.C., "Some comparisons of continuous and pulsed jets for excavation", Proceedings of the 1st International Symposium on Jet Cutting Technology, Paper B9, pp. 125-132, BHRA, Cranfield, Bedford, England, 1972.
- Cooley, W.C., "Rock breakage by pulsed high pressure water jets", Proceedings of the 1st International Symposium on Jet Cutting Technology, Paper B7, pp. 101-112, BHRA, Cranfield, Bedford, England, 1972.
- Edwards, D.G., Smith, R.M., and Farmer, G., "The coherence of impulsive water jets", Proceedings of the 6th International Symposium on Jet Cutting Technology, Paper C4, pp. 123-140, BHRA, Cranfield, Bedford, England, 1982.
- Fowell, R.J., "Mechanical rock excavation with water jet assistance", Proceedings of the International Conference Geomechanics 91, pp. 233-242, A.A. Balkema, Rotterdam, 1992.
- Frank, J.N., Fogelson, D.E., and Chester, J.W., "Hydraulic Mining in the U.S.A". Proceedings of the 1st International Symposium on Jet Cutting Technology, Paper E4, pp. 45-62, BHRA, Cranfield, Bedford, England, 1972.
- Geier, J.E., and Hood, M., "The effect of preweakening a rock surface by water jet kerfing on cutting tool forces", Proceedings of the 4th U.S. Water Jet Conference, pp. 97-102, Water Jet Technology Association, St. Louis, Missouri, USA, 1987.
- Henneke, J., and Baumann, L., "Jet assisted tunnel boring in coal-measure strata", Proceedings of the 4th International Symposium on Jet Cutting Technology, Paper J1, pp. 1-12, BHRA, Cranfield, Bedford, England, 1978.
- Hood, M., Li, X., Salditt, P., and Knight, G., "An advanced system for rock tunnelling -

- results from a field experiment". Proceedings of the 6th American Water Jet Conference, Paper No. 6, pp. 63-69, Water Jet Technology Association, St. Louis, Missouri, USA, 1991.
- Hoshino, K., Nagano, T., and Tsuchishima, H., "Rock cutting and breaking using high speed water jets together with TBM cutters", Proceedings of the 1st International Symposium on Jet Cutting Technology, Paper B6, pp. 89-98, BHRA, Cranfield, Bedford, England, 1972.
- Johnson, V.E., Kohl, R.E., Thiruvengadam, A., and Conn, A.F., "Tunnelling, fracturing, drilling and mining with high speed water jets utilizing cavitation damage", Proceedings of the 1st International Symposium on Jet Cutting Technology, Paper A3, pp. 37-55, BHRA, Cranfield, Bedford, England, 1972.
- Johnson, V.E., Conn, A.F., Lindenmuth, W.T., Chahine, G.L., and Frederick, G.S., "Self-resonating cavitating jets", Proceedings of the 6th International Symposium on Jet Cutting Technology, Paper A1, pp. 1-25, BHRA, Cranfield, Bedford, England, 1982.
- Kogelmann, W.J., Thimons, E.D., Virgona, J.E., and Weakly, L.A., "Water-jet-assist oil shale boom-miner development", Proceedings of the 5th American Water Jet Conference, Paper No. 2, pp. 11-25, Water Jet Technology Association, St. Louis, Missouri, USA, 1989.
- Kuzmich, I.A., Goldin, J.A., Ruthberg, M.I., and Frolov, V.S., "A combined method for rock breakage". Proceedings of the 6th International Symposium on Jet Cutting Technology, Paper G3, pp. 301-321, BHRA, Cranfield, Bedford, England, 1982.
- Labus, T.J., "A Comparison of pulsed jets versus mechanical breakers", Proceedings of the 6th International Symposium on Jet Cutting Technology, Paper F1, pp. 229-240, BHRA, Cranfield, Bedford, England, 1982.
- Labus, T.J., "Pulsed fluid jet technology", Proceedings of the 1st Asian Conference on Recent Advances in Jetting Technology, pp. 136-143, CI-Premier Pte. Ltd., 150 Orchard Road #07-14, Orchard Plaza, Singapore 0923, 1991.
- Mazurkiewicz, M., and Summers, D.A., "The enhancement of cavitation damage and its use in rock disintegration", Proceedings of the 6th International Symposium on Jet Cutting Technology, Paper A2, pp. 27-38, BHRA, Cranfield, Bedford, England, 1982.
- Moodie, K., and Artingstall, G., "Some experiments on the application of high pressure water jets for mineral excavation", Proceedings of the 1st International Symposium on Jet Cutting Technology, Paper E3, pp. 25-44, BHRA, Cranfield, Bedford, England, 1972.
- Nebeker, E.B., "Percussive jets - State of the art", Proceedings of the 4th U.S. Water Jet Conference, pp. 19-25, Water Jet Technology Association, St. Louis, Missouri, USA,

1987.

- Nikonov, G.P., and Goldin, Y.A., "Coal and rock penetration by fine, continuous high pressure water jets", Proceedings of the 1st International Symposium on Jet Cutting Technology, Paper E2, pp. 9-24, BHRA, Cranfield, Bedford, England, 1972.
- Ohga, K., Higuchi, K., and Sato, K., "Problems on the development of some machines assisted by water-jets in Japanese coal mines", Proceedings of the 11th International Symposium on Jet Cutting Technology, pp. 167-183, Kluwer Academic Publishers, London, England. 1992.
- Plumpton, N. A., and Tomlin, M.G., "The development of a water jet system to improve the performance of a boom-type roadheader", Proceedings of the 6th International Symposium on Jet Cutting Technology, Paper G1, pp. 267-282, BHRA, Cranfield, Bedford, England, 1982.
- Singh, M.M., Finlayson, L.A., and Huck, P.J., "Rock breakage by high pressure water jets", Proceedings of the 1st International Symposium on Jet Cutting Technology, Paper B8, pp. 113-124, BHRA, Cranfield, Bedford, England, 1972.
- Summers, D.A., and Henry, R.L., "The Effect of change in energy and momentum levels on the rock removal rate in Indian limestone", Proceedings of the 1st International Symposium on Jet Cutting Technology, Paper B5, pp. 77-88, BHRA, Cranfield, Bedford, England, 1972.
- Vijay, M.M., and Brierley, W.H., "Cutting, cleaning and fragmentation of materials with high pressure liquid jets", Proceedings of the 1st U.S. Water Jet Symposium, Paper No. V-4, pp. 1-12, Water Jet Technology Association, St. Louis, Missouri, USA, 1981.
- Vijay, M.M., and Grattan-Bellew, P.E., "An assessment of rotating high pressure water jets for drilling and slotting of hard ore-bearing rocks", Proceedings of the 3rd U.S. Water Jet Conference, pp. 231-247, Water Jet Technology Association, St. Louis, Missouri, USA, 1985.
- Vijay, M.M., and Yan, W., "Water jet cutting techniques for processing of hard rock material", Proceedings of the 9th International Symposium on Jet Cutting Technology, Paper K4, pp. 545-560, BHRA, Cranfield, Bedford, England, 1988.
- Vijay, M.M., Zou, C., and Tavoularis, S., "A study of the characteristics of cavitating water jets by photography and erosion", Proceedings of the 10th International Symposium on Jet Cutting Technology, Chapter 3, pp. 37-67, Elsevier Applied Science, London, England, 1990.
- Vijay, M.M., "Comparison of the performance of high-speed abrasive-entrained, cavitating and plain water jets for selective mining applications", Proceedings of the 6th American Water Jet Conference, pp. 195-212, Water Jet Technology Association, St.

Louis, Missouri, USA, 1991.

Vijay, M.M., and Grattan-Bellew, P.E., "The influence of properties of rocks on nozzle design for drilling and slotting with water jets", *International Journal of Water Jet Technology*, Vol. 1, pp. 117-133, 1991.

Vijay, M.M., "Ultrasonically generated cavitating or interrupted jet", U.S. Patent No. 5,154,347, October 13, 1992.

Vijay, M.M., Remisz, J., Tavoularis, S., Zou, C., and Hu, S.G., "A study of the practicality of cavitating water jets", *Proceedings of the 11th International Symposium on Jet Cutting Technology*, pp. 75-99, Kluwer Academic Publishers, London, England, 1992a.

Vijay, M.M., Remisz, J., and Shen, X., "Fragmentation of hard rocks with discontinuous jets", *Proceedings of the 3rd Pacific Rim International Conference*, pp. 201-224, Water Jet Technology Society of Japan, Tokyo, Japan, 1992b.

Wang, F.D., Robbins, R., and Olsen, J., "Water jet assisted tunnel boring", *Proceedings of the 3rd International Symposium on Jet Cutting Technology*, Paper E6, pp. X63-X74, BHRA, Cranfield, Bedford, England, 1976.

Watson, A.J., Williams, F.T., and Brade, R.G., "Impact pressure characteristics of a water jet". *Proceedings of the 6th International Symposium on Jet Cutting Technology*, Paper C2, pp. 93-106, BHRA, Cranfield, Bedford, England, 1982.

8. NOMENCLATURE

- d Nozzle orifice diameter, mm
- D Diameter of the exit hole of the plexiglass tube, mm
- d_e Equivalent nozzle orifice diameter, mm
- E_k Specific kerfing energy (J/cm^2 or MJ/m^2)
- E_v Specific energy (J/cm^3 or MJ/m^3)
- f Frequency of pulses (Hz)
- ζ porosity of the rock material (%)
- H_p Hydraulic power (kW)
- P Pump pressure (MPa)
- S Standoff distance (m)
- V_{tr} Traverse speed of nozzle (m/s)
- κ Permeability of the rock material (μD)
- ξ Grain size of the rock material (μm)
- ρ_r Dry bulk density of rock material (kg/m^3)
- σ_c Uniaxial compressive strength (MN/m^2)
- σ_t Uniaxial tensile strength (MN/m^2)

Table 1. Typical properties of mining rock samples (granite listed for comparison, Vijay & Grattan-Bellew, 1985 and 1991; Vijay, 1991).

Material	ζ	κ	ξ	ρ_r	σ_c	σ_t
Granite	0.61 - 2.65	Not measured	200 - 4400	2603 - 2649	139 - 175	5.3 - 10.0
Falconbridge	1.08 - 1.19	0 - 0.582	240 - 434	2820 - 2880	237 - 273	9.3 - 15.5
Inco	≈ 1.3	0 - 0.075	0 - 312	2910 - 4420	102 - 206	8.4 - 19.7
Noranda	0.74 - 2.2	0 - 0.072	103 - 341	2710 - 4260	92 - 227	5.2 - 27
Gneiss (Waste)	≈ 0	≈ 0	0 - 30	2741 - 2921	186 - 366	18 - 22

Table 2. Design specifications of nozzles shown in Fig. 3

Nozzle #	1A	1B	2	3A	3B	3C	4A*	4G*
d (mm)	1.78	1.60	1.78	1.78	1.78	1.78	3.05	3.05
d_e (mm)	1.78	1.60	1.78	1.78	1.78	1.78	1.78	1.78
d'							1.59	1.59
L/d_e	2.0	2.0	2.0	2.0	2.0	2.0	2.0	2.0
α	20°	20°	180°	20°	20°	20°	20°	20°
L' (mm)				23.8	28.2	32.7		
L''							0.0	30.5
θ								5°

*For the specifications of nozzles 4B to 4F see Vijay, et al., 1990 (designated as #7 to #11).

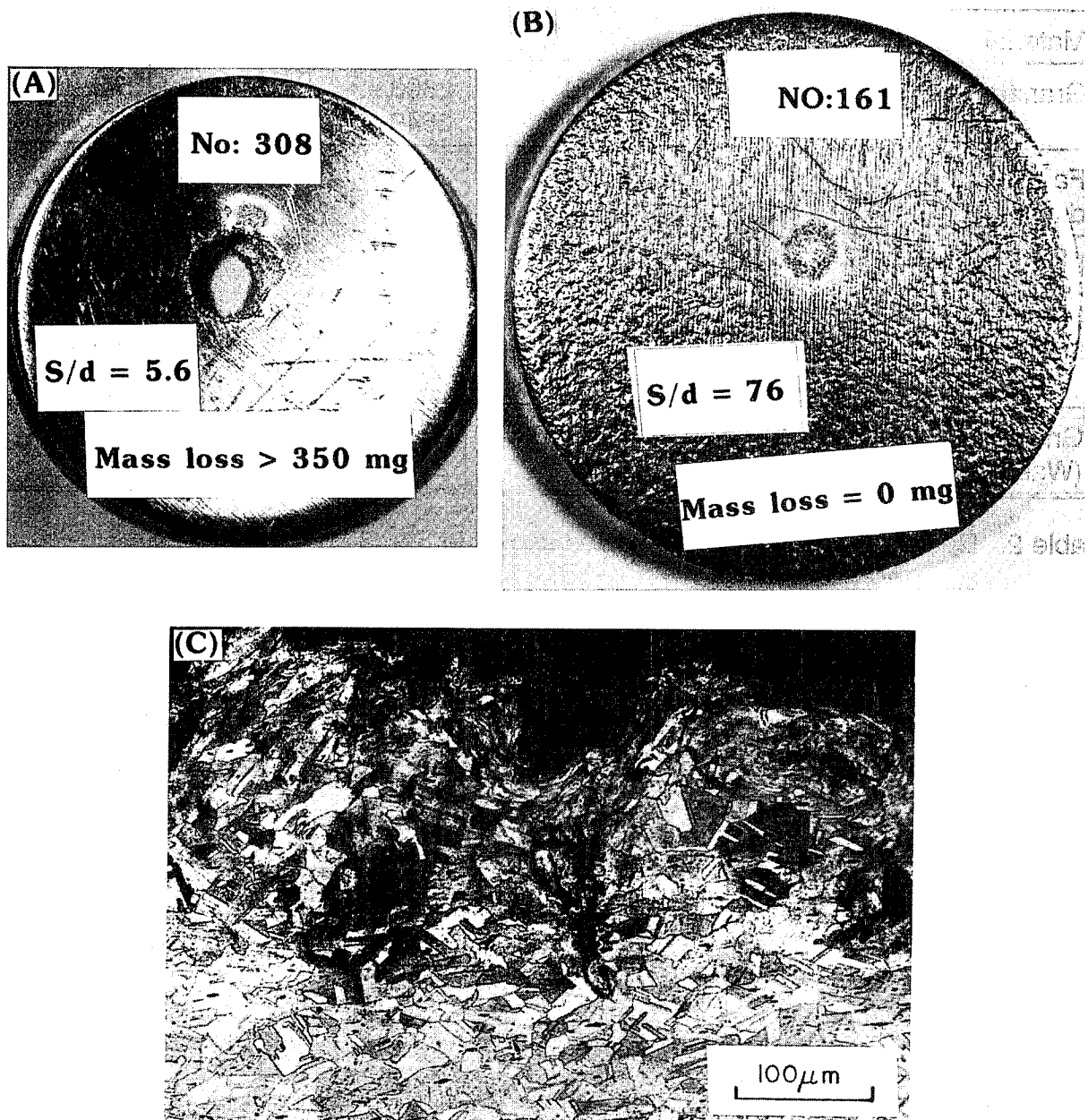


Fig. 1 Samples of aluminum (A & B) and annealed copper (C) exposed to high speed water jets issuing from different types of nozzles at 35 MPa. Metallograph of the thin section through the crater shown in (C) was taken from a Leitz Microscope (for details see: Vijay & Brierley, 1981 and Vijay, et al., 1990).

- | | |
|-----------------------------------|-----------------------|
| 1. TRANSDUCER | 5. HIGH PRESSURE PUMP |
| 2. TRANSFORMER | 6. JET |
| 3. NOZZLE | 7. SLUGS OR DROPS |
| 4. SIGNAL GENERATOR AND AMPLIFIER | 8. CAVITATION BUBBLES |

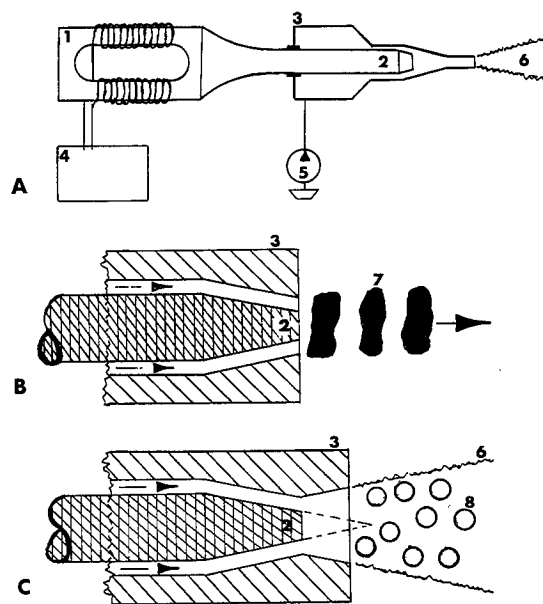
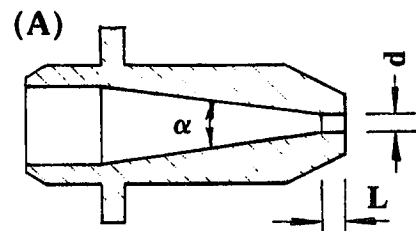
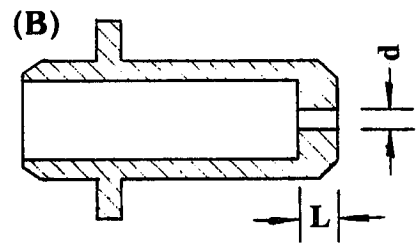


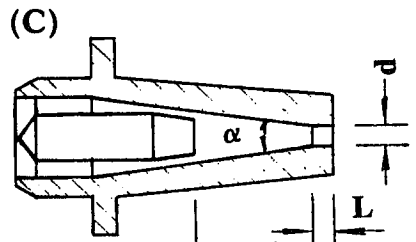
Fig. 2 Schematics of a nozzle device showing an electromagnetic transducer for generating high frequency (> 5 kHz) ultrasonic waves in a stream of high speed water. Depending on the design of the inner profile of the nozzle, the waves can be used to modulate the water stream to produce pulsed (B) or forced cavitating water jets (C) or both. The intensity of cavitation bubbles or size and shape of the pulses can be controlled by the amplitude and frequency of the waves.



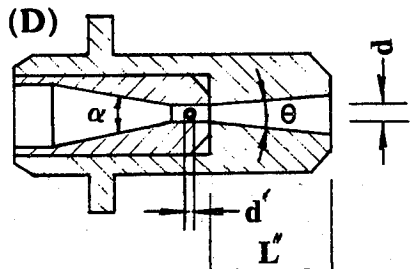
NOZZLES #1A & #1B



NOZZLE #2



NOZZLES #3A, #3B & #3C



NOZZLES #4A TO #4G

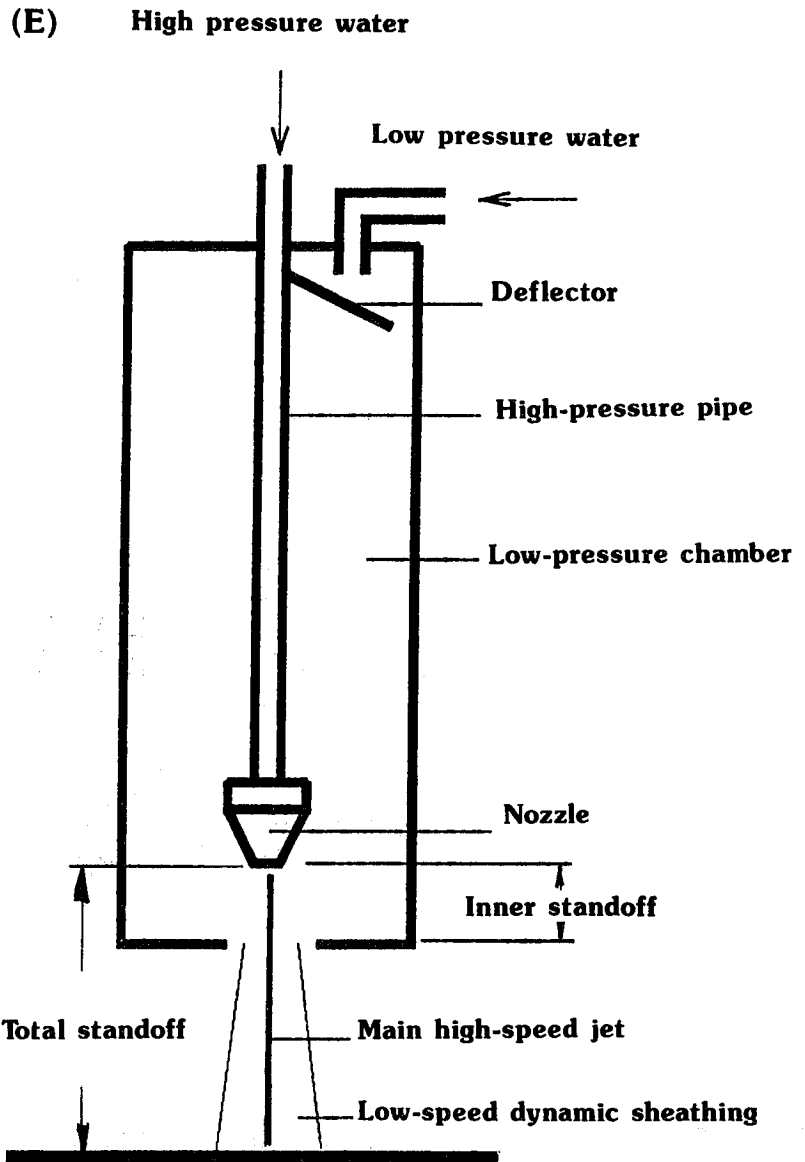


Fig. 3 Schematics of the nozzle configurations and the method of artificial submergence used in the investigation (Vijay et al., 1992a).
 (A) Conical entry nozzle (B) Straight entry nozzle (C) Nozzle with a centre-body and (D) Nozzle with a transverse pin. For specifications, see Table 2.

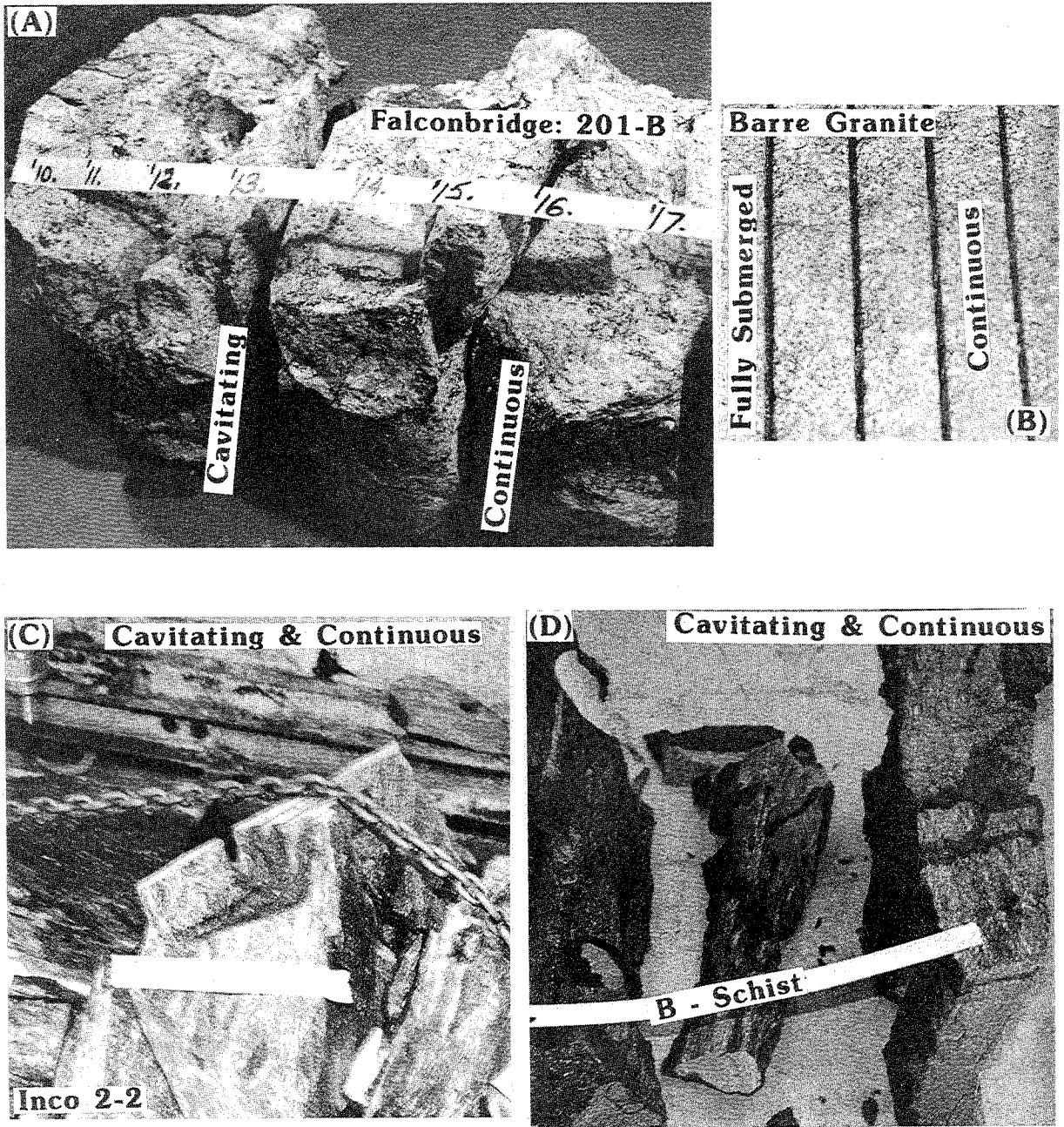


Fig. 4 Typical appearance of the rock samples after testing with cavitating (in air and artificially or fully submerged) and continuous water jets. Pressure: 103 to 138 MPa. Traverse speed = 0.005 & 0.05 m/s. Kerfs cut by cavitating jets were generally wider than those cut with continuous jets.

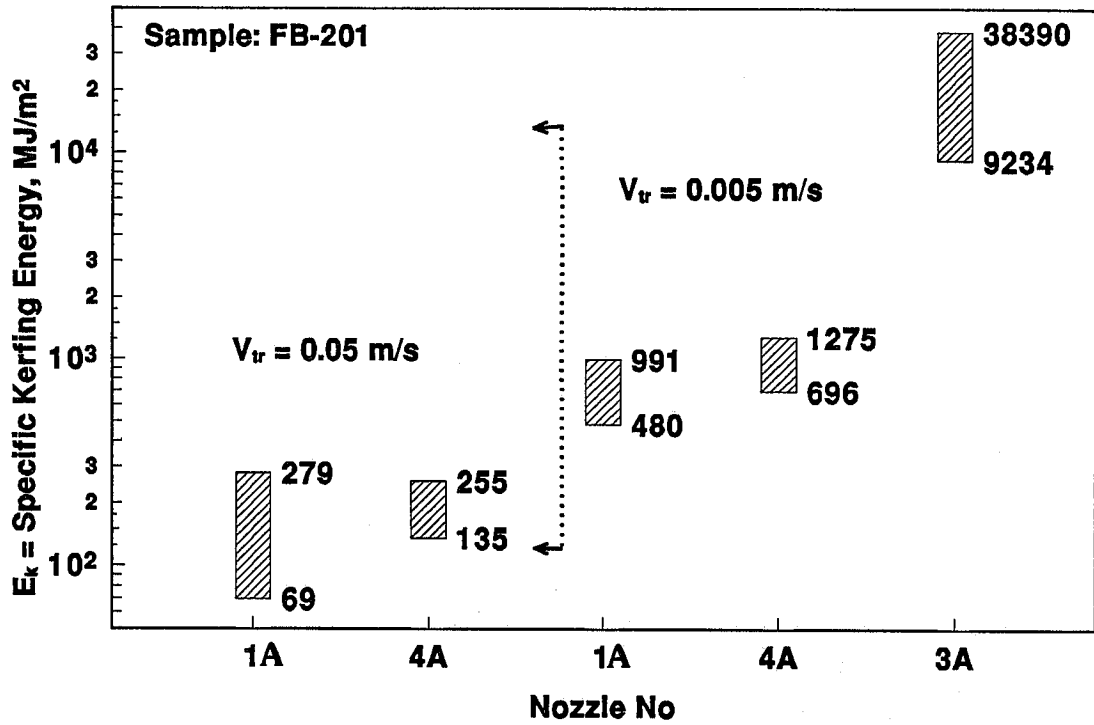


Fig. 5 Plot of the range of specific kerfing energies (E_k) obtained in artificially submerged experiments with the nozzles indicated

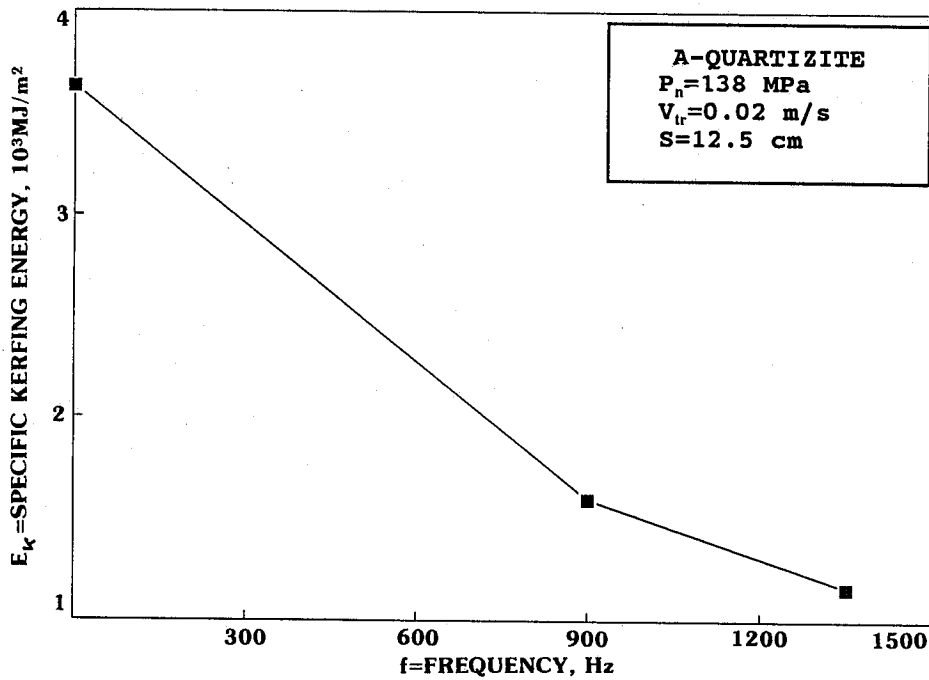


Fig. 6 Plot of the specific kerfing energy (E_k) against the frequency (f) obtained with mechanically interrupted jets

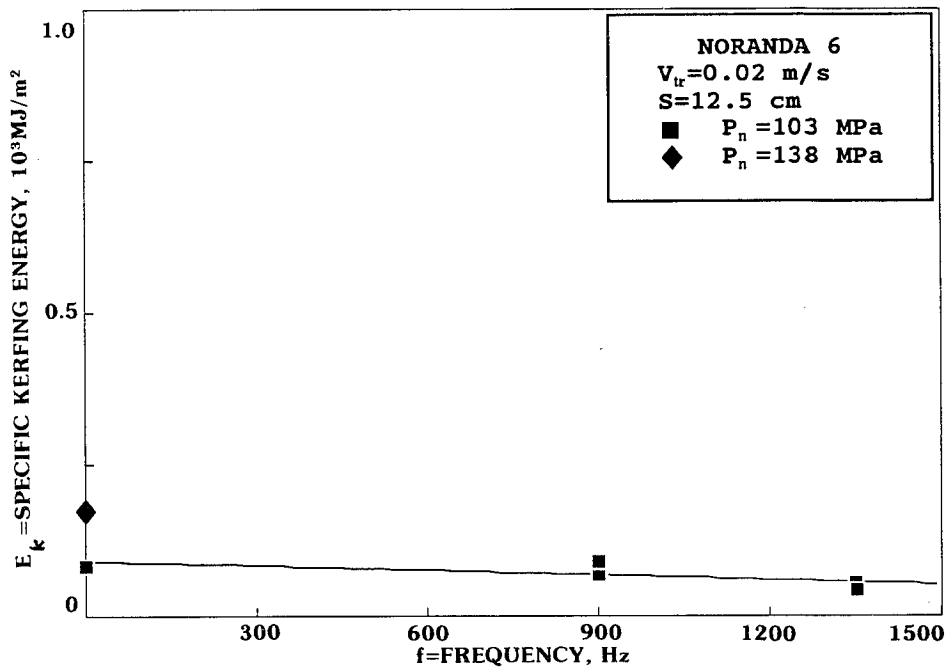


Fig. 7 Plot of the specific kerfing energy (E_k) against the frequency (f) obtained with mechanically interrupted jets

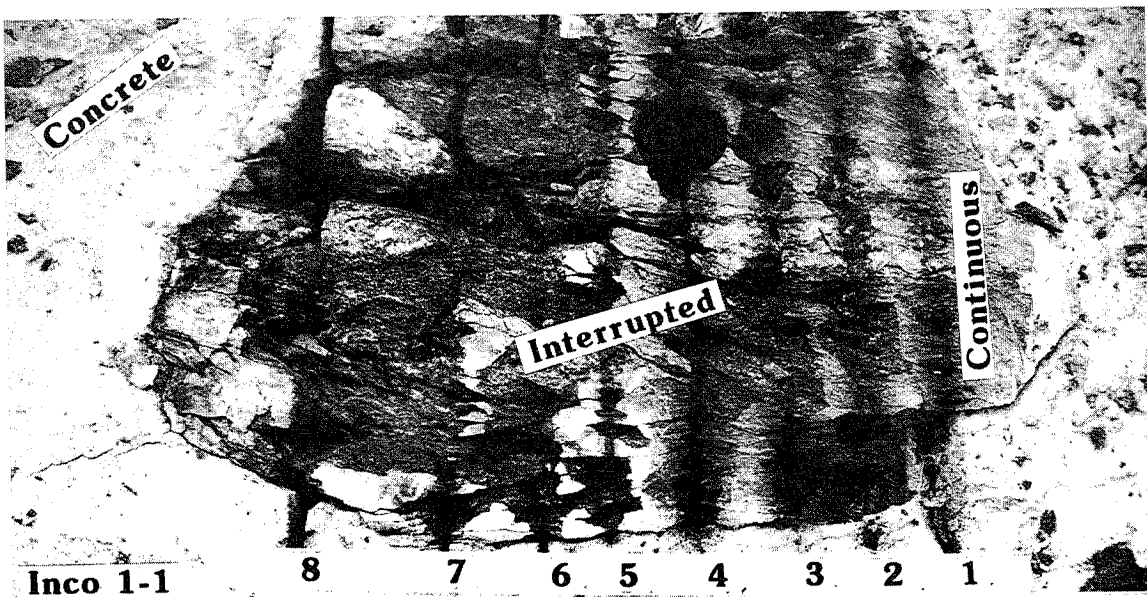
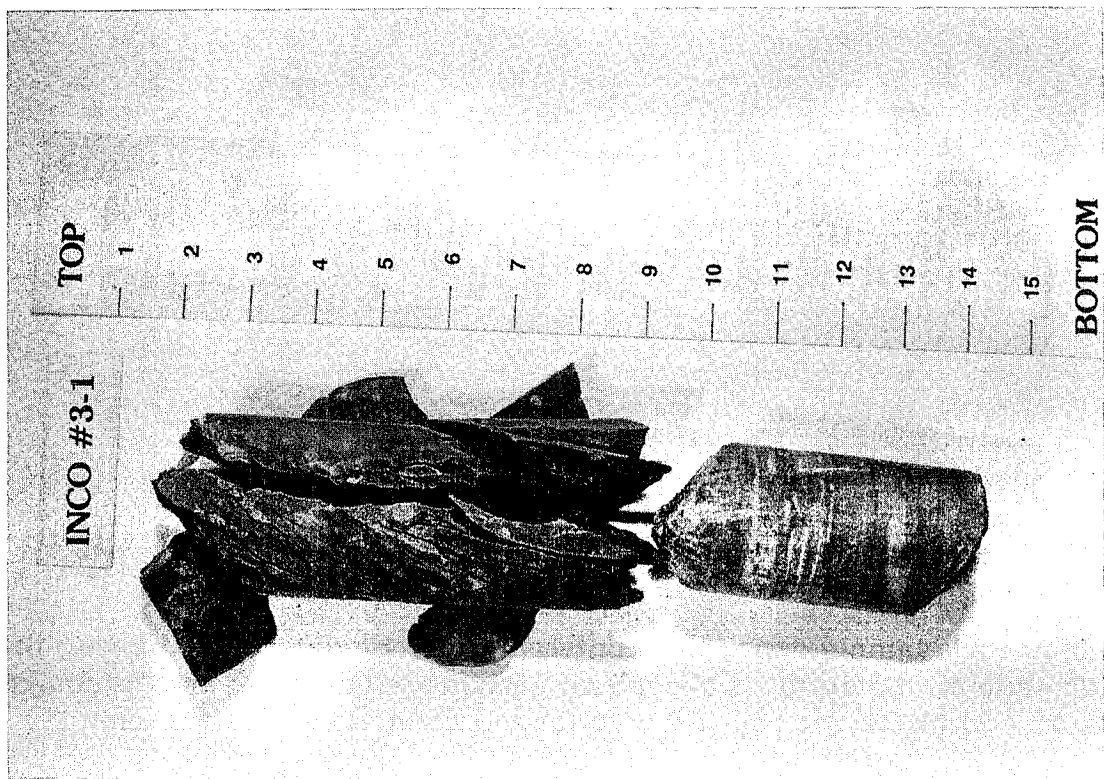
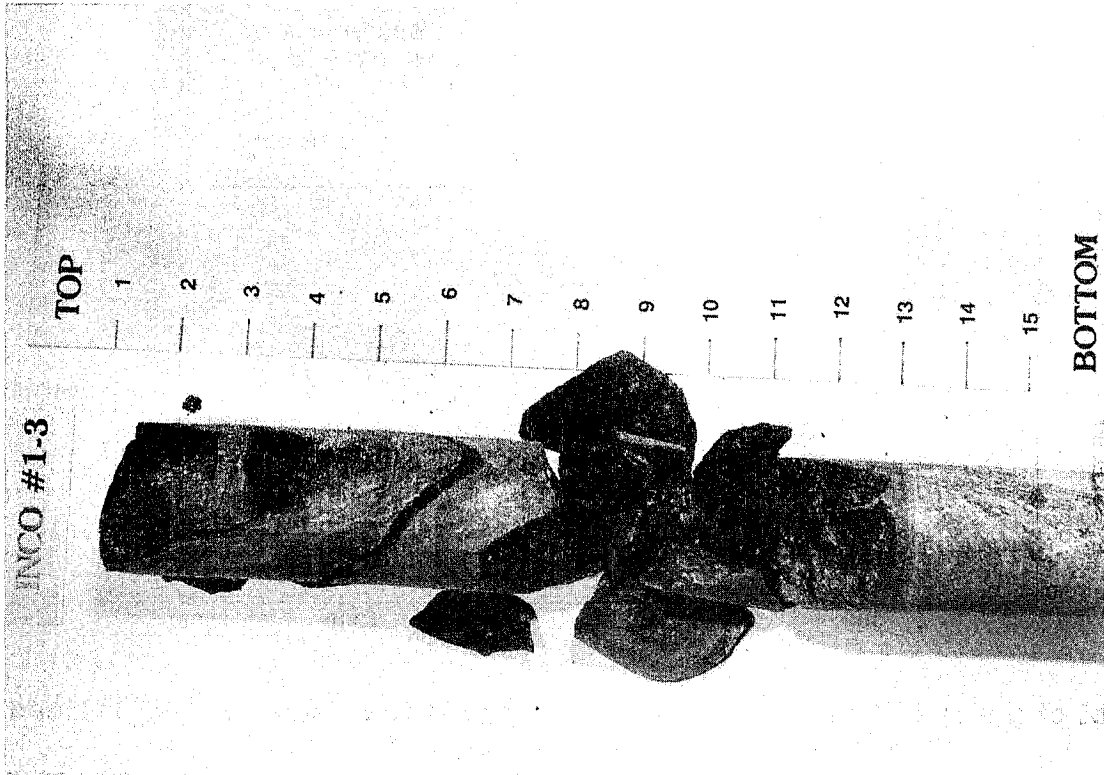


Fig. 8 An Inco rock sample exposed to different types of water jets showing the extent of damage on the surface. The extent of damage (initiation and propagation cracks and fractures) below the surface is defined as "preweakening"

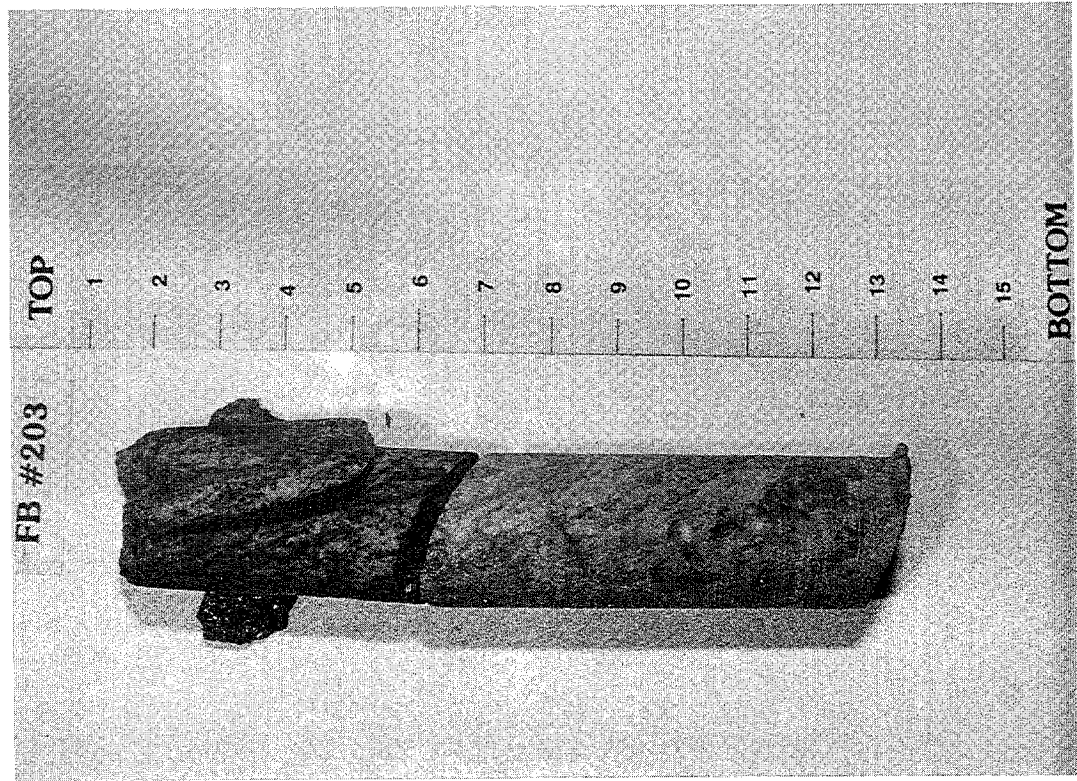


(A) Taken between slots #2 and 3

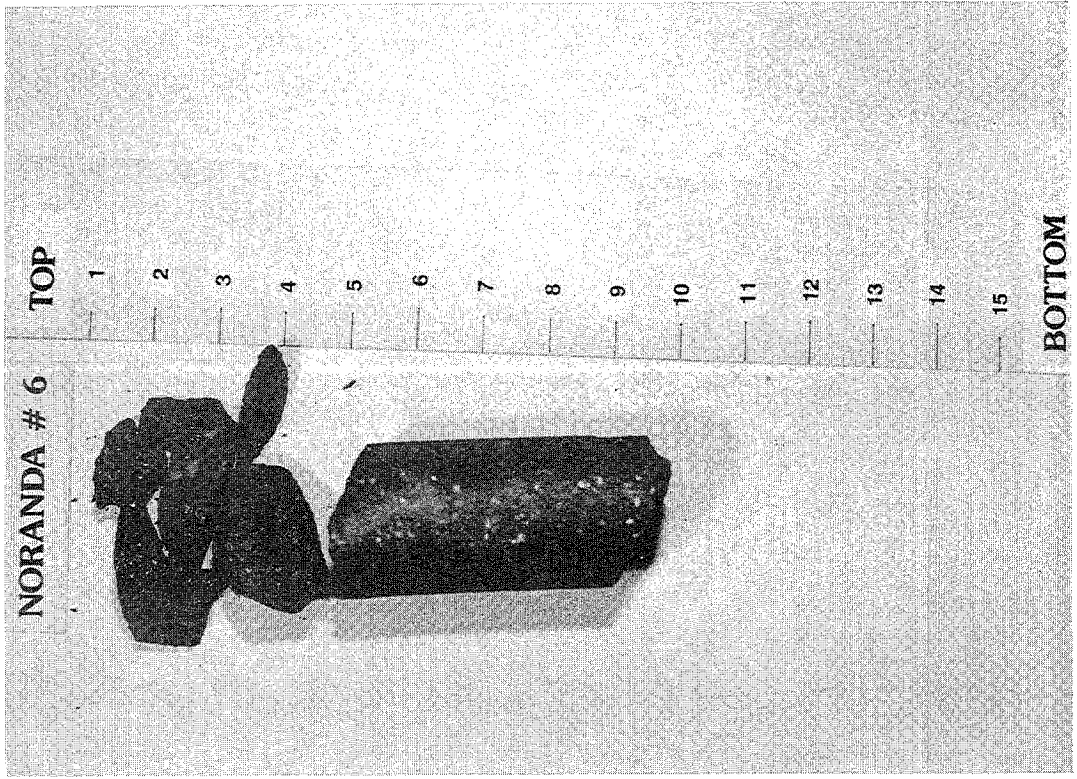


(B) Taken between slots # 6, 7 and 8

Fig. 9 Appearance of the cores taken from water jet treated Inco samples



(A) Falconbridge rock sample



(B) Noranda rock sample

Fig. 10 Appearance of the cores taken from water jet treated Falconbridge (A) and Noranda (B) samples

THE INFLUENCE OF ROCK PROPERTIES ON WATERJET PERFORMANCE

M. Agus, A. Bortolussi, R. Ciccu, W.M. Kim, P.P. Manca
Department of Mining and Mineral Engineering
Mineral Science Study Centre, CNR
University of Cagliari
Cagliari, Italy

ABSTRACT

The paper deals with the most recent results of rock cutting with high velocity water jets, concerning a number of igneous lithotypes having different origin and characteristics. In particular, it is shown that for heterogeneous materials of the same group the effect of mineral composition is generally important, whereas in the case of mono-mineral rocks porosity often plays the most important role. The statistical relationships linking specific energy to jet parameters on one side, and to rock-related properties on the other are given and discussed. Minimum specific energy can be correlated very well with propagation velocity of sound waves.

1. INTRODUCTION

Disintegration of rocks using high velocity water jets is strongly dependent on some fundamental material properties such as mineral composition, grain size, porosity features and mechanical strength. Though their effect on specific energy is known to most waterjet experts, no reliable relationships of general validity have hitherto been made available as a predictive tool.

On this subject, research is ongoing at the Waterjet Laboratory of the University of Cagliari, in the frame of a project aimed at demonstrating the feasibility of new technologies for stone quarrying and processing.

2. EXPERIMENTS

In order to obtain performance data, linear cutting tests have been carried out with a variety of lithotypes. Findings can be extended to deep kerfing using oscillating (or rotating) nozzles since rock behaviour to waterjet action is generally similar in both cases, i.e. cutting results are roughly proportional.

On this assumption the experimental burden was considerably simplified enabling a large collection of data to be gathered for establishing the correlation with the various material properties. Moreover reliability was improved due to a better representativity and homogeneity of rock samples.

2.1 Equipment

Cutting tests have been carried out using the facilities installed at the DIMM Waterjet Laboratory of the University of Cagliari, consisting of:

- A Diesel-driven triplex plunger pump generating a 54 l/min flowrate at 250 MPa.
- A hydraulically traversed carrier table.
- A waterjet lance connected to the pump by means of flexible hoses.

2.2 Instrumentation

Rock characterization was carried out using classic and advanced microscopy.

Sound velocity of P-waves across the rock samples was measured with the Pundit instrument of CNS Electronics using the 54 kHz probe.

Porosity features were assessed according to the technique of forced intrusion of mercury under a pressure of up to 400 MPa, using the Macropore Unit 120 for the initial degassing and the measurement of macropores and the Carlo Erba Porosimeter mod. 4000 for the assessment of porosity distribution. Rock fragments were 4 to 7 mm in size.

Specific gravity was measured by means of a pycnometer using petroleum ether; samples were crushed to a fragment size around 10 mm.

Mechanical properties were determined with the point load testing apparatus of Engineering Laboratory Equipment. This allowed a number of statistically meaningful tests to be carried out, accounting for the heterogeneity of the rock.

2.3 Materials

A variety of granite samples having different composition, texture and fabric was subjected to cutting tests under variable experimental conditions. Each rock sample was characterized by determining the minero-petrographic features and by measuring the relevant mechanical properties and some significant parameters related to them.

They are listed in Table 1 and identified with a letter.

2.3.1 Minero-petrographic characteristics

Minero-petrographic investigation was carried out according to the procedures suggested by rock petrography (Parfenoff et al., 1970).

In particular, average mineral composition was determined along directions parallel to the intended waterjet cuts, summing up the segments corresponding to each mineral crossed by the reference lines.

The length of the segments overlaying each individual crystal was taken as representative of the crystal size.

In the cases of extrusive and dyke rocks the ratio of phenocrysts to the microcrystalline or vitreous mass was also determined.

Texture and fabric features were also assessed though difficult-to-translate into quantitative parameters.

Plutonic rocks are generally characterized by a holocrystalline, hypidiomorphic structure and allotriomorphic in lithotypes P and R, porphyritic in lithotypes K, G, H, I and U.

Crystal size is mostly coarse, in the range of 1 to 5 mm, seldom fine (<1 mm) like in lithotype O, with marked heterogranularity in lithotypes having a porphyritic structure.

In volcanic rocks, the size of phenocrysts seldom exceeds 1 mm into a microcrystalline (lithotypes V and Y) or vitreous matrix (lithotypes W and X).

The following mineralogic features have been observed:

Quartz is generally xenomorphic, sometimes tending towards idiomorphic in small crystals inside the larger K-feldspar. Almost always it shows undulating extinction and considerable intragranular microfracturation; in some instances (lithotypes A and Q) microfractures are filled with secondary weathering phases (sericite).

The K-feldspars class is represented both by orthoclase and microcline crystals (this latter mainly occurring in lithotypes D, E, G, I, M and S), generally perthitic and often microfractured.

Plagioclase, in the form of idiomorphic or subidiomorphic crystals, is chiefly represented by the oligoclasic and oligoclase-andesinic terms in granites and by labradoritic terms in gabbroes and norites. Plagioclase is often strongly weathered (lithotypes Q, I and D) with formation of secondary micaceous phases (sericite).

Pyroxenes, found exclusively in lithotypes P, R, S and O, occur as xenomorphic crystals, often interstitial between plagioclase, showing intragranular fracturation. Typical of lithotype P is the diffusion of augite lamellae inside the clinoenstatite crystals.

Results of minero-petrographic analysis are summarized in Figures 1 and 2 and in Table 2.

2.3.2 Physical and mechanical properties

Properties of main interest are summarized in Table 3.

Porosimetry has been studied by determining the statistical distribution of pore size in the classes $+1 \text{ m}\mu$, $-1 \div +0.1 \text{ m}\mu$, $-0.1 \div +0.01 \text{ m}\mu$ and $-0.01 \text{ m}\mu$. In most granites the intermediate pore sizes are most frequent, whereas in the other lithotypes a greater proportion of smaller pores is encountered.

3. CUTTING RESULTS

The following jet parameters and experimental conditions have been considered in the experimental plan:

- Pumping pressure: from 50 to 250 MPa, step 10 MPa.
- Jet diameter: 0.8 and 1.25 mm.
- Traverse velocity: 1 and 4 m/min.

Linear cuts are characterized by different accuracy for the various lithotypes. In fact, neat and

straight edges were seldom obtained, whereas in many instances cut configuration was rather irregular, especially in the case of low-pressure jetting. Cutting rate as a function of pressure is represented by the curves of Figures 3 to 5, a) and b). Specific energy as a function of pressure is represented by the curves of Figures 6 to 8, a) and b).

4. DISCUSSION

4.1 Cutting rate

From the curves of Figures 3 to 5 the following considerations can be underlined:

Most curves are S-shaped, i.e. three phases can be distinguished and characterized by a gradient which first increases, then reaches an almost constant value and finally decreases until an asymptotic value is attained.

This means that in the first phase jet power is not sufficient for the complete promotion of the cutting mechanism. In the intermediate phase the process is fully developed while in the final phase efficiency falls progressively due to passive losses of power (jet friction on the kerf walls, interference between incoming jet and spent water).

In particular, in the case of nozzle diameter = 1.25 mm and traverse velocity = 1 m/min the three phases are present for most granites and for the basic plutonic rocks whereas for dyke rocks and for volcanic rocks, both characterized by a fine-grained or vitreous matrix, phase 1 is rather extended and phase 3 is likely to start beyond 250 MPa.

In the case of nozzle diameter = 1.25 mm and traverse velocity = 4 m/min the process is almost complete for all lithotypes except for hard volcanic rocks.

Finally, in the case of nozzle diameter = 0.80 mm and traverse velocity = 1 m/min only the first phase appears well developed, whereas phase 3 is lacking for almost all lithotypes. In fact jet energy is not sufficient even at the highest pressure reached. The only exception is represented by lithotype V, characterized by a very high porosity index.

4.2 Specific energy

Specific energy as a function of pressure is typically U-shaped, with a more or less flat bottom according to cases (see Figures 6 to 8). However, in many instances minimum value falls beyond 250 MPa and therefore only the decreasing portion of the curve appears within the explored range. This happens especially for the 0.80 mm jet, carrying insufficient power even at the highest pressure.

For all the rock samples studied, minimum specific energy for the 0.8 mm nozzle diameter is found at pressures roughly twice those corresponding to the minimum value for the 1.25 diameter at equal traverse velocity of 1 m/min.

For the same nozzle diameter (1.25 mm) minimum specific energy at 1 m/min traverse velocity occurs at intermediate pressures, roughly 1.5 times larger than in the case of 4 m/min.

Correspondingly, minimum values at 1 m/min are on average two to three times larger than those at 4 m/min, according to the toughness of the rock.

This is summarized in Table 4.

4.3 Statistical correlations

A - Mineral composition

The possible correlation between minimum specific energy and mineral composition has been studied for the holocrystalline lithotypes where the different components, having comparable crystal size, are almost evenly distributed in the rock mass. These include all the plutonic rocks except those showing a marked porphyritic texture, i.e. lithotypes A to S. Lithotype M is also excluded for having a markedly striped fabric.

To this end, minerals with a distinct fragile behaviour (quartz and K-feldspar) have been

considered separately from those having a lower elasticity modulus (plagioclase and mica) (Lama and Vutukuri, 1978; Rhzevsky and Novick, 1971), following the indication of a previous research on single crystal impingement (Agus et al., 1991). Specific energy is correlated with the proportion of each group of minerals, as shown in Figure 9.

In both cases a trend can clearly be distinguished, though the correlation coefficient is not very high, due to the presence of other factors inducing considerable scattering of data points.

It appears that specific energy decreases with the quartz and K-feldspar content whereas it increases with that of plagioclase and mica. Therefore, the elastic properties of the constituent minerals (and of the rock as a whole) appear to be very important, as pointed out elsewhere.

Indeed, for a rock characterized by a larger proportion of less brittle minerals, a greater amount of jet energy is likely to be lost in the form of plastic deformation, thus leaving less energy available for effective disintegration (Agus et al., 1992).

Moreover it happens that other factors, such as porosity and grain size, favouring rock disintegration with water jets, are affected by mineral composition, both generally decreasing with increasing plagioclase content. At the same time, mechanical strength (here represented by the point load test) increases with plagioclase content, due to the fact that intergranular bonds involving this mineral are generally stronger than those between the other constituents (Agus et al., 1991).

B - Grain size

The effect of crystal size is hardly evident if the average size of all constituents is taken into account (Vijay and Grattan-Bellew, 1991). However if the crystal size of brittle minerals is considered separately from the others, a feeble trend is disclosed as shown in Figure 10.

Actually specific energy slightly decreases/increases for rocks containing the more/less fragile components in the form of coarser crystals.

C - Porosity

Correlation of minimum specific energy with porosity index is quite inconsistent if the whole set of lithotypes is considered. However, if the investigation is restricted to the granites alone, thus reducing the influence of composition and grain size, the influence of porosity becomes clearly evident.

Roughly granites having double the porosity can be cut with half specific energy.

If only intermediate porosity is taken into consideration, i.e. that corresponding to pore sizes in the range between 1 and 0.01 micrometres, then correlation improves considerably for the whole set of rocks as shown in Figure 11.

D - Mechanical properties

As already pointed out by previous research, compressive strength is of little significance in rock disintegration with water jet (Summers, 1987). On the other hand, since fracture propagation due to traction forces appears to be the dominant mechanism, cutting results should be correlated with a suitable strength parameter (Erdmann-Jesnitzer et al., 1978).

The Point Load Test seemed appropriate for its capability of representing the resistance of the sample to tensile stresses. Moreover, the possibility of repeating the test on unshaped fragments allowed to collect enough data for each lithotype, accounting for the heterogeneity of the rock.

In spite of the considerable scattering, a certain correlation of point load test results with specific energy seems to exist as shown in Figure 12.

E - Sound velocity

Sound velocity is a measure of the compactness of a rock and therefore a good correlation with waterjet cutting results should have been expected.

Actually, as shown in Figure 13, all data points are reasonably well gathered along a straight line with a correlation coefficient higher than 0.9.

It can be suggested that sound velocity is assumed as a suitable global parameter for assessing

the amenability of a rock to disintegration with high velocity water jets.

From the above it ensues that any attempt to establish a reliable correlation between jet cutting results and single rock-related parameters is not fully successful, except for sound velocity which accounts globally for many influencing properties.

Probably a more accurate definition of specific energy by exploring traverse velocities higher than 4 m/min would have provided a better fitting.

5. CONCLUSIONS

The following conclusions can be drawn on the basis of experimental evidence regarding waterjet cutting of igneous rocks:

- Mineral composition has an important influence on waterjet disintegration which is favoured by the presence of quartz and K-feldspar (the more fragile constituents, markedly microfractured) and hindered by that of plagioclase and mica (showing plastic deformability).
- Textural features can also be important: generally, the coarser the crystal size of fragile components, the lower the energy needed for unit area exposed. On the other hand, disintegration is promoted when crystal size of deformable minerals is smaller.
- Porosity plays an important role too, especially that corresponding to pore sizes in the range between 1 and 0.01 m μ .
- Minimum specific energy can be correlated with point load strength, despite of considerable scattering of data points.
- Textural features also affect waterjet performance: in the case of extrusive rocks mineral composition plays a minor role.
- Minimum specific energy is very well correlated with the ultra-sound velocity of P-waves. This parameter can, therefore, be assumed for assessing the amenability of rocks to waterjet cutting.

ACKNOWLEDGEMENTS

The research work has been carried out with the financial support of EMSa (Sardinian Mining Body) within the projects approved by CNR (National Research Council) and MURST (Italian Ministry for Scientific Research)

The help provided by Professor R. Balia for the measurement of ultra-sound wave velocity and by Dr. C. Atzeni for the determination of porosity spectra is greatly appreciated.

REFERENCES

- M. Agus, A. Bortolussi, R. Ciccu, P.P. Manca, G. Massacci and M. Bosu, "Jet impingement tests on mineral crystals", *Proc. 1st Asian Conf. on Recent Advances in Jetting Technology*, Singapore, 6-8 May 1991, pp. 1-9.
- M. Agus, A. Bortolussi, R. Ciccu, P.P. Manca and G. Massacci, "Granite cutting with water jets", *Int. J. of Waterjet Techn.*, Vol. 1, N. 2, 1991, pp. 73-83.
- M. Agus, A. Bortolussi, R. Ciccu, P.P. Manca, G. Massacci and C. Atzeni, "A contribution to the understanding of waterjet cutting of rocks", *Proc. WJT 1992 Taiwan 3rd Pacific Rim Int. Conf. on Water Jet Technology*, Tainan, Taiwan, November 1992, 107-120.

- F. Erdmann-Jesnitzer, H. Louis and J. Wiedermeier, "Material behaviour, material stressing, principle aspects in the application of high speed water jets", *4th Int. Symp. on Jet Cutting Technology*, Canterbury, UK, April 1978, pp. 29-44.
- R.D. Lama and V.S. Vutukuri, *Handbook on Mechanical Properties of Rocks*, 1978, V. II. Trans. Tech. Publ..
- A.Parfenoff, C. Pomerol and J. Tourenq, *Mineraux en grains, methodes d'étude et détermination*, Masson et Cie, Paris, France, 1970, pp.170-171.
- V. Rhzevsky and O. Novick, *The Physics of the Rocks*, 1971, MIR Publ., Moscow, Russia.
- D.A. Summers, "Water jet cutting related to jet and rock properties", *Proc. 14th Symp. on Rock Mechanics*, Pennsylvania State University, AIME, 1987, pp. 569-588.
- M.M. Vijay and P.E. Grattan-Bellew, "The influence of properties of rocks on nozzle design for drilling and slotting with water jets", *Int. J. of Waterjet Techn.*, Vol. 1, N. 3, 1991, pp. 116-133.

TABLES

Table 1. List of rock samples included in the cutting experiments

PLUTONIC ROCKS

Lithotype		Origin	Lithotype		Origin
A - S.Giorgio White	g	Sardinia,	L - Cinza	gd	Portugal
B - "Sienite" T.	g	Sardinia,I	M - Tropical	g	Brazil
C - Pearl Grey	mg	Sardinia,I	N - Sardinian Red	g	Sardinia, I
D - Iksan	g	S. Korea	O - Diorite	t	Piedmont, I
E - Sinbuk	g	S. Korea	P - Africa Black	ga	Angola
F - Rosa Beta	g	Sardinia,I	Q - Green Labrador	g	Portugal
G - Indian Red	g	India	R - Preto S.G.	n	Brazil
H - Carmen Red	g	Finland	S - Verde Ubatuba	qm	Brazil
I - Porrino	g	Spain	T - Porphyry Red	fg	Sardinia, I
J - Montorfano	g	Piedmont, I	U - Porphyry Grey	bd	Sardinia, I
K - Ghiandone	mg	Sardinia			

VOLCANIC ROCKS

Lithotype		Origin	Lithotype		Origin
V - Ignimbrite	ri	Sardinia, I	X - Andesite	b	Sardinia, I
W - Basalt	r	Sardinia, I	Y - Rhyolite	a	Sardinia, I

Lithologic definition

g = granite	n = norite	qm = Q-monzonite	mg = monzogranite
t = tonalite	fg = F-granite	gd = granodiorite	ga = gabbro
bd = basic different.			
a = andesite	ri = rhyolitic ign.	r = rhyolite	b = basalt

Table 2. Minero-petrographic characteristics of volcanic rocks

Lithotype	Porph.Ind. %	Structure	Cryst.size (mm)	
			Phenocr.	Matrix
V	10	Vitroclastic	0.7	-
W	30	Porphyritic vitrophyric	0.9	-
X	30	Holocryst. porphyritic	1.0	<0.04
Y	5.5	Holocryst. porphyritic	0.7	0.20

Table 3. Physical and mechanical properties of the rock samples

Lithotype	P.Load Test MPa	Sound Vel. m/s	Porosity %	Sp. surf. cm ² /g	Spec.gravity kg/dm ³
A	37.9	5,001	0.80	0.12	2.57
B	62.4	4,052	0.71	0.14	2.67
C	53.6	4,760	0.80	0.05	2.69
D	29.6	4,013	1.10	0.13	2.61
E	37.7	3,951	0.90	0.04	2.55
F	47.3	5,626	0.63	0.04	2.67
G	72.4	5,829	0.40	0.06	2.45
H	23.0	4,846	0.30	0.02	2.58
I	37.2	3,010	0.50	0.03	2.58
J	54.6	4,200	0.66	0.02	2.61
K	49.2	4,510	0.68	0.03	2.80
L	--	--	0.40	0.01	2.45
M	41.7	5,910	0.40	0.04	2.62
N	49.0	4,520	0.70	0.09	2.46
O	54.3	4,257	1.10	0.07	2.80
P	110.7	7,393	0.34	0.01	2.89
Q	50.6	5,052	0.20	0.01	2.62
R	39.2	6,740	0.42	0.01	3.14
S	34.2	4,500	0.28	0.01	2.65
T	55.3	4,131	2.20	0.54	2.47
U	69.7	6,343	1.00	0.29	2.75
V	21.5	2,985	24.07	4.50	1.84
W	51.1	5,837	1.60	0.71	2.66
X	90.2	5,333	1.18	0.49	2.76
Y	72.4	3,970	11.92	3.67	2.95

Table 4. Minimum specific energy E_s and corresponding pressure P for the various experimental conditions (D = Nozzle diameter (mm), V_t = Traverse Velocity (m/min)).

Conditions	$D=1.25, V_t=1.0$		$D=1.25, V_t=4.0$		$D=0.80, V_t=1.0$	
	E_s	P	E_s	P	E_s	P
PLUTONIC ROCKS						
A - S.Giorgio White	22	100	8.5	160	27	> 250
B - "Sienite" T.	25	130	8.0	200	11	175
C - Pearl Grey	20	100	8.0	160	28	> 250
D - Iksan	20	140	7.5	200	22	> 250
E - Sinbuk	23	120	6.1	170	21	> 250
F - Rosa Beta	26.5	150	13.5	210	35	> 250
G - Indian Red	28	190	13.0	> 250	64	> 250
H - Carmen Red	24	140	9.5	180	50	> 250
I - Porrino	16	--	5.0	--	19	--
J - Montorfano	22	--	9.8	--	--	--
K - Ghiandone	22	--	9.1	--	--	--
L - Cinza	44.6	--	21.5	--	--	--
M - Tropical	41	170	20.5	200	32	> 250
N - Sardinian Red	25	--	13.3	--	--	--
O - Diorite	17	180	8.0	180	17.5	> 250
P - Africa Black	40	170	21.0	200	65	> 250
Q - Green Labrador	22	130	12.0	180	17	> 250
R - Preto S.G.	41	--	18.1	--	--	--
S - Verde Ubatuba	30	--	11.6	--	--	--
T - Porphyry Red	21	210	11.0	> 250	10.5	> 250
U - Porphyry Grey	280	140	25.0	210	210	> 250
VOLCANIC ROCKS						
V - Ignimbrite	12	160	5.5	180	12	230
W - Basalt	40	210	21.0	250	170	180
X - Andesite	60	> 250	48.0	230	230	250
Y - Rhyolite	20	--	9.6	--	--	--

E_s (kJ/cm²), P (MPa)

FIGURES

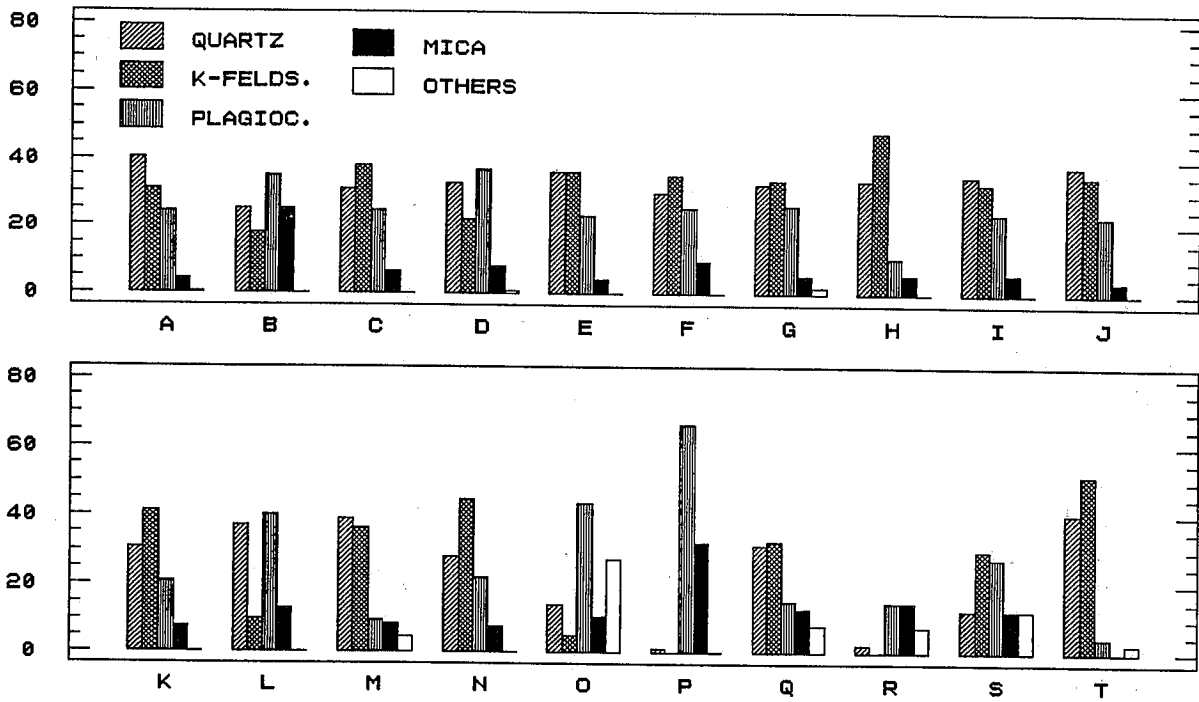


Figure 1. Bar diagram of the mineral composition (% proportion by linear size) for the various lithotypes tested.

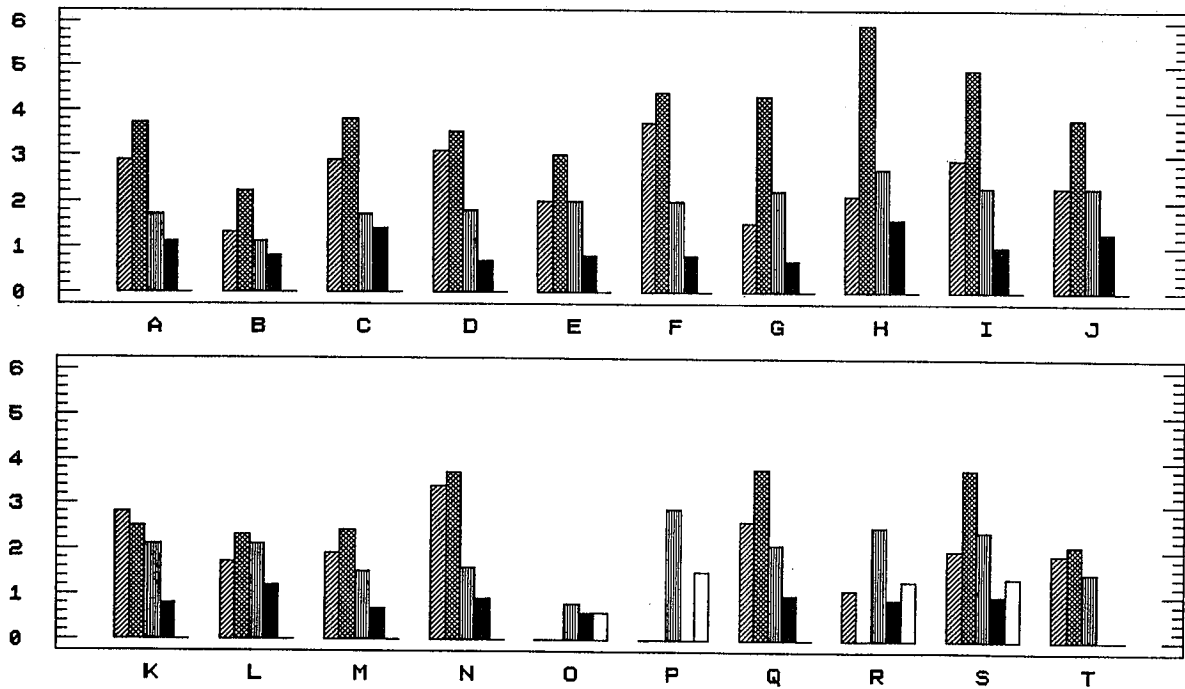
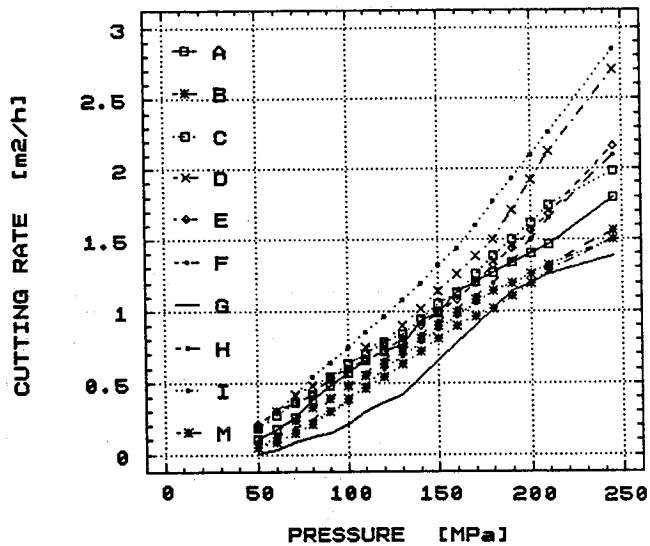
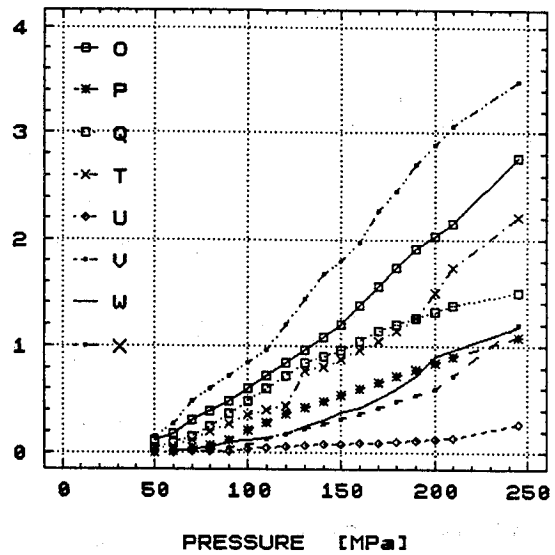


Figure 2. Mean grain size (cm) of each mineral component



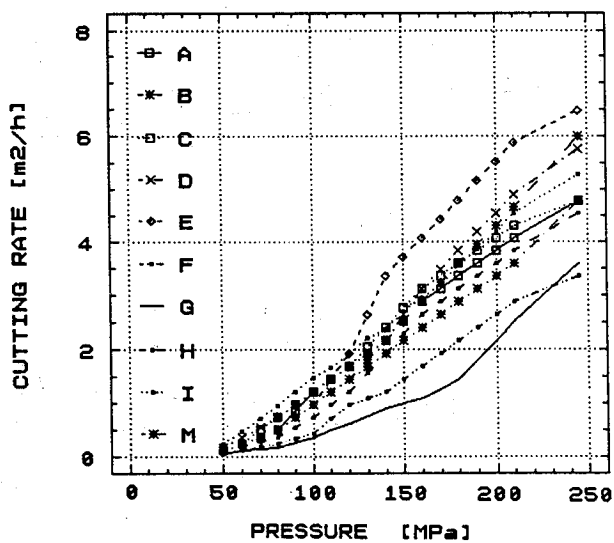
a)



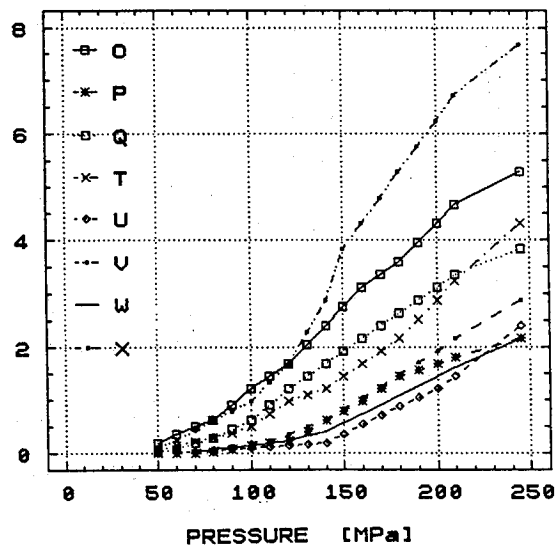
b)

Figure 3. Cutting rate versus pressure. Nozzle diameter: 1.25 mm; traverse velocity: 1 m/min.

a) granites; b) other lithotypes



a)



b)

Figure 4. Cutting rate versus pressure. Nozzle diameter: 1.25 mm; traverse velocity: 4 m/min.

a) granites; b) other lithotypes

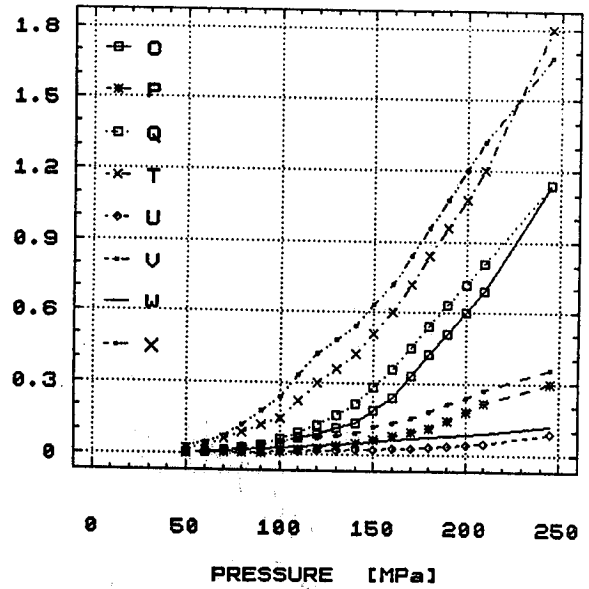
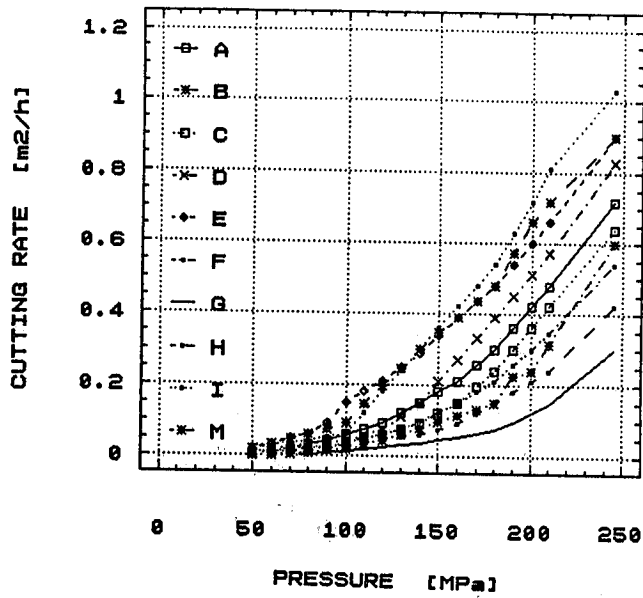


Figure 5. Cutting rate versus pressure. Nozzle diameter: 0.80 mm; traverse velocity: 1 m/min.
 a) granites; b) other lithotypes

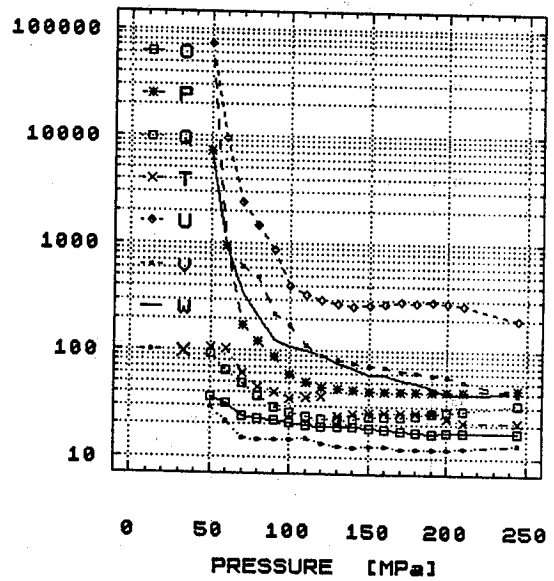
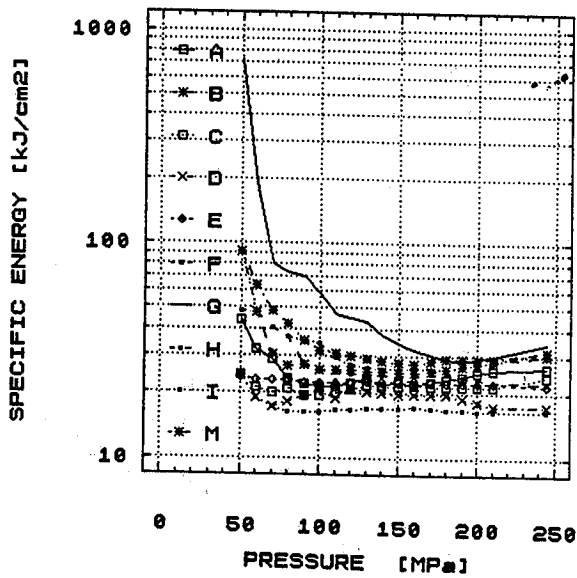
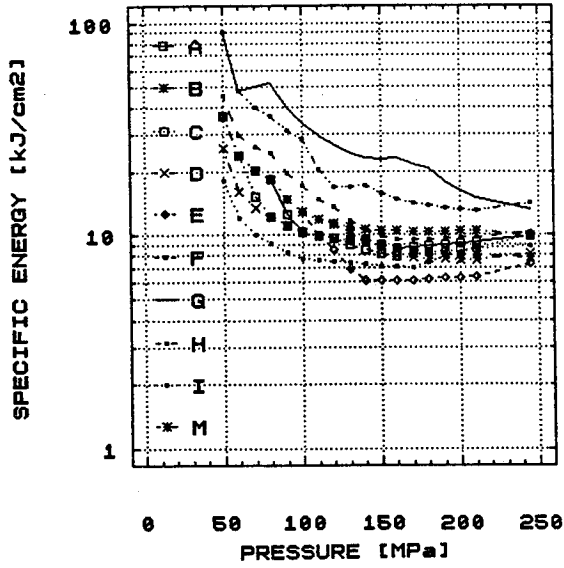
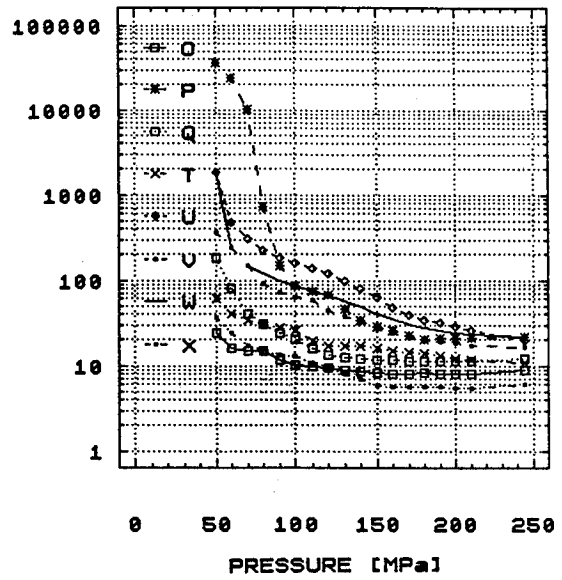


Figure 6. Specific energy versus pressure. Nozzle diameter: 1.25 mm; traverse velocity: 1 m/min.
 a) granites; b) other lithotypes



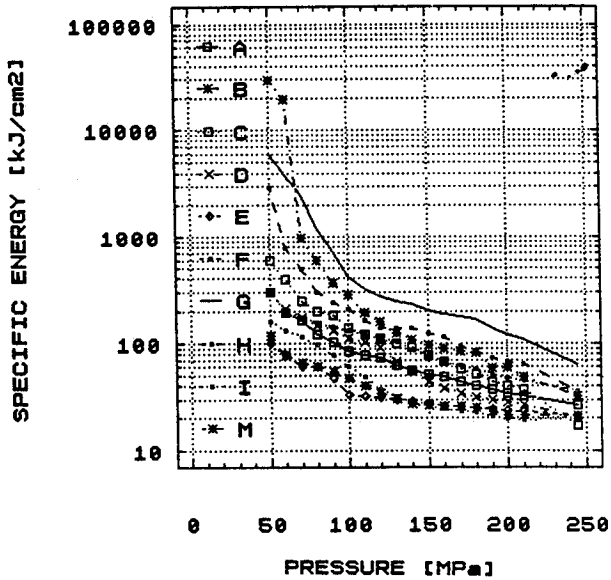
a)



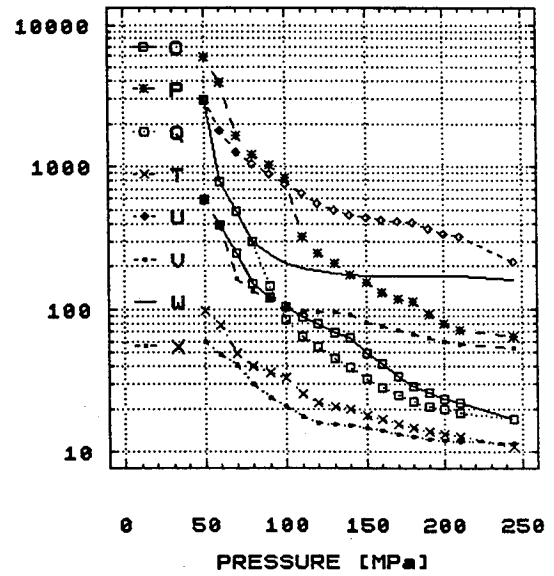
b)

Figure 7. Specific energy versus pressure. Nozzle diameter: 1.25 mm; traverse velocity: 4 m/min.

a) granites; b) other lithotypes



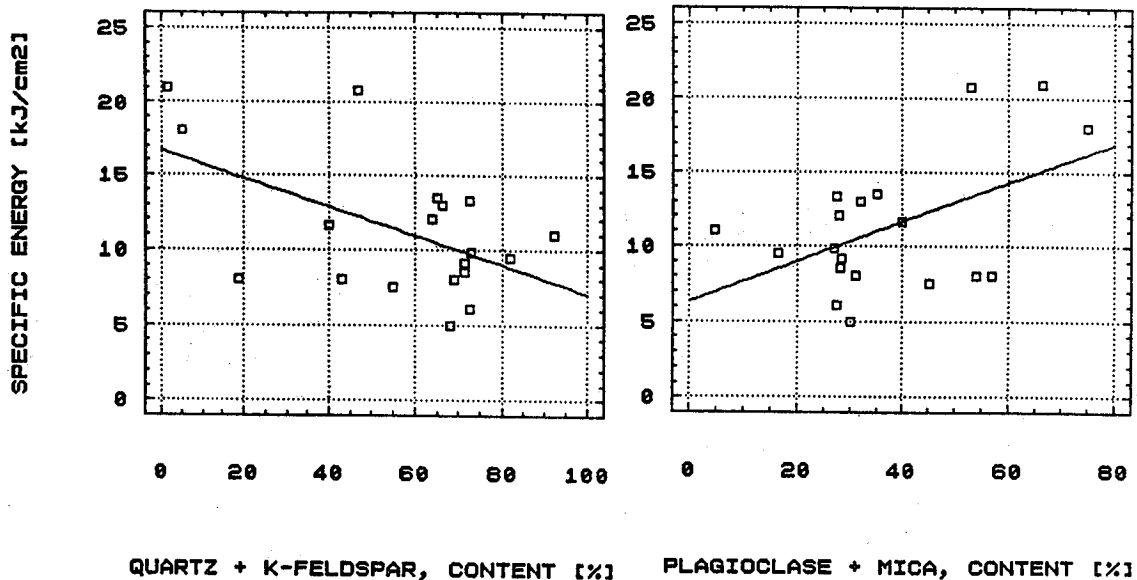
a)



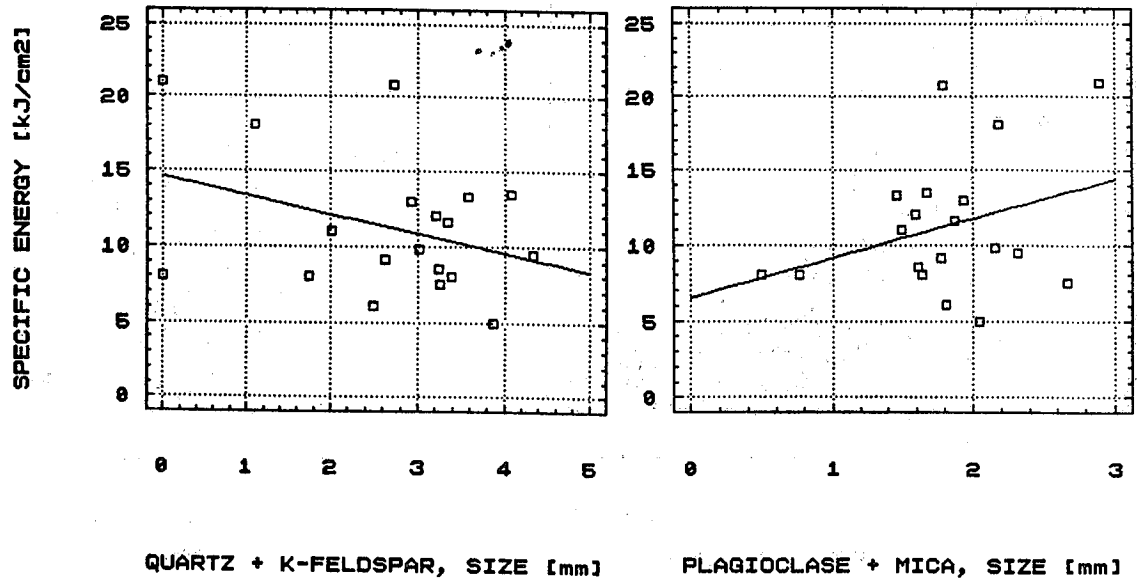
b)

Figure 8. Specific energy versus pressure. Nozzle diameter: 0.80 mm; traverse velocity: 1 m/min.

a) granites; b) other lithotypes



a) b)
 Figure 9. Correlation of cutting results with mineral composition.
 a) Minimum specific energy versus quartz + K-feldspar content
 b) Minimum specific energy versus plagioclase + mica content



a) b)
 Figure 10. Minimum specific energy versus average crystal size.
 a) Quartz + K-feldspar
 b) Plagioclase + mica

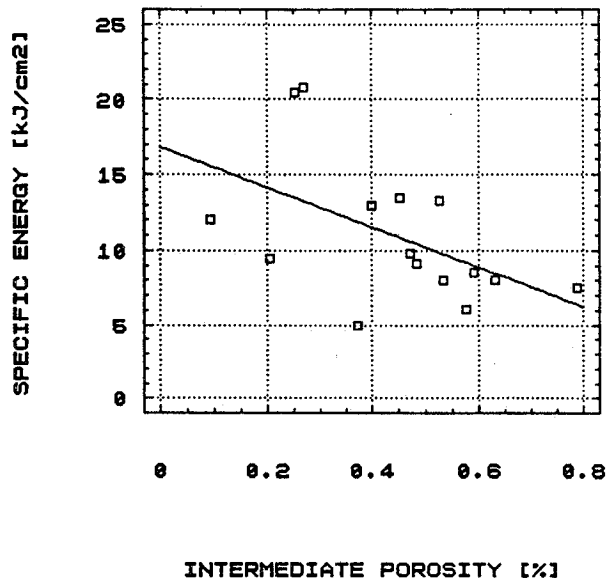


Figure 11. Specific energy versus intermediate porosity for the whole set of rocks studied.

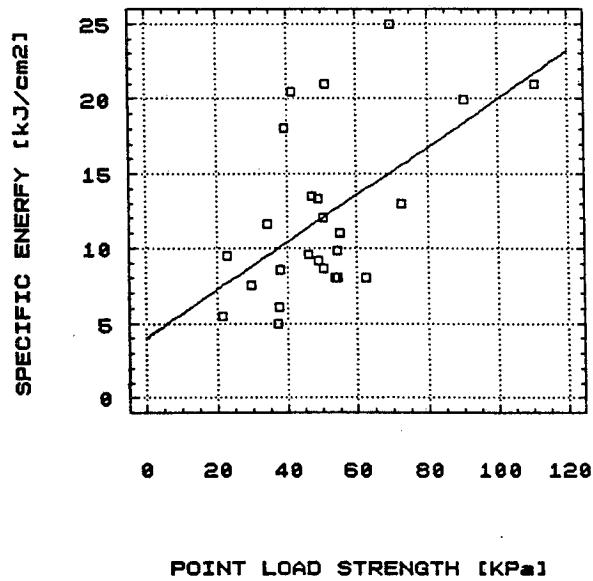


Figure 12. Minimum specific energy versus average point load strength.

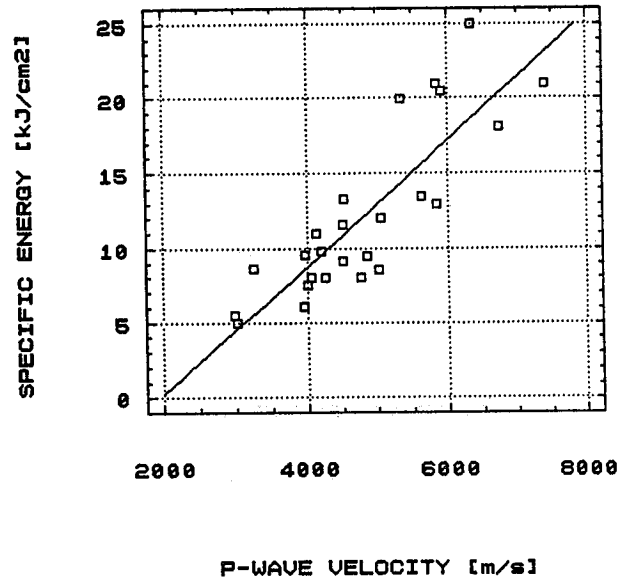


Figure 13. Correlation of specific energy with ultra-sound velocity of P-waves.

ABRASIVE WATER JET CUTTING OF PORTUGUESE MARBLES

R. M. MIRANDA, P. LOUSA
Instituto de Soldadura e Qualidade
Lisbon, Portugal

A. J. MOURAZ MIRANDA
Instituto Superior Técnico
Lisbon, Portugal

T. KIM
University of Rhode Island - USA

ABSTRACT

Earlier works suggested that rock hardness influences the rate of material removal and the type of erosion in water jet cutting. However, no systematic parametric study had been yet conducted on this topic.

The main objective of this study is to investigate the relationship between the calcareous rock properties and material removal characteristics in an abrasive water jet cutting environment. Three Portuguese calcareous stones are used in this experiment to determine the factors influencing the shape cutting profile as well as the quality of cuts.

1 - INTRODUCTION

Portugal is one of the major world producers of calcareous stones with a very wide range of varieties. However as far as the authors are aware, no systematic studies have been conducted on the machinability of these materials in a non-traditional cutting environment.

Recently an abrasive waterjet (AWJ) cutting system was introduced in Portugal for linear and shape cutting applications of stone plates, mainly marbles. The advantages of this new technology for mechanical processing of calcareous stones are:

- * Precise shape cutting can be achieved with a good surface finish;
- * AWJ cut kerf width is much smaller than that produced by the conventional cutting technologies;
- * AWJ cutting systems can be easily integrated with the existing CAD/CAM systems, thereby greatly optimizing the shape cutting process;
- * the system produces no dust, thereby significantly improving the working environment.

In Portugal, there is a wide range of calcareous stones used in construction industry. From these there are three different types of calcareous stones (Moca Creme, Lioz and Cristalino de Estremoz) with a unique composition including different petrographic composition and hardness.

The aim of this study is to determine the machinability and AWJ characteristics of these stones in terms of major AWJ process parameters, such as: pressure, transverse speed and stand off distance.

2 - EXPERIMENTAL PROCEDURE

Three different calcareous stones were tested, with commercial references: Moca Creme, Lioz and Cristalino de Estremoz, respectively with the following petrographic description (1): biomicritic with clastic argilous matrix; crystalline biosparite with steolite; and crystalline calcitic marble with medium to fine grain.

Microhardness of each stone was measured by means of a Vickers microhardness tester with a load of 0.5Kg and obtained average hardness as:

Moca Creme:	83 MHV0.5
Cristalino de Estremoz:	111 MHV0.5
Lioz:	114 MHV0.5

AWJ cutting trials were performed on 20mm thick plates, varying: pressure, cutting speed and stand-off distance.

A factorial design of experiments was used so 24 trials were made for each material. The testing conditions are listed in table 1. The water flow rates of 2.60, 2.95 and 3.20 l/min for corresponding pressures of 196, 245 and 294 MPa, were used.

All the other parameters were kept constant as listed below:

- sapphire diameter: 0.355 mm
- mixing tube diameter: 1.016 mm
- mixing tube length: 76.2 mm
- abrasive type: garnet
- abrasive grain size: 80 mesh
- abrasive flow (g/min): 200

For each sample cut, the measured values are:

- the kerf width at top and bottom faces;
- roughness (R_a and R_{max}) in three regions of the cut surface: at 1/4, half and 3/4 thickness measured from the top.

The morphology of the cut was observed under a scanning electron microscope.

3 - DISCUSSION OF RESULTS

Using the Tagushi analysis method, three groups of results were evaluated separately (see table 1).

The results of the measured kerf width on the top and bottom faces, indicate that no significant variation exists in the ranges tested. The kerf width plots as a function of the water pressure and traverse speed for all materials (figs.1 and 2), also reveals low significance. The results suggest that the kerf width is more dominated by speed than pressure except for very soft materials like Moca Creme. For the harder material, like Lioz, it was not possible to measure the kerf width at the bottom surface due to its irregularity.

Another interesting result generated from these tests was that Moca Creme reacted with a larger kerf width on the bottom face than the top face. This result is similar to the observations made by T.J.Kim et al. (2) for very porous materials. This is mainly due to the small amount of energy required for cutting this material and the jet divergence.

To confirm this phenomenon a second round of simple experiments was conducted by varying the pressure and the traverse speed keeping all other parameters constant. Results are presented in fig.3 and 4. The result shows that the kerf width does depend on the pressure and the traverse speed at the top surface, while at the bottom the behaviour is unpredictable. The kerf width ratio was plotted as a function of the two varied parameters (fig.5 and 6). The harder varieties of calcareous stones show pronounced V-groves with increased taper specially when the pressure was increased, while the softer stone shows straight edge cuts.

The surface roughness of Moca Creme was difficult to analyze because the roughness range was above the detection limit of surface roughness indicator used in this study. The peak-to-valley roughness measurement for two other stones (Cristalino de Estremoz and Lioz) indicates that the roughness increases with pressure as shown in fig.7.

Observing the AWJ cut surfaces of the same specimens, it was also noticed a variation of striation angle measured at the jet exit for each material. This clearly implicates a possible relationship between material hardness and the jet exit angle, which was investigated by Zeng and Kim (3,4) in advanced ceramic cutting. The result is illustrated in fig.8 showing that the exit angle increases as a function of the stone's hardness.

For a better understanding of the microstructure as well as the cut surface morphology of the stones subjected to AWJ erosion, a SEM analysis on each of the material tested was performed.

Moca Creme is a very porous calcareous stone with about 15% in volume of voids. Under SEM, it was observed that the material is constituted of small amounts of quartz (in small grains) and calcite (in large grains) in a matrix constituted of argilous and non-crystalline carbonate with a hardness of 1 in the Mohs scale.

Observation by a Scanning Electron Microscope indicates three different zones on the cut surface. One of the zones near the top surface, shows flat surface with lamellar argilous material. A trace of plastic deformation under steady conditions was also observed as shown in fig.9. Small aligned craters with romboedric calcites were seen as shown in figs.10 and 11. Around these craters a significant number of plastic deformation trace was also observed.

Going into the depth of the material, an increase of the number of craters is seen (figs. 12 and 13).

The divergency of the jet together with the larger number of craters on the bottom can be the main cause for the increase in the bottom taper.

A harder material, Lioz, is non-homogeneous and very dense. A SEM observation reveals two distinct zones: the first one that measures down to 1/3 of the thickness from the top surface and is mainly constituted of cleavage without plastic deformation (fig.14a and b) and the second one with fracture lines along the interface between the plate thick feldspate (a harder constituent) and the matrix. The cutting mechanism is dominated by cleavage of the romboedric calcite with small plastic deformation of the matrix and fracture along the interface of plate thick feldspate and the matrix.

Polysynthetic twinning may be due to the high shear forces exerted by the pressure jet and the small number of sliding systems, since feldspate has a monoclinic crystalline arrangement.

Cristalino de Estremoz is a very homogeneous material with almost no porosity. Near the jet impinged area, a network of small cracks is observed (fig.15a and b). Cleavage of the calcitic grains is predominant mainly near the top surface.

4 - CONCLUSIONS

- Stone hardness seems to play a key role on the cut profile geometry. Porous materials tend to show an inverted V-groove shape, while harder stones present a more regular behaviour.
- A significant influence of stone hardness and porosity was observed on the predominant cutting mechanism investigated under Scanning Electron Microscopy.
- Softer materials with high porosity contents tend to show a large number of craters with plastic deformation on the borders, while harder brittle materials show evidence of intergranular cracking and cleavage through the harder constituents.

5 - ACKNOWLEDGEMENTS:

The authors would like to thank JNICT and FLAD for their financial support. They also gratefully acknowledge ISQ for making available the necessary facilities to perform this investigation and Michael Memeteau for his assistance with data analysis.

6 - BIBLIOGRAPHY:

- 1 - "Portuguese Ornamental Stone Catalogue"- vol.I, D.G.G.M., 1983
- 2 - Kim, T., Zeng, J., Kee, W.J., "Effect of porosity in asphalt concrete on abrasive water jet cutting", Proceedings of the 1st Asian Conference on Recent Advances in Jetting Technology, pp.66, Singapore, 1991.
- 3 - Zeng, J., Kim, T., "Material Removal of Polycrystalline ceramics by a High Pressure Abrasive Water Jet - A SEM Study", International Journal of Water Jet Technology, vol.I, n.2, pp65-71, 1991.
- 4 - Zeng, J., Kim, T., "Development of an Abrasive Water Jet Kerf Cutting Model for Brittle Materials", Proceedings of the 7th Jet Cutting Technology, pp. 483, St. Andrews, Scotland, 1992.

Table 1 - Testing Conditions

SAMPLE NUMBER	Pressure(MPa)	Speed(mm/min)	Stand-off(mm)
1 - 1st group	196	200	2
2	296	200	2
3	196	400	2
4	296	400	2
5	196	200	3
6	296	200	3
7	196	400	3
8	296	400	3
9 - 2nd group	246	300	2.5
10	296	300	2.5
11	246	400	2.5
12	296	400	2.5
13	246	300	3
14	296	300	3
15	246	400	3
16	296	400	3
17- 3rd group	196	200	2
18	246	200	2
19	196	300	2
20	246	300	2
21	196	200	2.5
22	246	200	2.5
23	196	300	2.5
24	246	300	2.5

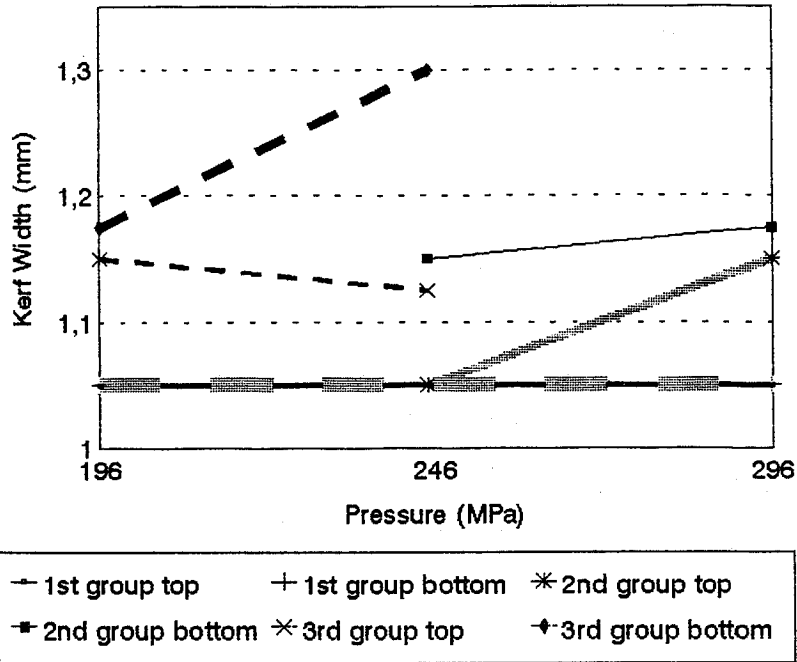


Fig.1 - Influence of cutting pressure on kerf width of Moca Creme

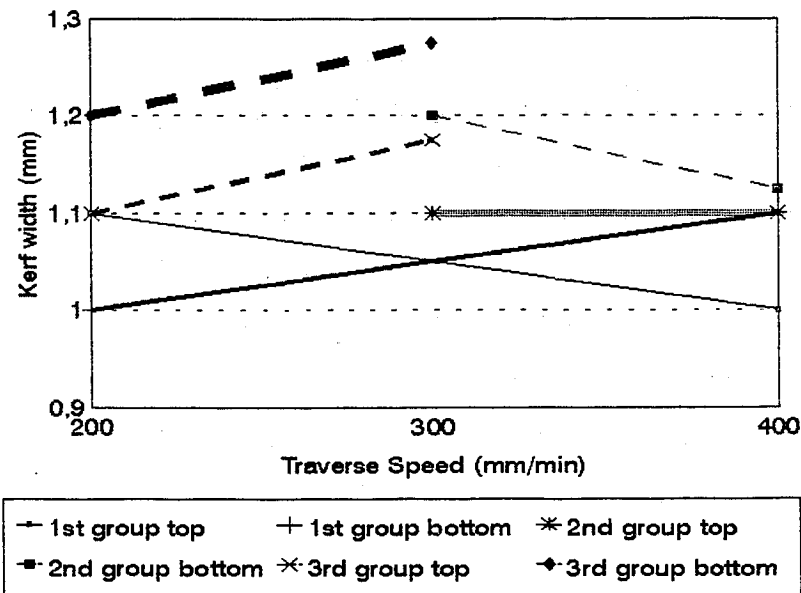


Fig.2 - Influence of cutting speed on the kerf width of Moca Creme

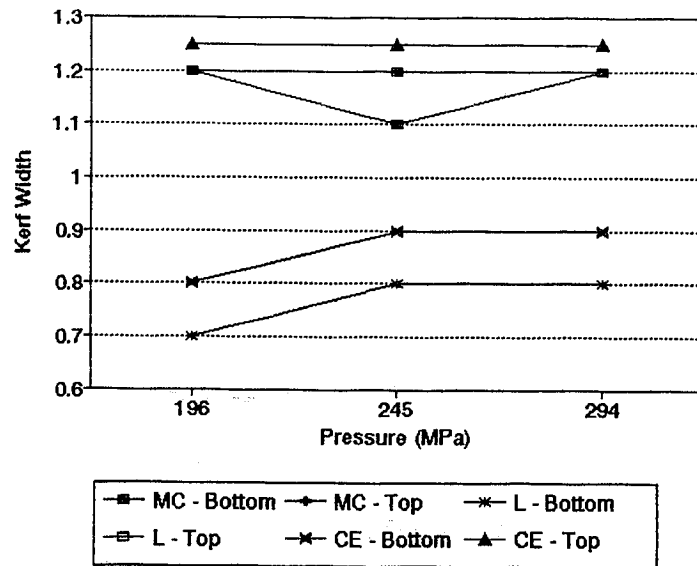


Fig.3 - Influence of cutting pressure on kerf width

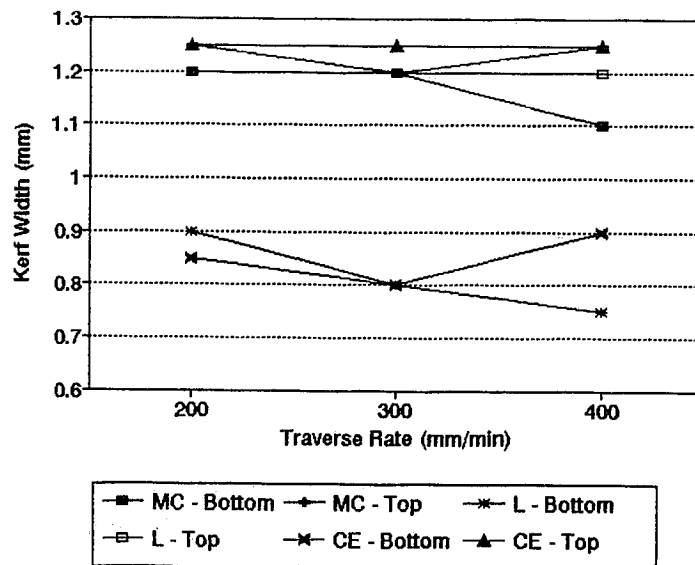


Fig.4 - Influence of cutting speed on the kerf width

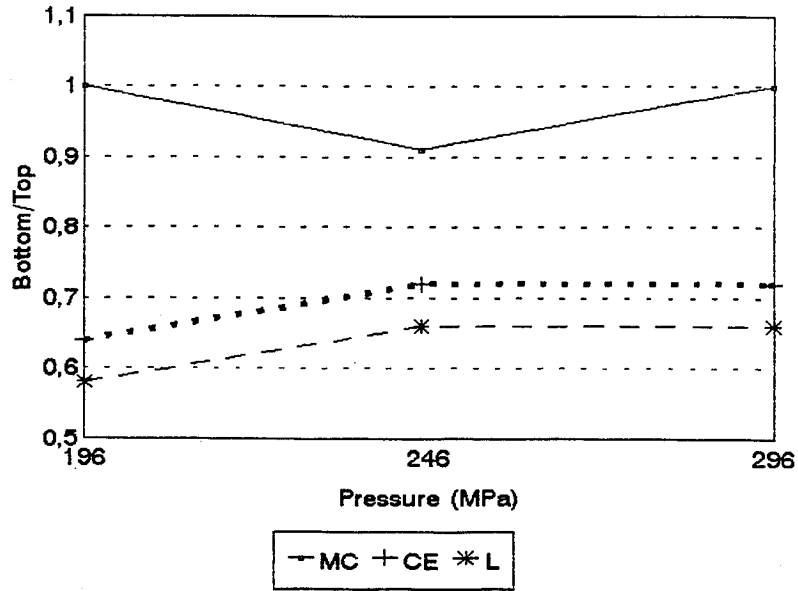


Fig.5 - Ratio between the kerf width at the bottom and the top with the cutting pressure

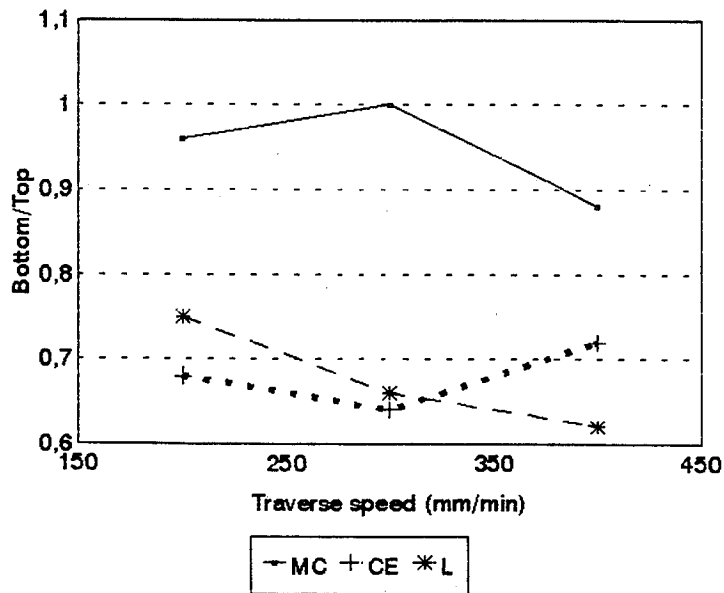
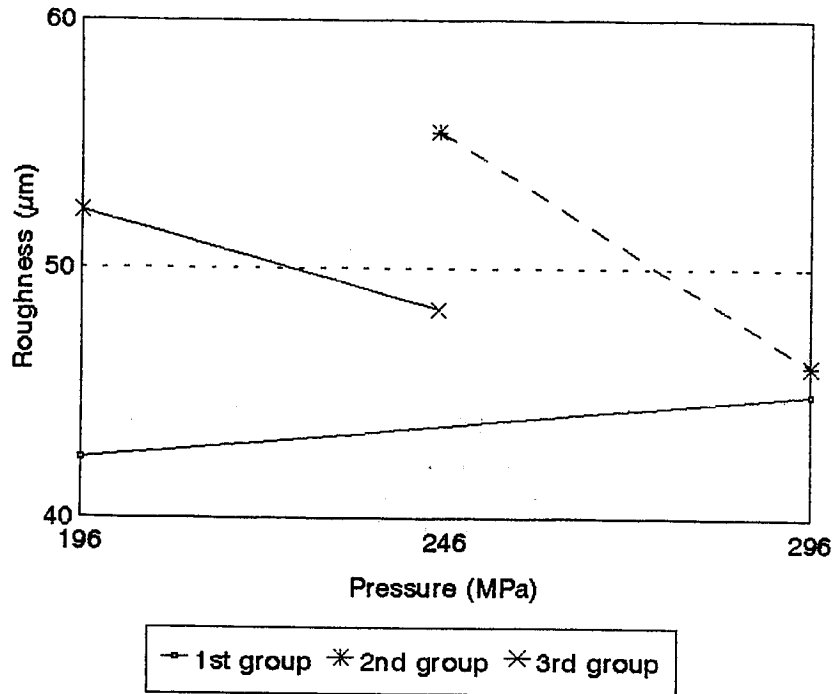
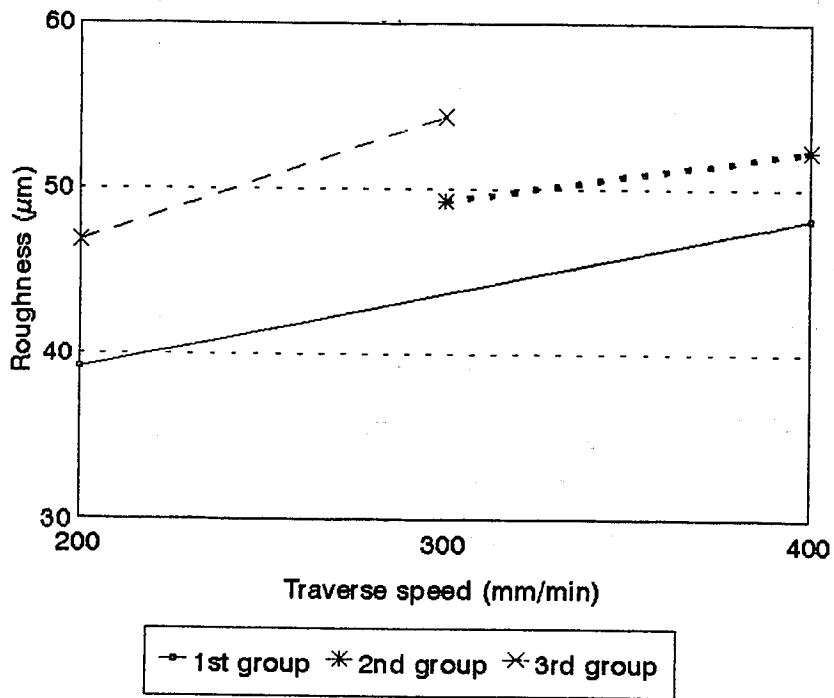


Fig.6 - Ratio between the kerf width at the bottom and the top with traverse speed



**Fig.7 -Variation of roughness of Cristalino de Estremoz at half thickness with:
a) Pressure;**



b) Traverse speed

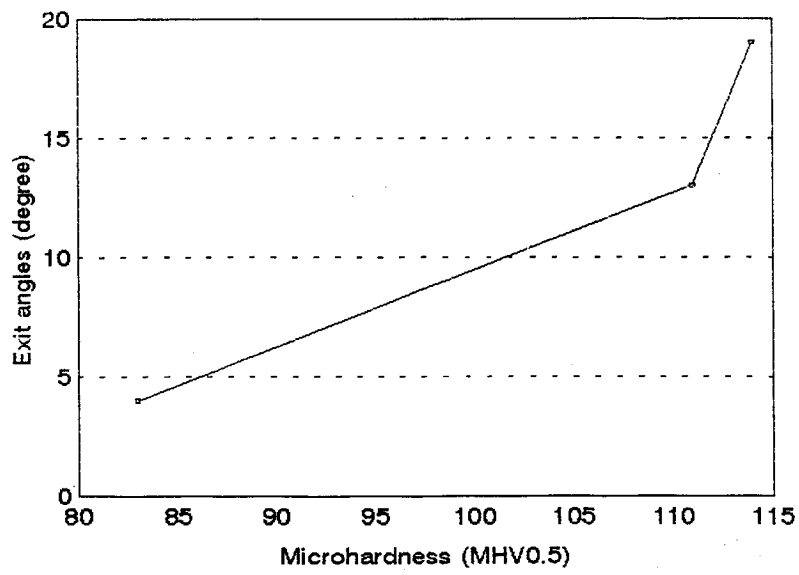


Fig.8 - Variation of angle of striation with stone microhardness

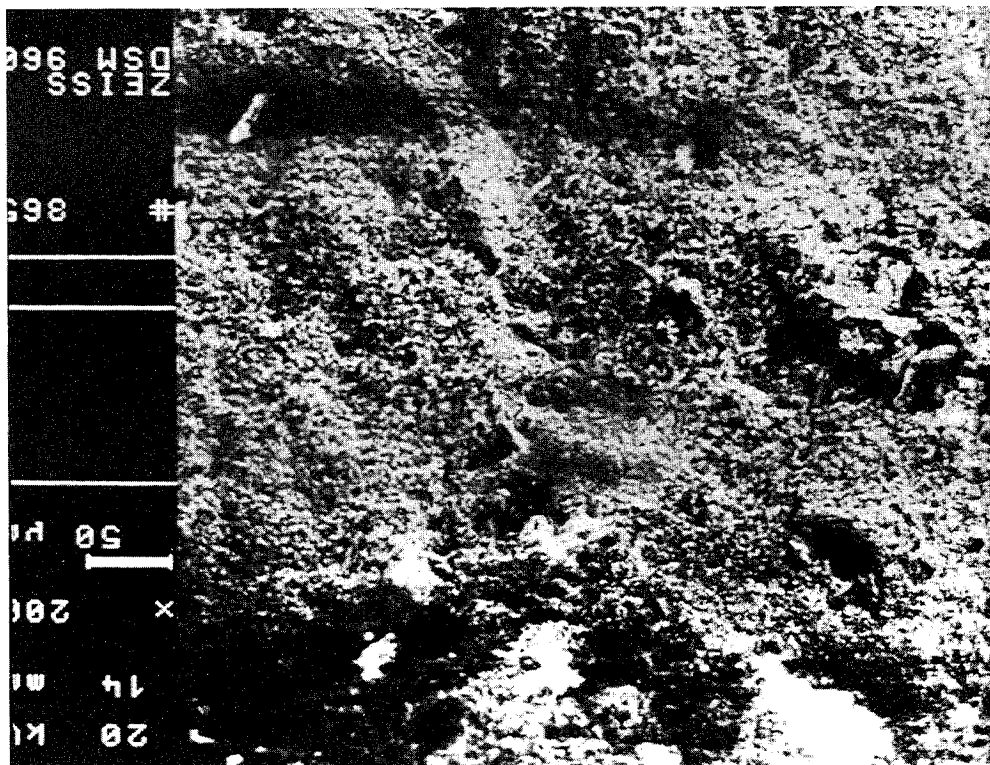


Fig.9 - Cut surface near the top

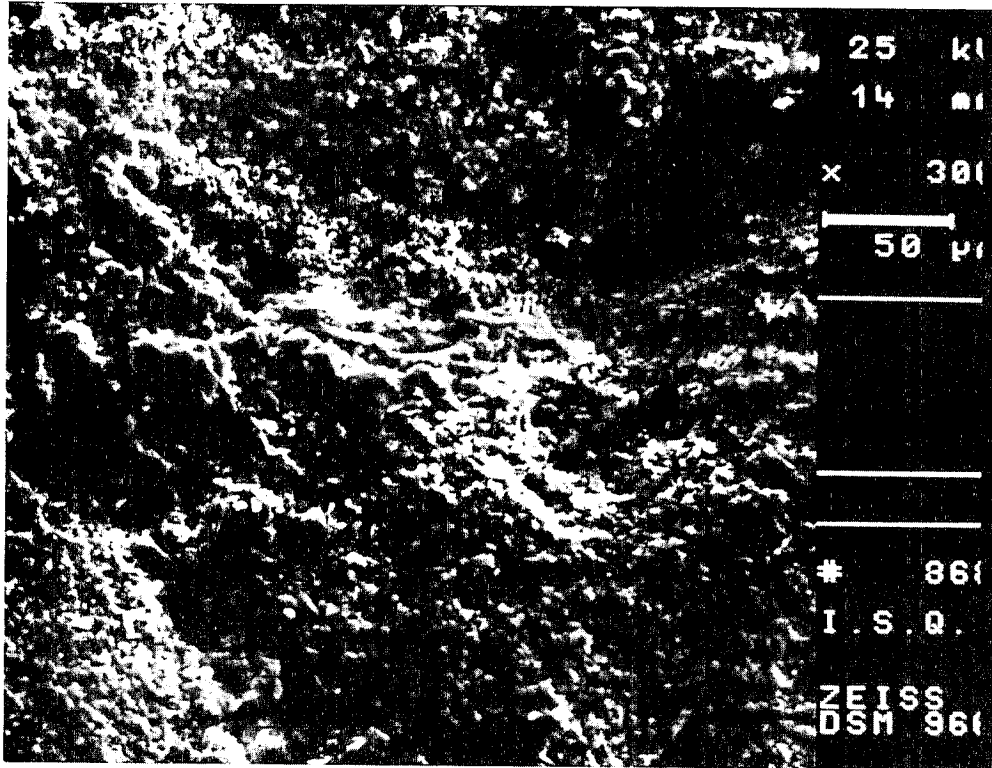


Fig.10 - Aligned craters with water jet flow direction

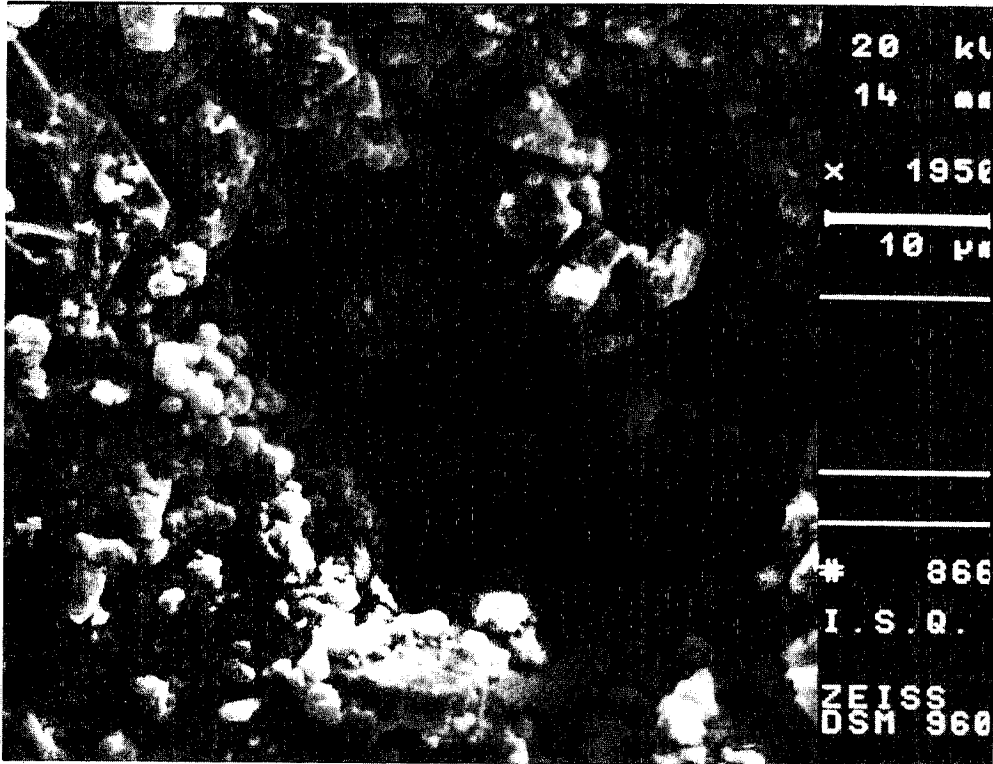


Fig.11 - Detail of a crater with rhomboedric calcitic grains

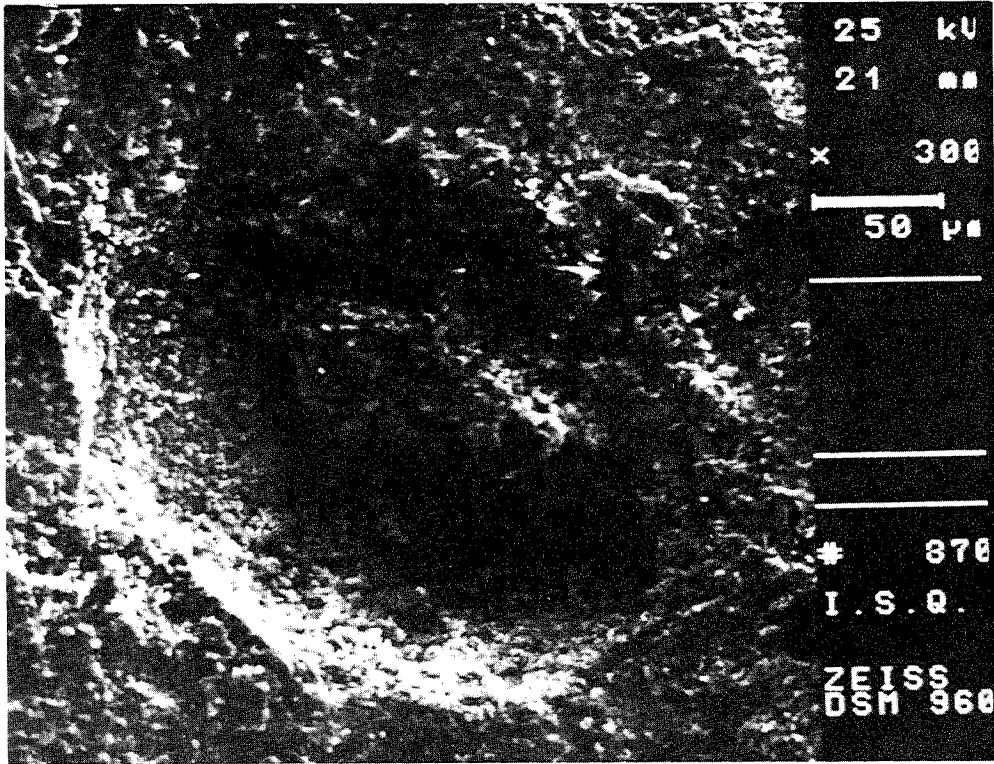


Fig.12 - Crater in the matrix near the bottom surface

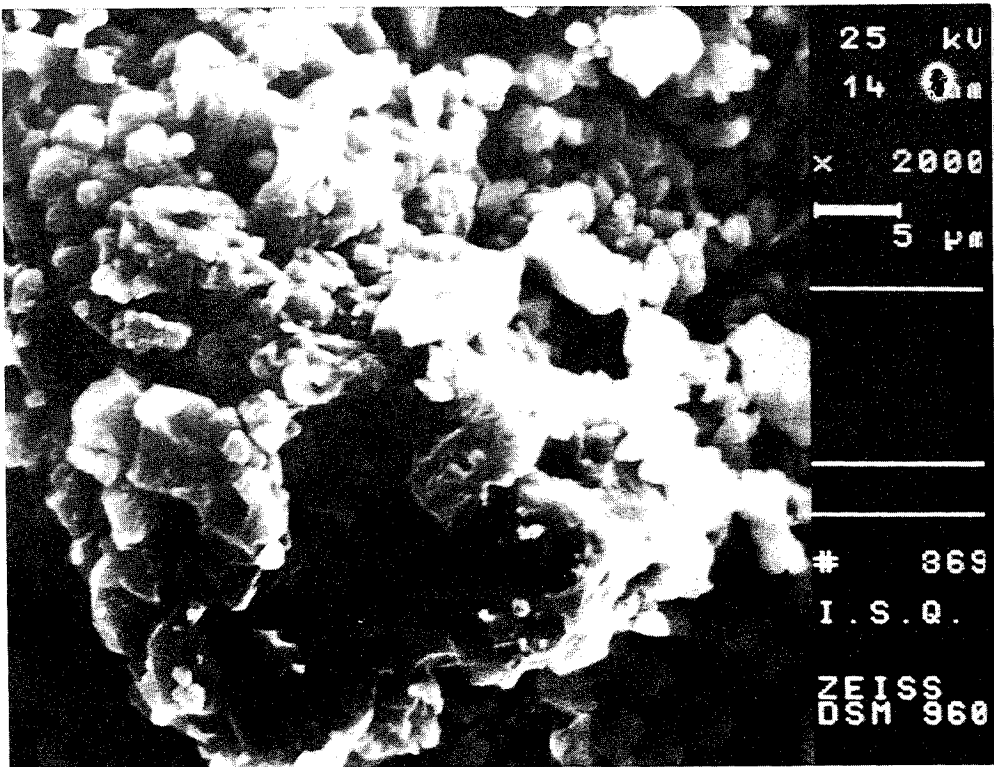


Fig.13 - Detail of porous crater

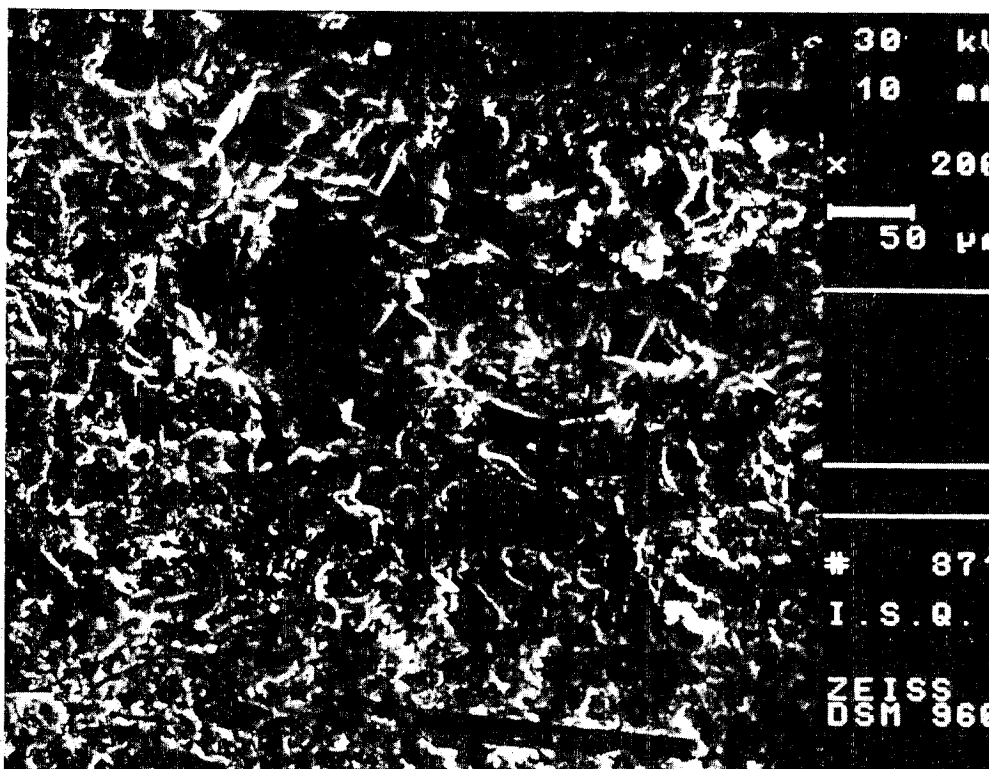
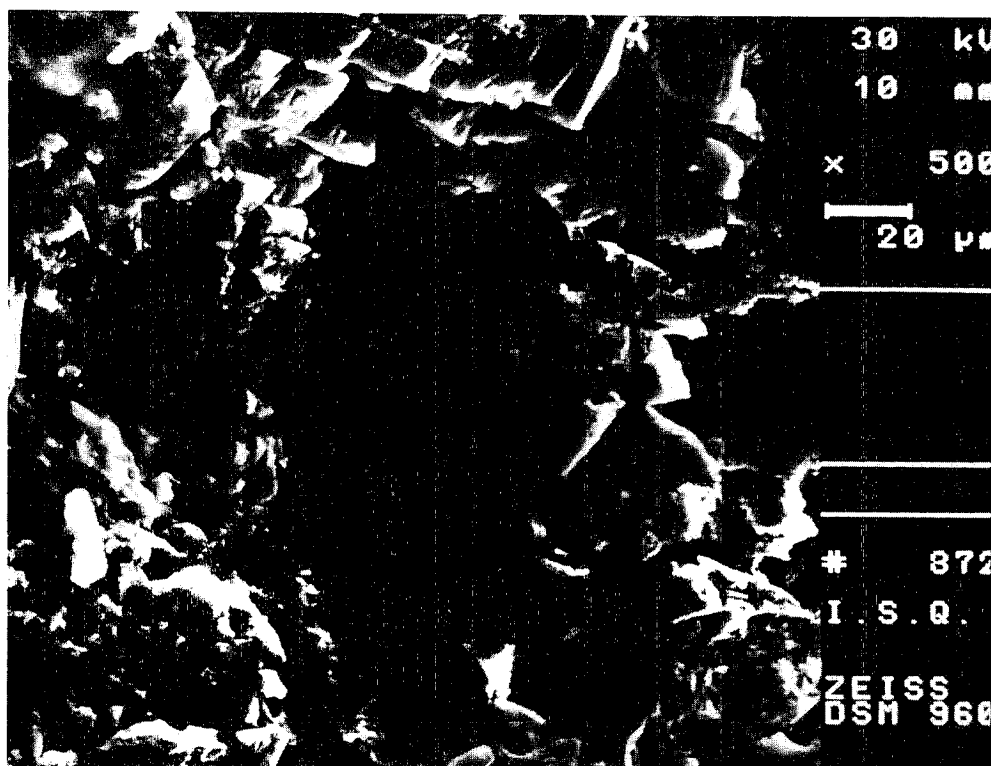


Fig.14 - a)- Cut surface view near the top surface with calcite cleavage and fracture lines along plate thick feldspate;



b) higher magnification of calcite cleavage

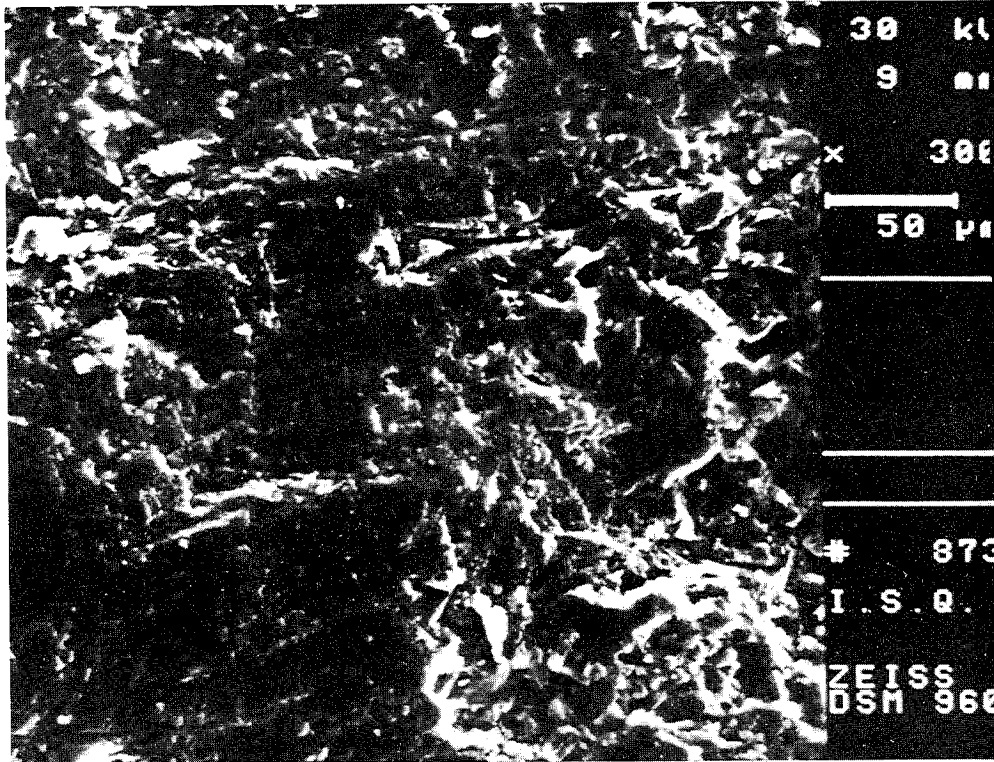
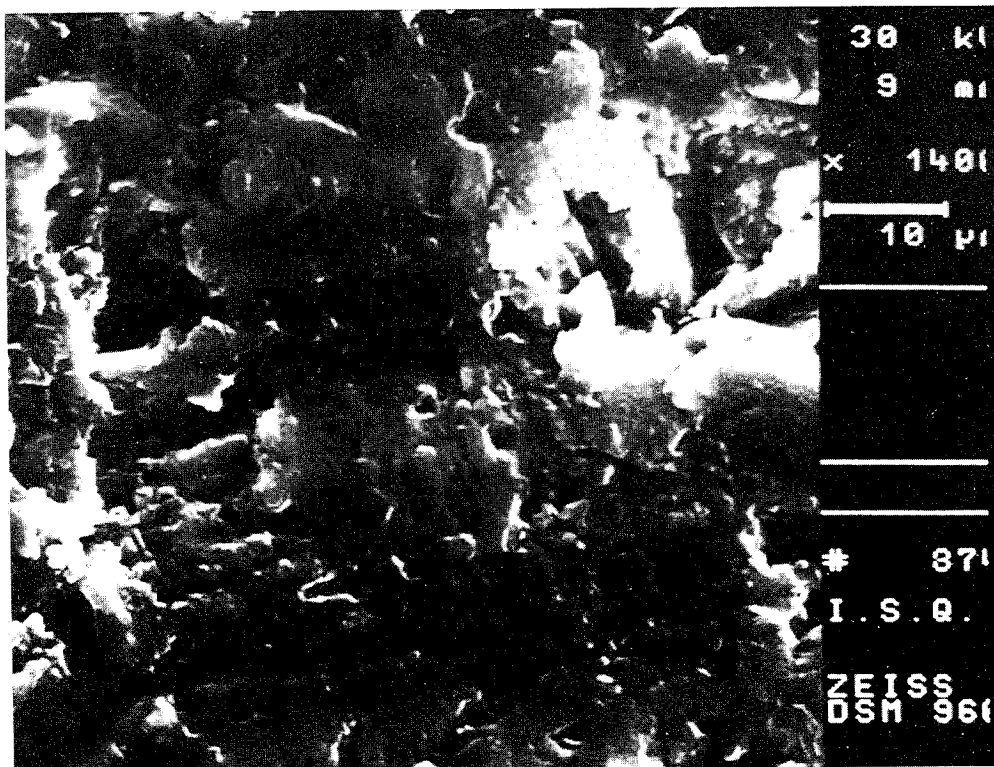


Fig.15 - a) Cut surface at half thickness. Fracture lines along the plate thick feldspates and plastic deformation of the matrix;



b) Detail of the plate thick feldspate with polysynthetic twinning along the fluid flow direction

DEVELOPMENT AND APPLICATIONS OF A HYDRAULIC PULSE GENERATOR

J. J. Kollé
QUEST Integrated Inc.
Kent, Washington U.S.A.

ABSTRACT

A compressed-water hydraulic pulse generator (HPG) has been developed for a variety of applications that require a high-energy pulse of water. Energy is stored in the HPG by compressing water to ultra-high pressure (200 to 400 MPa). A large, fast-opening valve discharges the compressed water resulting in a high-energy impulse. The HPG was originally designed for fragmenting and excavating hard rock. The pressures and loading rates generated by discharge through a nozzle fitted into a borehole are comparable to a gunpowder blast and result in multiple fracturing and fragmentation of hard rock. A prototype HPG with a discharge energy of 42 kJ has been built and used to demonstrate rock fragmentation. A 250-kJ HPG has also been fabricated and is currently undergoing testing for underground mining. Excavation productivity estimates and drilling requirements for this system are provided. Nonexplosive excavation techniques for hard rock provide significant advantages for mechanized mining including continuous mining capability, reduced ventilation requirements, enhanced safety, and reduced vibrations. A 22-kJ HPG has been tested as a means of fragmenting the saltcake that accumulates in nuclear waste storage tanks. The HPG has also been used as a seismic source and to drive a mechanical impact test system. Potential applications include high-energy-rate forming of metals, impact processing of materials, and launch of hyper-velocity projectiles.

1. INTRODUCTION

The hydraulic pulse generator (HPG), shown in Figure 1, was developed as a way of fragmenting and excavating hard rock (Kollé and Fort, 1988). This device uses the energy stored in a water-filled accumulator to generate an ultrahigh-pressure (300 to 400 MPa) water pulse through a large, 10- to 25-mm diameter, discharge valve. The energy of this pulse can be used to fracture rock or other materials, to drive a projectile, or to generate seismic waves. This paper describes the operating principles of the HPG and a variety of applications developed and demonstrated by QUEST Integrated, Inc.

2. WATER COMPRESSION

The HPG systems built to date have all used water as a working fluid. At ultra-high pressures, water is a compressible fluid. Figure 2 shows the compression of water based on data from Bridgman (1911) (remarkably, this appears to be the only data available on water compression at ultra-high pressure). Water compression data may be fit by an equation of the following form:

$$V/V_o = (1 + P/P_c)^c, \quad (1)$$

where V_o is the volume of a vessel filled with water at pressure, P , and V is the decompressed water volume; P_c and c are empirical constants. The best fit to Bridgman's data is given by $P_c = 370$ MPa and $c = 0.1671$.

The energy stored in a water-filled accumulator with volume, V_o , can be found by integrating the work of compression

$$W = \int_{V_o}^V P dV \quad (2)$$

which leads to

$$W = \frac{P_c(V^{1+1/c} - V_o^{1+1/c})}{V_o^{1/c}(1+1/c)} - P_c(V - V_o). \quad (3)$$

The charge energy per unit volume is illustrated in Figure 3. In practice there is an upper limit on the operating pressure of accumulators that is dictated by the materials used in their construction and safety considerations. As the operating pressure increases, the pressure vessel wall thickness must also increase. This means that, for a given external vessel dimension, the internal volume decreases. Figure 4 shows this relationship for the HPG design with safety factors ranging from 1.5 to 3.0; where safety factor is defined as the ratio between operating pressure and the pressure at which yield initiates on the inside surface of the vessel. A safety factor of 2.5 has been used in the design of HPGs that will be used in manned areas, (the actual safety factor is considerably higher since yield on the inner diameter of a thick-walled, ductile steel pressure vessel does not lead to catastrophic failure). Lower safety factors can be used for remote applications where higher energy/weight ratios are desired.

3. HPG OPERATIONS

The HPG discharges through a fast-opening valve contained within the pressure vessel. Initial tests on pulse generation used a rupture disc to release the pressure. A pilot-operated ball valve was then developed and later modified to a poppet design, as shown in Figure 5 (Kollé and Monserud, 1991). During charging,

an orifice maintains a positive pressure differential between the valve inlet and the pressure vessel. This causes the poppet to seat and seal the pressure vessel. For discharge, a two-way servo-valve on the inlet line to the HPG is activated to vent the inlet line. This generates a pressure imbalance that lifts the poppet from its seat, discharging the HPG. Once the poppet starts to lift, the pressure imbalance increases rapidly to a level equal to the total charge pressure; this causes the valve to open completely in a fraction of a millisecond. The servo-operated vent allows complete control over the discharge cycle using an electrical trigger. If the valve fails to open for any reason, the internal pressure will slowly discharge through the inlet orifice and vent valve.

Impulsive energies of up to 250 kJ have been generated by the HPG systems discussed in the following sections. The low compressibility of water means little heat is generated; the compression/discharge cycle is nearly adiabatic and efficiency is almost 100%. Consistent, repeated pulses may be generated at a cycle rate of 1 Hz with conventional ultrahigh-pressure power. The system may also be charged using a low-cost, air-driven pump if rapid cycle time is not a consideration. The discharge valve used on the HPG has only a single moving part and our first prototype has been discharged thousands of times without significant wear.

3.1 Rock Fragmentation and Excavation

Explosive blasting is the most efficient means of excavating hard rock, however, the use of explosives has a number of drawbacks. Explosive excavation is a cyclic process in which blastholes are drilled, the holes are loaded with explosive charges, the area is evacuated, explosives are detonated, the opening is ventilated, and the broken rock is removed. Chemical explosives generate toxic gas by-products that require extensive ventilation during underground tunneling or mining. In the deep level gold mines of South Africa, the drill and blast cycle takes 24 hours, with much of the time devoted to ventilation and personnel transport. Explosives have been banned from some urban areas because of vibration damage induced during the nearly simultaneous detonation of explosive charges required by the drill and blast operation. Explosives also present a safety hazard during storage and use. These considerations have led to an interest in developing nonexplosive, continuous excavation techniques suitable for hard rock (e.g., Haase and Pickering, 1991).

Our first HPG was designed for rock fragmentation and excavation (Kollé and Fort, 1988). In this application, the impulse pressure is directed into a discharge nozzle that is fitted into a borehole drilled in the rock. Figure 6 shows the pressure profile that results during discharge of a 30-kJ/300-MPa impulse into a 25-mm-diameter test chamber. The discharge nozzle for this test had a diameter of 23 mm and a length of 200 mm. The rise time and pulse duration shown here is comparable to that of a propellant charge, such as gunpowder, in a tamped hole.

The useful energy or "blasting strength value" (BSV) of high explosives is about 1500 kJ/kg (Lownds, 1986). A 20-L HPG at a pressure of 300 MPa releases 300 kJ of energy or the equivalent of 0.2 kg of high explosive. Johansson and Persson (1970) give the following relationship to estimate the amount of rock that may be blasted from bench using a given weight, q_b , of high explosive:

$$q_b = 1.45B^3(C_b + 0.07/B) \quad (4)$$

where $C_b = 0.35 \text{ kg/m}^3$ and B is the height and burden of the bench as shown in Figure 7. The equivalent hydraulic pulse energy can be found from $W = q_b BSV$. The volume of rock removed in this simple bench blast geometry is B^3 . Figure 8 shows the burden of rock that can be blasted using pulses generated by the HPG; a 250 kJ system should be capable of blasting a burden of 0.6 m, which amounts to about a metric ton of rock.

Figure 9 shows an HPG mounted on a backhoe along with an indexed rock drill. This system was used to excavate a large opening in Andesite (volcanic rock with a compressive strength of 74 to 263 MPa), as shown in Figure 10. These tests demonstrated the rock fragmentation and excavation capabilities of the HPG. The HPG used had a discharge energy of 42 kJ and a valve diameter of 11 mm. The excavation rate achieved by this system was limited by the relatively low discharge energy and by pressure losses in the

relatively small discharge valve. A 250-kJ system with a 25-mm-diameter discharge valve has now been built (Figure 1) and is undergoing testing for use in a deep level gold mine.

3.2 Nuclear Decontamination and Decommissioning

The HPG also has found a number of applications in the decontamination and decommissioning of nuclear facilities. These applications involve situations in which a mass of contaminated material must be fragmented to allow removal from a facility.

Our first system was designed to fit into the reactor vessel at Three Mile Island. The meltdown at this facility resulted in a mass of ceramic-like material pooled in the bottom of the reactor vessel. An HPG system was designed to enter the reactor and to break up the material. A 125-mm-diameter, 40-kJ system was fabricated and tested in a simulated reactor pool.

A second system has been designed for use in fragmenting and dislodging solid masses of radioactive salts that have formed in liquid waste storage tanks at the Hanford Nuclear Reservation (Monserud and Lilley, 1992). The salts have surprisingly high strength and must be dislodged from the single-shell wall of the tank and internal tubing without damage. The application requires deployment of the HPG from a robotic arm, so the reaction forces must be minimized. Finally, the amount of water discharged into the tank must be minimized since this increases the volume of radioactive material that must be handled.

Figure 11 shows the HPG end effector and recoil mount that was designed for this application. This system is 1-m long and weighs 50 kg. The HPG has a discharge energy of 22 kJ at 345 MPa through an 11-mm discharge valve. The reaction load during discharge was observed to be 1300 N. At 345 MPa the system was quite effective at fragmenting a saltcake simulant.

3.3 Impact Testing and Industrial Applications

A typical 250-kJ HPG discharge requires approximately 100 milliseconds, which corresponds to a power of 2.5 MW. This level of impulsive mechanical power may be applied to a variety of industrial and testing situations. A 42-kJ HPG has been used to power a mechanical impact test system for projectiles prior to launch at a hypervelocity test range at Arnold Engineering Development Test Center, Arnold AFB, Tennessee (Kollé, 1991a). A two-stage light gas gun (G-range) is used to launch 63.5-mm-diameter projectiles at velocities of up to 6 km/s. During the launch, the projectiles are subjected to base pressure spikes of up to 300 MPa. Structural failure of the projectile during launch can cause significant damage to the launcher and range track.

An impact tester, shown in Figure 12, has been built to simulate the duration and magnitude of base pressure spikes that occur during launch. This allows proof testing of projectile designs before launch. The projectiles are loaded into a launch tube simulator that incorporates a water-filled cavity at the projectile base. A 0.3 kg aluminum impactor cylinder is accelerated using the HPG to velocities of up to 200 m/s. The cylinder impacts the water cavity generating a pressure spike with a profile controlled by the elastic properties and dimensions of the impactor. The pressure spike is monitored with a pressure transducer. Figure 13 shows the pressure spikes generated by the test apparatus superimposed on the base-pressure profile generated by a gas dynamics model of a launch at G-range.

The HPG could also be used as a highly efficient pump stage in a two-stage light gas gun for launching hyper-velocity projectiles, as shown in Figure 14. The compressed water would be used to pump a volume of light gas (hydrogen or helium are typically used because of their high acoustic velocities). A pressure-release diaphragm then releases, allowing the gas to drive a projectile to hyper-velocities. Energy storage in compressed water is nearly adiabatic because of its low compressibility, the energy transfer in the gas is also adiabatic because of the speed at which the process occurs. It is thus possible to design a highly efficient launcher that transfers almost all of the energy stored in the water to the projectile. The energy discharged by a 500 kJ HPG is equivalent to the kinetic energy of a 10-g projectile moving at 11 km/s.

3.4 Seismic Source

The HPG may also be used to generate impulsive pressures in boreholes for rock mechanics and seismic studies. A 42-kJ HPG has been used to generate intense pressure pulses in 38-mm boreholes in granite, limestone and concrete in study of nonlinear attenuation of stress waves (Kollé, 1991b). This work is directed towards modeling of the coupling of nuclear explosions to teleseismic radiation. Figure 15 shows the experimental setup; the HPG is discharged into a shallow borehole in rock while the borehole pressure and ground acceleration at a small standoff are observed. Figure 16 shows impulse pressure profiles in the three materials and Figure 17 shows the ground velocity spectrum at a standoff of 0.4 m. These spectra show that the source produces a significant signal at frequencies of over 1 kHz.

The HPG was also discharged directly into the ground to evaluate coupling to a surface seismic signal. In these tests an accelerometer was used to record ground motion at a standoff of 10 m. Figure 18 shows the seismic signal resulting from three 300 MPa discharges into alluvium. The primary signal is a surface wave followed by reflections at a time lag of 300 and 400 ms.

The HPG provides a compact source of mechanical energy that may be used in a borehole for crosswell seismic work. An HPG borehole source concept is illustrated in Figure 19, this source could be configured to generate compressional and shear wave energy. Existing electromechanical borehole seismic sources are limited in energy output while explosive sources are poorly characterized. The HPG source offers high energy at frequencies of up to 1 kHz. The source magnitude and spectrum may be characterized with a pressure transducer. A well-characterized source may be used to log formation attenuation properties, which are an important indicator of the presence and mobility of formation fluids. In addition, a variable amplitude source can also be used to characterize the inelastic mechanical properties of the formation. In this application, the attenuation of the signal is monitored as the source amplitude increases. The onset of nonlinear attenuation can provide an indication of the elastic limit of the formation.

4. CONCLUSIONS

The development of a hydraulic pulse generator using compressed water has led to a number of applications requiring a source of impulsive mechanical power. The HPG has been demonstrated as an effective means of fragmenting rock and other hard materials including ceramics and saltcake. The pulse generation technique is compact, efficient, safe, and reliable. Applications currently under development include nonexplosive mining in deep-level gold mines, nonexplosive tunneling in urban areas, material removal in contaminated nuclear waste tanks, nonexplosive demolition of contaminated material, generation of compression and shear wave energy in boreholes, in situ rock mechanics testing, impact testing, materials processing, and hypervelocity projectile launch.

5. REFERENCES

- Bridgman, P. W., "Water, in the Liquid and Five Solid Forms, Under Pressure," in *Proc. Am. Acad. Arts Sci.*, Vol. 47, pp. 441-558, 1911.
- Haase, H. H., and Pickering, R. G. B., "Non-Explosive Mining: An Untapped Potential for the South African Gold-Mining Industry," *J. South African Inst. Min. Metal.*, Vol. 91, pp. 381-388, 1991.
- Johansson, C. H., and Persson, P. A., *Detonics of High Explosives*, Academic Press, London and New York, 1970.
- Kollé, J. J., "Impact Tester for Hypervelocity Projectiles," prepared for Arnold Engineering Development Center, Arnold AFB, Tennessee, under Contract No. F40600-91-C-0009, QUEST Technical Report No. 549, 1991a.

- Kollé, J. J., "Observations of Transition Level Stress Wave Attenuation Using a Hydraulic Impulse Source," prepared for Defense Advanced Projects Agency under Contract No. DAAH01-90-C-0698, QUEST Technical Report No. 517, 1991b.
- Kollé, J. J., and Fort, J. A., "Application of Dynamic Rock Fracture Mechanics to Non-Explosive Excavation," *Key Questions in Rock Mechanics: Proceedings of the 29th U.S. Symposium*, P. A. Cundall et al. (eds.), A. A. Balkema, Rotterdam, pp. 571-578, 1988.
- Kollé, J. J., and Monserud, D. O., "Apparatus for Rapidly Generating Pressure Pulses for Demolition of Rock Having Reduced Pressure Head Loss and Component Wear," U.S. Patent No. 5,000,516, 1991.
- Lownds, C. M., "The Strength of Explosives," *The Planning and Operation of Open-Pit and Strip Mines*, J. P. Deetlets (ed.), SAIMM, Johannesburg, South Africa, pp. 151-159, 1986.
- Monserud, D. O., and Lilley, R. C., "Hydraulic End Effector Inspection and Test Results," prepared for Lawrence Livermore National Laboratories under Contract No. B199069, QUEST Technical Communication No. 355, 1992.

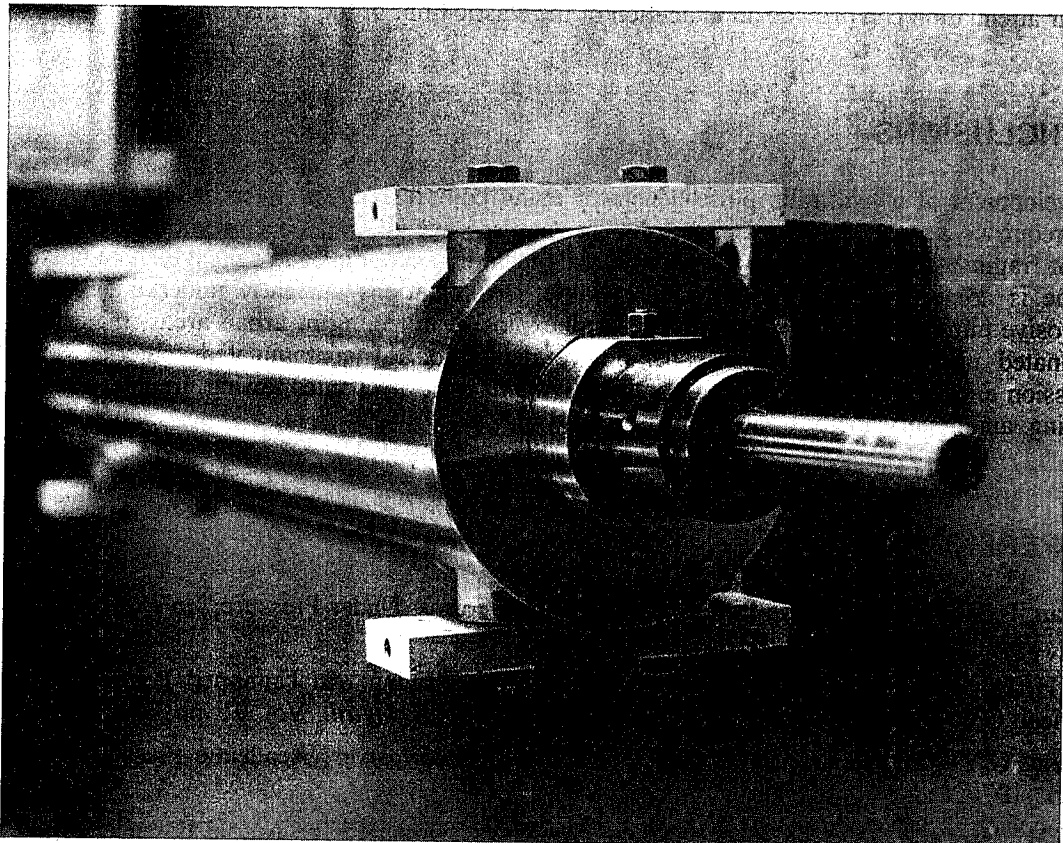


Figure 1. HYDREX Pulse Generator

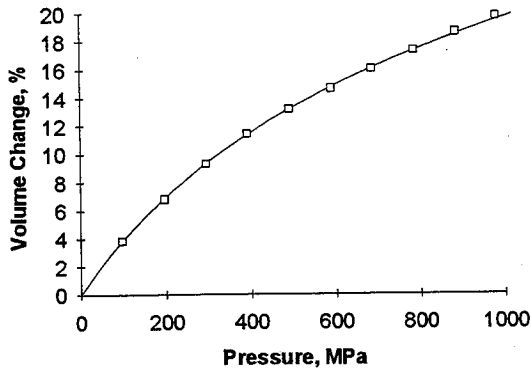


Figure 2. Compressibility of Water.
Data points from Bridgman (1911).
Curve fit equation given in text.

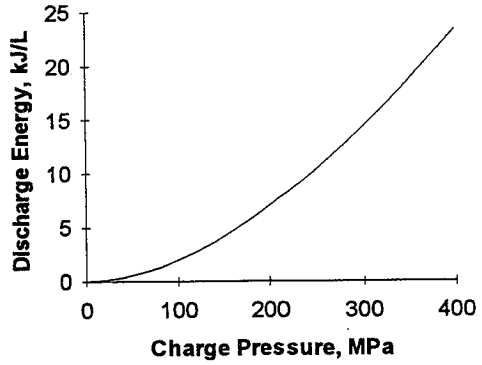


Figure 3. Stored Energy per Liter HPG Volume

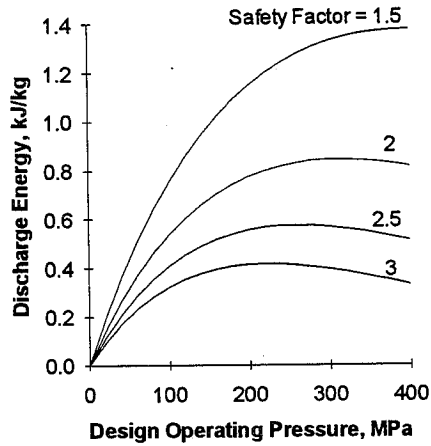


Figure 4. Specific Discharge Energy per Unit HPG Weight

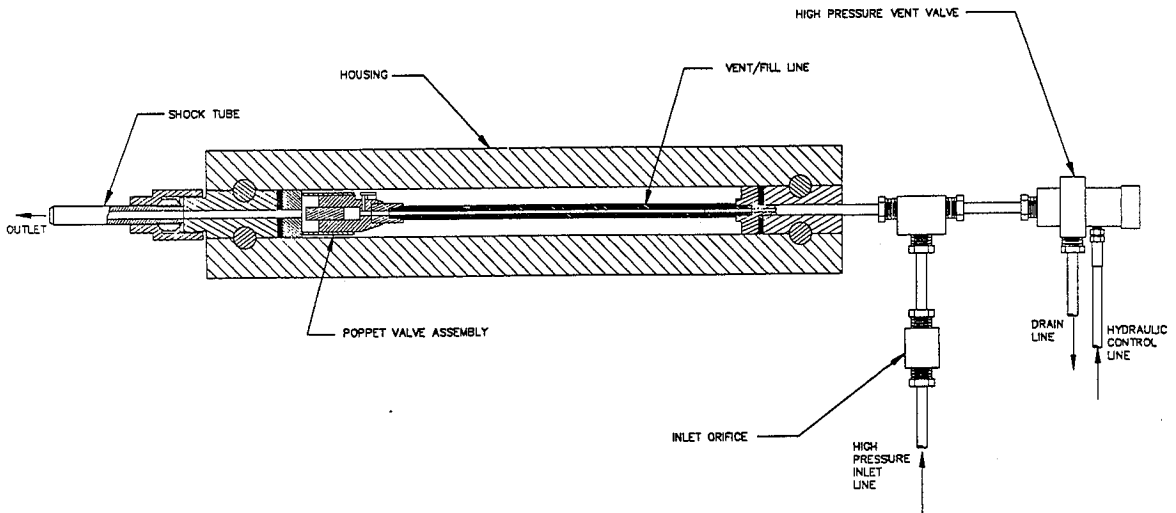


Figure 5. HPG System Configuration

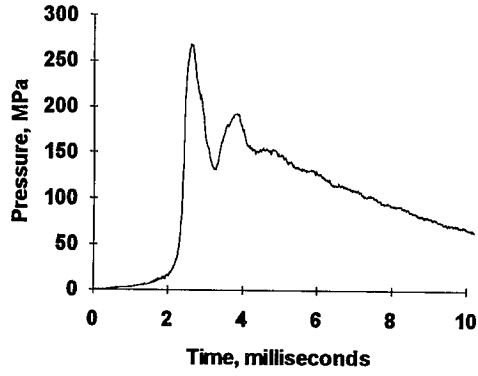


Figure 6. 30-kJ/300-MPa HPG Discharge into 25-mm Chamber with 1-mm Annular Vent

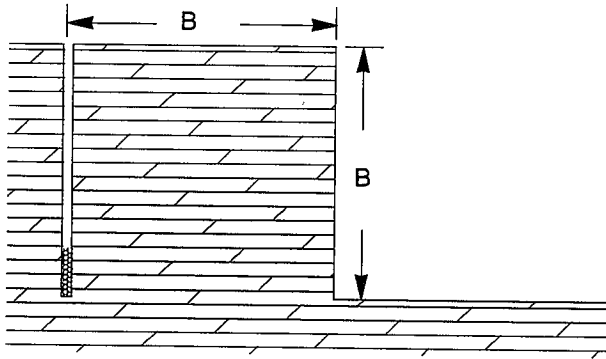


Figure 7. Bench Blast Configuration

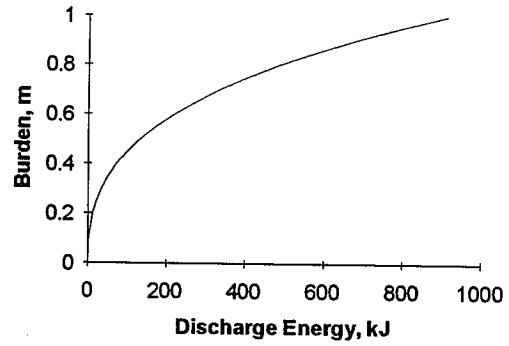


Figure 8. Benching Burden Estimate

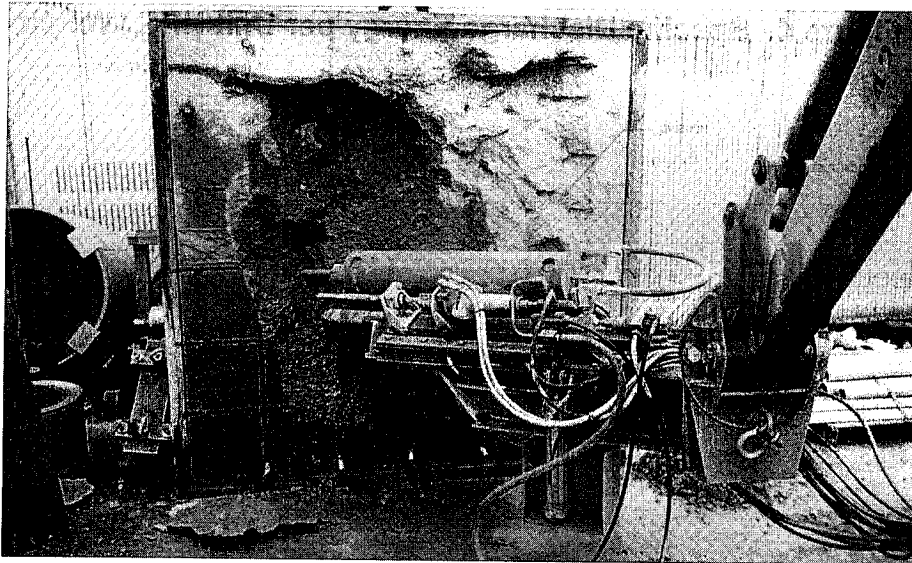


Figure 9. HYDREX Mounted on a Backhoe with Drilling and Indexing Mechanism

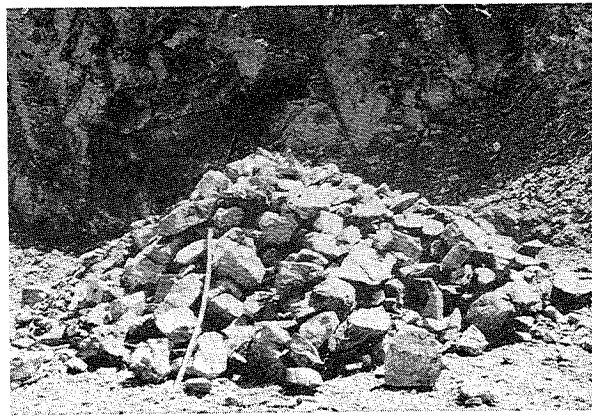
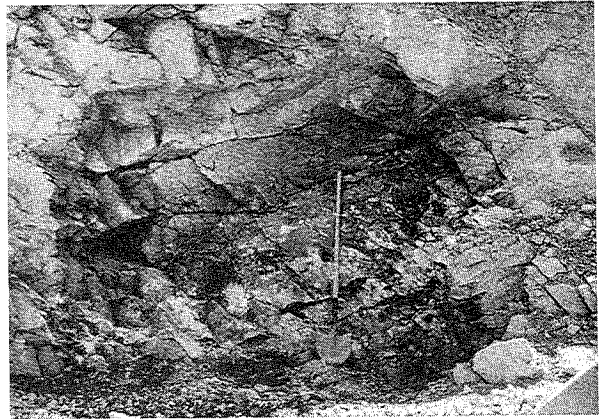
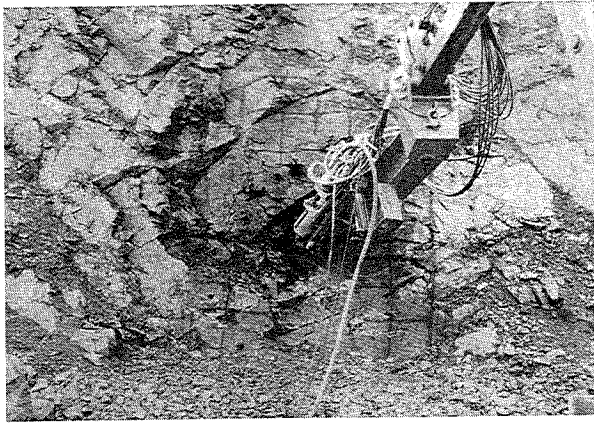


Figure 10. Test Excavation in Andesite

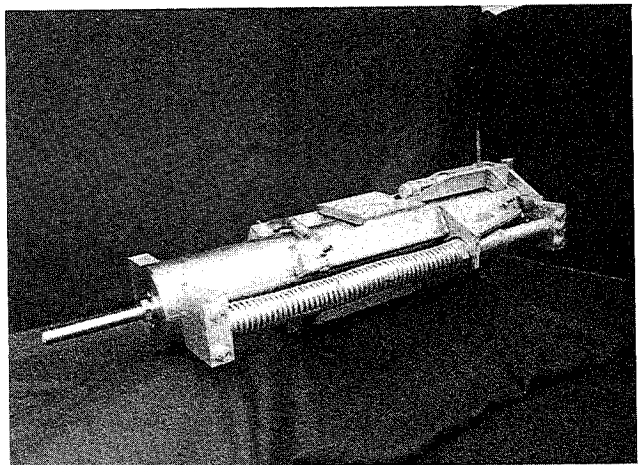
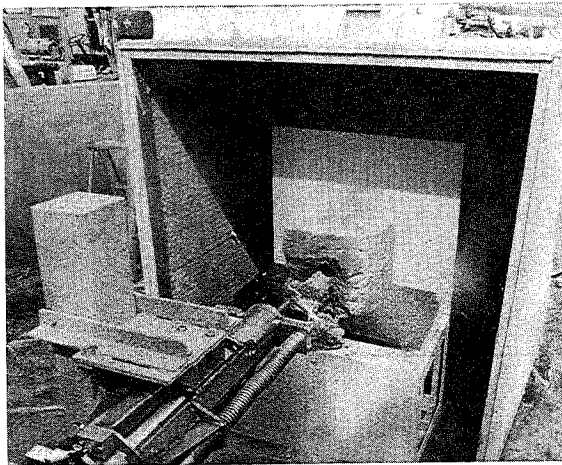


Figure 11. HPG End Effector with Recoil Mount for Saltcake Fragmentation

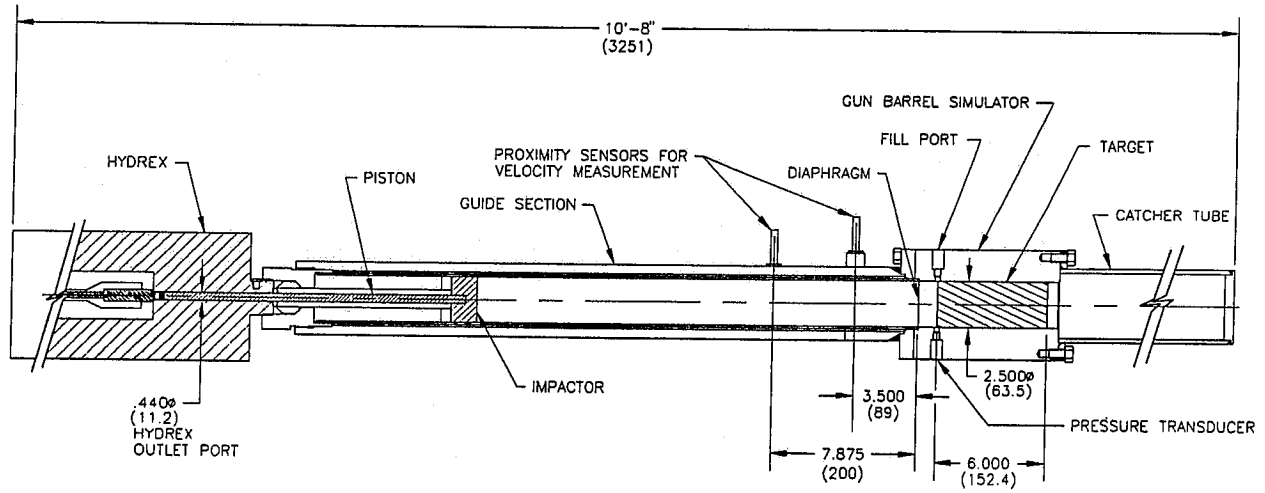


Figure 12. Impact Test Setup

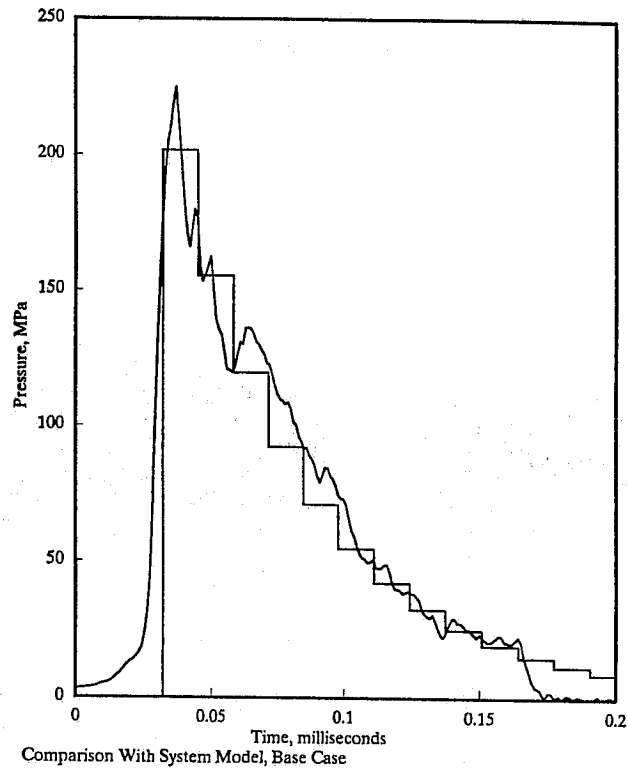


Figure 13. Impact Pulse Profile with Modeled Pulse Profile

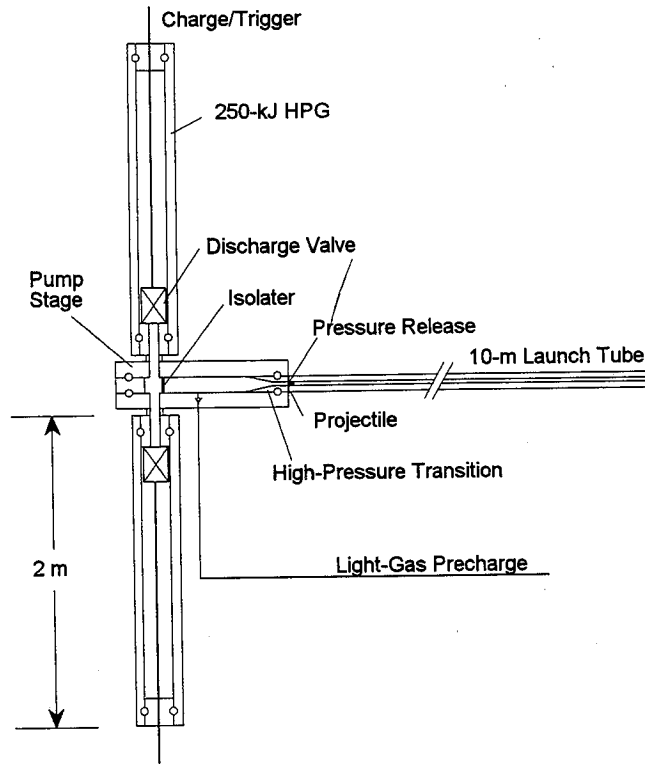


Figure 14. Hydraulic Two-Stage Light-Gas Gun

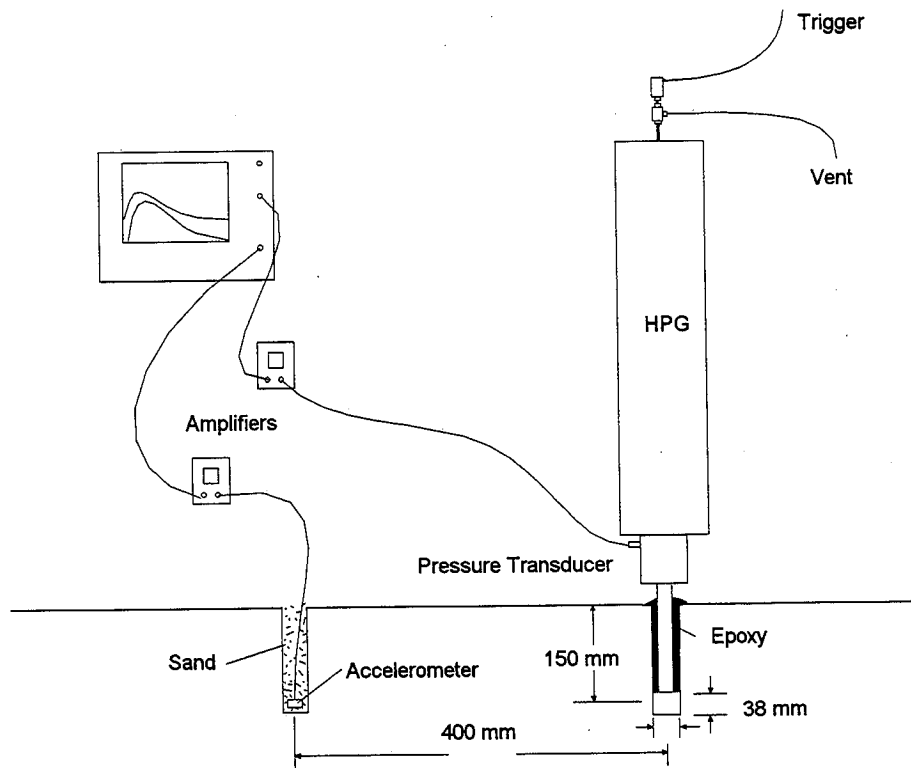


Figure 15. Seismic Coupling Test

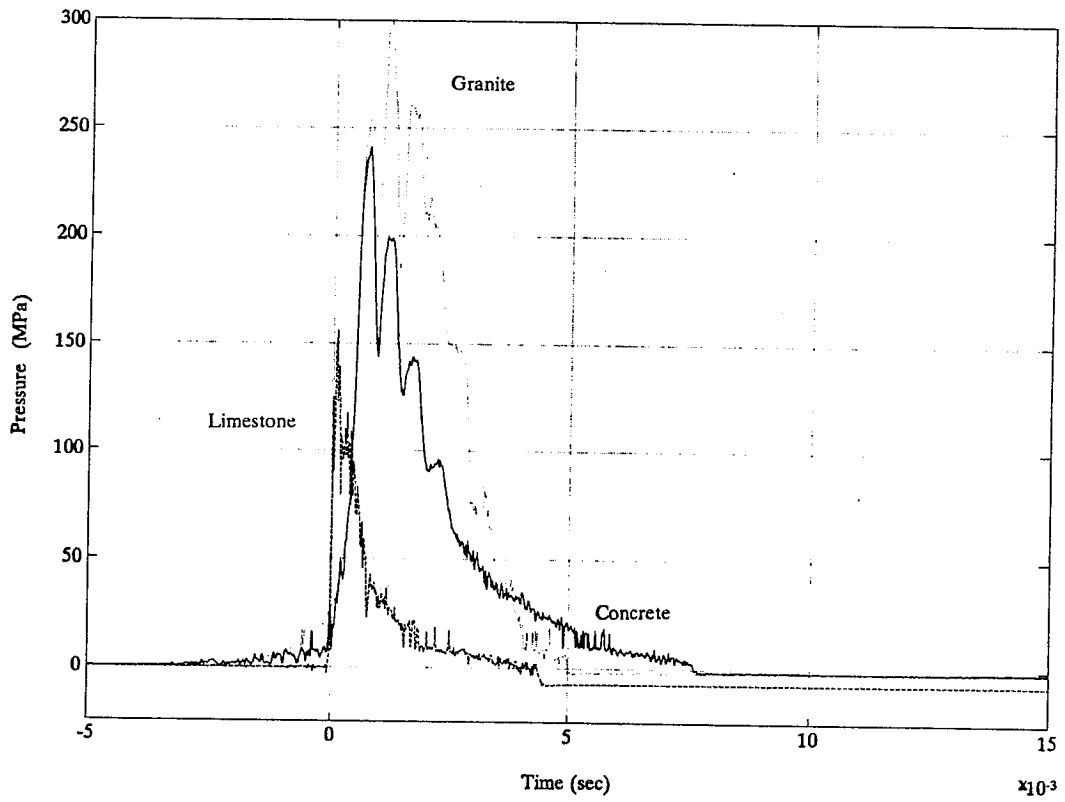


Figure 16. Impulse Pressures in Concrete, Limestone, and Granite

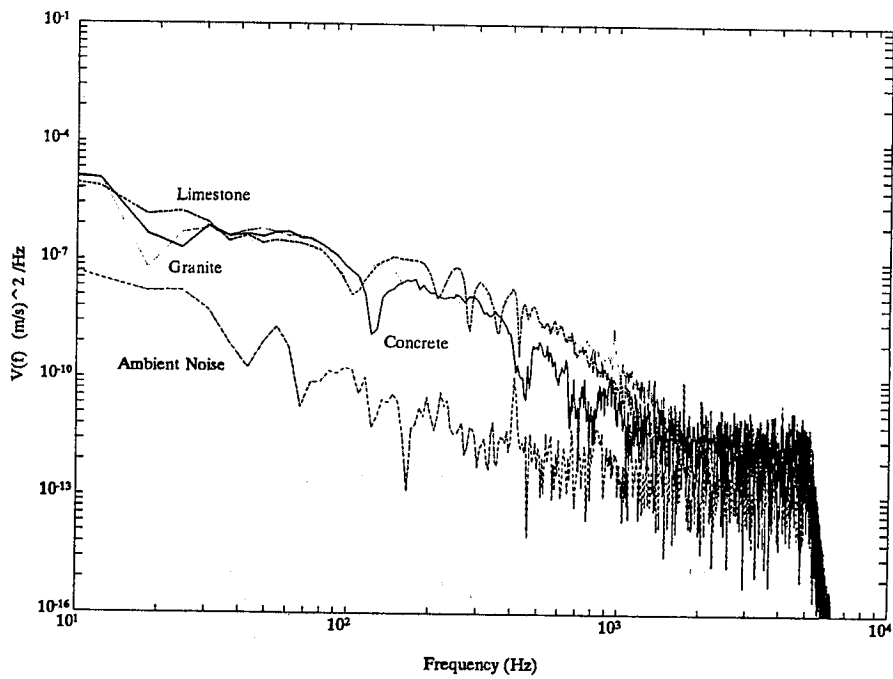


Figure 17. Ground Velocity Spectra

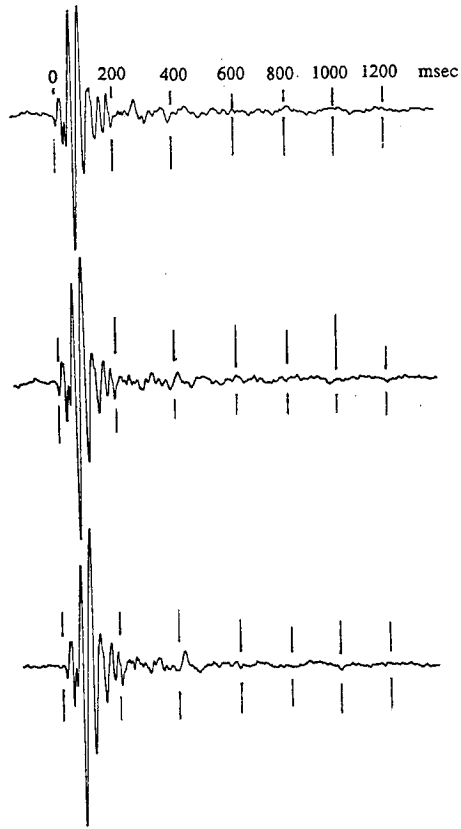


Figure 18. Surface Wave from Discharge in Alluvium, Demonstrating Source Repeatability

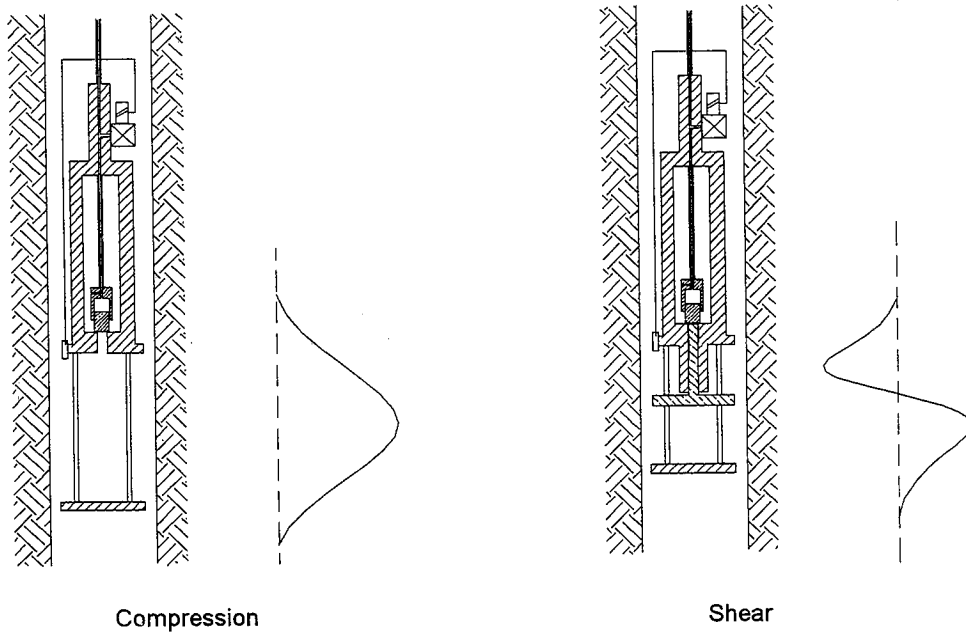


Figure 19. Hydraulic Borehole Source Configurations

Index of Authors

Agus, M.	427	Hai, Z.	287
Alba, H.H.	759	Hake, J.C.	829
Alkire, T.D.	351	Hanrahan, M.D.	389
Amundsen, B.	853	Harbaugh, D.J.	599
Arola, D.	43	Hashish, M.	205, 793, 829
Atherton, A.	801	Hlavac, L.	375
Ayers, G.	853	Hofacker, S.A.	613
Bamberger, J.A.	737	Horii, K.	747
Bocchi, M.	863	Hu, F.	337
Bondurant, P.D.	829	Hu, S.G.	233
Bortolussi, A.	427	Isobe, T.	747
Bothell, D.	793	Jia, B.	629
Bouix, M.	103	Jingming, M.	929
Burnham, C.	697	Johnson, S.T.	607
Butler, T.J.	523	Jun, H.	643
Capello, E.	157	Jura, W.	473
Carletti, F.M.	813	Kalukiewicz, A.	263
Carlson, G.	71	Kalumuck, K.M.	251
Chahine, G.L.	251	Kang, S-W.	71
Chalmers, E.J.	327	Kelley, D.P.	523
Chao, J.	27	Khan, A.K.	801
Cheng, D.	287, 515	Khan, M.E.H.	273
Chuan-lin, T.	537	Kim, T.J.	175, 443
Ciccu, R.	427	Kim, W.M.	427
Coleman, W.J.	829	Kiyohashi, H.	87
Craigen, S.J.	829	Klich, A.	473, 501
Crofton, P.S.J.	307	Kobayashi, R.	747
Crutchmer, J.	71	Kollé, J.	459
Da-jun, S.	653	Kotwica, K.	501
Da-zhong, C.	295	Kovacevic, R.	217
Do, B.	71	Kramer, P.	71
Duan, X.	515	Kyo, M.	87
Fanhua, L.	915	Lai, M.K.Y.	233
Fincher, H.	599	Laurinat, A.	119
Foldyna, J.	375	Lees, W.A.	307
Frederick, G.S.	251	Leyao, Z.	907, 915
Garrett, D.	71	Li, N.	629
Geskin, E.	27, 273	Lindeke, R.R.	801
Gracey, M.T.	689	Liu, B.	629
Groppetti, R.	157, 863	Liu, L.	287
Guo, C.	287	Louis, H.	1, 119
Guo, N.S.	1	Lousa, P.	443
Haber, Dr. Ing.	759	Mainbourg, B.	729

Manca, P.P.	427	Wang, C.	629
Martinec, P.	375	Wang, L.	217
Mazurkiewicz, M.	473, 501	Wangping, H.	653
McArthur, A.	701	Watson, J.D.	583
Meier, G.	1	Whalen, J.M.	883
Meier-Wiechert, G.	119	White, G.B.	829
Merle, C.	103	Wilhelm, Dipl.-Ing.	759
Miller, A.L.	485	Woodward, M.J.	397
Miller, D.S.	899	Woolman, R.F.	877
Ming-qing, Y.	295	Wright, D.E.	549
Miranda, A.J.	443	Yahiro, T.	747
Miranda, R.M.	443	Yanari, A.	813
Momber, A.W.	561	Yang, J.	907, 915
Monserud, D.O.	829	Yao, H.	629
Munoz, J.	191	Yasui, R.	813
Ogasawara, M.	87	Yeh, H.	65
Ohman, J.L.	363	Yoshida, H.	747
Öjmertz, K.M.C.	777	Yu, L.	515
Pontvianne, P.	729	Zacharias, F.	307
Qizhuang, Z.	907, 915	Zeng, J.	175
Raju, S.P.	141	Zhen-Fang, L.	537
Rankin, M.	663	Zhang, D.	629
Ramulu, M.	43, 65, 141	Zhang, Y.M.	217
Reitter, T.	71	Zi-Pu, C.	295
Remisz, J.	405, 573		
Remisz, W.	573		
Robertson, J.	337		
Romano, R.	863		
Savanick, G.A.	485		
Scharwat, F.E.	685		
Schibley, J.R.	843		
Schoenig Jr., F.C.	801		
Sepe, R.	697		
Sheng, Z.	653		
Shengxiong, X.	653		
Singh, P.J.	191		
Sionneau, M.	103		
Steele, D.E.	737		
Summers, D.A.	549		
Takei, M.	747		
Thode, J.	759		
Vasek, J.	375		
Vasseur, J.	103		
Veehuizen, S.D.	523		
Vijay, M.M.	233, 405		
Wang, F.X.	65		

SUBJECT INDEX

- accuracy 877
acoustic 217
adaptive 157, 863
aerospace 43
air 747
aircraft 599, 607, 613, 883
airfoil 883
algorithm 863
alignment 829
alluvial 363
almanide 375
aluminum oxide 777
aluminum 1, 43, 71, 157, 397,
777
ambient 251
ammunition 759
amplitude 27, 217
asphalt 561
assist 405, 501, 515, 523, 801
attenuator 327
automatic 829
automotive 607
Barton 375
basalt 549
bentonite 747
blast media 397
boiler 729
boiling 87
bore hole 473, 485
bread 103
bricks 363
brittle 43
CAD/CAM 157
candy 103
capital 175
carrier wave 65
cartridge 829
catcher 375
cavitation 233, 251, 273, 405
chemicals 697
chip 801
choking 295
clay 747
CNC 583, 843, 863
coal 473
coating 583, 599, 607
composite 883
compressibility 459
concrete 263, 573
constraint 863
contamination 389
control rod 729
control 157, 863, 899
corrosion 307
cost 175, 191, 843, 863, 877
crack 307
cutting wear 43
decontamination 701
deformable 71
deformation wear 43
dejunking 813
demilitarization 899
demolition 573
de-scaling 643
DIAJET 287, 295, 549, 899
diamond 793
diffusivity 87
disk cutter 501
displacement 27
disposal 697, 701
dissipation 119
dissolved 389
dolomite 549
dovetail 883
drag 141
drill 549
drilling 205, 523, 537, 883
droplets 71
ductile 43
dust 697
dynamics 27
effluent 689
electrochemical 307
empirical 141, 157
end-effector 27, 613, 843
environment 685, 689, 697,
701
EPA 689
erosion 43, 175
excavation 459
explosives 759
factorial 777
fatigue 307
feed 295
fettling 899
filtration 389
fines 363
fish 103
flushing 759
food 103
fouling 915
foundry 899
Fourier 1
fracture 43, 71, 405
frequency 27, 217
fringe 65
frozen 485
fumes 697
garnet 363, 375
gas well 523
glass 157, 191, 777
gold 485
grain 375, 427
granite 375
graphite/epoxy 43
groove 1
Hanford 737
hardness 443
hazard 701
health 663, 685
heat-exchanger 915
hole 883
holography 65
hydrostatic 307
hygienic 103
hyperbaric 251
impact 71, 87, 459, 537
impulse 459
inconel 729
injection 287
injection 643
insert 801
instability 295
integration 843, 853
intensifier 191, 327, 337
ion exchange 389
isopachic 65
isotopes 701
JAM 801
jet engines 583
junk 813
kerf 119
labor 191
laminates 43
laser 65
lathe 205
Laval 747
law 663
leadframe 813
leakage 737

SUBJECT INDEX (Continued)

- machinability 175
- machining 829, 863, 877, 899
- manipulator 613, 843, 877, 899
- marble 443
- market 899
- milling 119, 205, 777
- mineral 427
- missiles 759
- mixing 251
- momentum 141
- motor 27
- nitrogen 87
- noise 697
- nozzle 217, 251, 273, 549, 599, 829, 907
- nuclear 729
- numerical 71
- oil well 523, 537
- optical 65
- optimization 191, 863
- oscillating 537, 929
- paint 607, 613, 685
- particle 363
- PCD 793
- penetration 65, 141
- permafrost 485
- petrochemical 907
- photo elasticity 65
- pick 515
- piercing 141
- plumbing 853
- plutonic 427
- poisson's ratio 175
- polishing 793
- pollution 389
- polycarbonate 65, 141
- polymer 157
- porosity 427, 443
- porous 87
- precision 883
- pulse 405, 459, 537
- pump 327, 337, 351
- quick-connect 829
- radioactive 701
- radioactive 737
- radioactive 747
- radon 701
- rake 801
- recovery 629
- recycle 629, 689, 697
- rebuilding 561
- regulations 663
- remote 759
- resin 813
- risk 685
- robotic 613, 843
- rock 405, 427, 459, 523
- roughness 1
- rust 629, 643
- safe 759
- safety 663, 697
- sand 549
- sandstone 375
- saturated 87
- scarifier 573, 737
- shock 87
- SEM 777
- semiconductor 813
- sensor 829
- size, particle 363
- slat cake 737
- slotting 205, 929
- sludge 701
- slurry 287, 295, 629, 643
- solubility 389
- soluble 397
- sound velocity 427
- spacing 501
- spectra 27, 217
- spikes 327, 337
- spiral 747
- spray 583
- spreading 251
- standards 389
- standards 663
- statistical 157
- stator 883
- steel shot 549
- steel 119, 375, 777
- steps 1
- sterile 103
- storage 747
- stress 65
- striation 1, 27
- stripping 583, 599, 613, 685
- submerged 233, 251, 263, 537
- superposition 119
- suspension 793
- swinging 929
- swivel 853
- system 853
- tank 737
- TBC 583, 607, 883
- temperature 87
- thermal 87
- thermocouple 87
- titanium 1, 27, 191, 801
- tolerance 877
- tool changer 829
- tool 801
- topography 1
- traffic 561
- transient 141
- traverse 27
- treatment 389
- triplex 351
- tube 729
- turbulence 273
- turning 205
- valve 459
- variable displacement 327
- vessel 307
- vibration 27
- visualization 1, 65
- volcanic 427
- waste 389, 737, 747
- water 389
- water-hammer 71
- waviness 1
- waviness 205
- weakening 405
- wear 217
- weber 87
- well 523
- width 119
- wrist 843
- yield stress 71
- zircon 777